ELECTRON TRANSFER IN METAL-ORGANIC FRAMEWORKS: CONDUCTIVITY, CATALYSIS, AND GAS ADSORPTION FROM THE PERSPECTIVE OF DENSITY FUNCTIONAL THEORY

by

JENNA L. MANCUSO

A DISSERTATION

Presented to the Department of Chemistry and Biochemistry
and the Division of Graduate Studies of the University of Oregon
in partial fulfillment of the requirements
for the degree of
Doctor of Philosophy

September 2021

DISSERTATION APPROVAL PAGE

Student: Jenna L. Mancuso

Title: Electron Transfer in Metal-Organic Frameworks: Conductivity, Catalysis, and Gas Adsorption from the Perspective of Density Functional Theory

This dissertation has been accepted and approved in partial fulfillment of the requirements for the Doctor of Philosophy degree in the Department of Chemistry and Biochemistry by:

Carl K. Brozek	Chairperson
Christopher H. Hendon	Advisor
Michael M. Haley	Core Member
Ellen E. Eischen	Institutional Representative

and

Andrew Karduna	Interim Vice Provost for Graduate Studies

Original approval signatures are on file with the University of Oregon Division of Graduate Studies.

Degree awarded September 2021

DISSERTATION ABSTRACT

Jenna L. Mancuso

Doctor of Philosophy

Department of Chemistry and Biochemistry

September 2021

Title: Electron Transfer in Metal-Organic Frameworks: Conductivity, Catalysis, and Gas Adsorption from the Perspective of Density Functional Theory

Metal-organic frameworks (MOFs) have a rich chemistry characterized by a diverse assortment of organic and inorganic components supplemented by post-synthetic modification procedures. The application of a given framework can be dependent on the linker or node chemistry, the pore space, or the combined properties of each. Using experimental data as a starting point or for benchmarking purposes, density functional theory (DFT) calculations are invoked to understand the physical and electronic origins of functional MOF behaviors such as electronic conductivity, catalytic activity, and gas uptake. The size and geometry of inorganic nodes are found to be the dominant factor in determining to what extent charge is localized within individual linkers or nodes, as does the distance between them and their orientation. Large aromatic linkers that are stacked due to the layering of 2D sheets or their connectivity to 1D nodal chains can produce conductive pathways. Ion exchange is also explored both in terms of post-synthetic metal-cation metathesis to acquire thermally and photocatalytically active sites and inorganic anion exchange to tune gas sorption behaviors. This thesis provides insight into the intuitive construction of MOFs with purposeful electronic structure design for targeted applications.

CURRICULUM VITAE

NAME OF AUTHOR: Jenna L. Mancuso

GRADUATE AND UNDERGRADUATE SCHOOLS ATTENDED:

University of Oregon, Eugene
University of Queensland, Melbourne
Case Western Reserve University, Cleveland

DEGREES AWARDED:

Doctor of Philosophy, Computational Chemistry, 2021, University of Oregon
Master of Science, Chemistry, 2018, University of Oregon
Bachelor of Science, Polymer Science & Engineering, 2017, Case Western Reserve University

AREAS OF SPECIAL INTEREST:

Computational Chemistry
Coordination Chemistry
Materials Science
Photochemistry
Catalysis

PROFESSIONAL EXPERIENCE:

Teaching assistant, Case Western Reserve University Chemistry of Materials, 2014-2017

Teaching assistant, University of Oregon Organic Chemistry Laboratory 2014-2017

Intern, General Electric Lighting Division, Summer 2015

GRANTS, AWARDS, AND HONORS:

Dean's First Year Merit Award, University of Oregon, 2017

Graduate Student Award for Excellence in the Teaching of Chemistry, University of Oregon, 2018

PUBLICATIONS:

A. M. Wright, Z. Wu, G. Zhang, J. L. Mancuso, R. J. Comito, R. W. Day, C.H. Hendon, J. T. Miller, M. Dincă, "A structural mimic of carbonic anhydrase in a metal-organic framework", *Chem* 2018, *4*, 2894-2901.

A. J. Rieth, A. M. Wright, G. Skorupskii, J. L. Mancuso, C. H. Hendon, M. Dincă, "Record-setting sorbents for reversible water uptake by systematic anion exchanges in metal-organic frameworks", *Journal of the American Chemical Society* 2019, *141*, 13858-13866.

J. L. Mancuso and C. H. Hendon, "Titanium(IV) Inclusion as a Versatile Route to Photoactivity in Metal-Organic Frameworks", *Advanced Theory & Simulation* 2019, *2*, 1900126.

J. L. Mancuso and C. H. Hendon, "Porous Crystals Provide Potable Water from Air", *ACS Central Science* 2019, *5*, 1639-1641.

M. M. Cerda, J. L. Mancuso, E. J. Mullen, C. H. Hendon, M. D. Pluth, "Use of Dithiasuccinoyl-Caged Amines Enables COS/H_2S Release Lacking Electrophilic Byproducts", *Chemistry — A European Journal* 2020, *26*, 5374-5380.

H. C. Wentz, G. Skorupskii, A. B. Bonfim, J.L. Mancuso, C. H. Hendon, E. H. Oriel, G. T. Sazama, M. G. Campbell, "Switchable Electrical Conductivity in a Three-Dimensional Metal-Organic Framework via Reversible Ligand n-Doping", *Chemical Science* 2020, *11*, 1342-1346.

J. P. Bard, J. L Mancuso, C.-L. Deng, L. N. Zakharov, D. W. Johnson, M. M. Haley, "A highly fluorescent PN-heterocycle-fused pyrene derivative with strong self-dimerisation through hydrogen bonding", *Supramolecular Chemistry* 2020, *1*, 49-55.

S.-J. Lee, J. L. Mancuso, K. N. Le, C. D. Malliakas, Y.-S. Bae, C. H. Hendon, T. Islamoglu, O. K. Farha, "Time-Resolved *in Situ* Polymorphic Transformation from One 12-Connected Zr-MOF to Another", *ACS Materials Letters* 2020, *2*, 499-504.

M. LeRoy, A. M. Mroz, J. L. Mancuso, A. Miller, A. Van Cleve, C. Check, H. Heinz, C. H. Hendon, C. Brozek, "Post-Synthetic Modification of Ionic Liquids Using Ligand-Exchange and Redox Coordination Chemistry", *Journal of Materials Chemistry A* 2020, *8*, 22674-22685.

J. L. Mancuso, A. M. Mroz, K. N, Le, C. H. Hendon, "Electronic Structure Modeling of Metal-Organic Frameworks", *Chemical Reviews* 2020, *120*, 8641-8715.

J.-H. Dou, M. Q. Arguilla, Y. Luo, J. Li, W. Zhang, L. Sun, J. L. Mancuso, L. Yang, T. Chen, L. R. Parent, G. Skorupskii, N. J. Libretto, C. Sun, M. C. Yang, P. V. Dip, E. J. Brignole, J. T. Miller, J. Kong, C. H. Hendon, J. Sun, M. Dincă, "Atomically precise single-

crystal structures of electrically conducting 2D metal-organic frameworks", *Nature Materials* 2021, *20*, 222-228.

C. M. Levinn, J. L. Mancuso, C. H. Hendon, M. M. Pluth, "N-Methylation of Self-Immolative Thiocarbamates Provides Insights into the Mechanism of Carbonyl Sulfide Release", *Journal of Organic Chemistry* 2021, *86*, 5443-5451

K. N. Le, J. L. Mancuso, C. H. Hendon, "Electronic challenges of retrofitting 2D conductive MOFs to form 3D conductive lattices", *ACS Applied Electronic Materials* 2021, *3*, 2017-2023.

J. L. Mancuso, K. Fabrizio, C. K. Brozek, C. H. Hendon, "On the limit of proton-coupled electronic doping in a Ti(IV)-containing MOF", *Chemical Science* 2021, *Accepted.*

J. L. Mancuso, C. A. Gaggioli, L. Gagliardi, C. H. Hendon, "Coordination induced spin-crossover during ethylene dimerization in Ni(II)-MFU-4*l* ", *Journal of Physical Chemistry C* 2021, *Accepted.*

ACKNOWLEDGMENTS

I first wish to express sincere gratitude to my advisor Professor Christopher H. Hendon, whose unbridled enthusiasm and endless encouragement guided me not only to the fields of metal-organic frameworks and computational chemistry, but through this thesis: your patience and understanding were unwavering, and your diverse chemical knowledge made this journey not only fascinating, but fruitful. Thank you also to all of my co-authors on the journal articles included in this thesis, and those that have been omitted. Thank you for your hard work and thorough discussions in the preparation of each manuscript, and specifically Professor Carl K. Brozek whose insight provoked fruitful discussions across all areas of my thesis. I would also like to thank Professor Michael Haley for his sundry guidance from the very first day I stepped foot on the University of Oregon campus. Perhaps most importantly, special thanks to my friends and Hendon Materials Simulation colleagues Dr. Thomas Kasel, Dr. Austin Mroz, Khoa Le, Joshua Davis, Lillian Payne, and Min-Chieh (Jack) Yang for being my sounding boards and an unending supply of feedback, questions, support, and smiles. Finally, these investigations were supported in part by the National Science Foundation through the Division of Materials Research under grant no. DMR-1956403 awarded to Prof. Christopher H. Hendon. I also acknowledge support from the Extreme Science and Engineering Discovery Environment (XSEDE), which is supported by the National Science Foundation [ACI-1548562], the PICS Coeus High Performance Computer, which is supported by the National Science Foundation [1624776], and the University of Oregon High Performance Computer, Talapas.

Dedicated to my marvelous mother, Jinny Mancuso, fabulous father, B. Thomas Mancuso, superb sister, Dr. Jordan E. Mancuso, brilliant brother, Joe Mancuso, awesome Aunt, Beverley Mancuso, and glamorous grandmother, also Beverley Mancuso, for their unconditional love and support throughout my academic career. I would neither be here nor alive without each of you.

TABLE OF CONTENTS

Chapter Page

Chapter Page

Chapter Page

LIST OF FIGURES

Figure Page

Figure Page

Figure Page

Figure Page

Figure Page

LIST OF TABLES

Table Page

LIST OF SCHEMES

Scheme Page

CHAPTER I

INTRODUCTION

Chapter I will serve as an introduction to the fields of metal-organic framework (MOF) chemistry and density functional theory (DFT), followed by a literature review regarding the application of DFT to MOFs. These sections are excerpted from a previously published article, *Chemical Reviews* 2020, *120*, 8641-9715, and set the technical and historical context for each study presented in subsequent chapters, including the different computational approaches applied throughout as a function of structure, composition, and property of interest.

1.1 Introduction to Metal-Organic Frameworks

Since their conception,[1] metal–organic frameworks (MOFs) have attracted practitioners from organic, inorganic, and materials disciplines,[2–4] each with a shared interest in physical properties afforded by mixing multitopic organic linkers and metal ions or clusters (secondary building units, SBUs, or nodes).[5,6] The combination of SBUs with the multitude of linkers has enabled a seemingly infinite landscape of materials with modular properties,[7] all featuring one commonality: crystallographically ordered void spaces.[8,9] Porosity in conjunction with functional MOF components catalyzed interest in

these materials and atomically precise pores enable a series of heterogeneous gas storage[10–12] and separation technologies[13,14] as well as access to extremely high loadings of catalytically active centers.[15–18] In more recent embodiments, exotic electronic structures have been discovered,[19–21] providing a foundation for applications in high surface area electrodes in electrochemical devices[22–27]. Clearly, their diverse composition and structure enable a wealth of possible applications.

Many of these applications depend on the accessibility of the pores; pore topology is largely determined by the shape, size, and composition of the linkers.[28,29] Of course, the node composition and topology also play a determining role in the structure,[6] but there are far fewer synthetic handles available to modify and create novel inorganic clusters. Thus, the prediction of MOF properties is well-suited to computation,[30] as we can rapidly construct a large family of MOFs using only the geometry of the SBUs and a nearly endless selection of linkers.[31] Indeed, one of the most elegant aspects of MOF chemistry is the ability to transmetallate[32–36] and geometrically substitute one linker for another of similar geometry[37–39] enabling a broad gamut of structurally related materials.[36] Such isoreticularity is a cornerstone of the field[40–42] and has been a key focus for several years with notable successes (e.g., efficient absorption of water,[43–45] and as site isolated catalysts[46–48]).

Focusing on the organic and inorganic components separately, there is a rich history of both molecular and solid-state chemistries from which to draw insight. The design principles that underpin these fields can also be applied to MOFs, enabling subtle electronic control of the bulk MOF properties; chemists can use pre- and post-synthetic design of

organic linkers to augment the properties of the bulk material.[49] The power afforded by constructing materials from molecules should not be undersold; it is easier to modulate a molecular property than it is to post-synthetically modulate a material property. To illustrate this power, both the linker and the inorganic node have been used as hosts for molecular catalysts.[50,51] The paradigm of appending known, active, catalysts to MOFs, via either linker functionalization[52,53] or node modifications,[54–58] often only serves the purpose of supporting an otherwise homogeneous catalyst.[59] The fact one is able to append a catalyst to the surface of a solid without grossly diminishing its function highlights a key design principle[60]: the electronic structure of most MOFs does not impact the local electronic structure of the catalytically active site. In other words, from this limited perspective, most MOFs are not greater than the sum of their parts, they are merely an array of ordered molecules.

However, there are certain instances where the assembly and composition of a MOF clearly does augment the electronic properties of its constituents; they are more complicated than an array of molecules. For example, the ionization potential of benzene dicarboxylic acid is 9.9 eV,[61] yet when it is used to construct Zn-MOF-5,[12] Ti-MIL-125 (Materials Institute Lavoisier),[62] and UiO-66 (Universitetet I Oslo),[63] three examples of frameworks whose frontier orbitals are centered on benzene dicarboxylate (BDC) ligand, BDC exhibits ionization potentials of 7.3, 7.7, and 7.0 eV, respectively.[64] Given the energetics of the linkers are hence susceptible to augmentation depending on the electrophilicity of the metal ions/clusters, the assembly of the MOF itself can have an impact on the electronics of the system, even if the states themselves are largely localized.

This enables opportunities for MOFs in optical[65,66] and photocatalytic[67–69] applications, where the MOF structure and composition play a determining role in the chemistry of the localized states.

Thus, by making the assumption that all MOFs feature highly localized electronic states, we limit our ability to provide insight into some of their properties, particularly for materials with high levels of covalency at the metal–ligand interface[70] and for MOFs that feature extended inorganic connectivity (e.g., MOF-74[71]). Consider the family of champion electrically conductive 2D MOFs constructed from square planar metals and oxidized planar hexatopic linkers. The most studied scaffold, Ni_3(hexaiminotriphenylene)$_2$ ($Ni_3(HITP)_2$),[72,73] only assembles in the presence of chemical oxidants. Analyses of the electronic structure have revealed that the emergent properties of the framework are difficult to rationalize from molecular design principles alone, as the linkers should feature unpaired electrons, but the MOF itself shows no EPR signal.[73–75] Indeed, it is more appropriate to consider these sorts of MOFs from a solid-state perspective, where the orbitals delocalize to form bands[76,77] and the symmetry of the crystal becomes important for correct descriptions of electron energetics.

Regardless of the electronic character embodied by a given system, the immense chemical space spanned by MOFs and their limitless application is impossible to explore solely through experiment. In order to achieve timely discovery and development of functional materials for technologies related to renewable energy, catalysis, low-energy chemical separations, and more, theoretical approaches can be used to guide synthetic efforts. Collaboration between theory and experiment can reduce the chemical waste,

human effort, and inception period for life- and planet-saving technologies, accelerating material development and technological advancements. One theoretical approach to garner insight into the chemical origins of observable MOF behaviors is density functional theory (DFT). The following sections will first detail the development of DFT, followed by an explanation of the molecular and solid-state modeling approaches that can be applied to study MOFs, and their situational appropriateness.

1.2 Introduction to DFT

Given knowledge of the electronic wavefunction for a chemical system, we can compute any electrochemical or physicochemical property of interest. Unfortunately, our best tool to compute a wavefunction is an unsolvable equation. DFT is just one of several electronic structure theories designed to approximate the wavefunction of a molecule or material, using an iterative protocol that will be described below. The founding principles for the development of these quantum mechanical models also serve as the foundation for our modern understanding of chemical bonding. Quantum mechanical simulations therefore provide us subatomic insights that overlap with our conceptualization of chemical systems and allow us to more rapidly advance in all areas of chemistry. The following subsections will serve to build an understanding of the founding assumptions and approximations that facilitate computational chemistry based in the DFT construct. This will establish the basis for computational methods sections throughout the following chapters, and the context in which chemical conclusions are established.

1.2.1 The Rise of Quantum Mechanics

Math is our intellectual connection to the physical world. From the conception of the nucleus, chemical physicists have been attempting to quantify measurable properties to test their theories. Starting from the Bohr model of a quantum atom[78], the age of quantum mechanics was quickly ushered in. Einstein discovered the wave-particle duality of light[79], and De Broglie extended this concept to matter-waves like electrons[80]. From this, the mathematical foundation of modern electronic structure theory was established with Erwin Schrödinger's equation for the time-evolution of a matter wave in a many body system.[81] Considering electrons and nuclei as negative and positive point charges we can express the time-dependent, relativistic many body Schrödinger equation as:

$$\hat{T}\Psi + \hat{V}\Psi = -i\hbar\frac{d\Psi}{dt} \qquad \text{Eq. 1}$$

where $\hat{T}$ is the many-body kinetic energy operator and $\hat{V}$ is the many-body potential energy operator, whose summation we can define as an overall Hamiltonian operator, $\hat{H}$. In this expression, the many-body wavefunction Ψ contains the probability amplitude of every possible configuration of electrons and nuclei available to the system. However, the energy operator, $\hat{H} = -i\hbar\frac{d}{dt}$, where $\hbar$ is the Dirac constant, can be replaced with the energy eigenvalue, E, and we can modify the above expression to describe the ground state of a static, interacting many-body system.[82] The resultant time-independent, non-relativistic Schrödinger equation takes the form:

$$\hat{H}\Psi = \mathrm{E}\Psi \qquad \text{Eq. 2}$$

By this definition, the wavefunction of system is an eigenfunction of the Hamiltonian operator with energy as the corresponding eigenvalue. At this point, the Hamiltonian contains multiple kinetic and potential energy terms corresponding to electrons, e, nuclei, n, and the interactions between them such that:

$$\hat{H} = \hat{T}_e + \hat{T}_n + \hat{V}_{ee} + \hat{V}_{ne} + \hat{V}_{nn} \qquad \text{Eq. 3}$$

where $\hat{T}_e$ and $\hat{T}_n$ are the kinetic energy terms for electrons and nuclei, while $\hat{V}_{ee}$, $\hat{V}_{ne}$ and $\hat{V}_{nn}$ are the potential energy terms embodying electron-electron, electron-nucleus, and nucleus-nucleus interactions, respectively. Using classical definitions for each of these terms, Schrödinger was able to arrive at an exact solution for orbitals in a hydrogen atom. In particular, he was able to simulate the hydrogen emission spectra associated with the Bohr model for electronic orbital transitions by computing the relative energy of the quantized electronic states;[83] an emission corresponds to a quantum of energy that defines the difference in energy between two discrete orbitals. The agreement between Schrödinger's solution and the experimental hydrogen emission spectrum validated these theories of quantum mechanics.[84]

Using spherical polar coordinates, there are three important quantum numbers for the definition of a wavefunction, namely 1) the principal quantum number, *n*, which has a positive natural number value and indicates the quantized energy level of an orbital and the

relative distance from the nucleus, 2) the Azimuthal quantum number, l, which describes the shape of the region in space occupied by an electron and can be any integer from 0 to n-1, and 3) the magnetic quantum number, m_l, which defines the orientation of the region of space occupied by an electron with respect to a magnetic field, and can be an integer value from -l to l.[85] For a given set of principal quantum numbers, there are a fixed number of subshells which each contain a fixed number of orbitals. For example, if $n = 2$, $l = 0$ or 1, and in the $l = 0$ subshell, $m_l = 0$ while in the $l = 1$ subshell m_l can be -1, 0, or 1 meaning there are 4 possible orbitals to occupy in this shell, namely 1 s ($l = 0$) and 3 p ($l = 1$).

These quantum numbers are sufficient to describe the hydrogen atom, containing one nucleus and one electron. However, in the case of more than one electron, we must introduce an additional quantum number, m_s, corresponding to the magnetic moment of an electron within these orbitals. So, while the 1s orbital of a hydrogen atom contains a single electron, in a hydride this orbital contains to two of opposing spin. This points to an important law of quantum mechanics known as the Pauli exclusion principle: two or more identical fermions (particles with a half-integer spin) cannot occupy the same quantum state at the same time.[86] In the static, time-independent many body Schrödinger equation, this means we must ensure no two single particle wave functions are identical; in other words, the total wave function must be antisymmetric. The resulting complexity and dimensionality of analytical solutions to the Schrödinger equation are computational intractable, and some approximations need to be made in order to build to a usable theoretical construct to analyze molecules, and larger.

1.2.2 Founding Approximations of Density Functional Theory

The first approximation we make is the so-called **Born-Oppenheimer approximation** (BOA), which decouples the motion of electrons and nuclei.[87] Within this approximation, we assume that the positively charged nuclei are so much more massive than the negatively charge electrons, and therefore the timescale of their motion is so much larger, that we can separate the overall Ψ into a nuclear and electronic component. This assumption is valid at the limit of infinite atomic mass, however, there is some deviation between theory and experiment for very precise spectroscopic measurement of molecules.[88] The magnitude of this discrepancy is determined by the electron-nuclear coupling operator, which is inversely proportional the nuclear mass. Even so, calculations performed within the BOA recover helpful and reliable results.

Using the BOA[87], we can modify the Hamiltonian to construct an electronic wavefunction, Ψ_e, for a set of fixed nuclear coordinates, r_n, that neglects the $\hat{T}_n$ term as it goes to zero, and takes $\hat{V}_{nn}$ to be an effectively constant background potential in which the electron cloud resides. Thus, we are left with a Hamiltonian describing the kinetic and potential energy of electrons:

$$\hat{H}_e = \hat{T}_e + \hat{V}_{ee} + \hat{V}_{ne} \qquad \text{Eq. 4}$$

By invoking classical definitions for each of these terms we obtain a Schrödinger equation that is dependent on the position, r, of e electrons with the form:

$$E_e(r_n)\Psi_e(\mathrm{r}) = \widehat{H}_e\Psi_e(\mathrm{r}) = \left[-\frac{1}{2}\sum_e^i \nabla_e^2 + \frac{1}{2}\sum_{e_1\neq e_2}^i \frac{1}{|r_{ee}|} - \sum_n^j \sum_e^i \frac{Z_n}{|r_{ne}|}\right] \Psi_e(\mathrm{r}) \qquad \text{Eq. 5}$$

At this point, we require one further approximation because the electron-electron interaction term still cannot be solved. The next approximation is termed the **Hartree-Fock** (HF) approximation, and describes the motion of an electron in an n-electron system as a single electron moving within the field produced by the stationary nuclei and n−1 electrons of the system.[89] Within the HF approximation, electron motions can be considered as uncorrelated and the electronic wavefunction can be approximated by the product of one-electron wavefunctions.

$$\Psi_0 = \varphi_1\varphi_2 \ldots \varphi_n \qquad \text{Eq. 6}$$

This original approximation put forth by Hartree did not account for electron spin and therefore, solutions for two or more electrons would violate the Pauli exclusion principle. Fock[90] and Slater[91] later recognized and solved this problem by using a **Slater determinant** whose functional form is built from one-electron spin orbitals/wavefunctions $\varphi(x)$ where x is a spatial-spin orbital:

$$\Psi(x_n) = \frac{1}{\sqrt{n!}}\begin{vmatrix} \varphi_1(x_1) & \varphi_2(x_1) & \ldots & \varphi_n(x_1) \\ \varphi_1(x_2) & \varphi_2(x_2) & \ldots & \varphi_n(x_2) \\ \vdots & \vdots & \ddots & \vdots \\ \varphi_1(x_n) & \varphi_2(x_n) & \ldots & \varphi_n(x_n) \end{vmatrix} \qquad \text{Eq. 7}$$

By taking linear combinations of one-electron spin wavefunctions, antisymmetry is satisfied. As a result, the exchange energy of electrons is thought to be exact.

To solve for $\Psi(x_n)$ one more founding principle must be introduced: the **variational principle** states that the expectation value of the model Hamiltonian is an upper-bound to the exact ground state energy. Essentially, the Slater determinant that describes the ground state wavefunctions for a system will return the lowest possible eigenvalue; you will never find a solution to the overall electronic wavefunction that yields an energy eigenvalue lower than the true ground state energy. Therefore, we can iteratively solve for the HF wavefunction by minimizing the eigenvalues, or expectation values, of the Hamiltonian with respect to the single-electron spin wavefunctions.

This optimization procedure is called a **self-consistent field (SCF)** approach because in order to compute new orbitals, we need to compute the operator, which is determined by that same set of orbitals.[89] Basically, we need to know the solution to the equation to solve the equation. In addition to the solution being dependent on the initial guess and basis set, the energy expression, or model Hamiltonian, for the HF method includes a Coulombic expression accounting for the interaction of each electron within its spin orbital with the average charge distribution of all the other electrons. In other words, the new wavefunction for each electron is computed as a response to the average electronic field produced by all the other electrons. Using the SCF approach, a set of atomic coordinates is used, an initial guess is formed for the one electron wavefunctions in order to solve the Schrödinger equation and compute Ψ_1, which gives a new set of more accurate orbitals with which Ψ_2 is computed. This procedure repeats until the difference between

Ψ_x and Ψ_{x+1} is sufficiently low. The arbitrary threshold set for the value of this difference is called the convergence criteria.

One shortcoming of the HF approximation is that while electron exchange is computed exactly, the only correlation effect considered is Coulombic repulsion from electrons existing in a field of negative charge. As a result, the electron-electron repulsion term computed within the HF construct is overestimated. Indeed, one definition of the electron correlation energy is:

$$E_{correlated} = E_{real} - E_{HF} \quad \text{Eq. 8}$$

or, the difference between the real energy of a system, E_{real}, and the HF energy of that system, E_{HF}. There are several so-called post-HF methods that use a combination of wavefunctions to describe the ground state of a correlated system, through perturbation theory[92], configuration interaction[93] and coupled cluster[94], and other composite methods[95]. However, density functional theory (DFT) is the only approach to obtain an improved description of the electronic system while also making the solution more computational tractable.

1.2.3 Density Functional Theory and Exchange Correlation Functionals

A valuable development in electronic structure theory came when Hohenberg and Kohn showed that the ground state wavefunction for a gas of interacting electrons in an

external potential can be recovered with knowledge of only the electron density.[96] This led to the Kohn-Sham Formalism wherein the energy of a system is computed as a function of electron density, ρ. Taking our Hamiltonian expression under the BOA in terms of electron density we see:

$$E_0[\rho] = \hat{T}_e[\rho_0] + \hat{V}_{ee}[\rho_0] + \hat{V}_{ne}[\rho_0] \quad \text{Eq. 9}$$

The nuclear-electron term is treated as an external potential, V_{ext}, using a classical electrostatic potential:

$$\hat{V}_{ne}[\rho_0] = \int V_{ext}(r)\rho_0(\mathrm{r})dr \quad \text{Eq. 10}$$

However, the kinetic and potential energy terms associated with electrons and their interactions are poorly defined. In practice, this is overcome by expanding both terms and separating their components into separate functionals including known and unknown terms. The expanded energy expression takes the form:

$$E_0[\rho] = \hat{T}_e^{real}[\rho_0] + \frac{1}{2}\int \frac{1}{r_{e_1e_2}}\rho_0(\mathrm{r}_{e_1})\rho_0(\mathrm{r}_{e_2})\,dr_{e_1}dr_{e_2} + \int V_{ext}(r)\rho_0(\mathrm{r})dr \quad \text{Eq. 11}$$

$$+\hat{V}_{ee}^{QM}[\,\rho_0] + \hat{T}_e^{dev}[\rho_0]$$

Here, $\hat{T}_e^{dev}[\rho_0]$ is the unknown deviation of the reference system's kinetic energy from the real kinetic energy of the electron system, $\hat{T}_e^{real}[\rho_0]$, and $\hat{V}_{ee}^{QM}[\rho_0]$ is the unknown quantum mechanical expression that accounts for the deviation of electron behavior from a classical Coulombic potential. In principle, Kohn-Sham (KS) DFT is exact for both electron exchange and correlation, however, these two trailing terms have no know functional form. The various DFT functionals employed in literature correspond to different methods of approximating the exchange and correlation functional:

$$E_{xc} = \hat{V}_{ee}^{QM} + \hat{T}_e^{dev} \qquad \text{Eq. 12}$$

Perdew coined the term 'Jacob's ladder' with respect to the approximations of increasing complexity for this term, where each level is another rung closer to the heaven of chemical accuracy, **Figure 1**. [97]

The first rung on Jacob's ladder of density-functionals is the local density approximation (LDA), the simplest approximation for E_{xc} put forth by Hohenberg and Kohn.[96] LDA depends only on the electron density at each coordinate and assumes that electron density is evenly distributed through space. The E_{xc} term for LDA takes on the general equation:

$$E_{xc}^{LDA} = \int \rho(\mathrm{r}) F_{xc}[\rho(\mathrm{r})] dr \qquad \text{Eq. 13}$$

where F_{xc} is a functional describing exchange and correlation in a homogeneous electron gas. Spin-polarized systems can also be computed by considering two spin-densities, and this is often called the local-spin-density approximation (LSDA).[98] While LDA (LSDA) approaches can offer fast and reliable results in conventional metallic solids with loosely bound and highly delocalized electrons, it is not suitable for electronically anisotropic systems such as MOFs or most molecules.[99]

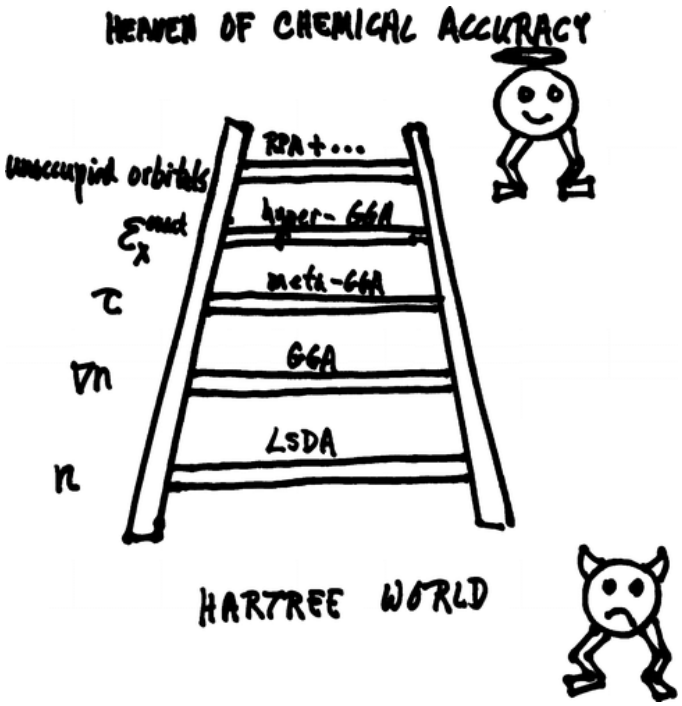

Figure 1. Jacob's Ladder as presented by Perdew et. al. showing steps with increasing levels of theory working towards the goal of chemical accuracy. Reproduced with permission from ref [100] Copyright 2009 American Chemical Society.

The second rung of Jacob's ladder is density-functional approximations based on the generalized gradient approximation (GGA). GGA functionals depend on the electron density at each coordinate *and* the local density gradient:

$$E_{xc}^{GGA} = \int \rho(\mathrm{r}) F_{xc}[\rho(\mathrm{r}), \nabla\rho(\mathrm{r})]dr \qquad \text{Eq. 14}$$

the density gradient expansion is not necessarily straight forward, and numerous F_{xc} functionals have been proposed. The Perdew-Burke-Ernzerhof (PBE) functional[101] and PBEsol[102] are two common variants, that latter of which is used extensively throughout this thesis. PBEsol is a corrected form of PBE that accounts for the changing exchange energy over a wide range of density gradients, which aids in the description of densely packed and porous solids.[102]

The next step from GGA functionals are meta-GGA functionals, which include the electron density, the local density gradient (or first derivative), *and* the second derivative of the electron density in their expression for E_{xc}. These functionals can be viewed as depending on the kinetic energy density of the spin orbitals as well. M06-L[103] is a meta-GGA functional that has been found to perform will for non-covalent interactions, and is used in Chapter 3 of this thesis.[104] Another approach to increasing the accuracy from GGA functionals is to incorporate a component of HF, or exact, exchange. These hybrid functionals compose the next rung of Jacob's ladder. PBE0, for example, is a hybrid functional that takes the local density gradient consideration from PBE and mixes in 25% of the HF exchange interaction description.

$$E_{xc}^{PBE0} = \frac{1}{4}E_x^{HF} + \frac{3}{4}E_x^{PBE} + E_c^{PBE} \quad \text{Eq. 15}$$

The form of this expression can be generalized for hybrid HF and GGA or LSDA functionals by replacing ¼ with a mixing parameter, a, and ¾ with $1 - a$ to incorporate HF exchange on a sliding scale. Beyond simple mixing, the HF exchange component can be controlled by parameters associated with short-range mixing, long-range mixing, and range separation. One example of a range separated hybrid functional used frequently in MOF literature and this thesis is HSE06. HSE06[105], uses an error function (erf) to screen the Coulomb potential associated with HF exchange. Using the erf and its complement (erfc), the exchange and correlation functionals can be decomposed into long-range (LR) and short-range (SR) components.[106] Doing so, another adjustable parameter, ω, can be introduced to control the range of the exchange interaction:

$$E_{xc}^{hybrid} = aE_x^{HF,SR}(\omega) + (1-a)E_x^{PBE,SR}(\omega) + E_x^{PBE,LR}(\omega) + E_c^{PBE}(\omega) \quad \text{Eq. 16}$$

For HSE06 $a = 0.25$ and $\omega = 0.20$. In general, when $\omega = 0$, the long-range terms are negated and effects become purely short-ranged (HSE06 is identical to the PBE0 functional in Equation 14). As $\omega \rightarrow \infty$, long range interactions begin to dominate. Section 1.3, on the application of DFT to MOFs, will discuss functional choice more thoroughly. However, there is one final theoretical consideration that is important to introduce.

1.2.4 Basis Sets

In practice, the SCF procedure developed by Hartree and Fock to 'relax' or equilibrate the geometric and electronic structure of a chemical system within the DFT construct begins with an input of atomic coordinates, typically obtained through some sort of crystallographic refinement. A 'basis set' of functions is then initialized that describe the electron density associated with those coordinates. To describe the overall electronic structure of chemical systems, we build molecular orbitals using linear combinations of these basis functions (plane-waves or atomic orbitals) as approximate solutions to the Schrödinger equation.

To perform molecular modeling of a discrete chemical system, basis functions describing each electron orbiting each nucleus are initialized. There will be at least one function per valence electron per atom as well as one or more functions describing the 'core' electrons that do not participate in bonding. The resolution of a given basis set increases with the number of basis functions. Different basis sets have different types and numbers of functions per electron. For example, in the family of Pople basis sets, 6-31G uses one contracted Gaussian type orbital (GTO) to describe the core electrons that is built from 6 primitive GTOs, while each valence electron is described by two separate functions, where one is another contracted GTO built from 3 primitive GTOs.[107] This basis set is called a double-ζ because there are two orbital functions used per electron. The triple-ζ basis set 6-311G takes the same form, but with an additional function per valence electron. In circumstances were the atomic orbital may be more diffuse or asymmetric than these GTOs can accurately describe, one can also add diffuse[108] or polarization[109] functions.

Diffuse functions, which are shallow Gaussian basis functions that better describe the tail in atomic orbital functions, may be necessary to describe longer-range bonding interactions such as hydrogen bonds and ligand fields as well as anions. Polarization functions are auxiliary functions with an additional node that supplement an atomic basis set and aid in the definition of hybridized orbitals, such as sp^3, or when there is asymmetric bonding. For example, while a minimal basis set for hydrogen would have one function describing the spherical 1s orbital, a p-polarization function can be added that helps describe the non-spherical bonding orbitals associated with an H-S bond. A chosen basis set must be 'large' enough, that is, have enough constituent functions to accurately represent the overall wavefunction. The more complex a bonding environment is, the more basis functions will likely be needed to describe the behavior.

In solid-state models that invoke periodic boundary conditions (PBCs), plane-wave basis sets are often used to describe the propagation of electronic bands. The use of these basis sets, including a discussion on reciprocal space and *k*-points, will be described further in section 1.3.1.1. For comparison with the above discussion regarding atom-centered basis sets, the precision of a plane-wave basis set is determined by the kinetic energy cut-off, where higher frequency cut-off values give higher resolution electronic descriptions. A typical cut-off value for MOFs is 400-600 eV.[110] The other consideration for basis-set accuracy is the classification and treatment of 'core' electrons. Within a plane-wave basis, core electrons—such as 1s, 2s, and 2p in phosphorus—that are tightly bound to the nucleus can only be described by high frequency waves, which are the computationally most expensive to compute, yet we garner the least electronic insight from their contribution to

our electronic structure solution. Therefore, to balance computational cost and accuracy, core electrons are typically approximated by a single effective core potential, or pseudopotential, that interacts with the surrounding particles.[111,112] These core-pseudopotentials are considered softer if they have lower cut-off energies, which are less computationally demanding, but with a trade-off for accuracy.[113]

Regardless of the basis set form, the variational principle is invoked to optimize the initial basis functions towards a minimized energy eigenvalue. (Remember: the orbitals with the lowest energy are the best approximation of the true system, and the orbitals with the lowest energy have the closest energy to the true system.) The SCF procedure begins with the initial system specifications, including atomic positions, the charge on those atoms, and the associated basis functions. Using this information, an initial density matrix will be generated, the Schrödinger equation will be solved to obtain new coefficients for the basis functions, and a new density matrix will be formed. If this new density matrix approximating the wavefunction is sufficiently similar to the previous density matrix by satisfying the stipulated convergence criteria, the iterative procedure is finished. If not, the new density matrix is used to solve the Schrödinger equation again and new orbital coefficients are obtained, repeatedly until the convergence criteria is met.

1.3 Application of DFT to MOFs

It is the molecule/material duality of MOFs that places them in the "nanoscale" gap, somewhere between molecule and material, **Figure 2**. Beyond a few simple design principles (e.g., presence of extended inorganic connectivity, stacking of conjugated

linkers, magnetism, etc.[114–116], which clearly depend on extended solid-state interactions, it is difficult to assess where the electronic structure and physical properties of new frameworks will lay on a spectrum between molecule and solid. This duality poses challenges for modeling MOFs, where computational chemists must decide to whether they model them as molecules or extended solids.

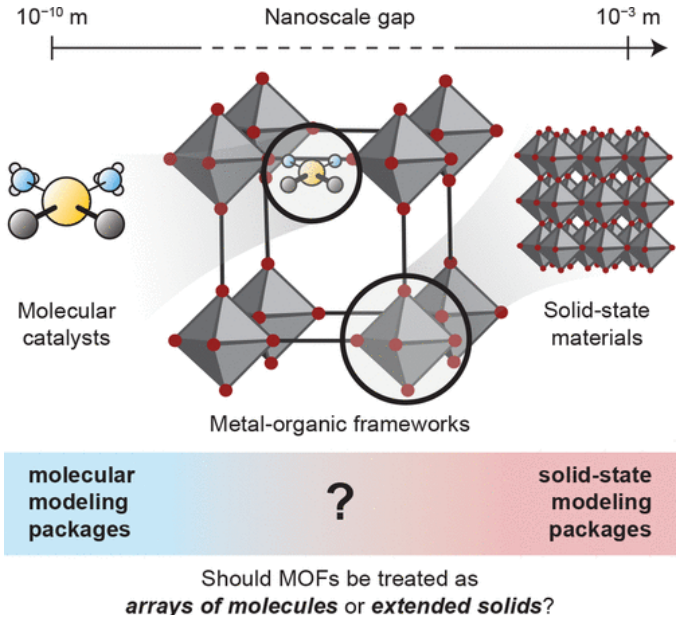

Figure 2. Metal–organic frameworks are uniquely positioned between the molecule, Å scale, and material, mm scale, and consequently behave as both molecules and extended solids. Reproduced with permission from ref. [110]. Copyright 2020 American Chemical Society.

Within the theoretical framework, the primary difference between solid-state and molecular software packages is the application of periodic boundary

conditions.[117] Practitioners are thus presented with a modeling paradox: should the material be treated as a bulk solid, in principle obtaining the correct electronic structure but with reduced capabilities to compute things like reaction transition states?[118] Or should one save computational time and model a truncated fraction using molecular software packages, enabling a broader array of computational tools and higher level of theory but perhaps sacrificing a proper description of the electronic structure?[119]

Of course, the ideal model would be one that treats the MOF as a periodic solid, but can readily apply high levels of theory (typically limited to molecular software packages) to important components in the material.[120] Ultimately, the purpose of a model is to help explain and predict experimental realities using the smallest possible computational system. Hence, it is not surprising that both molecular and solid-state modeling approaches have been fruitful in the MOF field, as the scaffolds may very well act more like one than the other.

1.3.1 Solid-State Modeling for MOFs

While it is certainly convenient to approximate extended MOF structures as finite molecules using the procedures discussed above, it is their crystallinity and ordered porosity that has stimulated many of the developments in the MOF field. Indeed, with the exception of rare amorphous variants,[121–125] MOFs are ordered solids. Thus, conventional solid-state modeling techniques can be applied where MOF crystals possess symmetry operations that enable the description of the extended material using a repeating unit. This section is intended to provide a background and some general calculation considerations

when modeling periodic MOF properties (section 1.3.2.1), including their electronic band gaps (1.3.2.2), and DOS plot interpretation (1.3.2.3).

1.3.1.1 Periodic Models and *k*-Points

Viewing MOFs as an extended array of molecules, each component (i.e., the linker and the prenucleated node) contains a family of molecular orbitals. Upon self-assembly of the MOF these electrons mix to form new molecular orbitals that expand over larger and larger regions of space. In principle, one could model a complete MOF crystallite (i.e., a *very* large chemical system as a molecule) and obtain the exact electron energetics and spatial distributions for all possible molecular orbitals in the material. Owing to symmetry, however, several of the molecular orbitals in the crystallite will be very similar in energy and centered on the same atoms. These geometric degeneracies enable a reduction in computational cost by modeling the associated electrons as interacting periodically in bands, **Figure 3**.

Electronic bands can be thought of as delocalized molecular orbitals whose energy depends on the extent of electronic interaction in crystallographic directions within the crystal. Indeed, Bloch's Theorem purports that for a nondefective material, the periodicity of the lattice describes the periodicity of the overall wave function.[126] Information on both the structural and electronic properties of a bulk sample can therefore be gleaned from a single unit cell (although the approach does not provide information about the surface chemistry at the grain boundaries of a crystallite). One way of thinking about the

construction of bands in solids is to first create molecular orbitals for all atoms contained within the computational cell, then, using harmonics, the electronic interactions with neighboring cells are computed.[127] By doing so, both the electronic properties of the discrete unit cell are recovered, as well as the influence of longer ranged (de)localization and electrostatics, which can only be observed by sampling beyond one computational cell.[128]

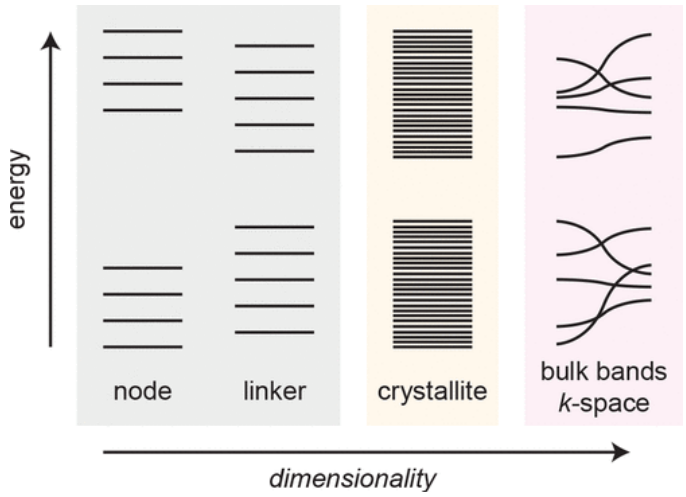

Figure 3: As size of a chemical system increases toward an infinite solid, the number of molecular orbitals becomes very large. For high symmetry materials, the crystallite can be described using a smaller, repeating unit, whose projection through reciprocal space generates electronic bands. Reproduced with permission from ref. [110]. Copyright 2020 American Chemical Society.

While it is convenient to visualize bands as large delocalized molecular orbitals in real space, they are often computed in reciprocal space (i.e. *k*-space) using Bloch's theorem paired with a basis set constructed from interfering planewaves to determine the combinations and populations of electronics bands. *k*-space vectors can be loosely thought to sample long-range interactions in the crystallographic directions defined by the *k*-vector. From experimental convention, a crystallographic unit cell (or conventional cell) contains the smallest chemical representation of a system that exhibits the same overall symmetry as the pristine lattice. Calculations using this geometry, composition, and associated lattice parameters will certainly be suitable for direct calculation of electronic properties, however, some space groups offer symmetry related primitive cells that contain a smaller repeating crystalline unit of lower symmetry.[129] Typically, calculations are run on the primitive cell unless the unit cell is required to capture magnetic ordering or structural deformations that cannot be described using the smallest repeating unit, some examples of which are shown in **Figure 4**.

Every ordered MOF crystallizes into one of 230 unique space groups,[130] each containing a series of high symmetry *k*-points.[131] The lowest crystal symmetry, *P*1, features no internal symmetry operations, all atoms in the cell are unique and must be explicitly computed, and hence there is only one high symmetry *k*-point in the first Brillouin zone, Γ. Chemically, the Γ-point is the equivalent of projecting the molecular orbitals contained within the unit cell in three dimensions: the electronics of the material are governed by the interactions captured explicitly within the computational cell rather than their interactions with neighboring cells. MOFs typically crystallize in high symmetry

space groups, and often feature more than one symmetrically *unique* *k*-point that will contribute to the total energy of the system, and hence should be sampled during the SCF.

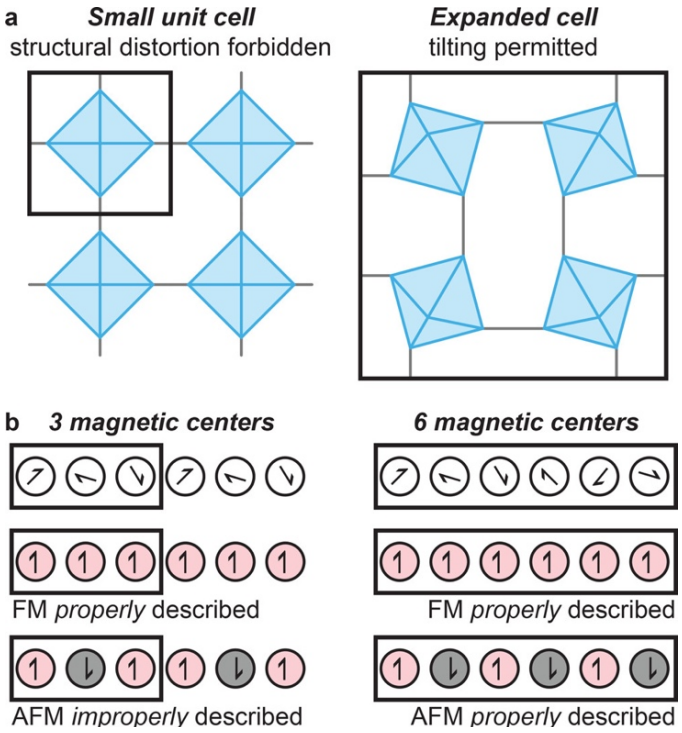

Figure 4. Although the smallest computational cell can save resources, an improper model may be recovered if a chemical interaction permeates beyond a single geometric cell. For example, (a) structural distortions are sometimes captured in temperature independent DFT (the ground state may feature titling of nodes);[132] and (b) magnetic ordering can be challenging if the unit cell contains an odd number of coupling metals (for example, the unit cell of Co_2Cl_2bis(1*H*-1,2,3-triazolo[4,5-*b*],[4,5-*i*])dibenzo[1,4]dioxin), (BTDD), contains 3 Co(II), which do prefer to order antiferromagnetically[133]). Reproduced with permission from ref. [110]. Copyright 2020 American Chemical Society.

Within crystals that feature anisotropic bonding (for example, graphene, 2D MOFs, etc.) certain crystallographic directions contribute more significantly to the bonding and stabilization of the system than others. In the 2D examples, the in-plane and out-of-plane interactions will contribute differently and sometimes seemingly unpredictably to the total energy of the system. It is hence good practice to sample as many *k*-points as possible to ensure a more tightly converged total electronic energy.

The selection of *k*-points depends on the crystal symmetry, and these *k*-points traverse the first Brillouin zone.[134] In practice, the contribution of each sampled *k*-point is taken as a weighted average (determined by symmetry) to recover the total system energy. The position of sampled *k*-points through the first Brillouin zone is computed with one of two philosophically dissimilar approaches: a Γ-centered Monkhorst–Pack, or a non-Γ-centered Monkhorst–Pack *k*-grid. The main difference is that the former forces sampling of the Γ, while the latter does not guarantee that any high symmetry points are sampled.[135] Crystal symmetry thus helps inform two key computational considerations: (i) the feasibility of using a computational primitive cell, and (ii) the *k*-path to explicitly examine how electron energies changed in the extended solid. Almost all of these considerations are enabled in freely available software, and high symmetry points of the first Brillouin zone can be found in online databases like the Bilbao Crystallographic Server.[131]

In principle, one would compute the total energy of a system by integrating over the entire first Brillouin zone or approximating the integration with the summation of a very large number of *k*-points. In practice, the total energy is asymptotically related to the

number of *k*-points and a convergence test is required to elucidate when a sufficiently dense grid has been invoked. We can distill the key considerations for *k*-grid generation and their impact on the material properties down to the following:

- In Bloch's theorem, planewave cutoff (i.e., the basis set) and the *k*-points are independent. Yet both affect the total energy of the system. Hence, to obtain converged results, it is good practice to benchmark the *k*-grid and basis set separately.

- Generally, sampling additional *k*-points provides better descriptions of long-range orbital interactions within a crystal system. Increasing *k*-grid density does not always reduce the total energy of the system that depends on the nature of the bonding and antibonding orbitals.[136] It is therefore difficult to predict the impact on total energy without first running the calculation.

- Empirically, a *k*-grid with a density of 25×(lattice parameter)$^{-1}$ provides an estimate of the *k*-point density required for a reasonable sampling of electronic interactions within the crystal.[129] Computational feasibility of the resultant grids relies on large lattice parameters, which typically infer large numbers of explicitly defined chemical interactions within the unit cell, the extent of electronic interactions rapidly diminishes in real space, hence why large crystals often show little dependence on increased *k*-point density. There is a trade-off between modeling large systems with many explicit electrons, versus small systems with many explicit *k*-points. Moreover, while a reduction to the primitive cell vastly

reduces the Slater determinant's size, it comes at the penalty of requiring several additional *k*-points (which contribute significantly to the computational time).

- In MOF chemistry, it is common to perform geometric optimizations with a sufficient *k*-grid at a lower level of theory, then refine the electronic structure with a single-point energy calculation at a higher level of theory; the size of the *k*-grid in either case is determined by MOF symmetry and resource availability.

- Importantly, there is no formal relationship between lattice parameter and *k*-point density; rather, large unit cells often contain sufficient descriptions of strong interactions, and hence long-range sampling does not overly alter the energetics of the system. Regardless of whether this is true for all MOFs, this procedure produces a highly reproducible systematic error in the total energy of the system that is acceptable in many cases.

- Most MOFs crystallize in high symmetry space groups, and it is good practice to include all high symmetry *k*-points in the computation of the total energy of the system, and ideally during the optimization routine.

Regardless of how many *k*-points are selected for the optimization routine, the material must be geometrically equilibrated (and the SCF must be converged) to ensure that the energetics are computed without spurious numerical fluctuation. A schematic of the general computational approach for solid-state materials is shown in **Figure 5**. Assuming that a structure has been optimized, the following sections discuss the computable properties and utility of using a solid-state model for MOF systems.

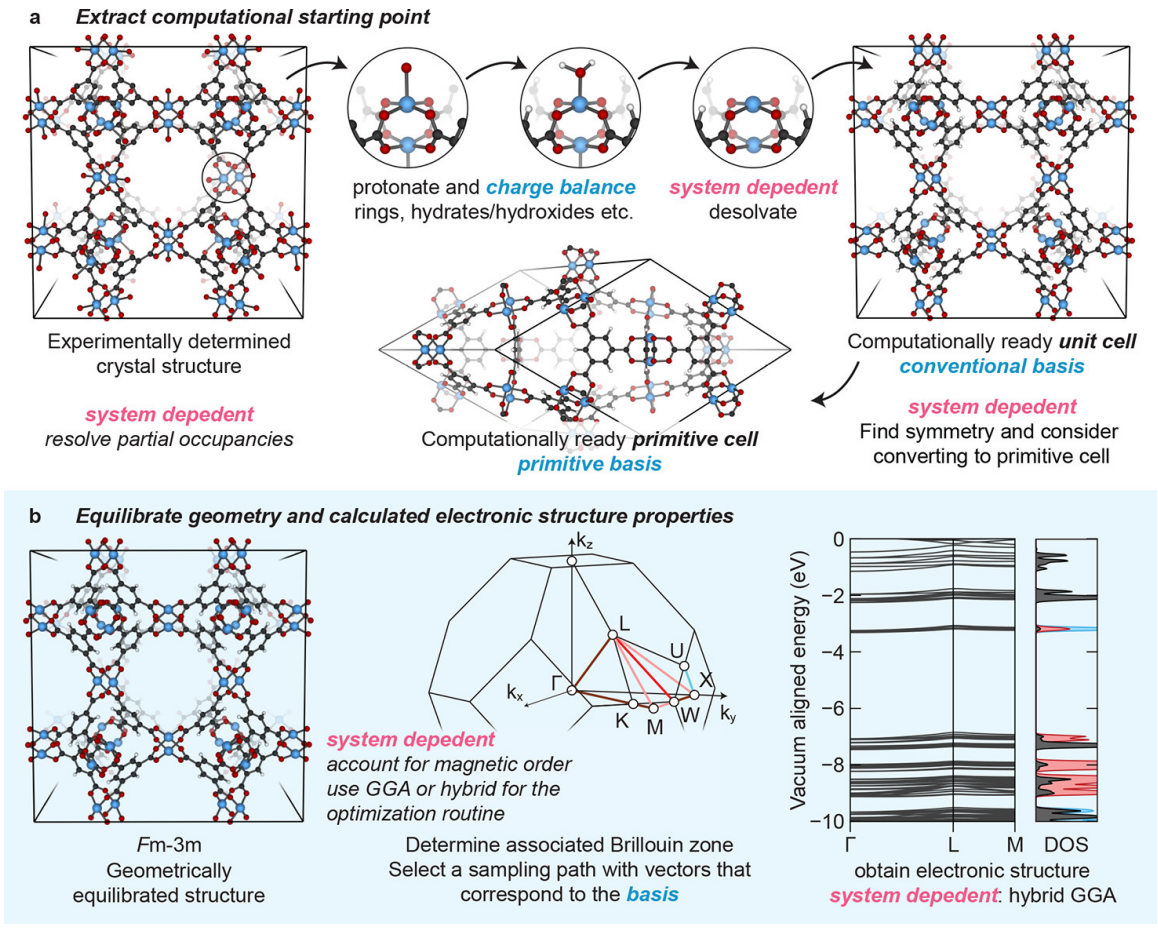

Figure 5: General computational approach used to obtain electronic structure properties from solid-state structures. (a) Beginning with an experimentally obtained crystal structure, partial occupancies must be resolved. Then, where applicable, protons must be added to charge balance the cell, in effect establishing the oxidation state of the metals. Extrinsic solvent may be removed to simulate the activated MOF. Symmetry can then be enforced and a computational primitive cell may be available. (b) The structure can then be equilibrated, and higher-level electronic structure properties can be obtained by sampling the first Brillouin zone, including electronic band structures and corresponding DOS. Reproduced with permission from ref. [110]. Copyright 2020 American Chemical Society.

1.3.1.2. Recovering Optical Properties

The ionic lattices of most MOFs feature a discrete electronic band gap, while some can be described as metallic (classified as having nonzero DOS at the Fermi level).[137] Within the subgroup of materials that feature electronic band gaps, their conductive properties depend on numerous other properties (e.g., the material's defect chemistry, the mobility of the charges, the electronic band gap, etc.). Because standard solid-state computations omit temperature, and without an exhaustive defect analysis, we are unable to assign the position of the Fermi level. In light of this, MOFs are largely insulating materials, but we note that they are interchangeably referred to as semiconductors in the literature.[138–141]

The fundamental energy gap, E_g, is defined by the lowest energy occupied-to-unoccupied transition in a system (independent of whether it is symmetry allowed);[142] its magnitude is the difference in energy between the VBM and CBM. Because of a derivative discontinuity and other localization errors associated with the exchange potential in semiconducting systems, GGA functionals systematically underestimate MOF band gaps.[143–145] Empirically, this systematic underestimation can be improved by incorporating a component of exact HF exchange into the Hamiltonian.[146,147] However, the computational expense associated with hybrid functionals[148] prompts the recovery of semiconducting properties from single-point calculations at this level of theory on a structure obtained using GGA.

MOFs with bands that exhibit different energies as a function of *k*-space (i.e., band dispersion) may exhibit an indirect band gap, schematically presented in **Figure 6** where

the VBM and CBM occur at different points in reciprocal space. In such cases, Γ-point sampling is insufficient to capture the dominant electronic influences. The lowest energy transition in an indirect band gap material requires the coupling of photon absorption/emission to a phonon mode in order to conserve energy and momentum because the wave vector at the top of the valence band does not match the wave vector at the bottom of the conduction band.[149] Indirect band gaps thus diminish the intensity but extend the lifetime of formed excitons by preventing recombination; indirect band gaps are desirable in photoactive solids for the enhancement of quantum efficiency.[150] Although there are almost no reported indirect-band MOFs,[151,152] the changing band gap energy in reciprocal space is a phenomenon ripe for exploration.

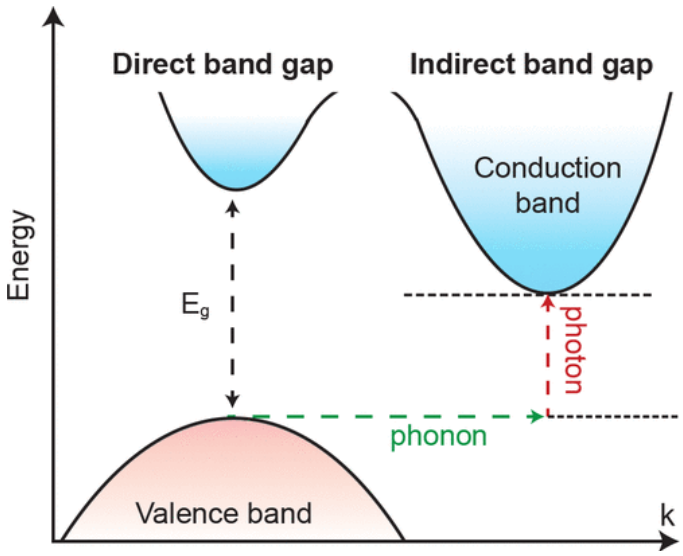

Figure 6. Illustration of the band gap in a semiconductor as a function of reciprocal space when the CBM and VBM are at the same point in reciprocal space (direct band gap) and when they are at different points in reciprocal space (indirect minimum absorption energy). Reproduced with permission from ref. [110]. Copyright 2020 American Chemical Society.

Certainly, most MOFs feature wide band gaps and highly localized electronic structures that give rise to flat bands with well-defined orbital contributions to the frontier states and direct gaps. The localization of electrons makes MOFs intriguing for photocatalytic applications,[69,153–157] as it affords one route toward accessing dense populations of high energy electrons localized on transiently reduced motifs,[158,159] discussed later in this chapter. Moreover, electronic structure may be tuned to desirable bulk properties, facilitated by the inherent modularity of MOFs.

Although the nature of band edges is material/composition dependent, the electronic band gap of a MOF can be modified by metathesis and functionalization of the linker and/or inorganic node. There are four possible frontier orbital orientations in MOFs, wherein the band edges are defined by (i) ligand-to-ligand, (ii) ligand-to-metal, (iii) metal-to-ligand, or (iv) metal-to-metal excitations, ultimately dictated by the material composition. Countless examples of DFT screenings are reported for band gap modulation via metal[160–165] and linker exchange[67,166–174] across the gamut of MOFs. MOF-5, for example, has been subject to numerous theoretical studies systematically exchanging components of the inorganic node[163,165,175–177] or the linker.[178–181] In one study, the authors made isovalent substitutions for both the inorganic oxo, as well as the transition metals, and from PBE (which systematically underestimates the band gap), these modifications shifted bulk MOF-5 (E_g = 3.6 eV) into the visible region, **Figure 7**.[182]

In a complementary study, both GGA and hybrid functionals showed tetrahedral Co(II) transmetalation in MOF-5 resulted in band gap reduction, and an eventual transition from semiconducting to metallic with two cobalt per node.[165] Experimental efforts revealed

that up to ~3 Co(II) per cluster could be incorporated in the presence of solvent, forming blue crystallites with octahedral Co(II).[176,183,184] Together, this indicates that in models assuming isogeometric substitution of tetrahedral Co(II), the resulting metallicity is likely an indication of material instability, Co(II) prefers to be octahedral in MOF-5.

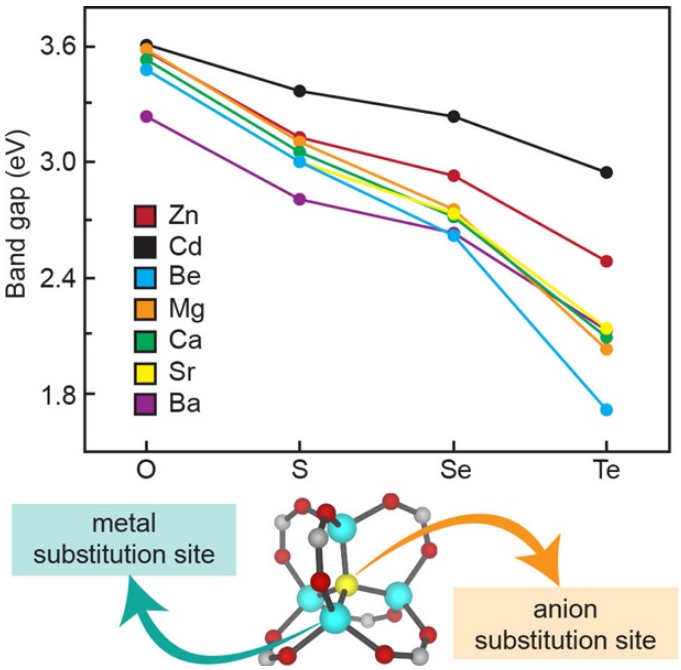

Figure 7. Evolution of the calculated PBE band gap (top) for X_4Y-MOF-5, where X is the substituted metal (X = Zn, Cd, Be, Mg, Ca, Sr, Ba) and Y is the substituted anion at the center of the metal node depicted in yellow (Y = O, S, Se, Te), Adapted with permission from ref [182]. Copyright 2014 American Chemical Society.

Still, transmetalation is a fruitful route to control the nature of band edges in an otherwise wide gap MOF. Several practitioners have examined the substitution of

transition metals in place of Zr(IV) in UiO-66,[185–187] however, it is inconclusive whether incorporation proceeds via transmetalation or node grafting.[188] The application of DFT has shown that certain metal ions seemingly reduce the band gap from the addition of states below or above the native conduction or valence band. For example, both Ce-[189,190] and Ti-substituted[191] UiO-66 install empty *f*- and *d*-orbitals, respectively, at the conduction band edge, reducing the requisite excitation wavelength. The installation of empty metal states at the conduction band edge of MOFs with ligand-centered excitations will be discussed further in Chapter 3 as a strategy for engendering linker-to-metal charge transfer for application in photocatalysis.

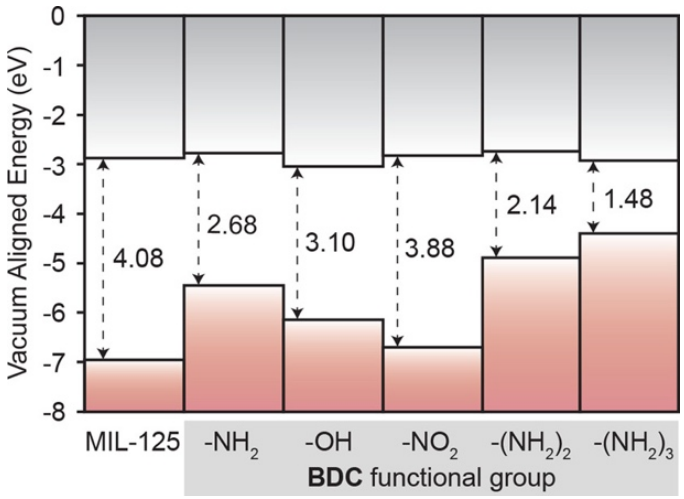

Figure 8. Fermi-aligned band edges of MIL-125 derivatives reveal the addition of states from organic functionalization raise E_F closer to the conduction band edge providing facile band gap modulation. Data obtained from ref [167]. Copyright 2018 AIP Publishing.

A more popular strategy, particularly in the realm of photocatalysis, is organic linker functionalization. For example, one study showed that the band gap of MIL-125, a MOF with an organic valence band and inorganic conduction band,[62,67] depends the electron donating or withdrawing ability of functional groups on the BDC linkers, **Figure 8**.[167] In most cases, the linkers can be installed presynthetically, however, linker exchange and postsynthetic functionalization[38,41,192,193] have proven effective to access structures that are otherwise in phase competition or would simply not self-assemble.[194]

Beyond electronic modulation of the band gap via linker and node functionalization, structural perturbation is also a route to alter the electronics of deformable MOFs; the physical structure is another variable parameter in MOFs that may exhibit flexibility or polymorphism. Perhaps the best example is conveyed through the breathing behavior of "wine rack" MOFs.[195–197] The open- and closed-pore structures of several monometallic forms of MIL-53 was computed using the HSE06 functional with Grimme's D3 dispersion correction.[198] The degree to which energy levels (e.g., valence band, conduction band, and band gaps) were perturbed by the strain was quantified with the deformation potential,[199] and the band gap was shown to depend on both the metal composition[198] and framework density **Figure 9**.[199] This pressure-induced band gap control was further demonstrated with the breathable MIL-47 framework, **Figure 9**.[198]

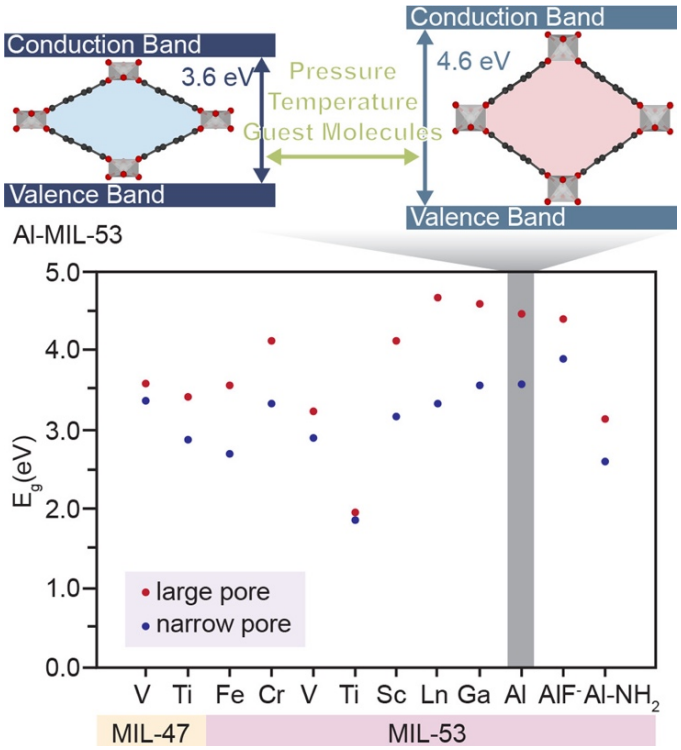

Figure 9. (a) MIL-53 is a prototypical example of th dynamic, ionic construction of MOFs instilling the framework with flexural freedom that alters its macroscopic properties, in this case, band gap energy. (b) the scatter plot shows through calculated band gaps of the narrow pore and large pore forms of several MIL-53 (with M(III) metal cations) and MIL-47 (with M(IV) metal cations) inorganic derivatives that the band gap of more condensed systems (i.e., the narrow pore form) is lower. Adapted with permission from ref [198]. Copyright 2015 American Chemical Society.

Because most MOFs feature large discrete band gaps, a tremendous amount of effort has been invested in understanding the electronic structure of a family of 2D MOFs that feature a narrow or zero electronic gap.[19,200–211] Many of these materials arrange to

form hexagonal pores and feature characteristic "Kagome" electronic bands arising from 3-fold degeneracy at certain *k*-points (usually denoted as the K point in hexagonal crystal systems, although strictly speaking the direction of the K vector does depend on the space group).[212,213] As shown in **Figure 10**, the Kagome bands occur in the conduction band at the K point as seen by the "Dirac cone". If appropriately modeled using SOC,[214] the bands themselves do not cross in *k*-space (the physics underpinning this effect are concisely presented in previously published work).[215,216] While this gap is often very small (10s of meV), the nondegeneracy of these states permits unusual physics.[217]

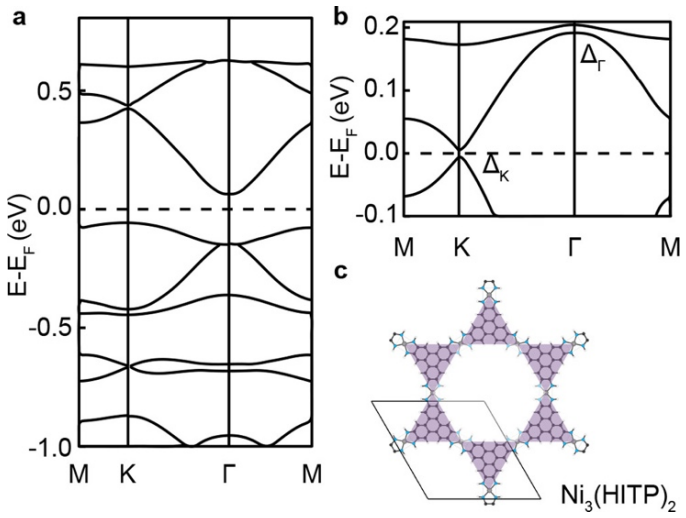

Figure 10: Electronic band structure of monolayer $Ni_3(HITP)_2$ (c) exhibits (a) closed-gap Dirac cones when spin–orbit coupling is ignored. These Dirac cones open upon spin–orbit coupling inclusion, (b), as seen by the enlarged view. Adapted with permission from ref [212]. Copyright 2014 American Physical Society.

Many of these exotic electronic properties are found in the most well-studied 2D MOF, $Ni_3(HITP)_2$.[218–221] For example, while both $Ni_3(HITP)_2$ and the Cu(II) analogue are predicted to be bulk metals due to delocalized π-electrons in the out-of-plane direction,[19] $Ni_3(HITP)_2$ features a narrow in-plane gap, and a Dirac cone in the conduction band, **Figure 10**.[73,219] This means the monolayer is only semiconductive, while the bulk solid is conductive. The out-of-plane stacking orientations have posed problems for modelers, because the anisotropic bonding leads to shallow potential energy surfaces, which provokes long computations and dissimilar electronic properties depending on stacking orientation, **Figure 11**.[222] Interestingly, the hexa-substituted benzene analogue features in-plane metallicity.[218]

While bulk models of $Ni_3(HITP)_2$ are metallic, a band gap is observed in monolayer models. The band gap observed in the monolayer models of $Ni_3(HITP)_2$ (**Figure 10**) can also be recovered by artificially elongating the intersheet distance. A band gap emerges at approximately 5 Å,[220] and the open metal-sites of square planar Ni(II) are exposed. Foster and colleagues proposed a retrofitting procedure to create a 3D connected version of the catecholate-based MOF based on this exposure.[220,223–225] The influence of metal identity on band gap has of course been assessed (Cu(II), Ni(II), Pt(II), Pd(II), as well as less common Ta(II), Rh(II), and Ir(II));[226] these studies reveal that the metal plays a role in balancing strong electron correlation effects and SOC, while linker redox state seemed to be one avenue to modulate the Fermi level.[227–230]

Interesting electronic phenomena are also observed in quantum mechanical simulations of isostructural frameworks where the linker motifs bond through sulfur atoms

rather than nitrogen. $Fe_3(HTTP)_2$ (HTTP = hexathioltriphenylene), for example, transitions from a bulk metal to having a discrete gap at low temperatures (130 K).[201] PBE-D3 calculations found an intersheet offset of ~1.25 Å to be the most stable stacking conformation by <100 meV per Fe(II) ion, indicating a shallow potential energy surface. [201] In that study, the material was predicted to be a metal in some sheet orientations, while in others, both the magnetism and geometric structure gave rise to the emergence of a band gap. Indeed, shallow PESs will continue to pose problems for computational chemists; the best effort with this family of 2D materials has been to use the experimental c-parameter and equilibrate within that restriction. Importantly, the slipped orientation perturbs the structure out of a hexagonal space group *P*6/*mmm* to orthorhombic *C*mcm.

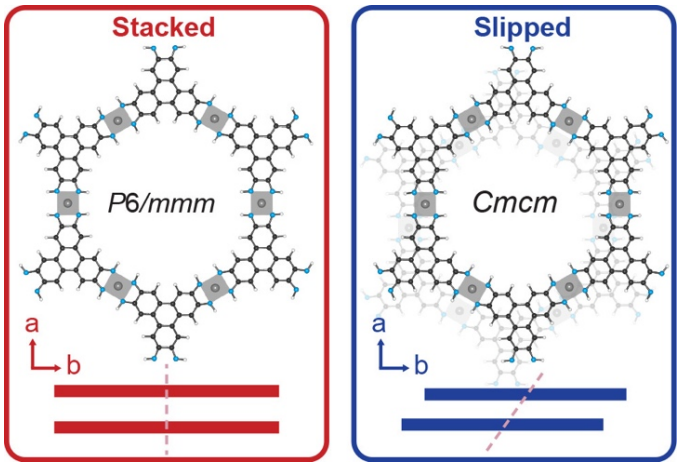

Figure 11. Both eclipsed and slipped stacking modes of $Ni_3(HITP)_2$. The out-of-plane stacking impacts both the π-delocalization of the aromatic systems in the van der Waals direction, as well the crystal symmetry. Reproduced with permission from ref. [110]. Copyright 2020 American Chemical Society.

In sum, MOF band gap energies can be effectively modified by altering the components on which frontier bands are localized, or adding new states within the existing band gap of a parent MOF through metathesis procedures. Both of these procedures enable predictive power in targeting material properties through systematic DFT studies. Although the band gap energy and frontier band identity play a role in determining the utility of a MOF in both light absorption and electrical applications, the lifetime of the charge carriers depends not only on the gap (or lack thereof) but rather on the charge. The following sections will discuss how the electronic band structure and DOS of a material can be used to predict electronic behaviors, among them charge mobility.

1.3.1.3 Analyzing Density of States Plots

DOS plots are critical to assessing electronic band parentage, providing information about the type of charge transport that may exist, be it ligand-to-ligand, metal-to-ligand, ligand-to-metal, or metal-to-metal fundamental gap. Hence, together with the electronic band structure and analysis of band dispersion, the DOS paints a comprehensive picture of the MOF's anticipated function.

The integral of the DOS indicates how many electrons occupy that energy level, and its parentage informs which atoms/orbitals are contributing to that energy level. Often, DOS plots are partitioned into atomic specific contributions (atom-projected DOS, pDOS) or orbital specific contributions (orbital-projected DOS), providing tremendous amount of insight into the nature of the bands in a material, as well as a lens through which the effects of linker functionalization, compositional substitutions, and interstitial influences may be

assessed.[166,167,231,232] The DOS is computed for all sampled *k*-points, enabling practitioners to examine the DOS at a single *k*-point, or the sum of them. The former can be helpful when MOF bands cross one another in *k*-space and has been used fruitfully in MOF calculations for systems with large unit cells.[233]

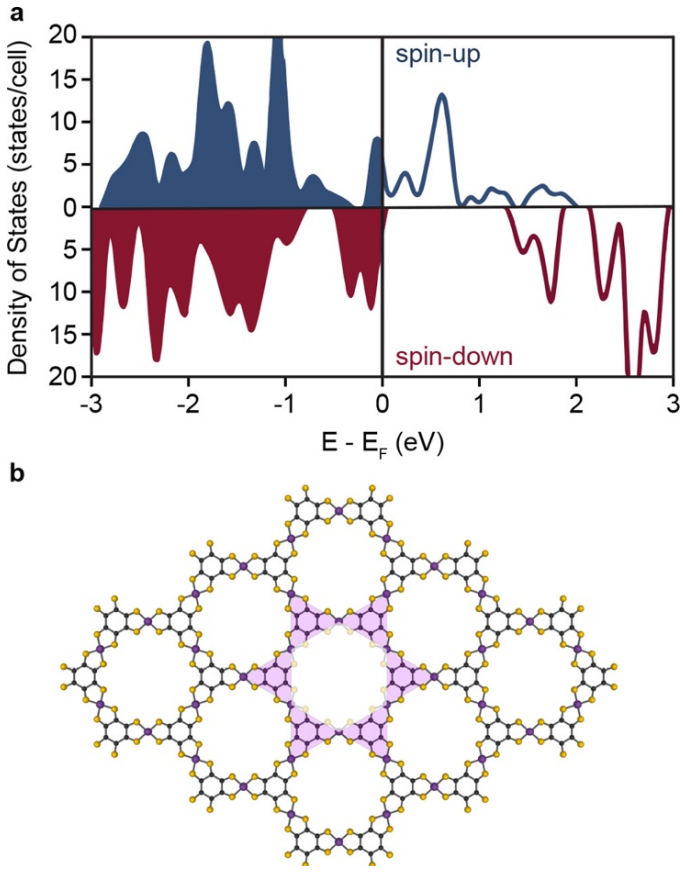

Figure 12. Spin-separated DOS (a) of the $Mn_3(HTB)_2$ Kagome lattice illustrated as the purple shading of the 2D planar $Mn_3(HTB)_2$ supercell (b) show the unique half-metallic property of being a metal in one spin-channel but a semiconductor in the other. Adapted with permission from ref [234]. Copyright 2014 American Physical Society.

In spin polarized materials, the DOS representation may be further partitioned by spin; the spin-refined DOS plot of a $Mn_3(HTB)_2$ (HTB = hexathiobenzene) monolayer reveals that the material is a "half-metal" with a band gap of 1.54 eV in one spin channel with metallic bands in the other, **Figure 12**.[234] Similar behavior was identified for Mn(II)-PBP (PBP = 5,5′-bis(4-pyridyl)(2,2′-bipirimidine)).[235] This knowledge is valuable because the spin bias afforded by the high degree of spin-splitting is advantageous for spintronic devices that require precise control over electron dipole orientation.[236]

DOS plots have also been helpful in determining the directionality of charge transport in conductive MOFs, as will be seen in Chapter 2 of this thesis. Charge hopping is likely the mechanism of electron transport in most MOFs, commonly promoted accessing mixed valency through either partial redox of the metal/linker or via photoexcitation.[237–240] Of the relatively conductive MOFs, those with the largest electrical conductivities typically contain an accessible iron redox couple.[241,242] One of the most conductive 3D MOFs, $Fe(tri)_2$ (tri = 1,2,3-triazolate), undergoes facile oxidation to yield an electrical conductivity enhancement from 10^{-9} to 10^{-1} S/cm.[243,244] From a hybrid GGA calculation, the pristine divalent material is predicted to have a band gap of 4.4 eV; partial oxidation of the framework creates midgap Fe(III) *d*-states seen in the DOS although (the density of these states is proportional to the extent of oxidation), decreasing the band gap to 1.5 eV, **Figure 13**.[241] The same design principle was used in a variety of other Fe containing MOFs, including $Fe_2(BDT)_3$,[233] $(NBu_4)_2Fe^{III}(dhbq^{-2/-3})_3$ (dhbq = 2,5-dioxidobenzoquinone/1,2-dioxido-4,5-semiquinone),[238] and $Fe_2(DSBDC)$ (DSBDC = 2,5-

disulfidobenzene-1,4-dicarboxylate).[245] In all cases, the authors attribute the increase in electrical conductivity to a loosely bound β-spin electron of Fe(II), which acts as the source of the enhanced rate of charge hopping.[246]

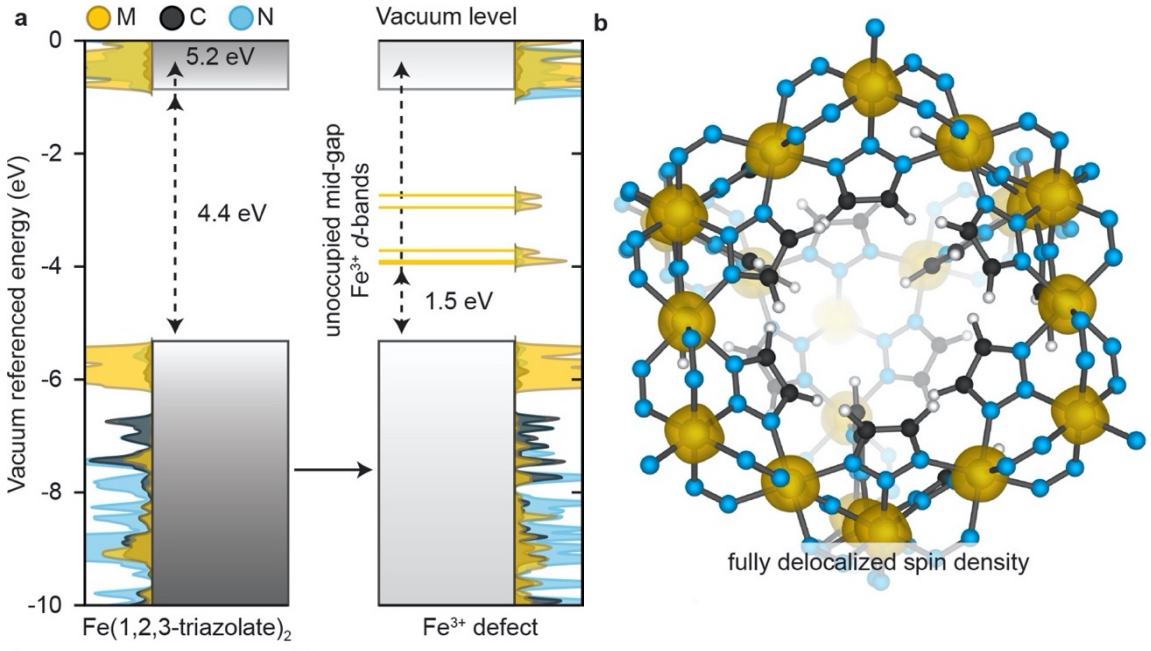

Figure 13. (a) The density of states for the Fe^{2+}-containing MOF, Fe(1,2,3-triazolate)$_2$ features the emergence of midgap Fe^{3+}*d*-bands. (b) The spin-density of the high spin Fe^{3+} defect is fully delocalized over all Fe atoms in the system. Image reproduced with permission from ref [241]. Copyright 2017 Royal Society of Chemistry.

There are also fleeting reports of Fe(III) reduction as a route to installing electron charge carriers (i.e., *n*-type doping). In a landmark publication, $Fe_2(BDP)_3$ (BDP = 1,4-

benzenedipyrazolate)[247] was reduced, enabling Fe(II) charge delocalization that mimics classic $d^{5/6}$ bimetallic molecular complexes.[248] Fractional reduction of $Fe_2(BDP)_3$ with potassium naphthalenide to yield $K_xFe_2(BDP)_3$ ($0 \leq x \leq 2$) accessed nearly a 10 000-fold conductivity enhancement experimentally.[247] Here, the authors performed their calculations on an approximate solid-state system, with the linkers being truncated to their inner-sphere pyrazolates, likely to reduce computational cost (**Figure 14**). Chemical reduction of the framework was modeled with periodic boundary conditions by adding a single electron to a six-iron super cell ($[Fe(pz)_3]_6$), in the absence of a potassium counterion. [247] The concept of ligand n-doping will also be discussed in Chapter 2 of this thesis.

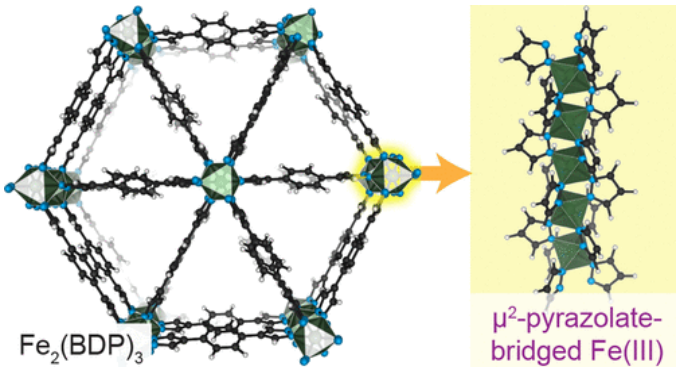

Figure 14. Directionality of charge motion in $Fe_2(BDP)_3$ was exploited in order to generate the electronic band structure and projected density of states for $Fe_2(BDP)_3$ upon elimination of the extended structure in two-dimensions to generate the 2-pyrazolate-bridged Fe(III) so that the 1D interactions that drive electron transport could be examined. Data obtained from ref [247]. Reproduced with permission from ref. [110]. Copyright 2020 American Chemical Society.

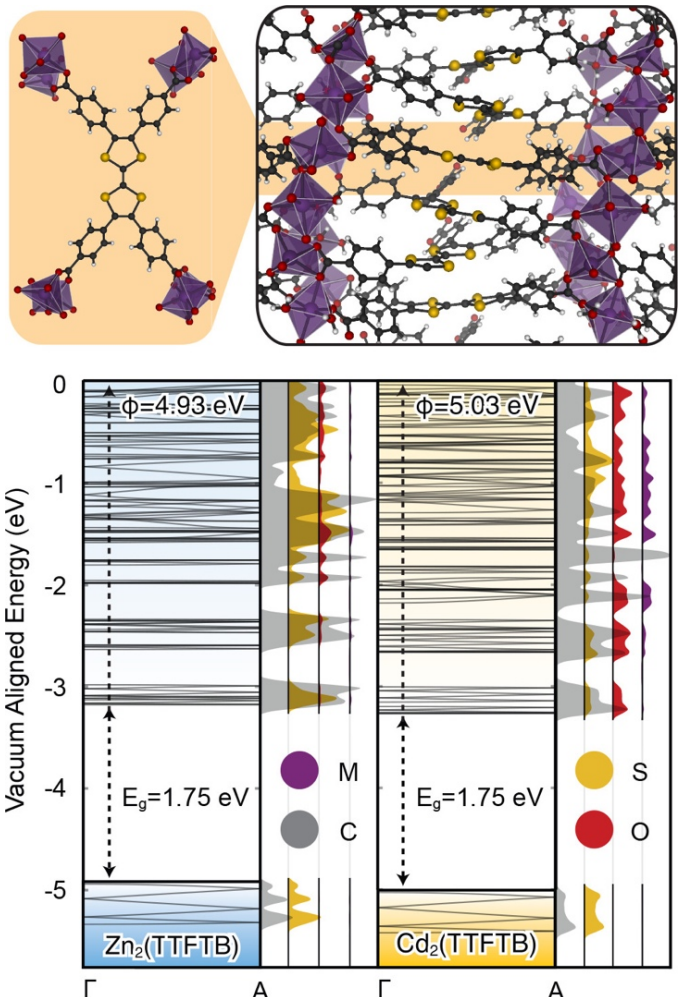

Figure 15. Electronic band structure and correlating density of states for M_2(TTFTB) where M = Zn or Cd shown as gray polyhedral, >300 meV band dispersion of a 6-fold degenerate valence band is observed. Reproduced with permission from ref. [110]. Copyright 2020 American Chemical Society.

Similar computational procedures have been applied to probe the oxidation of organic linkages. The family of M_2TTFTB (TTFTB = tetrathiafulvalene tetrabenzoate)

MOFs[249] have a valence band that is highly delocalized along the π-stacked TTFTB chain, **Figure 15**.[250] The directionality of charge transport was exploited such that only the out-of-plane lattice vector was sampled to assess band dispersion. Upon oxidation, the hole was free to hop along the extended π-stacked pathway. MOFs that feature the same linker but do not crystallize with extended π-overlap, feature much lower electrical conductivity.[251]

Obviously, DOS plots are instructive beyond the paradigm of visualizing possible charge transport pathways. A subtler invocation of pDOS plots was applied to a Ni/Co bimetallic ultrathin MOF nanosheet to indicate electronic coupling between metals.[252] Charge transfer between the metals was deduced visually by comparing the pDOS plots for monometallic Co- and Ni-MOFs and the mixed Co/Ni-MOF. The authors report that electronic coupling across metal centers results in an increase and decrease in the density of unoccupied e_g states for Ni and Co, respectively, due to a balance between electron–electron repulsion and π-donating abilities, **Figure 16**.

In sum, the electronic DOS provides a detailed view of the atomistic contributions to energy levels, which can be quite complex for large chemical systems. Information gleaned from these analyses gives modelers the ability to predict the locality and direction of electron transfer, which are important in catalytic applications. The DOS also helps classify a material as a metal or semiconductor/insulator based on the absence or presence of density at the Fermi level.

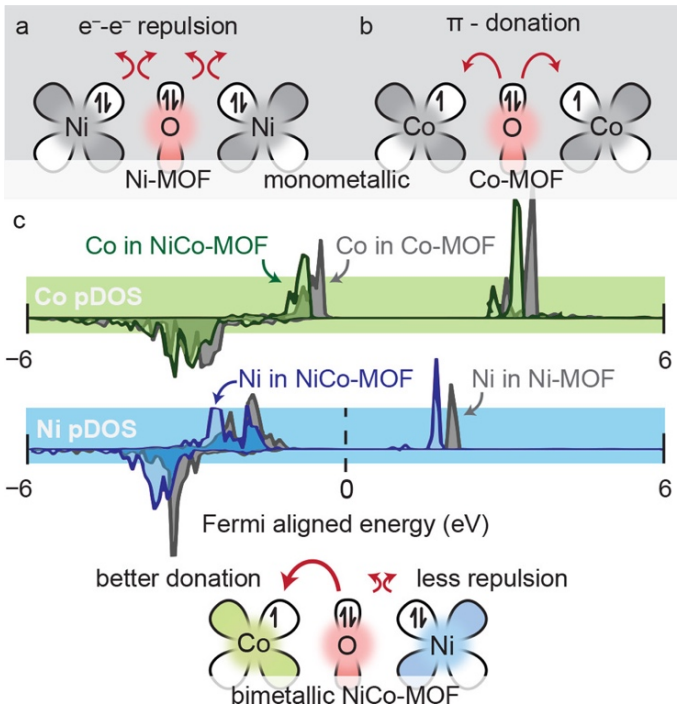

Figure 16. Fermi-aligned DOS of monometallic MOF nanosheets built with (a) Ni and (b) Co revealed the resultant alteration of *d*-state density associated with bimetallic species (c). Ni(II) species experience electron repulsion from inorganic oxo ligands, while Co(II) species experience π-donation from the inorganic oxo ligands. These individual effects behave cooperatively in the bimetallic species; the donation of electron density from oxygen to Co(II) diminishes electronic repulsion from Ni(II). Data obtained from ref [252]. Reproduced with permission from ref. [110]. Copyright 2020 American Chemical Society.

1.3.2 Molecular Modeling Approaches for MOFs

In situations where the bonding between node and linker is highly ionic and their arrangements are not dense, a portion of the framework may be extracted to reduce system size. Given the exponential scaling of computational expense with the number of electrons

in a system, this strategy can be invoked to save time and energy, or to facilitate the use of higher levels of theory. So-called "cluster modeling" is only valid when the property of interest pertains to a distinct active site, such as in the case of catalysis or small molecule adsorption, where MOF truncation will not impact the overall function and simply systematically eliminate bulk stabilization effects. The following subsections will outline the considerations for cluster extraction and geometric equilibration. Further, they will provide literature examples to evidence the functional utility of these procedures and demonstrate the diverse approaches to cluster definition afforded by the incredible variation in MOF composition and topology.

1.3.2.1 Cluster Extraction

Cluster models may be extracted from either experimental or computationally equilibrated structures.[253] Equilibrating the latter structures in their periodic forms prior to cluster extraction significantly improves electronic convergence of the cluster:[160] this is particularly important for MOFs that contain strained metal geometries.[254–256] In both cases, it is then common practice to simulate the pseudorigidity of the MOF by fixing the coordinates of terminal atoms/groups of atoms. However, the process of cluster extraction unquestionably results in the loss of some information, either electronic or steric. The challenge, more broadly, is in the construction of a model that contains the dominant geometric and electronic properties of the system, and modelers are prepared to make some (major) approximations in order to do so. The value of benchmarking cluster models by comparison to extended solids and experimental geometries cannot be understated.[257]

One of the early challenges in cluster extraction is the emergence of negative vibrational modes that correspond to the molecular cluster wanting to relax into a geometry dissimilar to the solid-state. These models often then feature low frequency negative vibrational modes associated with the structure not being in a local minimum. The imaginary frequency may persist after geometric relaxation and can impact the calculation of thermodynamic properties, such as Gibbs free energy and formation enthalpies.[258] The same vibrations may also be found in protocols where a low level of theory is used to obtain an equilibrated structure, followed by applying a higher level of theory to obtain electronic properties.[259–262] Yet each of these are common practices in the modeling community, and while this propagates a small error, it should be systematic if the procedure is applied consistently throughout.[263,264]

One method to eliminate negative frequencies simply and artificially replaces their magnitude with a value that reduces the effect of unphysical modes on the equations of state built using the quasiharmonic approximation.[265] In other words, if we assign these modes to vibrations associated with the formation of the pseudolattice, then we can arbitrarily adjust their contribution. While this is a somewhat crude correction scheme, the energetic implications of large-scale structural distortions are expected to be of much greater magnitude. Persistent negative frequencies associated with modes artificially impacted by model parameters, such as boundary treatment, are often ignored.[266,267] In practice, however, these modes can potentially be eliminated by subsequent optimizations or refining convergence criteria.

Beyond the geometric constraints placed on a cluster model, the other major challenge arises due to bond cleavage from the bulk. Regardless of the size or composition of the cluster model, extraction of an isolated region from an infinite solid will require installation of extrinsic passivating groups, rigidly altering the electronic structure, and sometimes the symmetry of the chemical system.[268] A significant amount of attention is paid to this stage of model development; improper passivation can inadvertently augment the charge of the cluster, the oxidation states of metals and ligands or, in the worst case scenario, cause calculations to oscillate and never converge (wasting both time and resources).[269]

Generally, MOF cluster models are formed by cleaving the material at a remote metal–linker interface (often the weakest bond in the material) and simply passivating the valence through addition of hydrogen (formally $H^{\bullet}$ prior to the self-consistent field routine, Figure 4d).[270] Alternative passivation options include the use of fluorine to emulate the electron withdrawing nature of the Lewis acidic metal cluster[271] or more elaborate orbital capping methods.[272,273] The only real mandate is that if a σ bond is cleaved in the extraction process, then a σ bond must be made in the passivation process. The same is true for other bond types, however cleaving through conjugated networks is generally a bad idea (e.g., it would be ill-advised to approximate an aromatic ring as *cis*-1,3-butadiene). Intuitively, the fewer bonds one cleaves, the less perturbed the electronics will be.

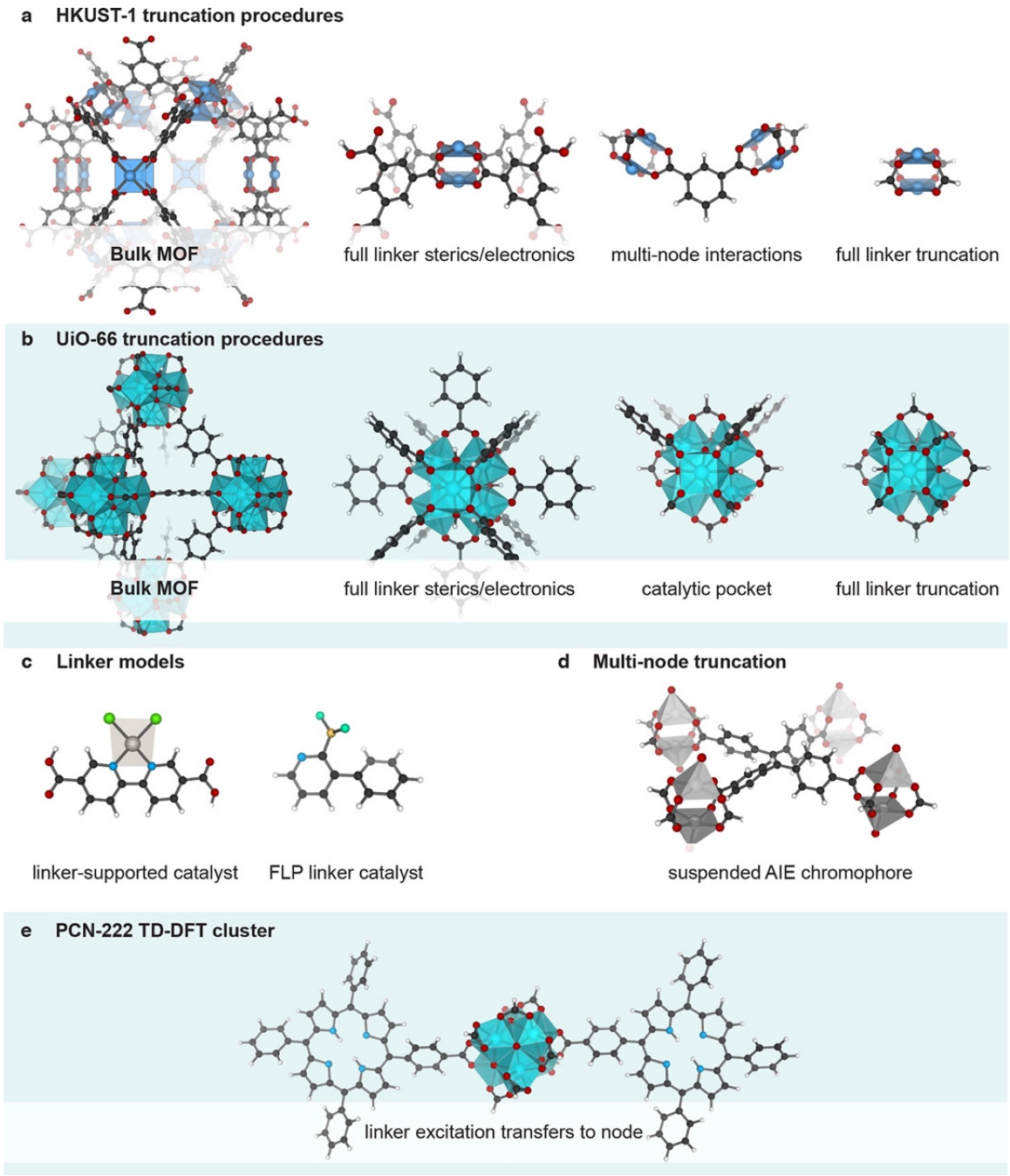

Figure 17. Various clusters used in computations of catalytic and photophysical transformations in MOFs. (a) HKUST-1 has been modeled using a single node passivated with protonated benzene tricarboxylic acid motifs, as well as formates. Furthermore, internode interactions have been captured by truncating to include two nodes. (b) UiO-66

is widely thought to be an ideal support for catalytically active metals by atomic layer deposition onto the nodes surface. There, the electronic structure of the ZrO motifs is relatively unperturbed by formate vs benzoate passivation, and models instead vary based on the extent in which they include the pseudopore created by the benzoate pocket. (c) Some models conjecture that the operative physics and chemistry of the MOF can be described entirely by a free ligand. The simplest cluster extraction is one that yields a free, protonated linker and its appendages. (d) Instances where the electronic structure of the linker is dependent on the chemistry of the nodes truncate to a full linker bound to all inorganic components. (e) Some studies include both complete nodes and linkers, in order to capture photophysical transformations that involve both the metal and ligand. Reproduced with permission from ref. [110]. Copyright 2020 American Chemical Society.

In practice, there is no real universal approach to extracting clusters from MOFs; practitioners will cleave whatever they think best captures the chemistry of the system. However, we can broadly summarize the mentalities arriving at the representative clusters shown in **Figure 17**:

- Approach 1 (intact nodes, the most commonly invoked), includes an explicit node (i.e., the inorganic component in the MOF), and the associated inner-sphere donor atoms from the anions. This approach is widely used because it enables a reasonable description of the operative chemistry at the node, enabling computations of node-supported catalysis[274,275] and gas sorption properties at open metal sites[276,277]

among others discussed below. In these models, the linkers must be neutrally terminated to some discrete approximate of the MOF linker (e.g., BDC approximated as formate, **Figure 17a**). There is some degree of creativity involved in this process because BDC, for example, can be approximated as a formate, a benzoate, or a protonated BDC (**Figure 17a,b**). To determine an appropriate degree of truncation a common practice is to begin with the smallest system (e.g., formate for BDC) and build outward toward inclusion of the full linker and beyond until the resultant analysis stops changing. The success of a given ligand truncation scheme depends on the purpose of the model (e.g., including aromatic motifs of linkers may be useful to simulate the pore environment). A mixed approach to linker truncation is commonly used for inorganic clusters with bulky ligands (such as the catalytic pocket model shown in **Figure 17b**) because the aromatics around the active site may play an allosteric role while remote ligands likely do not contribute to catalytic function, nor do they significantly alter the chemistry of the node.

- Approach 2 (intact linkers), a cluster of a MOF is created such that the complete linker is intact, and the node is accounted for in some creative way. In the simplest example, a linker can be extracted and passivated with protons, **Figure 17c**. Here, the Lewis acidity of the node is obviously poorly accounted for, but its effect may not be overly important (e.g., for studies relating to the geometry of a linker-supported catalytic metal). Full SBUs may be appended to linker termini where their influence controls the properties of interest (e.g., conformational restriction during optical transitions,[278] **Figure 17e**). Other exotic examples may include

complete linkers passivated by approximate nodes (e.g., nodes that are geometrically related to the MOF but contain more simple metals such as switching Fe^{2+} for Mg^{2+})[279].

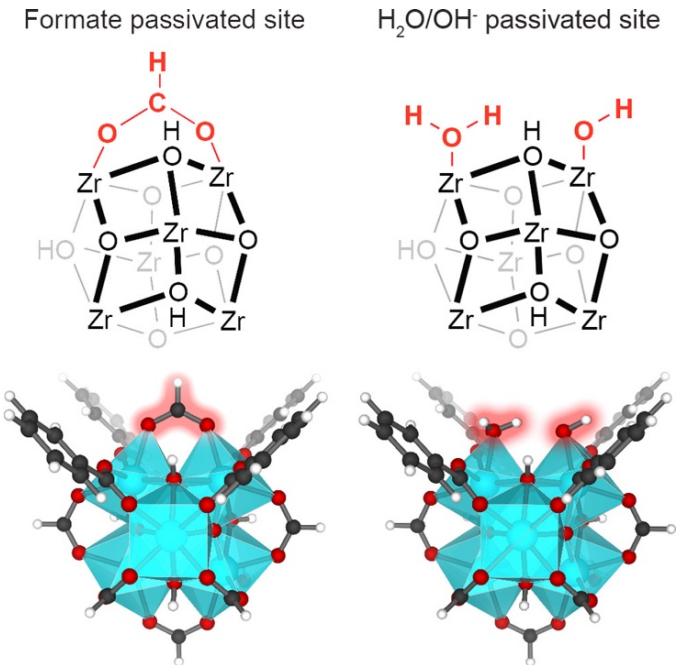

Figure 18: Cluster model of UiO-66 wherein one of the BDC linkers is passivated with a formate or the aqua/hydroxyl pair.[280] Reproduced with permission from ref. [110]. Copyright 2020 American Chemical Society.

Most models follow approach 1, and feature complete nodes passivated by some representative anions. As an illustrative example, the performance of UiO-66 and UiO-66-NH2 for the cross-aldol condensation of propanal with benzaldehyde has been assessed using both cluster and periodic models.[281] The cluster model was composed of one Lewis acidic $[Zr_6(\mu^3\text{-}O)4(\mu^3\text{-}OH)_4]^{12+}$ node, with pendant linkers modeled as formates on the

remote portion of the node, and benzoates on the active half (**Figure 18**). The idea of a mixed ligand model can be thought of as a method to locally simulate a pseudopore environment (i.e., approximating local steric interactions around the site of interest). In a related study, protonation of the active hydrate sites (**Figure 18**) was found to play a critical role in the reaction pathway of Fischer esterification due to the dual Brønsted acidity/basicity of water molecules coupled with the Lewis acid catalytic function of defective Zr(IV) centers.[282]

Naturally, the full linker must be present to study systems where the linker plays an operative role in the chemistry of the MOF (approach 2). In fact, there are both thermal and photocatalytic examples where a cluster model may be a single linker, **Figure 17c**, although inclusion of a complete linker and node are most common, particularly in photoapplications.[278,283,284] These "linker models" are familiar in inert MOF scaffolds that can support catalytically active linkers. For example, biphenyl dicarboxylate (bipydc) linkers hosting catalytically active species that were incorporated in UiO-67 derivatives can be modeled as the free acid with catalytically interesting metals bound through the N-donor, **Figure 17c**. The simulated platinum XANES data of the cluster model matches that of the same catalytic linker incorporating into the MOF indicating that electronic behavior of the linker-metal interaction was not overly affected by framework incorporation.[285–287]

Cluster models can also be used to study photophysical properties if the photoactive motifs are intact. In other words, the frontier states of a MOF may be individually assessed using isolated cluster models, provided there is no charge transfer between the components, i.e., when the valence and conduction band edges of the solid are centered on either the

linker, or separately, the node. However, many MOFs feature ligand-to-metal excitations, and models may even erroneously predict such excitations due to the truncation procedure. For example, a cluster model featuring a single Zr-oxo node suspended by hydrogen-passivated porphyrin linkers was generated to explore the nature of frontier orbitals responsible for photocatalytic oxidative amine couplings, **Figure 17e**.[288] From that model, the lowest unoccupied orbital is dominated by contributions from the Zr-oxo moiety, yet the experimental UV–vis response correlated with linker energetics suggests excited linkers may transfer charge to the inorganic node.

A linker-only model (approach 2) was also used to simulate modified UiO-67 hosting borane frustrated Lewis pairs (FLPs), **Figure 17c**.[289,290] Approximation of the MOF chemistry as a single proton-passivated linker was valid in this case because only the FLP centers were responsible for heterolytic dissociation of H_2 in the hydrogenation of CO_2 to methanol via formic acid.[289]However, the model apparently omitted critical interactions of reagents with the inorganic node; periodic calculations performed to assess the success of the cluster model identified strong interactions between H_2 and the node. As a result, the mechanistic analysis was performed with the climbing-image nudged elastic band (CI-NEB) method with the bulk structure modeled using periodic boundary conditions; however, inclusion of the node in the model may have been important.[290]

Beyond these examples, there have been more extreme cluster extractions designed to include the effects of pore encapsulation. The pore is thought to provide additional physical influence on properties such as site adsorptivity,[291] enantioselectivity,[292] and size selectivity[293,294] as functions of the pore volume, aperture, and composition. In such cases,

a complete description of the pore aperture and/or cage created within may be necessary to explain intrapore reactivity. Such was the case for a borylation catalyst incorporated as the linker of a UiO-67-analogue.[295] The heterogenized system exhibited >99% chemoselectivity toward a monoborylated product, far exceeding the selectivity of its homogeneous counterpart.[294] Gibb's free energy profiles were first recovered from the isolated linker model (**Figure 19d**), but it took the implementation of a large UiO-67-analogue cluster model, containing both the tetrahedral and octahedral pores of the MOF, **Figure 19a–c**, to deduce that selectivity of their catalytic reaction resulted from pore confinement restricting access to the diborylated product rather than local sterics or electronic interactions.[295]

Clearly, the size of a cluster model, i.e., the portion of the framework included in the model, will be different between MOFs of different chemical composition, but it can also vary when attempting to recover different information regarding the same scaffold. For instance, the Cu-dimer paddlewheel node found in Cu_3BTC_2 was approximated to cupric formate to study small molecule binding at its open metal site, Figure 4a, and similar binding energies of small gases were recovered using the cluster model, the periodic model, and experiment.[296] However, the same node required inclusion of complete BTC linkers (passivated with hydrogen) to account for their steric role while modeling a carbonyl-ene reaction.[297] In a different instance, the Knoevenagal reaction of malononitrile and benzaldehyde to 2-benzylidenemalonitrile was modeled at the Cu(II) site.[298] The authors noted the possibility of reagents binding to more than one node, thus two formate-passivated Cu-paddlewheels were included and linked together using a 1,3-benzene

dicarboxylate model of BTC, **Figure 17a**. This cluster was validated by implementing periodic interpolation schemes between intermediates identified through cluster modeling. The cluster model predicted that deprotonation of malononitrile creates a Brønsted acid from one organic linker, and the adjacent Cu(II) Lewis acid facilitates subsequent reaction steps both electronically and through geometric prearrangement. The periodic model, however, showed that adjacent Cu(II) sites from a *third* Cu paddlewheel, not included in the cluster model, provided additional stabilization that reduced the highest activation barrier by ~5 kcal/mol. One might conclude, then, that the cluster model should have included three SBUs for accurate electronic properties, although the mechanism itself was qualitatively constant.

Determining the appropriate extent of linker truncation for a model requires some chemical intuition, but the choice is aided by synthetic design. Modelers have learned a lot about their selection of both cluster models and defect passivating agents by simply examining the modulators used in experiment. Modulators are monotopic ligands with local geometry similar to the linker that primarily aid in prenucleation and organization of the inorganic clusters during MOF synthesis. The resulting crystals may host monotopic modulators that became trapped at the site of missing linkers. Formic acid is a common modulator added to metal-carboxylate mixtures to facilitate crystal growth. Hence, it should not be surprising that one of the most common truncation schemes is the simplification of aromatic carboxylate ligands to pendant formates.[299] The exclusion of phenyl motifs in BDC linkers might raise eyebrows, however formates are routinely found bound to Zr nodes in experiment due to the inherent defective nature of real materials.

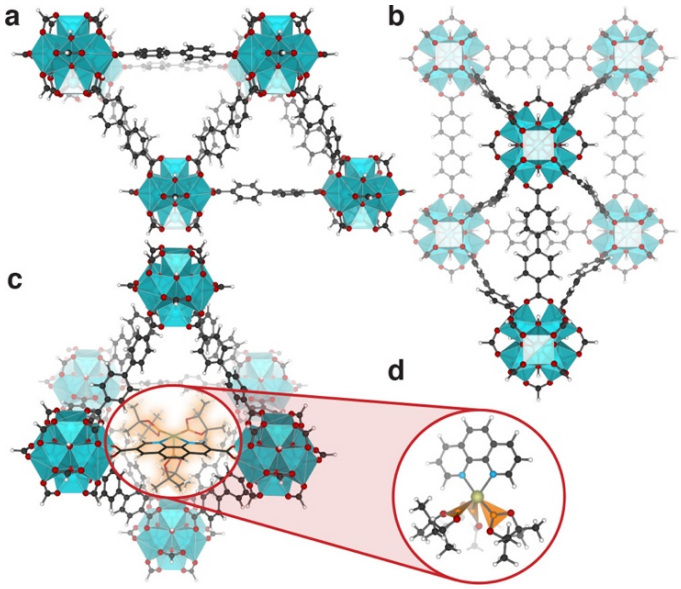

Figure 19. (a) Top and (b) side view of a modified UiO-67 scaffold. The model contained a complete description of both pores, enabling assessment of energetic barriers for product diffusion throughout, which seemingly enhanced selectivity for monoborylated products during catalytic methane borylation; the energetics of reaction pathways were compared with the pore cluster model (c) and linker cluster model (d) and similar reaction coordinated diagrams were recovered. Image adapted from data presented in ref [294]. Reproduced with permission from ref. [110]. Copyright 2020 American Chemical Society.

However, as illustrated by the pairing BDC, tetrakis(*p*-benzoate)pyrene (TBAPy), and BTC with the same Zr_6-oxo node to yield three dissimilar MOFs with increasing node connectivity, metal sites that are not coordinatively saturated can be passivated by hydroxy- or aqua-ligands depending on the charge compensating requirements, **Figure 20**. Linker vacancies are capable of hosting transition metal catalysts.[300–302] These have been widely studied in the UiO-66 and NU-1000 frameworks, which have periodic "defect sites",[303–

[306] while metal appendage to UiO-66 mandates the use of a linker-vacancy model (**Figure 17b**);[301] metals are thought to bind via two bonds formed with node-bound hydroxyls/hydrates.[307–309]

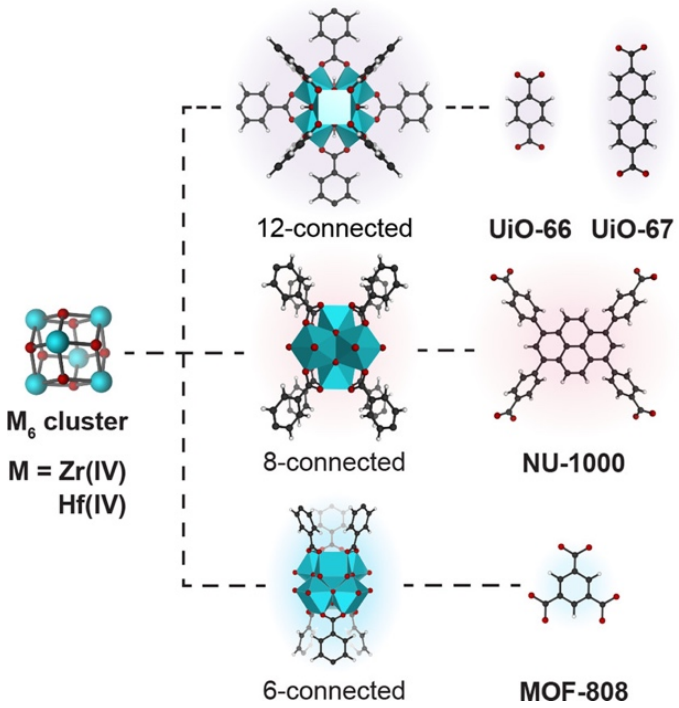

Figure 20: Connectivity of MOFs built from inorganic clusters can be varied by changing the directionality associated with the linker; ditopic BDC ligands create a 12-connected SBU, tetratopic TBAPy ligands form 8-connected SBUs, and triptoic BTC ligands for a 6-connected SBU. Reproduced with permission from ref. [110]. Copyright 2020 American Chemical Society.

Even without appended metals, the nucleophilic node-bound hydrates/hydroxides are thought to be active sites for the hydrolysis of nerve agents. A tremendous amount of

effort has been invested in the topic, and we will highlight a notable example: linker-vacant UiO-66 and MOF-808 models compared for the decomposition of Sarin (**Figure 21**).[309] The energetic pathway obtained from DFT was similar for both systems, yet the relative rates of detoxification experimentally are MOF-808 < UiO-66.[261,291] It was suggested that the mixed aqua and hydroxy coordination sphere in MOF-808 has the greatest capacity for thermal rearrangements to stabilize reaction species through hydrogen bonding.[309] The effect of linker truncation was assessed by comparing these results to a half formate–half benzoate capped model and the largest difference in energy along the reaction pathway was ~1 kcal/mol, bolstering speculations that the openness of catalytic sites on these nodes reduces the significance of linker identity in small molecule transformations, **Figure 21**.

Even if the electronic properties of the cluster remain intact in the extraction procedure, the excluded chemistry may have had an unforeseen operative role in a catalytic cycle. To model reaction conditions, the explicit inclusion of small molecules such as solvent or water may become important.[310] In one case, four explicit water molecules were included in a mixed ligand formate/benzoate cluster model of UiO-66-NH_2 (in addition to an implicit solvation model) to study the hydrolysis of phosphonate ester bonds in chemical warfare agents catalyzed by UiO-66-NH_2.[311] An experimental investigation of zirconia cluster based MOFs showed the presence of amines either in the MOF (UiO-66-NH_2) or the agent VX (*O*-ethyl *S*-diisopropylaminoethyl methylphosphonothiolate) significantly enhances the rate of hydrolytic decomposition.[312] Multiple water molecules were included to assess whether the amino groups were behaving as Brønsted bases to catalyze hydrolysis or passively tuning the hydrogen bonding network to increase the nucleophilicity of water

molecules around Zr(IV).[311,313] The *trans*-benzoate linkers across the active site were aminated, as adopted from the comparative study of UiO-66 and UiO-66-NH_2 for aldol condensation.[281] The transition state barrier for water addition was higher when the activated water molecule was coordinated to the aniline unit rather than the hydroxyl ligands of the node, suggesting the amino group does not electronically participate in the reaction, and is instead active in orienting the nucleophilic water molecules.

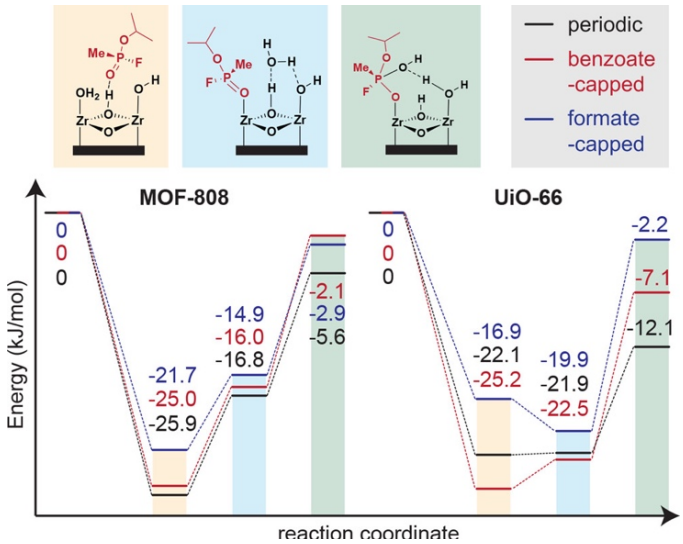

Figure 21. Comparison of free energy profiles for decomposition of Sarin on Zr-oxo nodes in defective UiO-66 and MOF-808 using periodic models and either benzoate or formate-capped cluster models. Subtle differences in predicted reactivity are noted depending on the capping agent used in the cluster model. Image produced from data presented in ref [309]. Reproduced with permission from ref. [110]. Copyright 2020 American Chemical Society.

Indeed, the extent of hydration (e.g., number of linker defects in UiO-66 or coordinated water molecules) can play a determining role in the catalysis.[281,314] Water exhibits a dual role in the hydrolytic reactions with nerve agents, where it functions as a gate-keeper for adsorption by blocking the Lewis acid sites on Zr-oxo nodes, in addition to acting as a nucleophile.[281,282] The necessary and endergonic displacement of water to initiate nerve agent hydrolysis makes its explicit presence an important consideration in these models.[261] Explicit consideration of CO_2 was further shown to hinder nerve agent degradation by preferentially binding to Lewis acidic sites.[315] Further, in the presence of CO_2, H_2O, and dimethyl methylphosphonate (DMMP), carbonate formation is preferred to DMMP decomposition. Although CO_2 prevents the hydrolytic degradation of DMMP on Zr(IV) sites, it was found to facilitate the desorption of its degradation products to regenerate the catalyst. Thus, cluster models concerned with enhancing reactivity or selectivity may benefit from explicit inclusion of small molecules that may be advantageous.

In summary, the process of cleaving and extracting clusters for catalytic modeling is somewhat of a case-by-case process. Depending on the active component, the cluster model may focus on a complete node or linker and additional subunits (e.g., additional nodes or linker components) are included if they play an electronic or steric role. To verify the results from cluster models, values can be compared to calculations performed on the bulk or experimental parameters; transition states and intermediates found from cluster modeling can be confirmed through interpolative procedures described in Chapter 3. The

following sections detail the modeling protocols practitioners employ once they have a cluster model at hand.

1.3.2.2 Geometry Constraints for Cluster Models

While the primary challenge of cluster model extraction is related to the chemistry of the truncation (i.e., how to cut the solid appropriately and passivate the dangling bonds), there are further considerations that must be addressed in order to obtain reliable computational data. The most important of these is how to appropriately geometrically equilibrate the cluster once it has been extracted; omission of the repeating framework provides additional degrees of freedom that may permit the molecular cluster to access conformations unattainable in the constraints of the lattice. To mediate this, geometric constraints are applied to certain atoms or functional groups to mimic the rigidity of a crystalline MOF.

The main objective of a geometric equilibration is to minimize forces on atoms and obtain a stable local minimum energy structure.[259] However, as previously alluded to, occasionally systems are so large that certain atoms must be frozen/fixed in their experimental positions in order to simplify the model; the same protocol is mandated in cluster extraction. Common atomic freezing procedures described herein for subsequent optimizations include freezing the passivating motifs, terminal nodes/linkers, or the *para*-carbons in BDC-containing MOF-clusters, as this still allows the ring face to rotate without expanding the pseudolattice.

As an example, the frozen *para*-carbons in a metal-appended NU-1000 derivative were sufficient to maintain the ligand orientation while studying hydrolysis of the phosphonate ester bond present in nerve agents.[261] The authors employed acetate-capped cluster models to assess the reaction profile for VX and 3,3-dimethyl-2-butanyl methylphosphonofluoridate, assuming the openness of the catalytic site would prevent significant contributions between the reagent and the surrounding linkers. No constraints outside of frozen *para*-carbons were applied to this cluster yet the directionality of the framework appeared to be maintained, pointing to the geometric rigidity of the Zr-oxo nodes. In a different study, benzoate linkers were employed to study the degradation of methylparaxon on the NU-1000 node.[316,317] The hydrogen atoms *para* to the carboxylate were again kept fixed, and reasonable quantitative agreement was found between theory and experiment. In sum, freezing a *para*-positioned atom does allow for ring rotation, while preventing distortion of the pseudolattice.

Maihom, Limtrakul, and colleagues examined CO oxidation of N_2O on HKUST-1 analogues (M_3BTC_2, M = Cr, Fe, Co, Ni, Cu, and Zn).[318] The model included four BTC linkers bound to one cupric paddlewheel, and the terminal carboxylic acid protons were kept fixed. In this case, the ligands were unlikely to deform throughout the reaction. However, this example serves as particularly pedagogical: one can imagine a circumstance where a reaction pathway involves major distortions to the active metal site that may be stabilized by improperly allowing the ligands to unbind throughout or artificially expanding/contracting the coordination bond lengths.

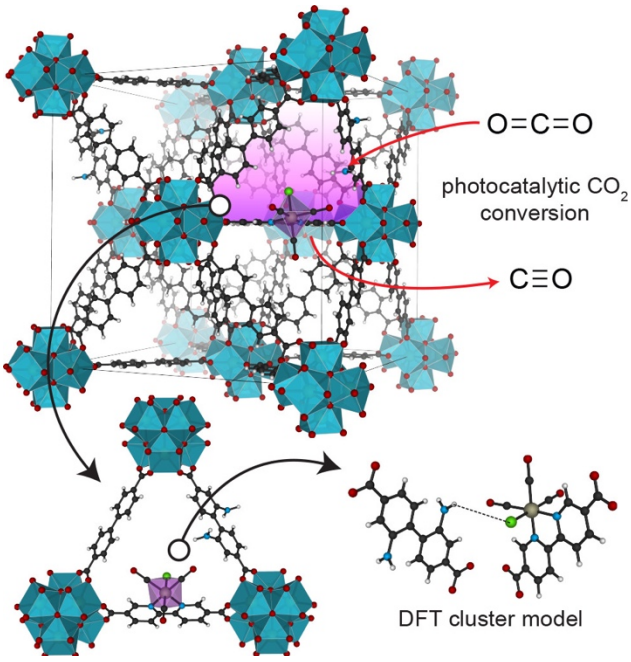

Figure 22. Isolation of the target clusters from a mixed-linker UiO-67 derivative bearing aminated and catalyst-loaded linkers; linker arrangement was maintained without directionality imposed by inorganic components by constraining carboxylate oxygens.[319] Reproduced with permission from ref. [110]. Copyright 2020 American Chemical Society.

Finally, in perhaps the most extreme application of atom constraints, a study by Ryu, Kim, Choi, Kang, and colleagues featured a linker-bound catalyst, $ReI(CO)_3$(2,2′-bipyridine-5,5′-dicarboxylate), which performed CO_2 reduction. The photocatalytic response of the MOF was observed to increase with the concentration of aminated-bpy linkers,[319] and EXAFS revealed bonding interactions between the amine-functionalized linkers and catalytic linkers that indicated ligand cooperativity. A creative cluster model featuring the catalyst linker complexed with an amine-based linker in close proximity was

taken from the experimentally refined crystallographic structure to explore the energetic reaction profile, **Figure 22**. To model framework rigidity, the carboxylates were constrained throughout the study. Indeed, this is an excellent example of a *model*: the operative chemistry was captured in their "cluster", even though its construction is somewhat esoteric.

In sum, there are numerous combinations of optimization and truncation protocols one could follow, and it is not immediately clear which yields the most reliable results. Indeed, the best solution depends on the chemistry of each framework, and the purpose of the model; it is thus difficult to be prescriptive, and once again benchmarking schemes comparing relative cluster model sizes, ab initio, or experimental data is strongly encouraged. Still, the breadth of modeling capabilities available to molecular models is worth the structural simplifications because the electronic insights gleaned from extensive and high-level studies build design principles that guide MOF developments in every field in which they are applied.

1.4 Bridge

Clearly, the methodologies applied to MOFs are as diverse as their chemistry. In Chapter 2, which pertains to electronic conductivity (the most material-like behavior of MOFs), all studies invoke periodic boundary conditions to capture the long-range bonding order that facilitates charge transport throughout the scaffolds. Each of the MOFs investigated have dense arrangements of aromatic linkers joined through π-orbital overlap that give rise to dispersive electronic bands along the k-vector associated with that

crystallographic direction. However, in the case of 2D graphene analogs, this is supplemented by in-plane conjugation between the metals and linkers such that even monolayers must be described within solid-state modeling paradigms. The metallic nature of these species enables the recovery of electronic band structures using the GGA functional, PBEsol; however, the accurate assessment of charge-hopping regimes in gapped materials requires the use of a hybrid functional such as HSEsol06.

In the case of catalytically active MOFs (discussed in Chapter 3) the scaffolds of interest have large pore volumes to facilitate mass transport and strongly ionic interfaces that give rise to localized electronic bonding. The photocatalytic studies described at the beginning of Chapter 3 also necessitate an accurate recovery of the electronic band gap. This means periodic boundary conditions must be used to account for the effects of increasing dimensionality, and the hybrid functional HSEsol06 is used so the difference in energy between occupied and unoccupied states is not underestimated. Conveniently, the associated redox reactions for photoactive scaffolds can be viewed through a thermodynamic lens such that clunky transition state algorithms can be foregone. However, the study pertaining to thermal catalysis in Ni(II)-MFU-4*l* presented later in the chapter adopts cluster modeling procedures to facilitate comprehensive transition state analyses and consideration of multiple competing pathways. For the cluster models, a meta-GGA functional (M06-L) is invoked, but periodic models using the GGA functional PBEsol are instituted as a benchmark to ensure the energetic of ordering of intermediate geometries is only systematically perturbed by model truncation.

The MFU-4*l* scaffold is also studied in Chapter 4; the coordinatively unsaturated Zn(II) metal site undergoes post-synthetic cation metathesis to achieve high catalytic activity, but inorganic ligand exchange to achieve gas adsorption behavior that mimics an enzymatic active site. Similar cluster models are invoked for both studies due to the localized nature of the properties in question, which occur at pore-isolated active sites on nodes that are electronically insulated from one another. Subsequent studies in Chapter 4 describe post-synthetic inorganic ligand exchange that function as structural motifs in a 1D nodal chain. These studies adopt periodic boundary conditions because altering the primary coordination sphere of the metal atoms corresponds to long-range structural perturbations that can only be captured by accounting for the extended structure. Further, an accurate description of the pore is necessary when considering pore-filling dynamics.

Despite their disparate structure, bonding, and function, each MOF probed throughout this thesis is a piece of a larger puzzle. The real questions being posed, and answered, herein being: when are MOFs greater than the sum of their parts, and how do we intuitively combine organic and inorganic building blocks to achieve electronic structures that facilitate a desired function. In each investigation reported hereafter, computational models are built and used to obtain key insights into the electronic structure of the MOFs in question. In turn, the model parameters and resultant findings inform future computational modeling endeavors and the construction of design principles that will help the enhance MOF functionality for each purpose described.

CHAPTER II

MATERIALS WITH DISPERSIVE ELECTRONIC BANDS

Chapter II of my dissertation pertains to the most conventional treatment of MOFs as solids. Charge transport pathways are explored using traditional condensed matter physics concepts including the construction of electronic band structures and atom- or orbital-projected DOS plots. These graphical representations of electronic structure help to understand the chemistry of conduction pathways and which components give rise to conductive bands near the Fermi level of metallic MOFs (Section 2.2), or valence and conduction bands of semiconducting MOFs (Section 3.3). This chapter begins with an introduction to the solid-state modeling procedures invoked for the investigations in the subsequent subsections that is excerpted from my first author published literature review, *Chemical Reviews,* **2020**, *120*, 8641-9715. Section 2.2 also contains previously published work, *Nature Materials* **2021**, *20*, 222-228, which was co-authored by experimental collaborators Jin-Hu Dou, Maxx Q. Arguilla, Yi Luo, Jian Li, Weizhe Zhang, Lei Sun, Luming Yang, Tianyang Chen, Lucas R. Parent, Grigorii Skorupskii, Nicole J. Libretto, Chenyue Sun, Min Chieh Yang, Phat Vinh Dip, Edward J. Brignole, Jeffrey T. Miller, Jing Kong, Junliang Sun, and Mircea Dincă, and my PI Christopher H. Hendon. There we explore structure-property relationships for charge transport in 2D MOF graphene analogs

using single crystal data in combination with theoretical crystal structure analysis. Section 2.3 also contains previously published work, *Chemical Science* **2019**, *11*, 1342-1346, co-authored by experimental collaborators Hanna C. Wentz, Grigorii Skorupskii, Ana B. Bonfim, Evan H. Oriel, Graham T. Sazamad, and Michael G. Campbell as well as my PI Christopher H. Hendon. There we see how MOF crystallinity can be used to develop charge transport pathways through the alignment of redox active organic motifs. Experimental details and discussion from the articles detailed in Section 2.2 and 2.3 can be found with the supporting information in Appendix A and B respectively.

2.1 Fundamentals of Charge Transport in Molecular Solids

The ionic metal-organic interface that results in localized bonding throughout bulk MOFs and benefits the aforementioned applications of as adsorption, catalysis, and charge storage, can be tuned through the spatial and energetic overlap of metal and linker orbitals. Towards this end, a compelling family of MOFs is the 2D graphene analogs composed of square planar divalent metal centers and hexasubstituted, tritopic organic linkers that yield π-d conjugation in the plane of connectivity and π-π interactions between the layers. These band-type transport materials have been tuned through heteroatom and metal variations to provide porous electrode materials with conductivities rivaling conventional materials but with superior tunability. The studies detailed below will explore the structure-property relationships associated with enhanced conductivity in these materials and alternative strategies to induce charge transport in formerly insulating materials based on component pre-organization and redox active components.

2.1.1 Recovering Electronic Band Structures

Electronic band structures (EBSs) are a plot of electronic energy as a function of *k*-space (i.e., electron momentum). The shape of the bands provides tremendous amounts of information about material properties, including the potential to transport charges, overall material stability and, to the trained eye, even the composition. Given that MOFs are self-assembled from discrete molecules, it is somewhat unsurprising most feature localized (i.e., flat) electronic bands that facilitate the use of cluster models. However, through development with a complement of experiment and theory, there are increasing examples of MOFs featuring curved (i.e., dispersive) bands and interesting MOF applications that rely on the description of bulk electronic structure. Thus, this section will discuss the calculation and implications of MOF electronic band structures.

The electronic band structure is simply constructed by sampling the energy of electrons at various *k*-points. The difference in energy between the bottom and top of the band at two dissimilar *k*-points is referred to as the bandwidth, or band dispersion, and is essentially a measure of the "curviness" of the bands. Higher band dispersion means more mobile charge carriers and also indicates something about the extent of orbital overlap and long-range interactions in that crystallographic vector. Because these plots ultimately depict electron momentum, the second derivative of a band near a high symmetry *k*-point (sometimes called special points) yields the effective mass of a charge carrier in that band.

Perhaps it is somewhat intuitive that a highly symmetric crystal would feature a large degree of electronic degeneracy within the unit cell; it is less intuitive to imagine how crystal symmetry affects the bulk electronic properties, i.e., those that extend beyond a

single computational cell. As mentioned in the previous section, the material should be properly equilibrated using all of the high symmetry *k*-points in addition to a dense grid between them. Practically, however, this is often impossible, but also unnecessary; generally flat-banded materials (like MOFs) can be described with Γ-only sampling because the insulating interface between the metal and ligand is sufficiently accounted for by explicit orbital interactions within the computational unit cell.[21,320,321] It is, however, typically good practice to sample all labeled high symmetry *k*-points for the given space group,[135,322,323] as presented in the *Bilbao Crystallographic Server*,[131] ensuring that the total energy has included all important long-range interactions.[324]

Although the chemical connectivity in MOFs is usually highly symmetric, MOFs themselves have highly anisotropic electron density through the crystallographic unit cell: there are pores! Thus, it is expected that the electronic band structures should contain some interesting information, albeit subtle, arising from the periodic absences of electron density. Indeed, one paradigm in the conductive MOF literature is whether the charge carriers are more delocalized through-space or through-bonds.[325,326] The band structure sheds light on this. Consider two similar scaffolds made from π-stacked triphenylene-based linkers: in the case of Ln(hexahydroxytriphenylene), the inorganic nodes form continuous ionic bonds throughout the material,[327] whereas in $Ni_3(HITP)_2$ the sheets are nonbonded. In both cases, the greatest band curvature is found to be centered on the linker, but associated with the out-of-plane direction. In other words, the conductivity mode is "through space". [325,326] The delineation of "through-bond" or "through space" should not be confused with that between band or hopping conduction, which are separate

mechanisms that can be distinguished by the presence of an activation energy associated with the conduction. [325,326,328,329]

Electronic band structure calculations primarily serve to graphically identify crystallographic directions in which electrons are highly delocalized and strongly interacting. Such plots contain a significant amount of information when paired with the crystal structure and a map of the high symmetry *k*-points for the MOFs parent space group. The analysis can be further complimented by quantitative analysis of the electronic band dispersion (a concept we have already introduced), and most importantly, the density of states.

2.2 Crystallization and Structure-Property Relationships for 2D MOFs

Imparting conductivity to MOFs, previously considered as insulating materials, provides new opportunities for materials research and facilitates applications that harness both porosity and electronic delocalization in extended crystalline lattices.[330–335] The unusual combination of porosity and excellent conductivity in MOFs with 2D π-conjugation has led to the development of a variety of potential applications, ranging from batteries[336–338], supercapacitors and fuel cells[339–341] to electrocatalysts[342] and chemiresistive sensors[343]. To develop 2D π-conjugated MOFs with chemically addressable electrical properties and/or redox activities, it is important to grow large single crystals[344,345], which facilitate single-crystal electrical device fabrication and atomic-resolution structural characterization by diffraction techniques—both of which are critical for understanding how physical properties relate to structure. Nonetheless, to date, 2D MOFs with well-resolved crystal structures remain scarce[330]; most, if not all, of these

MOFs can only be obtained as nanocrystalline powders that also exhibit heavily disordered interlayer stacking[326,332,346,347]. Typically, the structures of 2D π-conjugated MOFs cannot be determined rigorously; instead, they are simply implied by matching experimental powder X-ray diffraction (PXRD) patterns with those simulated from hypothesized models[331,348]. This status quo does not provide any information on the stacking sequence of the 2D layers or on the content of the pores. The lack of studies on single-crystal structures has significantly impaired the determination of structure−property relationships that drive the materials discovery process and are critical for the continued development of this class of porous conductors.

2.2.1 Ligand Design Strategy for Single-Crystal Growth

Controlling crystal growth in 2D conductive MOFs is difficult because in-plane growth (that is, growth in the *ab* plane) requires continuous formation and breakage of strong metal–ligand bonds, whereas growth normal to the covalent sheets (that is, in the *c* direction) is governed by much weaker π-stacking interactions. Because the latter are much more reversible, they usually dominate growth but are too weak to enforce long-range translational symmetry, causing severe stacking disorder. Consequently, these materials exhibit long needle- or thread-like morphology, with severely stunted in-plane growth such that the *ab* dimensions of typical MOF crystallites rarely exceed several hundred nanometres. Crystal growth in these systems is further complicated by the unusually complex chemistry. Indeed, MOFs in this class are often the result of reactions involving four components: the protonated organic ligand, a metal-ion source, a base that

deprotonates the ligand in situ, and an oxidant that oxidizes the ligand in situ. Traditional strategies for controlling crystal growth in such systems involve systematically changing the reactant concentration or order of addition, or controlling the reaction temperature and time. Nevertheless, these approaches do not fundamentally alter the anisotropic growth directions of a given crystallite and have yielded only marginal improvements in the crystal dimensions.[349]

Instead of relying on these traditional methods for controlling crystal growth, we sought to fundamentally rebalance the in-plane and out-of-plane growth of conductive 2D MOFs by altering the ligand electronic structure (**Figure 23a**). The molecular and electronic structure of the ligand core influences both the in-plane crystal growth, by modifying the nature of the metal–ligand bond, and the π-stacking between the 2D sheets. For this particular class of 2D conductive MOFs, we hypothesize that a large, electron-deficient ligand core with reduced electron density at the metal-binding site will increase the acidity of the metal-binding functional group, resulting in a more pronounced reversibility of the metal–ligand bond and higher in-plane crystallinity. These design principles are exemplified by the ligand 2,3,7,8,12,13-hexahydroxytetraazanaphthotetraphene (HHTT) (**Figure 23a**; see Appendix A for synthesis). The choice of this ligand is inspired by concepts in organic electronics, whereby enlarging the π-conjugation and embedding heteroatoms into the backbone result in stronger non-covalent interactions between adjacent molecules.[350–353] Here, the tetraazanaphthotetraphene core features a larger π-conjugated plane than the triphenylene core (such as in 2,3,6,7,10,11-hexahydroxytriphenylene, HHTP) in archetypical 2D MOF

ligands, which should favor stronger inter-ligand interactions and more ordered π-stacking, as demonstrated in closely related organic π-based systems.

To assess the relative electronic structures of HHTT and HHTP we invoked molecular models of the acid form of both linkers. The geometry optimizations for the ground and charged states were performed using DFT as implemented in Gaussian09 at the B3LYP/6-31G** level. The electrostatic potential (ESP) maps of the molecules were calculated with an isovalue of 0.0004 from the total electron density obtained at the same level of theory. As can be seen in **Figure 23a**, the three peripheral pyridinic nitrogen atoms in HHTT significantly decrease its electron density and consequently lower the energy of the lowest unoccupied molecular orbital (LUMO) relative to that of HHTP. This should increase the acidity of the catechol groups in HHTT relative to HHTP and is similar to why more acidic carboxylates yield more crystalline MOFs than less acidic triazoles and pyrazoles[354]; the former should promote higher crystallinity in the *ab* plane.

Our hypothesis is further substantiated by calculations that specifically compare the pK_{a1} values of HHTP and HHTT. Following previously a previous published procedure[355,356], we computed the pKa for catechol, HHTT, and HHTP using the hybrid functional B3LYP with the larger basis set 6-311+G**. The neutral and deprotonated models were optimized in both the gas phase and aqueous phase using the conductor-like polarizable continuum (CPCM) solvation model with the dielectric of water. Gibbs free energy was then computed using **Equations 17-19**, the terms in which correspond to the arrows in **Scheme 1**. The concentration of water is defined as 1 mol/L, hence, log[H_2O] is

zero. To benchmark our methodology, we compared our computational pKa of catechol (9.33) to the experimental value (9.45) and find the error to be less than 1.3%.

$$\Delta G_{sol} = \Delta G_g + \Delta G_{solv}(A^-) + \Delta G_{solv}(H_3O^+) - \Delta G_{solv}(HA) - \Delta G_{solv}(H_2O) \quad \text{Eq. 17}$$

$$pK_a = \frac{\Delta G_{sol}}{1.364} - \log [H_2O] \quad \text{Eq. 18}$$

$$pK_a(corrected) = pK_a(calculated) - 4.54 \quad \text{Eq. 19}$$

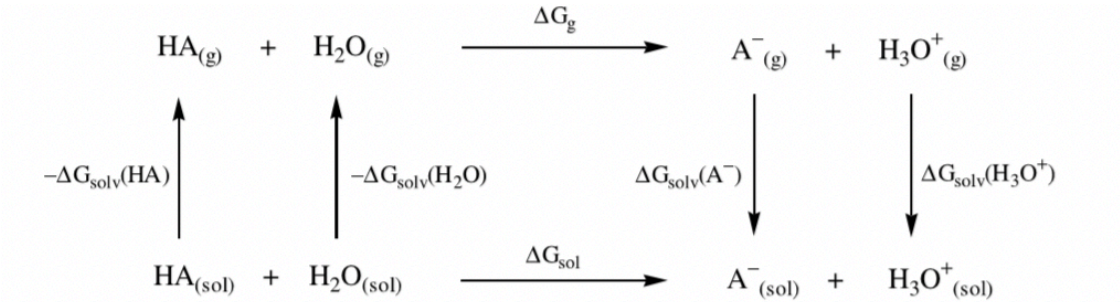

Scheme 1. Thermodynamic cycle corresponding to Equation 1 for the calculation of pKa values using DFT.

Using the above methodology to compute theoretical pKa values for HHTT and HHTP we predict that the latter (pK_{a1} = 6.06) is one order of magnitude more acidic than the former (pK_{a1} = 7.39). Therefore, the HHTT core should promote a higher degree of both in-plane and out-of-plane crystallinity (**Figure 23b**). Further modulation of the interlayer interactions should be possible by employing different metal ions that prefer either square-planar or octahedral coordination. The latter prefer axially coordinated solvent molecules whose hydrogen bonding interactions compete with π-stacking and facilitate additional

dynamic crystallization to limit crystal defects[357]. We optimized and investigated the three core parameters, namely precursor concentration, solvent identity, and reaction temperature, to exploit the advantages of the HHTT ligand in terms of improving the size and degree of crystallinity of the resulting 2D MOF (App. A Table A1).

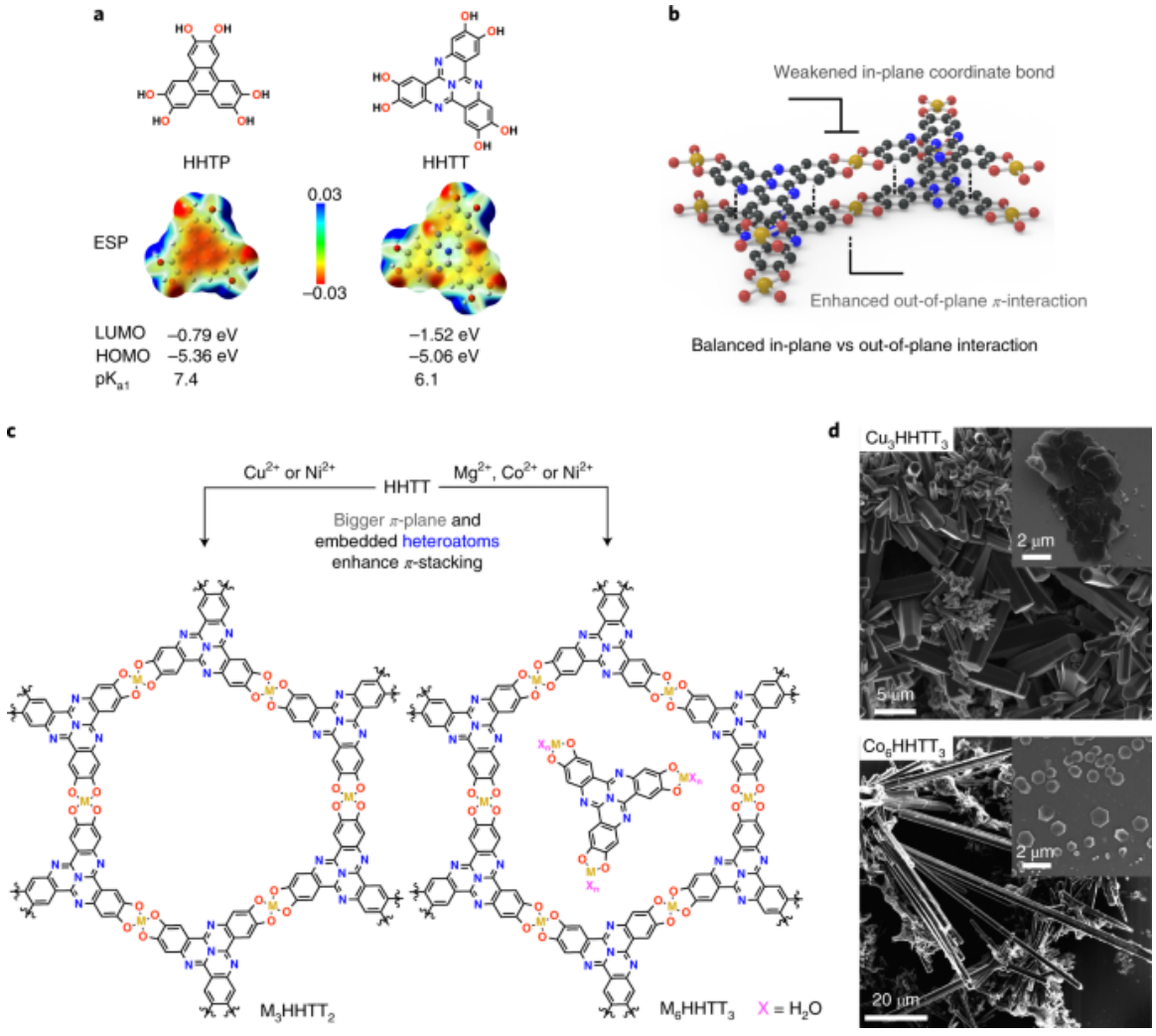

Figure 23. Design strategy and synthetic conditions for the growth of single crystals of 2D MOFs. (a) Chemical structures of HHTP and HHTT with electrostatic potential (ESP) maps and computed pK_{a1} values. Computed energy values (referenced to vacuum)

of the highest occupied molecular orbital (HOMO) and lowest unoccupied molecular orbital (LUMO) of HHTT and HHTP highlight the more electron deficient character of the former. (**b**) Schematic illustration of the conductive 2D MOF stacking lattice. **(c)** Molecular design strategy for creating porous and dense 2D MOFs. Axially coordinating water molecules in M_6HHTT_3 are omitted for clarity. **(d)** Scanning electron microscopy (SEM) micrographs of Cu_3HHTT_2 and Co_6HHTT_3 that can be isolated on-demand with either rod- or plate-like (inset) morphology by varying the synthetic conditions (see Methods in Appendix A).

Reactions of HHTT with a variety of divalent metal ions in mixtures of *N*,*N*-dimethylformamide (DMF) and water produce a family of 2D π-conjugated MOFs, M_mHHTT_n ($m = 3$, $n = 2$ for Cu^{2+} and Ni^{2+}; $m = 6$, $n = 3$ for Co^{2+}, Mg^{2+}, Ni^{2+}; see **Figure 23c**). Single crystals exhibiting rod- or plate-like morphology and ranging in size from 5 μm to 200 μm can be grown for all five materials, with the structural type correlated with the preferred geometry around the metal ion (**Figure 23d**, See App. A, Table A1, Fig. A9). The high quality and relatively large size of the crystals facilitated atomic-resolution structural analysis by single-crystal X-ray diffraction (SXRD), continuous rotation electron diffraction (cRED) and high-resolution transmission electron microscopy (HRTEM), which can all be found in Appendix A.

2.2.2 Structural Details of M_3HHTT_2 Crystals

Metals that prefer square-planar coordination yield 2D honeycomb sheets with the formula M_3HHTT_2 ($M = Cu^{2+}$ or Ni^{2+}), which feature eclipsed packing and vacant pores. Structures refined through cRED experiments provided an excellent starting point for geometric equilibration with DFT. Experimentally, it was determined that these sheets stack in perfectly eclipsed AA fashion. To corroborate this result and benchmark our model parameters, full geometric and electronic equilibration of periodic Cu_3HHTT_2 models with AA and AB stacking in both ferromagnetic (FM) and antiferromagnetic (AFM) ordering of the metals between the sheets was performed. These calculations were performed in the Vienna *ab-initio* Software Package (VASP) using a projector –augmented plane-wave basis with a 500 eV plane-wave cut-off. All structures were initialized using the atomic coordinates obtained for the primitive cell using cRED and geometrically equilibrated with the GGA functional PBEsol using electronic convergence criteria of $1x10^{-6}$ eV and a *k*-grid of 2x2x4. The results found that AA stacking with AFM coupling between the sheets to be lowest in energy, consistent with experiment (Appendix A).

Although the exact stacking sequences in other 2D conductive MOFs are unknown, perfectly eclipsed AA stacking is considered rare. Here, it likely results from the enhanced π-stacking interactions between HHTT cores in neighboring sheets. A more convincing indication of the strong π-stacking in Cu_3HHTT_2 is the unusually small interlayer distance of 3.19 ± 0.02 Å. This interlayer distance is shorter than that in any other 2D MOF and is even shorter than the stacking distance of graphene sheets in natural graphite.[327] Due to the success of our linker design, a cofacial stacking arrangement and

high degree of crystallinity give rise to a Brunauer–Emmett–Teller (BET) apparent surface area of of $1{,}360 \pm 20\ m^2\ g^{-1}$, as determined through N_2 adsorption isotherms, which is considerably higher than those reported for other 2D conductive MOFs, and is in line with the slightly larger pore size of this material.[326]

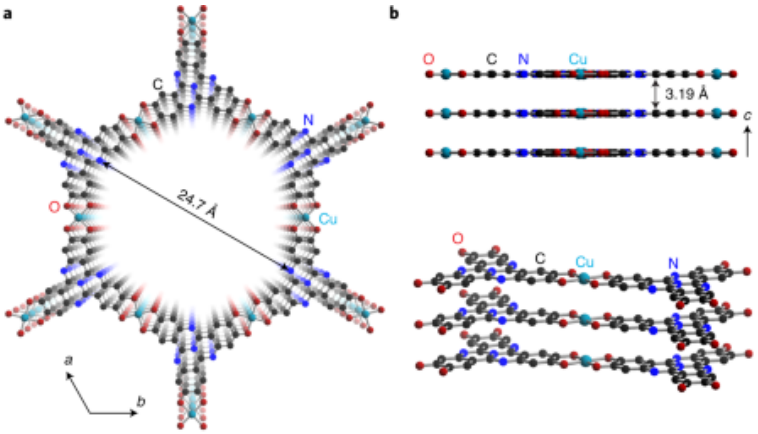

Figure 24. **(a)** A portion of the Cu_3HHTT_2 crystal structure along the *c* direction. **(b)** Views parallel to the *ab* plane. Hydrogen atoms are omitted for clarity.

2.2.3 Guest Molecule Inclusion in Crystals of M_6HHTT_3

Metal ions that do not easily accommodate a square-planar geometry, instead preferring octahedral coordination, form similar SBUs with two equatorially oriented catechol groups, but also feature axially coordinated water molecules and give materials with the formula $[M_3(HHTT)_2(H_2O)_6 \cdot M_3(HHTT)(H_2O)_{12}]$[330] ($M_6HHTT_3$, $M = Co^{2+}$, Mg^{2+} and Ni^{2+}) (**Figure 25a**). Despite coordination to only one catechol group, the cobalt centers in the guest molecules share a similar $[CoO_6]$ SBU. As a representative example, single crystal x-ray diffraction of Co_6HHTT_3 crystals and the corresponding computational

structural optimizations reveal that the axial water molecules disrupt the π-stacking observed in Cu_3HHTT_2, increase the interlayer spacing to 3.2–3.3 Å (**Figure 25b**) and cause slippage of the 2D honeycomb M_3HHTT_2 sheets into a staggered ABC packing motif (**Figure 25c**). The staggered packing eliminates the 1D pores, and the remaining open space is occupied by well-defined $Co_3(HHTT)(H_2O)_{12}$ clusters centered in the hexagonal pockets defined by the 2D sheets (**Figure 25a,c–f**). These molecular clusters have no direct bonding with the extended framework sheets (**Figure 25a**) but engage in extensive hydrogen bonding interactions with neighboring MOF layers (**Figure 25c**).

The ability for Ni^{2+} to form both square-planar and octahedral complexes with medium-weak oxygen donor ligands allows for synthetic control of the crystal growth product using a DMF:H_2O solvent continuum. DMF is more effective in disrupting the strong π-stacking between the sheets than water.[358] Indeed, the reaction between Ni^{2+} and HHTT in the presence of DMF (App. A Table A1) yields large crystals of Ni_3HHTT_2 that are identical to Cu_3HHTT_2 and retain the close interlayer spacing of 3.19 Å. In the absence of DMF, Ni^{2+} and HHTT form $[Ni_3(HHTT)_2(H_2O)_6 \cdot Ni_3(HHTT)(H_2O)_{12}]$ (Ni_6HHTT_3), a dense network that is essentially identical to Co_6HHTT_3 with only small variations stemming from the difference in interlayer interactions owing to hydrogen bonding and the solvent content. Having access to both crystal structures with Ni^{2+} allows use to establish structure-property relationships with metal identity as a controlled variable. The behavior of Ni^{2+} in this system establishes the identity of the metal ion as an important variable in defining the stacking sequence in 2D conductive MOFs in addition to the molecular and electronic structure of the ligand.

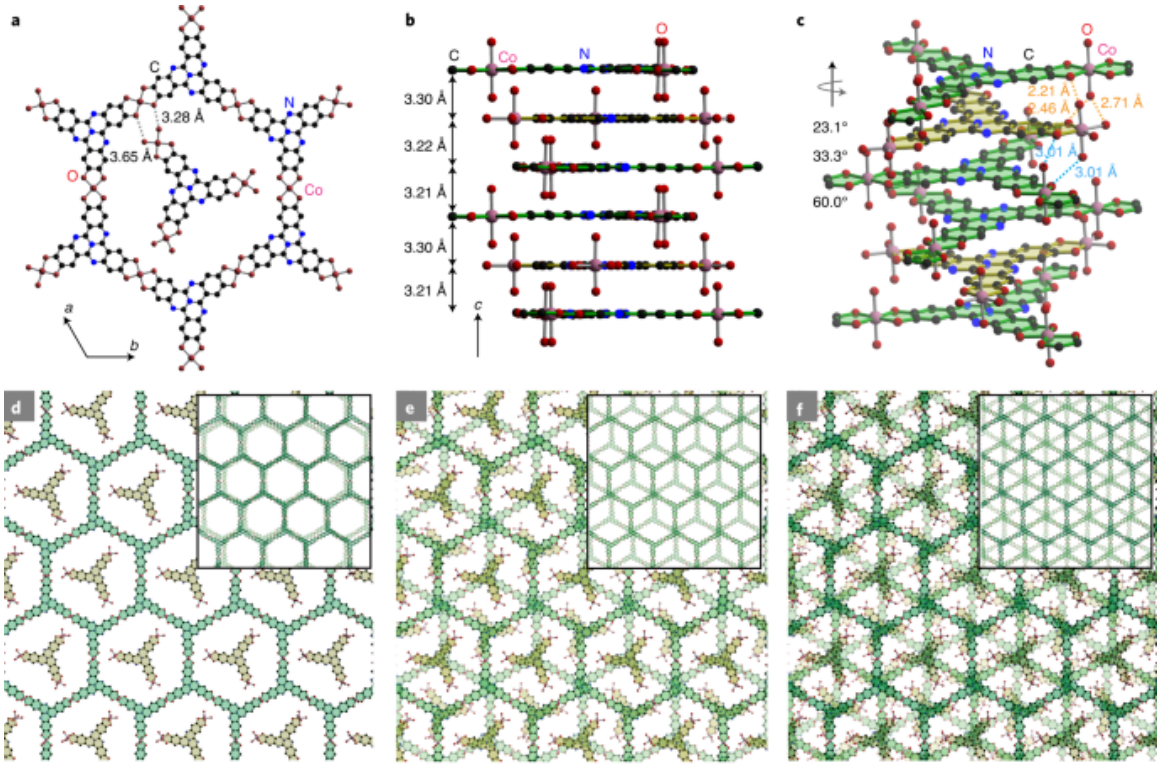

Figure 25. (a) Portion of the Co_6HHTT_3 crystal structure viewed along the *c* direction. The long O–O distances suggest that no hydrogen bonds are formed between the molecular clusters and the Co_3HHTT_2 sheets. (**b**) View along the *ab* plane showing an $(ABC)_n$ triple sheet stacking motif. (**c**) Spatial relationships between molecular and extended Co-HHTT units. The sheets and molecular units are indicated in green and yellow, respectively. The interlayer hydrogen bonds are represented by orange and blue dashed lines. (**d**–**f**) Structural representations of single, double and triple layers of Co_6HHTT_3. The insets in **d**, **e** and **f** show views normal to the two closest A layers, one AB layer set, and an ABC stack, respectively. All guest molecules are omitted for clarity.

2.2.4 Anisotropic Electrical Transport in 2D MOF Single Crystals

The large single crystals of MOFs made from HHTT provide a unique opportunity for understanding anisotropic charge transport in this class of materials. Four-probe devices were fabricated by electron-beam lithography from large hexagonal plates or hexagonal rods of different materials to probe in-plane and out-of-plane electrical transport, respectively (**Figure 26a,b**, App. A Figs. A58–A65). The room temperature conductivity values, summarized in **Figure 26c**, reveal several surprising trends that are qualitatively explained well by the structural data; DFT calculations, exploring the band structure as well as the charge and spin distribution for each M_mHHTT_n MOF, provide deeper insights into the qualitative trends observed for conductivity data. The calculations assumed that all metals are in the formal oxidation state +2, as confirmed by investigations of their absorption edge positions via X-ray absorption near-edge spectroscopy (XANES) and X-ray photoelectron spectroscopy (XPS) (App. A Figs. A38–A43 and A67–A69), with the charge on Co and Cu further supported by electron paramagnetic resonance (EPR) measurements (App. A Fig. A66a,b). Based on charge neutrality, the HHTT ligands within the extended sheets were assumed to be triply oxidized (that is, $HHTT^{3-}$), a formal charge assignment that is further supported by the presence of an organic radical in EPR (App. A Fig. A66). Conversely, the HHTT ligands of $M_3(HHTT)(H_2O)_{12}$ clusters centered in the hexagonal pockets were assumed to be fully reduced (that is, $HHTT^{6-}$), supported by the elemental analysis data.[330] EBS diagrams and corresponding DOS plots reveal a positive correlation between the proximity of occupied metal-based *d*-states near the Fermi level and the in-plane conductivity (**Figures 27 and 28**).

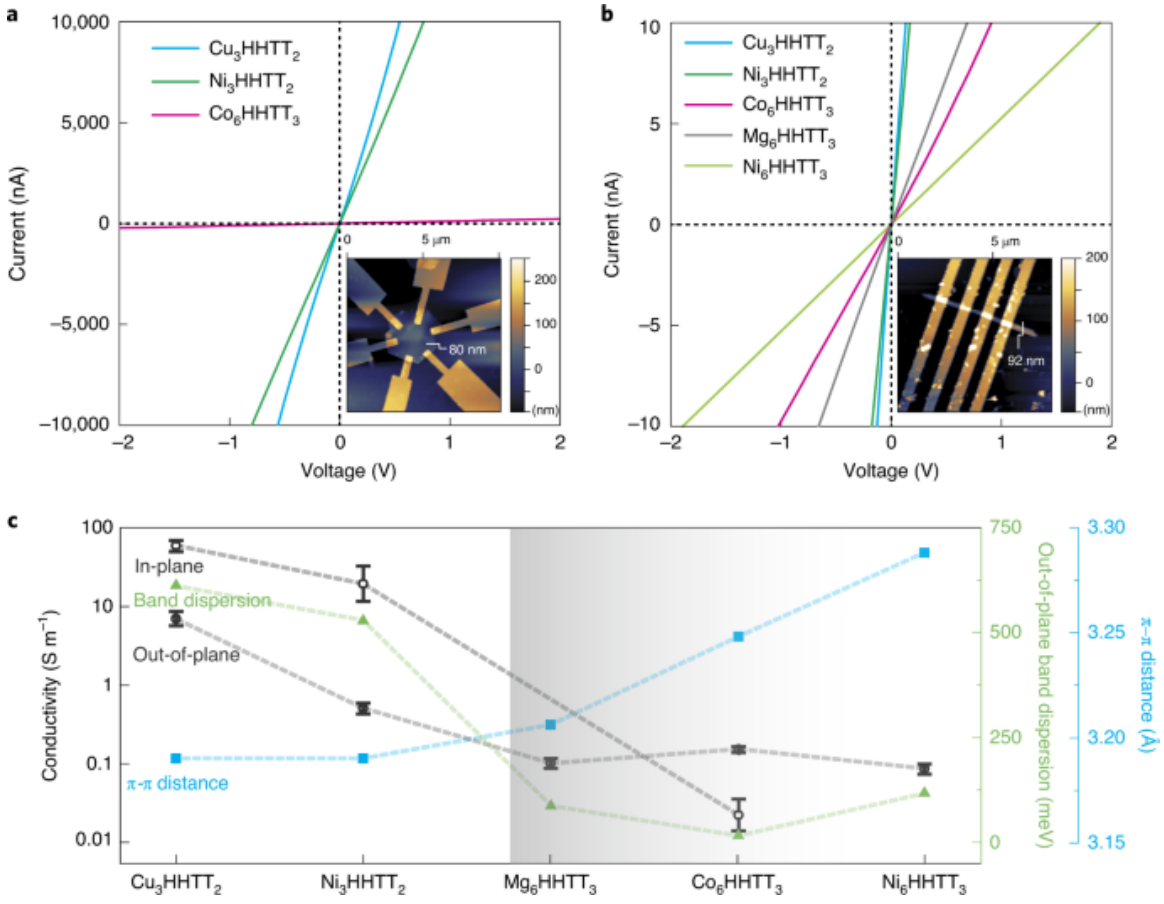

Figure 26: Electrical transport data for 2D M_mHHTT_n MOFs. (a) In-plane van der Pauw *I–V* curves measured from electron-beam devices made from hexagonal single-crystal plates. (**b**) Out-of-plane four-probe *I–V* curves measured from electron-beam devices made from single-crystal rods. In both **a** and **b**, the linearity of the *I–V* plots confirms ohmic behaviour, with the slope variation depending on the crystal orientation and MOF identity. The insets show representative AFM images and the thicknesses of the in-plane and out-of-plane Cu_3HHTT_2 devices. (**c**) Single-crystal conductivity data (in-plane and out-of-plane), out-of-plane band dispersion and π-stacking distance of 2D M_mHHTT_n MOFs (average and standard deviation obtained from 10 devices). The gradient to the right of the graph separates the three dense HHTT-based analogues.

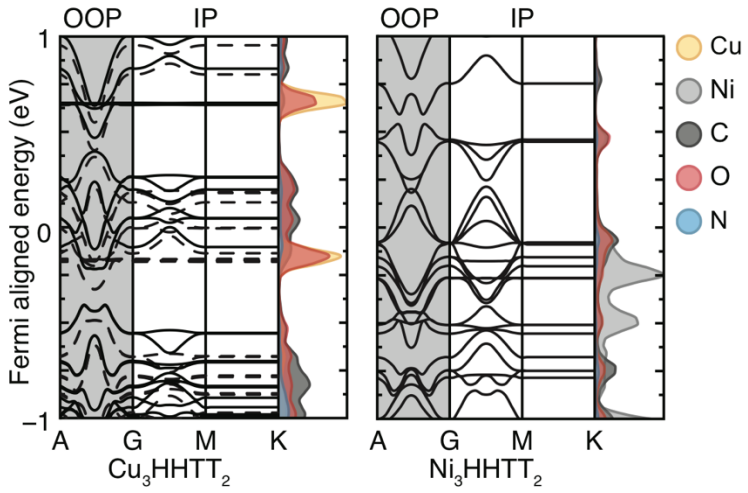

Figure 27. Electronic band structure and DOS of **Cu_3HHTT_2** and **Ni_3HHTT_2**. Both systems exhibit metallic electronic band structures, evidenced by the non-zero density of states at the Fermi level. The Cu variant converged to a ferromagnetic ground state. In both cases the materials are metallic in both the in plane, and out of plane k-vectors. We can reconcile the experimentally lower out of plane conductivity with dislocation defects (i.e. the 2D sheets slipping, reducing out of plane orbital overlap).

The first relationship we observe between conductivity and structure is that the in-plane conductivity of the porous, eclipsed phase M_3HHTT_2 ($M = Cu^{2+}$ or Ni^{2+}) is expectedly higher than its out-of-plane conductivity, whereas the dense staggered phase Co_6HHTT_3 shows higher out-of-plane conductivity. Notably, the in-plane conductivity of ~100 S m^{-1} observed for Cu_3HHTT_2 compares favourably with the highest conductivity reported for any MOF. **Figure 26c**.[359] Given the narrower band dispersion associated with conductive states in the M_6HHTT_3 systems compared with the M_3HHTT_2 species (**Figures 27**, **28**), we surmise that the molecular clusters residing within the pores of the former

contribute towards transport normal to the 2D sheets and potentially also impede transport within the sheet (**Figure 26c**).

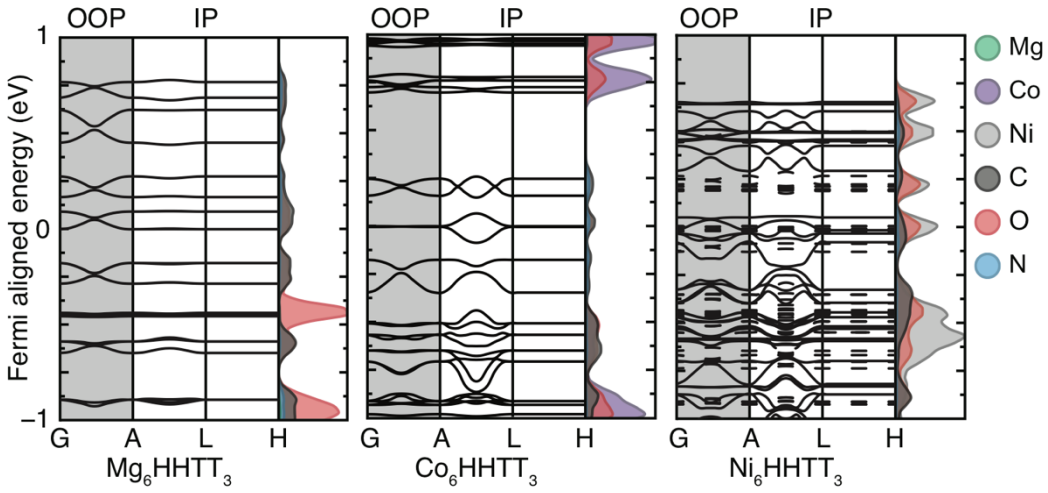

Figure 28. Electronic band structure and DOS of **Co_6HHTT_3, Mg_6HHTT_3** and **Ni_6HHTT_3.** All three systems are metallic, although they feature low density of states at the Fermi level. In addition, the band dispersion is heavily reduced compared to the porous analogues, suggesting that charge carriers are more localized in these structures. Here the Co system converges to an antiferromagnetic electronic orientation, while the Ni material orders ferromagnetically.

The second trend me observe is that the eclipsed phases are more conductive than the staggered phases in either crystallographic direction. This is most evident in the two phases made from Ni^{2+} (Ni_3HHTT_2 is approximately 10 times more conductive than Ni_6HHTT_3) and is clearly correlated with the much closer stacking distance in the former.

More generally, the out-of-plane conductivity for all MOFs is inversely related to the interlayer π–π distances, with the exception of Mg_6HHTT_3, where the metal-based *d* orbital is absent. Finally, within the more conductive eclipsed group M_3HHTT_2, the Cu analogue is more conductive than the Ni analogue in both directions. Conversely, within the dense staggered phase M_6HHTT_3 ($M = Mg^{2+}$, Co^{2+} and Ni^{2+}), the out-of-plane conductivities are nearly identical for all three materials.

The eclipsed phase M_3HHTT_2 ($M = Cu^{2+}$, Ni^{2+}) has widely dispersed bands consisting of orbitals from both metal ions and ligands at the Fermi level in both in-plane and out-of-plane directions, whereas the dense phase M_6HHTT_3 ($M = Co^{2+}$, Mg^{2+}, Ni^{2+}) has relatively narrow bands at the Fermi level. This significant difference indicates that the high conductivity observed in the porous phase is a result of effective orbital mixing. In the in-plane direction, the energy matching between the orbitals of square-planar Cu^{2+} or Ni^{2+} ions and those of the radical-state ligands leads to in-plane π-conjugation; in the out-of-plane direction, the strong interlayer π–π interaction and the lack of steric hindrance from axial ligands give rise to a dense packing motif. Both of these factors result in well-mixed orbitals, which translate to dispersed bands and efficient charge transport. By contrast, in the dense staggered phase, the guest monomer interpenetration and the coordinating axial solvent interfere with the in-plane π-conjugation and interlayer packing, respectively, giving rise to ineffective orbital mixing, narrow bands and consequently inefficient charge transport in both directions.

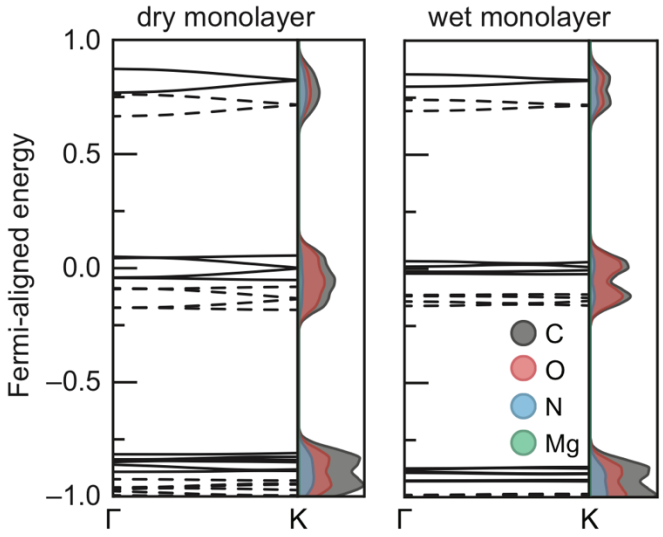

Figure 29. Electronic band structures corresponding to the contiguous monolayer of Mg_2HHTT_3 with and without coordinated water molecules (i.e. square planar and octahedral coordination spheres for dry and wet monolayer respectively) show how axial aqua ligands impede intralayer conjugation and reduce conductivity.

The contrast between the band diagrams of the two structure types also rationalizes their different trends for anisotropic transport and the important influence of metal ions on conductivity. In the eclipsed phase M_3HHTT_2, the in-plane charge transport is highly efficient owing to effective π-conjugation, resulting in higher in-plane conductivity than out-of-plane conductivity. The metal ions participate in charge transport and contribute charge carriers, thus significantly affecting conductivity and resulting in higher conductivity in Cu_3HHTT_2 with d^9-Cu^{2+} ions than that in Ni_3HHTT_2 with d^8-Ni^{2+} ions. On the other hand, in the dense phase, interlayer charge hopping is dominant owing to the absence of in-plane π-conjugation, which gives rise to the opposite anisotropy. The

electronic band structures for a contiguous monolayer of Mg_2HHTT_3 with and without axial aqua ligands shown in **Figure 29** demonstrate the reduction in band dispersion in the case of a wet layer due to disruption of the in-plane π-bonding. Indeed, charge transport in the dense staggered phase is mainly ligand based. Since there is little contribution from metal ions, the out-of-plane conductivities among the three analogues in this phase are nearly identical. Overall, the theoretical data helps support experimental observations that reveal the decisive influence of the extent of π-conjugation and the packing motif on electrical conduction in 2D π-conjugated MOFs, highlighting a design principle for future development of this class of materials.

2.2.5 Conclusions

We presented atomically precise structural data for an important class of conductive MOFs and established clear correlations between structure and transport properties in these materials. Molecular modeling of HHTT and HHTP was invoked to confirm hypotheses regarding the electronic property modulation afforded through heteroatom inclusion, designed to balance crystallization dynamics. The single crystal growth enabled by these linker modifications afforded high resolution structural refinement and direction-dependent conductivity measurements and therefore direct comparison between theoretical values obtained from pristine unit cells and experiment. Single-crystal devices reveal anisotropic conductivity trends that can only be explained with the aid of high-resolution structural data and quantum mechanical insight from electronic band structures and DOS plots. The metal-dependent crystal structures, and in particular the ability to recover both

morphologies with Ni(II), granted a unique opportunity to understand the impact of coordinated donor molecules, monomer intercalation, and layer ordering on band transport in conjugated MOFs. The structure–conductivity relationships elaborated herein provide a blueprint for a well-guided approach towards the design and development of porous, conductive 2D MOFs.

2.3 Switchable Conductivity from Redox Doping of ZnNDI

Electrically conductive porous metal–organic frameworks (MOFs) have emerged as a fascinating class of materials with potential impact in a wide variety of applications, enabled by the development of chemical design strategies that overcome the longstanding problem of inherent insulating behavior in porous crystalline solids.[326,360,361] For example, the development of layered 2D MOFs with extended π–d conjugation has led to record-setting conductivity values while maintaining permanent porosity in some cases.[330,331,362,363] Engendering conductivity in 3D MOFs has been significantly more challenging, but recent work has shown that open-shell metal centers and/or organic ligands can be used to increase charge carrier density, coupled with either through-bond or through-space charge transport pathways.[326,364] Guest@MOF strategies have also been developed to impart conductivity on otherwise insulating framework materials, by insertion of electroactive guest molecules or polymers into the MOF pores.[334,365–367]

One strategy, with the potential to be quite general, is to make use of redox-active components in the MOF.[368] Redox manipulation of a stable, insulating MOF can be used to increase electrical conductivity while maintaining structural integrity, and both chemical

and electrochemical doping approaches can be envisioned. Examples of this strategy to date have been dominated by redox-active metal centers in the secondary building units (SBUs), and iron-based SBUs have shown particular promise.[369] For example, partial reduction of the Fe(III) centers to Fe(II) in the material $Fe_2(BDP)_3$ (BDP = 1,4-benzenedipyrazolate) results in electrical conductivity increases up to four orders of magnitude.[335] Similarly, partial aerobic oxidation of Fe(II) centers in $Fe_2(BDT)_3$ (BDT = 1,4-benzeneditetrazolate) leads to tunable conductivity values that span five orders of magnitude.[370] Analogous approaches that make use of ligand-based redox activity in 3D MOFs are less developed, and have focused primarily on materials with non-innocent semiquinone or dithiolene-type linkages.[327,371,372] Furthermore, there have been no examples of reversible redox processes that can be used to reversibly modulate conductivity in a 3D MOF, for either metal- or ligand-based approaches.

In this work, we show that n-doping of the redox-active naphthalene diimide (NDI) organic ligands in the microporous pyrazolate MOF ZnNDI (**Figure 30a**) can produce a greater than one-million-fold enhancement in conductivity. The ligand-based reduction can be performed reversibly without altering the structure of the framework, and the extent of ligand reduction can be used to tune the material's conductivity over several orders of magnitude. To the best of our knowledge, this represents the first example of appreciable electrical conductivity in a 3D MOF as a result of reductive ligand doping. Furthermore, while redox switching has been used to control conductivity in 1D and 2D coordination polymers,[373,374] this is the first demonstration of reversible switching between two different stable redox states with dramatically different conductivity values for a 3D MOF.

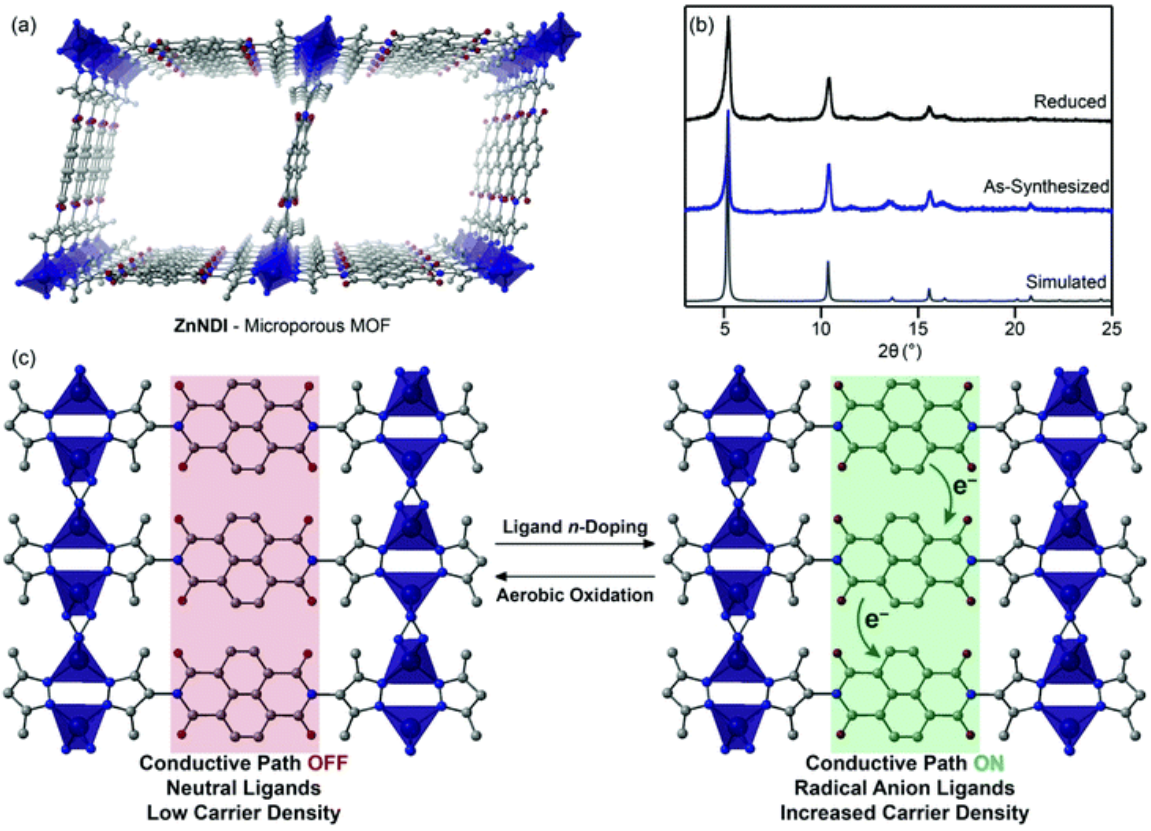

Figure 30. (a) Structure of the microporous MOF ZnNDI; (b) PXRD data demonstrating that the MOF structure remains intact after ligand reduction; (c) the ordered stacks of NDI ligands undergo reversible reduction to their radical anion form, creating a through-space charge transport pathway *via* NDI hopping that results in increased electrical conductivity.

Redox activity of NDI-based ligands in MOFs has previously been used for applications such as electrochromic devices.[375–377] The NDI subunits of the ligands typically exhibit well-behaved electrochemistry, displaying reversible reduction processes to their $NDI^{\cdot -}$ radical anion and NDI^{2-} dianion states. In this work, we make use of the

known fluoride-induced reduction of NDIs as a mild chemical doping strategy that can reversibly transform the neutral ligands in ZnNDI to their radical anion form;[378,379] while the specific mechanism of NDI reduction in the presence of fluoride is still a matter of debate in the literature, recent work suggests a complex solvent-mediated pathway.[380,381] The ordered stacks of $NDI^{\cdot -}$ ligands generated in this manner form a charge transport pathway that dramatically increases the framework's conductivity (**Figure 30c**). Supramolecular organization has been shown to both promote and stabilize the formation of NDI radical anions,[382] and the rigid ordering provided by the crystalline MOF provides advantages compared to solution-phase approaches toward conductive stacks of NDI radicals.[383]

2.3.1 Results and Discussion

As synthesized ZnNDI (procedure reported in Appendix B) is a white powder, consistent with an electronically insulating material. Indeed, the conductivity value of the neutral material is below the limit of detection for our instrumentation ($\leq 10^{-14}$ S cm^{-1}). UV-vis measurements collected from thin films of as-synthesized ZnNDI grown on the surface of glass slides (**Figure 31**) display absorption maxima at 360 and 380 nm, assigned to $\pi \rightarrow \pi^*$ transitions in the neutral NDI ligands. However, chemical reduction of these neutral ligands carried out by soaking ZnNDI in DMF solutions of tetra-*n*-butylammonium fluoride (TBAF), was shown to increase conductivity through an increase in charge carrier concentration.

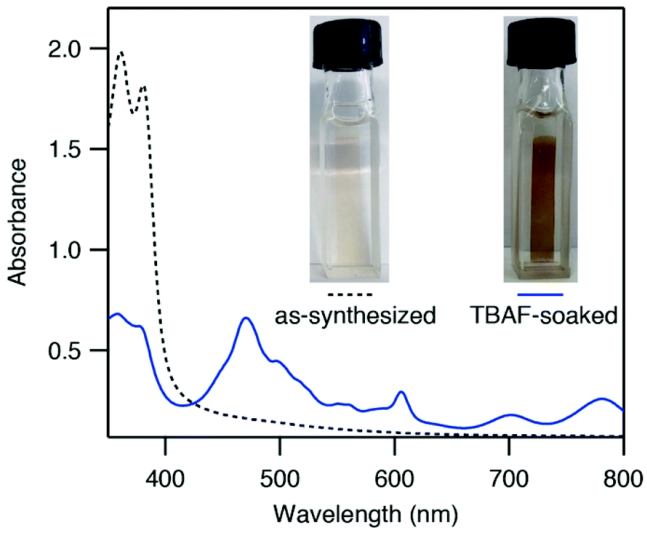

Figure 31. UV-vis data of a ZnNDI thin film before and after soaking in a TBAF solution (60 mM in DMF, 14 hours), showing conversion of the neutral NDI ligands to their radical anion form; the inset shows optical images of the films.

Upon placing ZnNDI films into a TBAF solution the color gradually darkens, accompanied by a decrease in intensity for the neutral NDI features and the appearance of new features throughout the visible region (λ_{max} = 471, 607, 701, 784 nm, **Figure 31**). These features are characteristic of $NDI^{\cdot -}$ radical anions,[384] and correspond well to spectroelectrochemical data for the reduction of ZnNDI.[375] The spectral features from reduced linkers persist after film removal from the TBAF solution under inert atmosphere, stable for up to 1 month. However, the spectrum of neutral ZnNDI is recovered upon exposure of the sample to air or brief soaking in non-deoxygenated DMF. Similar to the thin films, bulk powder samples of ZnNDI exhibited a color change from tan/yellow to

black after reduction. It is clear from these data that linker reduction corresponds not only to an increase in conduction band occupancy, but a reduction in the electronic band gap.

Quantitative EPR measurements were used to determine the extent of linker reduction in ZnNDI samples. Different degrees of ligand reduction were achieved by soaking with varying amounts of fluoride, and no structural changes or degradation were observed by PXRD or SEM at 20%, 50%, or even 90% reduction. Room temperature conductivity values recovered with 2-probe measurements on pressed-pellet samples showed that conductivity increased as the extent of linker reduction increased. At 90% linker reduction, an average conductivity value of 2×10^{-7} S cm^{-1} was achieved, compared with average values of 1×10^{-9} and 3×10^{-10} S cm^{-1} for 20% and 50% reduction, respectively. While the maximum conductivity observed for ZnNDI-A does not approach record values for conductive MOFs, it is commensurate with other 3D MOFs featuring electroactive ligands and redox-inert metal centers. The most direct point of comparison is the well-studied family of porous tetrathiafulvalene (TTF)-based MOFs, which display average pressed-pellet conductivity values ranging from 10^{-9} to 10^{-6} S cm^{-1}.[385–389] Pivotally, the stable reduction of NDI linkers in this MOF can be used to tune the conductivity of the material and enhance the conductivity by up to 10^{6} S cm^{-1}.

DFT calculations were used to understand the origin of the electrical conductivity increase upon ligand reduction. Both the neutral and reduced species were optimized with PBEsol.[101] as implemented in VASP,[390–392] using the PAW plane wave method[393] and a 500 eV planewave cutoff basis set. A Γ-centered 1x1x1 k-grid was converged to ionic and electronic criteria of 0.005 eV and 1×10^{-6} eV, respectively. The HSEsol06[394]

(PBEsol+25% HF) level of theory was used to recover more accurate band-gap energies using the same convergence criteria. Band structures were constructed using the structure from our optimization, sampling at explicit *k*-points along the high symmetry path. Electron energies were aligned to the vacuum using a previously reported method.[395] Reduction was modeled by addition of electrons to the system. These data were used to demonstrate the radical locality rather than their energies.

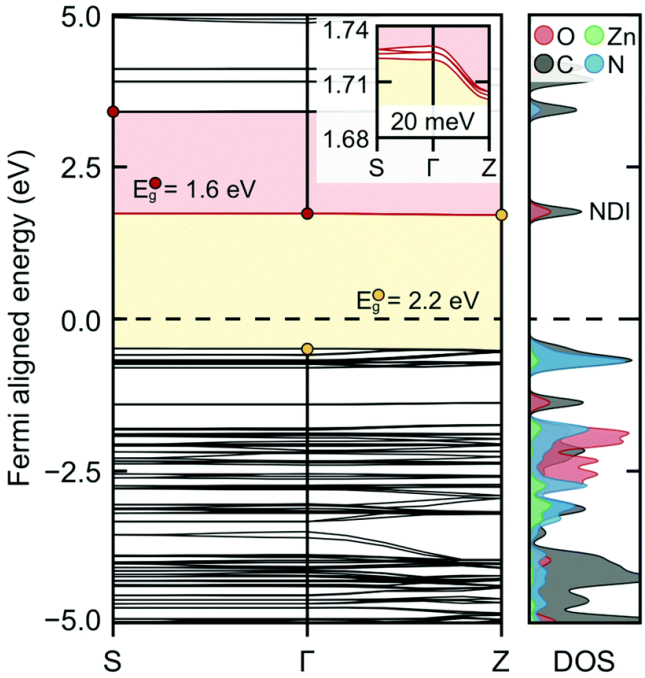

Figure 32. Calculated electronic band structure and density of states for ZnNDI. In its neutral form, ZnNDI has a 2.2 eV band gap, which red-shifts to 1.6 eV upon population of the conduction band by ligand reduction.

The electronic band structure and projected density of states for the optimized ZnNDI structure are shown in **Figure 32**. The conduction band is defined by the NDI

ligand orbitals, as clearly shown by the charge density associated with this electronic state (**Figure 33a**). Curvature of the conduction band indicates electron mobility in that direction upon population *via* reductive doping (shown in the figure inset; *Z* corresponds to an out-of-plane 0, 0, 1/2 vector). Explicit calculation of ZnNDI with a single electron added to the system indicates spin delocalization over the NDI ligands (**Figure 33b**). Overall, these calculations support that electron conduction occurs *via* NDI hopping in the reduced ZnNDI materials. The distance from between carbon nuclei in adjacent linkers is ~7.3 Å and defined by the coordination sphere of the inorganic node. NDI reduction results in the emergence of super-gap excitations (**Figure 32**, red), indicating a shift to a narrow gap material as the conduction band is populated; this is consistent with our experimental observation of new red-shifted bands in the UV-vis data. Decreasing the distance between linkers would undoubtedly enhance conductivity values associated with ligand reduction.

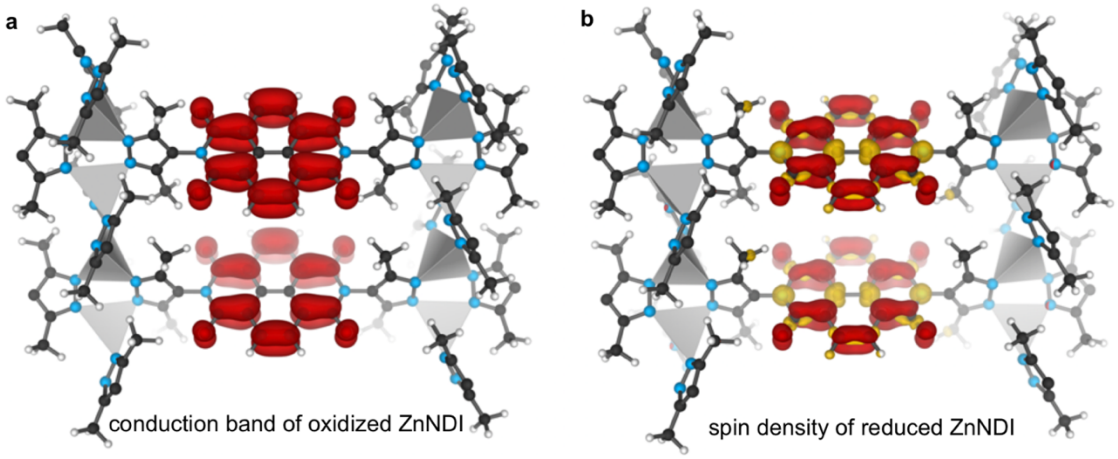

Figure 33. Visual plots of (a) the charge density associated with the conduction band of neutral, as synthesized ZnNDI, and (b) the associated spin density from its occupation in reduced ZnNDI.

2.3.2 Conclusion

We have reported the first example of electrical conductivity enhancement in a porous 3D MOF *via* ligand n-doping. Utilizing MOF crystallinity to generate conduction pathways and incorporating reducible components represents a clear design principle for engendering typically insulating frameworks with charge transport capability. We find that the extent of ligand reduction in the redox-active MOF ZnNDI can be rationally varied, resulting in electrical conductivity values that span over six orders of magnitude, but neither stoichiometric one electron reduction of the linkers nor the NDI dianion state are accessible. This work also represents the first demonstration of a 3D MOF that can be reversibly switched between two different stable redox states with dramatically different conductivities. Even so, the broad range of accessible conductivities is quite low (1×10^{-14} to 6×10^{-7}) and dependent on the fabrication of a given sample. The theoretical electronic band structure of this material exhibits negligible dispersion of the electronic bands, consistent with hopping transport and these low conductivity values. The utility of this framework for reductive sensing rests not only on a fast, measureable and reversible response, but also on cyclability and reproducibility. Future work will aim to improve switching times and maximum conductivity values as well as framework stability.

2.4 Bridge

In this chapter, periodic boundary conditions were invoked to sample discrete vectors between high symmetry points in the Brillouin zone of MOFs with long-range

bonding order. The electronic band dispersion resolved from pristine unit cells along vectors in momentum space that correlate with real-space crystallographic directions directly correlated with direction-dependent single-crystal conductivity measurements along those same vectors. We observe an acute sensitivity of through-band charge transport pathways within conjugated layers and along π-stacked organics to solvent coordination and ion intercalation; solvent coordination impacts both interlayer spacing and in-plane conjugation. Conductivity along both in and out-of-plane crystallographic vectors in the eclipsed, porous arrangements adopted by Ni(II) and Cu(II) showed greater conductivity with the spin-unpaired d^9 Cu(II) relative to the spin-paired d^8 Ni(II). However, Cu(II)-based bands appear flat while Ni(II)-based bands demonstrate dispersion out of plane suggesting there is conduction through the overlapping d^8 orbitals in the *c*-direction, but not d^9. The organic linkers and their interaction across the single metal atom nodes play the dominant role in defining overall conductivity. Unpaired d-electrons from ions such as Co(II) and Cu(II) likely facilitate communication between in-plane linkers. Hydrogen bonding between layers reduces the metal dependency on conductivity by shifting the dominant charge transport regime to charge-hopping. However, Co_6HHTT_3 demonstrates the most effective in-plane conductivity (c.f. Mg(II) and Fe(II))

In the final section, we present a 3D MOF whose inter-linker spacing is predetermined by the node. Through-band transport is not observed, as demonstrated by negligible dispersion in the electronic bands. However, redox activity of the linkers enables electronic n-type doping to obtain switchable conductivity in the scaffold—a notable first for MOFs—albeit with the accompaniment of scaffold degradation and poor cyclability.

Clearly, high conductivity in MOFs can be enhanced by obtaining the densest association of redox active components. The dynamic metal-organic interface likely precludes the use of these scaffolds for applications where there are significant, repeated changes to internal charge and current in the presence of other coordinating molecules, e.g. water. Still, the defined arrangement of internal components is helpful to attain desirable charge transfer properties and define charge transport pathways. In the next chapter, I will demonstrate how separation of charge across the metal-linker interface, rather than communication, benefits charge storage, photoactivite, and catalytic applications. The same DFT model parameters necessary to describe charge-hopping in semiconducting MOFs with poorly dispersive bands like ZnNDI, translate to the recovery of photoproperties in other semiconducting MOFs.

CHAPTER III

MATERIALS WITH FLAT ELECTRONIC BANDS FOR CATALYSIS

Chapter III of my dissertation builds from the methodologies invoked in Section 2.3 of the previous chapter where a hybrid functional is used to recover accurate electronic band gap energies. This chapter contains two main sections pertaining to 1) photocatalysis, where the activation barrier is taken to be the fundamental band gap as described in Section 3.1.1, and 2) thermal catalysis, where saddle-point searching algorithms are used to established kinetic activation barriers as described in Section 3.2.1. The introductions for both sections contain excerpted portions from my first author literature review (*Chemical Reviews,* **2020**, *120*, 8641-9715.) to contextualize my own contributions to the field. Section 3.1 begins with a review of the computational approaches relevant to photocatalysis viewed through a thermodynamic lens, leading up to two computational investigations of Ti(IV)-containing MOFs that solid-state theory. The first, in section 3.1.3, explores the general utility of Ti(IV) atoms for accessing photoactivity in MOFs, both natively through direct synthesis, and post-synthetically through transmetalation. This is a previously published study (*Advanced Theory & Simulation* **2019**, *1900126*.) co-authored by my PI, Christopher H. Hendon. A subsequent investigation of proton-coupled electron transfer in one natively Ti(IV)-containing MOF is found in Section 3.1.4 which pertains to

hydrogenation catalysis. This work inspired, and was supplemented by, experimental work performed by Kevin Fabrizio from the group of Carl K. Brozek who are co-authors on the manuscript under review at *Chemical Science* at the time of writing. Experimental details from this work can be found along with the Supplementary information in Appendix C.

Section 3.2 explores thermal catalysis, where the localized nature of MOF electronic structure is exploited to afford high densities of non-interacting active sites. Since only the relative energy change of local bonding rearrangements is of interest, cluster modeling methods are used. This section begins with an explanation of transition state finding methodologies, leading into a mechanistic investigation of selective ethylene dimerization in Ni(II)-substituted MFU-4*l* (Section 3.2.2), which is submitted to the Journal of Physical Chemistry C at the time of writing. This work is co-authored by Laura Gagliardi and Carlo Alberto Gaggioli who identified the minimum energy crossing point between the singlet and triplet spin-surfaces following dimerization.

3.1 Photocatalysis

The localization of charge (i.e., flat bands) of most scaffolds and the ability to tune the size and parentage of the electronic band gap[396] makes MOFs interesting candidates for photoredox catalysis. Photoexcitation provides one route to accessing transient, exotic redox states,[156,397,398] and can further be used to promote an electron from the MOF to pore interstitials (e.g., absorbed polyoxometalates[399] or nanoparticles[400]).

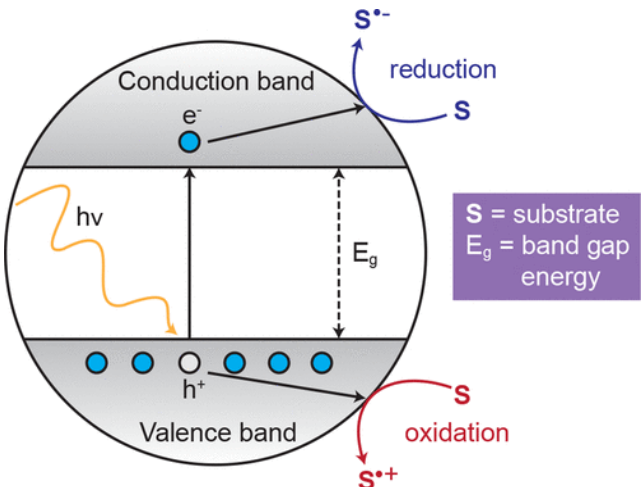

Figure 34. Photoexcitation of a valence electron to the conduction band minimum enables redox catalysis. Upon light absorption and excitation, electrons that populate the conduction band travel to the lower energy vacant states of an acceptor, while holes formed in the valence band exchange with electrons from higher energy occupied states of a donor. Reproduced with permission from ref. [110]. Copyright 2020 American Chemical Society.

Photocatalysis is predicated on the photocatalyst forming high energy, transient holes, and/or electrons, a process which is governed by (i) the photopromotion (e.g., band gap), (ii) relative alignment of vacant and occupied states in the catalyst and reactants (e.g., electron affinity and ionization potential/workfunction), and (iii) exciton lifetime.[47] Furthermore, there are four possible excitations in MOF materials, and they depend on the composition of the material: (i) ligand-to-ligand, (ii) ligand-to-metal, (iii) metal-to-ligand, and (iv) metal-to-metal excitations. In all cases, photoexcitation yields a hole in the valence band and an electron in the conduction band, which are then primed to do work, **Figure 34**.[401] The following subsections will discuss the utility of DFT in

quantifying activation barriers, and identifying the modes and direction of charge transfer in photoactive MOFs. Then, the application of these methodologies will be discussed for the development of design principles associated with long exciton lifetimes and stable photo-doped structures utile for either charge storage or selective hydrogenation.

3.1.1 Quantifying Activation Barriers

Experimentally, the energy of activation is quantified as the optical gap of a material, defined by the lowest energy dipole-allowed transition.[142] The fundamental gap, which is the difference in energy between the highest occupied and lowest unoccupied states in the material, is either close or identical in energy to the optical band gap.[142] Therefore, in theory, the fundamental electronic band gap is adopted as an approximation of the excitation wavelength.[402]

The computation of band gaps for solid systems is discussed in Chapter 1 (section 1.3.2.2), however, an accurate description of both the band gap and the valence band ionization potential are paramount for the prediction of photocatalytically relevant properties (i.e., hybrid functionals are necessary).[147] Again, the contribution of electron exchange is of particular importance when studying electronic transitions in metal ions.[145] Yet, the computational expense associated with hybrid functionals[148] prompts the recovery of optical and redox properties of MOFs from a single point hybrid functional calculation on a structure obtained using GGA theory. This technique is prominent in MOF literature and was applied to study the impact of metalation on the photocatalytic properties

of a porphyrinic MOF for water splitting and CO_2 reduction;[161] geometry optimizations were performed using PBEsol, followed by HSE06 to recover electronic properties. In all cases, the porphyrin alone was a chromophore; only the addition of Fe introduced new low-laying states. These midgap orbitals were used to justify the improved catalytic ability of the Fe porphyrin compared to other metals.

Static DFT recovers ground-state electron densities and may provide a poor description of the unoccupied orbitals populated upon photoexcitation. Methods like TD-DFT permit calculation of excited state electron configurations, i.e., the energy of a system is recovered when electrons are not placed in the lowest possible orbitals/higher-level Kohn–Sham orbitals are occupied.[403] The optical gap can be found by identifying the first excited state; a simple task in molecular modeling packages, but rarely attempted in the solid-state.[404] When invoking periodic boundary conditions, the fundamental gap is thus taken as an approximate activation energy, however, the optical gap is narrower than the fundamental gap because of the exciton binding energy. This disparity between experiment and theoretical approximations can be observed in computations of HKUST-1. The electronic band gap is ~3.5 eV using HSE06, but the material is strongly blue colored.[405,406] Conveniently, the localized electronic states in highly ionic MOFs again grants the opportunity to sensibly model local electronic structure with high levels of theory like TD-DFT by reducing the computational system to a cluster model.[21] Linker-to-linker transitions specifically offer increased control over band edge positions via molecular chemistry and functionalization.[407,408] In one study, amino- and nitro-functionalized UiO-66 showed band gap reduction using HSE03.[235] The same study also examined

hydroxylated and dehydroxylated metal centers of UiO-66, revealing that hydroxylation increased the band gap of the bulk material, likely owing to the increased ionicity at the node/linker interface.

Indeed, the implementation of TD-DFT for MOF cluster structures has generally been successful in the case of linker-centered excitations. TD-DFT was also effectively applied to a series of UiO-66 derivatives when studying the origin of band gap perturbations as a result of varying linker identity.[169] Calculations were performed on cluster models of the hydrogen-passivated linkers, and HOMO–LUMO energies showed excellent agreement with values obtained from periodic calculations. Experimental adjustments to the optical response were found to be the result of additional linker states corresponding to the added functional groups.

The impact of framework rigidification and the chemical environment on the optoelectronic properties of light adsorbing molecules upon MOF inclusion is of interest to dampen unproductive photodecay.[409] TD-DFT simulations of 4′,4″,4‴,4⁗-(ethene-1,1,2,2-tetrayl)tetrakis(([1,1′-biphenyl]-4-carboxylic acid)), a luminescent linker incorporated into MOF-5, were performed in the free and lattice-constrained cluster geometries.[410] Consistent with experimental results on the bulk MOF, TD-DFT showed the HOMO–LUMO gap was blue-shifted by ∼400 meV upon MOF inclusion due to a resultant conformational change and differences in terminal Lewis acidity; these data were in qualitative agreement with experiment.

While linker-to-linker transitions are more prevalent in MOFs than metal-to-ligand, ligand-to-metal, and metal-to-metal, the latter three transitions offer additional routes

toward band gap modulation beyond organic functionalization. Band gap modulation of MOFs featuring metal-to-metal transitions can typically be accessed by substitution of transition metals into and onto nodes in otherwise wide gap scaffolds.[411,412] These materials then show standard crystal field splitting patterns related to their local ligand environment. Perhaps more interesting are linker-to-metal and metal-to-linker transitions; the electron and hole become spatially separated within MOFs featuring these transitions, giving rise to prolonged exciton lifetime.[413]

Perhaps the most exciting photophysical avenue in MOF chemistry is the control of ligand-to-metal excitations, as they are analogous to redox noninnocent molecules[414] while boasting potentially very large populations of photoaccessed reduced, site-isolated metals. Indeed, MOFs are able to stabilize excited-state radicals (e.g., with metals or linkers that yield a reasonable reduced product upon photoexcitation). The propensity of MOFs for electron storage was demonstrated in a series of landmark studies where the authors showed that MIL-125 could support photoaccessed Ti(III) in the presence of a sacrificial reductant.[415,416] The general approach invokes stabilization of the excited state by a cation (i.e., either proton or sodium) coupled electron transfer into the valence band hole of the photoexcited MOF. The generality of this approach is yet to be determined.

In sum, the activation energy recovered from static DFT is most often reported as the fundamental band gap. Recovering experimental semiconductor band gaps in the solid-state empirically requires the inclusion of exact exchange in the Hamiltonian, however, molecular cluster models can be employed when frontier bands are localized on isolated

components and are minimally perturbed by MOF incorporation. To obtain more accurate descriptions of the orbital interactions involved in excitation processes, post-DFT methods can be applied. However, the higher resolution quantum mechanical insights may mandate geometric or active space restrictions that diminish their ability to provide a realistic MOF model.

3.1.2 Predicting Charge Transfer Phenomena

Because most MOFs have flat bands, an exhaustive electronic band structure calculation is often a waste of computational resources. Instead, photocatalytic MOF chemistry can be explained using conventional DOS plots, which illustrate the orbitals contributing to each band.[417] In a photocatalytic reaction, from the ground state, absorption of a photon may promote an electron into the conduction band: the excited electron and hole are in kinetic competition between exciton recombination and the desired electron transfer.[418] The exciton binding energy, which drives recombination, is the attractive Coulombic force that must be overcome to separate a hole and electron[419] and thus decreases exponentially as a function of distance.[420] Photocatalyst design for systems with flat bands benefits from localization of the excited electron on a separate component from its ground state.[421]

Many MOFs have wide band gaps stemming from valence and conduction bands centered on the organic linker, which are commonly conjugated systems dominated by π–π^* transitions (e.g., MOF-5 and Zr^{IV}-UiO-66).[302,422–425] Wide gap materials, particularly, can host chromophores that sit mid gap relative to the bulk material. For example, a

chromophore similar to the green fluorescent protein was appended to the biphenyl linker of a zinc-based MOF to inhibit low energy vibrational modes that deplete its signaling response.[426] Similarly, UiO-67 has been employed as an immobilization platform for a rhodium-based photocatalyst through postsynthetic linker exchange.[427] [Cp*Rh(bpydc)$_3$]Cl$_2$ (bpydc = 2,2′-bipyridine-5,5′-dicarboxylic acid) performs the photoreduction of CO_2 to formate. DOS of the hybrid material revealed that the frontier states were defined by the new d–d transitions of rhodium, indicating the framework played a passive support role.

MOFs composed of late transition metals or metals with high quantum numbers will typically feature ligand-to-ligand transitions because the organic components have lower ionization potentials and higher electron affinities than the Lewis acidic metals.[428] Early experimental work presumed that the zinc-oxo clusters in MOF-5 operate as ZnO quantum dots via a ligand-to-metal charge transfer.[429,430] There, the GGA functional PBE, known for overstabilizing strongly bonded states, places the zinc orbitals closer to the conduction band edge. However, this was later debunked using a higher level of theory (HSEsol06)[431] paired with experiment: MOF-5 features primarily ligand centered excitations, **Figure 35**.[432] Higher energy conduction bands may also be populated via a multiphoton absorption process, although the prediction of the explicit energetics will depend heavily on the functional used.[433]

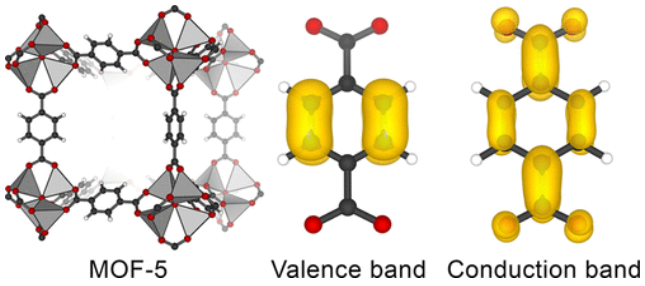

Figure 35. Valence and conduction band extrema projected at the Γ-point. The linkers are shown in isolation for clarity. Data obtained from ref [64]. Reproduced with permission from ref. [110]. Copyright 2020 American Chemical Society.

Unlike d^{10} MOFs, those constructed with Ti(IV) have reported photoaccessible Ti(III) states as evidenced by EPR and transient absorption spectroscopies, in addition to theory.[421,434–437] Nodes built from the other d^0 ions (Zr(IV) and Hf(IV)) do not exhibit metal-based states near band edges, although Ce(IV)-UiO-66, which has empty *f*-orbitals, exhibits a conduction band dominated by metal orbitals.[438] Powerfully, ligand-centered valence bands can be modulated by changing the organic motif with negligible perturbation to the conduction band if it is metal-based.[439] A renowned example of band gap modulation through organic linker functionalization is reduction of the MIL-125 band gap from the UV to visible light region through amino-functionalization,[440] and the same principles have been applied to other MOFs.[441–444] DOS plots show that electron donation from the amino group formed shallow midgap states at the valence band. Subsequent analysis with DFT established that the band gap could be further tuned by adjusting linker functional groups and the concentration of functionalized linkers.[445] Experimentally, it was observed that

MIL-125-NH_2 indeed exhibited an optical gap in the visible range and, interestingly, the minimum band gap was reach at >50% linker substitution.[446] This observation leaves us wondering whether their observation was catalysis enabled by surface sites, or rather that the material became limited in quantum efficiency. Either way, this example highlights the symbiosis of theory and experiment by showing that visualization of the DOS is an indispensable tool for analyzing the band edges of photoactive system.

Section 3.1.3 will demonstrate that analyzing DOS plots in this way is especially beneficial for the fruitful modulation of exciton separating MOF species that can be selectively tuned from both band edges. Powerfully, in addition to modulating the energy of the valence band through linker substitution, the chemical identity and energy of the conduction band can be modified through metal substitution without affecting organic valence bands. Section 3.1.4 will then explore the utility of localized bonding in photoactive materials composed such that optical excitation results in metal-to-linker charge transfer, *i.e.* exciton separation.

3.1.3 Ti(IV)-Inclusion as a Route to Photoactivity in MOFs

Photocatalysts offer a unique advantage over conventional thermal catalysts as they harness a ubiquitous source of energy, light, to perform chemical transformations. Photocatalytic materials absorb photons equal to, or greater than, their band gap energy to produce high-energy electrons and low-energy holes.[447] These charges may then perform oxidative and reductive chemistry enabling applications in water purification,[448] renewable

fuel generation,[449–451] and CO_2 conversion.[452–454] The prospect of solar-to chemical energy conversion for both catalytic and energy applications makes development of new scaffolds that absorb visible light to promote novel single and multielectron redox processes a key synthetic target.[455] In general, the desired attributes for a photocatalyst are i) a narrow band gap enabling the absorption of photons in the visible range; ii) valence and conduction band edges aligned with reactant potentials for efficient electron transfer upon excitation; iii) long exciton lifetimes to reduce competition between recombination and the desired catalytic transformation; and iv) an ability to modulate reactivity and selectivity by altering the structure and composition. Transition metal oxides possess some of these desirable attributes.[456] Their elemental diversity and various accessible oxidation states provide a medley of transition metal oxides to select for a given catalytic function.[457,458]

TiO_2 is the champion photocatalyst because of its high efficiency and stability, low cost and toxicity, and earth abundancy.[459] When irradiated, Ti^{III} is formed through charge transfer from oxygen to titanium.[460,461] This separation of electron–hole pairs enables redox processes such as photodegradation of organic dyes[461,462] and renewable fuel production.[449] The large electronic band gap (3.0 eV),[463] however, limits the usable wavelengths from the solar spectrum. Efforts to close the electronic band gap through compositional and morphological alterations have been successful.[464,465] However, manipulation of rigid inorganic lattices can be synthetically difficult and leads to adverse effects such as material instabilities or high recombination rates near defects.[466] TiO_2 could thus be improved upon by designing a material with similar, but more readily tunable, electronic properties.

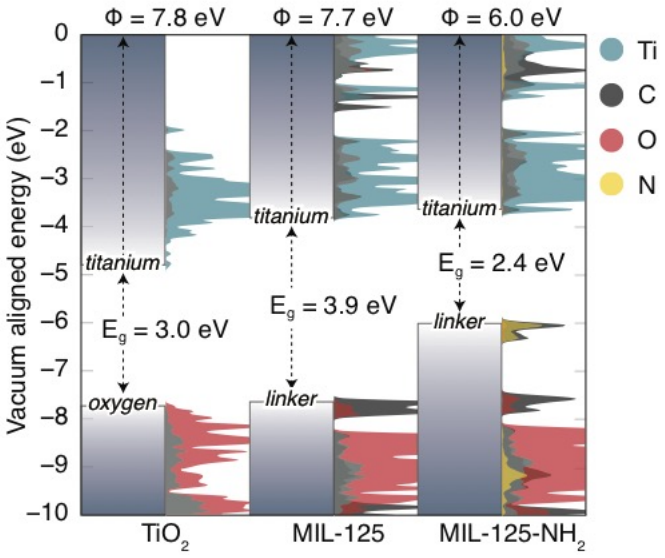

Figure 36. Band edge diagrams and theoretical density of states for TiO_2, MIL-125, and MIL-125-NH_2 show the familiar MOF confinement effects (wider band gap with reduced dimensionality of the metal-oxide cluster compared to bulk). Amino-functionalization is presented to demonstrate that because MOFs feature organic valence bands, additional BDC functionality affects their energetics.

MOFs are a class of compositionally diverse, high surface area, crystalline materials. Some embodiments contain metal-oxide clusters (i.e., nodes) crystallographically orders and separated by anionic organic linkers. MIL-125,[62] for example, is constructed from $[Ti_8O_8(OH)_4]^{12+}$ inorganic building blocks interconnected by benzene dicarboxylate (BDC) linkers. Like TiO_2, the conduction band edge is dominated by titanium d-states; photoexcitation yields a transient Ti^{III} (**Figure 36**).[421] Unlike TiO_2, the valence band edge of MIL-125 is localized on an organic source of titanium-bound oxygen, BDC. Further, inherent MOF porosity facilitates valuable trapping of the low-

valent titanium species through bulk reduction of the framework by small molecules in the pore. Addition of up to eight electrons per node can be achieved in the presence of charge stabilizing counterions.[415,416]

While both TiO_2 and MIL-125 have native band gaps in the UV, the valence band of MIL-125 can be tailored through organic substitution. Amino functionalization of the BDC linker brings the optical gap into the visible range (a reduction in band gap by approximately 1.5 eV), intensifying the harvestable solar wavelengths—a phenomenon reminiscent of nitrogen doping in anatase TiO_2.[440,446,467] Varying the electron donating ability of organic functional groups enables higher fidelity band gap tunability.[445] Independent of the functional group, the conduction band edge remains unaltered, and the lowest energy exciton is spatially separated. In other words, the optical gap is attributed to a linker-to-metal charge transfer (LMCT). Separated Ti^{III} species and valence band holes are then poised to perform reduction (e.g., Cr(VI)-to-Cr(III)[468]) or oxidation (e.g., amines-to-imines[469]), respectively. The reactivity of MIL-125 thus parallels TiO_2, but has the advantages of inherent porosity (enabling higher active site accessibility) and electronic customizability (allowing band gap tunability and energy level matching).

Other Ti^{IV}-containing MOFs (e.g., NTU-9,[437] COK-69,[470] PCN-415[471]) demonstrate photoactivity similar to MIL-125—it is the metal ion, Ti^{IV}, that makes these frameworks unique. MOFs composed of BDC and other d^0 group 4 metals (i.e., Zr^{IV} or Hf^{IV}) do not feature the same reactivity because the unoccupied Zr and Hf orbitals lay closer to the vacuum level—their conduction bands are localized on their organic motifs.[188,472,473] Thus, there remains value in the development of new scaffolds consisting

of Ti^{IV}. This may be achieved in two ways; i) construct new scaffolds featuring Ti^{IV} through direct syntheses,[471] or ii) coalesce the favorable properties of an existing framework, such as pore size or water stability, with Ti^{IV} character through transmetallation. In both cases, the question remains whether Ti^{IV} will define the conduction band independent of MOF structure or composition.

Despite the relative maturity of metal-exchange procedures, there are surprisingly few examples of Ti^{IV}-substituted MOFs.[474] Ti^{III}, however, undergoes more facile exchange (e.g., Zn^{II}-MOF5[475] has been successfully transmetallated with Ti^{III}, but there are no reports of Ti^{IV}-MOF-5 to date)[412] and, once incorporated, can be oxidized by a single electron to the desired form.[476] It should be noted that titanium can be incorporated into seemingly non-exchangeable MOFs (e.g., UiO-66 and other ceramics) by appendage through atomic layer deposition and wet impregnation, but the inner-shell Ti^{IV} ligands then depend on the synthetic conditions.[188,477] In principle these Ti^{IV} could also be photoactive, but position of the unoccupied titanium orbitals demonstrate a mild dependence on the non-MOF ligands. In any case, transmetallation or direct synthetic approaches to incorporating Ti^{IV} may be a worthwhile endeavor for the development of novel photocatalysts.

Developing design principles such as targeting scaffolds with organic valence and Ti-conduction band character can narrow the vast chemical space of potential photoactive MOFs. Density functional theory is useful for this, as photocatalytic function is derived from the material band gap and exciton localities—both are properties readily obtained from theory.[478] Thus, this study seeks to demonstrate that metal-exchanged systems

containing Ti^{IV} are interesting synthetic targets because organic valence bands and Ti-centered conduction bands subsist independent of MOF structure of composition.

3.1.3.1 Results ad Discussion

To begin, the effect of ligand identity and MOF structure on the energetics of Ti^{IV} must be decoupled. A series of BDC-containing MOFs, MOF-5, MIL-125, PCN-415, Zr^{IV}- and Hf^{IV}-UiO-66[472,473] were selected as candidates to compare the native Ti(IV) containing scaffolds (i.e. MIL-125, PCN-415) with transmetallated variants (e.g. Ti-MOF-5).[476,479] Other non-BDC based frameworks, MOF-74 and MFU-4*l*, were then selected as scaffolds to isolate the importance of ligand field strength on the transmetallated Ti orbitals. These transmetallated frameworks are presented in contrast to other native Ti-containing scaffolds; COK-69, NTU-9.

All structures were optimized with PBEsol[101] as implemented in VASP[390,391,480] using the PAW plane wave method[393] and a 500 eV planewave cutoff basis set. A Γ centered 2 × 2 × 2 k-grid was converged to ionic and electronic criteria of 0.005 eV and 1×10^{-6} eV, respectively. The HSEsol06[394] (PBEsol+25% HF) level of theory was used to recover more accurate band-gap energies using the same convergence criteria, and a Γ-only sampling of the first Brillouin zone. Parent scaffolds were fully optimized and referenced to the vacuum potential by subtracting the background potential applied to the unit cell as located within the center of the largest pore.[110] This value was obtained using the open-source code MacroDensity[395] by sampling the potential at the origin of unit cell – a

plateaued potential was identified at this location by performing a scan of the potential change across the diagonal of the unit cell.

For metal-substituted derivatives, one metal per unit cell was exchanged, and the unit cell shape and volume were constrained to the parent framework parameters over the course of the optimization. Titanium was kept in the 4+ oxidation state by including chlorides in its coordination sphere, saturating the octahedral environment with water in the case of MFU-4*l*. For MOF-74, two electrons were removed from the unit cell and the vacant coordination site was again passivated with water. Metal substitution resulted in a dipole across the unit cell, preventing accurate vacuum level alignment. Thus, the lowest native metal orbital in the conduction band of each substituted material was aligned to that of the parent material. This strategy assumes that native metal orbitals of the remote unsubstituted node will be negligibly perturbed by metal-exchange due to the insulating nature of metal–oxygen bonds.

From the HSEsol06 level of theory[394] (using the procedure detailed above), band edge diagrams and corresponding DOS plots were obtained for each of the native Ti^{IV}-MOFs (**Figure 37**). Analogous to TiO_2, the DOS of each native titanium-containing MOF features a conduction band minimum (CBM) centered on titanium. The workfunction and parentage of the valence band maximum (VBM) for all species are additionally localized on the linker. The BDC valence of PCN-415 lays somewhere between that of MIL-125 and Zr^{IV}/Hf^{IV}-UiO-66, attributed to the fact that PCN-415 has a hybrid node consisting of both Ti^{IV} and Zr^{IV}. Thus, the valence band energy is somewhat determined by the relative Lewis acidity of the node. In comparison, the conduction bands of both Zr^{IV} and Hf^{IV} BDC

derivatives lack photoaccessible metal-based states despite their d0 configuration (**Figure 37**), indicating that a ligand-to-ligand transition is favored for hafnium- and zirconium-bound MOFs. This produces neither spatial separation nor stable excited organic radicals, and consequently low photocatalytic activity.

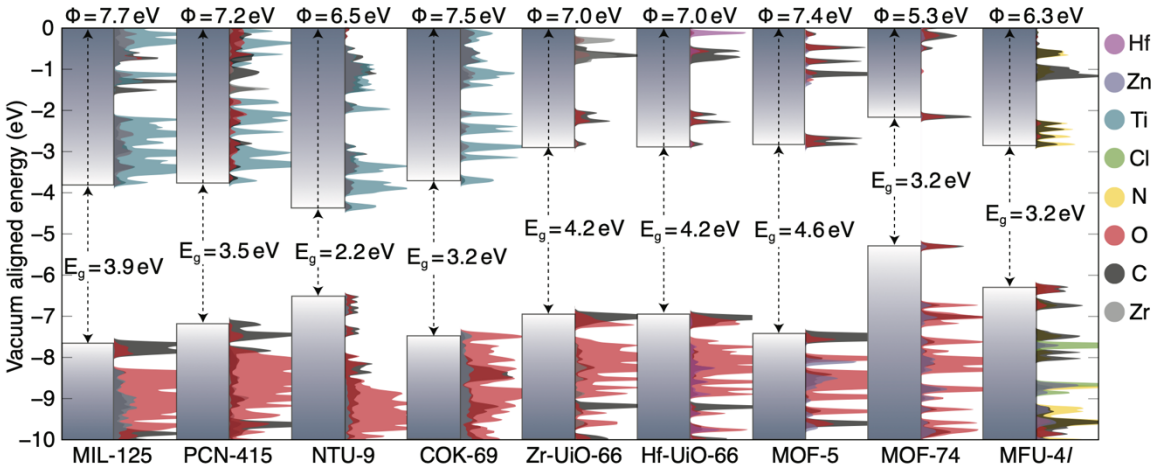

Figure 37. Ti orbitals define the conduction band in Ti-based MOFs. Other non-Ti MOFs (e.g., Zr^{IV} and Hf^{IV}-UiO-66, MOF-5, MOF-74, and MFU-4*l*) feature higher energy, organic-centered conduction bands that are less ideal for photocatalysis. In all cases, the valence bands are composed of linker-centered orbitals.

The real utility of Ti^{IV} would be realized if the conduction band of any transmetallated MOF was persistently centered on Ti, independent of the ligand scaffold surrounding it. Fortunately, there is a wealth of experimental and theoretical literature that demonstrate the emergence of conduction band states centered on titanium in these scenarios. The resultant LMCT is predicted by DOS plots[434,436,439] and electronic band

diagrams[435,481] from DFT performed by other groups and evidenced experimentally by a range of spectroscopic methods.[476,482–486] Thus, transmetallation of MOFs with an organic VBM presents an opportunity to instill the beneficial photocatalytic property of long-lived, spatially separated excitons, formed with a tunable wavelength, in virtually any scaffold. However, remembering the distinct lack of literature on Ti^{IV}-transmetallated frameworks, a careful selection of transmetallated frameworks can be used to paint a comprehensive picture of the persistence of Ti-orbitals in otherwise Ti-free materials by computing the electron energetics of MOFs whose ligands impose vastly different field strengths.

MOF-5, Zn-MOF-74, and MFU-4l feature native ligand-to-ligand transitions because Zn^{II} is d^{10}, placing the next unoccupied metal-centered orbital far above the CBM (+1.6 eV greater than the electron affinity of bulk MOF-5, +1.5 eV for bulk Zn-MOF-74, and +1.8 eV for bulk MFU-4l). However, each framework is known to maintain structural integrity through post-synthetic metal exchange,[476,487,488] and BDC and triazole lay on either end of the ligand field spectrum. The propensity for Ti^{IV} to form octahedral coordination environments mandated that Ti^{IV}-substituted MOF-74, MFU-4*l*, and MOF-5 require additional ions and neutral ligands. Our selection is presented in **Figure 38**; in sum, Cl^- and H_2O were added to achieve charge neutrality and octahedral coordination.

The persistence of Ti^{IV} states defining the CBM in transmetallated frameworks without perturbing the valence band (**Figure 38**) is particularly remarkable as the Ti-orbitals again lay mid-gap relative to the organic orbitals, independent of ligand field strength. More importantly, despite the differences in ligand field strength, the Ti-orbitals in MIL-125, PCN-415, COK-69, Ti^{IV}MOF-5, Ti^{IV}-MOF-74, NTU-9, and Ti^{IV}-MFU-4l all

have similar electron affinities (≈4 eV), fluctuating due to variation in ligand field strength,[489] suggesting that one could target similar photocatalytic transformations by simply installing Ti^{IV} in essentially any metal-cluster based MOF without dramatically changing its reductive ability.

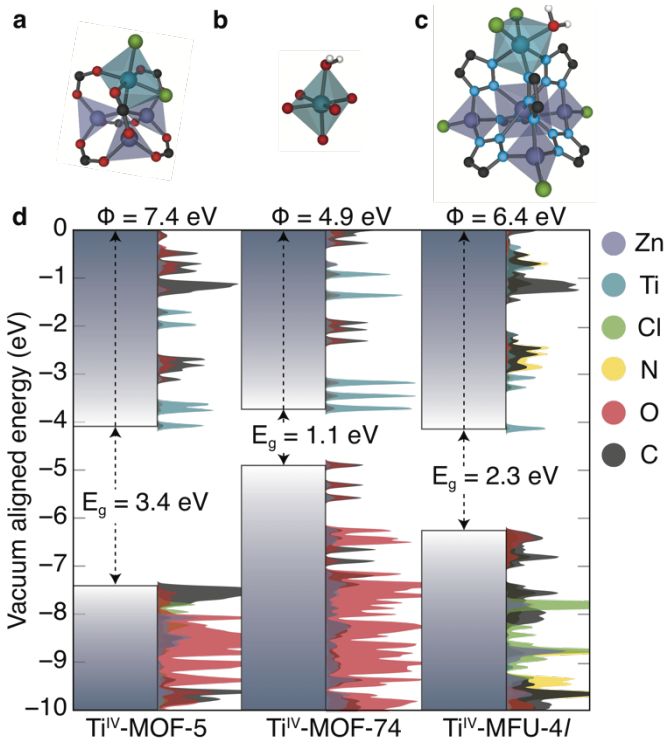

Figure 38. Ti^{IV}-substituted nodes of the post-synthetically exchangeable MOFs. a) MOF-5, b) MOF-74, and c) MFU-4l are passivated with adventitious Cl^- and H_2O. d) Their electron energy diagrams and density of states reveal that titanium-based states define the conduction band extrema in all frameworks, supporting the hypothesis that its incorporation will generally provide access to LMCT from organic-based VBMs.

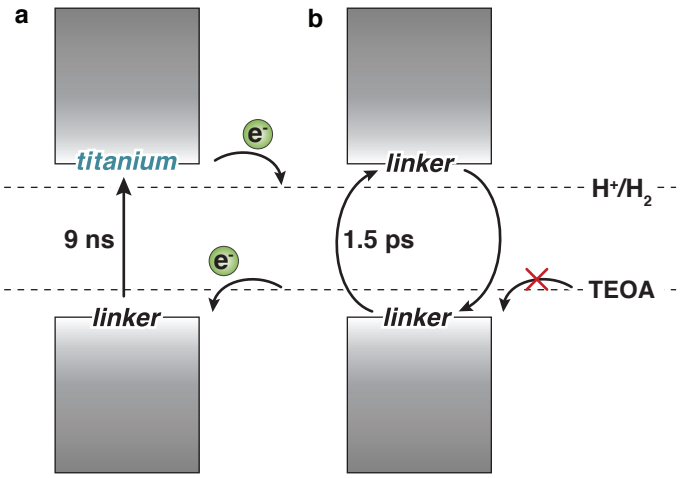

Figure 39. (a) MOF systems with long-lived excitons (i.e., LMCT), such as MIL-125, facilitate photodoping and catalytic reduction via Ti^{IV}. (b) Scaffolds with highly localized excitations, such as UiO-66, recombine faster than catalytic redox can occur.

The incorporation of titanium can thus be viewed as a comprehensive design route to metal-based frontier conduction bands; the modular nature of valence band energetics should not be overlooked. It is their reducing power that determines the ability to "photodope" the framework (i.e., store electrons in the conduction band via excitation and subsequent reduction of the framework-bound hole with an extrinsic reductant). Considering the general scheme of MOF photoactivity shown in **Figure 39**, excitation followed by framework reduction results in the storage of electrons in the conduction band only if the rate of reduction is faster than that of exciton recombination. These rates are determined partially by spatial separation of the electron and hole (a property related to the structure of the MOF itself), and the energetics of the hole in the valence band (a property related to the identity of the ligand). Recombination rates are usually unfavorably fast in

frameworks where the valence and conduction band edges are centered on organics.[421] Thus, while the linker appears to play a relatively benign role in determining the conduction band energetics of Ti-based MOFs, the valence band does play an operative role in the photocatalytic activity of a given MOF, particularly when looking beyond single electron photocatalytic processes.

3.1.3.2 Conclusions

In sum, the results presented in this section demonstrate that metal-exchanged MOFs exhibit similar properties to those that are natively constructed from titanium. Independent of ligand field (where carboxylates and triazoles represent extremes in ligand field strength), titanium orbitals sit mid-gap, relative to the organic orbitals. As a result, metal-exchange becomes a very important strategy to accessing photocatalytic frameworks otherwise unattainable through direct approaches. Furthermore, the utility of Ti^{IV} in MOF-based photocatalysts lays the foundation for other studies of equally rare high-valent metal compositions (e.g., Fe^{III}, V^{V}, etc.) Other metal-oxide clusters, including zirconium and hafnium-based nodes, feature linker-centered frontier states when interconnected by organic components. Titanium can hence be viewed as a unique element to target MOF photoactivity due to its predictable energetic positioning. Experimentalists are encouraged to continue in pursuit of Ti^{IV}-containing frameworks (either through direct routes or transmetallation) as it is both the ligand and metal that contribute to the framework's ability to perform photocatalysis/multielectron energy storage. Continuing investigation of these modular scaffolds will reveal fundamental principles for general photocatalyst design.

3.1.4 Thermodynamic PCET Doping Limit in MIL-125

By coupling to the motion of protons, electrons can enter reactivity patterns, charge storage, and electron transport pathways that would be difficult to achieve otherwise, through a mechanism known as proton-coupled electron transfer (PCET).[490] In net, the reaction can be thought of as a hydrogen atom transfer, and is consequently invoked in various chemical processes found in enzymes[491,492], chloroplasts[493,494], hydrogen fuel cells[490,495], and reductive catalysts[496–498]. However, achieving selective PCET depends on knowledge of the relative redox potentials of the reagents. With the appropriate frontier energy level alignments, PCET can be either thermally or photochemically promoted in both molecular and solid-state manifolds,[499–503] but mismatched energetics creates pitfalls ranging from sluggish kinetics to undesirable H_2 formation or back-hydrogenation to reform reactants.[504] There is hence a desire to leverage the PCET manifold to, for example, suppress the hydrogen evolution reaction (HER) by stabilizing the e^--H^+ pair (H*) below that of the NHE (-4.4 eV relative to vacuum[505]).

In conventional solid-state scaffolds, the ill-defined nature of surface-active sites hinders catalyst design for selective PCET reactivity. For instance, the surface of TiO_2 — a semiconductor known to perform HER[449] — features a broader array of active sites, beyond the idealized (101)-Anatase surface presented in **Figure 40**,[490,506,507] limiting efforts to identify and tune specific localities for selective reactivity other than H_2 formation. Conversely, molecular catalysts offer well-defined single-atom active sites with wide synthetic tunability, but suffer from poor

recyclability[508]. Combining the best of both approaches, metal-organic frameworks (MOFs) combine the benefits of heterogeneous catalysis and synthetic modularity.[509–512] Previous studies in MOF catalysis have primarily focused on thermally driven reactions at either the linker or node using intrinsic[513–515] and extrinsic[516–518] catalytically active metals. Conversely, MOF photoredox chemistry[401,468,519] typically focuses on electron transfer between the inorganic and organic MOF components[520], shuttling electrons to interstitial molecular catalysts[521–523] or guests[524–527].

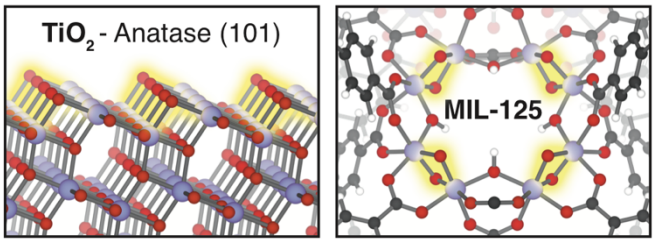

Figure 40. TiO_2-based materials can be reduced via PCET, with a corresponding $Ti^{IV/III}$ reduction, and O-H formation. Depicted are Lewis basic μ^2-oxo sites on TiO_2 (shown is the (101)-Anatase surface). In a MOF analogue, octameric $Ti_8(\mu^2\text{-}O)_8(\mu^2\text{-}OH)_4$ clusters offer four isolated pairs of bridging O per node(highlighted in yellow). These sites are thought to host extrinsic cations (e.g., H^+, Na^+, etc.), affecting the reduction potential of vicinal Ti^{IV} centers.

However, one burgoening area of MOF research has been the exploration of the chemistry afforded by the compositional similarity between inorganic clusters in

MOFs, and their conventional dense-phase semiconducting counterparts, **Figure 40**.[528] In particular, a central theme of our research is the study of chemical opportunities enabled by the Lewis basic inorganic ligands in the inorganic clusters. Such anions are prevelent in Ti-MOFs, and it is these scaffolds that have been shown to stabilize H*, while also enabling the specific design of a well-defined, PCET active site.[529–533]

In the seminal report, UV irradiation in the presence of alcohols caused MIL-125 to turn from colorless to black.[62] The color was shown to persist indefinitely, returning to colorless upon exposure to air. The authors attributed the apparent bandgap reduction to the formation of Ti^{III} centers stabilized by protons liberated from the oxidation of alcohol by the photogenerated holes, *i.e.,* PCET from the solvent to the framework, **Scheme 2**. EPR later validated the presence of Ti^{III} centers and,[421] paired with electronic structure calculations, rationalized their formation by identifying the conduction band minimum (CBM) origin as Ti *d*-states in the pristine MOF — a general property extending to all reported Ti^{IV}-containing MOFs.[513]

Scheme 2. As posited by Dan-Hardi et al., MIL-215 forms Ti^{III}-OH motifs upon photo-promoted reactions with primary and secondary alcohols (R' = H or alkyl respectively).

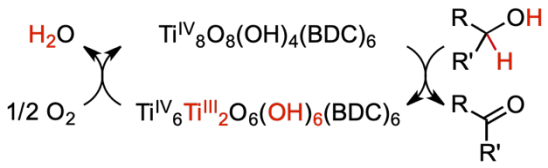

The reversible colorless-to-black transformation, spectroscopic evidence of Ti^{III}, and aldehyde formation observed in irradiated MIL-125[62] demonstrates that the MOF is undergoing photochemical electronic doping, *i.e.,* photodoping. Kinetically, this process requires that rate of exciton recombination be slower than hole quenching, wherein a sacrificial reductant (alcohol) diffused to the photogenerated hole. Although subsequent reports have detected small quantities of H_2 evolved from this process[534,535], these data suggest that a significant portion of the Ti^{III}-OH^+ pairs generated through photodoping remain indefinitely stable,[62,415,416] suppressing H_2 formation. This is further supported by the requirement for MIL-125 and other Ti-containing MOFs to use a co-catalyst to promote H_2 formation.[471,525]

The maximum charge capacity, i.e., relative stability of Ti^{III} centers, of MIL-125 shows a strong cation dependence. Recent studies by the Mayer group demonstrated that Na^+-based chemical reductants enable stoichiometric reduction of all eight Ti centers per node,[416] while the PCET-based photodoping strategy only two H* per Ti octamer.[415] Since Na^+ is undoubtedly less stabilizing than H^+ (which forms a covalent bond with bridging oxos), we hypothesize that H_2 formation sets the thermodynamic limit to PCET-based charge storage in MIL-125: in the low-charging regime, the energies of electron-proton pairs are more stable relative to HER, but exceed the redox potential of HER in the high-charging regime. Further, stoichiometric reduction of the Ti centers can only be achieved with Na^+ because the Na^+/Na redox couple lays far more negative (closer to the vacuum level) than

the new conduction band of the all-Ti^{III}-MOF. Consequently, we surmise that the charge storage capacity of MOF nodes depends on both the redox potentials of the metal ions and the node nuclearity or, more specifically, the presence of inorganic anions to accept protons.

Here, we sought to understand the limits to PCET-based charge storage in MIL-125. To do so, we have combined electronic structure calculations and experiments to identify the microscopic origin of 1) the stability of Ti^{III}-OH^+ pairs towards H_2 evolution in the low-charging regime, and 2) the thermodynamic limit to the number of Ti^{III}-OH^+ that can accumulate. We find the inorganic oxo units in the MIL-125 clusters accept the protons liberated after PCET photodoping, thereby stabilizing the e^-/H^+ pairs against H_2 formation by spatially separating them as Ti^{III}-OH^+ units. From this study, we offer a more general design principle for forming MOFs with the potential to act as transfer hydrogenation catalysts, *but not dehydrogenation catalysts*: the incorporation of Brønsted-basic inorganic inner sphere ligands paired with redox-active metals may achieve controllable PCET reactions in MOFs. In other words, we offer a general observation of accessing non-equilibrium reactivity in MOFs featuring metal oxide clusters.

3.1.4.1 Results and Discussion

While the CBM of a semiconductor provides an estimate for the reduction potential of that material (*i.e.,* the electron affinity),[536,537] it alone is insufficient to assess the thermodynamic tendency to host additional electrons because the ground

state structure does not account for local reorganization (for example, distortions due to ion pairing, or reduction in bond order) upon conduction band population. Computational chemistry is well-suited to study both instantaneous reduction of the MOF, as well as the emergent structural deviations. Using plane-wave DFT we are able to compute the ground state electronic structure for MIL-125 and subsequent PCET products. Using a vacuum level alignment[395], the conduction band minimum of MIL-125 sits at -3.7 eV, closer to the vacuum level than H_2 formation from H^+ (-4.4 eV, **Figure 41a)**. We note that functionalization of the linkers does not dramatically affect the CBM position, as it is composed of inorganic metal-oxo orbitals. Together, one might anticipate that electrons that occupy the conduction band would be sufficiently high in potential to reduce protons.

Upon irradiation, in the presence of a primary or secondary alcohol, the MOF becomes black, **Figure 41b**. Due to the persistent color change, these experiments indicate that there is at least one doped configuration that suppressed H_2 formation, otherwise MIL-125 would fade back to colorless over time without exposure to air. We hence surmise that MIL-125-H* is a thermodynamic minimum on the potential energy surface of hydrogen transfer. In the simplest case, where a single H* is added to a bridging oxo, our calculation reveals that the newly formed "mid-gap" state, a half-occupied, Ti-centered orbital (**Figure 41c**) that has an electronic potential of -4.5 eV, ~100 meV more positive of H^+/H_2 reduction potential (shown in purple, **Figure 41a**). Hence, we offer that the PCET product should be thought of as a stable Ti^{III}-OH moiety rather than an ill-defined H*.

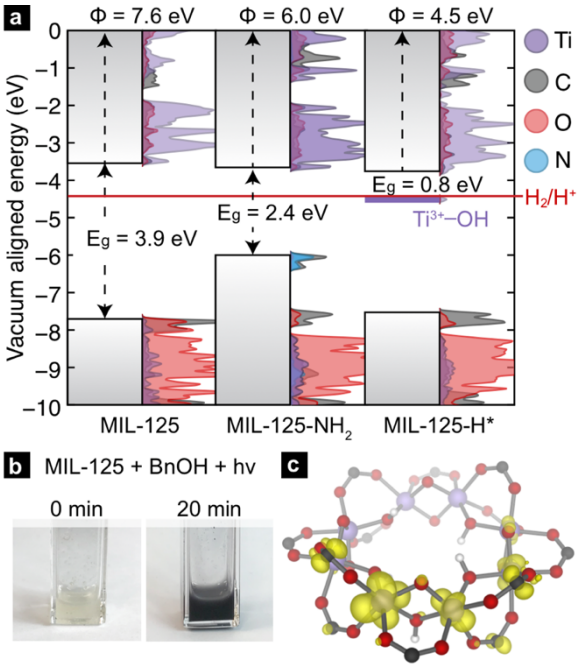

Figure 41. (**a**) Vacuum-aligned DOS plots show that pristine and organo-functionalized derivatives of MIL-125 both have CBMs above H^+/H_2 (-4.44 eV, shown in red). A new mid-gap state emerges upon H* addition, with a potential 100 mV below H^+/H_2. (**b**) Proton and electron addition via photoillumination is evidenced by a colour change, which persists as long as the MOF is kept free from oxidants. (**c**) Electronic structure calculations of the H* adduct reveal that additional electron localizes on a Ti near the adatomic proton, bound to μ^2-oxo ligands.

However, the recent experimentation by Saouma *et al.* revealed an apparent thermodynamic limit of two protons and two electrons per Ti_8 node.[415] It remains unclear whether the two protons would preferentially adhere to vicinal μ^2-oxos or in some other configuration. It is further unclear why only two reductive events can

occur in excess alcohol. Lastly, we wanted to understand the thermodynamic origin of that two-electron limit. To assess this energetic landscape, we developed an assortment of models containing two hydrogen atoms at various positions around the nodes, **Figures 42**. From these calculations, we find that the addition of two hydrogen atoms to MIL-125 yields consistently HER-positive mid-gap Ti^{III} states. The most stable configuration arises from the addition of two additional H* on geminal μ^2-oxos (**Figure 42c**, second column). When the H* are added to μ^2-oxos on different nodes (**Figure 42c**, fifth column), connected by benzene dicarboxylate (BDC), is disfavored by up to 11.3 kcal/mol, **Figure 42d**. In that case, the Ti^{III} radicals delocalize through the π*-system of the linker (see App. C Fig. A1). We find, however, that if the two hydrogen atoms are added to different nodes and not connected by a common linker, the reduction potential is stabilized to the same level as a single addition (approximately 60 mV positive of HER).

We also examined the 2H*-per-node limit presented by Saouma, **Figure 43**. Practically, this amounts to four hydrogen atoms per computational cell, and several observations may be made from these calculations. First, we note that isolated vicinal pairs of protons/electrons result in additive density of the mid-gap states. Second, same-node-separated protons result in splitting of the mid-gap DOS, and this process is energetically disfavored both in terms of formation energy (**Figure 43**, lower panel) and potential to reduce protons. Third, we note that the four separated protons on a single node is more than twice the energy of two protons on a single node (from **Figure 43**, column four, ~21 kcal/mol, and **Figure 42**, column

three, ~8 kcal/mol). We can hence make the general conclusion that the adatomic hydrogenic atoms thermodynamically prefer to add across pairs of bridging oxos. Kinetically, we also expect that alcohol radicals would react with pairs of bridging oxos before diffusing unreacted to distant oxo units.

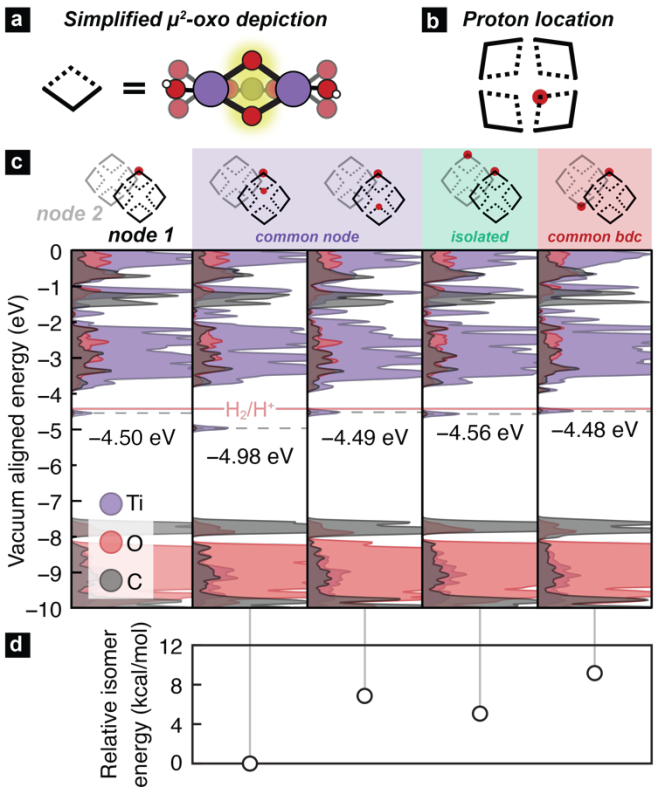

Figure 42. (a) A schematic of a portion of the Ti_8 node, highlighting the μ^2-oxos, and simplifying them to diamonds, whose central apexes represent the bridging oxos. **(b)** A node represented by our simplified notation. The unit cell of MIL-125 contains two nodes, thus (**c**) the vacuum-aligned atom-projected DOS plots contain two nodes per DOS plot, with the depicted PCET product shown above. The Fermi level (*i.e.* the gas phase reduction potential) is denoted by the dotted gray lines.

As yet, these calculations have not identified the chemical origin of the MIL-125 doping limit of two H* per node. Thus, we further explored higher H* loadings, up to the stoichiometric hydrogenation of the μ^2-oxo units, and we determined a thermodynamic doping limit of four e^-/H^+ pairs per node within certain configurational parameters. In order for HER to remain suppressed with more than four PCET events at the same node, neighboring nodes must be in the fully oxidized Ti^{IV}-state (App. C Fig. A3 and A4). HER remains suppressed when six H* are added to a single node, but the presence of a hydrogenated μ^2-oxo pair on the adjacent node facilitates H_2 formation. Meanwhile, four H* per node are stable with respect to HER as long as two pairs coexist on each node, or all four localize on one, App. C Fig. A3 and A4**)**. Higher loadings become progressively less stable (App. C Table A1), and beyond 4 electrons per the node (*i.e.,* 50% doping), the occupied states are split such that many configurations exceed the reduction potential of H^+; an extreme example is presented in App. C Fig. A3. Importantly, these calculations suggest as many as six Ti^{III}-OH pairs can be accumulated on one MIL-125 node despite the previously observed limit of two. Finally, we also note that examined stabilizing the Ti^{III} with adatomic Na^+, App C. Fig. A5. A similar effect is observed (a metastable mid-gap Ti^{III}–ONa^+ state is half populated). In this case, the electron sits negative to HER, but should not form protons since there is no H^+ available to reduce and, calculations would hence agree with the previous observation that stoichiometric reduction of Ti^{III} is achieved in the presence of Na^+.

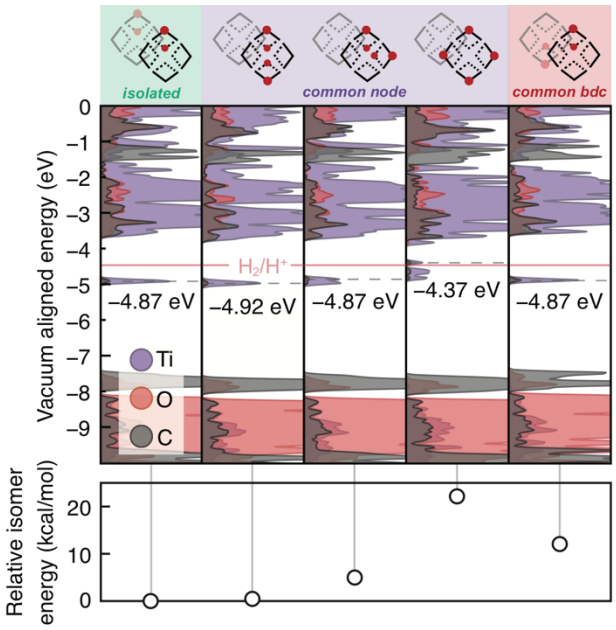

Figure 43. At the experimental limit presented by Saouma *et al.*, two hydrogen atoms per node, the MOF appears electronically indistinguishable from one another, unless a single hydrogen atom is added to each one μ^2-oxo per pair in a single node. While this structure may still be accessible, it is only kinetically stable compared to H_2 formation.

In summary, computations have uncovered two possible thermodynamic explanations for the observed limit to PCET-based charge storage in MIL-125; i) e^-/H^+ pairs accumulate until protons are reduced, generating H_2 or ii) e^-/H^+ pairs accumulate until saturating the available cluster orbitals, at which point alcohol oxidation would cease. To test these possibilities, we sought to experimentally quantify MOF cluster photo-charging and associated H_2 evolution by irradiating

MIL-125 for varying durations in the presence of a) excess of benzyl alcohol and b) stoichiometric quantities (four alcohol molecules per cluster), respectively. Scenario 1 serves to test whether MIL-125 can continuously consume alcohol, while scenario 2 serves to test whether the clusters cease charging after complete reduction of the clusters. The reaction was monitored by comparing benzylaldehyde ^{1}H NMR signals with those of an internal standard (see Appendix C for further experimental detail).

Quantification by ^{1}H NMR of unreacted benzylic alcohol at each time point relative to the amount of aldehyde generated provided an indirect measure of H_2 evolution and other side-reactions, *i.e.*, any deviation from 1:1 would imply an e^-/H^+ "leak". The percent reduction of clusters in MIL-125 by one-electron and one-proton was found to increase with increasing irradiation time, and all materials retained the white-to-black color change after irradiation, supporting the computational insights that e^-/H^+ pairs remain stable towards HER in the low-charge regime. Because photocharging ceases prior to complete cluster reduction, we surmise that HER must serve as the thermodynamic limit, and yet scarce H_2 can be tracked by us and other groups, and most of the ethanol remains unreacted. Kinetic factors therefore likely prevent further reduction and subsequent H_2 generation. Specifically, depletion of ethanol near Ti-oxo clusters during photodoping would prevent continued accumulation of charges because exciton recombination would outcompete hole quenching due to the slow diffusion of new ethanol molecules. This kinetic-based explanation requires further investigation.

To further test the hypothesis that e^-/H^+ pairs are stabilized against H_2 evolution in MIL-125 during photodoping, we sought to measure their redox potentials during the photodoping process. Decamethylferrocenium [$FeCp^*_2{}^+$][415] was employed as an *in situ* optical redox indicator of the photodoped MOF suspension by monitoring the absorption feature at 778 nm, attributable to a LMCT transition[538]. We were able to recover the Fermi level of our solution through the Nernst equation by determining the ratio of [$FeCp^*_2{}^+$] to [$FeCp^*_2$],[539,540] and assuming redox equilibration between all species in the suspension, this value also reports the redox potential of the photodoped MOF at that time point. Hence, we can compare this value to the known redox potential of HER in acetonitrile (-624 mV vs Fc^+/Fc)[541] as further proof that the electron-proton pair is stabilized against recombination.

A steady-state concentration of all redox-active species in the mixture was obtained after 23 h of irradiation, at which point MIL-125 had photoreduced 48.2% of the original [$FeCp^*_2{}^+$], yielding a steady-state redox potential of –588 mV vs Fc^+/Fc, just +36 mV milder than that of the electrochemical potential of HER. The comparatively positive potential of photodoped MIL-125 helps explain the lack of detectable H_2 generation and supports our computational results that estimate the Ti^{III}-OH^+ mid-gap state to sit ~100 meV more stable than HER. The slight difference between experimental and computational results can be easily attributed to accounting for the true H^+ activity of the suspension, which is considerably lower than the pH = 0 conditions defined for NHE. In other words, the true redox potentials

of photodoped MIL-125 sit energetically even farther from vacuum than HER and closer to the calculated results. Remarkably, given that 1.25 equivalents of Fc^{*+} per Ti atom were introduced for this experiment, 48.2% reduction would imply that each MIL-125 cluster supports approximately five Ti^{III}-OH pairs, on average, in excellent agreement with our computational predictions of the thermodynamic limit to MIL-125 charge storage.

Cation-induced electrostatic stabilization of the MIL-125 clusters can account for the considerable increase in charge storage when performed with Fc^{*+} compared to normal photodoping conditions. During the optical redox indicator experiment, each electron that transfers from MIL-125 to Fc^{*+} must be associated with a H^+ liberated from alcohol oxidation. Therefore, when the MOF-Fc^{*+} reaches steady-state conditions the H^+ activity is higher than during normal photodoping conditions. We expect that these additional cations impart strong electrostatic stabilization of the $Ti^{IV/III}$ redox couples. Additionally, we expect that the increased concentration of H^+ increase the likelihood of achieving the specific arrangement, as outlined above by our calculations, that permit up to size Ti^{III}-OH pairs per cluster. The impact of cations on the redox potentials of Ti-MOFs has been recently investigated by us and will be a fruitful strategy for photoredox reactivity.

3.1.4.2 Conclusions

In sum, a combined computational and experimental study has been used to explain the microscopic origin of PCET-based charge storage MIL-125 as arising

from the inorganic oxos of the clusters. These motifs accept the H^+ liberated during the photodoping reaction, thereby providing Coulombic stabilization and separation from the otherwise highly reducing photogenerated Ti^{III} center. Computational and experimental results place the redox potential of these Ti^{III}-OH^+ pairs at reduction potentials more stable than HER in the low-charging regime.

The lack of gaseous byproduct from the oxidation of alcohol molecules within MIL-125 pores is seen to result from electron delocalization across $Ti^{III/IV}$ redox couples and the covalent association of a functional counter-ion. Single PCET events, or those that occur at remote active sites, yield conduction band electrons too low in energy to afford molecular hydrogen formation from the associated protons. Paired events at geminal μ^2-oxo ligands further suppress HER. We identified routes for hydrogen loading exceeding 4 H* per node, and certain spatial configurations allowed for up to 50% reduction of Ti-sites. With this in mind, the spatial distribution of PCET sites formed under kinetic conditions is likely to inhibit access to this configuration, as evidenced by experiment. Irradiation of MIL-125 in the presence of benzylic alcohol showed negligible hydrogen formation, consistent with HER suppression. Quantitative ^1H NMR suggests, nevertheless, that photodopant concentrations of only 20% were obtained with excess reductant over 18 h, but as many as five Ti^{III} could be stabilized in each cluster when performed with an optical redox indicator.

The extent of e^-/H^+ accumulation is therefore likely due to a thermodynamic limit set by HER and electrostatic interactions of the electrolyte medium.

Kinetically, they may be inaccessible due to depletion of sacrificial reductant. While these results suggest H_2 must evolve during steady-state charge accumulation, this work and previous studies imply minimal H_2 generation. We therefore expect kinetics to be slow for accessing the states that are unstable towards HER. It is also notable that a few photodoped states in the low-charge regime were computed to be unstable towards HER, while the vast majority are stable. Therefore, the accumulation of e^-/H^+ pairs and minimal H_2 generation may stem from the greater probability of e^-/H^+ finding stable arrangements. In all, this study indicates MOFs featuring inorganic clusters with redox-active early transition metals and inorganic basic sites could offer a platform to stabilize excited electrons in the conduction band, broadening the gamut of photochargeable materials.

3.2 Thermal Catalysis

With a few notable exceptions,[326,339,542–546] the application of MOFs in heterogeneous catalysis draws on concepts deeply rooted in molecular chemistry.[511] The modular nature of the node and linker enables access to molecularly precise, site-isolated reactive sites[515] while also affording different local chemistry to molecular analogues.[547–549] Yet, MOFs are uniquely dissimilar to molecular analogues: their porosity engenders an additional modular parameter, and subtle differences in coordination environment of node-incorporated metals compared to conventional homogeneous catalysts make MOFs ideal for accessing novel reactivity, and for performing fundamental mechanistic studies.

Generally, design strategies targeting specific reactions have included incorporation of catalytically active linkers,[550] the formation of SBUs that are intrinsically catalytic,[514,551] and using encapsulation of catalytic species in the pores (examples are shown in **Figure 42**).[552,553] Post synthetic modification methods[476] such as cationic metal exchange,[554] linker exchange,[555,556] linker functionalization,[557–559] and atomic layer deposition (ALD)[54,477] have been further utilized to tune existing scaffolds and provide access to materials that are otherwise inaccessible through direct synthesis.

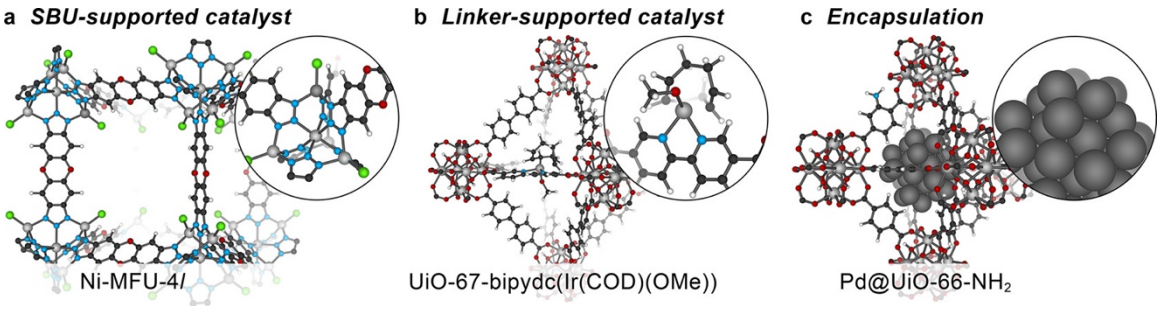

Figure 44. Some avenues for appending molecular catalysts. (a) Ni transmetalation in MFU-4*l* yields a catalyst capable of selective olefin oligomerization.[551] (b) Ligand exchange in UiO-67 enables the support of Ir(COD)(OMe) (COD = cyclooctadiene), a catalyst for C–H borylation of arenes.[561] (c) Encapsulation of Pd in amino-functionalized UiO-66 catalyzes the hydrogenation reactions.[562,563] Reproduced with permission from ref. [110]. Copyright 2020 American Chemical Society.

Computational analysis of catalytic mechanisms and active site geometries requires the identification of key intermediates and transition states that determine the overall efficiency of the catalytic cycle. Such studies are more sophisticated than simple geometry optimizations of ground state materials as they include computationally intensive transition state search methods based on saddle point searching or interpolative schemes.[560] However, once these structures are identified; screening various chemical modulations becomes relatively simple.

Unfortunately, transition-state searching can sometimes feel like finding a needle in a haystack; if the chemical system has more than four atoms, the potential energy surface (PES) has more than three dimensions and from there the PES becomes very complicated, very quickly. To simplify the challenge of determining the appropriate gradients to follow (both transition state searches and generally in modeling), it is helpful to extract clusters using the procedures discussed in Chapter 1. Molecular modeling in catalytic studies of MOFs is seemingly requisite to accomplish the exhaustive analyses necessary to determine both reaction pathways and their driving force.[564] The following sections discuss the use of cluster models (and a handful of solid-state examples) for computational kinetic studies including transition state searches and saddle point search methods.

3.2.1 Kinetics and Transition State Modeling

Conventional ground-state DFT methods provide very precise estimates of geometries at intermediate points along a reaction pathway. Transition states are geometries that correspond to saddle points on the PES, and are the highest energy

configuration that exists along the lowest energy pathway between two intermediates. This section proceeds with the assumption that the intermediate structures, either solid-state or cluster, have been initially equilibrated.

The transition state is a saddle point on the PES that lies along the minimum energy path between intermediates, i.e., the dominant reaction pathway, and accordingly has exactly one negative (i.e., imaginary) frequency corresponding to a single direction of molecular motion with no restoring force. Analogous to ground-state equilibrations that converge to a minimum point on the PES, transition-state optimizations self-consistently converge to a saddle-point. Saddle point search methods generally take one of two forms: (i) interpolation methods, which step through a series of geometric configurations obtained by interpolating between the coordinates of "known" reactants and products, and (ii) surface walking algorithms, which are based on assessing the local gradients or Hessian matrices.[565] Ultimately, the various saddle point finding methods differ only in the manner with which they traverse the PES, but should in principle yield the same result.

3.2.1.1 Interpolation Algorithms

One intuitive approach to find the transition state between intermediates is to construct a "chain-of-states" along the MEP by interpolating coordinates between the known reaction intermediates.[566] Interpolative schemes optimize a series of static chemical configurations referred to as images along the PES between the reactants and products to create a 2D energy profile; the resolution (and expense) of interpolation schemes is a function of the number of images as well as the chemical system, and their convergence

relies on having a well-converged description of the starting materials and products.[567] Still, constructing a chain-of-states both reduces computational cost by limiting the degrees of freedom to sample, and ensures extracted geometries belong to the appropriate reaction coordinate.

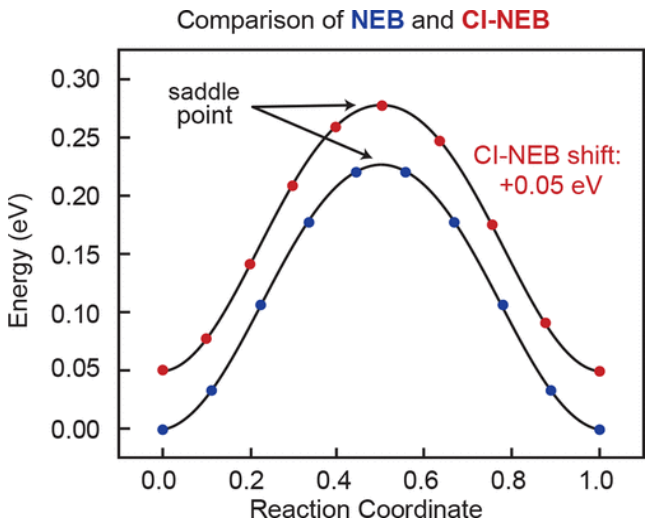

Figure 45. An illustrative representation of how pure interpolative schemes (e.g., NEB, blue) may overlook the true saddle point, but refinement schemes that employ gradient searching methods in addition to interpolative ones, such as CI-NEB (red) or subsequent transition state searches with surface-walking methodologies identify the saddle point. Image adapted from ref [570]. Reproduced with permission from ref. [110]. Copyright 2020 American Chemical Society.

The most common interpolation methods are the string[568–570] or NEB approaches,[571–574] which have been widely applied in inorganic surface catalysis[575,576] and

ion diffusion,[577–579] and more recently to MOFs.[580–582] The various incarnations differ both in their convergence scheme and the reaction coordinate spacing kept between images. Importantly, the images obtained from interpolation algorithms that define the MEP may not necessarily contain the true transition state structure, and the results are often improved by the addition of a surface-walking algorithm to locate the true transition state using the highest energy structure, **Figure 45**.[570]

String Methods: The string method gets its name from the equal spacing kept between its connected "string" of images, achieved through a repositioning step after each SCF iteration.[568] Various embodiments of the string method have been developed: the simplified method[569] seeks to increase accuracy of the highest energy structure and computational efficiency, while the growing string method[570] adds more images until a complete reaction path and transition stare are identified.[570] Other alternatives exist (e.g., climbing image string, which is analogous to CI-NEB[583]) but are highly uncommon in MOF literature because the cluster modeling alternative generally provides higher fidelity data from smaller model sizes. In fact, string methods have only recently been applied to MOFs and are limited to the diffusion of gas throughout the pores.[584–586]

Nudged Elastic Band: Analogous to the string method, the NEB approach initializes a "chain-of-states" or "band" between the reactant and product configurations with images at fixed distances along the reaction path (n.b.: here, band does not refer to an electronic band, and to avoid ambiguity we will be explicit in our discussion of NEB). However, in

NEB, the geometric perturbations between images along the PES is governed by spring forces applied along the band, hence the "elastic" band.[574,587] This chain-of-states converges to the MEP by optimization of each individual image and minimization of the spring force acting parallel to the band, as well as the true forces acting perpendicular to the reaction path. The result is a scan of the potential energy surface between reactants and products that traverses a saddle point; if the exact transition state is of interest, the highest energy structure obtained using NEB should be further refined.[573,588]

The climbing-image variant of NEB, CI-NEB, is the most widely used interpolation-based algorithm in MOF modeling,[572,589] and has also found success in solid-state transition state searches along simple reaction coordinates.[572,590,591] The climbing image, or the highest energy conformation, obtains a high resolution convergence to the saddle point without increasing the number of images by moving up the PES along the band, and down the PES perpendicular to the band, by way of the energy gradient without considering the spring forces.[572] CI-NEB was employed with PBEsol-D3 to assess the activation of hydrogen gas by UiO-66 with one linker per primitive cell functionalized with 1-(difluoroboranyl)-4-methyl-1*H*-pyrazole (UiO-66-P-BF_2).[592] The MEP and saddle point energy provided by CI-NEB demonstrated that activating H_2 via dissociative adsorption is a lower energy pathway than a reaction of H_2 with adsorbed CO_2.

In a related system, the transfer of hydrogen from palladium nanoparticles encapsulated in NH_2-UiO-66 (Pd@NH_2-UiO-66) to 2,3,5-trimethylbenzoquinone (TMBQ) was studied.[552] Thermodynamically stable configurations of palladium nanoparticles up to 32 atoms large encapsulated in the NH_2-UiO-66 pore were first determined with AIMD

and refined at the Γ-point using DFT optimization with the PBE-D2 method.[101,593] Subsequent CI-NEB calculations with the Pd_{28} cluster revealed that increased catalytic activity likely stems from enhanced TMBQ binding due to cooperativity between the palladium nanoclusters and the NH_2 linker moieties.[552] This study benefited from an interpolative method because surface-walking algorithms would struggle to navigate the multitude of low-frequency modes in the PES of H_2 adsorption and desorption on a palladium surface.

In both cases, however, the dissociation and reaction of H_2 or H* (i.e., surface adsorbed H•) are readily performed via linear interpolation: at the time of writing, we are unaware of any examples of more complicated molecular transformations modeled using this approach. In short, it is easy to interpolate the trajectory of a proton; it is more difficult to interpolate the complicated trajectory of multiple atoms moving in 3D space.

3.2.1.2 Surface-Walking Algorithms

Surface-walking algorithms (e.g., quasi-Newtonian methods)[594–596] are often employed to refine transition state guesses from other methods such as NEB.[597] Occasionally called eigenvector following, these techniques proceed self-consistently by maximizing the energy along one local eigenmode of the Hessian while minimizing the energy along all other modes.[598] A good initial guess is critical because the transition state found as a result of these algorithms may follow an incorrect gradient, neglecting to connect the reactant to the desired product geometries.[599]

Minimum mode finding algorithms, such as the dimer method,[600] calculate only the lowest eigenvalue and corresponding eigenvector. The "dimer" consists of two configurations of the system close together on the PES that are displaced by a fixed geometric distance. As an example, the dimer method was employed to study the kinetics of hydrogen migration in cluster models of single metal atoms deposited on the node of MIL-125-NH_2.[601] The activity of MIL-125-NH_2 for the photoreduction of CO_2 to formate depends on the photogeneration of a Ti(III) active site via LMCT stabilized by hydrogenation of bridging oxo atoms. Here, the mechanistic differences between deposited Au and Pt were compared, and differences in H* binding energies were used to rationalize differences in reactivity. The diffusion barrier for hydrogen migration from the metal atoms to the bridging oxo units that facilitate Ti(IV) reduction, determined using the dimer method, showed the spillover mechanism was facile in the case of Pt loading and inhibited by the different preferential binding of Au to the lattice.

The most widely used embodiment, the "improved" dimer method, proceeds with fewer gradient calculations than the string or NEB methods.[602] However, the dimer method still suffers from difficulties with systems containing many low-frequency modes and with identifying a transition state along the targeted reaction coordinates. Again, this method works particularly well for protonic transition states and other one- or low-dimensional chemical events.

3.2.1.3 Combining Interpolative and Surface-Walking Methods

The most efficient way to locate transition states is through a combined interpolative and local saddle point search approach.[571] In this way, the interpolative scheme generates a reasonable initial guess for the transition state structure along the MEP, and a local surface-walking (saddle point searching) algorithm is then used to equilibrate the transient geometry. In the molecular software package Gaussian,[603] for example, both interpolation and surface-walking methods are used in the synchronous transit-guided quasi-Newton (STQN) approach to elucidate the structures of activated complexes.[604] If only a transition-state structure guess is provided, the Berny algorithm is used to converge to the saddle point.[605] When structures are provided on either side of the activated complex, a quadratic synchronous transit approach gets close to the quadratic region of the MEP, and the saddle-point is refined using a quasi-Newton or eigenvector following approach (QST2).[606] The uphill search direction for optimizing transition states is chosen based on the tangent of the synchronous transit path, and the eigenvector for this ascent direction is then fed into the quasi-Newton or eigenvector following algorithm to refine the saddle point.[607] QST3 additionally employs a transition state guess between the intermediates, which may increase the accuracy of the interpolated path mitigating the risk of calculation failure yet comes at a computational deficit.[608]

The STQN procedure was adopted to compare the catalytic efficiency of NTU-180, a Cu-paddlewheel-based MOF, for propylene carbonate formation from CO_2 and propylene oxide, in the presence of tetrabutylammonium bromide (TBAB).[609] To isolate the effects of pore confinement and node construction on the overall efficiency, the reaction

energetics were compared across four models: (i) gas phase calculations without the presence of catalysts (e.g., without TBAB or NTU-180), (ii) in the presence of TBAB alone, (iii) on a hydrogen passivated Cu_2 paddle-wheel/TBAB cluster model, and (iv) a large NTU-180/TBAB model featuring six Cu_2 paddle-wheel units and 24 ligands. The lowest activation barrier for cycloaddition was exhibited by the NTU-180/TBAB model highlighting the importance of both confinement and Lewis acid Cu(II) sites in stabilizing the epoxide ring-opening step.

The catalytic activity of Fe_2M (Fe^{3+}, M = Ti^{2+}, V^{2+}, Cr^{2+}, Mn^{2+}, Fe^{2+}, Co^{2+}, Cu^{2+}, and Ni^{2+}) mixed valent nodes found in PCN-250 were investigated for the oxidative dehydrogenation of propane using N_2O as the oxidant.[610] Cluster models containing formate-passivated Fe_2M mixed valent nodes showed that oxygen-binding energy is strongly correlated with the N_2O and C–H activation barriers; we highlight the C–H activation barrier descriptor, **Figure 46**. Identifying the transition states played an operative role in determining the optimal metal identity for oxidative dehydrogenation of propane using N_2O. Moreover, increasing HOMO energy of the cluster model, facilitated by varying metal identity in Fe_2M, increases the oxygen bond strength due to the increased ability to donate electrons ultimately resulting in a decreased N_2O activation. Four materials were synthesized (M = Mn, Fe, Co, and Ni), and the calculated trend agrees with experiment, revealing, PCN-250(Fe_2Mn) ~ PCN-250(Fe_3) > PCN-250(Fe_2Co) > PCN-250(Fe_2Ni); this is unsurprising considering the increasing electronegativity of the transition metals.

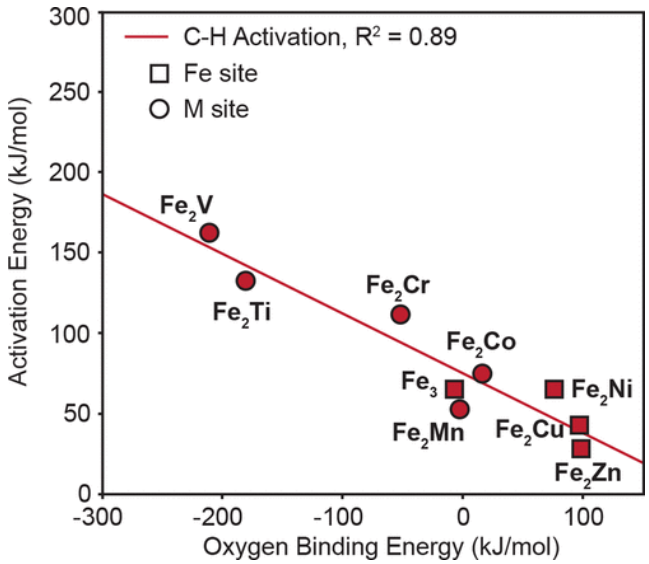

Figure 46. Lowest free energy M = O bond (M = Ti, V, Fe, Mn, Co, Ni, Cu, Zn) and the activation energies for C–H dehydrogenation are correlated. The shape of the data point indicates whether the reaction occurs on the Fe (square) or M (circle) site of the cluster. Reproduced with permission from ref [610]. Copyright 2019 American Chemical Society.

In periodic systems, NEB can be used to find an approximate saddle point in the potential energy surface, which can be further refined by applying CI-NEB with or without subsequent invocation of the dimer method. The images for CI-NEB may still straddle the true saddle point, thus surface-walking algorithms are preferred. Open metal sites in PCN-250 were screened for C–H activation with N_2O using the PBE-D3(BJ) level of theory; the rate limiting step was found to be metal oxidation using the CI-NEB+dimer method.[611] A similar procedure also used the CI-NEB+dimer method combined with high-throughput screening of adsorption studies in derivatives of HKUST-1[612] as well as the development

of an apparent universal descriptor for C–H activation (discussed in more detail later in this section).[613] This balance of procedures provided by interpolation and gradient analysis is effective because CI-NEB is a high accuracy interpolative scheme that ensures a structure between the provided intermediate minima.

3.2.2 Selective Olefin Dimerization in Ni(II)-MFU-4*l*

Fossil fuel dependence creates an uncertain future for energy production and crucial chemical commodities derived from crude oil.[614] One such commodity is 1-butene, a linear α-olefin produced and consumed on the megaton scale,[615] used in diesel production and as a precursor to other value-added products.[616,617] Traditionally, 1-butene is a product of oligomerization or fragmentation and typically yields a Schulz-Flory C_n-backbone distribution of products (*i.e.,* alkenes of various carbon lengths).[618,619] While most 1-butene comes from petroleum cracking processes, it can also be formed selectively through ethylene dimerization.[615] Since the ethylene precursor can be produced from bioethanol through dehydration, selective dimerization provides a route to 1-butene.[620,621]

Current industrial ethylene dimerization technologies employ homogeneous Ni(II) and Co(II) catalysts[622–624] which have some shortcomings compared to heterogeneous catalysts (*e.g.* heterogeneous architectures in principle allow for continuous processing with longer catalyst lifetimes and recyclability).[625] However, conventional solid surface-anchored active sites tend to be poorly characterized, or feature an array of reactivity based on differences in local chemical environment.[626] Ideally, a good ethylene dimerization

catalyst would bridge both technologies, allowing for molecular design of catalytic sites in heterogeneous scaffolds. [627]

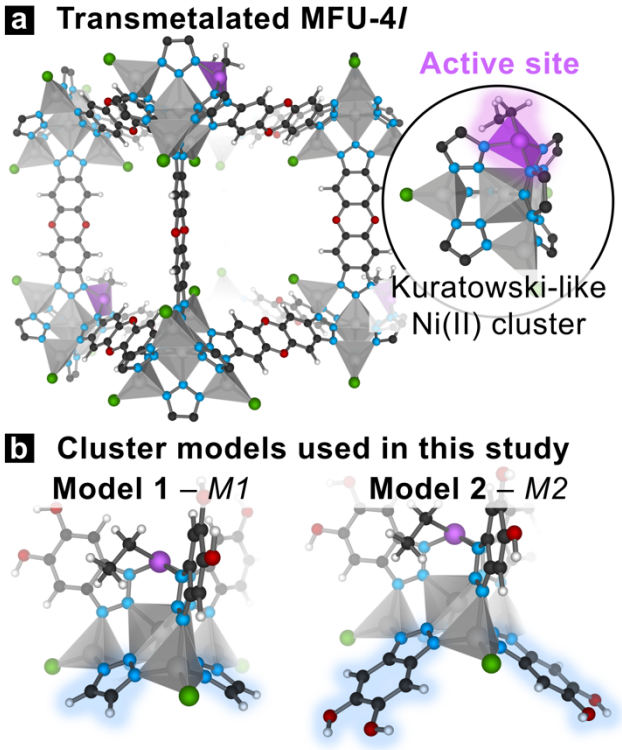

Figure 47. (a) MFU-4*l* feature Kuratowski clusters that host distorted square planar Ni(II) upon metal exchange. (**b**) Computationally, these clusters can be truncated from the parent MOF by peripheral triazines (Model 1, M1), or with inclusion of the aromatic diol (Model 2, M2). Both models are used in this study.

Metal-organic frameworks (MOFs) are an emergent class of porous,[628] crystalline catalysts[292,629,630] that are potentially useful for the conversion of ethylene to 1-butene.[631–

[633] The ability to create site-isolated active sites[110], through either pre- or post-synthetic syntheses[634,635], has enabled the precise design of molecular-like catalytic sites anchored periodically throughout the MOF scaffold. Building on the success of homogeneous nickel-based ethylene dimerization catalysts, MOFs featuring isolated Ni(II) sites with precisely tuned inner-sphere ligation have offered a promising heterogeneous alternative to current industrial catalysts.[636–638] These nickel-based MOFs can be directly synthesized[639] or obtained through post-synthetic grafting[640], deposition[54,305], and metathesis[641]. Yet, state-of-the-art MOF catalysts are still known to produce the undesired product 2-butene, as well as a marginal amount of 1-hexene.

1-Butene selectivity achieved within Ni(II)-MOF catalysts has been attributed to higher activation barriers for chain propagation than termination (and subsequent release of 1-butene).[642] Selectivity towards the α-olefin product has been rationalized comparing the activation barriers for isomerization with β-hydride elimination (BHE).[642] Yet the magnitude of these differences in activation barrier have been relatively small (*e.g.,* 0.5 kcal/mol difference between chain termination and propagation for Ni(II)-NU-1000[642]) or thermally accessible (*e.g.,* 3.5 kcal/mol difference in primary and secondary Ni-alkyl binding along the isomerization route for Ni(II)-MFU-4*l*, computed along a consistent Ni(II) singlet pathway).[643]

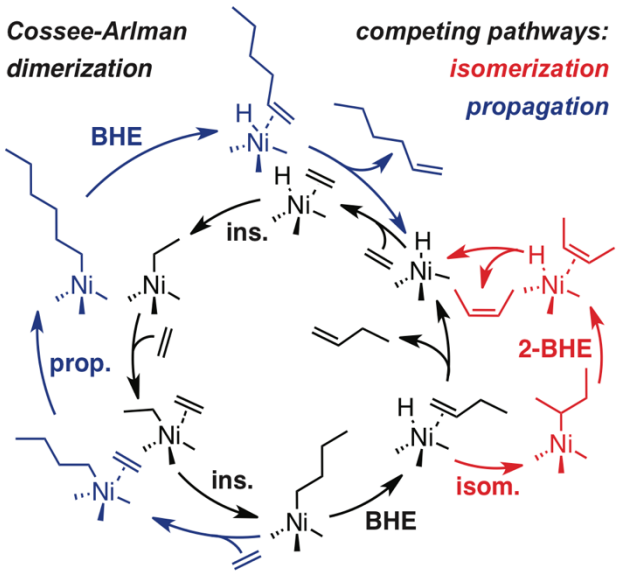

Figure 48. Ni(II) catalysts have been shown to dimerize ethylene through the Cossee-Arlman mechanism – the same mechanism through which higher-order olefins are produced (propagation pathway shown in blue). The isomerization pathway to form 2-butene is shown in red. Selectivity for a single insertion to the C4 product is contingent on β-hydride elimination (BHE) occurring prior to, and faster than, isomerization (*i.e.,* H-insertion to the α-carbon and subsequent BHE).

In a recent experimental report, the Ni(II)-containing MOF Ni(II)-MFU-4*l* achieved 1-butene selectivity rivaling current industrial technologies.[551] The ethylene dimerization is thought to occur at the Kuratowski-type secondary building unit (SBU, see **Figure 47**)[551]. While the conventional Kuratowski cluster is a pentanuclear Zn(II),[644,645] at least one peripheral Zn(II) may be exchanged for Ni(II). These sites bear a close resemblance to the scorpionate reagent cavity of the catalytically active molecular scaffold, nickel tris(pyrazolyl)borate, that affords high 1-butene selectivity.[646] Ni(II)-MFU-4*l*

exhibits >96% selectivity for the C_4 product 1-butene, exceeding the 81% selectivity achieved with the homogeneous analog.[551] Ethylene dimerization in this material is known to proceed via the typical Cossee-Arlman-type mechanism (**Figure 48**) as determined through isotopic labeling experiments in conjunction with density functional theory (DFT) calculations.[643] Yet, the driving force for the exceptional selectivity of this catalyst for the linear α-olefin product over the internal olefin, 2-butene, remains largely unknown.[622]

Here, we employ quantum mechanical simulations to elucidate the underlying electronic forces that drive 1-butene formation and prevent isomerization and propagation. We present a mechanistic investigation along both accessible spin surfaces (singlet and triplet) and compare the zero-point energy (ZPE) corrected free energy profiles of ethylene dimerization and competing pathways over Ni(II) in both MFU-4*l* and a homogeneous trispyrazolyl borate analog. We show that intersystem crossing (ISC) at critical transition states (which we refer to as spin-switching) contributes to selectivity for 1-butene.[647] This spin-switching mechanism highlights an overlooked aspect of MOF catalysis — the ability to access a non-ground state potential energy surfaces during chemical transformations, and promotes the requirement to look beyond the crystallographic structure of MOFs to understand their reactivity.

3.2.2.1 Results and Discussion

Native tetrahedral Zn(II)-Cl sites found in MFU-4*l* are catalytically inert, yet the post-synthetic modification of these sites *via* transmetalation with Ni(II), and subsequent treatment with an initiator such as methylaluminoxane, yields a catalytically active species,

Figure 47b.[551] There, Ni(II) obtains a 4-coordinate distorted square planar geometry, and a ground state singlet, **Figure 49**. However, tantamount to ethylene dimerization is the requirement for the metal to dynamically bind ethylene to an open-metal site.[648] It should not be surprising, then, that throughout the course of a catalytic cycle a change in inner-sphere ligation – per the other idealized geometries shown in **Figure 49** – may also affect the spin surface, potentially inducing ISC.[649–652]

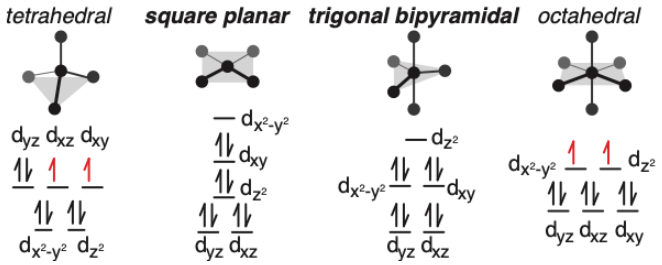

Figure 49. The spin-state of a transition metal-containing system will be dependent on both ligand field strength, which determines the d-orbital spitting energy, and the coordination number and geometry. Throughout the course of a catalytic cycle each of these parameters is dynamic.

Given the conventions of crystal field splitting and the configurations in **Figure 49**, both tetrahedral and octahedral Ni(II) complexes are expected to be ground state triplets, while both square planar and five-coordinate species are expected to be singlets.[653] This variability presents an inherent modeling challenge: how should one treat a transition state that likely undergoes a spin reconfiguration upon the dynamic binding or insertion of a reagent?

To assess the dimerization and propagation pathways in Ni(II)-MFU-4*l,* we first isolated two cluster models to evaluate the impact of peripheral ligands on the Kuratowski cluster, **Figure 47b**. The cluster models were taken from a bulk model built from the parent MFU-4*l* scaffold and equilibrated with periodic boundary conditions. The unit cell for MFU-4*l* contains two pentanuclear Zn(II) nodes (App. D Fig. A5). By exchanging a single Zn(II) per unit cell with Ni(II), Ni(10%)-MFU-4*l* is formed. Bulk Ni(10%)-MFU-4*l* was fully optimized using the PBEsol-functional[101] as implemented in the Vienna *ab-initio* Software Package (VASP)[390–392] using a 500 eV cutoff for the projector-augmented-wave plane-wave basis. The ionic and electronic energy convergence criteria of 0.005 eV and $1x10^{-6}$ eV were applied to a 2x2x2 Γ-centered *k*-grid. All solid-state optimizations proceeded with the same methods.

Two cluster models were extracted from the optimized periodic structure, and any bonds severed in the extraction process were passivated with the addition of hydrogen atoms (H•) to saturate the valence orbitals.[110] Both models keep the secondary building unit containing the entire Zn_4Ni inorganic unit and six connecting triazolate motifs intact. Since steric effects at the catalytic active site are a long-known contributor to selectivity for short-chain olefins over longer chains or polymers[654], the bistriazolatedibenzodioxin (BTDD) linkers around the active site were bisected, inclusive of the dioxin oxygen atoms in both models. In Model 1 (M1, **Figure 47b**), the, linkers on the opposite side of the cluster were truncated to the pyrazolate motif to reduce computational expense. To ensure this approximation did not result in asymmetric electronics that impact the reaction cycle, we compared the Cossee-Arlman dimerization pathway recovered using M1 with a second

model in which all linkers were truncated at the dioxin motif (M2, **Figure 47b**) on both the singlet and triplet energy surfaces. The coordinates of terminal oxygen or carbon atoms were kept fixed in M2 and M1, respectively, to mimic lattice stabilization from MOF incorporation in extracted cluster models.[110]

Consistent with prior investigations of ethylene dimerization in Ni(II)-containing MOFs[642] and similar systems[651] computations were performed on molecular cluster models using the M06-L[103] functional as implemented in Gaussian09.[603] Metal atoms (Zn/Ni) were treated with a doubly polarized triple-ζ basis set (def2-tzvpp) while all other atoms were treated with a polarized split-valence basis set (def2-svp).[655] Vibrational analysis was performed at 298.15 K to obtain thermodynamic quantities, including the zero-point energy correction, and confirm potential energy surface minima and saddle-points with zero and one imaginary frequency, respectively. The gas-phase ΔG is computed at 298.15 K to account for the zero-point energy. The same methods were employed to compute triplet and singlet energy pathways for the homogeneous analogs.[646]

Following the Cossee-Arlman dimerization mechanism previously determined to be the active pathway for ethylene dimerization Ni(II)-MFU-4*l*[643] we compared the energetics of Model 1 and Model 2 along the main reaction pathway. With both models, we found that alkyl-bound species (4-coordinate) favor a triplet spin-state, and no equilibrium geometry could be identified for olefin-bound species in the triplet state (*i.e.,* the ethylene does not bind to the metal). The inclusion of extended allosteric ligands, M2, showed resulted in a smaller difference between the singlet and triplet spin surfaces at stationary points throughout the reaction by 2.3-4.0 kcal/mol. Regardless, the same reaction

profile was recovered using both models, including predicted ISC events and relative activation barriers between reaction steps. M1, **Figure 47b**, was thus selected for further analysis to balance computational cost and electronic structure accuracy while exploring both spin surfaces along each competitive reaction pathway, as detailed in **Figure 48**. We additionally considered β-hydrogen transfer as an alternate chain termination event, but found the activation energy for this pathway to be >30 kcal/mol larger than for the expected BHE pathway, indicating this pathway is likely inactive (App. D, Table A1).

By plotting the reaction profile of a single catalyst turnover to yield 1-butene on the triplet state energy surface (**Figure 50**, blue) relative to the singlet energy surface (**Figure 50**, red), it is apparent that the spin-surfaces repeatedly intersect throughout the lowest energy mechanistic pathway (**Figure 50**, dotted black lines). Hydride insertion and elimination events are expected to take place on the singlet spin surface; the transition state energies for ethylene to ethyl conversion and butyl to 1-butene conversion recovered from singlet configurations are 12.6 and 12.3 kcal/mol lower in energy than the triplet configurations. However, the resulting alkyl-substituted active sites exhibit lower energy triplet geometries. At key stationary points throughout the dimerization pathway, we see that the triplet and singlet energy differences diminish as chain length, *i.e., the* electron-donating ability of the metal-bound alkyl, increases: the triplet geometry is 9.2 kcal/mol, 7.4 kcal/mol, and 2.8 kcal/mol more stable than the singlet geometry for Ni^{II}(H), Ni^{II}(Et), and Ni^{II}(Bu), respectively.

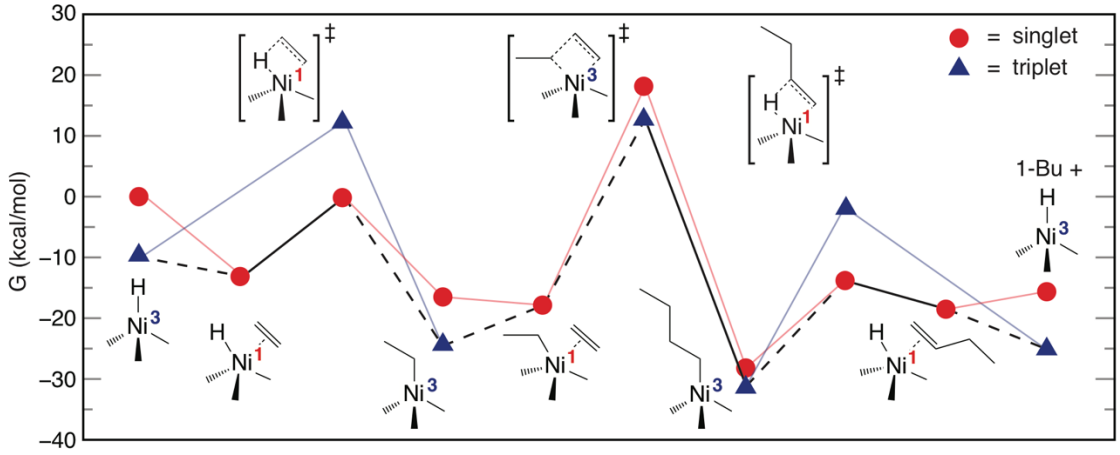

Figure 50. The singlet (red circles, red lines) and triplet (blue triangles, blue lines) dimerization energy surfaces experience repeated crossing when plotted with the singlet Ni-H species and two free ethylene molecules as the absolute reference, indicating the lowest energy reaction route (black lines) incorporates both spin-surfaces, *i.e.* the Ni(II) spin-state is dynamic throughout the catalytic cycle. Atom economy is maintained throughout the cycle by including one or zero equivalents of free ethylene in the free energy of each intermediate along the reaction coordinate.

We expect the triplet $Ni^{II}(H)$ system to play a significant role as an energetic sink to accelerate 1-butene expulsion from the singlet configuration (last step in **Figure 50**).[656] Experimental investigation of the same catalyst for propylene dimerization found reinsertion of 1-butene to be slow and product distribution to be dependent on the primary olefin insertion event, consistent with nickel-alkyl species in the triplet state functioning as intermediates.[657] This is consistent with the recovered spin-switching mechanism where 1-butene desorption is favored only through relaxation to the stable ground-state triplet of

the tetrahedral nickel-hydride. While 1-butene desorption is uphill in energy by 2.8 kcal/mol on the singlet spin-surface, spin-switching affords exergonic product release that is downhill in energy by 6.4 kcal/mol.

Taking a closer look at the coordination sphere of Ni(II) in each spin state, we find the active site geometry for the triplet Ni^{II}(R) MOF species is distorted square planar, **Figure 51a**. A similar geometric trend is observed for the analogous homogeneous catalyst $Tp^{Mes}NiCl$[646], but we note that Ni(II) is more labile in the molecular complex, as the singlet features a partial dissociation of the N-donor ligand (**Figure 51b**) and β-hydrogen-bonding with the unbound nitrogen. Within the MOF, the alkyl chain tail bisects two neighboring BTDD ligands in both the singlet and triplet configurations, likely to mitigate steric interactions between the growing chain and the linkers. Consistently along the lowest energy pathway, the non-triazolate ligand (H, Et, Bu, Hex) is nearly axial in the triplet state. However, olefin approach, especially under high pressures, can further distort the triplet towards the more open distorted square planar ligand arrangement that allows for the side-on association of the small ethylene molecule in the singlet state. This coordination-induced spin-switching phenomenon has been observed in other Ni(II) complexes with rigid N-donor ligands.[650,652,658,659] We note that the axial position of the growing alkyl chain and orientation of linker protons that point directly at the active site likely shield the metal from coordinating larger olefins and inhibits subsequent transformations of preferentially desorbed 1-butene products to longer olefins or isomers.

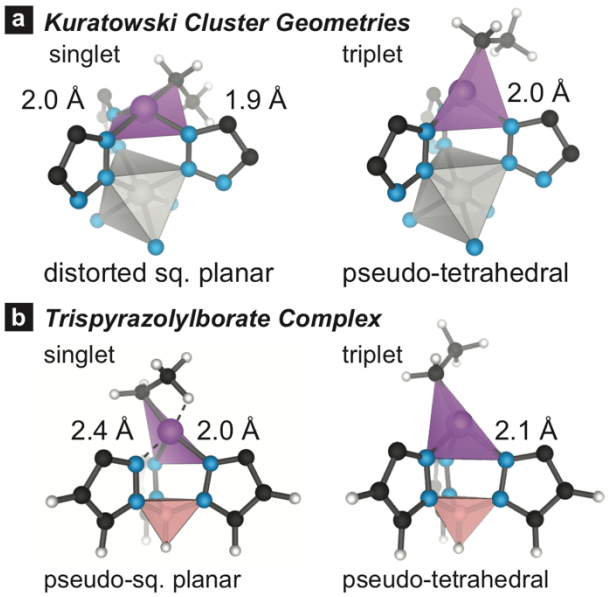

Figure 51. Ni(II)-alkyl species adopt a distorted square planar geometry in the singlet state and a seesaw geometry in the triplet state in both homogeneous and MOF-incorporated active sites. The selected bond lengths depicted for these systems show reduced Ni-N bond lengths in the Kuratowski cluster (**a**) relative to the molecular catalyst (**b**), but the Ni-N bond for both triplet geometries is equivalent. The symmetry of the triplet geometry is likely reinforced in the crystal lattice, evident from the large singlet-triplet gap computed with periodic boundary conditions.

To examine the feasibility of ISC, we explored the spin-surface intersection along the reaction coordinate for olefin insertion to yield Ni^{II}(Bu). While spin-orbit coupling may be used to assess these transitions, it is often impermissible due to system size. Here, the system contains first-row transition metals and organics, so spin-orbit coupling effects are likely to be small. Therefore, the minimum energy crossing point (MECP) will lie close in

energy to the transition state in the adiabatic surface and is a good approximation to the transition state computed with spin-orbit coupling.[660] The computation of the minimum energy crossing point (MECP) was performed using a program described by Harvey et al.[661] interfaced with the Gaussian package and the computational details described above. By analyzing each spin surface between $Ni^{II}(Et)(\eta^2\text{-}Et)$ and $Ni^{II}(Bu)$, we find that the MECP occurs after C-C formation. At this point, Ni(II) can spin-switch from singlet to triplet, enabling a pathway to form the $Ni^{II}(Bu)$ intermediate.

Olefin coordination to $Ni^{II}(Bu)(\eta^2\text{-}Et)$ is 10.3 kcal/mol lower in energy and seemingly functions as a potential well. Thus, to perform BHE on the singlet PES, the system would have to expel the bound ethylene to pass through the MECP to triplet $Ni^{II}(Bu)$. However, butyl chain orientation following the insertion step must enable olefin approach for ethylene adsorption to occur. Previous work suggested a free energy penalty associated with displacing the hydrocarbon chain for ethylene association.[662] Ethene coordination was found to be disfavored in the presence of a butyl chain due to the requisite rotation to afford coordinative approach. Resultantly, C-C coupling proceeded on mobile active sites that detached upon ethylene coordination to adopt the preferred square planar Ni(II) complex. This release of bonding constraints is unattainable in the MOF. Conveniently, the MECP geometry is similar to the activated complex for BHE (App. D Fig. A4**)**; the β-agostic interaction facilitates BHE by reducing the necessary reconfiguration. The MECP is lower in energy than the BHE transition state energy on the singlet PES by 6.8 kcal/mol (App. D Fig. A4), so the rate-determining barrier for BHE is still the singlet transition state.

To assess the implication of ISC on overall 1-butene selectivity, we additionally explored the net energetic pathways for isomerization to the C_4-product 2-butene and propagation to the C_6-product 1-hexene by identifying the lowest energy spin configuration for each intermediate and activated complex at each step of the reaction, **Figure 52**. Evidently, double bond migration is effectively suppressed despite the thermodynamic stability of the internal olefin (**Figure 52**, red). In order to form 2-butene, following BHE an α-hydride insertion must occur rather than 1-butene desorption. This hydride shift forms a 2°-alkyl species that is responsible for the subsequent hydride elimination step to 2-butene. While the 2°-alkyl intermediate is 1.6 kcal/mol more stable than the 1°-alkyl intermediate, the Gibbs free energy of the α-hydride insertion transition state necessary for its formation is 5.2 kcal/mol greater than the preceding BHE and 0.6 kcal/mol greater than the $Ni^{II}(H)$ starting point, whereas BHE is 4.7 kcal/mol lower in Gibbs free energy from the same starting point. Importantly, α-hydride insertion is in direct competition with the barrierless release of 1-butene, favored relative to isomerization by 16.0 kcal/mol. Combined with the 5.2 kcal/mol higher transition state energy for α-hydride insertion relative to BHE, 1-butene formation and release is more likely to occur than isomerization to 2-butene.

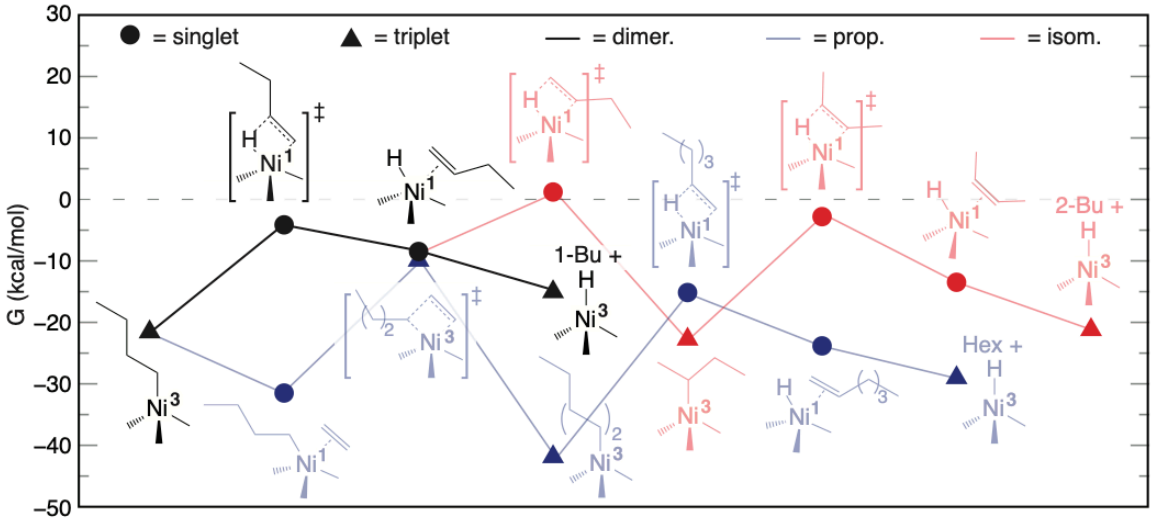

Figure 52. The lowest energy reaction pathways for ethylene dimerization, propagation, and isomerization *via* the Cossee-Arlmann mechanism are overlaid to reveal that following the first ethylene insertion to form a C4-paraffin, isomerization to 2-butene is endergonic by ~0.6 kcal/mol while 1-butene formation and propagation remain exergonic relative to the nickel hydride species. The barrier for BHE (**black**), however, is 17.3 kcal/mol while α-hydride insertion (**red**), 2°-BHE (**red**), and propagation (**blue**) have activation barriers of 9.6 kcal/mol, 19.9 kcal/mol, and 22.3 kcal/mol, respectively. The activation barrier to propagation is >5 kcal/mol larger in magnitude than the barrier that leads directly 1-butene release. For isomerization, while the activation barrier to isomerization from the preceding intermediate is lower than that of BHE, the activated complex is 5.2 kcal/mol higher in Gibbs free energy than that of BHE. Further, this transformation is in direct competition with 1-butene release, which is exergonic by 6.4 kcal/mol.

While the pathway for isomerization is endergonic relative to the nickel hydride species on the triplet surface, both BHE and propagation barriers are entirely downhill from the nickel hydride species (plus two or three equivalents of free ethylene in the case of C_4 and C_6 products, respectively) by 4.7 and 9.9 kcal/mol. At first glance, the propagation pathway seems roughly equivalent to the primary insertion pathway with a more stable product. Indeed, the conversion of C-C π-bonds to C-C σ-bonds is the thermodynamic driving force for common polymerization catalysts.[663,664] However, the activation barrier for propagation is 5.0 kcal/mol greater than the barrier for 1°-BHE, driving the equilibrium towards chain termination events. By these calculations, propagation and isomerization pathways should be similarly disfavored. Yet, product distribution analysis of Ni^{II}(10%)-MFU-4*l* at 298 K shows a greater preference for 2-butene formation than hexene formation—with isomerization products suppressed at high ethylene pressures.[551] Indeed, the noted dependence of 1-butene selectivity with Ni^{II} ethylene dimerization catalysts on ethene pressure is unaccounted for in isolated equilibrium structures.[551,665] It is possible under reaction conditions restricted to the MOF pore space that hexyl formation is hindered not only by internal steric effects but also by nearby reaction species within a MOF unit and the kinetic limitations of displacing the butyl chain to bind the additional ethylene.

Indeed, the additional parameter of pore encapsulation seems to be a dominant factor in controlling ultimate chain length. MOF incorporation of olefin dimerization catalysts frequently corresponds to increased selectivity for shorter-chain olefins; however, local active site geometry is thought to be the primary steric influence.[666,667] Here, the pore size (diameters ranging from 12.0 Å to 18.6 Å[668]) is large enough that van der Waals

interactions from remote portions of the scaffold should have a negligible effect on chain growth (1-butene ~6 Å).[395] However, chain elongation within the radial influence of the MOF pore chemical potential could be hindered by the resultant electronic forces of the pore itself, or the reaction mixture species confined within the same effective "nanoreactor".[669]

Within the confines of porous materials containing catalytic sites, reaction kinetics are governed not only by active site electronics but by the convoluted interplay of local reaction mixture concentrations and relative diffusion kinetics. Given that 1-butene is the primary product from ethylene dimerization while 2-butene and 1-hexene are secondary products formed from prolonged surface sojourns or product re-adsorption, solvation and diffusion kinetics must play a dominant role in MOF-encapsulated ethylene dimerization catalysts. Indeed, the reactivity of ethene in zeolitic mesopores was found to be governed by an intrapore condensation regime.[670] The authors later demonstrated in (Ru)HKUST-1 that C_4+ products are preferentially desorbed into pores in the presence of liquid ethylene.[671]

To understand the implications of MOF incorporation on both selectivity and spin-state, we finally compared the reaction profile of our cluster model with the homogeneous catalyst that inspired its design on both spin surfaces, App. D Fig. A3. In homogeneous systems, where only the local active site is defined, bulky ligands are shown to favor linear chain formation rather than hinder propagation, while more open active sites afford greater rates of BHE and, therefore, a Schulz-Flory distribution of oligomers rather than polymers.[672,673] Contrary to the pre-determined Kuratowski cluster geometry where BTDD

linkers connect six metals from two different nodes, the Tp^{Mes} chelating ligand of the single metal homogeneous analog can dissociate an N-donor to accommodate changes to the coordination environment without necessitating a change in spin-state. The active site can be opened for BHE to occur on the singlet surface, while the mesityl functionalities provide the steric blockage necessary to prevent isomerization.

The entropic freedom of catalysts in the solution phase affords equilibrium structures for olefin-bound intermediates on both spin surfaces. The singlet geometry for $Tp^{Mes}Ni^{II}(Et)$ exploits its entropic freedom to grant a β-agostic interaction with the bound alkyl functionality (App. D Fig. A5b). Yet, the pseudo-tetrahedral triplet geometry remains lower in energy by 15.6 kcal/mol for $Ni^{II}(H)$ and 5.6 kcal/mol for both $Ni^{II}(Et)$ and $Ni^{II}(Bu)$ (App. D. Fig. A3). Still, olefin coordination results in significantly higher energy structures for the triplet configuration (e.g. 19.5 and 20.3 kcal/mol for $Ni^{II}(H)(\eta^2\text{-Et})$ and $Ni^{II}(Et)(\eta^2\text{-Et})$, respectively). It is, therefore, possible that the same spin-switching phenomenon afforded by MFU-4*l* is active in the Tp^{Mes} analog. Yet, unlike in the MOF-catalyst, the only species more stable as triplets than singlets are the four-coordinate alkyl intermediates. Rather than olefin dissociation, followed by association, direct olefin substitution may occur such that no ISC occurs in the solution phase. The more labile coordination geometry means that unlike in the MOF-based catalyst, the ligand sphere of the molecular complex can distort to accommodate olefin association leading to propagation, and the wider transition state geometries associated with isomerization, lowering 1-butene selectivity.

Thermally accessible spin-switching events are known for other Ni(II) trispyrazolyl borate systems.[674] 4-coordinate molecular Ni(II) diimine chain transfer

polymerization catalysts also exhibited natural spin-switching between low-spin square planar geometries and high-spin tetrahedral geometries throughout the catalytic cycle.[675] Structural changes to the ligands, such as altering the location and direction of steric bulk, granted synthetic spin-state control by the resultant coordination geometry distortions, consistent with our results. Closer to the explored catalyst structure, 4-coordinate Ni(II)-Me complexes with strongly donating tris-carbene borate ligands exhibit the same seesaw geometry observed here in the triplet state, as well as the distorted square planar geometry of the singlet (**Figure 51**).[676] Although the carbene system resulted in a more stable singlet state than the triplet, tuning electron density around the metal atom to distort the ligand field could easily alter the preference. Indeed, the similarity in geometries between the singlet and triplet states precludes hysteresis that would prevent rapid interconversion between states.[677]

In homogeneous complexes, the flexible Ni(II) coordination sphere can be both distorted and rigidified by multidentate ancillary ligands with strong electron-donating abilities to facilitate ISC and BHE.[649,651,678,679] Here, the mutual accessibility of spin-surfaces known for Ni^{II} systems with rigid N-donor ligands is accessed through post-synthetic cluster incorporation from heterogenization in a MOF. Thus, with knowledge of how ligand spheres affect coordination geometry and the subsequent material spin state, it is possible to tune the singlet-triplet energy gap and control ISC events. By comparing transition state geometries with spin-state geometries, we can target reaction pathways by targeting the corresponding spin-state. Beyond nitrogenic ligand spheres, molecular

complexes including both nitrogenic and phosphoric donors yield exceptional electrocatalytic hydrogen uptake kinetics and may be attractive future targets.[680,681]

3.2.2.2 Conclusions

In sum, we have found that post-synthetic incorporation of Ni(II) into the scorpionate-type MFU-4*l* nodes induces ISC and electronically disfavors isomerization. The electronic barriers for propagation and are similarly greater than pathways leading to 1-butene. The computed activation barriers for propagation and isomerization steps are 5.2 kcal/mol and 5.1 kcal/mol greater than 1-butene formation, respectively. 1-Butene selectivity is afforded, in part, by a geometrically restricted active site that is both open enough to favor BHE and sufficiently narrow to disfavor non-linear chain growth. This work also highlights the critical role of intersecting spin-surfaces in transition metal-mediated catalytic pathways.

However, the size and similarity of these barriers in idealized DFT models compared with the larger contribution of 2-butene over C_6 products in experimental product distributions signifies a divergence from ideality and hence the complexity associated with reaction mixtures contained in mesoporous scaffolds. Indeed, the reaction barriers to follow alternative pathways vary by less than 1 kcal/mol between the MOF cluster and homogeneous structural analog despite a more than 20% increase in 1-butene selectivity, implicating pore-confinement effects in the higher activity and selectivity of MFU-4*l*. While pore walls do not directly hinder chain growth in this large pore MOF, solvation effects from pore-confined liquids are known to accelerate both hydrogen transfers and 1-

butene desorption.[670,671] C_4 α-olefin selectivity is thereby enhanced because isomerization and propagation events are prevented from taking place.

We propose the contribution of transient triplet state species accessed through effectively barrierless ISC events further favors product expulsion due to the condensed nature of $Ni^{II}(H)$ and the sizeable triplet-singlet energy gap associated with this specific species (9.2 kcal/mol compared with 2.8 kcal/mol for $Ni^{II}(Bu)$). Other materials capable of merely grafting catalytic components cannot provide the same inherent bulk stabilization of the distorted ligand sphere that we find facilitates BHE. Indeed, the mutual dependence of geometry and electronic configuration enables fine-tuning of overall transition metal reactivity. The accessibility of unique coordination geometries from lattice stabilization is encouraging properties for MOF catalyst design.

3.3 Bridge

MOFs with highly ionic linker-node bonding and pore space separating the internal components are beneficial as photocatalysts because the localization of excited states and charge from dopants facilitates active site densities. The same is true for MOFs used as thermal catalysts. However, recovery of the fundamental band gap associated with thermodynamic photocatalytic activation barriers necessitates the use of both periodic boundary conditions and hybrid functionals; on the other hand, kinetic activation barriers for local bonding rearrangements in thermal catalysts can be recovered using molecular cluster models where the level of theory used to recover electronic energies can also be used for geometry optimizations in ground state species and activated complexes.

In this chapter, I demonstrated through the use of Ti(IV) that d^0 metals from the first row of the periodic table give rise to metal-based conduction band states that accept electrons from the organic linker upon MOF excitation. This compositional design principle for achieving spatial separation of an electron and hole can be generalized to any scaffold capable of post-synthetic Ti(IV) incorporation via transmetalation. I further demonstrated that nodes capable of accepting excited electrons in this way, and also feature inorganic basic sites, such as MIL-125, can be stably charged with hydrogen atoms through photodoping up to half the nodal nuclearity. Here, the valence band hole is plugged by an electron, and the associated proton is spatially separated therefrom. The delocalization of electrons within a node through Ti(IV)/Ti(III) redox coupling and the covalent association of a counterion energetically stabilizes the dopant states such that molecular hydrogen formation is suppressed. Building MOFs with inorganic clusters that feature basic sites and d^0 metals prone to redox coupling upon reduction are therefore fruitful targets for both charge storage materials and high activity hydrogenation photocatalysts.

In the area of thermal catalysis, MOFs with localized electronic structure have long acted as host scaffolds to heterogenize homogeneous catalysts. While the inert nature of many nodes enables the incorporation of catalytically active linkers, here we probed the use of innate MOF chemistry and post-synthetic functionalizations thereof to access unique chemical behavior. Indeed, Ni(II)-substituted MFU-4*l* was synthesized as a structural analog to a homogeneous catalyst; yet, the rigid nature of the nodal Kuratowski cluster geometry restricted the geometric flexibility of non-native d^8 metals such that unique spin character was adopted. However, the desorption kinetics governed by pore-confined olefin

solvation seem to also play a dominant role in the selectivity of this, and other, porous solid-state ethylene dimerization catalysts.

In the next chapter, we will see that the dense arrangement of metal atoms within an inorganic cluster show cooperativity, despite their lack of communication with neighboring nodes. This will be demonstrated through gas adsorption, where the chemisorptive uptake of the ligand-exchanged MFU-4*l* node is nonlinear with respect to its nuclearity. In a departure from cluster-based chemistry, we will then explore the use of periodic boundary conditions to analyze long-range structural perturbations to the pore space and active site from the exchange of structural inorganic ligands, and how these inorganic ligand substitutions modulate ligand field strength in a way that grants subtle electronic control over metal active sites. The MOF family discussed in these latter studies is obtained from the direct mixing of Ni(II) and BTDD linkers rather than Zn(II) clusters and BTDD linkers followed by transmetallation with Ni(II).

CHAPTER IV

MATERIALS WITH FLAT ELECTRONIC BANDS FOR GAS UPTAKE, STORAGE, AND CONVERSION

Chapter IV of this thesis begins with a brief explanation of how the methods extensively reviewed in previous chapters are applied to study gas adsorption. The following sections include content from three published studies co-authored by experimental collaborators in which computational approaches to recover physical and electronic structure parameters grant key insights into the electronic origin of adsorption trends, uptake capacity, and pore-filling pressures observed in experiment. Section 4.2 is taken from a previously published article (*Chem,* **2018**, *4*, 2894-2901.) that is co-authored by experimental collaborators and my PI: Ashley M. Wright, Zhenwei Wu, Guanghui Zhang, Robert J. Comito, Robert W. Day, Christopher H. Hendon, Jeffrey T. Miller, and Mircea Dincă. As with previous chapters, since the experimentation performed by these authors is beyond the scope of a theoretical thesis, I have recapitulated the details necessary to understand the implications of my simulations and their benchmarking. All experimental methods and details can be found in Appendix E with the Supplementary Information from this article. This first study surrounds that same parent scaffold as the last section of the previous chapter, MFU-4*l*. However, inorganic anion exchange, rather than metal cation

exchange, is used to modulate the scaffold reactivity. Yet, the same cluster modeling approach is used. Section 4.3 and 4.4 also explore inorganic anion exchange in a family of MOFs with the same BTDD linker as MFU-4*l*, but with a different structure: in this family of MOFs, the inorganic anions play a structural role along continuous 1D nodes in hexagonal pores. The node dimensionality and our interest in the pore space enforces the use of periodic boundary conditions (PBCs) must be used. In Section 4.3, I use PBCs to describe a change in pore dimensions with anion exchange and to understand the role of these anions in modulating the relative humidity at which pore-filling will occur in water-harvesting MOFs (*Journal of the American Chemical Society* **2019**, *141*, 13858-13866.). The co-authors on this study are again experimental collaborators and my PI: Adam J. Rieth, Ashley M. Wright, Grigorii Skorupskii, Mircea Dincă, and Christopher H. Hendon. In Section 4.4, PBCs are again needed to describe the effect of long-range perturbations that effect small molecule binding, but discrete interactions at the open metal centers. This study, co-authored once again by similar experimental collaborators and my PI (Julius Oppenheim, Ashley M. Wright, Adam J. Rieth, Christopher H. Hendon, Mircea Dincă), explores how modulating the ligand field strength along with linker orientation facilitates control over the scaffold's adsorption selectivity for discrete gas molecules.

4.1 Models for Gas Uptake, Separation, and Conversion

Due to the incredible porosity of MOFs, and their unparalleled capacity for structural and electronic modulation with isoreticular chemistry, they have been used to host guest molecules since their earliest conception[1,682,683]. So-began the age of size and shape selective

MOF adsorbents controlled by pore aperture and topology.[684–687] Research in this area during the subsequent decades revealed the practical utility of coordinatively unsaturated, or open metal sites, for strong selective binding of smaller molecules based on electronic interactions.[687–689] In a salient example of how atom-specificity and exchangeability in MOFs can afford both selective catalytic function and gas adsorption, we take a different look at the MFU-4*l* scaffold used here as a biomimic of the carbonic anhydrase active site. In this different capacity, molecular modeling approaches are still appropriate due to the cluster-based MOF and localized nature of bonding interactions. Next, this chapter highlights one family of materials, M_2X_2BTDD[690–692], where metal and inorganic linker exchange can be used for coarse and fine tuning of discrete small molecule interactions with the MOF metal sites as well as pore filling phenomena.

Obviously, key modeling decisions relevant for gas adsorption in MOFs depend on the target application and nature of the active site. Molecular cluster models are sufficient to describe direct active-site interactions that govern adsorbate binding strengths and selectivity when those sites are isolated on electronically insulated components. Periodic models must be invoked to recover the overall pore topology that governs pore-filling dynamics, and embody an accurate portrayal of MOF connectivity in the instance of long-range order: e.g. the π-stacked aromatic linkers in Chapter 1 and the 1D inorganic node discussed in Sections 4.3 and 4.4.

4.2 A Structural Mimic of Carbonic Anhydrase in a MOF

Metal-organic frameworks (MOFs) are promising platforms for biomimetic studies of metalloenzymes.[693–696] The connecting ends of organic linkers in MOFs, such as carboxylates and triazoles, are comparable to the ligands that make up the active sites in metalloenzymes. Consequently, the metal nodes are attractive targets for biomimetic chemistry. The advantages of performing biomimetic chemistry in MOFs over traditional homogeneous systems include (1) site isolation, preventing unwanted bimetallic reactivity and in turn allowing for sterically unhindered metal sites;[697] (2) tunable pore environments, affording hydrophilic or hydrophobic channels, which can mimic the channels found in the enzymes;[695] and (3) higher stability than with enzymes,[698–701] potentially leading to broader use of biomimetic chemistry in industrially relevant applications.

Carbonic anhydrase (CA) is a ubiquitous zinc metalloenzyme that catalyzes the hydration of carbon dioxide. The active site of CA features a divalent zinc in a N_3ZnOH coordination environment, where the zinc exhibits a tetrahedral geometry featuring three histidine groups and a hydroxide (or water) **(Figure 53)**.[702] Much has been learned about CA through modeling the active site with synthetic analogs,[703] such as $Tp^{(tBu,Me)}ZnOH$ (Tp = tris(pyrazolyl)hydroborate), which reacts reversibly with CO_2 and catalyzes oxygen atom exchange between CO_2 and H_2O.[704–706] Accessing similar Tp-like environments within MOFs would afford site-isolated examples of CA. One material whose secondary building units (SBUs) are almost exact structural mimics of the active site in CA is MFU-4l ($Zn_5Cl_4(BTDD)_3$ **1**, where $BTDD^{2-}$ = bis(1,2,3-triazolo[4,5-*b*],[4′,5′-*i*])dibenzo[1,4]dioxin) (**Figure 53**).[479,668,707–710] The SBUs, or metal nodes, in this material

feature four peripheral zinc chloride sites that are coordinated by three triazoles in C_3 symmetry analogous to the Tp ligand and, accordingly, CA (**Figure 53**).

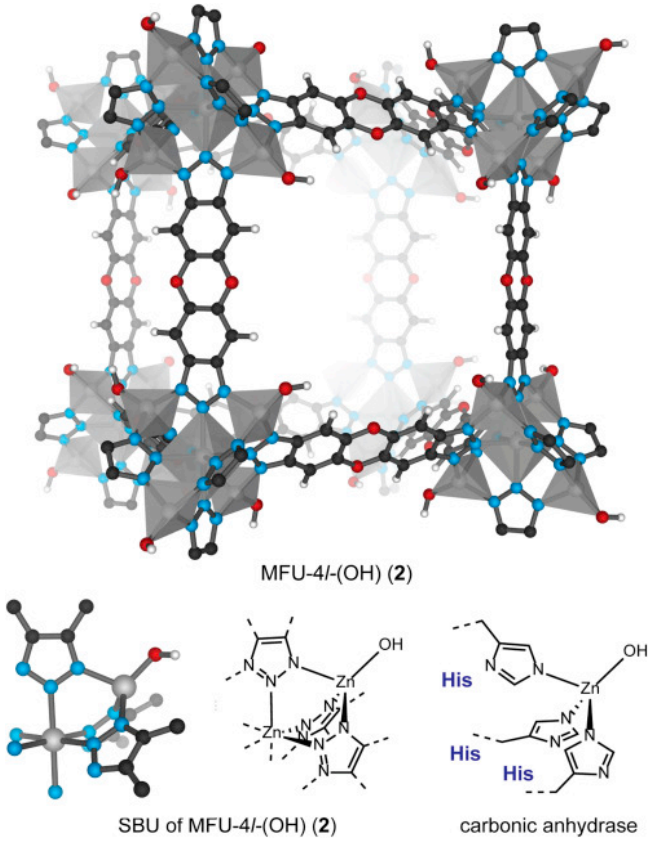

Figure 53. Structure of MFU-4*l*-(OH) (Top) and Comparison of the Active Site in Carbonic Anhydrase with the Peripheral Zinc in MFU-4*l* (Bottom) The structure of MFU-4l-(OH) (**2**) was modeled from the XYZ coordinates of an extended lattice DFT model.

In this article, we demonstrate that the metal node of MFU-4*l* (**1**) can be modified by anion exchange to create a biomimetic model of CA. The addition of organic hydroxide

affords MFU-4*l*-(OH) (**2**), where original terminal N_3Zn–Cl centers are quantitatively transformed to terminal N_3Zn–OH units. Characterization by X-ray absorption spectroscopy confirms the installation of the hydroxide unit, and subsequent reactivity studies show that **2** reacts with CO_2 and catalyzes oxygen atom exchange between H_2O and CO_2 as well as the hydrolysis of 4-nitrophenyl acetate (4-NPA), consistent with the activity of CA.

4.2.1 Results and Discussion

Although the terminal chlorides in MFU-4*l* are known to exchange with a variety of other anions, hydroxide exchange using KOH has been reported to cause decomposition.[488] However, we found that anion metathesis with hydroxide was possible through the addition of 10 equiv (2.5 equiv per peripheral zinc) of tetrabutylammonium hydroxide, [TBA][OH], to a suspension of **1** in methanol, which yielded MFU-4*l*-(OH) ($Zn_5(OH)_4(BTDD)_3$, **2**) as a beige microcrystalline solid. Analysis of **2** by powder X-ray diffraction confirmed the retention of crystallinity (Appendix E Figure A1). Full experimental details of functional group characterization, and all experiments herein, can be found in **Appendix E**.

One way theory helps experimentalists characterize their products is through simple structural comparison. Quantitative fitting of the EXAFS region provided a satisfactory fit for the Zn–Cl bond distance of 2.17 Å in **1** and for the Zn–O bond distance of 1.93 Å in **2**. To compare with single crystal data, an extended lattice calculation on **2** (**2-DFT**) was performed using the PBEsol functional to as implemented in VASP and a 500 eV planewave cutoff with a Gamma-only k-grid. The starting structure was obtained from the

crystallographically determined MFU-4*l* xyz coordinates by replacing Cl with OH groups. The computed Zn–O bond distance of 1.84 Å was in good agreement with the EXAFS fitting (1.85 Å for comparable molecular analogs) and with CA itself (1.9–2.1 Å).[703]

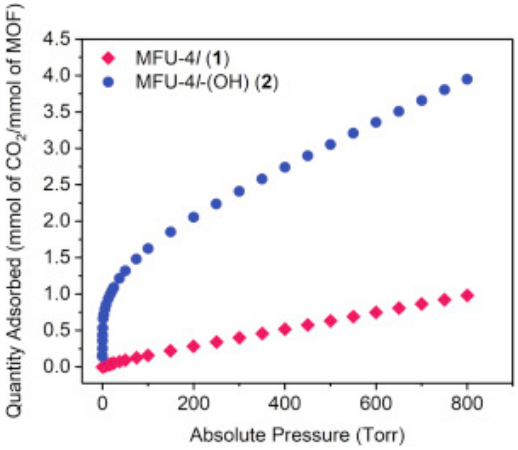

Figure 54. CO_2 Isotherm at 298 K for MFU-4l (1; Red Diamonds) and MFU-4l-(OH) (2; Blue Circles) showing steep uptake up to 1 CO_2 molecule per node and a shallower slope up to the stoichiometric uptake of 4 CO_2 molecules per node.

A critical step in CO_2 hydration by CA is CO_2 insertion into the Zn–OH bond. After confirming the installation of the Zn–OH group, we probed its reactivity with CO_2 by measuring its CO_2 adsorption isotherm at 25°C (**Figure 54** and App. E Fig. A3). Notably, the adsorption isotherm profile featured a significant uptake of CO_2 between 0 and 17 Torr, corresponding to 0.86 mmol of CO_2 per g of MOF. Importantly, this is equivalent to 1.0 mmol of CO_2 per mmol of MOF or the insertion of CO_2 into one of four Zn–OH sites in each SBU. The isotherm profile became shallower, and uptake of the remaining ~75% CO_2 occurred over a large pressure range of 17–800 Torr. The total CO_2 adsorption

capacity at 800 Torr was 3.41 mmol/g (4.05 mmol of CO_2 per mmol of MOF), which coincides with the total number of Zn–OH sites (3.36 mmol/g) in the MOF. The initial steep uptake supports a strong interaction between **2** and the first CO_2 equivalent (per SBU), most likely stemming from the insertion of CO_2 into the Zn–OH bond, a unique CO_2 capture mechanism that has been observed only once before in a MOF.[711] After the initial steep uptake, the isotherm profile became shallower with increasing coverage, suggesting a change in the interaction between the MOF and CO_2 or a shifting of the hydroxide-carbonate equilibrium with increasing CO_2 pressure.

To gain insight into this apparent transition between adsorption regimes, we modeled CO_2 insertion into the Zn–OH bond by using DFT (PBE/6-311G**). To do so, we used a truncated model of the SBU, $Zn_5(OH)_4(BTA)_6$ (BTA = benzotriazole), extracted from the periodic structural optimization. Subsequent optimization of the cluster model gave a Zn–O(H) bond distance of 1.85 Å and Zn–N bond distances of 2.02–2.05 Å, consistent with the EXAFS fit and extended lattice DFT model. Binding energies were calculated from the difference in energy between the MOF or cluster after bicarbonate formation and the sum of the energy of the MOF or cluster with one less bicarbonate and free CO_2. Due to computational expense, we were not able perform full optimizations on the bulk solid-state material after CO_2 additions, and instead only allowing the local node-bicarbonate structure to relax. There was reasonably good agreement between the molecular and solid-state bicarbonate formation enthalpies of the first addition of CO_2 (–50.4 and –60.7 kcal/mol, respectively). The disparity is due to our constrained relaxation parameters. Binding enthalpies of subsequent CO_2 additions to the $Zn_5(OH)_4(BTA)_3$ cluster

were obtained by performing with full optimizations and were found to be less favored than the first addition, ranging from –42.0 to –37.8 kcal/mol (App. E Table A7). This trend of decreasing binding enthalpy is in qualitative agreement with the experimental data. We postulate that the conversion of the highly basic –OH to weakly basic –OCO_2H perturbs the coordination environment of the SBU enough to weaken the nucleophilicity of the remaining three Zn–OH sites within a given metal node. Given that the nucleophilic strength of Zn–OH correlates with its reactivity toward CO_2,[712] less nucleophilic Zn–OH units shift the Zn–OH + CO_2 ⇌ Zn–OCO_2H equilibrium to the left. A comparable trend of initially high heat of adsorption to lower heat of adsorption was observed in $[M^{II}M^{III}(OH)Cl_2(bbta)]$.[711]

These cluster models were also used to aid in experimental characterization through simulated spectroscopy. To determine the nature of the chemisorption interaction, our experimental collaborators monitored the reaction between **2** and CO_2 by DRIFTS. While no spectral changes occurred with the addition of CO_2 to **1**, the addition of CO_2 to **2** resulted in the formation of new bands in the DRIFT spectrum that are consistent with the formation of zinc-bicarbonate, the product of CO_2 insertion in CA (App. E Fig. A21). The cluster models used to obtain free energy changes upon subsequent binding were also used to simulated IR spectra and confirm the changing –OH group IR frequency upon CO_2 insertion (**Figure 55**).

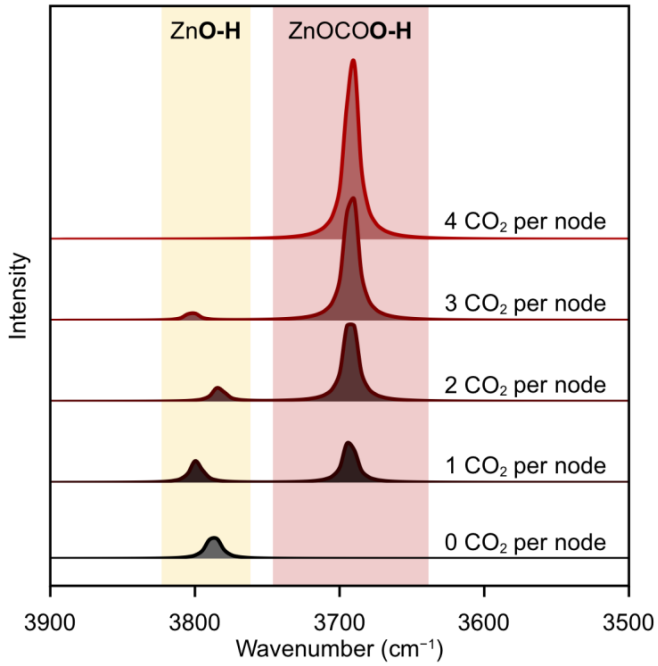

Figure 55. Simulated IR spectra for $Zn_5(OH)_{4-n}(CO_3H)_n(BTA)_3$ (n = 0–4). The unscaled vibrational frequencies are shown for the ZnO–H and ZnOCOO–H. The variation of the Zn-OH is due to variation in the symmetry of the cluster.

We further illustrated the critical role of the hydroxide ligand in CO_2 uptake by comparing the experimental CO_2 sorption properties of **1** and **2**. MOF **1**, containing a Zn–Cl bond and a saturated metal center, showed a CO_2 adsorption capacity at 800 Torr of 0.98 mmol of CO_2/mmol of MOF (1.23 mmol of CO_2 per g of MOF), which is approximately four times smaller than the overall capacity of **2** (**Figure 54**). The zero-coverage Q_{st}, 20 kJ/mol, was also significantly lower than the Q_{st} of **2** (App. E. Figs. A16–A19). Most notably, at 17 Torr, **2** adsorbed 0.99 mmol of CO_2 per mmol of MOF, which is approximately 300 times more CO_2 than **1** (0.0031 mmol of CO_2 per mmol of MOF) at

the same pressure. The large uptake at low pressures demonstrates the potential utility of CO_2 insertion into the M–OH bond for CO_2 sorption applications.

4.2.2 Conclusion

In summary, we have demonstrated that the metal nodes of MFU-4*l* can be functionalized to create a high-fidelity biomimetic model of the CA active site. Reactions performed by the enzymes, such as CO_2 insertion into the Zn–OH groups of the metal nodes and hydrolysis of 4-NPA, are mimicked in the MOF. These results demonstrate a rare example of functionalizing a MOF metal node to mimic the activity of an enzyme. The nascent field of biomimetic chemistry in MOFs holds potential for future understanding of enzyme chemistry by isolating the reactivity of distinct components and also performing enzyme-inspired reactions in stable frameworks. For instance, the insertion of CO_2 into a metal-hydroxide bond could lead to CO_2 separations with limited energy cost in regeneration of membranes.

Models of the extended solid were used to compare against experimental EXAFS data and benchmark the cluster models used to compute the relative energy of subsequent CO_2 insertions into the four Zn-OH motifs per node. Cluster models were additionally employed to perform vibrational analysis and build simulated infrared spectra for MOF nodes with increasing ratios of bicarbonate groups. These spectra helped confirm chemisorption taking place and correlated with the growth of new peaks observed in DRIFTS spectra with increasing concentrations of CO_2. Together, theory and experiment demonstrated the $N_3Zn(II)$-OH active site in MFU-4*l* was uniquely active for the uptake

and conversion of CO_2 compared to with the halide ligand site in the parent material. Periodic models confirmed the chemical motifs describe by PXRD and benchmarked cluster models used to simulate vibrational spectra and free energy changes. The relative energy of subsequent CO_2 insertions computed with DFT suggest a reduced basicity of all -OH groups within a node given chemisorption at one. This indicates some intranodal electronic communication, consistent with previous investigations (Section 3.1.4.1), while electronic isolation of each node is maintained such that cluster modeling is still appropriate.

4.3 The Onset of Pore-Filling for Water Sorption in MOFs

The capture of water vapor at low relative humidity (0–40% RH) can be used to drive heat transfer,[713–720] (to trap atmospheric water vapor,[714,721–725] or for dehumidification.[726–730] Recent advancements in the design of porous materials for these applications have moved next-generation water sorbents closer to applicability,[714,716,725,727,728] but methods to precisely control the hydrophilicity of a sorbent are still needed. Complicating sorbent design, the mechanism of water uptake at low relative humidity remains incompletely understood due to the complex nature of the water phase-change process as well as the difficulty of accurately simulating the properties of water.[731,732]

In order to achieve maximum thermal efficiency, a porous material should have a high capacity for water and should adsorb water reversibly and in a stepwise fashion at a precise RH.[715] Additionally, although nontrivial, it is highly desirable to have synthetic

control over the position (% RH) of the water uptake step.[668,733,734] The % RH whereupon a pore fills with water determines the driving force for heat transfer and, concomitantly, the temperature required to release water from the sorbent: more hydrophilic sorbents are capable of creating greater temperature gradients but also require more energy to cycle back to the dry state.[715] In the case of atmospheric water capture, the % RH of the uptake step determines the applicable climatic region.[723,725]

Outside the confines of a porous material, water condensation occurs at 100% RH. In porous materials, water begins to occupy the voids at lower RH with decreasing pore diameter,[735] and complete saturation occurs near 0% RH in some cases.[713,736,737] Additionally, the hydrophilicity of the pore interior, modifiable via ligand functionalization,[733,734,738] cation exchange,[668] as well as exchange of supporting ligands,[739] plays a role in determining the RH at which the pore will fill. These empirical design rules have guided the development of sorbents with impressive performance, even though the underlying hydrogen bonding structure of water in confined pores, which undoubtedly influences the position of the pore filling step, remains unclear. Indeed, water in confinement and along interfaces can have properties very different from that of bulk water, as the pore structure or interface itself impose restrictions on the complex hydrogen bonding structures.[740,741] Metal–organic frameworks (MOFs) provide an ideal platform for interrogating the hydrogen bonding structure of confined water because their modular nature allows for tuning of the pore size, metal ion, and hydrophilicity without altering the overall framework topology.[742] In addition to precisely controlling the water uptake step position, the stability of water sorbents is also of paramount importance because

applications for water harvesting or heat transfer will require active materials capable of undergoing thousands of adsorption cycles. This is an important practical consideration that only rarely is addressed in the academic literature.[743]

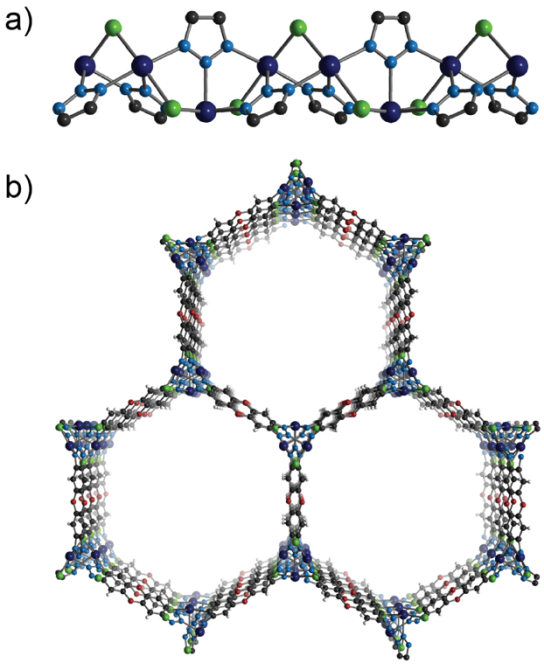

Figure 56. The structure of Ni_2Cl_2BTDD (1-Cl). (a) The infinite chain secondary building unit viewed along the c-axis. (b) View down the c-axis.

Recently, our experimental collaborators reported a MOF that captures record quantities of water in the humidity region relevant for many applications.[714] The water uptake capacity in this material is optimized: because the pore size is at the "critical diameter"[735,744] for water capillary condensation during pore-filling, its high water capacity is completely reversible, without appreciable hysteresis. This minimizes the energy input

required for cycling between the hydrated and dry states. The champion material, synthesized from the ligand bis(1H-1,2,3-triazolo[4,5-b],[4′,5′-i])dibenzo[1,4]dioxin (H_2BTDD) and $CoCl_2 \cdot 6H_2O$, exhibits a capacity of nearly 1 g of H_2O g^{-1} of MOF.[714] Here we report that the Ni^{2+} variant, Ni_2Cl_2BTDD, can be synthesized with greater crystallinity and porosity than previously possible, enabling it to match the capacity of the Co^{2+} material. We further show through extended cycling experiments that the decreased lability of Ni^{2+} [745] leads to excellent long-term stability well beyond that of the Co^{2+} analogue. Finally, we demonstrate that Ni_2Cl_2BTDD undergoes facile anion exchange whereby hydroxide, fluoride, or bromide anions isostructurally replace native chloride ligands (**Figure 56**). These anion metathesis manipulations modulate hydrogen bonding interactions between water and the pore wall, resulting in stark differences in water uptake at low RH for the different anion-containing MOFs. Fundamentally, these structural perturbations provide a platform to investigate the hydrogen-bonding structure of confined and interfacial water during the pore-filling process by diffuse reflectance infrared Fourier transform spectroscopy (DRIFTS). Beyond tuning the hydrophilicity, the series of halogens modulates the pore size of the respective MOFs in a nonintuitive way, with the larger bromide yielding the shortest a and b cell parameters. This subtle variation leads to critical changes in the hydrogen bonding structure of water within the pore. Consequently, pore filling occurs at substantially lower relative humidity (RH) in Ni_2Br_2BTDD. This is counterintuitive because below 5% RH the bromide derivative is the least hydrophilic. Importantly, the introduction of bromide maintains exceptional water stability, with negligible loss of capacity after 400 adsorption cycles. These systematic synthetic

variations further our fundamental understanding of water in confinement and provide a promising new adsorbent with record water capacity at low (<25%) RH and excellent long-term stability. Data and methods associated with the uptake measurements can be found in **Appendix F.**

To understand the impact of anion exchange on structural parameters, periodic models were constructed with, and compared to, powder x-ray diffraction refined coordinates. Computationally, all structures were fully optimized within the DFT construct using PBEsol[746] as implemented in Vienna *Ab-Initio* Software Package (VASP)[113,390,391,480] with a projector-augmented-wave plane wave basis set. A 500 eV plane-wave cutoff was employed with a 2 x 2 x 2 k-grid. Calculations were performed with spin polarization and Ni atoms were initiated as, and optimized to, the high-spin state. Close inspection of the experimental structural parameters of the anion-exchanged MOFs revealed a surprise expansion of the a, b parameters from 38.5282(5) Å for Ni_2Cl_2BTDD to 38.6092(5) Å upon fluoride exchange, despite the expected contraction of the c parameter upon replacing the larger Cl– with F– (Table 1). The computational optimization of the two idealized, fully exchanged fluoride and chloride structures by DFT confirmed this unexpected trend and predicted that the bromide-exchanged analogue, Ni_2Br_2BTDD, should have an even narrower pore due to a further reduction of a and b by at least 0.1 Å relative to Ni_2Cl_2BTDD (Table 1). Furthermore, owing to its larger covalent radius, Br– should protrude into the pore to a greater extent than any of the other anions, further narrowing the pore diameter and potentially leading to water uptake at lower RH due to increased confinement.

Table 1: Unit cell and select crystallographic parameters determined by Rietveld Refinement and DFT for Ni_2X_2BTDD frameworks, X=F, Cl, Br, I, OH demonstrating good agreement.

DFT	***a,b***	***c***	**Ni-N_1**	**Ni-X**	**Ni-X-Ni**
Ni_2F_2BTDD	38.846	7.663	1.91	2.02	100.4°
$NiCl_2BTDD$	38.507	7.932	1.92	2.33	87.9°
Ni_2Br_2BTDD	38.364	8.009	1.92	2.46	83.8°
$Ni_2(OH)_2BTDD$	38.897	7.807	1.92	1.99	104.0°
Rietveld	***a,b***	***c***	**Ni-N_1**	**Ni-X**	**Ni-X-Ni**
$Ni_2F_{0.83}Cl_{0.17}BTDD$	38.609	8.093	2.02(2)	2.06(2)	112.2(2)
$NiCl_2BTDD$	38.528	8.189	2.04(2)	2.38	92.4(2)
Ni_2Br_2BTDD	38.425	8.208	2.03(1)	2.50	87.4(2)

Despite the seemingly small reduction in pore diameter, a water isotherm for the Ni_2Br_2BTDD material indicates that the pore-filling step shifts substantially, from 32% RH at 25 °C for the Cl– and F– derivatives to 24% RH for the Br– analogue (**Figure 57a**). As a consequence, Ni_2Br_2BTDD adsorbs a record 64% water by weight below 25% RH, a humidity value that is within the relevant range for many applications in heat transfer and atmospheric water capture.[723,747] Notably, the total volumetric water uptake at 95% RH for Ni_2Br_2BTDD (**Figure 57b**) is only 15% lower than that of the chloride parent material. In the very low humidity region (below 15% RH), where hydrogen bonding interactions with

the framework are expected to dominate, the water uptake for Ni_2Br_2BTDD is expectedly lower than that for either the chloride or fluoride analogues, which presumably establish stronger hydrogen bonding interactions with the first water molecules entering the pores (App. F Fig. A10.1)

Ni_2Cl_2BTDD is a strong candidate for water sorption applications, with a record reversible water uptake below 32% relative humidity. Because of the inertness of Ni^{2+}, it exhibits exceptional stability toward water cycling, in excess of that previously reported for the analogous Co^{2+} material. Introduction of anions with greater potential for hydrogen bonding interactions, such as F^- or OH^-, did not lead to shifts in the water uptake step profile toward lower RH, though these anions did promote increased water adsorption at very low RH. These results indicate that, as long as nucleation sites exist for water, further increasing the pore wall hydrophilicity does not change the position of the water uptake step. Contraction of the accessible pore diameter by just 0.1 nm as indicated by models of the extended solid and Rietveld refinement of crystallographic parameters, as well as modification of the polarity of initially adsorbed H_2O by the introduction of Br^- results in a pore-filling step at lower RH by 8%. The resulting Ni_2Br_2BTDD material has the greatest capacity, measured gravimetrically or volumetrically, of any material below 25% RH. The capacity of 0.64 g of water per g^{-1} of MOF achieved below 25% RH is a new record in this partial pressure region relevant for many applications in heat transfer and atmospheric water generation, which represents a large leap forward achieved via precise pore size control and polarity modification not possible in other materials.

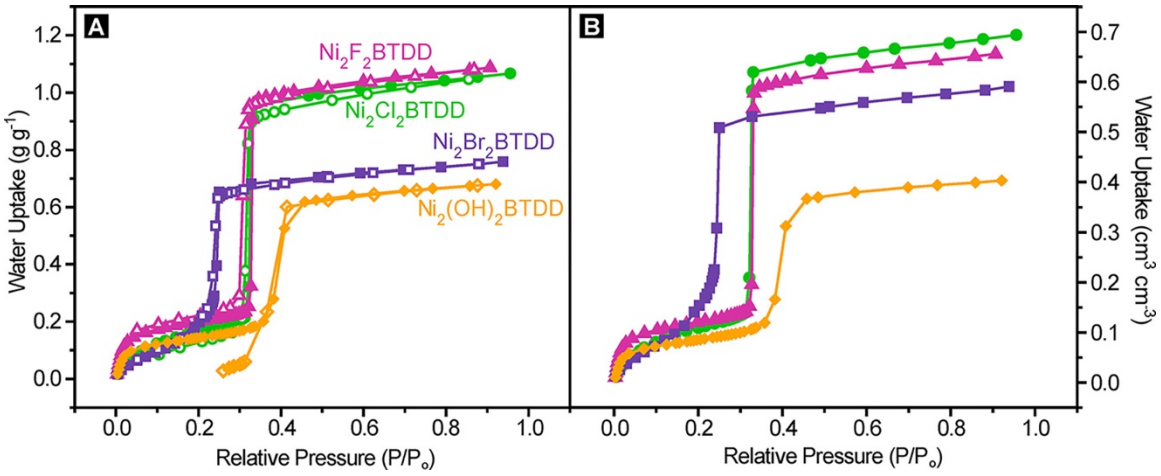

Figure 57. (a) Water vapor adsorption (closed symbols) and desorption (open symbols) isotherms of Ni_2Br_2BTDD, Ni_2Cl_2BTDD, $Ni_2F_{0.83}Cl_{0.17}BTDD$, and $Ni_2(OH)_2BTDD$ measured at 25 °C. (b) Adsorption isotherms converted to volumetric units using the material density.

4.4 Divergent Adsorption Behavior Controlled by Primary Coordination Sphere Anions

Metal-organic frameworks (MOFs) are a class of highly porous crystalline materials employed for a variety of applications, particularly that for the uptake, storage, separation, and catalytic conversion of gases.[748–750] The atomically defined scaffolds (barring defect sites) can be easily tailored through a barrage of synthetic methods—including cation and linker exchange, post-synthetic functionalization of both metal and linkers, and post-synthetic metalation of metallolinkers—allowing specific adsorbate-adsorbent interactions to be fine-tuned.[687,751–753] These aspects allow for the realization of high capacity, selective solid-state adsorbents for gas separations. In particular, MOF

adsorbents have the potential to increase the efficiency of separations in which the relative volatility of the adsorbates is low; here conventional materials and distillations struggle to chemically differentiate between components of the mixture, as in alkane/alkene separations.[754,755]

Ethene, or ethylene, is a crucial feedstock for the production of global chemical commodities including ethylene glycol,[756] styrene, ethylene dichloride[757], and numerous polymers,[758] that is primarily obtained from high energy processes in oil refineries, that further invoke costly separation schemes.[759] Ethene is also relevant in the agricultural industry where it is used to control the ripening rates of fruits and vegetables, and other aspects of plant growth and development.[760–762] To improve the sustainability of the chemical industry, we seek to both access petrochemical derived chemicals through more energy efficient transformations beginning with sustainable building blocks such as biomolecules and replace distillation separations with passive membrane technologies.[763,764] The effluent of reactors either consuming or producing ethene molecules host other small molecule species. For example, CO and H_2 are byproducts in the oxidative coupling of methane to ethene and ethane[765–767] and the reduction of CO_2 to ethene.[768] While ethane/ethene separations are facilitated in MOFs by π-π interactions between olefins and open metal sites (OMS, also referred to as coordinatively unsaturated metals), the selectivity for ethylene over other π-acids such as carbon monoxide requires subtler chemical tunability.[769]

The idealistic goal of specifically tailoring frameworks with high sorption capacities to select for target species demands a detailed understanding of the structure-

function relationships within the frameworks. Small molecule binding affinity with OMS is governed by the adsorption geometry, orbital interactions, and relative electronegativity, which are in turn controlled by MOF topology and composition. Prior investigations focus on tuning adsorption strengths through direct metal substitution.[770] Here we demonstrate how manipulating the primary coordination sphere of individual metals imparts sufficient structural and electronic variation to create divergent trends in electronically similar gases, namely ethene, carbon monoxide, and hydrogen gas.

Modifications to the primary coordination sphere of OMS (either through steric hinderance or electronic perturbation) can have a substantial impact on gas sorption properties.[771] For example, it has been demonstrated that O_2 binds more strongly to $Co_2(OH)_2BBTA$ than to Co_2Cl_2BBTA (an isoreticular framework to the titled Ni_2X_2BTDD), likely due hydrogen bonding interactions from the hydroxide as well as changes to the partial charge on the metal center enabling charge transfer to O_2.[772] Examples such as this are atypical as modifications can significantly alter framework topology and be detrimental to porosity, crystallinity, or OMS accessibility.[773–775] Resultantly, there are few systems in which the primary coordination sphere can be systematically varied and structure-function relationships elucidated. Yet, both metal and inorganic ligand exchange in Co_2X_2BBTA and Ni_2X_2BTDD yield topologically consistent scaffolds.

We recently reported a series of triazolate OMS MOFs, M_2Cl_2BTDD (M = Mn, Co, Ni; H_2BTDD = bis(1H-1,2,3-triazolo[4,5-b],[4′,5′-i])dibenzo[1,4]dioxin) (**Figure 56**), that feature the same chain of alternating -M-X-M-X- units in the secondary building unit

(SBU) as the BBTA MOF.[770] The primary coordination sphere features halogens that can undergo post-synthetic anion exchange resulting in a family of Ni_2X_2BTDD (X = OH, F, Cl, Br) materials with the same chemical topology.[692] These isostructural and compositionally dissimilar materials have been demonstrated to have varying water sorption properties (due to changes of the hydrogen bonding networks). The network cooperativity in such system prevents isolated characterization of the metal-adsorbate interaction.

Here we demonstrate that the direct metal-adsorbate interactions for conventional π-acceptors (CO, C_2H_4, H_2) also vary in the family of Ni_2X_2BTDD frameworks, allowing for the harnessing of the spectrochemical series to control the Ni d-orbital potential. Variation of the X-type ligand (X = OH, F, Cl, Br) alters the electron density at the Ni site, with opposing adsorption behaviors for the studied adsorbates. Unlike what would be predicted, based on the molecular orbital assumption in which a series of π-acceptors respond similarly, we find that the isosteric enthalpy of adsorption for CO increases with heavier halogens, that for ethylene decreases, and that for dihydrogen remains nearly constant. While our initial inclinations were to attribute these differences to steric restrictions about the larger adsorbates and halogens, the combination of experimental and computation evidence suggests differential electronic behaviors whereby CO and H_2 act as σ-donors, while C_2H_4 behaves as a π-acceptor. The insights drawn from electronic structure analyses benchmarked to isosteric adsorption enthalpies will have implications for the future design of MOFs for selective gas separation applications.

4.4.1 Results and Discussion

$Ni_2(OH)_2BTDD$ (**1-OH**), Ni_2F_2BTDD (**1-F**), and Ni_2Br_2BTDD (**1-Br**) were synthesized according to literature by soaking Ni_2Cl_2BTDD (**1-Cl**) in solutions of KOH, CsF, and CsF followed by TMSBr respectively.[692] It has been previously demonstrated that each of these frameworks remains crystalline, and that **1-OH** and **1-Br** are quantitatively exchanged while that for **1-F** proceeds to $Ni_2F_{0.83}Cl_{0.17}BTDD$

To test the impact of the anion on the binding strength of various adsorbates, we measured variable temperature adsorption isotherms with activated samples of **1-X** (X = OH, F, Cl, Br) for CO, C_2H_4, and H_2. With all three gases, the isotherms displayed type I character indicating that the relative pressure of the gases is insufficient to form multilayer surface coverage **(Figure 58)**.[776] The uptake capacities at 1 bar and 298 K show that the metal site coverage is substoichiometric ranging from 14-59% for CO and 43-74% for ethylene (**Table 2**). Typically, OMS MOFs near room temperature display CO and ethylene isotherms that saturate near a value stoichiometric to that of the metal site as the adsorbates have preferential coordination to the metal sites.[777,778] Notably, the uptake capacity is considerably reduced for **1-OH**, possibly indicating a weakened interaction between **1-OH** and each adsorbate. The H_2 capacity at 1 bar and 77 K is in excess of the metal content, ranging from 174-252% per metal site, suggesting the formation of a multilayer or the presence of BTDD-bound sites. Still, the total quantity adsorbed is not a precise metric by which to interpret sorption data, as such, we measured the isosteric enthalpy of adsorption and used these values to benchmark computational models.

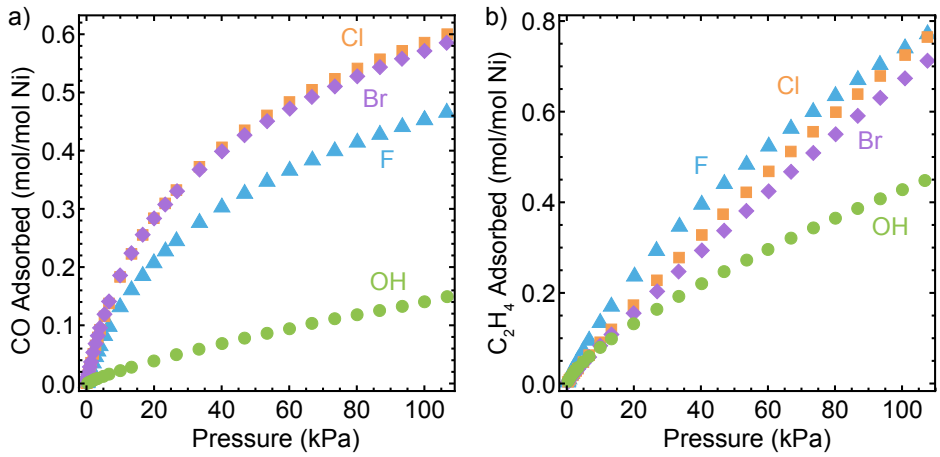

Figure 58. (a) Carbon monoxide and (b) ethylene adsorption isotherms for 1-X materials at 298 K

Experimental adsorbate binding energies were recovered by averaging the isosteric enthalpies of adsorption extracted from four different models used to fit variable temperature adsorption isotherms (**Figure 59**, unfilled shapes, see Appendix G for experimental details). Transitioning from F to Cl to Br, the isosteric enthalpy of adsorption for CO increases from 31 to 45 kJ/mol. The enthalpy for 1-Br at 45 kJ/mol is large relative to similar MOFs, which typically range from 20 to 50 kJ/mol (App. G Table A5.1). In contrast, the enthalpies for ethylene follow a reverse trend, decreasing from 33 to 20 kJ/mol. An enthalpy of 20 kJ/mol is quite small for the interaction of ethylene with OMS MOFs, which typically fall between 20 and 60 kJ/mol (App. G Table A5.2). The H_2 enthalpies are only weakly dependent upon the identity of the anion (7.0-7.6 kJ/mol). These magnitudes are indicative of weak physisorption.[779] Still, the strength is comparable to other materials with H_2 binding energies at open coordination sites, which typically range from 5-15 kJ/mol.[780,781]

Table 2. Summary of adsorption isotherm data and computational binding energies for CO, C_2H_4, and H_2 with Ni_2X_2BTDD frameworks, X=F, Cl, Br, I, OH

Gas	Anion	Total uptake capacity at 1 bar,[a] (mol gas/mol BTDD)	Open metal sites occupied at 1 bar,[a] (%)	Q_{st} (kJ/mol)[b]	Theoretical Binding Energy (HSEsol06)
CO	**F**	0.91	45	31.00 ± 1.61	32.74
	Cl	1.17	59	39.02 ± 0.16	41.44
	Br	1.14	57	44.56 ± 0.75	44.42
	OH	0.29	14	16.42 ± 1.17	31.79
C_2H_4	**F**	1.48	74	32.98 ± 0.40	25.07
	Cl	1.45	73	22.31 ± 0.24	23.62
	Br	1.35	67	19.80 ± 0.65	20.79
	OH	0.86	43	23.23 ± 1.14	13.06
H_2	**F**	4.51	225	7.09 ± 0.02	9.78
	Cl	4.78	239	7.63 ± 0.01	12.90
	Br	5.04	252	7.62 ± 0.01	12.38
	OH	3.47	174	7.00 ± 0.01	-

[a] CO and ethylene at 298 K and dihydrogen at 77 K, [b] Averaged over Unilan, Virial, Sips, and Dual-Site Langmuir models

In the case of **1-OH**, a substantial decrease in the isosteric enthalpy of adsorption for both CO and C_2H_4 is observed, accompanied by a large decrease in the uptake capacity. The decrease in uptake capacity suggests that access to the OMS is impeded. However, no decrease is observed in the uptake of dinitrogen at 77 K indicating the pores are not clogged and there are negligible differences in the PXRD pattern compared to **1-Cl**, so no significant structural changes should be present (for example if the ligands bent at the dioxin ring).[692]

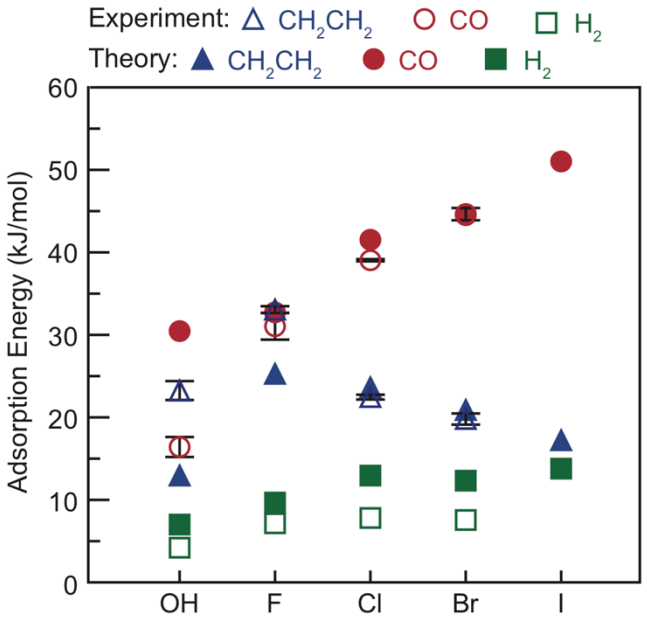

Figure 59. Comparison between the experimentally determined isosteric adsorption enthalpies for carbon monoxide (blue empty triangles), ethylene (red empty circles), and dihydrogen (green empty squares) with the theoretical adsorption energies computed at the HSEsol06 level of theory from PBE-D3 optimized geometries (solid shapes) show excellent agreement for halide derivatives, but some disparity in the case of hydroxyl ligands and adsorbates with pi-systems.

Electronic insights into the divergent adsorbate behaviors were obtained through periodic density functional theory (DFT) models at the HSEsol06 level, which have been validated with agreement to the experimental isosteric binding enthalpies, **Figure 59**. All structures were fully optimized within the DFT construct as implemented in the Vienna *Ab-Initio* Software Package (VASP)[782] using the PBEsol[746] GGA functional. A project-augmented-wave plane wave basis set was employed with a 500 eV plane-wave cutoff. To

prevent anomalous phasing interactions within adsorbate binding models a 1x1x1 k-grid was used. Spin-polarized calculations were performed and a high-spin state was enforced on Ni atoms consistent with our previous study.[692] The energy of "free" adsorbates were computed using the same methods in a unit cell containing >20 Å of vacuum. Binding energies were computed from the difference in energy between empty frameworks plus the adsorbate and the adsorbate-bound frameworks.

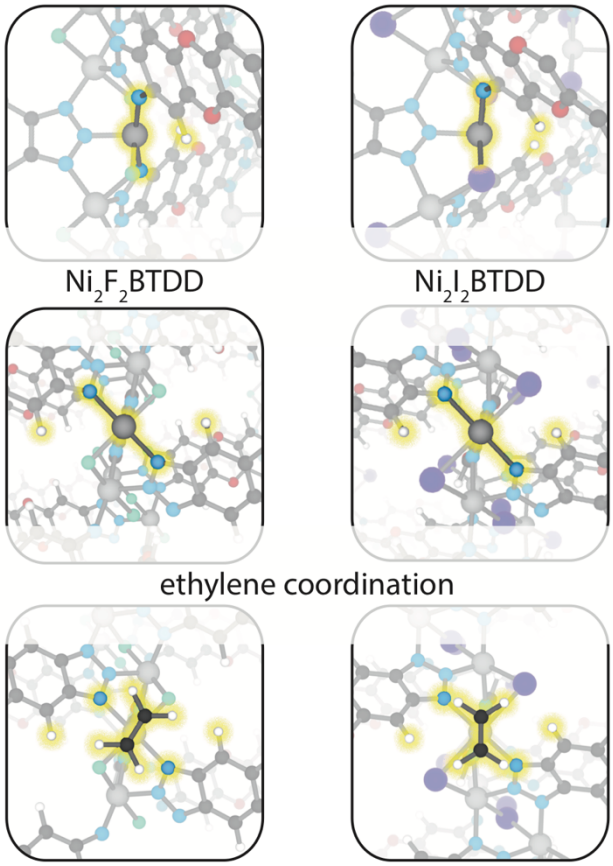

Figure 60: Definition of linker-linker dihedral angle. The smaller this dihedral angle, the less "open" the binding pocket is due to steric hindrance from the BTDD.

Together, the experimental and computational data indicate these behavioral differences originate from a combination of subtle geometric and electronic differences between ligand exchanged species and the binding mode of each gas on nickel sites in this family of MOFs. While each gas interacts with the same active site, their molecular orientations and orbital symmetries are varied. From a geometric perspective, the subtle linker rotations that occur due to expansion of the nodal pillar with bromide and iodide exchange which reduce pore diameter,[692] sterically encumber the active site with respect to the η^2-binding mode of ethylene (**Figure 60**). The resultant rotation hinders the ideal overlap between π-orbitals on ethylene and d-orbitals on Ni. However, due to the terminal binding mode of CO and small kinetic diameter of H_2 their binding is unperturbed by geometry.

From an electronic perspective, inspection of the partial charge density plots (**Figure 61a**) for adsorbate binding reveals that the terminal binding mode of CO to Ni is dominated by σ-interactions, while the η^2-binding mode for ethylene has mostly π-character. Greater σ-donation from CO is also observed from the increase in electron density at the Ni site after binding, while the greater influence of π-backbonding to ethylene induces partial oxidation of the metal center (App. G Table A2.2). Further, the electron density on Ni decreases as X is exchanged down the halogen group, promoting the CO σ-donor interaction and impeding the ethylene π-accepting interaction. The increased capacity for σ-interaction is also revealed in the calculated density of states (DOS); with heavier halogens, the conduction band shifts to more negative energies and closer to the Fermi-level (**Figure 61b,** App. G Fig. A2.1). This computational description supports the

conclusion drawn from the infrared spectroscopy discussed above, where the blue shifted CO stretching frequency indicates a nonclassical metal carbonyl complex in which σ-interactions dominate.

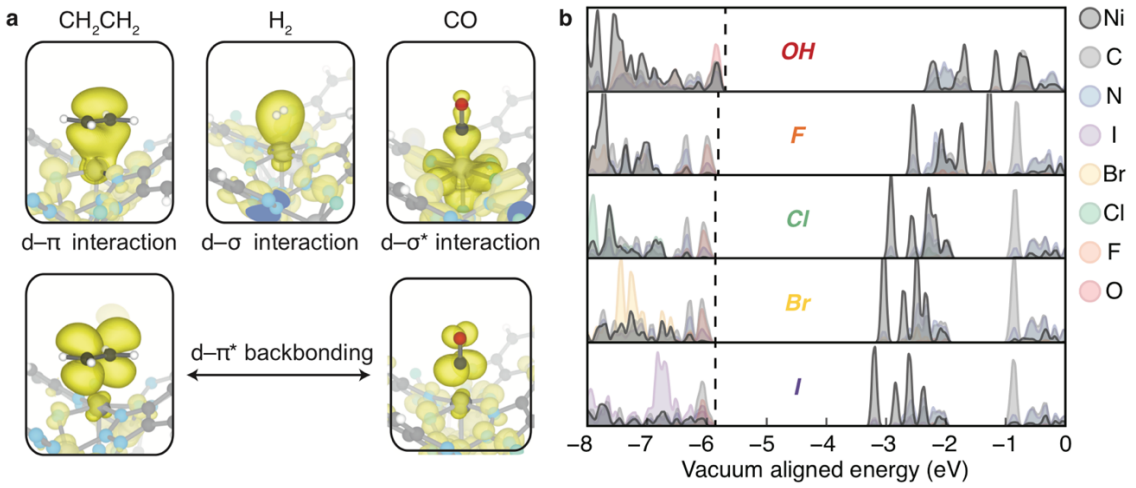

Figure 61. (a) Charge density depictions of the electronic states associated with adsorbate binding, shown here for the Ni_2F_2BTDD derivative, reveal the divergent orbital interactions between MOF and molecule for ethylene (binding through the π-system), dihydrogen (binding through a σ-bond), and carbon monoxide (binding through a σ*-orbital). **(b)** Vacuum aligned atom-projected density of states (DOS) plots at the HSEsol06 level of theory for each Ni_2X_2BTDD species theoretically investigated reveal that the reduction in ligand field strength down the group of halides modifies the conduction band potential so the band gap is reduced. The reduced potential of unoccupied d-states is a barometer for adsorption trends, however the major consideration for π-acid adsorption strength turns out to be whether the molecule functions as a σ-donor or π-acceptor.

Given that the isosteric enthalpy of adsorption for dihydrogen is weakly correlated with that of carbon monoxide, we expect the Ni-H_2 interaction is also one of σ-donation. Indeed, the charge density of binding orbitals (**Figure 61a)** depicts the active d-σ-interaction—distinct from the d-σ*-interaction of CO binding—and the charge on nickel generally increases upon H_2 binding (App. G Table A2.2**)**. The weak binding recovered for H_2 both in experiment and theory likely results from its low polarizability relative to the other adsorbates, in addition to weak orbital overlap from greater spatial and energetic disparities between H and Ni.[783]

One last piece of experimental evidence that corroborates our computational model comes from DRIFTS of **1-Cl** does with CO (App. G Fig. A3.1). The difference spectrum reveals that as the CO concentration increases, a new peak at 2170 cm^{-1} grows in. The new CO stretching frequency is higher than that for free CO at 2143 cm^{-1}, indicative of the non-classical metal carbonyl interaction identified computationally. This type of interaction has been previously noted in a series of structurally related M_2(dobdc) analogues ($dobdc^{4-}$ = 2,5-dioxido-1,4-benzenedicarboxylate, M = Mg, Mn, Fe, Ni, Zn).[777] Non-classical metal carbonyls typically involve a σ-bonding interaction (that causes a depletion of electron density from the anti-bonding HOMO of CO) with minimal to no π-backdonation from the CO π* orbitals.[784] As such, the formally Ni(II) sites in Ni_2X_2BTDD most likely do not participate as π-donors (or at least the d-π interaction is insufficient to compete with the σ interaction). It has been demonstrated, empirically, that the binding energy of non-classical metal carbonyls has a linear relationship with the difference in energy between bound and free CO stretching frequencies (Δv).[785] As the Δv vs. ΔH_{ads} of **1-Cl** lies on this relationship,

it is suggestive that the nickel-CO interaction is purely electrostatic in nature (App. G Fig. A4.1). This further provides evidence that the increasing isosteric enthalpy of adsorption from **1-F** < **1-Cl** < **1-Br** is the direct result of the OMS becoming a stronger Lewis acid.

4.4.2 Conclusions

In conclusion, we have probed the effect of inorganic anion exchange within Ni_2X_2BTDD on adsorbate interactions with various gaseous conventional π-acceptors and uncovered divergent behaviors that reveal dominant σ-donor behavior. The expected trending of adsorption energies for similar π-acceptors does not hold; CO, C_2H_4, and H_2 each demonstrated unique trends. The CO-nickel interaction is dominated by σ-interactions, causing an increase in electron density on the nickel and a blue shifting of the C-O stretching frequency (non-classical metal carbonyl). The H_2-nickel interaction also has σ-character, but demonstrates a weak physisorption interaction likely due to high metal valency and the absence of π-backbonding. Yet, the C_2H_4-nickel interaction proceeds as expected, with π-backbonding interactions that decrease the electron density on the nickel atom. Coupled with steric factors, these subtle differences in electronic interaction culminate in isosteric enthalpy of adsorption trends that increase, remain constant, and decrease for the three gases moving down the halogen group. These results suggest that the subtle fine-tuning of metal sites enabled by post-synthetic ligand metathesis in OMS MOFs will enable highly selective gas separations.

4.5 Bridge

The relatively long history of MOF adsorbents is culminating in studies focused on understanding how to fine-tune the selectivity through electronic interactions between discrete active sites and molecules much smaller than the pores and their apertures. The dominant interactions that govern pore-filling dynamics are intermolecular within the confined media. For example, we show that in water harvesting applications the structural parameter of pore-diameter is of the utmost importance to permit favorable hydrogen-bonding interactions between surface adsorbed water molecules the rest of the pore-confined media. In Ni_2X_2BTDD this can be controlled through the identity of the X anion along 1D nodal pillars that expands and contracts pores with an inverse relationship to anion diameter. Yet, the ligand field modulations and subtle structural perturbations afforded by this inorganic ligand exchange also affords controllable selectivity of small molecule adsorption at the open metal sites. The adsorption strength of each molecule is governed by the geometry of the binding mode and symmetries of the associated orbital interactions. To strongly bias an OMS for one π-acid over another, the preferred binding mode and relative strength of σ- and π-interactions must be accounted for along with any minor geometric perturbations that result from compositional alterations. In this family of materials, solid-state modeling techniques were necessary regardless of the property of interest due to the nodal connectivity. However, cluster modeling techniques were applied to MFU-4*l* -OH despite it being constructed with the same ligand because the geometric perturbations involved in the nonstructural ligand exchange and chemisorption of CO_2 did not have long-range impacts for the overall MOF. Further, while the relative adsorption

strengths of subsequent small-molecule binding indicated some cooperativity between metal ions in a given cluster, these are electronically isolated from one another making the molecular approximation of the active sites valid.

Clearly, inorganic clusters functioning as MOF nodes have immense utility. In the current chapter, I showed how inorganic ligands, when structural, offer both electronic and geometric perturbations that are subtle enough to fine-tune adsorbate interactions through both electronic and steric factors. Small adjustments to pore diameter afford significant differences in pore-filling behavior for interacting media such as the hydrogen bonding networks within water. The ability to exchange inorganic ligands, even those that are non-structural, further afford access to heterogeneous active sites capable of mimicking other well-defined active sites such as in the enzyme carbonic anhydrase. While each metal points into isolated pores, the nuclearity of the node is also relevant to determine the stoichiometric ratio of CO_2 to bicarbonate conversion.

In previous chapters, the same MFU-4*l* scaffold underwent post-synthetic transmetallation to achieve Ni-based active sites that demonstrated higher activity than the associated homogeneous catalyst. Here, the stoichiometric incorporation of Ni(II) was consistent with the bicarbonate formation at Zn(II) sites in MFU-4*l*-OH. The number of metal ions in a given isolated node was also relevant for the hydrogen storage capacity of MIL-125 undergoing photodoping through PCET, where only half as many hydrogen atoms could be loaded as metal ions in the node such that Ti(III)/Ti(IV) redox coupling could be maintained. Clearly, the cluster-based chemistry of MOFs is heavily impacted by their nuclearity and can be controlled and understood by monitoring the effects of

perturbations in the primary coordination sphere. Between Chapter III and Chapter IV it is evident that d-orbital occupancy and ligand field strength are two synthetic handles that, together with innate cluster chemistry, will give rise to fruitful modifications pertaining to MOF selectivity as catalysts and adsorbents in a given scaffold.

CHAPTER V

FINDINGS AND FUTURE OUTLOOK

This thesis employed density functional theory to recover physical and electronic structure parameters for a class of porous and crystalline coordination materials, metal-organic frameworks. The ability for reagents to diffuse into MOF pores means chemical reactions are not limited to the surface. Further, the crystallographic order of these pores ensures the spatial distribution of active sites that are typically also electronically isolated. As a result, MOFs have high densities of non-interacting active sites and demonstrate relatively high catalytic activity and steep gas uptake isotherms. Additionally, individual pore cavities can be thought of as "nanoreactors" that increase the local effective concentration of reactants and products, in turn governed by relative mass transport properties. Large surface areas are also attractive across fields of renewable energy technologies. For example, porous electrodes that can host electrolytic solutions could be used for the development of supercapacitors.[339] Conductive MOFs with accessible coordination sites can also be developed as electrochemical chemosensors.[786–788] Yet, perhaps the most important chemical property of MOFs is the dynamic nature of their structural coordination bonds between organic anions and inorganic cations.

Since MOFs embody a combination of organic and inorganic chemistry they can only be conceptualized through the consideration of both disciplines. The synthetic flexibility afforded by the simple recipe of mixing charge balancing cations and anions facilitates an astounding degree of chemical diversity across the possible MOF space. Post-synthetic modifications including, but not limited to, metal and linker metathesis exponentially increase the number of possible MOF scaffolds. Yet, very little of this chemical space has actually been explored due to anthropogenic biases.[789] Computational methods are one strategy to broaden the horizons of synthetic efforts by identify promising MOF scaffolds and derivatives. In order to perform large-scale screening studies that pinpoint desirable structures and compositions, chemical descriptors must be established to expose them. Thus, understanding structural and electronic properties that control selective interactions, transformations, and efficient charge transfer is of the utmost importance to advance the field of MOFs for any application. Importantly, the accuracy of high-throughput methods depends on the agreement between computational parameters and experimental outcomes. Therefore, fundamental studies combining theory and experiment are key to the thoughtful and efficient development of the field.

The goal of this thesis has been to inform synthetic pursuits by understanding the electronic origins of observable behaviors such that general guidelines could be proposed for forming a MOF with specific functional characteristics. Through the theoretical investigation of MOF conductors, catalysts, and adsorbents we have gleaned valuable insight into the nature of native and transmetalated active sites for small molecule adsorption and chemical conversions, as well as the orbital interactions that direct and

dictate charge transport pathways. As expected, there is a delicate interplay between structure, composition, and chemical behavior. Throughout the studies presented in the preceding chapters, we uncovered some electronic structure anomalies that are imperative to establishing reliable computational models and therefore descriptors. Yet, we also identified some general design principles that appear to hold true regardless of topology and chemical make-up.

In Chapter 2, the most conventional solid-state behavior of MOFs was explored: conductivity. Electronic band structures (EBS) and their corresponding density of states (DOS) plots are prominent graphical tools to depict and comprehend the relationship between connectivity and charge transport pathways. There is limited electronic linker-node (ionic bond), node-node (linker spacers), and linker-linker (node size and geometry) communication in most MOFs. This electronic insulation gives rise to localized electronic bonding, which manifests in non-dispersive (i.e. flat) electronic bands. However, dense arrangements of redox active components such as mixed-valent metals or linkers and crystallographically defined columns of aromatic organic molecules give rise to mobile charge carriers.

2D MOF graphene analogs are the most conductive family of neutral MOFs. However, the weak van der Waals interactions between layers are significantly weaker, and therefore more reversible, than the coordination bond between metal and linker in plane. The heavily disordered interlayer stacking in crystals of these materials precludes atomically resolved structural refinement and the specific measurement of in- (bonding plane) and out-of-plane (direction of layer stacking) conductivity. Using basic physical

organic chemistry concepts, we were able to modify the organic linker and remedy this by balancing the in- and out-of-plane bonding strengths such that larger crystal domains could be achieved. By enlarging the aromatic linker surface area and incorporating heteroatoms to increase linker acidity, the metal-metal repulsion was reduced and π-π stacking interactions were enhanced between layers. Single crystals could be grown of two distinct phases, depending on the d-orbital occupancy and therefore coordination number of the metal.

Later transition metals with more saturated valence orbitals (i.e. Cu(II) and Ni(II)) adopted four-coordinate square planar ligand spheres, while more oxaphilic metals with fewer d-electrons (i.e. Mg(II), Co(II), and Ni(II)) coordinated axial aqua ligands to adopt octahedral geometries. Crystals formed with square planar metals have eclipsed π-stacked layers and hexagonal pores (porous phase), while crystals built with octahedral metals form a hydrogen bonding network that give rise to staggered layers with occluded pores whose negative space is occupied by molecular complexes (dense phase). Notably, Ni(II) species have more malleable coordination spheres and could adopt either structure. Indeed, the flexibility of nickel cations in terms of coordination geometry and chemistry has them featured in every application explored in this thesis.

The clear delineation between charge-hopping regimes in the dense crystals and band transport regime in the porous crystals reinforces the importance of orbital overlap. We show that axial water ligands reduce band dispersion by hindering the in-plane conjugation through distortion of the metal-orbitals and localization of electron density. The hydrogen bonding network between intercalated molecules and staggered layers

disrupts charge flow insulating each layer. Metal identity had a negligible impact on conductivity by charge hopping between linkers. Importantly, the lack of porosity undermines the most desirable trait of highly conductive MOF electrodes. Yet, these structures may be interesting from the standpoint of proton conductivity or self-doping. An ongoing area of research in the water-coordinated MOFs described herein and those similar is the protonation state of the ligand-sphere. Based on a combination of the charge-neutrality principle and EPR data, we hypothesize that contiguous layers host two aqua ligands while the intercalated monomer complexes have one hydroxyl ligand per Mg atom such that all metals are divalent cations and all linkers are trivalent anions. However, structural refinement procedures are blind to protons, and it is also possible that the layers and molecular complexes charge balance each other, or that linkers in the molecular complexes are hexavalent anions.

In general, for 2D MOFs, strengthening and balancing bonding interactions between metal and linker and between sheets is an electronic pathway for identifying metal-linker combinations that will simplify device fabrication through facile crystallization into a single phase. Strategies to overcome sheet-slipping structural distortions and phase purity should also be developed. Elsewhere, we have taken metallic 2D layers and shown 3D arrangements of conductive MOFs with permanent porosity can be obtained through retrofitting procedures with ligating pillars.[790] Here, we saw that Co(II) prefers an octahedral coordination site upon native construction of 2D conductive MOFs. However, when incorporated into the same octahedrally coordinated crystal structure as Ni(II) the cobalt species demonstrated in-plane conductivity while the nickel species did

not. In the square planar coordination sphere adopted when there is in-plane conjugation in the sheets, Cu(II) demonstrated more dispersive electronic bands than Ni(II) and higher conductivity in both directions.

With variable loading concentrations, mixed metal frameworks could demonstrate more effective charge transport properties. Experimentally, binary combinations of Co, Ni, and Cu with HITP linkers were synthesized that demonstrate continuous variation in structural parameters, band gap, and conductivity values between those of the pure MOFs based on the metal ratios.[791] While, large differences in metal diameter and bonding can negatively impact crystallinity, the fabrication of MOF alloys is another fruitful strategy for tuning the electronic structure. To explore this combinatorial chemical space for different metal combinations and linkers, electronic structure theory calculations that assess electronic band topology will be invaluable.

As previously mentioned, most MOFs do not exhibit metallic character and band transport, but do feature the electronic anisotropy that results from mixing organic and inorganic components in a vacuous arrangement. Charge hopping is the more typical electron conduction mechanism in MOFs due to these bonding properties. By constructing pillars of NDI linkers defined by Zn(II)-nodal chains, we showed that 3D connected linkers can be conductive, and that reducing those linkers yields an increase in conductivity due to an increase in charge carriers. However, the d-orbital spacing is much larger than in the 2D graphene analogs that experience charge hopping (nucleus to nucleus distance of 7.3 Å in ZnNDI and 3.2 Å in Ni_6HHTT_3) and therefore the conductivity is much lower ($<1x10^{-12}$ S/m vs. ~0.1 S/m). Another difference is that the Fermi level of ZnNDI lies within an

electronic band gap. This type of scaffold challenges conventional solid-state models built from plane-wave basis sets, and we must adopt hybrid functionals to accurately assess the band gap for bulk semiconductors. The computational expense associated with hybrid functionals coupled with the size of MOF unit cells makes full geometric equilibration intractable in current implementations of DFT; this will only be made possible but increasing the computational efficiency of these methods or increasing the usable computing power beyond current hardware. Until then, optimization of the electronic wavefunction for a GGA-derived structure at the hybrid level of theory is acceptable, and provides reliable results relative to experimental measurements as is further demonstrated in the studies of photoactive MOFs in Chapter 3.

In Chapters 3 and 4 we move away from single atom nodes and conductive scaffolds to explore the reactivity of transition metal active sites in discrete inorganic clusters. First, a thermodynamic lens was applied to understand the optical properties of photocatalytic MOFs. By observing the vacuum-aligned band edge potentials of Ti(IV)-containing scaffolds and the atom-projected DOS we were able to understand the compositional origin of band edges and recognize that transmetallation with Ti(IV) should be a general design principle for accessing light-absorbing MOFs. The ability for linkers to funnel excited electrons to Ti(IV) and reduce the metal to Ti(III) can be used to prevent exciton recombination and promote reactions known to be mediated by titanium radical active sites such as epoxide ring-opening.[792] The presence of basic sites within the electron-accepting inorganic cluster further enables hydrogen storage. IVCT from intranode Ti(III)/Ti(IV) redox coupling promotes exciton stabilization not present in Zr(IV) or

Hf(IV) scaffolds[421] that enables PCET from solvent molecules where, like the exciton hole and electron, the hydrogen electron and proton are spatially separated into distinct orbitals. IVCT and the covalent association of a counterion stabilizes the reduced framework with respect to HER.

Clearly mixed-valency is a utile characteristic for MOFs. The electronic coupling between redox partners facilitates electron conduction through charge-hopping when there is long-range order in a dense arrangement of the redox active component. In the case of more local electron exchange, IVCT between two of the same metals (e.g. Ti(III)/Ti(IV)) or two different metals (e.g. Ti(III)/Fe(III))[793] is an important modulator of reactivity. The delocalization of "hot" electrons not only stabilizes excitons, but also grants access to unique oxidation states through either through photoexcitation or reduction. Here again, bimetallic frameworks are interesting targets for future studies. Ce-O-Ti active sites, for example, are known to be highly effective for catalytic reduction of NO_x with NH_3.[794]

Moving from the ground state and thermodynamic perspective, this thesis also probed kinetic reactivity in a Ni(II) transmetallated MFU-4*l* scaffold. By comparing activation barriers, we are able to understand the relative probability of different reaction pathways. However, our cluster and periodic models were both ultimately insufficient to describe intrapore reactivity. First of all, because both these models are restricted to a single spin state while both the singlet and triplet spin states were active in the investigated mechanism. We identified at least one crossing point for these spin surfaces, however it is possible that the true ground state and transition state wavefunctions have contributions from both spin states; a situation that could only be described with post-DFT methods such

as configuration interaction. Single wavefunction ground states may be provide insufficient descriptions of many transition metals with multiple accessible open-shell states. Theorists must be careful to consider all relevant spin-states with each change in coordination number, oxidation state, and ligand sphere.

Secondly, an important consideration omitted from DFT models is the description of flow properties. At the end of Chapter 3 we saw how mass transport behavior of pore-confined fluids can facilitate selectivity in olefin reactions by promoting the desorption of longer chains to be replaced by smaller species, and therefore the formation of kinetic products. The Scorpionate-type active site provided by the SBU of Ni(II)-MFU-4*l* is empirically understood to favor short chain products. The position of linker protons likely limits olefin approach and therefore propagation, especially with larger Ni-alkyl groups. Also, as hydrocarbon length increases, possibly even to just C4, the product is thought to be preferentially solvated such that short chain, unisomerized products are obtained. Molecular dynamics simulations or other statistical mechanics methods that account for solvent interactions and relative concentrations of reactants and products in the pores are needed to understand the solvation energetics and mass transport properties of MOFs with different pore and aperture sizes and geometries. Still, by isolating the local, pore, and macroscopic effects in different cluster, periodic, and dynamic models, we can begin to understand how different parameters interact and build across scale levels. Further, we can individually optimize factors at each length and time scale to achieve the most efficient or effective composition and topology to maximize the efficacy and selectivity of passive separation membranes, chemosensors, and catalysts.

Finally, Chapter 4 looks at the role of structure and electronics on gas binding and pore filling. Small molecule binding strengths in MOFs are relevant not only to understanding gas selectivity and uptake reversibility, but also catalytic activity where binding energies can be used as descriptors for reactivity. In the first study, the MFU-4*l* scaffold is used with its native metal ions and hydroxyl ligands but still studied with the molecular cluster methods used for the mechanistic study on the scaffold. We see that chemisorption of CO_2 at one of four Zn(II)-OH motifs in the MFU-4*l*-OH node impacts the energetics of subsequent binding events at the other three sites, supporting the idea of charge delocalization within nodal clusters identified in the study of MIL-125. This chemisorption study also upholds the incredible atomic specificity of MOF-active sites: they are able to mimic the reactivity of highly evolved enzyme active sites.

While an isolated SBU model was sufficient to embody the intranode cooperativity of CO_2 binding in the MFU-4*l* scaffold, PBCs were necessary to describe structural and electronic perturbations to the 1D node and pore of Ni_2X_2BTDD species, X=OH, F, Cl, Br, and I. Post-synthetic ion metathesis of these bridging inorganic anions (X) produced a continuous spectrum of ligand field and steric effect trends based on halogen size and polarizability. In the context of water harvesting, pore diameter should be optimized in hydrophilic MOFs to achieve pore-filling at the lowest possible RH. Larger ions not only protrude more into the pore, but induce linker rotations down the 1D nodal chain that further contract the pore space. In the context of selective gas adsorption, H_2, CO, and C_2H_4 all exhibited different trends in their binding energy down the halide group because of their different binding modes and orbital symmetries. The linker rotations with larger anions

that reduced pore diameter, e.g. iodide, also rotated the olefin coordination axis of C_2H_4 in a way that disrupts the π-d bonding. On the other hand, the reduced ligand field of more polarizable anions lowers the conduction band edge and benefits the terminal binding mode of CO that is unperturbed by linker crowding. From the perspective of discrete gas and reagent interactions with transition metal active sites, these studies show how explicit knowledge of coordination geometries and electronic structure trends will aid in the specific design of active sites by tuning the orbital interactions through steric enforcement of certain binding modes or specific design of active sites with appropriate orbital symmetry.

Of course, dynamics effects must also be factored in when developing MOF adsorbents and membranes. Those that exhibit guest-induced structural changes due to conformational flexibility, such as breathing behaviors, must be monitored as a function of time—a dimension that is by definition absent in KS-DFT calculations.[795] In these cases, theorists must look beyond static simulations to provide a holistic description of gas uptake.[796] Binding energies, like those published in the aforementioned articles, and studies that highlight the important parameters governing small molecule-MOF interactions serve as a beneficial foundation for high-throughput and machine learning algorithms. However, conformational degrees of freedom and the stability of guest-promoted phases may also be relevant.

Past developing an understanding of pore-confined reaction and flue gas mixtures, dynamic modeling procedures, in addition to static simulations, will be beneficial for understanding the role of solvent and other spectator molecules in the formation of MOFs

and post-synthetic exchange procedures. Such knowledge will benefit the design of synthetic routes to access idyllic scaffolds based on theory. Crystal domain size and reproducibility is a major factor limiting the industrial implementation of these record-breaking materials. In addition to controlling the dispersion, concentration, and structural precision associated with cation and anion exchange, this knowledge will enrich our understanding of crystallization processes in general.

To study alloy formation, transmetallation, and doping, "defect" formation energy calculations are going to be valuable for the future of MOF modeling. Computational simulations of the electronic structures associated with defective materials will be an important area of research for MOF chemistry, in particular for understanding trends in defect concentration and the favorability of mixed-component MOF formation. The ability to compute defect formation energies and simulate the perturbed electronics of post-synthetically exchanged MOFs, chemically or electronically doped MOFs, and MOF alloys, will help understand doping limits and the accessible spectrum of modulable properties.

In the quest for new functional scaffolds, decisions regarding the coordination motif and geometry also affect framework stability to water, base, acid, pressure, and temperature. Indeed, MOF stability under operating conditions is a determining factor for industrial implementation, as well as cost of production and reproducibility. High-valent ions such as Ti(IV) and Zr(IV) have a strong attraction to carboxylate motifs and therefore often produce more stable frameworks. Yet, Ti(IV)-based frameworks that undergo long-term or repeated reduction may degrade due to reduced bond strength as demonstrated in

the ZnNDI scaffold. One possible work around or strategy to increase photodopant capacity, is to incorporate Ti(IV) into formally M(III)-containing scaffolds where photoreduction may be favorable up to higher loadings. More typical degradation mechanisms such as ionic bond hydrolysis can be kinetically blocked.[354] For example, nonpolar functional groups near coordination bonds can prevent the hydrolysis events that nucleate MOF degradation.[797] When functionalizing linkers, whether for electronic or physical structure modulation, one must account for the rotational degrees of freedom accessible to linkers. Different linker orientations can give rise to different phases with different properties.[798] Using the relative energy of linker orientation arrangements, statistical models can be built to predict the distribution of these arrangements.

Overall, the future of MOF development will likely rely on high-throughput screening procedures and machine learning algorithms that employ DFT-derived data and concepts to identify promising frameworks for the adsorption, conversion, or transport process of interest. Machine learning algorithms will help determine what combination of descriptors, or features, produces the most consistent chemical effects. There will be some interplay from topological analysis, compositional analysis, and relative adsorption energetics.[799] The sensitivity of MOFs to degradation and other dynamic factors may also be influential in screening processes. The size and scope of data sets necessary for machine learning approaches and high-throughput procedures necessitates expansive libraries of comparable computational results. Notably, data recovered for the same or similar systems using different types or levels of theory are incomparable. A challenging aspect of using computational data for screening procedures is therefore the poor transferability of a given

model. The lack of generality for functional, basis set, and other important model parameters makes it so the construction of highly accurate models is challenging and requires extensive benchmarking. Here, we largely invoked relative trends observed in theory to explain trends observed in conductivity, reactivity, and selectivity. In the future, more generalizable approaches may be adopted.

Altogether, the works in this thesis highlight the role of structure on chemical properties and the utility and effects of ion exchange. The combination of ligand identity and transition metal identity determine the coordination geometry, d-orbital occupancy, ligand field, and therefore spin state. Redox coupling between redox active components, like large aromatic linkers or metal cations, facilitates charge delocalization that, given an appropriately dense and structurally related arrangement of components, can elicit charge transport pathways. Another strategy is to use single atom transition metal nodes that share efficient d-orbital overlap with organic linkers that have extended conjugation. With these components, electronically conductive 2D layers can be built. Conductivity can be even more effective when the aromatic linkers stack, and layers align in an eclipsed conformation. In these frameworks, metal-identity controls interlayer spacing, intersheet displacement, and charge carrier concentration. Maximum orbital overlap provides maximum conduction.

Beyond linker and node substitutions, single atom metal or ligand substitutions are invaluable to 1) install discrete active sites and 2) tune bulk electronic properties. Synthesis or transmetalation with Ti(IV) grants light-absorbing MOFs by installing metal d-states that lower the conduction band edge and accept electrons from excited linkers. Native

metals cooperate with linker chemistry to determine crystallographic order; transmetalation procedures can install metals into ligand spheres and coordination geometries that would be inaccessible through direct synthetic approaches, e.g. Ni(II)-MFU-4*l* as opposed to Ni_2X_2BTDD. The inclusion of metal ions in non-native coordination spheres can achieve unique reactivity, such as the spin-crossover mechanism of ethylene dimerization at Ni(II) active sites in MFU-4*l*. Inorganic ligand exchange can be used to modulate ligand field strength and active site chemistry—when these ions play a structural role, they can also be used to tune steric factors. Individually, these ideas offer conceptual understanding of how to manipulate MOF electronic structure and target more effect materials for conductivity, catalysis, and gas adsorption. Together, they represent a summation of pieces belonging to the larger puzzle of intuitive MOF design.

APPENDIX A

EXPERIMENTAL DETAILS AND SUPPLEMENTARY INFORMATION FROM:

Atomically precise single-crystal structures of electrically conducting 2D metal-organic frameworks (*Nature Materials*, **2021**, *20*, 222-228.)

Jin-Hu Dou, Maxx Q. Arguilla, Yi Luo, Jian Li, Weizhe Zhang, Lei Sun, **Jenna L. Mancuso**, Luming Yang, Tianyang Chen, Lucas R. Parent, Grigorii Skorupskii, Nicole J. Libretto, Chenyue Sun, Min Chieh Yang, Phat Vinh Dip, Edward J. Brignole, Jeffrey T. Miller, Jing Kong, Christopher H. Hendon, Junliang Sun & Mircea Dincă

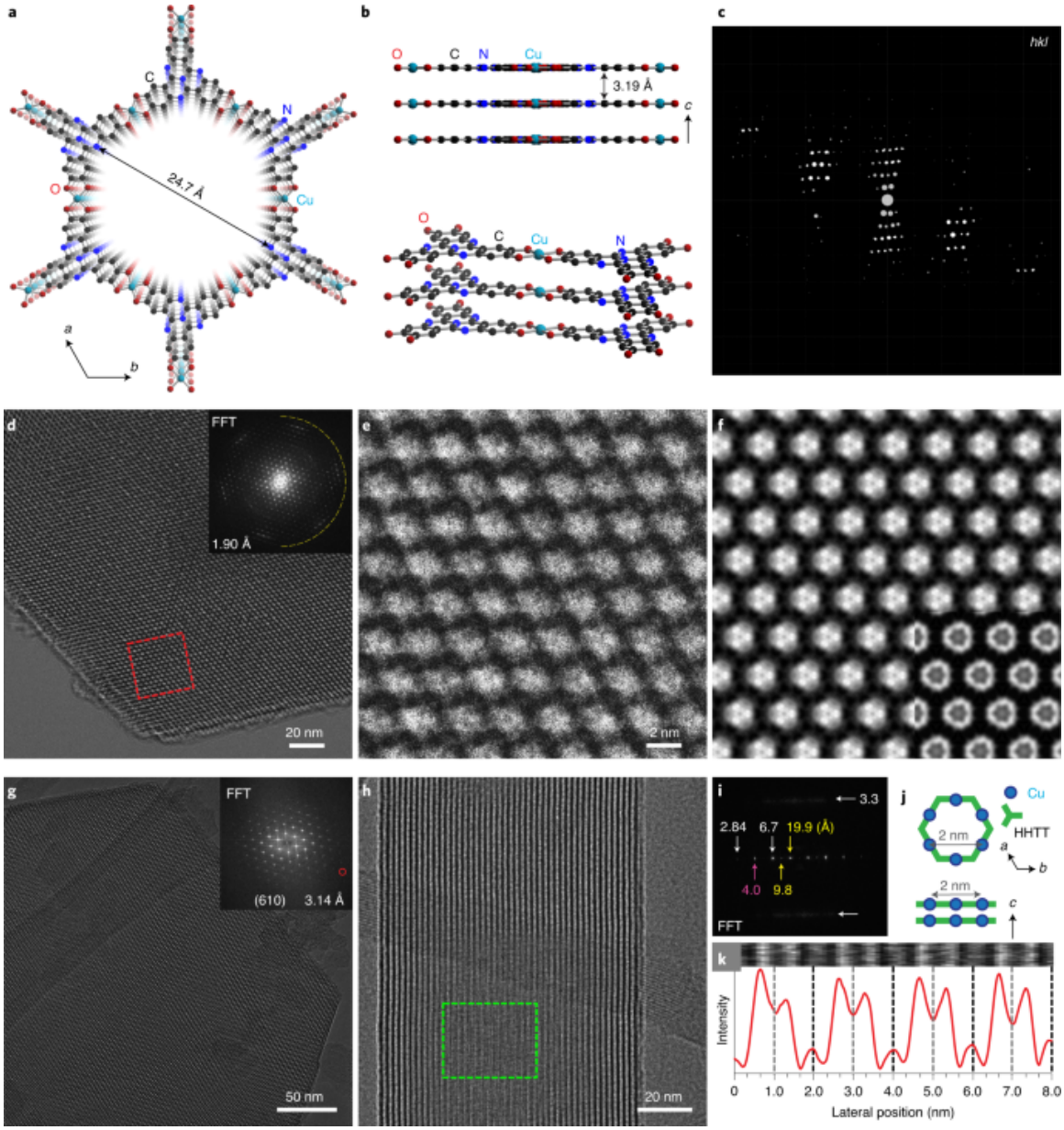

Fig. A1. Single-crystal structure of Cu_3HHTT_2 derived from cRED and HRTEM (a) A portion of the crystal structure along the *c* direction. **(b)**, Views parallel to the *ab* plane. Hydrogen atoms are omitted for clarity. (**c**) 3D reciprocal lattices of a Cu_3HHTT_2 rod with a maximum resolution of 1.5 Å (*hkl* corresponds to reciprocal space indices). (**d**) Cryo-EM image of a Cu_3HHTT_2 plate (inset: FFT). **(e)** High-magnification image from the red

square in **d**. (**f**z averaged experimental image (inset: simulated HRTEM image). **g**, Low-magnification image of ~1 μm Cu_3HHTT_2 plate (inset: FFT of the micrograph). **h**, HRTEM image of a Cu_3HHTT_2 rod imaged normal to the *c* direction. **i**, FFT of the image from the green square in **h**, evidencing the eclipsed stacking in the reciprocal lattice. **j**, Schematic of Cu_3HHTT_2 structure to illustrate imaging directions. **k**, Average intensity in the *c*-direction measured along the *a*-direction from the image in **h**.

Cu_3HHTT_2 forms single crystals that present either as 5-μm-wide hexagonal plates or as 10-μm-wide hexagonal rods (**Figure 23d**, Appendix A, Fig. A9). The crystals are of sufficient size and quality to allow structural refinement by cRED with a resolution of ~1.5 Å (**Figure 24c**, Appendix A, Figs. A22-S24). The highly ordered nature of HHTT-based MOFs is also highlighted by near-atomic-resolution HRTEM down to 1.9 Å. This resolution is remarkable given the well-known beam sensitivity of similar materials.[347,800–808] The HRTEM images show that the crystals of Cu_3HHTT_2 exhibit long-range order across the whole crystallite and along all three crystallographic directions (Fig. A1k, Fig. A56 in App. A). Micrographs exploring the in-plane arrangement (Fig. A1d,e,g) show a well-resolved extended honeycomb framework (bright contrast) and pores (dark contrast) with a pore size of 2.1 nm. The simulated HRTEM image matches well with the averaged experimental image obtained for thick and thin crystals, and the thickness obtained from the image simulation is also consistent with the atomic force microscopy (AFM) results (Figs. A1f, A54, A55 and A63). Micrographs exploring the stacking direction (Fig. A1i) show atomically flat sheets with an interlayer spacing of 3.3 Å. Fast Fourier transform

(FFT) of these images shows good agreement with eclipsed stacking between the sheets (Fig. A1c,d,i; for additional information on HRTEM, see Figs. A48–A56). Altogether, the HRTEM data are in excellent agreement with the more detailed structure derived from cRED and reveal important additional features that are not distinguishable with the latter. Thus, close examination of the crystal edges reveals termination by Cu^{2+} (and likely the coordinating solvent) rather than organic ligands (Fig. A48c,d), which is probably due to the excess stoichiometry of Cu^{2+} during synthesis. Remarkably, the HRTEM data reveal isolated in-plane moiré superlattices (Figs. A56 and A59) from twisted overlapping neighbouring sheets, suggesting that the single crystals are potentially exfoliatable. Moiré superlattices have recently attracted attention owing to their ability to modulate the electronic band structures of the underlying single sheets in graphene and other 2D van der Waals materials.[809] The large crystals of HHTT-based materials may provide interesting opportunities to explore similar effects in MOFs in the future.

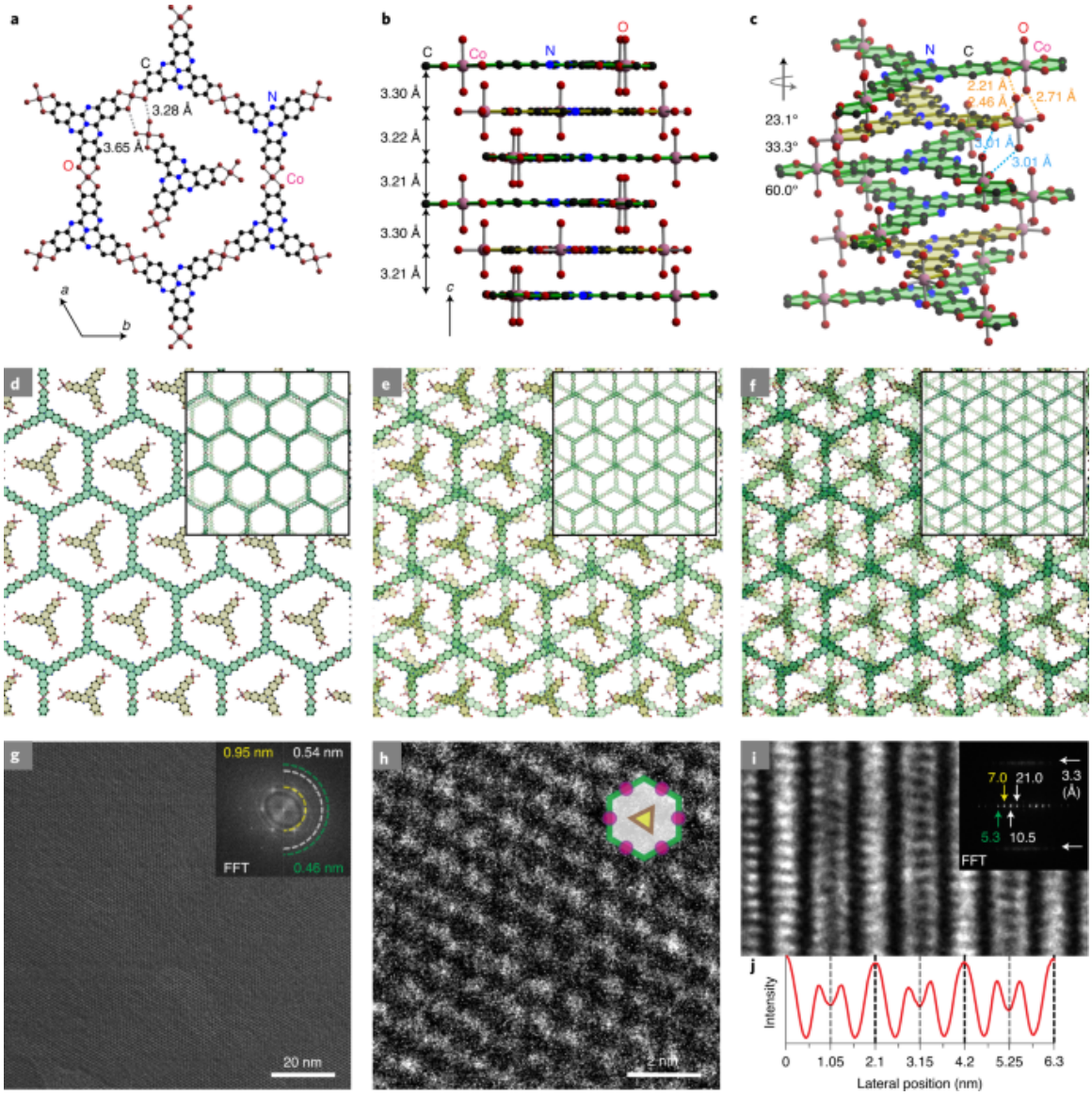

Fig. A2: Single-crystal structure of Co_6HHTT_3 derived from SXRD and HRTEM. (**a**) Portion of the crystal structure viewed along the *c* direction. The long O–O distances suggest that no hydrogen bonds are formed between the molecular clusters and the Co_3HHTT_2 sheets. (**b**) View along the *ab* plane showing an $(ABC)_n$ triple sheet stacking motif. (**c**) Spatial relationships between molecular and extended Co-HHTT units. The sheets and molecular units are indicated in green and yellow, respectively. The interlayer

hydrogen bonds are represented by orange and blue dashed lines. (**d**–**f**) Structural representations of single, double and triple layers of Co_6HHTT_3. The insets in **d**, **e** and **f** show views normal to the two closest A layers, one AB layer set, and an ABC stack, respectively. All guest molecules are omitted for clarity. **g**, HRTEM images of a Co_6HHTT_3 plate with long-range lattice fringes extending across the entire crystal. Inset: FFT of the micrograph. **h**, High-magnification micrograph where intra-pore clusters are visible, as indicated by a primary hexagonal periodicity of 0.95 nm, approximately half of that of Cu_3HHTT_2, which does not contain guest clusters. **i**, HRTEM image of a Co_6HHTT_3 rod imaged normal to the *c* axis. Inset: FFT from the image in **i**, revealing an interlayer stacking of ~3.3 Å. **j**, Average intensity of the image in **i**, integrated down the *c* direction and measured across the *a* direction (lateral position, left to right).

As with Cu_3HHTT_2, HRTEM analysis of Co_6HHTT_3 confirms long-range ordering and reveals honeycomb lattice fringes that extend throughout the crystal lattice, with lattice periodicities resolved down to 4.6 Å (Figs. A2g and A58). Contrast analysis of the HRTEM data at high magnification further reveals the in-pore Co_3 clusters that are clearly distinguishable from the extended lattices (Fig. A2h). Surprisingly, lattice fringes that extend along the length of the crystallographic *c* axis exhibit alternating high- and low-contrast fringes spaced at 1.05 nm (Fig. A2j). The emergence of high- and low-contrast fringes in Co_6HHTT_3, not observed in Cu_3HHTT_2, also confirms the presence of staggered in-pore clusters (Fig. A1h–k). Mg_6HHTT_3 presents structural features that are essentially

identical to those of the Co analogue, as expected for Mg^{2+} ions, which prefer octahedral coordination (Figs. A32–A34 and A59).

Owing to its ability to form both square-planar and octahedral complexes with medium-weak oxygen donor ligands, Ni^{2+} showcases the crystal growth and product selectivity control facilitated by ligands with the characteristics of HHTT. We surmised that in the DMF:H_2O solvent continuum, DMF would be more effective in disrupting the strong π-stacking between the sheets than water (Fig. A47).[358] Indeed, the reaction between Ni^{2+} and HHTT in the presence of DMF (Supplementary Table 1) yields large crystals of Ni_3HHTT_2, whose structure, revealed by cRED down to a resolution of 1.5 Å, is identical to that of Cu_3HHTT_2 and retains the close interlayer spacing of 3.19 Å (Figs. A20, A21, A24–A27 and A54). In the absence of DMF, Ni^{2+} and HHTT form $[Ni_3(HHTT)_2(H_2O)_6 \cdot Ni_3(HHTT)(H_2O)_{12}]$ (Ni_6HHTT_3), a dense network that is essentially identical to Co_6HHTT_3 (Figs. A28, A29, A33–A36 and A57), with only small variations stemming from the difference in interlayer interactions owing to hydrogen bonding and the solvent content.

Materials and Methods

Materials

All commercially available chemicals were used without further purification unless otherwise noted. All air- and water- sensitive reactions were performed under a nitrogen atmosphere. Column chromatography was performed with silica gel. All yields refer to isolated yields.

Nuclear Magnetic Resonance (NMR)

^{1}H and ^{13}C NMR spectroscopy were recorded on Bruker AVANCE III spectrometers (500 MHz). All chemical shifts are reported in parts per million (ppm). $CDCl_3$ (7.26 ppm), DMSO-*d6* (2.50 ppm) and CD_2Cl_2 (5.32 ppm) were the references for ^{1}H NMR chemical shifts, $CDCl_3$ (77.00 ppm), CD_2Cl_2 (54.00 ppm) and DMSO-*d6* (39.52 ppm) were the references for ^{13}C NMR chemical shifts.

Mass Spectrometry

Mass spectra were recorded on a Bruker Apex IV Fourier Transform Ion Cyclotron Resonance Mass Spectrometer.

N_2 Adsorption-desorption Analysis

The nitrogen adsorption measurements were performed on a Micromeritics ASAP 2020 Surface Area and Porosity Analyzer. An oven-dried sample tube equipped with a TranSeal^{TM} (Micromeritics) was evacuated and tared. The sample was transferred to the sample tube, which was then capped with a TranSeal^{TM}. The sample was heated to 120 °C, as determined by thermogravimetric analysis, under a dynamic vacuum of 4 mTorr until the outgas rate was less than 2 mTorr/minute. The evacuated sample tube was weighed again and the sample mass was determined by subtracting the mass of the previously tared tube. The N_2 isotherm was measured using a liquid nitrogen bath (77 K). Ultrahigh purity grade (99.999% purity) N_2, oil-free valves and gas regulators were used for all the free

space correction and measurement. Fits to the Brunauer-Emmett-Teller (BET)[810] equation satisfied the published consistency criteria.[811]

Powder x-ray Diffraction (PXRD)

Synchrotron PXRD patterns were obtained at beamline 11-BM of the Advanced Photon Source (APS), using a wavelength of 0.517045 Å. Diffraction patterns were collected at 100 K. Data points were collected every 0.001° (2θ step) in a range from -6 to 28° 2θ are scanned over a 34° 2θ range, with data points collected every 0.001° 2θ (actual 2θ/step is 0.0009984375°) and scan speed of 0.1 s/step. The 11-BM instrument uses X-ray optics with two platinum-striped mirrors and a double-crystal Si(111) monochromator, where the second crystal has an adjustable sagittal bend[812]. Ion chambers monitor incident flux. A vertical Huber 480 goniometer, equipped with a Heidenhain encoder, positions an analyzer system comprised of twelve perfect Si(111) analyzers and twelve Oxford-Danfysik $LaCl_3$ scintillators, with a spacing of 2° 2θ.[813] Analyzer orientation can be adjusted individually on two axes. A three-axis translation stage holds the sample mounting and allows it to be spun, typically at ~5400 RPM (90 Hz). A Mitsubishi robotic arm is used to mount and dismount samples on the diffractometer.[814] Oxford Cryosystems Cryostream Plus device allows sample temperatures to be controlled over the range 80-500 K when the robot is used. The diffractometer is controlled via EPICS.[815] Data are collected while continually scanning the diffractometer 2θ arm. A mixture of NIST standard reference materials, Si (SRM 640c) and Al_2O_3 (SRM 676) is used to calibrate the instrument, where the Si lattice constant determines the wavelength for each detector. Corrections are applied for detector

sensitivity, 2θ offset, small differences in wavelength between detectors, and the source intensity, as noted by the ion chamber before merging the data into a single set of intensities evenly spaced in 2θ. Background of PXRD patterns were corrected by Bruker Diffrac. Suite EVA software. The unit cell parameters were determined directly from the synchrotron PXRD pattern by TREOR,[816] and the diffraction intensities were extracted by Le Bail fitting using JANA2006.[817]

The laboratory PXRD patterns were obtained with Bruker Advance II diffractometer equipped with a θ/2θ Bragg-Brentano geometry and Ni-filtered CuKα radiation ($K\alpha_1$ = 1.5406 Å, $K\alpha_2$ = 1.5444 Å, $K\alpha_1/K\alpha_2$ = 0.5). The tube voltage and current were 40 kV and 40 mA, respectively. A scan rate of 2 seconds per step and a step size of 0.02° was adopted. Samples for PXRD were prepared by placing a thin layer of the appropriate material on a zero-background silicon crystal plate.

Single-crystal X-ray Diffraction (SXRD)

The synchrotron SXRD data were collected at the Beamline BL17B1, BL19U1 of Shanghai Synchrotron Radiation Facility (SSRF) with λ = 0.9840 and 0.82654 Å. All the datasets of single- crystal MOFs were collected at 100 K, and the data were accordingly processed with CrysAlisPro (version 1.171.37.35), HKL3000, and APEXII software packages, depending on the instrument setup. The structure solution and refinement were carried out using the SHELXT[818] and SHELXL[819]. In order to increase the completeness, two datasets of Co_6HHTT_3 and four datasets of Mg_6HHTT_3 were merged to refinement. According to the intensity statistics table for the whole dataset (PRP file), the resolution of Co_6HHTT_3

and Mg_6HHTT_3 were cut off to 0.90 Å and 1.05 Å, respectively. Solvent masking was applied during structure refinement. The structure was refined anisotropically. Crystal data and details of the structure refinement for single-crystal Co_6HHTT_3 and Mg_6HHTT_3 are given in Tables S2-S3.

High Resolution Transmission Electron Microscopy (HRTEM)

HRTEM images were obtained with a spherical aberration corrected FEI Titan 80-300, operated at an accelerating voltage of 300 kV equipped with a Gatan K2 in-situ direct electron detector (at the Center for Functional Nanomaterials (CFN), Brookhaven National Laboratory (BNL)). Samples were drop-cast onto Cu TEM grids from powder dispersed in methanol. The TEM dose rate was maintained between 4.8 $e^-/Å^2/s$ and 18.7 $e^-/Å^2/s$. We note that no damage to the MOF structures were detected during brief exposures at these dose conditions, but higher doses would cause significant and rapid structural damage. All image acquisition was done using Digital Micrograph 4.0 software at 0.3 s exposure time (~1.5 – 5.6 e- /$Å^2$ cumulative dose per image), with focusing done adjacent to the region imaged to minimize beam exposure prior to image acquisition (standard low dose imaging protocols). Analysis of the raw HRTEM data (.dm4), including FFT and intensity profile analysis, was done using FIJI ImageJ software (https://imagej.net/Fiji/).

Cryo-EM images of Cu_3HHTT_2 in Figs. A1d, A1e and A54 were obtained with a Titan Krios G3i transmission electron microscope operated at an accelerating voltage of 300 kV with Gatan BioQuantum-K3 energy filtered detector. Images in Fig. A53 were obtained

with a Talos Arctica G2 transmission electron microscope operated at an accelerating voltage of 200 kV with Falcon3EC direct electron detector.

3D Electron Diffraction Technique, Continuous Rotation Electron Diffraction (cRED)

3D ED data were collected under cryo-condition (95K) using the cRED method implemented in software *Instamatic*[820,821]. All the datasets were collected using a JEOL JEM2100 TEM (LaB6 filament, ASI Timepix camera) operating at 200 kV. The reciprocal space reconstruction was carried out using the program REDp[822], and the reflection intensity extraction was conducted by the program XDS[823]. Using the intensities obtained from 3D ED data, the structures were solved ab initio by the software package *SHELXT* [818].

Absorption spectra (UV-vis)

Absorption spectra were recorded on PerkinElmer Lambda 750 UV-vis spectrometer under ambient conditions.

X-ray absorption spectroscopy (XAS)

XAS experiments were performed at the 10-BM beamline at the Advanced Photon Source (APS) at Argonne National Laboratory. All measurements for the Co-, Ni-, and Cu-MOFs were performed at the K edges of Co (7.709 keV), Ni (8.333 keV), and Cu (8.979 keV) in transmission mode in fast scan from 250 eV below the edge to 550 eV above the edge. Each scan took approximately 10 minutes. Samples were pressed into a stainless-steel sample holder and placed in a sample cell. The cell was sealed and transferred to the

beamline for measurement. For reference, the locations of the white line and X-ray absorption near-edge spectroscopy (XANES) energy (inflection point of the leading edge) are noted for representative spectra at each edge. The XANES measurements of the compounds provide critical information about the oxidation states of the metal centers.

X-ray Photoelectron Spectroscopy (XPS)

XPS was performed at the Harvard Center for Nanoscale Systems (Cambridge, MA, USA) on a Thermo Scientific K-Alpha system equipped with an Al source and 180° double focusing hemispherical analyzer and 128-channel detector using a 400 μm X-ray spot size.

Scanning Electron Microscopy (SEM)

SEM was conducted at the Harvard Center for Nanoscale Systems (Cambridge, MA, USA) on a Leo Supra 55VP FEG SEM or on a Zeiss Ultra 55 SEM with an InLens detector and an operating voltage of 4 kV.

Optical microscopy (OM)

OM images were obtained by Leica S6 E stereoscopic microscope.

Atomic force microscopy (AFM)

AFM images were acquired on a Cypher Atomic Force Microscope from Asylum Research using silicon probing tips with mid-range mechanical properties (f = 300 kHz, k = 26 N/m) from Oxford Instruments. The scan rates are 0.5-2 Hz depending on the scan size.

Thermogravimetric Analysis

Thermogravimetric analysis (TGA) was performed on a TA Instruments Q500 Thermogravimetric Analyzer at a heating rate of 2.0 °C/min under a constant stream of air of 5 mL/min on a platinum pan. The analysis (Figure A7-A11) revealed similar behavior for the 5 materials, with apparent elimination of guest solvent molecules before 100 °C, at which stage the material fully retains its structure by PXRD. Dehydration of the nodes appears to be concurrent with the thermal decomposition of the framework, which starts above 100 °C and continues until full decomposition at 800 °C.

Electron Paramagnetic Resonance (EPR)

EPR measurements were performed on solid MOF powders diluted in potassium bromide with a Bruker EMX spectrometer at 9.37 GHz. Simulations of EPR were performed with the EasySpin package4 in Matlab (R2018b).

Elemental Analysis

Elemental analyses were performed by Robertson Microlit Laboratories, 1705 US Highway 46, Suite 1D, Ledgewood, NJ 07852.

Device Fabrication and Characterization

Samples of rods, or plates were suspended in hexane and drop-cast onto Si/SiO_2 substrates having pre-patterned marks for optical alignment and registration. The samples were then annealed at 60 °C for 12h in a vacuum oven. 2 layers of MMA and 1 layer of

PMMA were coated onto the chips, and the layers were baked at 85 °C for 5 minutes in a vacuum oven. Electron beam lithography at 30 kV was used to pattern contacts, and 5 nm Ti/250 nm Au were evaporated using an electron beam evaporator. Subsequently, the sample was soaked in acetone for a 24h lift-off process.

All electrical measurements were performed at room temperature in vacuum (10^{-5} mbar) in the dark. van der Pauw or four-probe configurations were adopted for plate- or rod-like crystals to minimize effect of contact resistance.[359,387] For van der Pauw measurements in figure 4A, four probes were connected to a source meter (Keithley 2450) through triax cables (Keithley model 7078-TRX-10). I-V curves were collected by scanning the current from -10 μA to 10 μA with a step size of 0.5 μA, speed of 5 number of power line circles (NPLC), and delay time of 2 ms, and measuring voltage at each step (for Co_6HHTT_3, –20 nA to 20 nA with a step size of 0.5 nA was applied). For detailed van der Pauw method calculation, please see the reference[387].For four probe rod measurements in figure 4B, linear I–V curves were obtained by supplying a current with range of –10 nA to 10 nA with a step size of 0.5 nA (Keithley 2450). Current was supplied through the outer two probes, while voltage was measured through the inner two probes. At least ten plates and rods of each MOF were measured.

Synthesis of 2,3,7,8,12,13-Hexahydroxytricycloquinazoline (HHTT)[824]

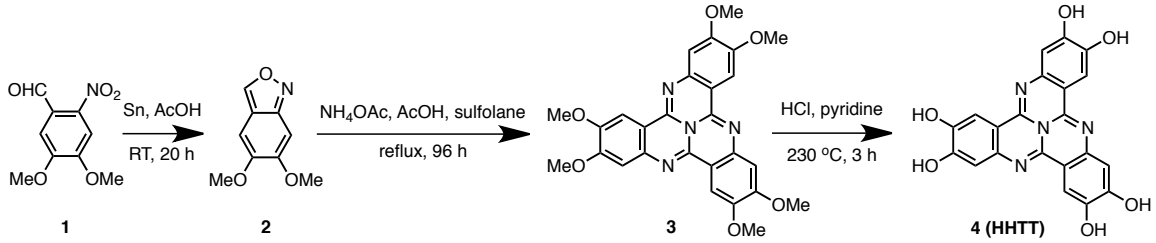

5,6-Dimethoxyanthranil **2**

Tin powder (13 g, 110 mmol) was added in portions to a stirred solution of 4,5-dimethoxy-2- nitrobenzaldehyde **1** (5 g, 23.7 mmol) in glacial acetic acid (300 mL). The resulting mixture was stirred at room temperature for 20 h before being worked up with ether and water. The organic layer was dried over anhydrous sodium sulfate and concentrated under vacuum. The residue was purified by silica gel column chromatography eluted with 8:2 hexanes/ethyl acetate followed by recrystallization using hexanes/ethyl acetate, affording 1.84 g (44%) of 5,6-dimethyoxyanthranil **2** as white rod-like crystals. ^{1}H NMR (500 MHz, $CDCl_3$): δ = 8.75 (1H), 6.70 (1H), 6.57 (1H), 3.88 (3H), 3.82 (3H) ppm. ^{13}C NMR (125 MHz, $CDCl_3$): δ = 155.10, 154.28, 151.70, 149.78, 113.95, 93.89, 90.90, 55.88 ppm.

2,3,7,8,12,13-Hexamethoxytricycloquinazoline **3**

To a mixture of sulfolane (100 mL) and glacial acetic acid (25 mL) was added ammonium acetate (12 g, 156 mmol) and 5,6-dimethyoxyanthranil **2** (4 g, 22.33 mmol). The reaction mixture was refluxed for 96 hours and cooled down to room temperature, after which water was added. The resulting greenish-yellow solid was collected by suction filtration, washed with water and methanol, and dried under air to give 789 mg (20% yield) of 2,3,7,8,12,13-

hexamethoxytricycloquinazoline **3**. ^{1}H NMR (500 MHz, CD_2Cl_2): δ = 7.68 (3H), 6.89 (3H), 3.97 (9H), 3.96 (9H) ppm.

2,3,7,8,12,13-Hexahydroxytricycloquinazoline (HHTT) **4**

A mixture of 2,3,7,8,12,13-hexamethoxytricycloquinazoline **3** (800 mg, 1.6 mmol) and pyridine hydrochloride (27 g, 234 mmol) was heated to 240°C for 3 hours and then cooled down to room temperature. Water was then added to the mixture, and the resultant black precipitate was collected by suction filtration, washed with water, and dried under vacuum to yield 328 mg (50%) of 2,3,7,8,12,13-hexamethoxytricycloquinazoline **4**. ^{1}H NMR (500 MHz, DMSO-*d6*): δ = 10.06 (3H), 9.64 (3H), 7.58 (3H), 6.72 (3H) ppm. ^{13}C NMR (125 MHz, DMSO-*d6*): δ = 151.96, 145.43, 143.43, 110.67, 109.38 ppm. Elemental analysis (calcd., found for: C (60.58, 60.55), H (2.91, 2.85), N (13.46, 13.48). Mass spectrometry analysis (HHTT = M, calc. $[M+H]^+$ = 417.0000, found 417.0001).

Synthesis of Cu_3HHTT_2

Cu_3HHTT_2 rod (fiber)

In air, to a 20 mL scintillation vial containing the solution of 0.077 mmol (1.0 equiv, 32.0 mg) of HHTT in 0.2 ml DMSO, the solution of 0.192 mmol (2.5 equiv, 48.0 mg) $CuSO_4 \cdot 5H_2O$ in 1.6 mL deionized water was added, inducing the formation of a cloudy red precipitate. Then the mixture was transferred into a 20 mL teflon sleeve of a parr bomb.

The parr bomb was then closed and left at 140 °C for 12 hours. After cooling to room temperature, the bomb was opened. The resulting black powder was centrifuged, and washed twice with each of water, DMSO, ethanol and acetone. Elemental analysis, (calcd., found for $Cu_3(HHTT)_2(H_2O)_{0.2}(CH_3C(O)CH_3)_{0.1}(DMSO)_{0.2}$: Cu (18.40, 18.97), C (49.49, 49.06), H (1.38, 1.43), N (10.81, 10.75).

Cu_3HHTT_2 plate (flake)

In air, to a 20 mL scintillation vial containing the solution of 0.120 mmol (1.0 equiv, 50.0 mg) of HHTT in 0.9 mL DMF, the solution of 0.180 mmol (1.5 equiv, 45.0 mg) $CuSO_4 \cdot 5H_2O$ in 2.1 mL deionized water was added, inducing the formation of a cloudy red precipitate. Then the vial was closed and left at 85 °C for 12 hours. The resulting black powder was centrifuged, and washed twice with each of water, DMF, ethanol and acetone.

Synthesis of Ni_3HHTT_2

Ni_3HHTT_2 rod (fiber)

In air, to a 20 mL scintillation vial containing the solution of 0.048 mmol (1.0 equiv, 20.0 mg) of HHTT in 0.2 ml DMF, the solution of 0.120 mmol (2.5 equiv, 30.0 mg) $Ni(OAc)_2 \cdot 4H_2O$ in 0.8 mL deionized water was added, inducing the formation of a cloudy red precipitate. Then the mixture was transferred into a 20 mL teflon sleeve of a parr bomb.

The parr bomb was then closed and left at 140 °C for 12 hours. After cooling to room temperature, the bomb was opened. The resulting black powder was centrifuged, and washed twice with each of water, DMSO, ethanol and acetone. Elemental analysis, (calcd., found for $Ni_3HHTT_2(H_2O)_{0.6}(DMSO)_{0.1}$: Ni (17.34, 17.38), C (49.92, 49.85), H (1.37, 1.44), N (11.04, 11.01).

Ni_3HHTT_2 plate (flake)

In air, to a 20 mL scintillation vial containing the solution of 0.024 mmol (1.0 equiv, 10.0 mg) of HHTT in 0.2 mL DMF, the solution of 0.036 mmol (1.5 equiv, 15.0 mg) $Ni(OAc)_2{\cdot}4H_2O$ in 0.8 mL deionized water was added, inducing the formation of a cloudy red precipitate. Then the vial was and left at 85 °C for 12 hours. The resulting black powder was centrifuged, and washed twice with each of water, DMF, ethanol and acetone.

Synthesis of Co_6HHTT_3

Co_6HHTT_3 rod (fiber)

In air, to a 20 mL scintillation vial containing the solution of 0.038 mmol (1.0 equiv, 16.0 mg) of HHTT in 0.2 mL DMF, the solution of 0.096 mmol (2.5 equiv, 24.0 mg) $Co(OAc)_2{\cdot}4H_2O$ in 0.8 ml deionized water was added, inducing the formation of a cloudy grey precipitate. Then the mixture was transferred into a 20 mL teflon sleeve of a parr

bomb. The parr bomb was then closed and left at 120 °C for 12 hours. The resulting black powder was centrifuged, and washed twice with each of water, DMF, ethanol and acetone. Elemental analysis, (calcd., found for $Co_6(HHTT)_3(H_2O)_{15.3}(DMF)_{0.2}$: Co (18.86, 18.79), C (40.75, 40.81), H (2.69, 2.62), N (9.12, 9.15).

Co_6HHTT_3 plate (flake)

In air, to a 20 mL scintillation vial containing the solution of 0.038 mmol (1.0 equiv, 16.0 mg) of HHTT in 0.4 mL 1,3-Dimethyl-2-imidazolidinone (DMI), the solution of 0.096 mmol (2.5 equiv, 24.0 mg) $Co(OAc)_2 \cdot 4H_2O$ in 1.6 mL deionized water was added, inducing the formation of a cloudy red precipitate. Then the vial was closed and left at 85 °C for 12 hours. The resulting black powder was centrifuged, and washed with water, DMI, ethanol and acetone.

Synthesis of Mg_6HHTT_3

Mg_6HHTT_3 rod (fiber)

In air, to a 20 mL scintillation vial containing the solution of 0.048 mmol (1.0 equiv, 20.0 mg) of HHTT in 0.2 mL DMF, the solution of 0.096 mmol (2.0 equiv, 20.6 mg) $Mg(OAc)_2 \cdot 4H_2O$ in 0.9 mL deionized water was added. Then the solution of 0.480 mmol (10.0 equiv, 39.4 mg) of anhydrous sodium acetate in 0.9 mL deionized water is added to

the mixture, inducing the formation of a cloudy grey precipitate. Then the mixture was transferred into a 20 ml teflon sleeve of a parr bomb. The parr bomb was closed and left at 120 °C for 12 hours. The resulting black powder was centrifuged, and washed twice with each of water, DMF, ethanol and acetone twice. Elemental analysis, (calcd., found for $Mg_6HHTT_3(H_2O)_{17.2}(DMF)_{0.3}$: Mg (8.54, 8.61), C (44.92, 44.98), H (3.22, 3.19), N (10.08, 10.03).

Mg_6HHTT_3 plate (flake)

In air, to a 20 mL scintillation vial containing the solution of 0.038 mmol (1.0 equiv, 16.0 mg) of HHTT in 0.4 mL DMF, the solution of 0.077 mmol (2.0 equiv, 16.5 mg) $Mg(OAc)2{\cdot}4H2O$ in 0.9 mL deionized water was added. Then a solution of 0.385 mmol (10.0 equiv, 31.6 mg) of anhydrous sodium acetate in 0.9 mL deionized water was added to the mixture, inducing the formation of a cloudy red precipitate. Then the vial was closed and left at 85 °C for 12 hours. The resulting black powder was centrifuged, and washed twice with each of water, DMF, ethanol and acetone.

Synthesis of Ni_6HHTT_3

Ni_6HHTT_3 rod (fiber)

In air, to a 20 mL scintillation vial containing the solution of 0.019 mmol (1.0 equiv, 8.0 mg) of HHTT in 3.0 mL deionized water, which was sonicated for 60 minutes. Then the solution of 0.048 mmol (2.5 equiv, 12.0 mg) $Ni(OAc)_2 \cdot 4H_2O$ in 1.0 mL deionized water was added, inducing the formation of a cloudy red precipitate. Then the vial was closed and left at 85 °C for 12 hours. The resulting black powder was centrifuged, and washed with water, DMF, ethanol and acetone, twice for each solvent. Elemental analysis, (calcd., found for $Ni_6(HHTT)_3(H_2O)_{16.7}(DMF)_{0.1}$: Ni (18.62, 18.76), C (40.02, 40.08), H (2.78, 2.83), N (8.96, 9.01).

Ni_6HHTT_3 plate (flake)

In air, to a 20 mL scintillation vial containing the solution of 0.019 mmol (1.0 equiv, 8.0 mg) of HHTT in 10.0 mL deionized water, which was sonicated for 60 minutes. Then the solution of 0.048 mmol (2.5 equiv, 12.0 mg) $Ni(OAc)_2 \cdot 4H_2O$ in 2.0 mL deionized water was added, inducing the formation of a cloudy red precipitate. Then the vial was closed and left at 85 °C for 12 hours. The resulting black powder was centrifuged, and washed with water, DMF, ethanol and acetone, twice for each solvent.

Table A1. Synthesis conditions of M_mHHTT_n MOFs

MOFs	Packing mode	Coordination # of metal	Temp (°C)	Solvent (ml)	Reaction time (h)	Ligand+ Metal (mg)
Cu_3HHTT_2 rod	porous	4	140	0.2 DMSO +1.6 H_2O	12	32+48
Cu_3HHTT_2 plate	porous	4	85	0.9 DMF +2.1 H_2O	12	50+45
Ni_3HHTT_2 rod	porous	4	140	0.2 DMF +0.8 H_2O	12	20+30
Ni_3HHTT_2 plate	porous	4	85	0.2 DMF +0.8 H_2O	12	10+15
Co_6HHTT_3 rod	dense	6	120	0.2 DMF +0.8 H_2O	12	16+24
Co_6HHTT_3 plate	dense	6	85	0.4 DMI +1.6 H_2O	12	16+24
Mg_6HHTT_3 rod	dense	6	120	0.2 DMF +1.8 H_2O	12	20+20.6
Mg_6HHTT_3 plate	dense	6	85	0.4 DMF +1.8 H_2O	12	16+16.5
Ni_6HHTT_3 rod	dense	6	85	4.0 H_2O	12	8+12
Ni_6HHTT_3 plate	dense	6	85	12.0 H_2O	12	8+12

As is shown in Table A1 and described in the main text, we were able to isolate both rod- and plate-like crystals for the five MOFs we reported. Based on experimental observation described in Table A1, plate-like morphology is favored by using more dilute precursor solutions (Ni_6HHTT_3, Ni_3HHTT_2, Mg_6HHTT_3), solvents disfavoring pi-pi stacking interaction (Cu_3HHTT_2, Co_6HHTT_3) (see Fig. A44 and discussion below), or

lower reaction temperature (Cu_3HHTT_2, Ni_3HHTT_2, Co_6HHTT_3, Mg_6HHTT_3). It has been shown in the literature that weakening of the ligand pi-pi stacking promotes the in-plane growth of 2D MOFs.[825] We believe the same principle can be applied to the morphological preferences we observed for the HHTT MOFs. Aggregation process due to pi-pi stacking are reversible equilibrium processes. Upon dilution, the equilibrium shifts towards breaking of the pi-pi stacking due to thermodynamic effects, thus promoting in-plane growth. It is worth noting that such effect is subtle in most systems. For Ni_6HHTT_3, where this effect is most pronounced, it only requires a three-fold dilution to completely eliminate the rod- like crystals from the plate-like once. A similar concentration dependence has been reported in the synthesis of the structurally similar 2D MOF of Cu_3(hexahydroxytriphenylene)$_2$,[349] where a more dilute solution is used to obtain the plate-like morphology. The effect of solvent is most pronounced for Cu_3HHTT_2 and Co_6HHTT_3MOFs, where substituting DMSO with DMF or DMF with DMEU contributes to formation of larger plates-like crystals. As demonstrated in Fig. A44, the nature of solvent has significant effect on the aggregation of HHTT molecules. Here, we believe that the solvent disruption of pi-pi stacking increases in the order of DMSO < DMF < DMI. Plate-like morphology is promoted by application of solvents that have stronger disruption of pi- pi stacking. Finally, lowering the reaction temperature facilitates growth of plate-like crystals for Cu_3HHTT_2, Ni_3HHTT_2, Co_6HHTT_3, and Mg_6HHTT_3. Whereas a reaction can be affected by temperature in multiple ways, including thermodynamics, kinetics, as well as solubility of the precursors, intermediates, and products involved, hereby we focus on the effect of temperature on the competition between in-plane and out-of-plane growth. As

discussed in the main text, the in- plane growth of the MOFs is stunted by the strong and less reversible in-plane metal-ligand bonding interactions. Such driving force dominates the crystal growth process at low temperature, leading to a preference over plate-like morphology. A complete understanding of these aforementioned processes is beyond the current study, and further experiments are currently underway in our lab to explore the applicability of these principles to the synthesis of other 2D conductive MOFs.

Assignment of X in Mg_6HHTT_3

As discussed in the main text, Mg_6HHTT_3 has formula of $[M_3(HHTT)_2(H_2O)_6 \bullet M_3(HHTT)(H_2O)_{12}]$, revealing the X groups in **Figure 23c** being water molecules. We made this assignment based on the following reasons. As shown by the crystal structure acquired from cRED analysis, X are determined to be terminal oxygen atoms coordinated to the metal atoms. Yet, crystallographic analysis does not reveal further detail about the nature and charge of the oxygen atom due to limited resolution of the hydrogen atoms. Nevertheless, we assign X to be water molecules by comparing our structures with previously reported crystal structures in the Cambridge Structure Database (CSD) of metal complexes with similar coordinating environments, i.e. complexes containing catechol-derived bidentate ligands and coordinating water/hydroxyl/oxo groups. The strongest piece of evidence comes from the structurally analogous 2D conductive MOF of Co_6HHTT_3reported by Yaghi et al. (HHTP = hexahydroxytriphenylene), which is composed of layers of isolated Co3(HHTP) molecular

complexes sandwiched between extended 2D $Co_3(HHTP)_2$ sheets.[330] In Co_6HHTT_3, which has identical metal and ligand charge states of +2 and -3 to M_6HHTT_3, water molecules are observed to fill in the open coordination sites of the octahedral cobalt centers that remained upon coordination to the o-dihydroxyl groups on HHTP. Consequently, in an analogy of charge neutrality principle, we assign the oxygen atoms in M_6HHTT_3 to be originated from water. This assignment is further supported by a similar observation for the molecular complexes of Co, Ni, and Mg with catecholate-derived ligands. Among all of such reported complexes we could find in the CSD with a well-characterized crystal structure, water is only found for terminal ligand, whereas hydroxyl and oxo groups are found solely as bridging ligands between multiple metal centers.[826–835] Based on these points, we assign the X groups in M_6HHTT_3 to be coordinating water molecules.

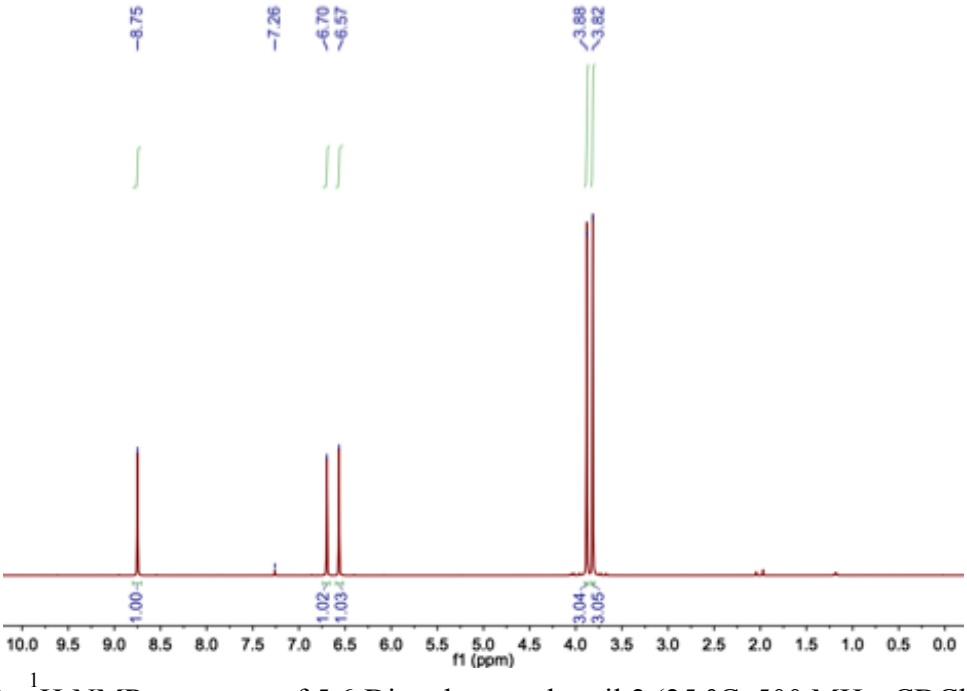

Fig. A3. ^{1}H-NMR spectrum of 5,6-Dimethoxyanthranil **2** (25 °C, 500 MHz, $CDCl_3$).

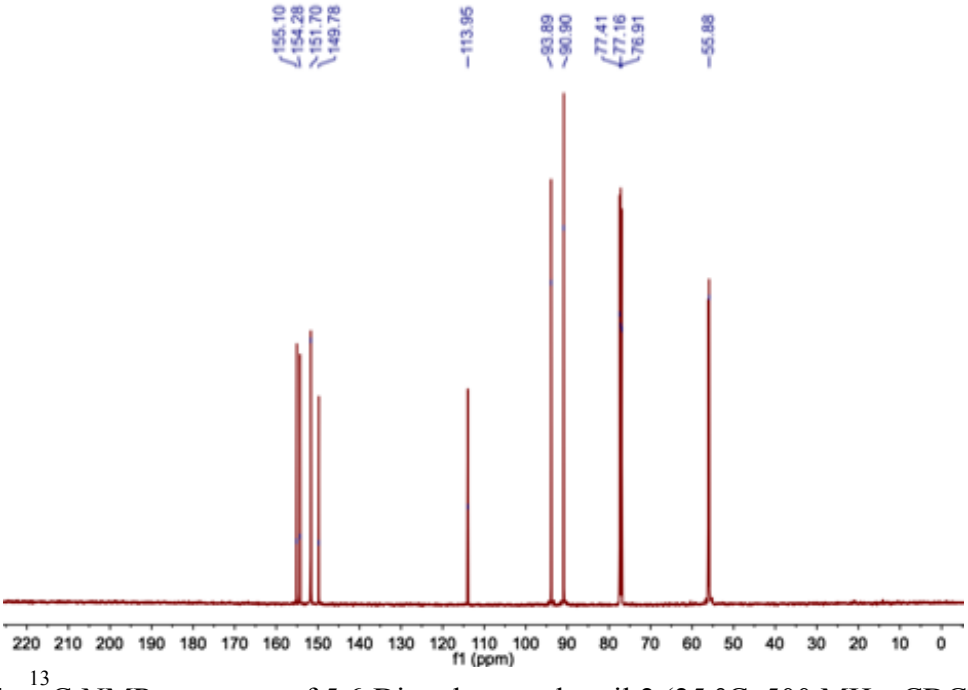

Fig. A4. ^{13}C-NMR spectrum of 5,6-Dimethoxyanthranil **2** (25 °C, 500 MHz, $CDCl_3$).

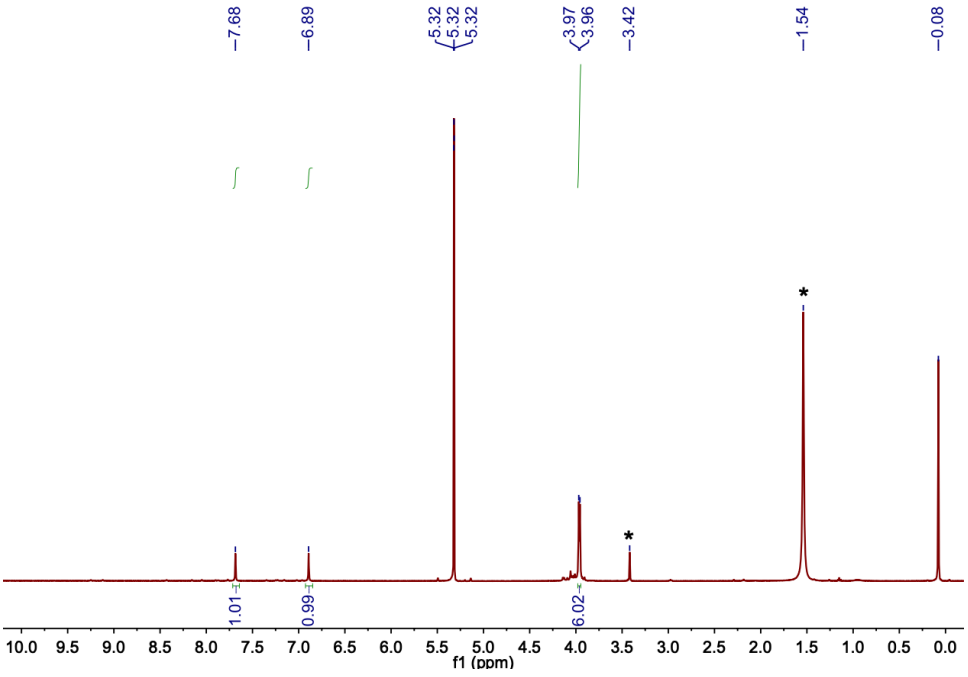

Fig. A5. ^{1}H-NMR spectrum of 2,3,7,8,12,13-Hexamethoxytricycloquinazoline **3** (25 °C, 500 MHz, CD_2Cl_2). * marks the residual H_2O (1.54 ppm) and methanol (3.42 ppm).

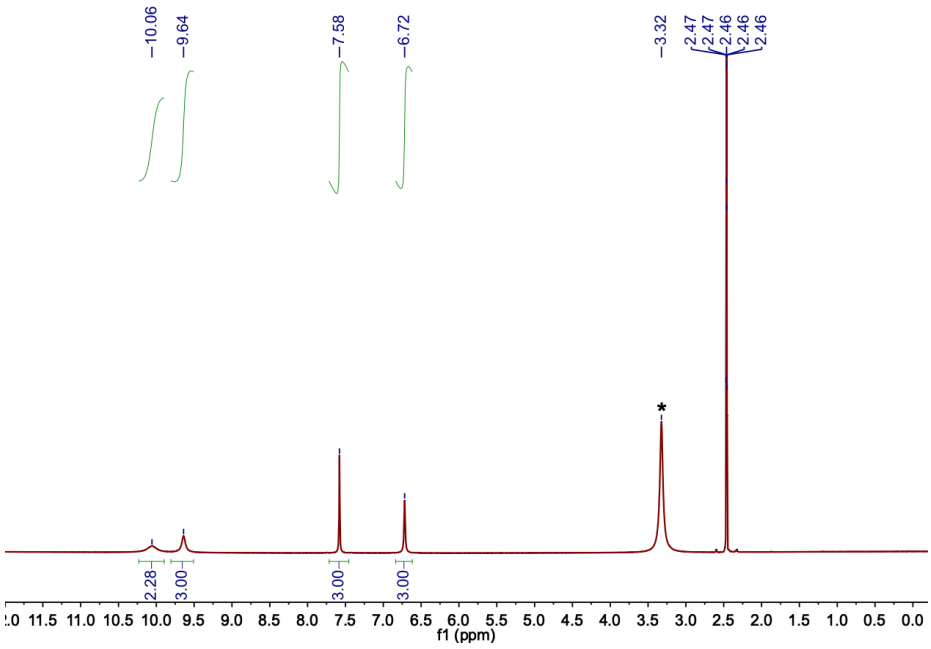

Fig. A6. ^{1}H-NMR spectrum of HHTT **4** (25 °C, 500 MHz, DMSO-*d6*). * marks the residual H2O (3.32 ppm).

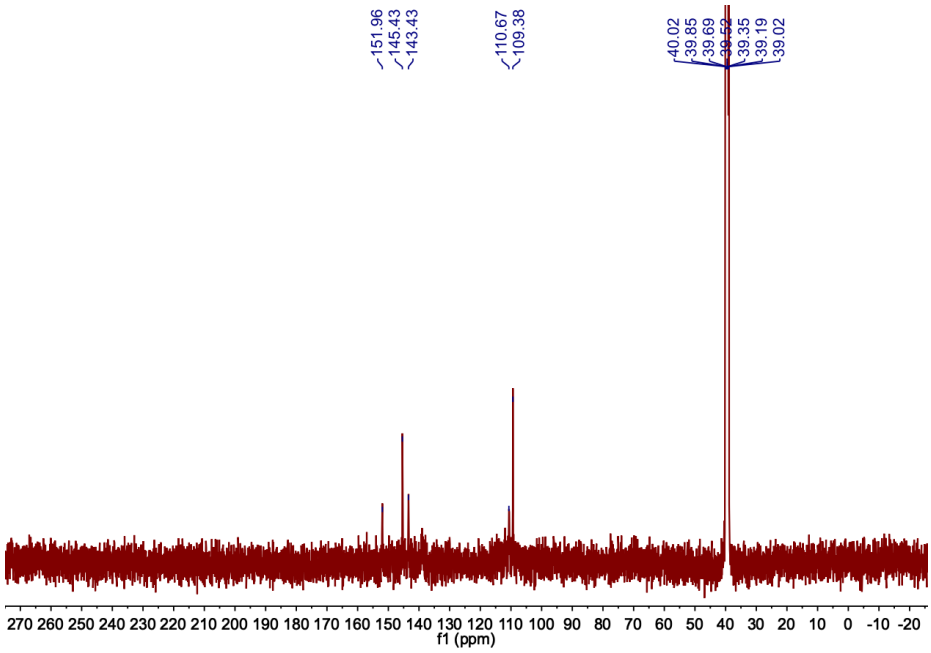

Fig. A7. ^{13}C-NMR spectrum of HHTT **4** (25 °C, 500 MHz, DMSO-*d6*).

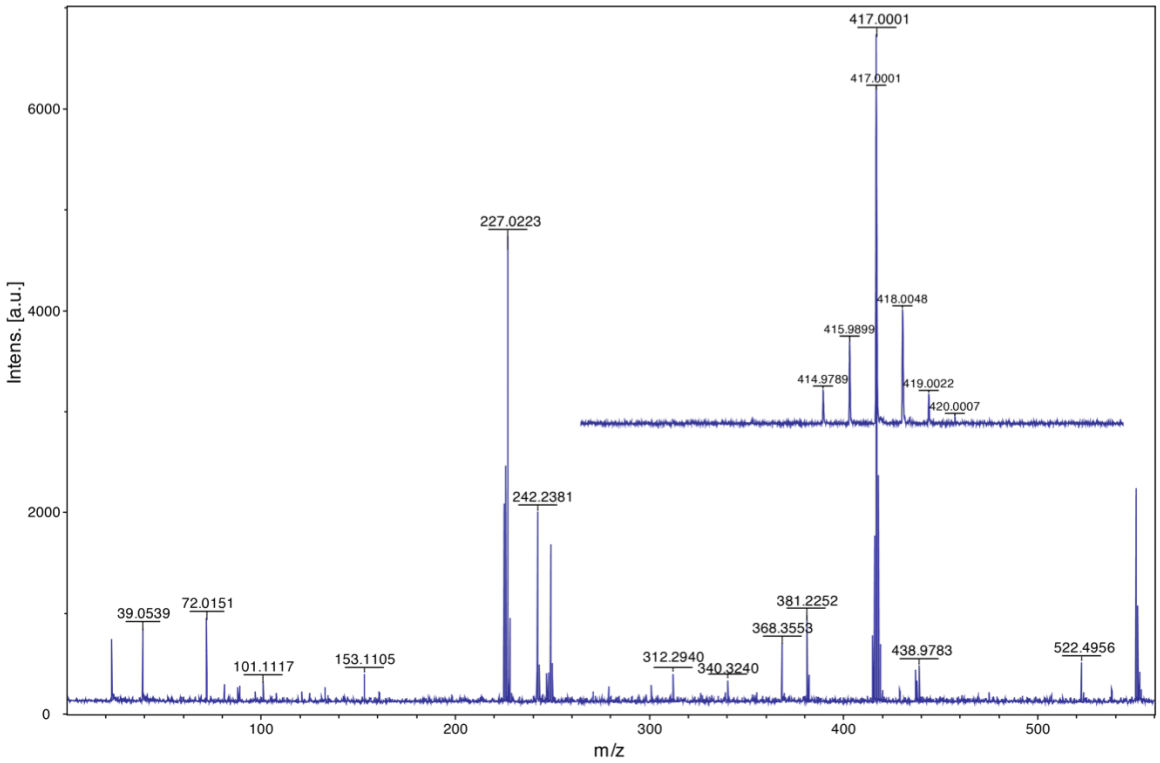

Fig. A8. Mass spectra of HHTT **4** (HHTT = M, calc. $[M+H]^+$ = 417.0000, found 417.0001).

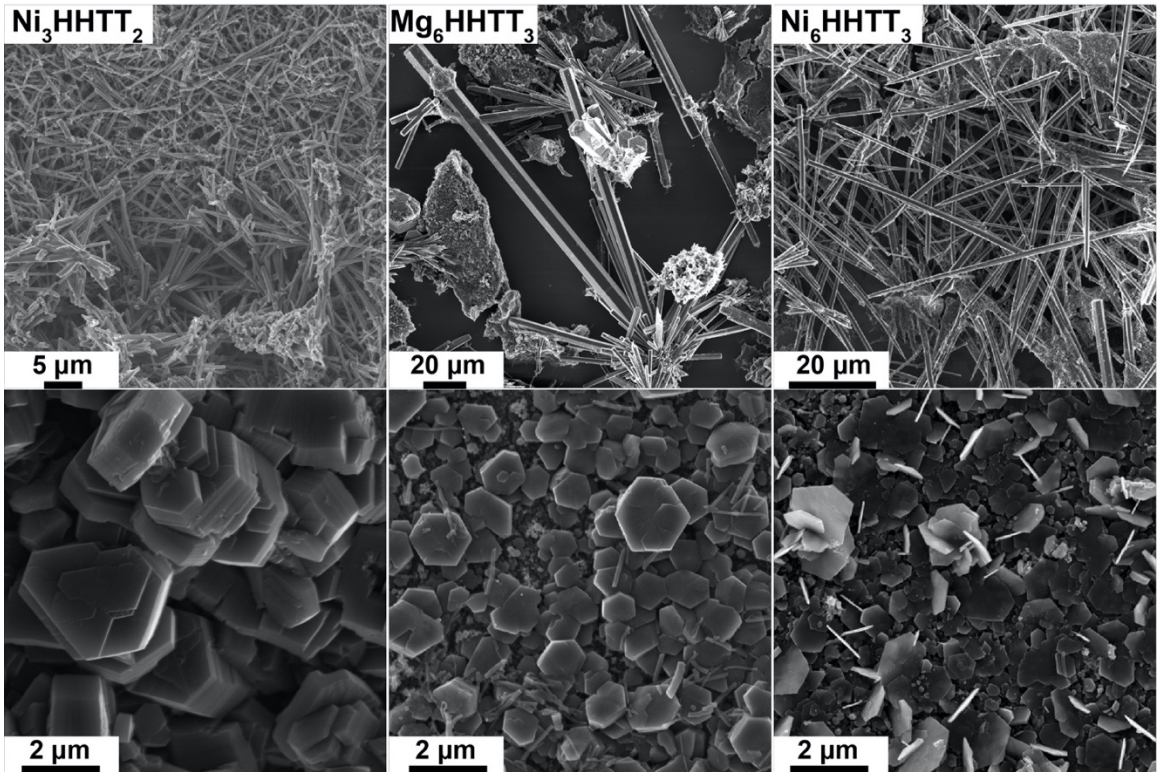

Fig. A9. SEM micrographs of 2D M_mHHTT_n MOFs that can be isolated on-demand with either rod- (top) or plate-like (bottom) morphology by varying the synthetic conditions.

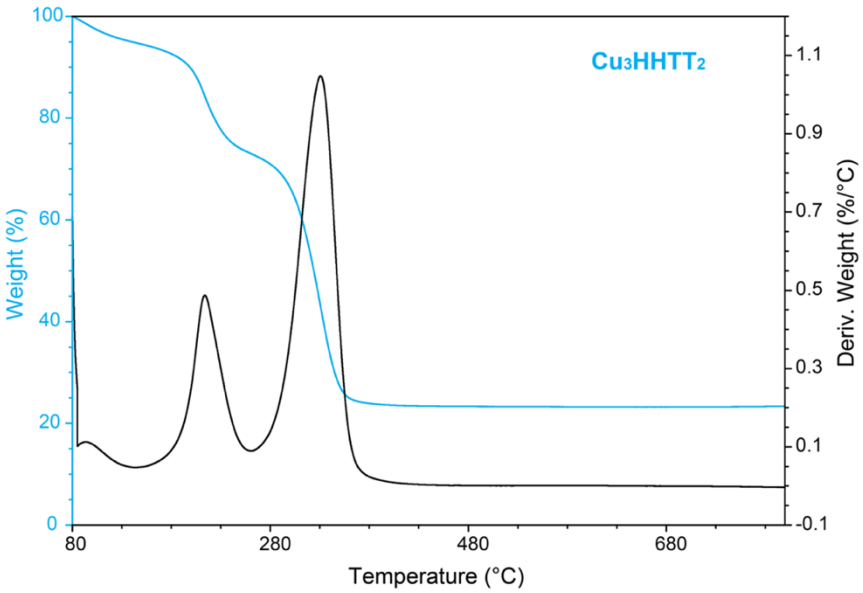

Fig. A10. TGA plot for $\mathbf{Cu_3HHTT_2}$. Blue: remaining relative mass percentage; black: derivative of the weight percentage change.

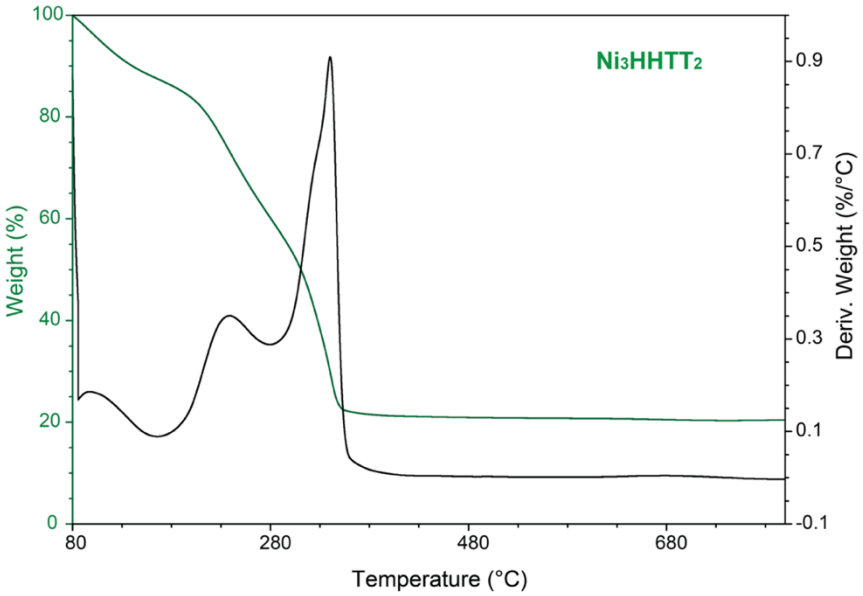

Fig. A11. TGA plot for $\mathbf{Ni_3HHTT_2}$. Green: remaining relative mass percentage; black: derivative of the weight percentage change.

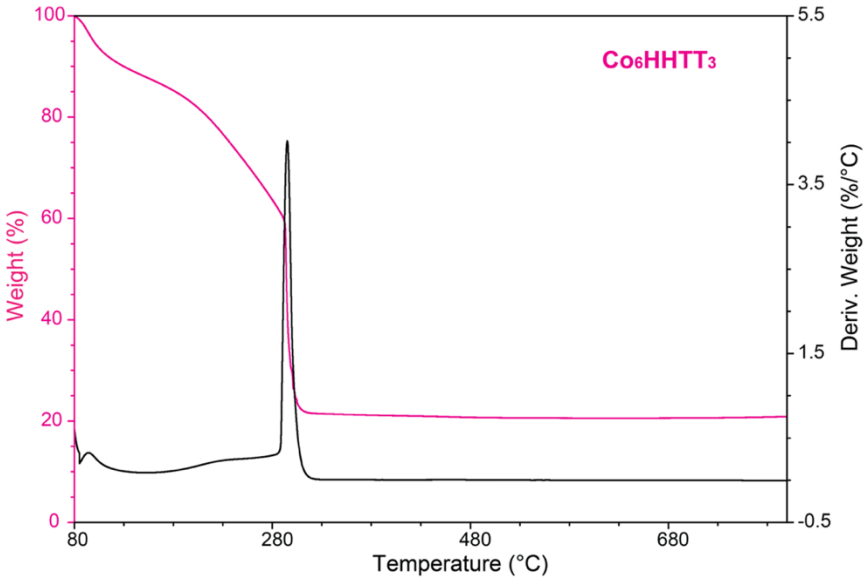

Fig. A12. TGA plot for $\mathbf{Co_6HHTT_3}$. Pink: remaining relative mass percentage; black: derivative of the weight percentage change

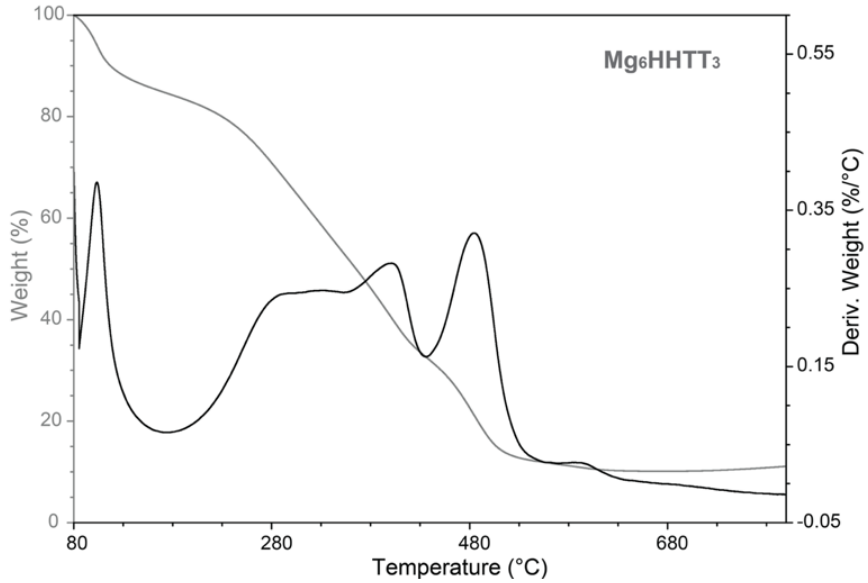

Fig. A13. TGA plot for $\mathbf{Mg_6HHTT_3}$. Gray: remaining relative mass percentage; black: derivative of the weight percentage change.

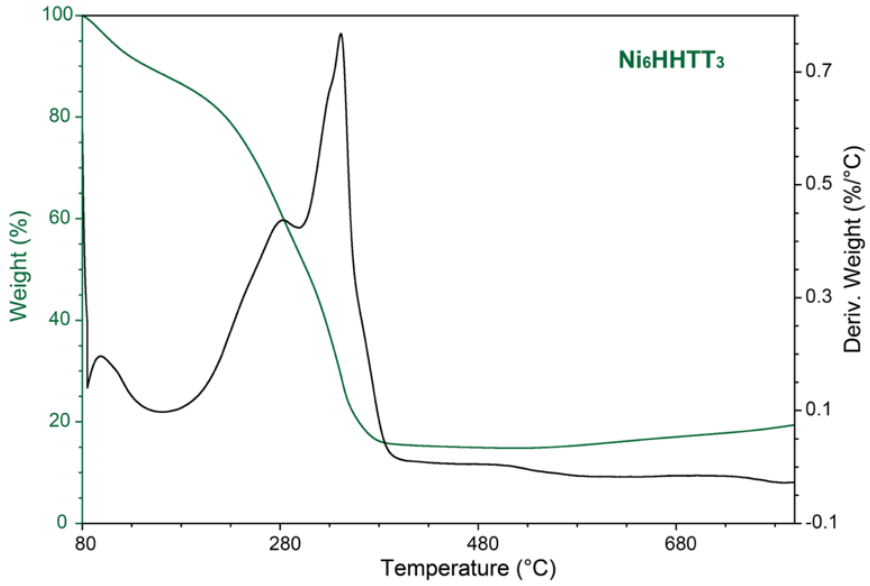

Fig. A14. TGA plot for **Ni_6HHTT_3**. Green: remaining relative mass percentage; black: derivative of the weight percentage change.

The stacked 2D sheets form 1D hexagonal pores with a diameter of 2.3 nm, which is in good agreement with the average pore size of 2.1 nm obtained by fitting a N_2 absorption isotherm to Cu_3HHTT_2 of an activated material (App. A, Fig. A15). Fitting the N_2 adsorption isotherm of Cu_3HHTT_2 to the Brunauer–Emmett–Teller (BET) equation gives an apparent surface area of $1{,}360 \pm 20$ m² g^{-1} (App. A Fig. A16).

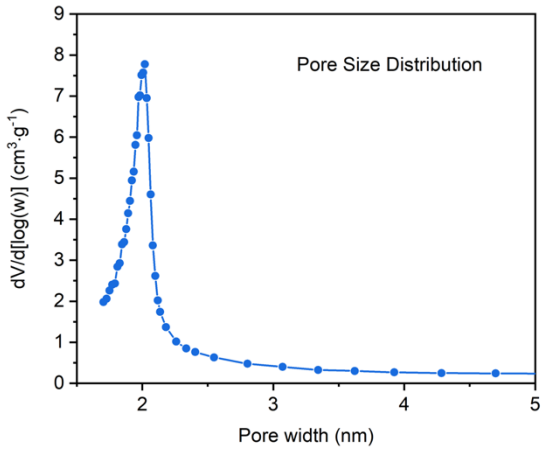

Fig. A15. Barrett-Joyner-Halenda (BJH)[836] pore size distribution curve using the Kruk-Jaroniec-Sayari correction[837] for hexagonal pores for **Cu_3HHTT_2**. Pore size: 2.1 nm.

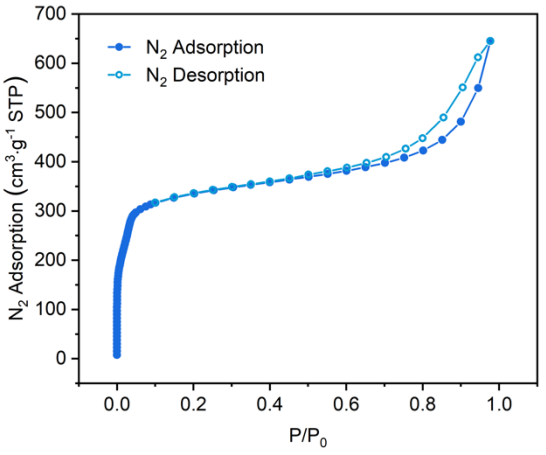

Fig. A16. Nitrogen adsorption isotherms for **Cu_3HHTT_2** at 77K. The isotherm was fit to the BET equation to give apparent BET surface areas of 1360±20 m2/g. The C value of the BET fitting was 155.

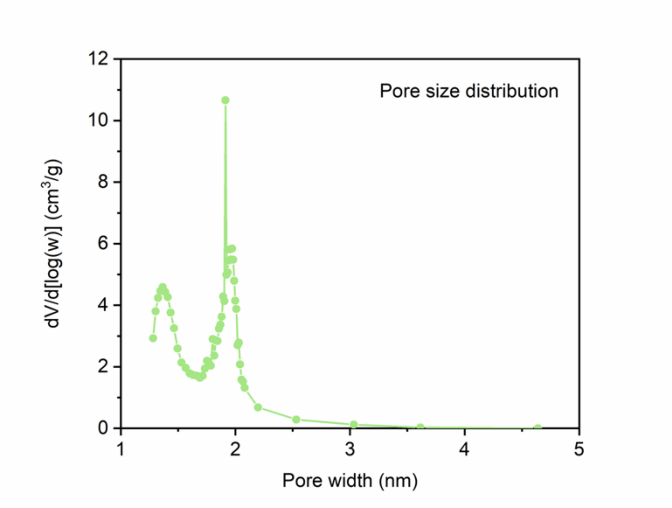

Fig. A17. Barrett-Joyner-Halenda (BJH)[836] pore size distribution curve using the Kruk-Jaroniec-Sayari correction 18 for hexagonal pores for Ni_3HHTT_2. Pore size: 1.9 nm.

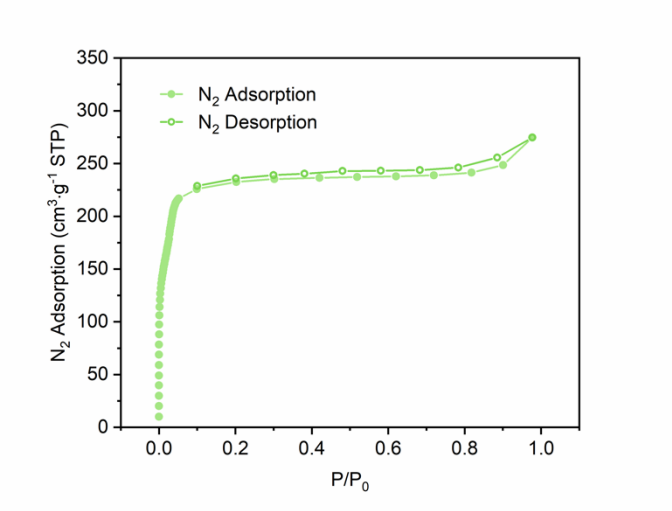

Fig. A18. Nitrogen adsorption isotherms for Ni_3HHTT_2 at 77K. The isotherm was fit to the BET equation to give apparent BET surface areas of 1114±11 m2/g. The C value of the BET fitting was 83.

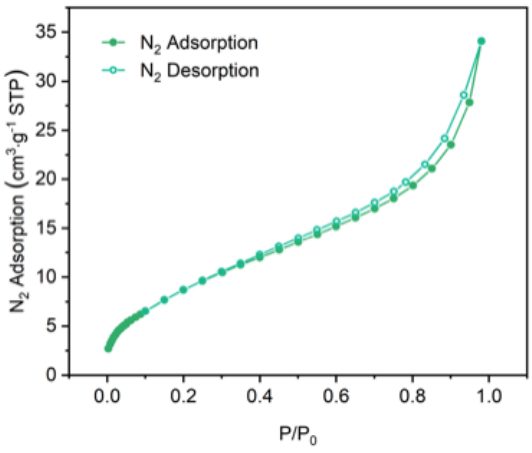

Fig. A19. Nitrogen adsorption isotherms for **Ni_6HHTT_3** at 77K. The isotherm was fit to the BET equation to give apparent BET surface areas of 25.6 ± 0.2 m2/g. The C value of the BET fitting was 97.0.

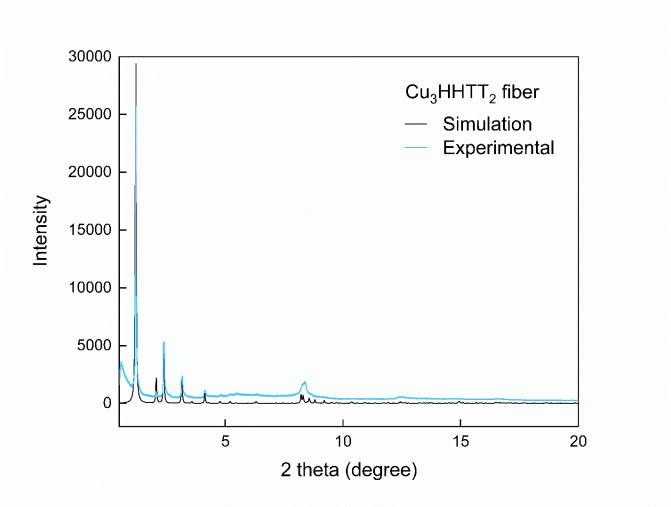

Fig. A20. Experimental (in blue) and simulated (in black) Synchrotron PXRD patterns for **Cu_3HHTT_2** rod (fiber).

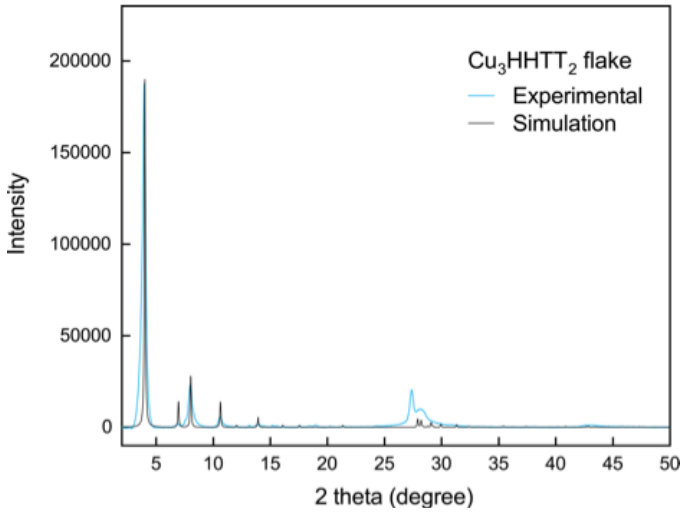

Fig. A21. Experimental (in blue) and simulated (in black) Laboratory PXRD patterns for **Cu_3HHTT_2**plate (flake). For presentation purposes, the background was subtracted.

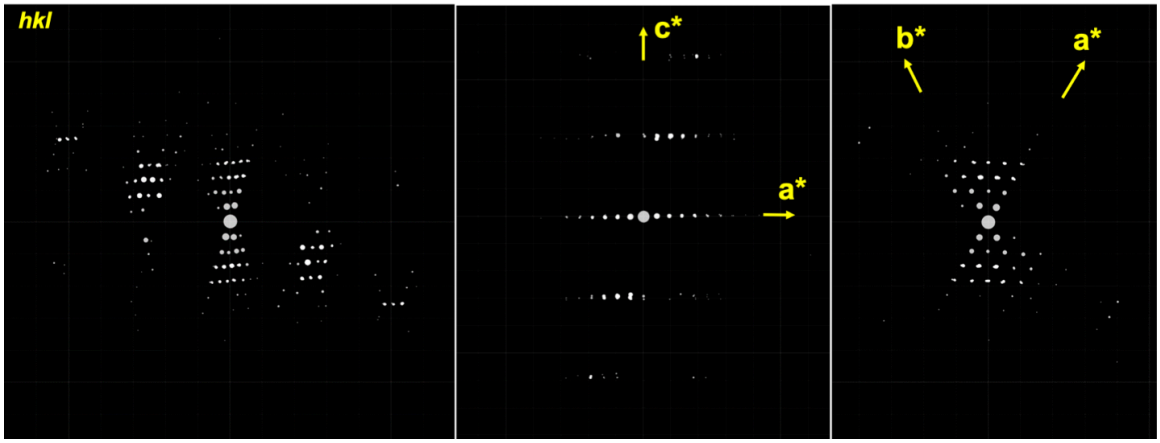

Fig. A22. 3D ED data for **Cu_3HHTT_2** rod. a) overview of the 3D reciprocal lattice; b) 3D reciprocal lattice along b* axes; c) hk0 slice cut from the 3D reciprocal lattice.

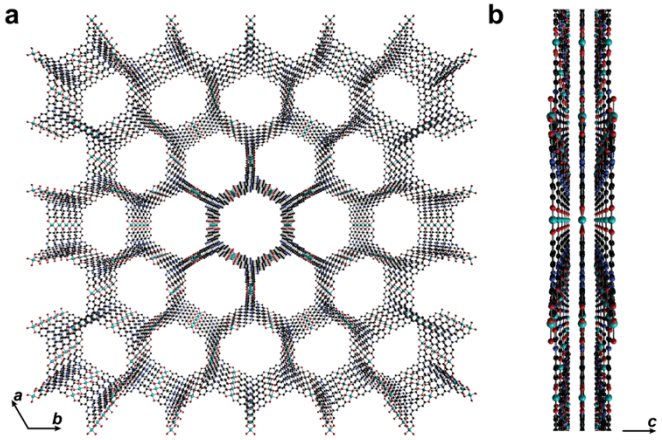

Fig. A23. (a) Multi-layer stacking for **Cu_3HHTT_2** viewed along the *c* direction and (b) *a/b* direction. C atoms, black; N atoms, dark blue; Cu atoms, turquoise; H atoms are omitted for clarity.

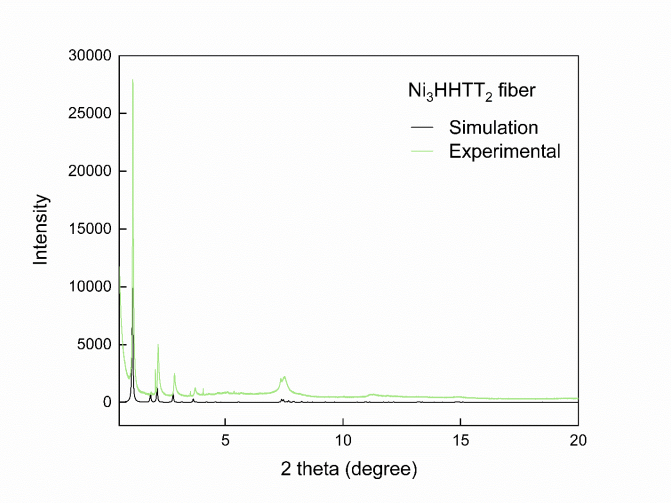

Fig. A24. Experimental (in green) and simulated (in black) Synchrotron PXRD patterns for **Ni_3HHTT_2** rod (fiber).

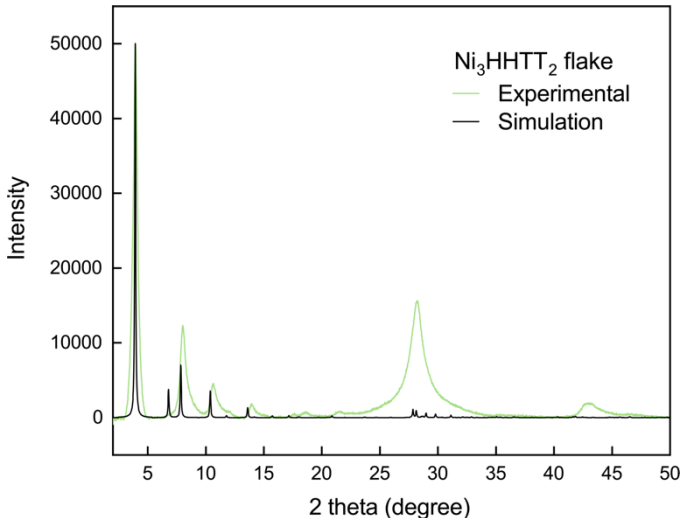

Fig. A25. Experimental (in green) and simulated (in black) Laboratory PXRD patterns for **Ni_3HHTT_2** plate (fiake). For presentation purposes, the background was subtracted.

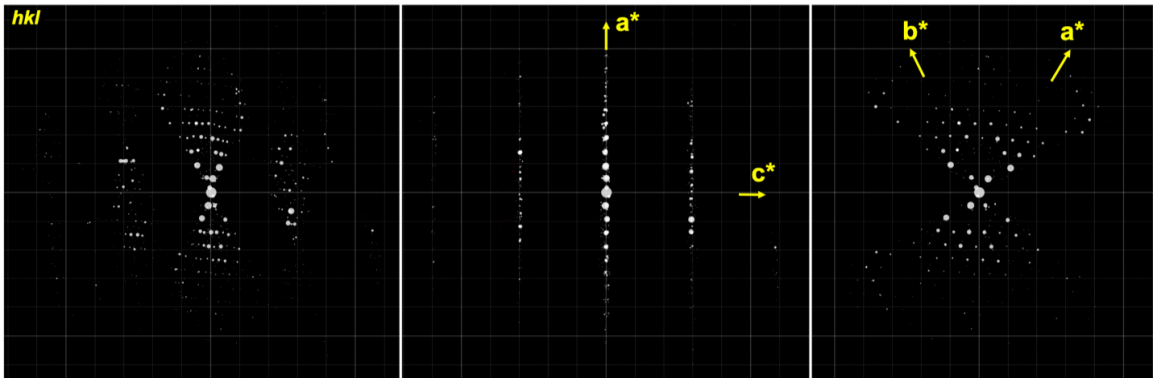

Fig. A26. 3D ED data for **Ni_3HHTT_2** rod. (left) overview of the 3D reciprocal lattice; (center) 3D reciprocal lattice along b* axes; (right) hk0 slice cut from the 3D reciprocal lattice.

Table A2. Crystal data, data collection, and structure refinement parameters for **Co_6HHTT_3**.

Empirical formula	$Co_{18}\ C_{189}\ N_{36}\ O_{108}$
Formula weight	5562.99
Crystal system	Hexagonal
Space Group	R-3c
Unit cell dimensions (Å)	a = 26.065(4)
	c =19.459(4)
V (Å^3)	11449(4)
Z, ρ_{cal} (g/cm^3)	2, 1.614
Absorption coefficient (mm^{-1})	3.258
F(000)	5472.0
Theta range (°)	1.5663 – 23.633
	-29 <= h <= 29
	-29 <= k <= 29
	-20 <= l <= 20
Reflections collected/unique	89262/1760
Completeness (%)	91.4
Data/parameter	1760/83
Goodness	1.585
Final R indices [I > 2σ(I)]	R_1 = 0.1282
	wR_2 = 0.2446

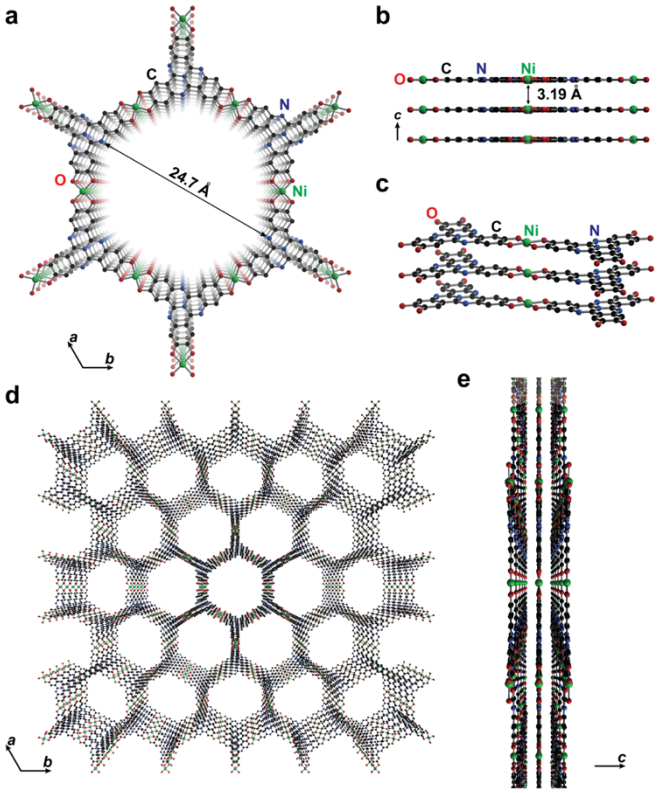

Fig. A27. (a). Crystal structure representation of **Ni_3HHTT_2** viewed along the c direction. (b) Layer stacking and (c) metal-ligand connectivity of the square planar coordination environment in **Ni_3HHTT_2**. (d) Multi-layer stacking for **Ni_3HHTT_2** viewed along the *c* direction and (e) *a/b* direction. H atoms are omitted for clarity.

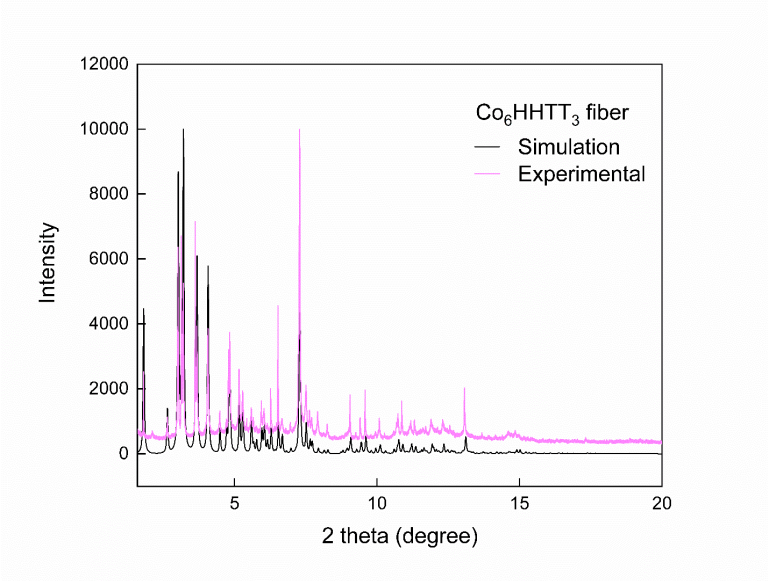

Fig. A28. Experimental (in pink) and simulated (in black) Synchrotron PXRD patterns for **Co_6HHTT_3** rod (fiber).

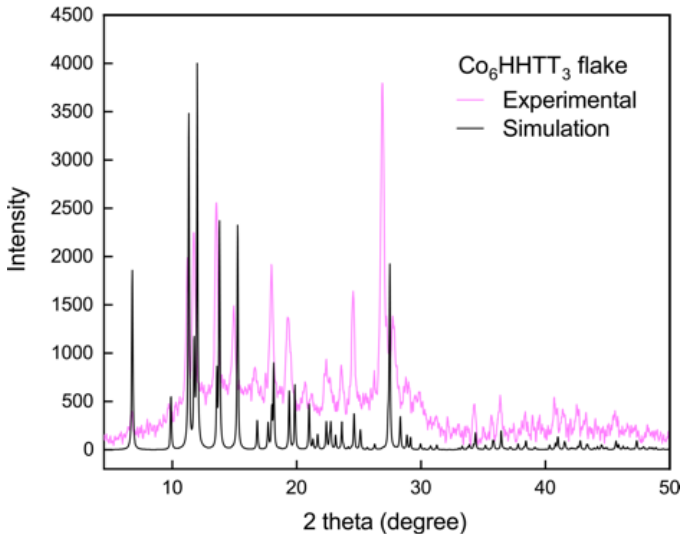

Fig. A29. Experimental (in pink) and simulated (in black) Laboratory PXRD patterns for **Co_6HHTT_3** plate (flake). For presentation purposes, the background was subtracted.

Table. A3. Crystal data, data collection, and structure refinement parameters for **Mg_6HHTT_3**

Empirical formula	$Mg_{18}\ C_{189}\ N_{36}\ O_{108}$
Formula weight	4939.83
Crystal system	Hexagonal
Space Group	R-3c
Unit cell dimensions (Å)	a = 26.122(4)
	c =19.740(4)
V (Å^3)	11665(4)
Z, ρ_{cal} (g/cm^3)	2, 1.433
Absorption coefficient (mm^{-1})	0.239
F(000)	4932
Theta range (°)	2.152 – 33.172
	-29 <= h <= 29
	-29 <= k <= 29
	-20 <= l <= 20
Reflections collected/unique	8251 / 1603
Completeness (%)	89.7
Data/parameter	1603/104
Goodness	2.794
Final R indices [I > 2σ(I)]	R_1 = 0.1526
	wR_2 = 0.4171

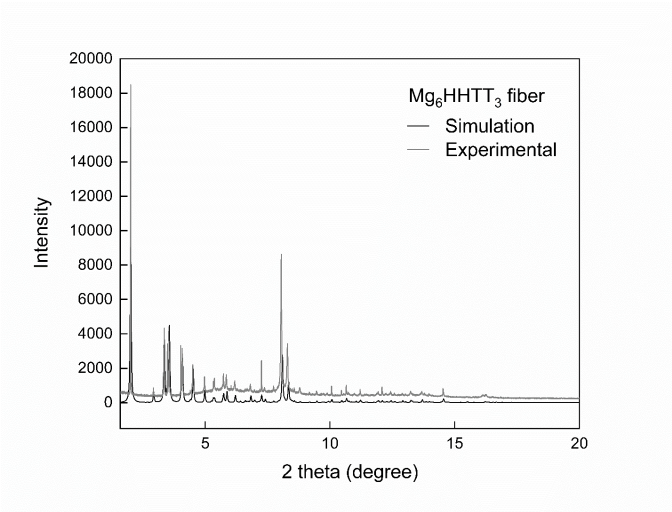

Fig. A30. Experimental (in gray) and simulated (in black) Synchrotron PXRD patterns for **Mg_6HHTT_3** rod (fiber).

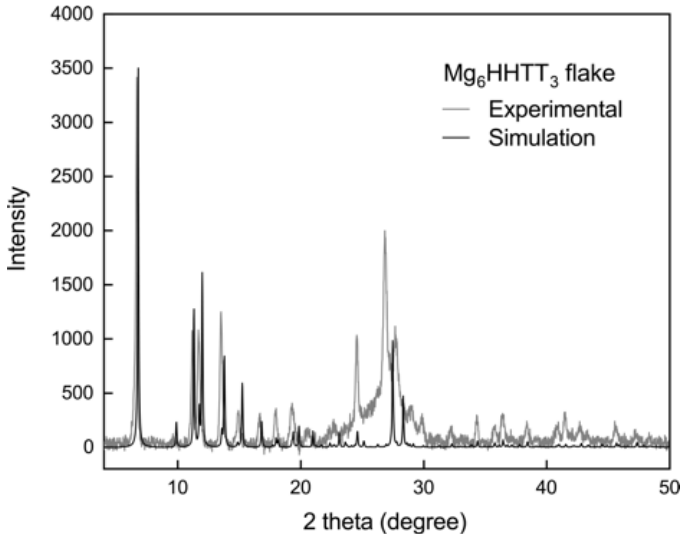

Fig. A31. Experimental (in gray) and simulated (in black) Laboratory PXRD patterns for **Mg_6HHTT_3** plate (flake). For presentation purposes, the background was subtracted.

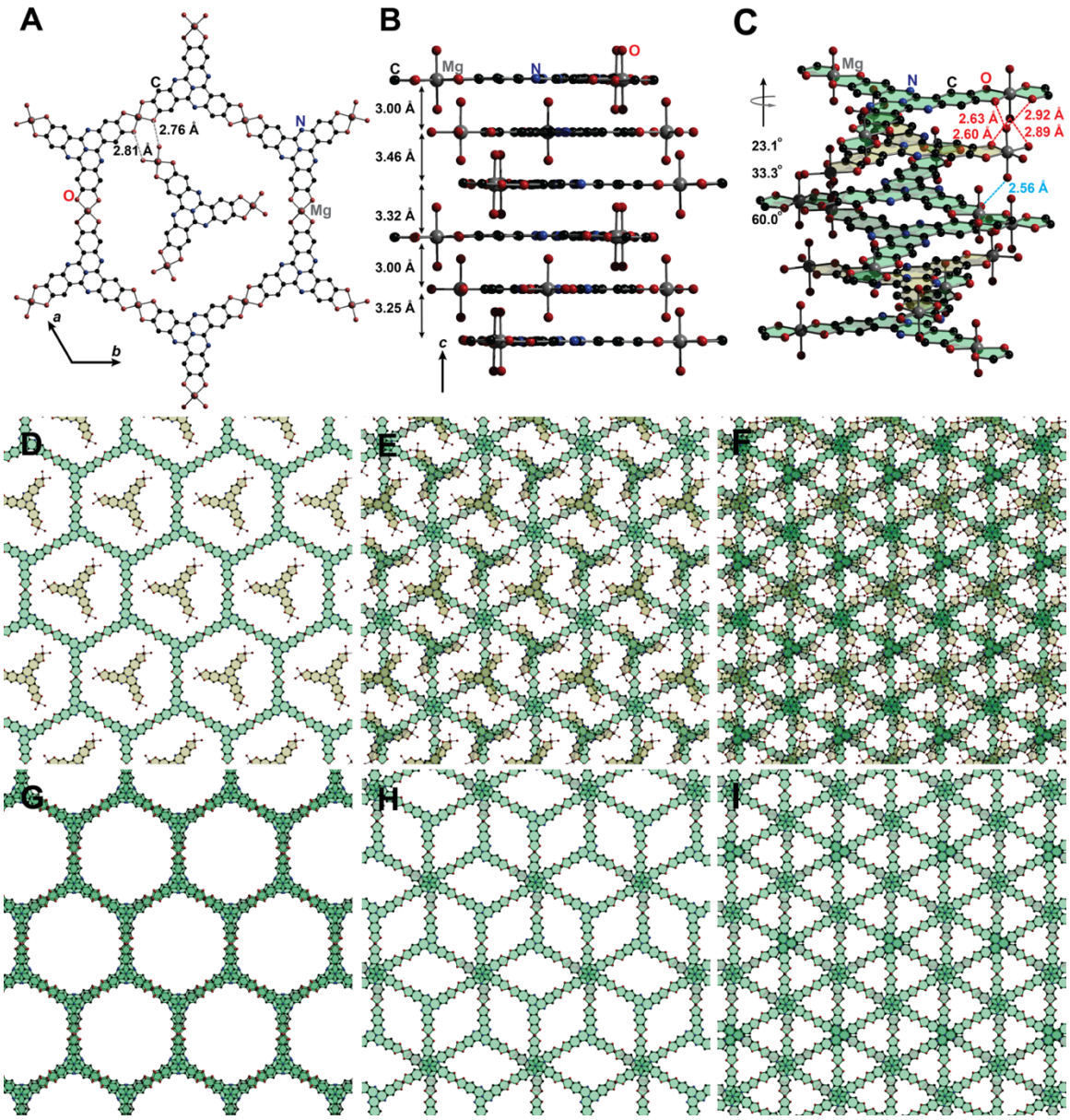

Fig. A32. Single-crystal structure of Mg_6HHTT_3. (a). Crystal structure representation of Mg_6HHTT_3 viewed along the c direction. (b) Structural view along the a/b-plane in one-unit cell, showing interlayer stacking distances and the octahedral coordination sphere of the magnesium centers. (c) Spatial relationships of the Mg3HHTT units in each layer. The framework-based and molecular units are colored in green and yellow, respectively. The

Mg_3HHTT units in each layer are related by screw axes of 23.1, 33.3, and 60.0 degrees. Interlayer hydrogen bonds are illustrated by red and blue dashed lines. (d, e, f) Structural representation of single, double, and triple layers of Mg_6HHTT_3. (g), (h), and (i) illustrate the stacking geometries between the first and fourth, first and second, as well as the first, second, and third layers, respectively. All guest molecules in the pore are omitted for clarity in the insets. The framework-based and molecular units are colored in green and yellow, respectively.

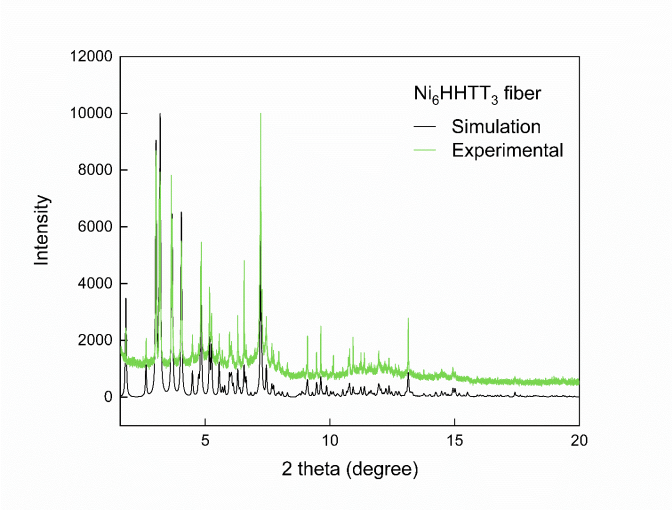

Fig. A33. Experimental (in green) and simulated (in black) Synchrotron PXRD patterns for **Ni_6HHTT_3** rod (fiber). The background was subtracted.

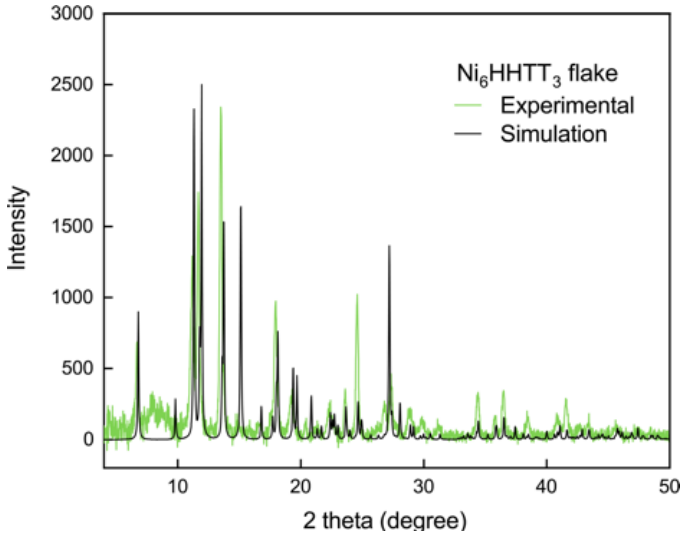

Fig. A34. Experimental (in green) and simulated (in black) Laboratory PXRD patterns for **Ni_6HHTT_3** plate (flake). For presentation purposes, the background was subtracted.

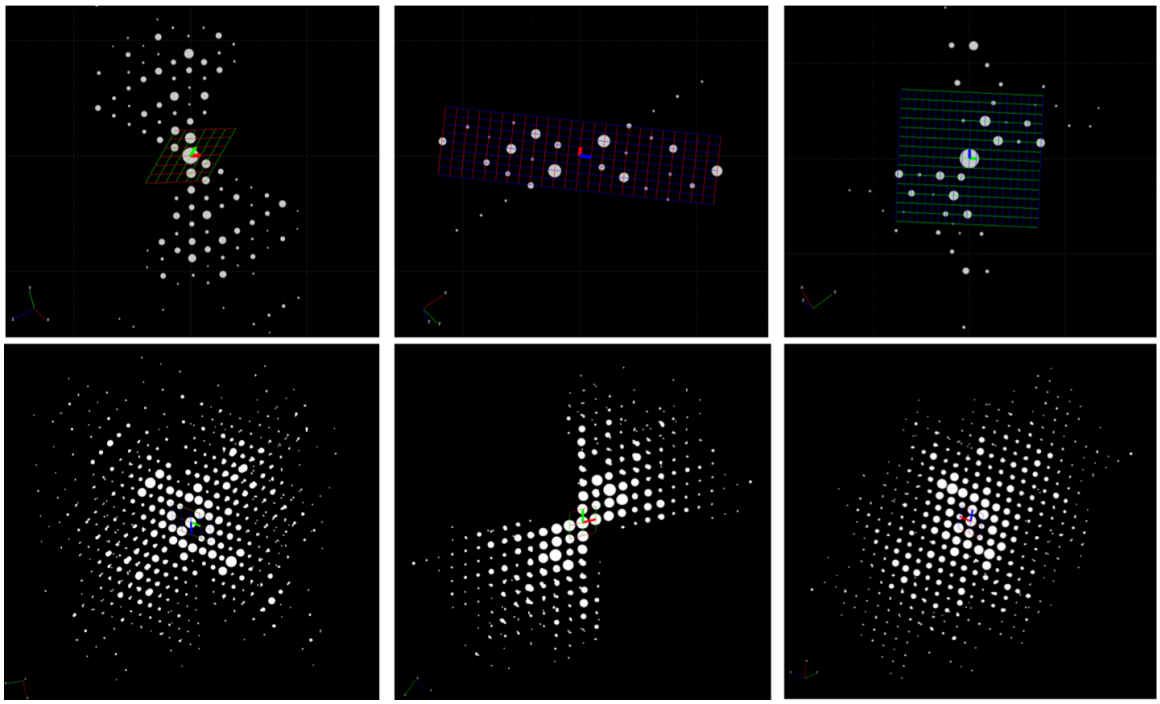

Fig. A35. (hk0) (up left), (h0l) (up center), (0kl) (up right) slices cut from the reconstructed reciprocal lattice of $\mathbf{Ni_6HHTT_3}$. 3D-RED data projection of $\mathbf{Ni_6HHTT_3}$ along [001] (bottom left), [010] (bottom center), [100] (bottom right) zone axes, respectively.

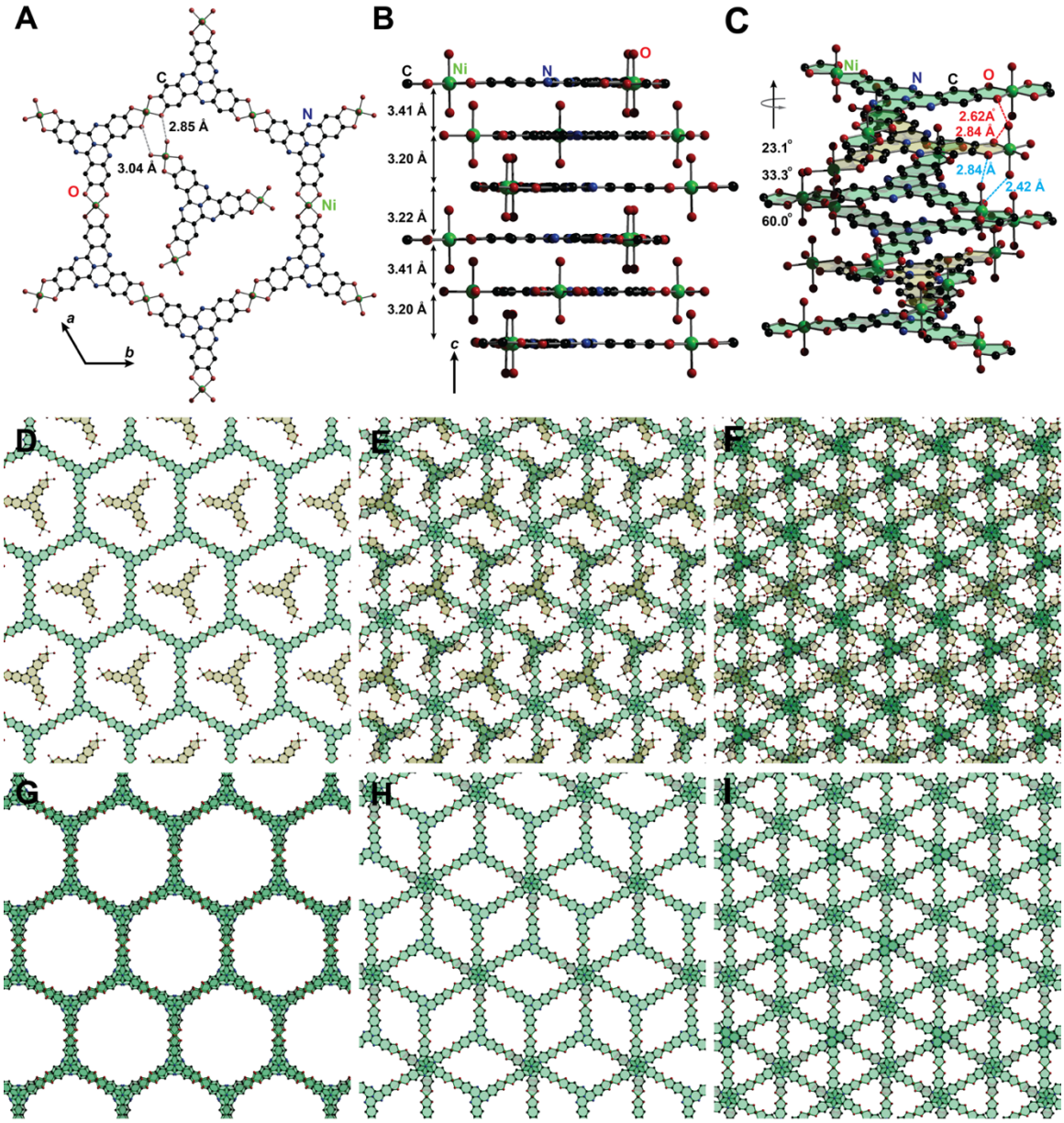

Fig. A36. Single-crystal structure of **Ni_6HHTT_3**. (a). Crystal structure representation of Ni_6HHTT_3 viewed along the c direction. (b) Structural view along the a/b-plane in one-unit cell, showing interlayer stacking distances and the octahedral coordination sphere of the nickel centers. (c) Spatial relationships of the Ni_3HHTT units in each layer. The framework-based and molecular units are colored in green and yellow, respectively. The

Ni_3HHTT units in each layer are related by screw axes of 23.1, 33.3, and 60.0 degrees. Interlayer hydrogen bonds are illustrated by red and blue dashed lines. (d, e, f) Structural representation of single, double, and triple layers of Ni_6HHTT_3, with one, two and three atomic layers, respectively. (g), (h), and (i) illustrate the stacking geometries between the first and fourth, first and second, as well as the first, second, and third layers, respectively. All guest molecules in the pore are omitted for clarity in the insets. The framework-based and molecular units are colored in green and yellow, respectively.

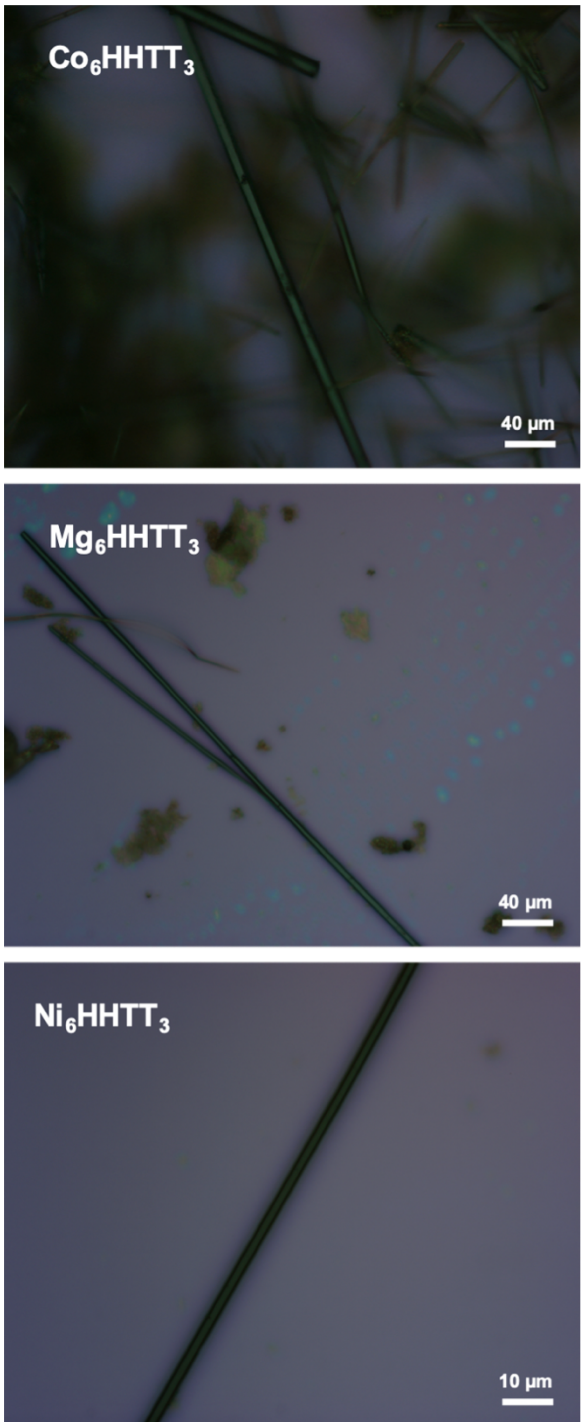

Fig. A37. Optical microscopy images of single-crystalline $\mathbf{Co_6HHTT_3}$, $\mathbf{Mg_6HHTT_3}$ and $\mathbf{Ni_6HHTT_3}$

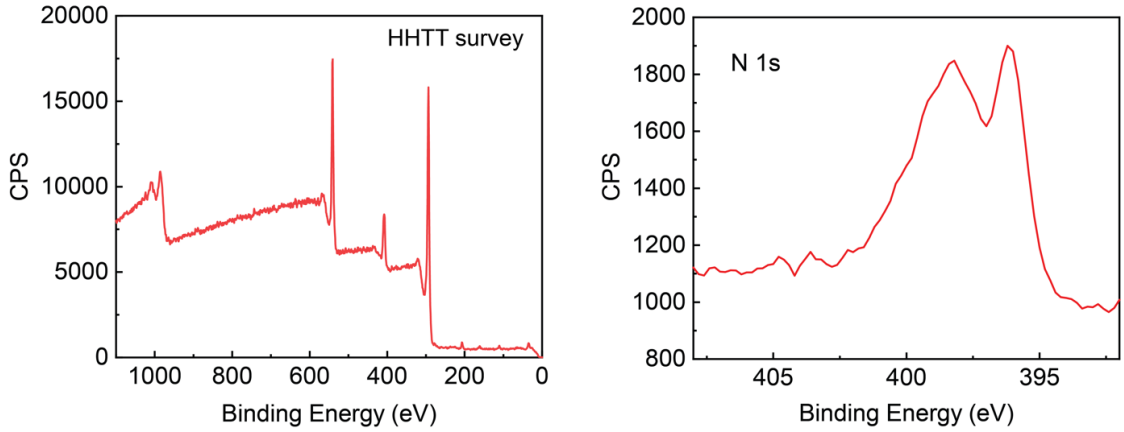

Fig. A38. XPS spectra of **HHTT** ligand survey and the N(1s) region. The N(1s) region has two peaks that corresponds well to the structure of the ligand.

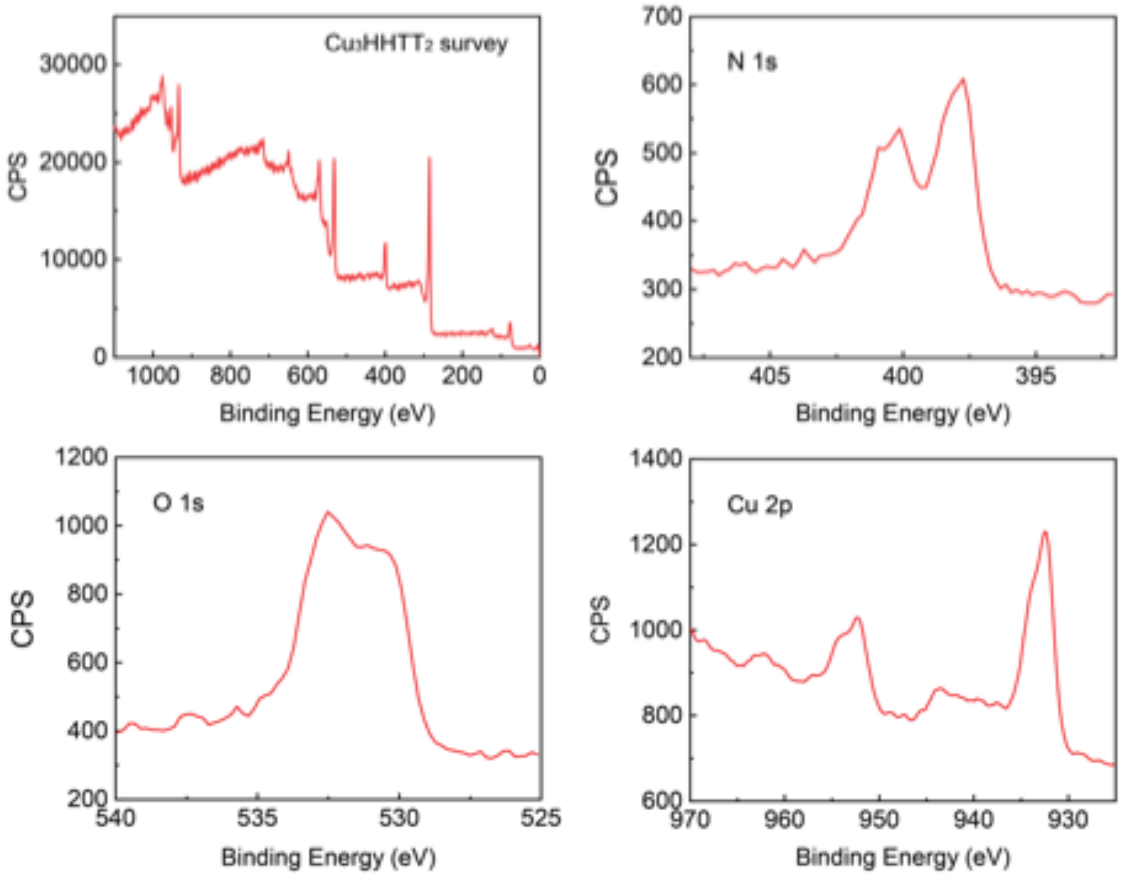

Fig. A39. XPS spectra of **Cu_3HHTT_22** survey and the corresponding N(1s), O(1s) and Cu(2p) region. Cu(2p3/2) peak has a binding energy of 933 eV, indicating the presence of Cu(II) in **Cu_3HHTT_2.**

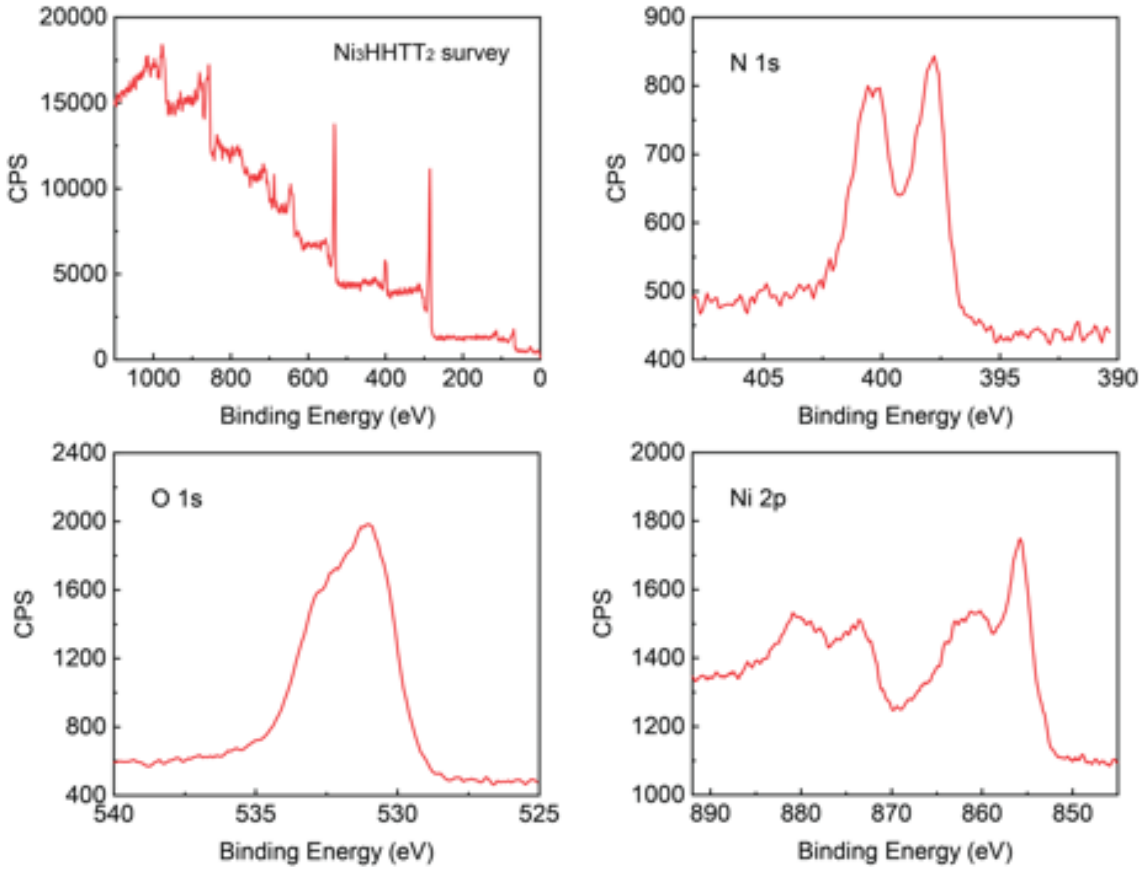

Fig. A40. XPS spectra of **Ni_3HHTT_2** survey and the corresponding N(1s), O(1s) and Ni(2p) region. Ni(2p3/2) peak has a binding energy of 856 eV, indicating the presence of Ni(II) in **Ni_3HHTT_2.**

Co_6HHTT_3 can be grown as large hexagonal rods, approximately 20 µm in diameter and 200 µm in length, which are amenable for single-crystal X-ray diffraction analysis (**Figure 23d,** App. A Fig. A41).

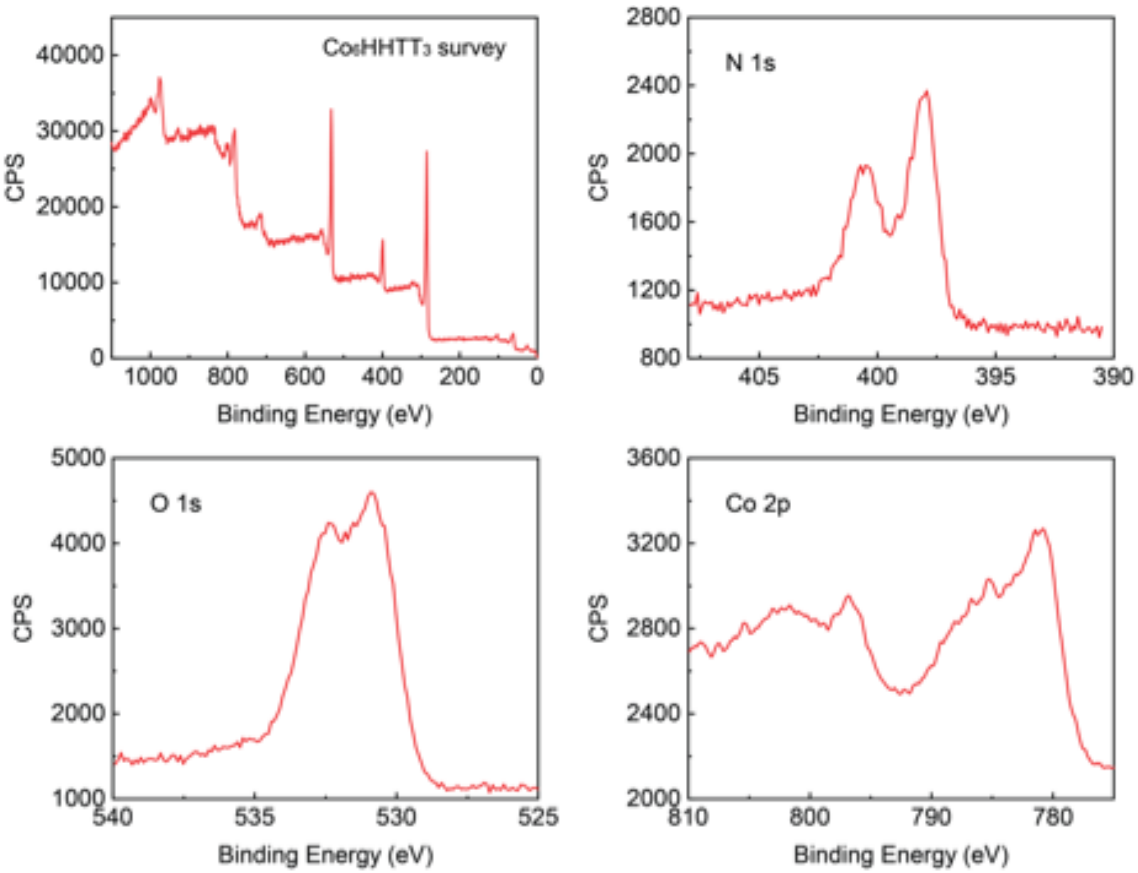

Fig. A41. XPS spectra of $\mathbf{Co_6HHTT_3}$ survey and the corresponding N(1s), O(1s) and Co(2p) region. Co(2p3/2) peak has a binding energy of 933 eV and a clear satellite feature at the binding energy of 785 eV, indicating the presence of Co(II) in $\mathbf{Co_6HHTT_3}$.

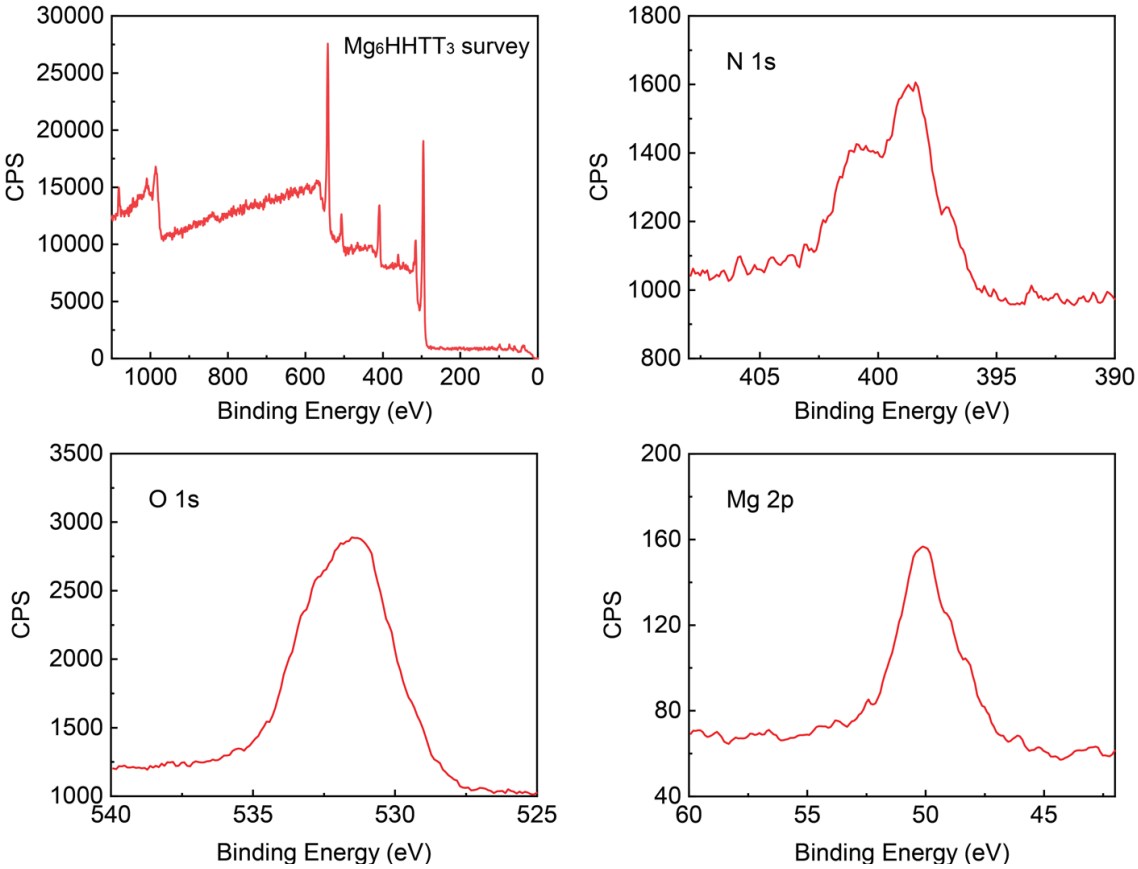

Fig. A42. XPS spectra of **Mg_6HHTT_3** survey and the corresponding N(1s), O(1s) and Mg(2p) region. Mg(2p) peak has a binding energy of 50 eV, indicating the presence of Mg(II) in **Mg_6HHTT_3.**

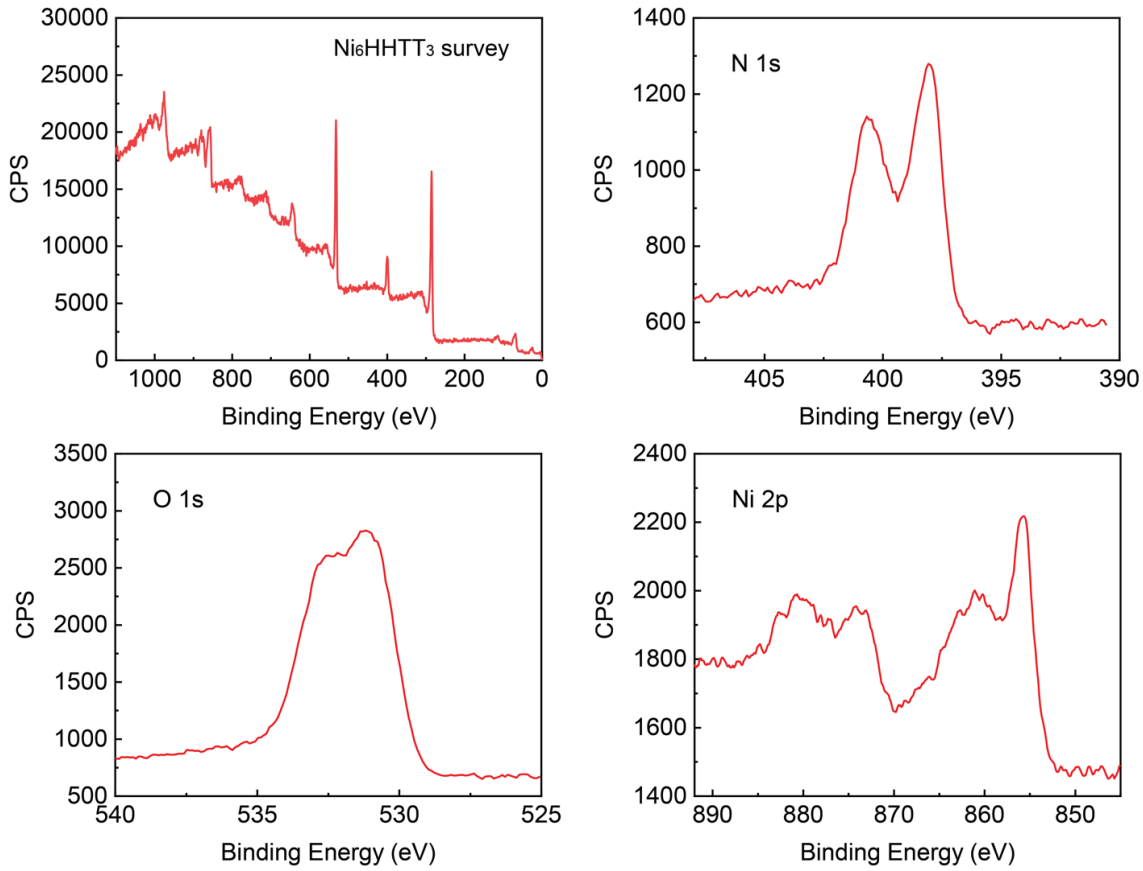

Fig. A43. XPS spectra of **Ni_6HHTT_3** survey and the corresponding N(1s), O(1s) and Ni(2p) region. Ni(2p3/2) peak has a binding energy of 856 eV, indicating the presence of Ni(II) in **Ni_6HHTT_3.**

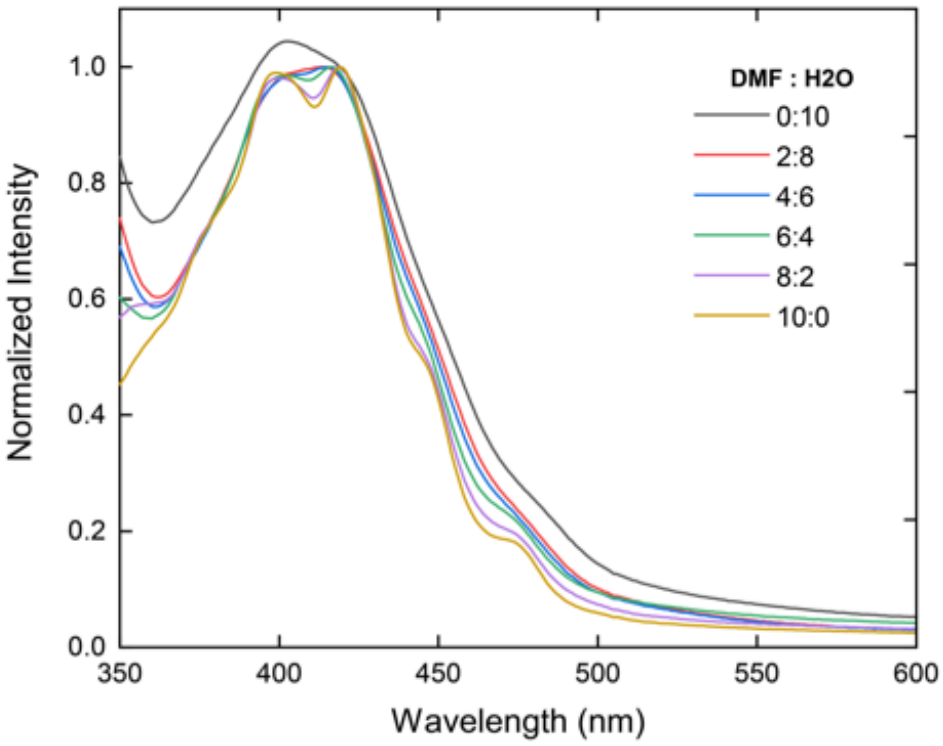

Fig. A44. Normalized absorption spectra of DMF/Water solutions (1×10^{-5} M) of **HHTT**.

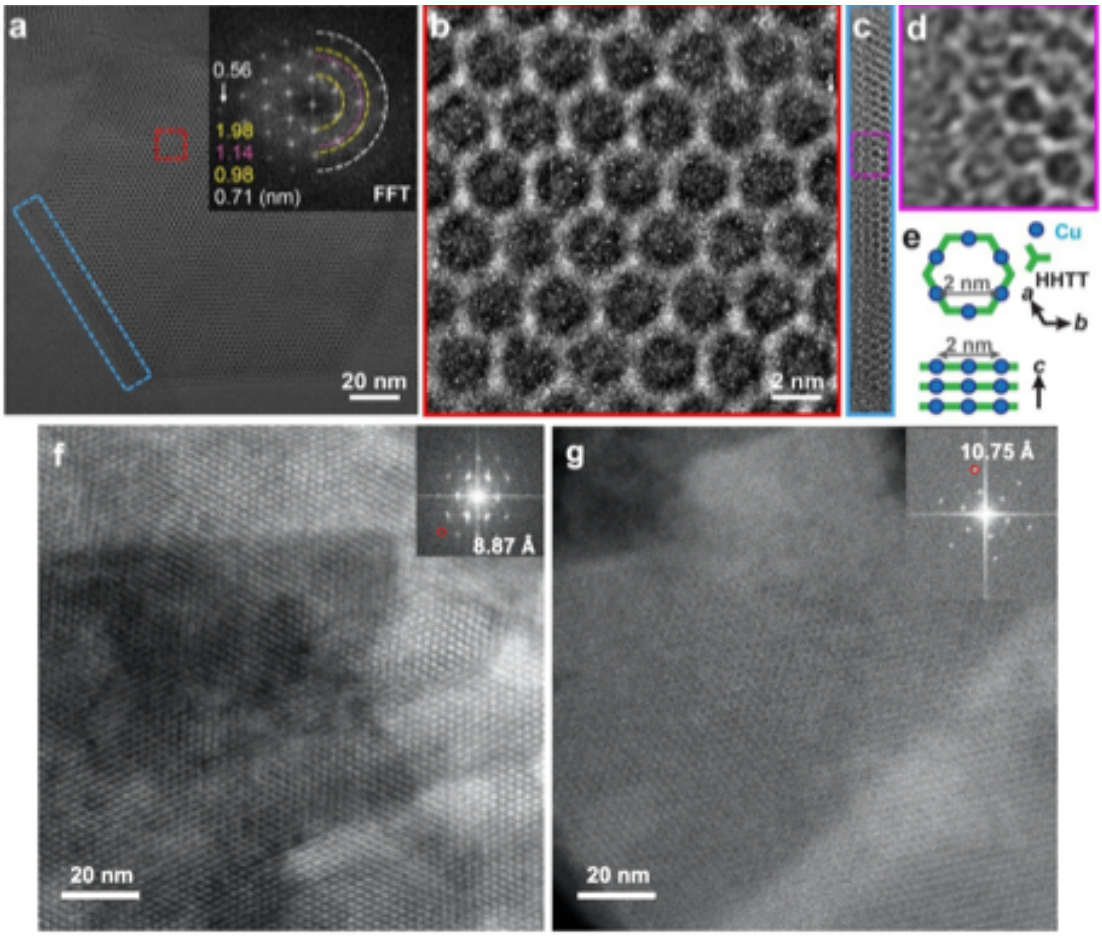

Fig. A45. (**a**) HRTEM image of a Cu_3HHTT_2 plate, with long-range lattice fringes extending across the entire crystal domain. Inset: FFT. (**b**) High-magnification HRTEM image down the *c*-direction illustrating the real-space extended 2D framework (bright contrast) and pores (dark contrast) [red box in (**a**)]. (**c**) High-magnification HRTEM image of a crystal edge [blue box in (**a**)]. (**d**) Higher magnification of part of the image in **c**, illustrating the sharp faceting of the hexagonal Cu_3HHTT_2 crystal and termination by copper ions [purple box in (**c**)]. (**e**) Schematic of Cu_3HHTT_2 structure to illustrate imaging directions. (**f**,**g**) STEM images for Cu_3HHTT_2 obtained at 80 kV with JEOL and Titan, respectively.

Discussion of electron microscopy phase contrast in Fig. A45a

The intensity of the honeycomb edge-centers (Cu/O atoms) and corners (C/N atoms) seems surprising at first glance, but is less surprising based on the meta data of the image in question (Figure A46a, b). The pixel size in Fig. A46a (and Fig. A46b) is 0.447 Å, and as a result, each pixel contains the scattering signal generated by multiple atoms, all those within a 0.223 Å radius (essentially the Cu-O bond length), shown in the figure below (red circle is c.a. 0.45 Å pixel diameter, while green circle is c.a. 0.25 Å pixel diameter required for single atom per pixel). This is critical; though we can consider the image in d/e a "lattice-resolution" image, it is not an atomic- resolution image (multiple atoms per pixel).

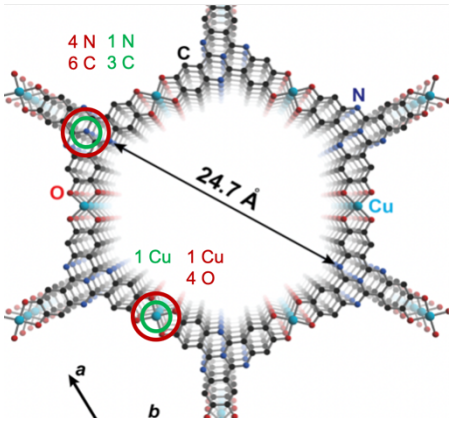

Fig. A46. Schematic representation of a single pore of Cu_3HHTT_2 single crystal.

We can approximate TEM elastic scattering probability, which is responsible for scattering intensity in TEM, using the total Rutherford elastic scattering cross section, given as[817]:

$$\sigma_{Ruther} = (5.21 \times 10^{-21})\left(\frac{Z^2}{E^2}\right)\left(\frac{4\pi}{\alpha + \alpha^2}\right)\left(\frac{E + 511}{E + 1022}\right)^2 cm^2$$

$$\alpha = (3.4 \times 10^{-3})\left(\frac{Z^{2/3}}{E}\right)$$

atom/cluster	Z	α	σ_{Ruther}
Carbon	6	4.14721E-05	2.63357E-19
Nitrogen	7	4.14721E-05	3.23449E-19
Copper	29	0.000106977	2.15201E-18
Oxygen	8	4.53333E-05	3.8648E-19
4N, 6C	64	0.000181333	6.18283E-18
1Cu, 4O	61	0.000175621	5.79949E-18
1N, 3C	25	9.68986E-05	1.76565E-18
1Cu	29	0.000106977	2.15201E-18
3N, 3C	39	0.000130337	3.1944E-18
1Cu, 1O	37	0.000125842	2.97788E-18

Note that the total Rutherford cross section does not account for the angle of scattering (included semi-angle 0˚to 180˚), which causes the size of the Objective Aperture affecting the fraction of scattered electrons blocked from reaching the TEM camera (controls pixel intensity). Despite this simplification, the total Rutherford cross section is useful to compare the respective magnitude of scattering from different pixels (contains single atoms or multi-atom clusters). Based on the structure and elemental composition of this MOF (Fig. A47), the pixel size would have to be small enough to contain on a single nucleus (pixel size < 3 Å) for pixels containing Cu atoms to generate more scattering intensity than the pixels at the honeycomb corners, which would contain only C or N atoms.

Due to the 0.447 Å pixel size (approximated by the red circles in Fig. A47), it is not unexpected that the hexagons' corners, which are composed of C/N-ring clusters (c.a. 4-Nitrogens and 6- Carbons, Z_{total} = 64) can generate higher pixel intensity than the hexagons' edge centers, which are composed of the CuO4 clusters (Z_{total} = 61). The pixel

size would have to be the size of the green circle (or smaller for the Cu atoms pixels to generate higher pixel intensity than the hexagons' edge centers.

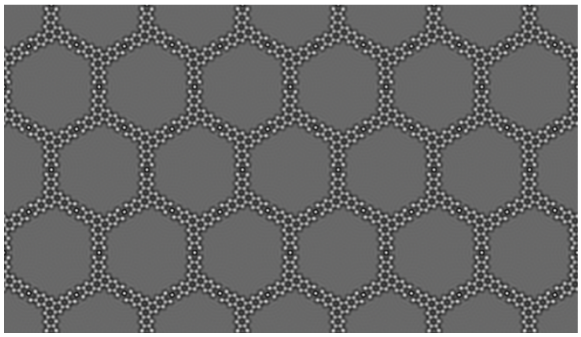

Fig. A47. HRTEM image simulation of lattice at c.a. 0.15 Å pixel size (thickness = 100 nm, defocus = 0 nm, Cs = 0 mm, Cc = 0 mm, Voltage 300KV)

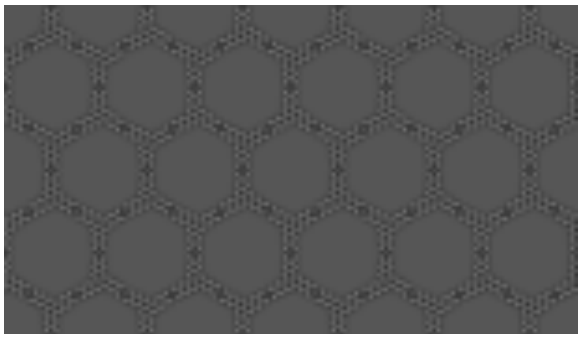

Fig. A48. Image in Fig. A47 with reduced resolution, pixel size has been increased to c.a. 0.75 Å (binned by 5 using bilinear interpolation)

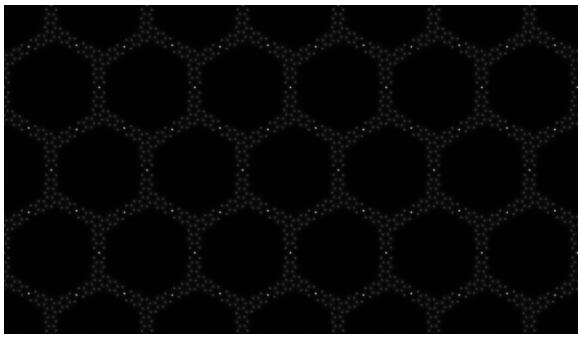

Fig. A49. HRTEM image simulation of lattice at c.a. 0.15 Å pixel size (the same simulation condition with image in Fig. A47 except defocus value. The defocus value is -100nm).

Fig. A50. Image in Fig. A49 with pixel size increased to c.a. 1.5 Å (binned by 5 using bilinear interpolation, then 1.5 Å Gaussian blur applied).

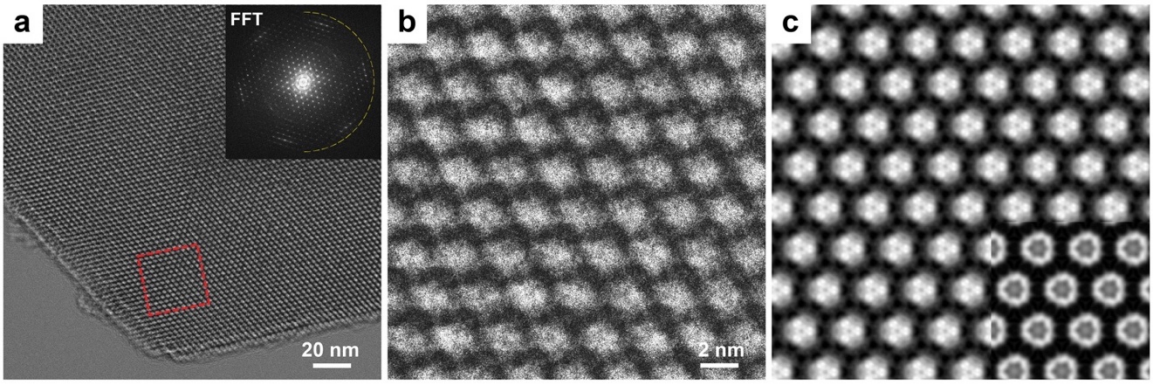

Fig. A51. (a) Cryo-EM image of **Cu_3HHTT_2** thick plates (inset: FFT). (b) High-magnification HRTEM image from a, red square. (c) Averaged experimental image processed with CRISP software[838] (inset: simulated HRTEM and structure model). Simulation conditions: voltage = 300 kV, Temperature = 80 K, sample thickness =12.8 nm, defocus = -200 nm, spherical aberration = 2.7 mm, chromatic aberration = 1.0 mm. Simulation software: QSTEM (www.qstem.org).

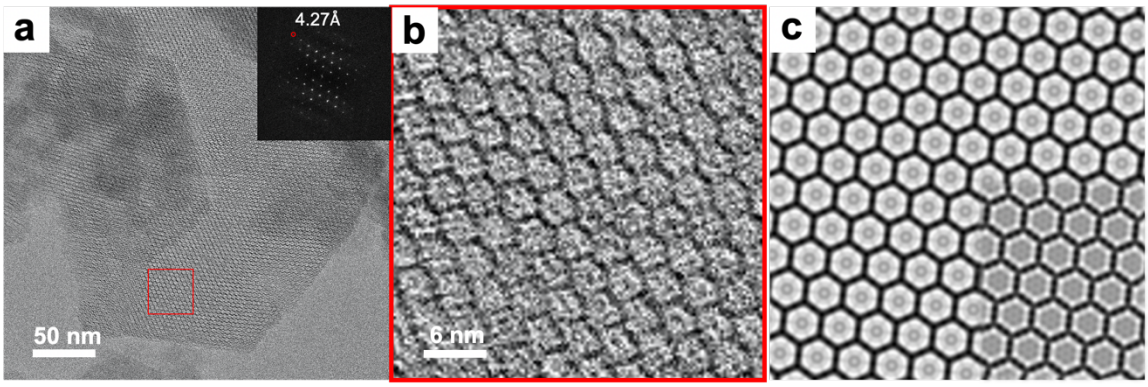

Fig. A52. (a) Cryo-EM image of $\mathbf{Cu_3HHTT_2}$ thin plates (inset: FFT). (b) High-magnification HRTEM image from a. (c) averaged experimental image processed with CRISP software[838] (inset: simulated HRTEM and structure model). Simulation conditions: voltage = 200 KV, Temperature = 80 K, sample thickness = 3.2 nm, defocus = -120 nm, spherical aberration = 2.7 mm, chromatic aberration = 1.0 mm. Simulation software: QSTEM (www.qstem.org)

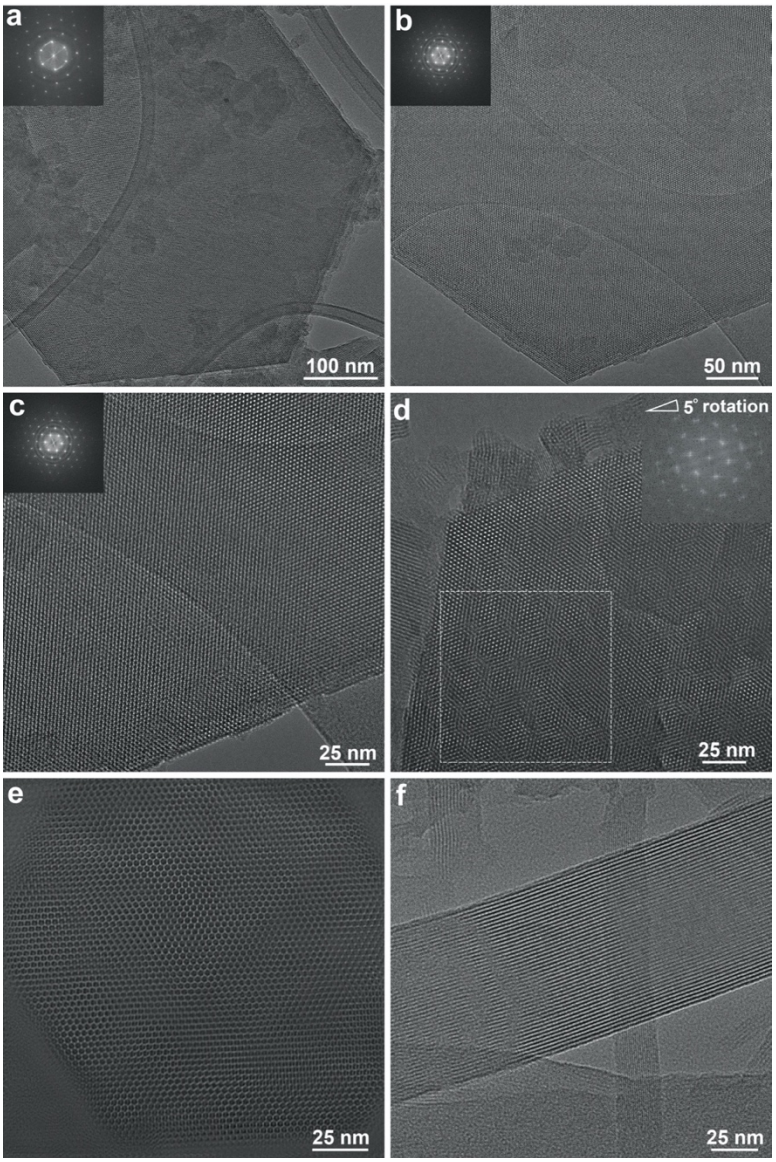

Fig. A53. HRTEM and FFT of **Cu_3HHTT_2** (a) A low magnification image and FFT of a Cu_3HHTT_2 plate around 700 nm in diameter. (b) Low and (c) high-magnification images of a Cu_3HHTT_2 plate around 400 nm in diameter; inset: FFT. (d) Moiré pattern observed from a double-layer Cu_3HHTT_2plate, the rotation angle is calculated to 5 degree from the inset FFT. (e) Fourier filtered and magnified image of Fig. A45a.(f) A low magnification image of the same Cu_3HHTT_2 rod as in Figure 2L and 2M.

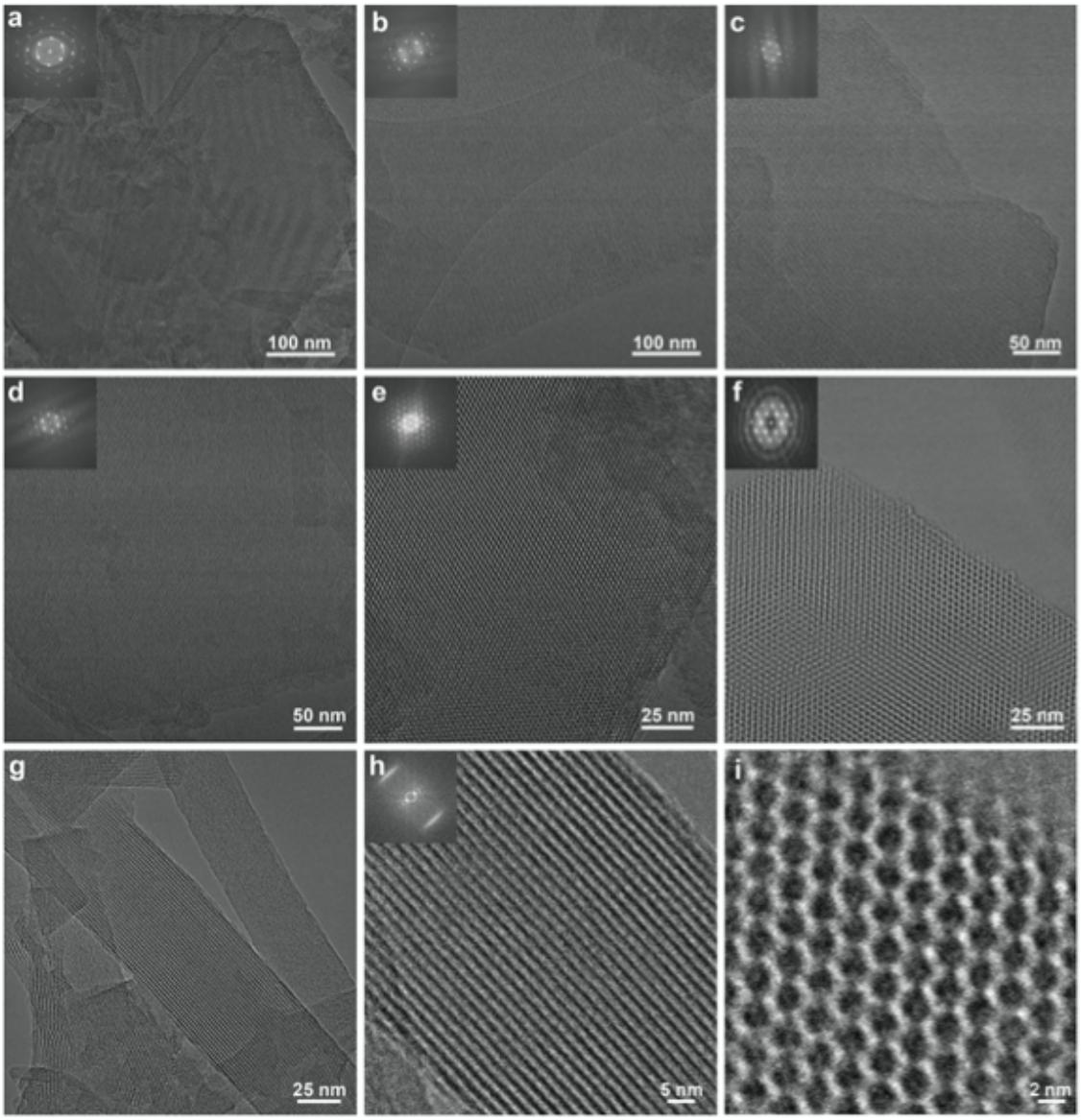

Fig. A54. HRTEM and FFT of **Ni_3HHTT_2** (a,b) Two low magnification images and FFT of the Ni_3HHTT_2 plates around 700 nm in diameter. (c,d,e,f) High magnification images and FFT of Ni_3HHTT_2 plates around 400 nm in diameter. (g) Low and (h) high-magnification images of Ni_3HHTT_2 rod, which are analogous to Cu_3HHTT_2. (i) High magnification image and FFT of Ni_3HHTT_2 plate, same sample as (f).

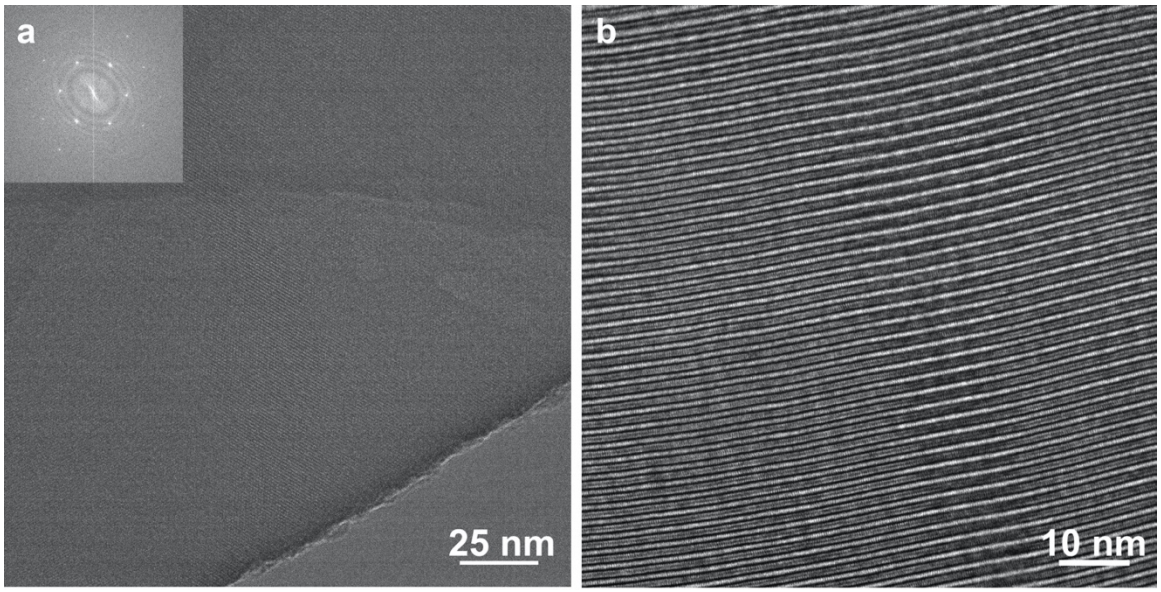

Fig. A55. HRTEM and FFT of **Co_6HHTT_3** (a) Low magnification image and FFT of the Co_6HHTT_3 plate. (b) Low magnification image of Co_6HHTT_3 rod, same sample as Fig. A2I.

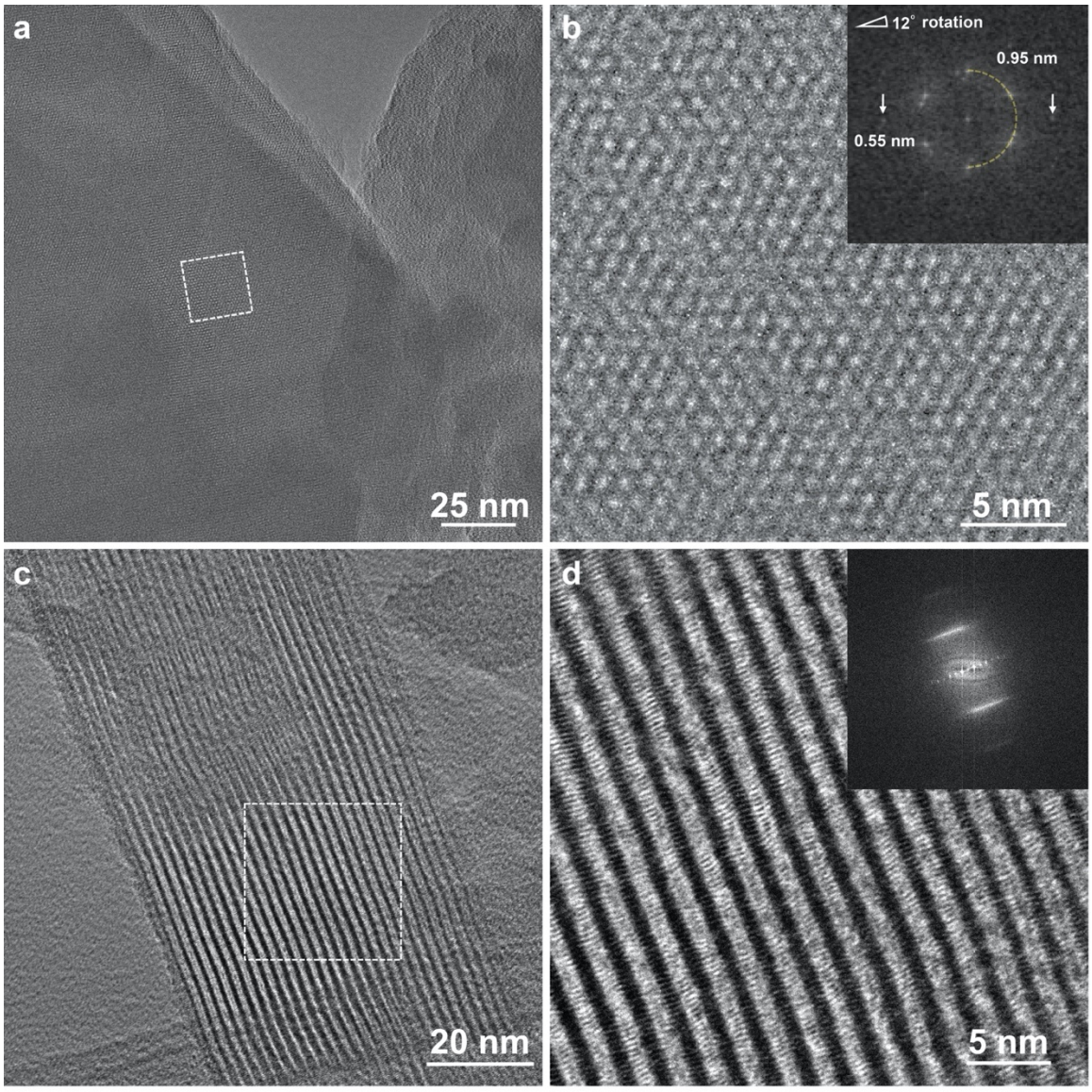

Fig. A56. HRTEM and FFT of **Mg_6HHTT_3** (a) Low magnification image of the Mg_6HHTT_3 plate. (b) High magnification image and FFT of Mg_6HHTT_3 plate, Moiré pattern observed from the Mg_6HHTT_3 plate, the rotation angle is calculated to be 12 degree from the inset FFT. (c) Low and high-magnification (d) images of Mg_6HHTT_3 rod, inset: FFT. Which are corresponding to Co_6HHTT_3

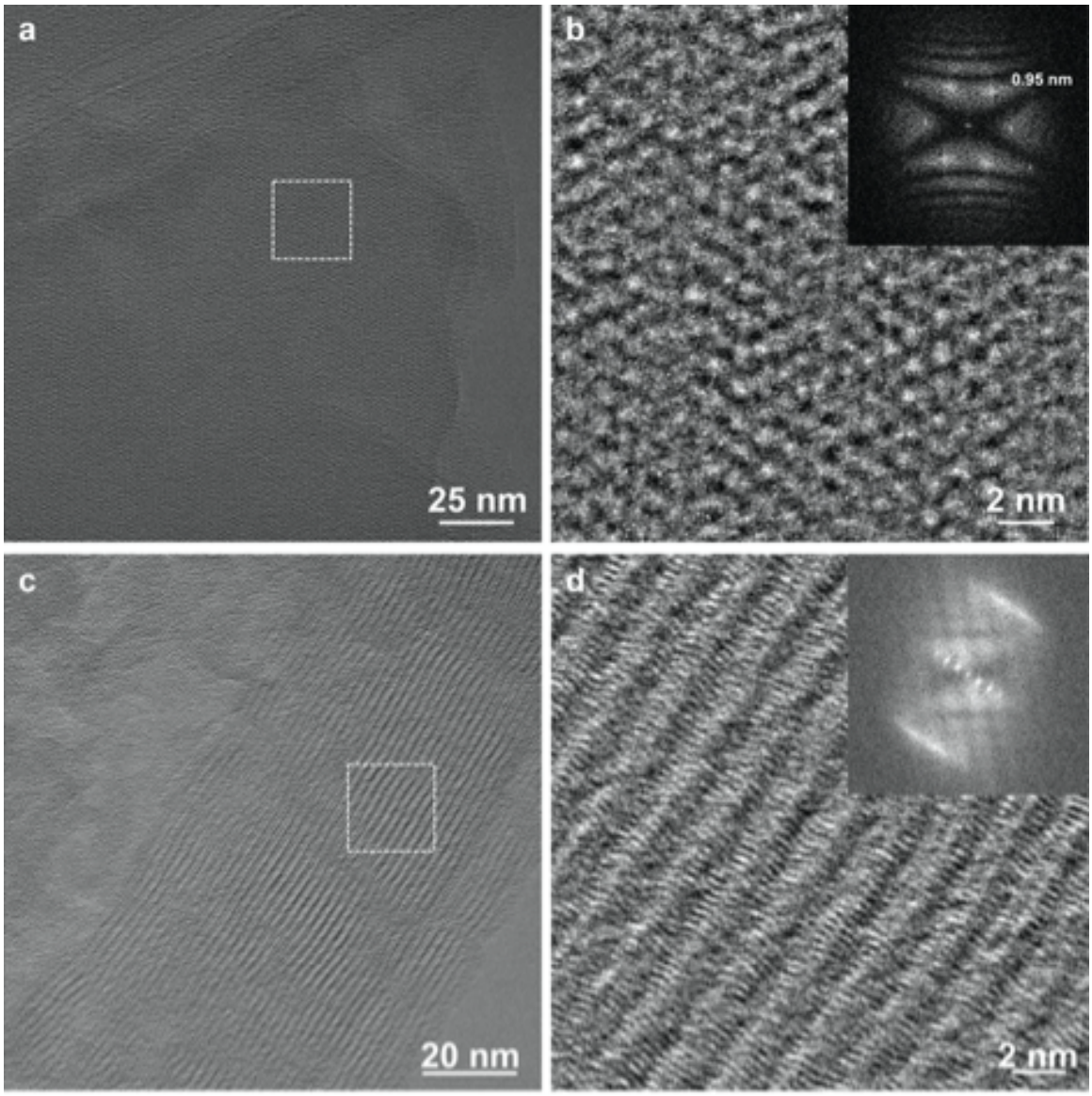

Fig. A57. HRTEM and FFT of **Ni_6HHTT_3** (a) Low magnification image of the Ni_6HHTT_3 plate. (b) High magnification image and FFT of Ni_6HHTT_3 plate. (c) Low and (d) high-magnification images of Ni_6HHTT_3 rod, which are analogous to Co_6HHTT_3 and Mg_6HHTT_3, inset: FFT.

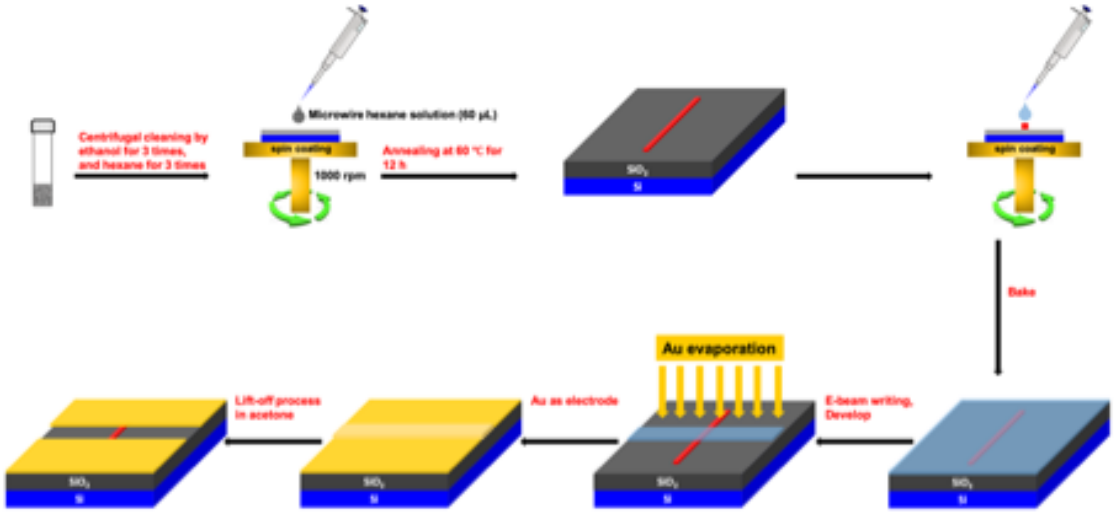

Fig. A58. Diagram of E-beam device fabrication process.

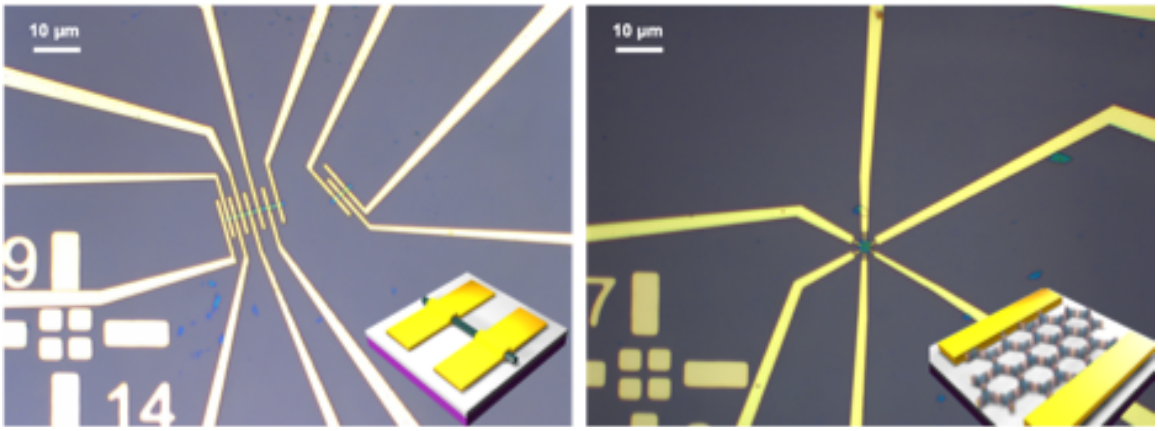

Fig. A59. Optical images of (left) multiple-probe out-of-plane and (right) in-plane multiple-probe

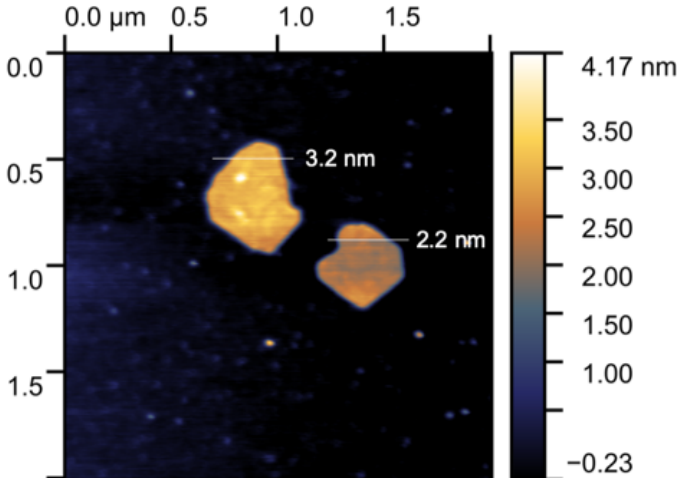

Fig. A60. 2D AFM scan and height profile from white line, **Cu_3HHTT_2**.

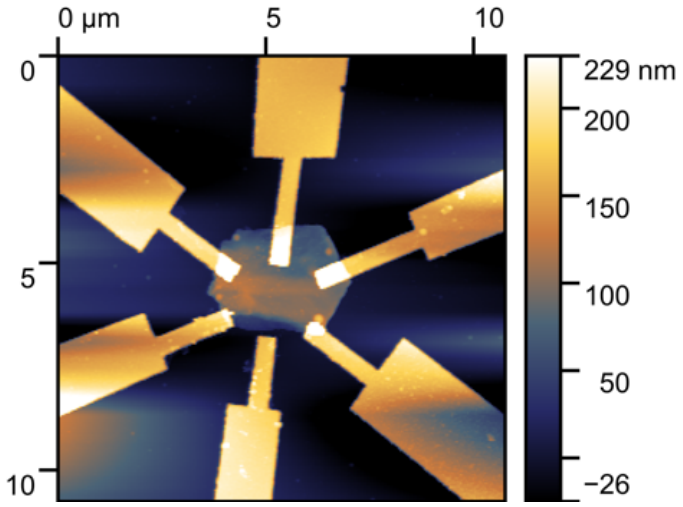

Fig. A61. 2D AFM scan of representative **Cu_3HHTT_2**E-beam device.

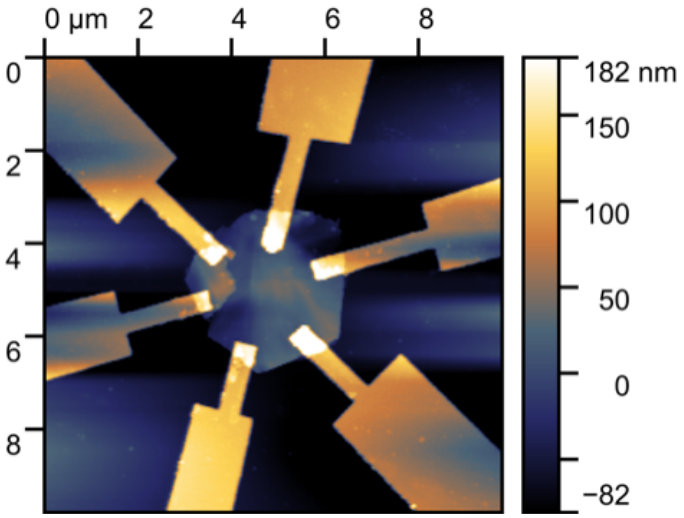

Fig. A62. 2D AFM scan of representative $\mathbf{Ni_3HHTT_2}$ E-beam device.

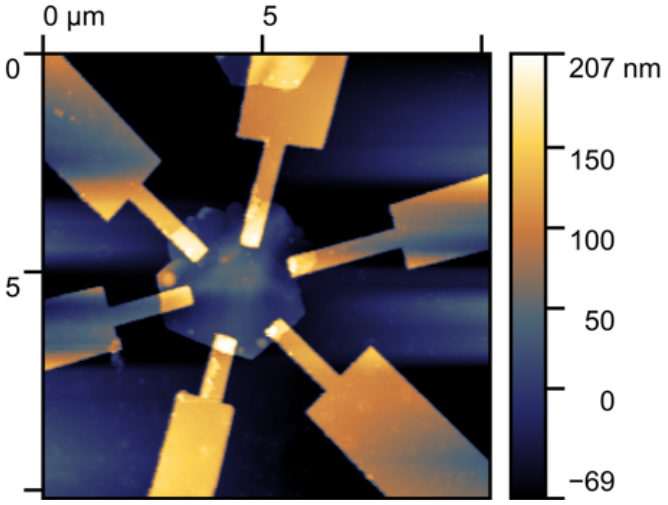

Fig. A63. 2D AFM scan of representative $\mathbf{Ni_3HHTT_2}$ E-beam device.

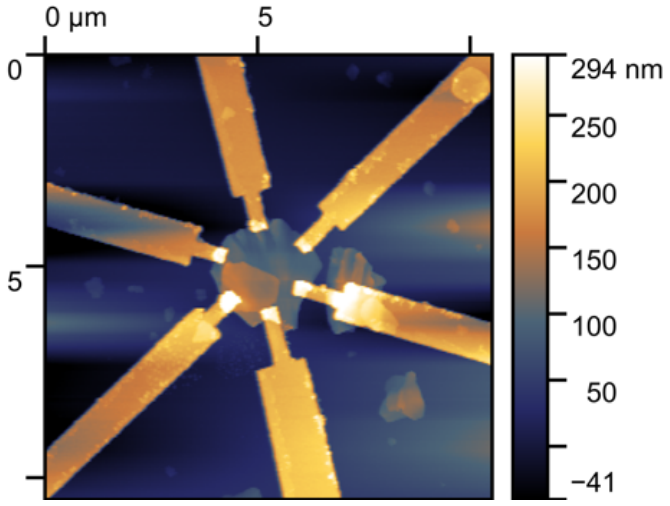

Fig. A64. 2D AFM scan of representative $\mathbf{Co_6HHTT_3}$ E-beam device.

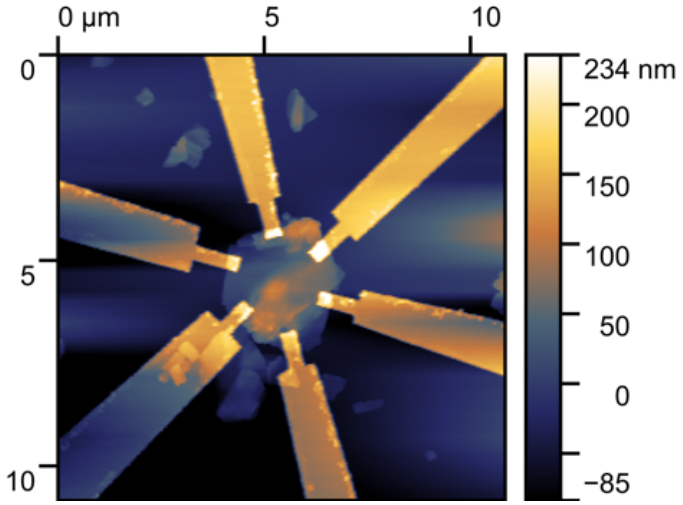

Fig. A65. 2D AFM scan of representative $\mathbf{Co_6HHTT_3}$ E-beam device.

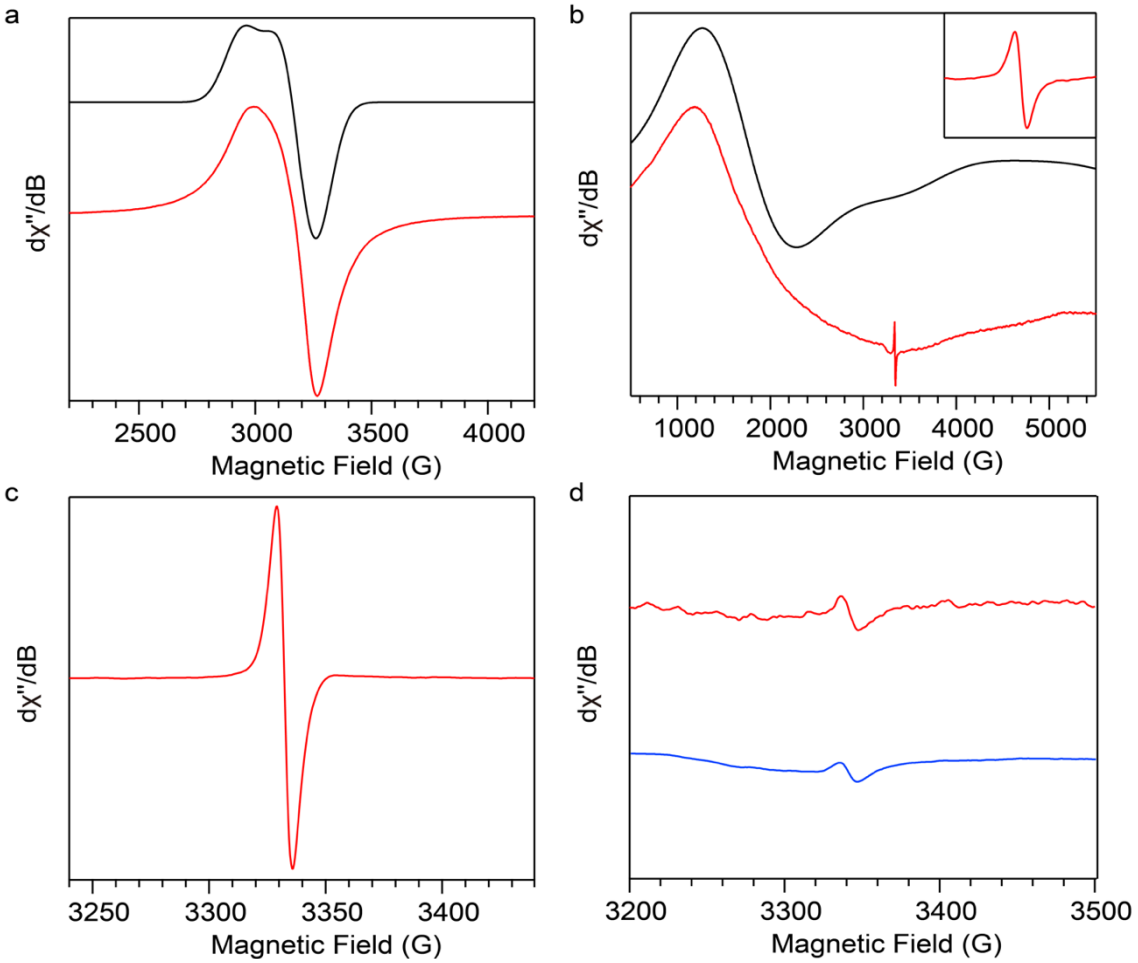

Fig. A66. X-band EPR spectra of (a) **Cu_3HHTT_2**, (b) **Co_6HHTT_3**, (c) **Mg_6HHTT_3**, (d, red) non-porous **Ni_6HHTT_3**, and (d, blue) porous **Ni_3HHTT_2** diluted in dry powder of potassium bromide measured at 20 K with microwave power of 0.05 mW. The inset of (b) is a zoom-in view of the signal of the HHTT-based organic radical centered at 3340 G. The black traces in (a) and (b) are fits for Cu_3HHTT_2 and Co_6HHTT_3, respectively, as described below.

Discussion of EPR results and peak assignments

The EPR of the HHTT-based MOFs corroborates our assignment of the metal oxidation states and the ligand charge states. For Co_6HHTT_3, a sharp signal with g = 2.00 agrees well with the typical g-value for S =1/2 organic radical, supporting our assignment of the ligand to be $HHTT^{3-}$ in Co_6HHTT_3. The broad features centered around 1189 G and 3340 G can be attributed to the S = 3/2 spins of the high-spin Co^{2+} center, proven by the reasonable match between the experimental signal and the simulated spectrum with $g_{\parallel}$ = 1.90, $g_{\perp}$= 2.20, and D = +0.5 cm^{-1}, values typical for high-spin Co^{2+}. This supports our assignment of the cobalt centers to be Co^{2+} in Co_6HHTT_3. Although the data interpretation is limited by significant line broadening, the tentative simulation suggests weak ligand-field anisotropy at the cobalt center, expected for a Co^{2+} with hexacoordinated oxygen-based ligand environments. For Cu_3HHTT_2, the broad signal in the range of 2500 – 4000 G agrees well with the signal expected for a Cu^{2+}-based S = 1/2 spin, as shown by the close match between the experimental trace and the simulated spectrum with $g_{\parallel}$ = 2.08, $g_{\perp}$= 2.28. Although no hyperfine coupling to Cu^{2+} can be observed due to line broadening, the g-values lie in typical range for Cu^{2+}, supporting our assignment of the coppers to be Cu^{2+} in Cu_3HHTT_2. Unlike Co_6HHTT_3, no signal related to HHTT-based organic radical can be seen, likely due to its weak intensity relative to the Cu^{2+}-based signal. For Mg_6HHTT_3, a sharp signal with g = 2.00 agrees well with the typical signal for organic radical with S = 1/2, which supports our assignment of the HHTT to have -3 charge state in Mg_6HHTT_3. The absence of any other signals in the spectrum of Mg_6HHTT_3 agrees with the close-shell nature of Mg^{2+}. Finally, the EPR signals of the non-porous Ni_6HHTT_3 and the porous

Ni_3HHTT_2 both display signals at g = 2.00. For both phases, such signal typical for organic radical support our assignment of the ligand to be $HHTT^{3-}$. The absence of any other signal agrees with the nickel centers being octahedral or square-planar Ni^{2+} (S = 1 or 0, respectively), which is commonly EPR-silent in X-band measurements.

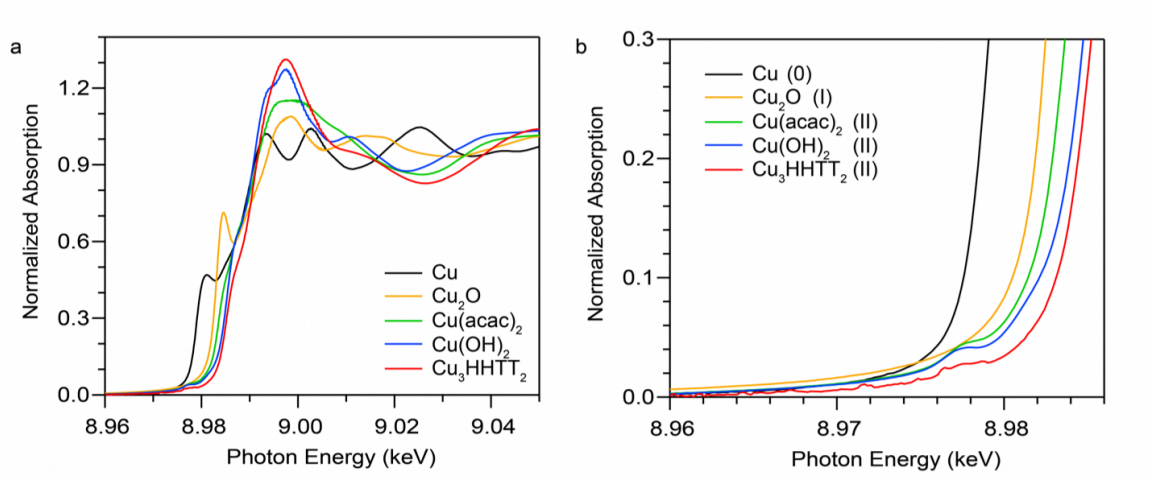

Fig. A67. (a) The X-ray absorption spectra for Cu (black), Cu2O (orange), Cu(acac)2 (green), Cu(OH)2 (blue), and **Cu_3HHTT_2** (red) at the Cu K edge (8.979 keV), with enlarged pre-edge region depicted in (b).

The XAS of Cu_3HHTT_2 corroborates our assignment of the oxidation state and ligand environment of the copper centers by comparison with known copper standards of Cu, Cu_2O, $Cu(OH)_2$, and $Cu(acac)_2$ (Fig. A50a). The pre-edge energy of $Cu_3HHTT_2$of 8.9776 keV matches well with the value for $Cu(OH)_2$ (8.9775 keV) and $Cu(acac)_2$ (8.9776 keV), supporting our assignment of the copper centers in Cu_3HHTT_2 to be Cu^{2+} (Fig. A51b).

The close match between the pre-edge features and XANES of Cu_3HHTT_2, $Cu(OH)_2$, and $Cu(acac)_2$ again shows the similarity in the ligand-field environment of the Cu^{2+} centers in the three materials, all based on weak-field anionic oxygenic ligands in a square-planar ligand field.

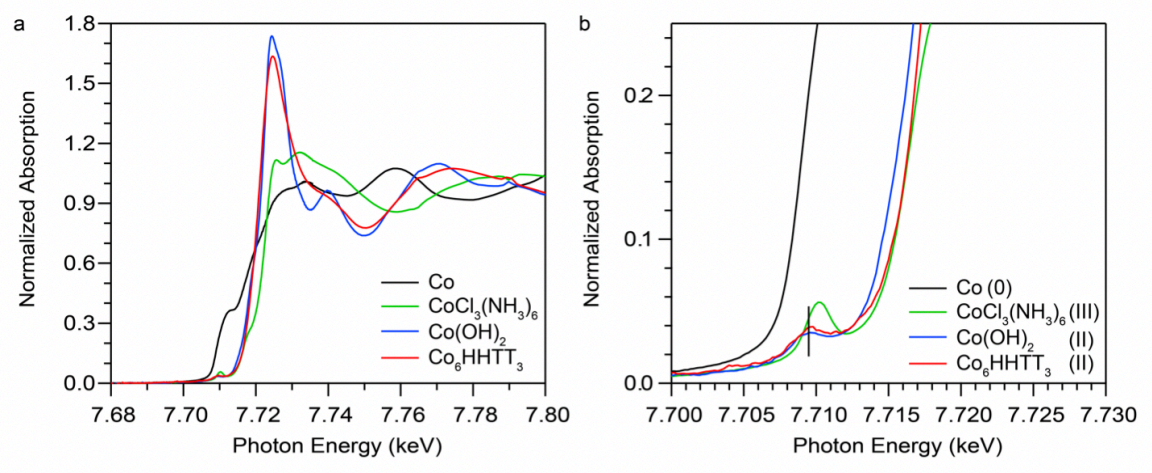

Fig. A68. (a) XAS for Co foil (black), $CoCl_3(NH_3)_6$ (green), $Co(OH)_2$ (blue), and **Co_6HHTT_3** (red) at the Co K edge (7.709 keV), with enlarged pre-edge region depicted in (b). The black solid line in (b) marks the pre-edge position of **Co_6HHTT3**.

The XAS of Co_6HHTT_3 corroborates our assignment of the oxidation state and ligand environment of the cobalt centers by comparison with known cobalt standards of Co foil, $Co(OH)_2$, and $CoCl_3(NH_3)_6$ (Fig. A48a). The XANES pre-edge position of Co_6HHTT_3 is measured to be 7.7093 keV. This value matches best with the value for the Co^{2+} standard

$Co(OH)_2$ (7.7093 keV), while deviating from the values of the compounds containing Co^0 (Co foil, none) and Co^{3+} ($CoCl_3(NH_3)_6$, 7.7104 keV) (Fig. A48b). This supports out assignment of the cobalt centers to be Co^{2+} in Co_6HHTT_3. The close similarity between the Co_6HHTT_3 and $Co(OH)_2$ pre-edge as well as XANES region can also be understood based on the similarity in the ligand-field environment of the Co^{2+} centers in the two materials, both with weak-field oxo- and/or hydroxyl-ligands and pseudo- octahedral symmetry.

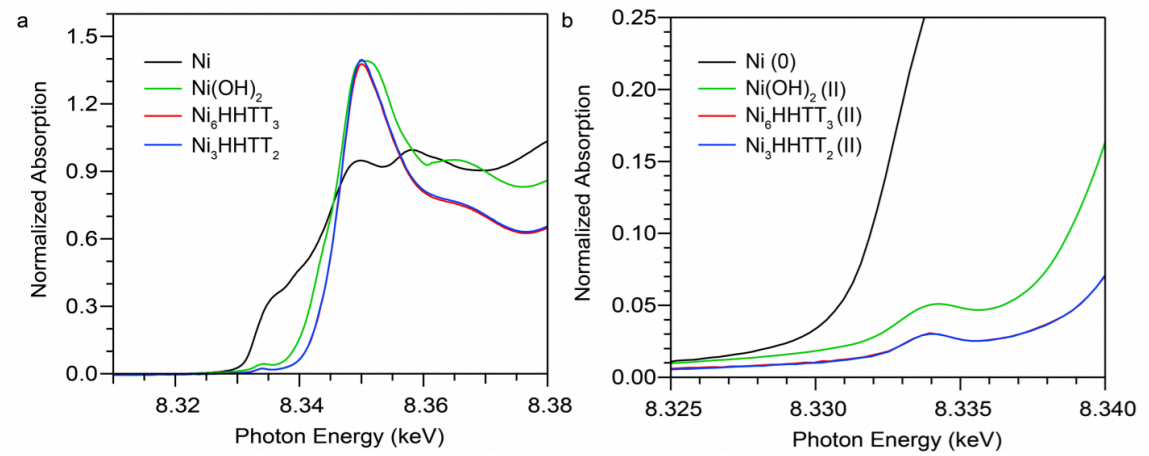

Fig. A69. (a) The X-ray absorption spectra for Ni (black), $Ni(OH)_2$ (green), dense **Ni_6HHTT_3** (green), and porous **Ni_3HHTT_2** (red) at the Ni K edge (8.333 keV), with enlarged pre-edge region for the four compounds depicted in (b).

The XAS of Ni_6HHTT_3 and Ni_3HHTT_2 corroborates our assignment of the oxidation state and ligand environment of the nickel centers by comparison with known nickel standards of Ni and $Ni(OH)_2$ (Fig. A49a). The XANES pre-edge position for Ni_6HHTT_3 and Ni_3HHTT_2 (both at 8.3340 keV) are close to the value observed for the Ni^{2+} standard $Ni(OH)_2$, agreeing with our assignment of the nickel centers to be Ni^{2+} in both Ni-HHTT MOFs (Fig. A49b). Moreover, the XANES regions for both phases are nearly identical and similar to that of $Ni(OH)_2$, as expected due to the similar oxo-/hydroxyl-based octahedral ligand-field environment of Ni^{2+} centers in the three materials.

APPENDIX B

EXPERIMENTAL DETAILS AND SUPPLEMENTARY INFORMATION FROM:

Switchable Electrical Conductivity in a Three-Dimensional Metal-Organic Framework via Reversible Ligand *n*-doping (*Chemical Science*, **2020**, *11*, 1342-1346.)

Hanna C. Wentz, Grigorii Skorupskii, Ana B. Bonfim, **Jenna L. Mancuso**, Christopher H. Hendon, Evan H. Oriel, Graham T. Sazama, and Michael G. Campbell

Experimental Details Omitted from Manuscript

ZnNDI was synthesized according to the reported procedure as a microcrystalline tan/yellow powder; PXRD analysis confirmed the expected structure (**Figure 30b**).[733] Time-lapse UV-vis data shows a rapid initial reaction followed by a slower reduction process over several hours (Fig. A4). After approximately 14 hours no further spectroscopic changes are observed. This is likely due to initial reduction of surface-exposed NDI ligands, followed by slower reduction of ligands throughout the framework, limited by diffusion of charge-balancing TBA^+ cations into the pores;[377] consistent with this interpretation, the mesoporous MOF-74 analogue Ni-NDISA (33 Å pore diameter,

compared to 16 Å for ZnNDI) undergoes complete reaction with TBAF in minutes rather than hours.[379] In contrast to data reported for NDI-based small molecules in solution,[378] we do not observe further reduction to the NDI^{2-} dianion form in ZnNDI upon longer soaking times or with increased amounts of fluoride, even though the ligand dianion is electrochemically accessible.[375]

In order to qualitatively evaluate the effect of soaking time on ligand reduction, we performed UV-vis measurements using thin films of ZnNDI grown on the surface of glass slides (**Figure 31**). The pale films of as-synthesized ZnNDI display absorption maxima at 360 and 380 nm, assigned to $\pi \rightarrow \pi^*$ transitions in the neutral NDI ligands. Upon placing the film into a TBAF solution the color gradually darkens, accompanied by a decrease in intensity for the neutral NDI features and the appearance of new features throughout the visible region (λ_{max} = 471, 607, 701, 784 nm). The spectral features for the reduced MOF persist after removal from the TBAF solution if kept under an inert atmosphere, but rapidly decrease in intensity upon exposure to air (App. B Fig. A5). The spectrum of neutral ZnNDI is recovered after brief soaking in DMF that has not been deoxygenated (App. B Fig. A6). Reduced ZnNDI is stable for at least 1 month after isolation if kept under an inert atmosphere.

To examine the effect of ligand reduction on conductivity, bulk samples were soaked in DMF solutions of TBAF for 24 hours. Different degrees of ligand reduction were achieved by soaking with varying amounts of fluoride (designated samples A–C; details below). After isolation by filtration, washing with fresh DMF and Et_2O, and vacuum

drying, the reduced samples were characterized by PXRD to ensure that no structural changes or degradation occurred (**Figure 30b**). Scanning electron microscopy also showed no significant changes in morphology after reduction (Fig. A7 and A8).

The extent of ligand reduction in ZnNDI was evaluated using quantitative EPR, with samples prepared as a 5% w/w mixture in an eicosane matrix. Quantitation of spins in this manner led to values of 7.5×10^{17} spins per mg for ZnNDI-A, 5.0×10^{17} spins per mg for ZnNDI-B, and 2.0×10^{17} spins per mg for ZnNDI-C. Calculating based on the general formula $[(TBA)_x(ZnNDI)]$, where one TBA^+ cation is incorporated per NDI ligand reduced to its radical anion form, the EPR data indicates the extent of ligand reduction to be approximately 90%, 50%, and 20% for samples A, B, and C, respectively (details of EPR data collection and analysis are given below). The ability of NDI-based MOFs to accommodate high degrees of ligand reduction while maintaining structural stability is also supported by previous studies on electrochemical reduction.[375–377]

Room temperature conductivity values (pressed-pellet, 2-probe) for the reduced samples were measured, as shown in **Figure A**. Pellets of ZnNDI-A, with 90% of its ligands reduced to their radical anion form, displayed an average conductivity value of 2×10^{-7} S cm^{-1}, with a maximum observed value of 6×10^{-7} S cm^{-1}. All measured samples of ZnNDI-A displayed conductivity values at least 10^6 higher than the neutral material. Samples ZnNDI-B and ZnNDI-C, with lower degrees of ligand reduction, displayed average values of 1×10^{-9} and 3×10^{-10} S cm^{-1}, respectively, demonstrating that the doping level can be systematically varied in order to tune the conductivity of the material.

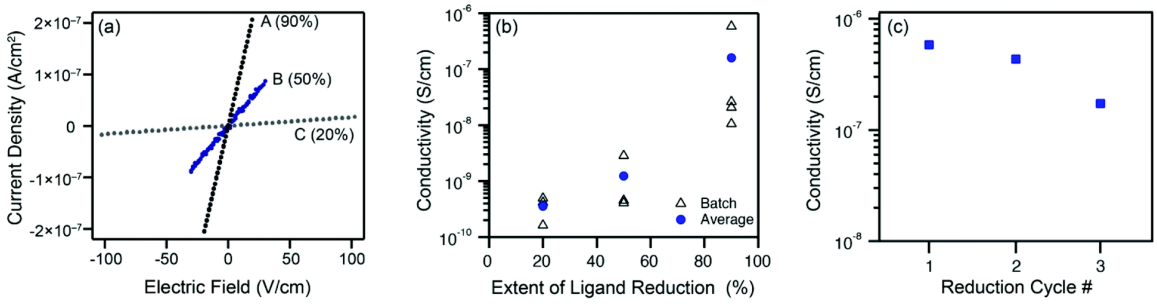

Figure A. Pressed-pellet conductivity measurements (2-probe, room temperature) on samples of ZnNDI after varying degrees of ligand reduction: (a) representative *I*–*V* curves, normalized for pellet size (extent of ligand reduction indicated in parenthesis); (b) conductivity values taken from multiple synthetic batches, showing systematic variations in conductivity as a function of ligand reduction; (c) conductivity of a single sample of ZnNDI-A that was subjected to three cycles of ligand reduction followed by aerobic re-oxidation. The neutral, as-synthesized MOF displays conductivity $\leq 10^{-14}$ S cm^{-1}.

Materials and Methods

General. All manipulations were carried out under an inert atmosphere of nitrogen or argon unless otherwise noted. Anhydrous solvents were obtained by filtration through drying columns[839] on an mBraun system, except for *N*,*N*-dimethylformamide which was purchased from Sigma-Aldrich (anhydrous, 99.8%) and sparged with argon prior to use. Bulk powders and thin films of the MOF ZnNDI were synthesized according to the literature procedures.[733] Tetra-*n*-butylammoniumfluoride(TBAF;1.0MinTHF)was purchased from Sigma-Aldrich.

Spectroscopy. UV-vis spectra were measured on a Varian Cary 5000 spectrophotometer, with MOF thin films on glass slides placed in DMF solutions in quartz cuvettes. EPR spectra were measured on a Bruker EMX spectrometer.

Powder X-ray Diffraction. PXRD data were recorded on a PANalytical XPert3 diffractometer with a Cu Ka X-ray source and PIXcel 1d detector, in a Bragg-Brentano geometry.

Scanning Electron Microscopy. ZnNDI powders were spread on a conductive carbon tape and then coated by a Au-Pd (1:1 mixture) layer by Cressington 108 sputter coater for 20 seconds (few nanometers of conductive Au/Pd layer). SEM imaging was performed using a Zeiss Sigma VP operating at 15 kV. To better understand the topological structure of the samples, secondary electron (SE) detector was used with positive 300 volts applied to its Faraday cage to enhance the signal-to-noise ratio. The working distance was kept around 5.2 mm and remained consistent through the imaging of particles at different locations.

Experimental Procedures

Details of Fluoride Soaking Procedure. In a nitrogen-filled glovebox, three 25 mg portions of ZnNDI were dispensed into separate 20 mL vials, then 7 mL DMF was added to each along with a magnetic stir bar. To vial **A** was added 200 μmol of TBAF (200 μL of a 1.0 M TBAF solution in THF), to vial **B** was added 50 μmol TBAF, and to vial **C** was added 25 μmol TBAF. The vials were capped and the suspensions were stirred gently (200 rpm) at room temperature. After 24 hours, each suspension was filtered and the recovered

black solids were washed with fresh DMF followed by Et2O, then dried under vacuum. Samples **A-C** prepared in this manner were stored under nitrogen as dry powders prior to further measurement.

Electrical Conductivity Measurements. Conductivity measurements were performed under a dry N_2 atmosphere at 302 K in an MBRAUN MB-200B glovebox using a home-made two-contact probe pressed pellet setup.[387,840] Dried bulk powder samples of MOF were loaded into dry glass tubes and pressed between two stainless steel rods, which also served as current collectors. The cell was then moved inside a hydraulic press, which was hand-tightened fast. Linear I-V curves were then obtained using a Keithley 2450 sourcemeter connected to the cell with test leads. The applied voltage was varied depending on the resistance of the pellet, but was generally within −1 to +1 V, except for the least conductive samples where voltage limits were raised to ±5-10 V. Following the initial measurement, the cell was allowed to stand for 15 minutes, and retightened by hand. I-V curves were then recollected, and this process was repeated several times until the change in resistance between measurements was minimal. Pellet thicknesses were obtained with a Mitutoyo micrometer after the electrical measurements, using the arithmetic mean of five measurements for each pellet. To test the as-synthesized material, a Keithley 6517B high resistance electrometer was used, and voltages up to ±50 V were applied without any measurable current response above background noise level.

EPR Data Collection and Analysis

Samples were prepared in a nitrogen-filled glove box by mixing powdered eicosane with the MOF sample to be measured in known w/w mixtures. Powdered samples were put into precision-bore 4 mm OD quartz EPR tubes, and sample height was measured in order to determine total sample volume. Samples were large enough to fill the entire resonator for all measurements. All measurements were performed at room temperature.

A 2D Field-Power experiment was used to create a power curve for Sample A (Figure S1), which was used to determine a non-saturating microwave power. A microwave power of 0.2996 mW was chosen for all quantitation scans, well within the linear regime of the power curve.

Extrapolation of the linewidth vs. power curve to zero-power shows a minimum linewidth of 7.383 G, largely due to inhomogenous broadening (b = 1.47).

An eicosane blank showed no background, and all samples had a Q value of 4800 in the resonator. Scans were 236 G wide, providing ample baseline for accurate integration. Single integration was performed on each spectrum before baseline correction to provide better correction before double integration for quantitative values. A modulation amplitude of 0.40 G at 100 kHz was also used for all spectra. Spin quantitation of the samples was performed by double integration of the spectrum, and calculation of absolute spins according the equation:

$$n_s = \frac{DI}{\frac{c}{f(B_1, B_m)} \times \{G_R \times C_t \times n\} \times \{\sqrt{P} \times B_m \times Q \times n_B \times S \times (S+1)\}}$$

Where *c* is the point sample calibration factor (provided by resonator manufacturer); *B1* is the microwave magnetic field; B_m is the modulation amplitude; *f*(*B1,Bm*) is the spatial distribution of *B1* and B_m (also provided by resonator manufacturer); G_R is the receiver gain, C_t is the conversion time; *n* is the number of scans; *P* is microwave power; *Q* is the quality factor of the resonator; n_B is the Boltzmann temperature correction; *S* is electronic spin; and n_S is the absolute number of spins. Using the calculated spins/mm^3, the sample w/w, and the sample volume and mass, the total number of spins/mg MOF were calculated. The extent of ligand reduction was then calculated based on the general formula [(TBA)*x*(ZnNDI)], in which one charge-balancing TBA^+ cation is required for each NDI ligand in the MOF that has been reduced to its radical anion form.

Supplemental Data Figures

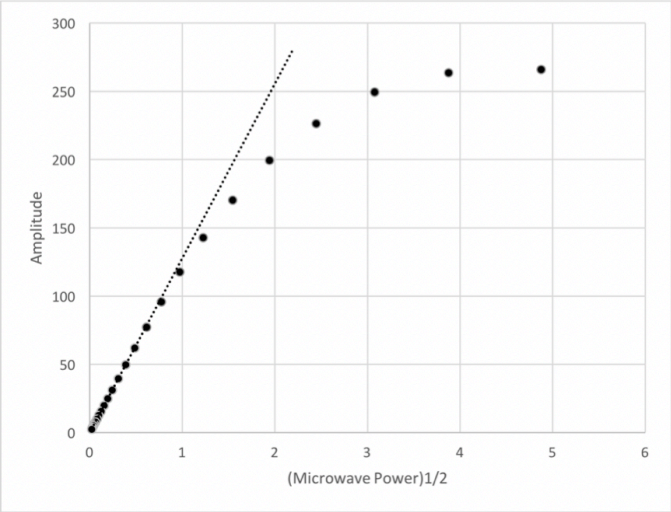

Figure A1. Microwave power curve measured for sample A

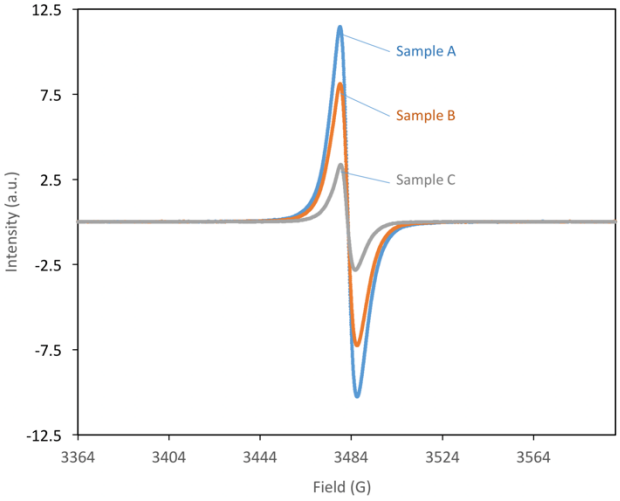

Figure A2. Isotropic EPR spectra of doped samples A–C.

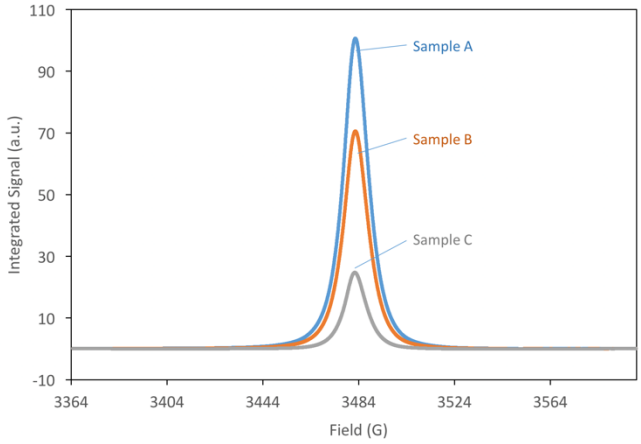

Figure A3. Singly integrated EPR spectra of doped samples A–C.

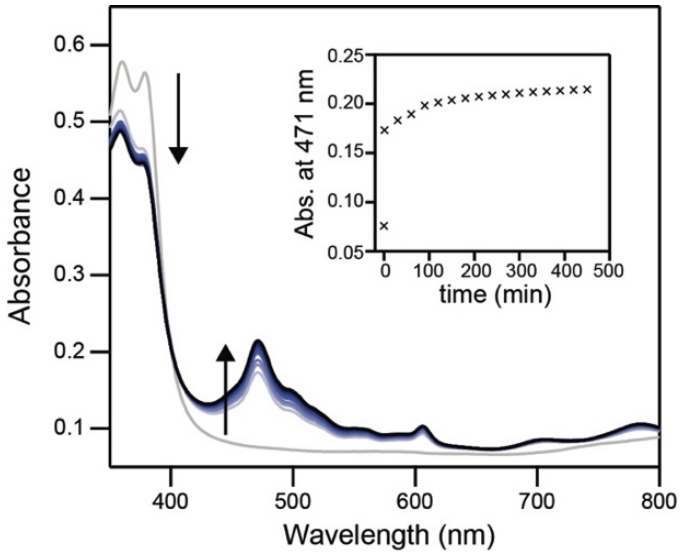

Figure A4. Time-lapsed UV-vis spectra of a ZnNDI thin film exposed to fluoride (60 nM TBAF in DMF), showing a fast initial reduction followed by gradual continued reduction over the course of several hours.

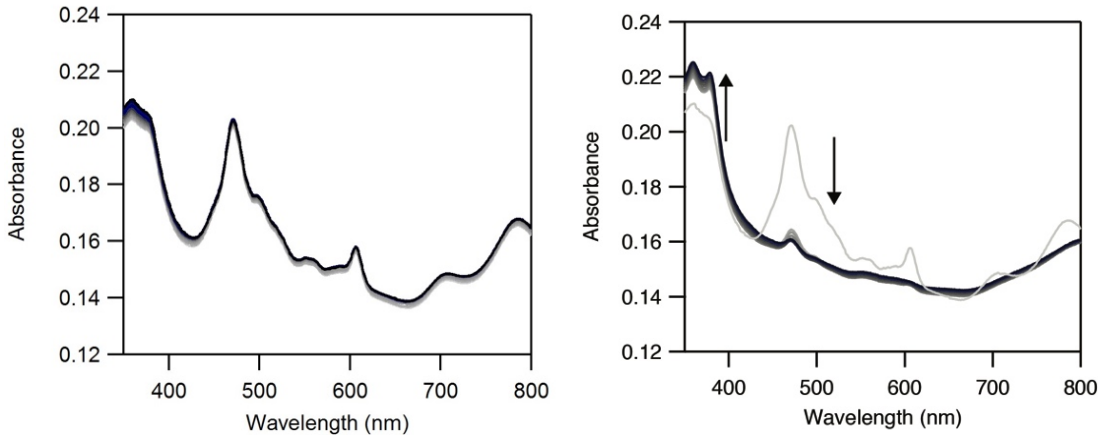

Figure A5. *(left)* Time-lapsed UV-vis spectra (3 hours) after removal of a ZnNDI thin film from a TBAF/DMF solution, in a sealed cuvette under N2. *(right)* Time-lapsed spectra (10 min) after opening the cuvette to air.

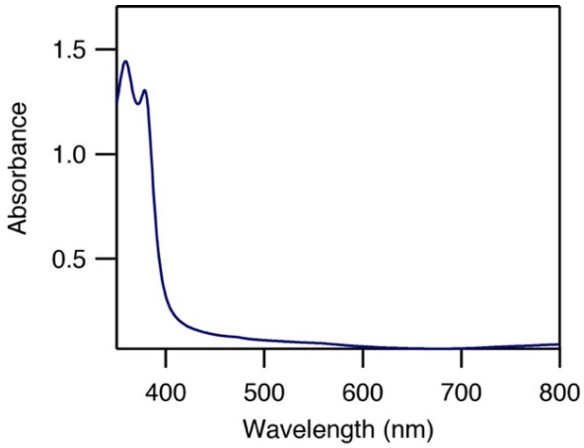

Figure A6. UV-vis spectrum of a ZnNDI thin film after reduction followed by soaking in aerated DMF, displaying an identical spectrum to the as-synthesized neutral material.

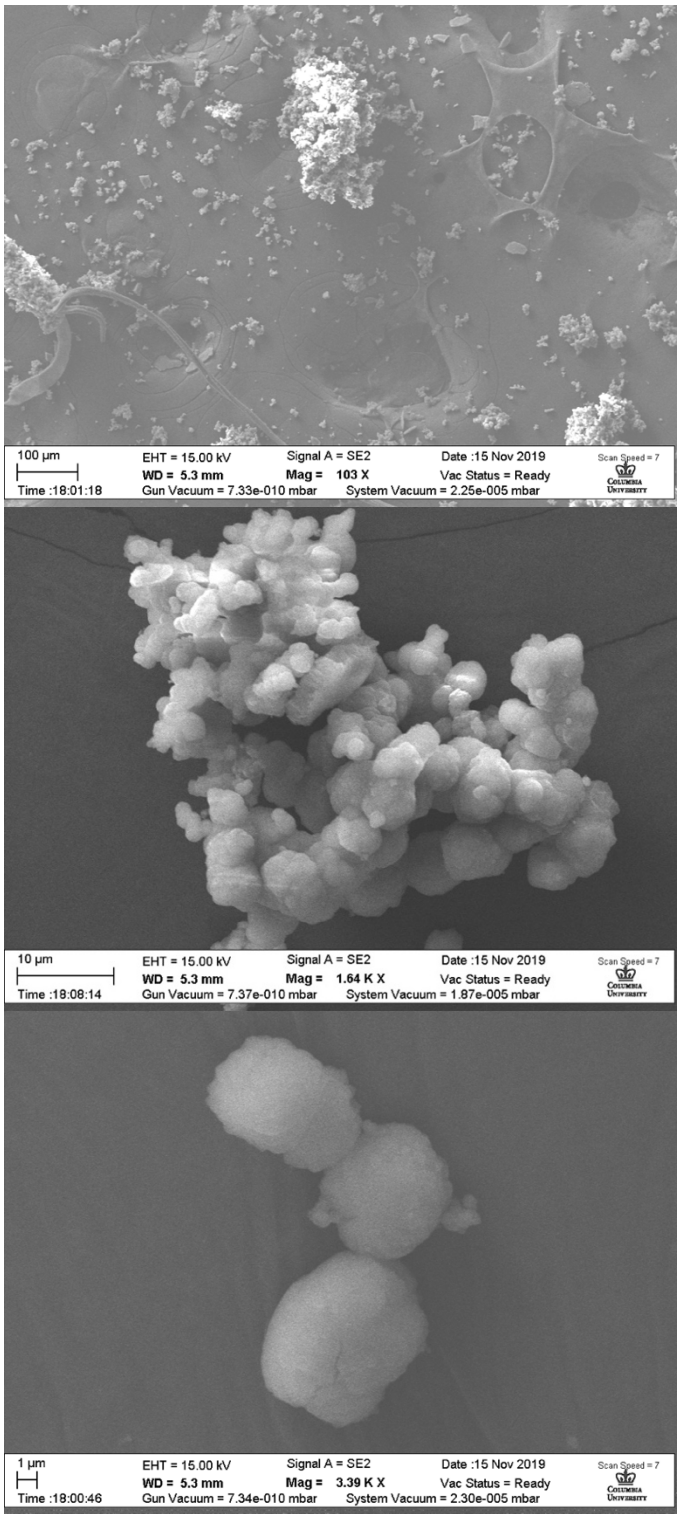

Figure A7. SEM images at different magnification levels for as-synthesized ZnNDI.

APPENDIX C

EXPERIMENTAL DETAILS AND SUPPLEMENTARY INFORMATION FROM:

On the thermodynamic limit of proton-coupled electronic doping in a Ti(IV)-containing MOF

Jenna L. Mancuso, Kevin Fabrizio, Carl K. Brozek, Christopher H. Hendon

Experimental Discussion Omitted from Main Text

Quantification by ^{1}H NMR of unreacted alcohol at each time point relative to the amount of aldehyde generated provides indirect measure of H_2 evolution and other side-reactions. After 20 minutes of irradiation in the presence of stoichiometric quantities of benzylic alcohol, an average of 2% of the clusters in MIL-125 accumulated one-electron, one-proton. Importantly, stoichiometric conversion of each alcohol to the corresponding aldehydes was observed. In a separate experiment, excess alcohol and a 2-h irradiation led to just 6% of the clusters storing an average of one electron, whereas irradiation for 18 h led to reduction of 20% of the clusters, with Ti^{III} per cluster, on average. All materials retained the white-to-black color charge after irradiation, supporting the computational insights that e^{-}/H^{+} pairs remain stable towards HER in the low-charge regime.

To further test the hypothesis that e^{-}/H^{+} pairs are stabilized against H_2 evolution in MIL-125 during photodoping, we sought to measure their redox potentials during the photodoping process. Considering that previous reports of photodoped MIL-125 shares

similar redox potentials to decamethylferrocenium [$FeCp^{*}_{2}{}^{+}$][415], we sought to use the latter as an optical redox indicator of the photodoped MOF suspension. By measuring the concentration of [$FeCp^{*}_{2}{}^{+}$] *in situ* through monitoring the absorption feature at 778 nm, attributable to a LMCT transition[538], the ratio of [$FeCp^{*}_{2}{}^{+}$] to [$FeCp^{*}_{2}$] can be determined and related through the Nernst equation to calculate the solution Fermi level, **Figure 45**.[539,540] Assuming redox equilibration between all species in the suspension, this value also reports the redox potential of the photodoped MOF at that time point. Hence, we can compare this value to the known redox potential of HER in acetonitrile (-624 mV vs Fc^{+}/Fc)[541] as further proof that the electron-proton pair is stabilized against recombination. Toward this aim, the mixture was dispersed in an air-free quartz cuvette, irradiated with a broadband photolysis lamp, and stopped intermittently to measure UV-vis spectra.

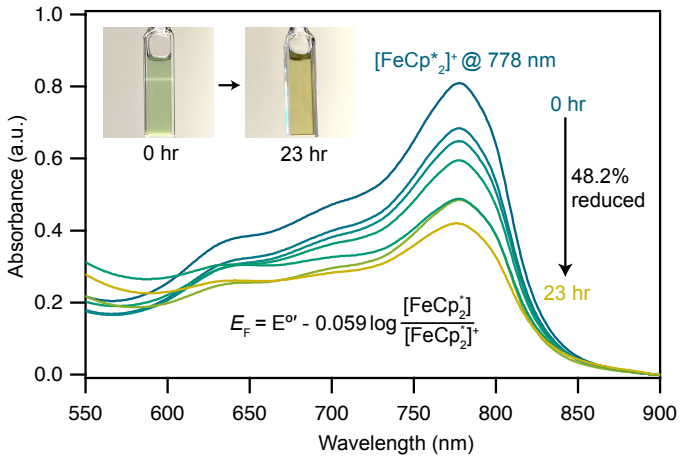

Figure A1. Electronic absorption spectra collected at various illumination times between 0 and 23 h during photochemical reduction of MIL-125 powder nanocrystals in the presence of 25 mM [$FeCp^{*}_{2}$][BF_4] in a MeCN/EtOH mixture.

Figure A1 shows that irradiation of the MOF-ethanol mixture induces a decrease in the [$FeCp^*_2^+$] absorption bands, signaling reduction by photodoped MIL-125. As a control, [$FeCp^*_2^+$] does not undergo photoreduction in the absence of MIL-125 (App C. Fig. A9). After 23 h of irradiation, the absorption bands of [$FeCp^*_2^+$] stopped decreasing, indicating a steady-state concentration of all redox-active species in the mixture. Analysis of these spectra indicate MIL-125 photoreduced 48.2% of the original [$FeCp^*_2^+$], yielding a steady-state redox potential of –588 mV vs Fc^+/Fc, just +36 mV milder than that of the electrochemical potential of HER.

Table A1: Compilation of total energy changes in two node unit cell with increasing numbers of hydrogen atoms (*i.e* PCET events) paired at bridging oxo pairs between titanium atoms (Figure 3a) in a computational unit cell containing two inorganic nodes, computed on a PBEsol optimized structure at the HSEsol06 level.

H* pairs / cell	ΔE from empty (eV)	ΔE from empty per pair (eV)	ΔE to release single H_2 (eV)
2	-0.67	-0.67	0.67
4 – same node	-1.38	-0.69	0.72
6	-1.76	-0.59	0.38
8 – same node	-0.41	-0.10	**-1.34**
4 – 2 per node	-1.40	-0.70	
8 – 4 per node	-2.16	-0.54	
16 – 8 per node	-3.12	-0.39	

The coupling of unpaired H*-donated radicals through BDC antibonds is made more apparent at higher loadings. If four PCET events occur at the same node (**Figure 44**, equivalent to 2 e^{-1}/node throughout the material) each titanium is partially reduced and the conduction band states are nearly entirely localized within the node; in contrast, isolating the PCET events between different titanium pairs forces spin density through the linker antibonds onto the metals of adjacent nodes, **Figure A3**.

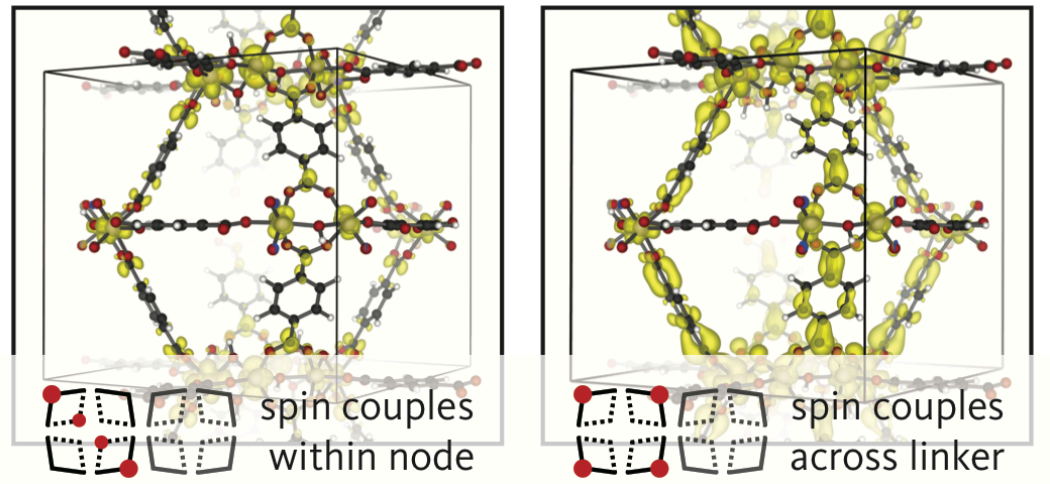

Figure A2. The spin density for all four conduction band electrons when four PCET events occur on a single node a) localizes within the node when matched between disparate sets of titanium pairs, but b) fill organic antibonding orbitals when the individual PCET are spread across each μ^2-oxo pair within the node.

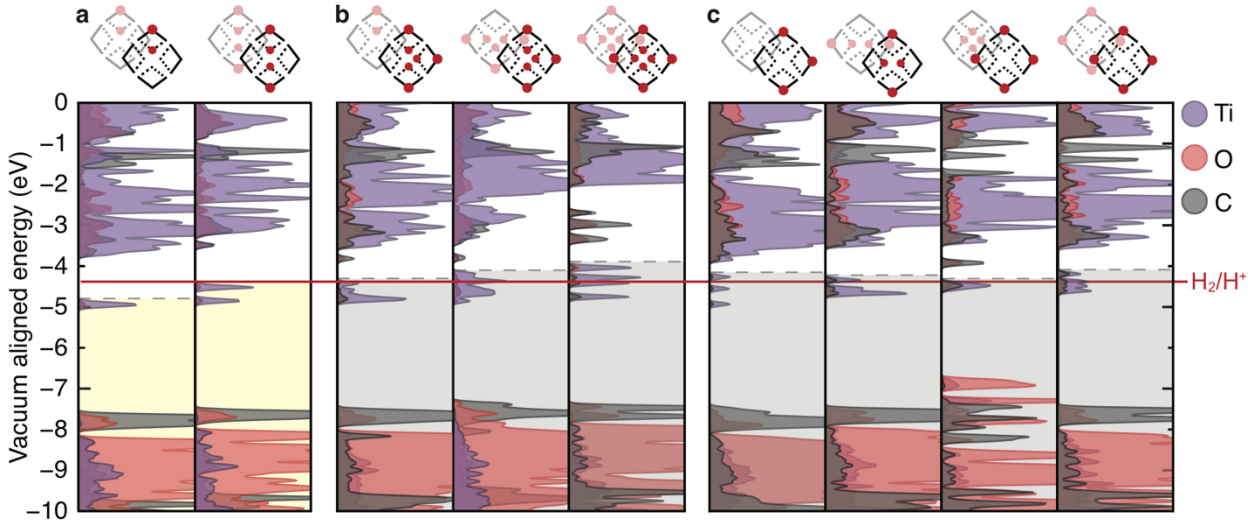

Figure A3. Atom-projected density of states for a range of configurations and dopant concentrations sampled for this study that were otherwise not discussed in the body of the article—the most favorable conformations occur when bridging oxo pairs are both protonated during subsequent/concurrent PCET events as is apparent in the purple and red sections depicting a range of two and four PCET event possibilities.

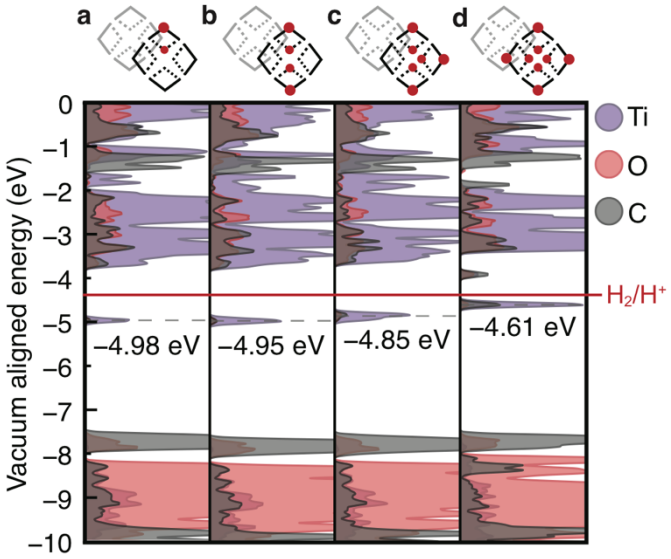

Figure A4. Atom-projected density of states for MIL-125 with (a) two, (b) four, (c) six, and (d) eight pairs of PCET events adding to the same bridging oxo pairs of the same node showing the reaction is net-favorable up to full saturation of the node – however this too can be forced by application of a chemical reductant and coordinating Na^{+} counterions.[416]

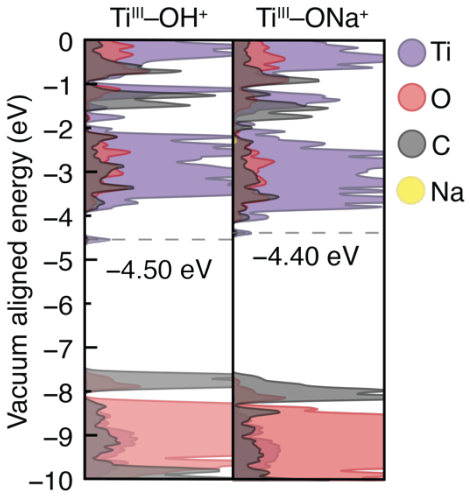

Figure A5. A comparison of proton-coupled and sodium coupled reduction of MIL-125.

Experimental Methods

MIL-125 was synthesized according to an adapted literature procedure[62] wherein, terephthalic acid, *N,N*-dimethylformamide and methanol were added to a Pyrex jar and sonicated for ca. 5 min to ensure complete dissolution. Under an N_2 environment, titanium (IV) ethoxide was added to the mixture. The reaction mixture was sealed under N_2 and heated at 150 ºC for 18 hr. Next, the solid product was collected via sequential centrifugation, and subsequent washing with DMF, methanol, and acetone to remove pore-trapped solvent. All q-^{1}H NMR experiments were referenced to 1,3,5-trimethoxybenzene in DMSO-d_6 and irradiated using a mercury arc lamp. The photoreduction of $[FeCp^*_2]^+$ took place in a MeCN/EtOH mixture such that the ratio of Ti^{IV} was 1Ti:1.25 $FeCp^*_2{}^+$ F. Full details are found below.

Materials and Characterization

All commercial chemicals were used as received unless stated otherwise. Titanium (IV) ethoxide (99.99%-Ti, Strem Chemicals), terephthalic acid (98% Sigma Aldrich), *N,N*-dimethylformamide (DMF, ACS grade, Fisher Scientific), methanol (HPLC grade, Fisher Scientific), 1,3,5-trimethoxybenzene (99.0%, Sigma Aldrich), benzyl alcohol (BnOH, 100%, Alfa Aesar), and dimethyl sulfoxide-d6 (DMSO-d6, Cambridge Isotope). Solvothermal syntheses were conducted in 100-mL Duran Schott bottles unless otherwise stated. Sample purity was verified by powder X-Ray diffraction (PXRD) with a Bruker D2 Phaser benchtop diffractometer. Photoirradiations were carried out using a mercury arc lamp. H NMR spectra were recorded at 600 MHz, d1 = 30 s, on a Bruker Advance-III-HD NMR spectrometer.

MIL-125 Synthesis

Following a procedure adapted from Dan-Hardi et. al,[62] terephthalic acid (0.748 g, 4.50 mmol), *N,N*-dimethylformamide (DMF, 9 mL) and methanol (1 mL) were added to a Pyrex jar and sonicated for ca. 5 min to ensure complete dissolution. Under an N_2 environment, titanium (IV) ethoxide (0.684 g, 3 mmol) was added to the mixture. The reaction mixture was sealed under N_2 and heated at 150 ºC for 18 hr. The contents were isolated by sequential centrifugation and decanting the mother liquor. To clean the product, the material was soaked in fresh DMF (10 mL x 3), methanol (10 mL x 3), and acetone (10 mL x 3). The product was dried using Schlenk line technique under dynamic vacuum at 180 ºC and transferred into a N_2 glovebox for analysis.

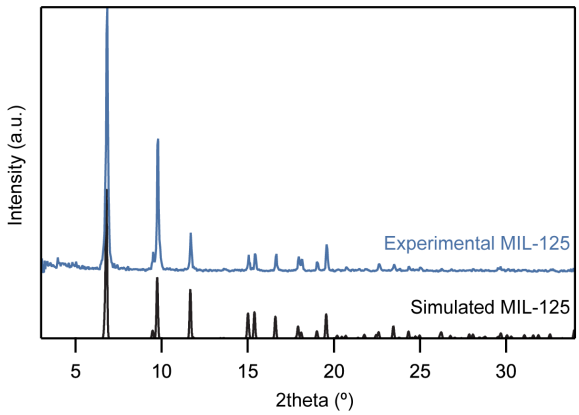

Figure A6: Experimentally determined powder X-ray diffraction pattern versus the simulated pattern for MIL-125.

q-^{1}H NMR Photodoping In an N_2 glove box, MIL-125 (10 mg) was placed in an air-free quartz cuvette with a small stir bar, DMSO-d6, and an amount of BnOH (added either neat, or dilute in DMSO-d6). The cuvette was sealed and irradiated with a mercury arc lamp while stirring. The solution was then centrifuged after irradiation, the liquid is decanted, and the standard (1,3,5-

trimethoxybenzene, 10 mg) was added for quantitative analysis. After dissolution, an aliquot was taken for ^{1}H NMR and mixed with additional deuterated solvent.

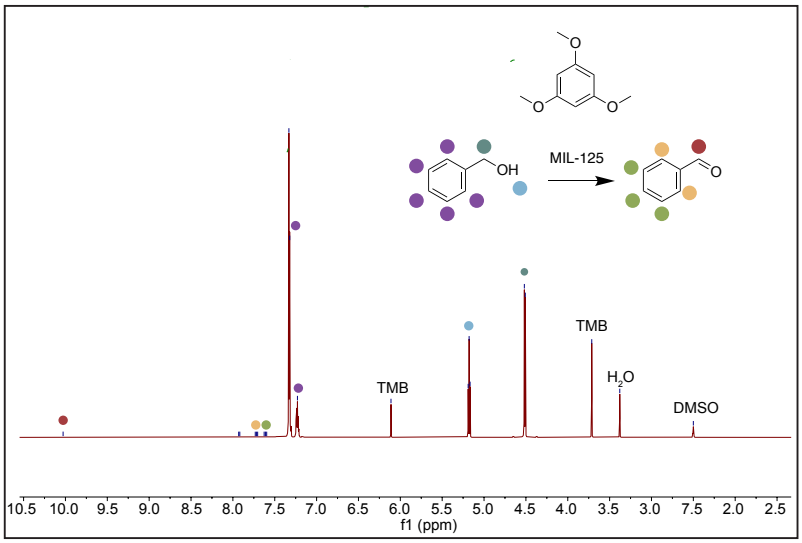

Figure A7: ^{1}H NMR spectra for an excess amount of BnOH. A large amount of BnOH is still present in solution, marked by difference in relative peak integrations, with the small emergence of expected shifts corresponding to benzaldehyde around 10 ppm.

Preparation and Reduction of [FeCp$_2$][BF$_4$]* In an N_2 glovebox, FeCp*$_2$ was weighed into a Schlenk flask and dissolved in ca 5 mL hexanes. In air, benzoquinone was dissolved in ca 5 mL of ethyl ether, and HBF_4 was added. The FeCp*$_2$ and benzoquinone solutions were combined by cannula transfer, creating a cloudy dark-green mixture. This solution was left to stir for one hour, and let stand for 30 minutes, yielding a green precipitate. The flask was transferred to a benchtop N_2 glovebox, where it was vacuum filtered and washed with dry hexanes (~40 mL). Once transferred into an N_2 glovebox, the powder was dissolved in dry MeCN. The concentration of the solution was tested via UV vis by way of a dilution of 100 µL in 3 mL MeCN in an air-free quartz

cuvette with pathlength 1 cm, and the concentration was determined to be 25.09 mM by the 30 min irr. abs value at 778 nm for an absorptivity coefficient of 488 L mol^{-1} cm^{-1}. 1 mg of MUV-10 (Ca) was added to a mixture of 250 µL of stock $[FeCp^*_2]^+$, 200 µL dry ethanol (excess), and 3 mL dry MeCN for a total ratio of 1Ti:1.25 $FeCp^*_2{}^+$. The cuvette was irradiated with a mercury arc lamp, and the UV-vis spectra were recorded after allowing the powder to settle. After 23 hr of irradiation with a mercury arc photolysis lamp, the vibrant green solution had reached a steady yellow color, indicative of $FeCp^*_2$ formation. Using the initial absorbance values at t=0 hr and 23 hr, a relative concentration of $FeCp^*_2{}^+$ to $FeCp^*_2$ can be calculated, and thus, a solution state Fermi level can be calculated using the Nernst equation displayed in **Figure 45.**

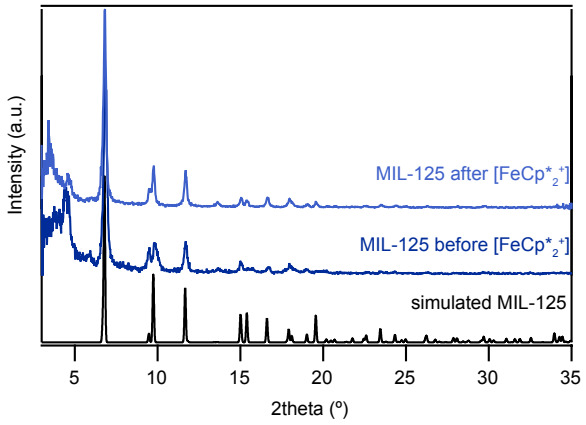

Figure A8: PXRD of MIL-125 before and after treatment with $FeCp^*_2{}^+$, displaying a full retention of its crystalline lattice and Bragg reflections.

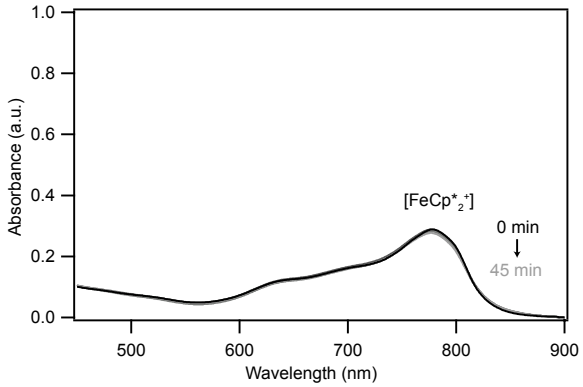

Figure A9: Solution state UV-vis of a mixture of neat $FeCp^*_2{}^+$ and ethanol, showing no reduction in absorbance after 45 min irradiation.

APPENDIX D

SUPPLEMENTARY INFORMATION FOR:

Singlet-to-Triplet Spin Transitions Facilitate Selective 1-Butene Formation During Ethylene Dimerization in Ni(II)-MFU-4*l*

Jenna L. Mancuso, Carlo A. Gaggioli, Laura Gagliardi, Christopher H. Hendon

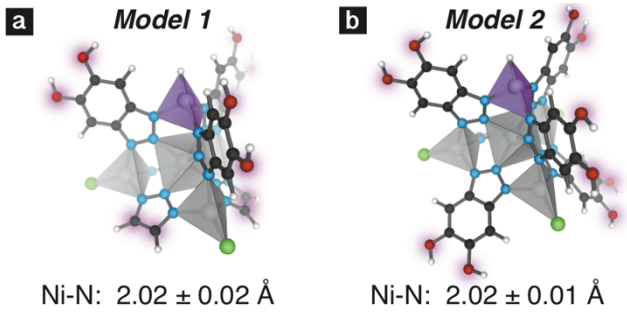

Figure A1: Truncated cluster models 1 and 2 were extracted from the bulk optimized metal-hydride species of Ni(10%)-MFU-4*l* and constrained during subsequent optimizations at the terminal crystallographic atoms (highlighted in purple) which were passivated with hydrogen atoms permitted to optimize during all geometric relaxations. Both models maintain the Zn_4Ni cluster and triazolate linkers of the secondary building unit and bisected BTDD linkers inclusive of the dioxin oxygen atoms for linkers around the active site to maintain their steric and electronic effects. a) Model 1 features triazolate motifs approximating the three linkers opposite the Ni(II)-active site in an effort to reduce computational expense, while b) Model 2 features six equivalently truncated linkers to detect the presence of spurious electronic dipoles that may cause deviations between the free energy profile of reactions occurring at the MOF-based Ni(II) active site and the reduced symmetry of Model 1. Both models, regardless of truncation, recovered identical active site geometries for each reaction step.

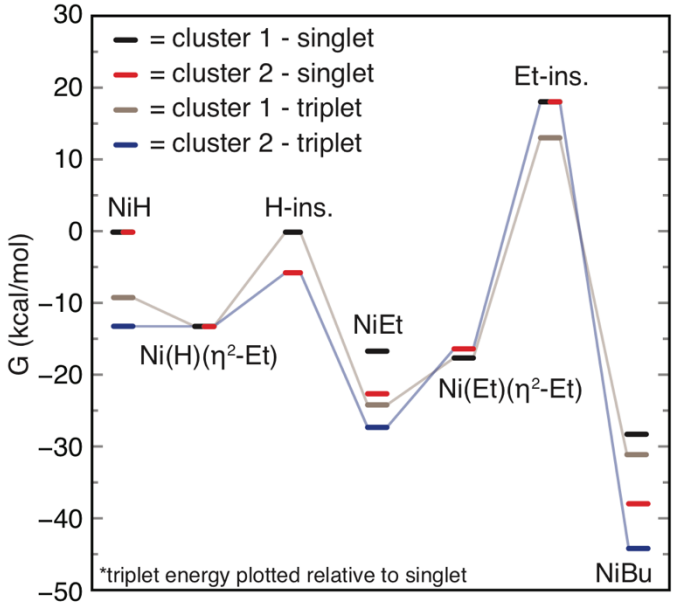

Figure A2: Energy profile comparison for cluster 1 (M1) and cluster 2 (M2) on both the singlet and triplet energy surfaces for butyl formation following the dimerization pathway shown in Figure 1. The net reaction pathways, shown in gray and blue for M1 and M2 respectively, follow the same qualitative reaction pathway including spin-crossing events.

β-hydrogen transfer pathway energetics

One hypothesis for high 1-butene selectivity unexplained by small differences in activation barriers predicted by prior quantum mechanical simulations was an alternative chain termination mechanism. Experimental labelling studies have shown that metallacycle formation does not occur in Ni(II)-MFU-4*l*, however we proposed beta-hydrogen transfer (BHT) *via* a 6-membered transition state could offer a lower energy route to BHE. However, rather than forming a loose 6-membered ring, the hydrogen being transferred forms a strong association with the Ni(II) center causing "ring" strain, **Figure A3**. The

activation barrier to 1-butene formation through this route is subsequently significantly higher than any other point along the pathway which means this route is unlikely and certainly does not contribute to explain the high 1-butene selectivity observed for this MOF, **Table A1**.

Table A1: Activation barriers for Kuratowski cluster model 1 pertinent to reaction kinetics for ethylene dimerization relative to isomerization and propagation pathways nonselective for the linear α –olefin.

Transition State	**Spin State**	**E_a (kcal/mol)**	**ΔG (kcal/mol)**
H-insertion	Singlet	13.2	9.2
Et-insertion	Triplet	30.8	22.3
BHE	Singlet	17.2	-4.7
Propagation	Triplet	22.3	-9.9
BHE (C6)	Singlet	26.6	-15.5
Isomerization	Singlet	22.4	0.6
BHE (2°-alkyl)	Singlet	19.9	-3.5
BHT	Singlet	64.9	32.8

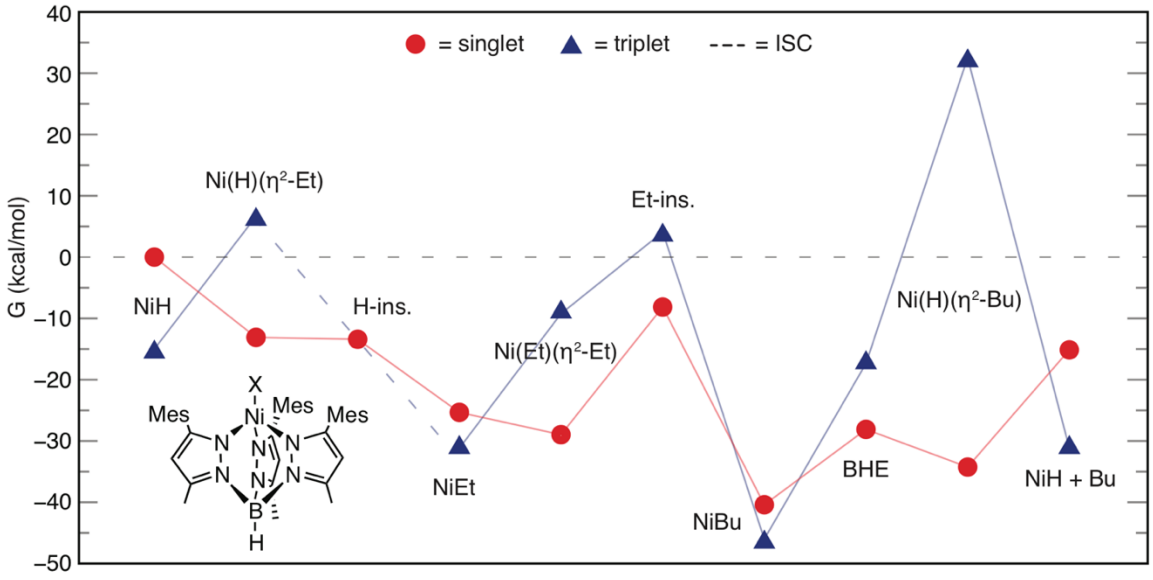

Figure A3: Reaction coordinate energy diagram for ethylene dimerization along the Cossee-Arlman dimerization route in $[Tp^{Mes}Ni]^+$ where Tp^{Mes} = HB(3-mesitylpyrazolyl)$_3$ (depicted in bottom left corner) for both singlet and triplet spin surfaces. While the transition state most certainly exists, we were unable to isolate the hydride insertion step for ethyl formation in the triplet state. However, consistent with subsequent hydride transfer barriers being higher in energy than the associated singlet, the Gibbs free energy is expected to be more positive making this step kinetically disfavored since the preceding triplet intermediate (NiH) is lower in energy than the corresponding singlet configuration.

Table A2: Lowest energy activation barriers for the homogeneous Ni(II) TpMes catalyst to compare competitive pathways for dimerization, namely isomerization and propagation pathways.

Transition State	Spin State	E_a (kcal/mol)	ΔG (kcal/mol)
H-insertion	Singlet	8.21	-13.6
Et-insertion	Singlet	21.0	-8.25
BHE	Singlet	12.4	-28.5
Propagation	Triplet	22.2	-21.0
BHE (C6)	Singlet	10.8	-43.2
Isomerization	Singlet	17.3	-23.6
BHE (2°-alkyl)	Singlet	29.6	-12.9

Table A3: Tabulated raw free energy values including the zero-point energy correction for all computed species recovered using the Computational Methods detailed in the main text reported in Hartrees. Pentacoordinated species with η^2-olefins were computationally nonisolable for MOF cluster models and demarcated by a hyphen. Other species either not computed or recovered for other models are labelled N/A.

Raw Free Energy	Model 1 - Singlet	Model 1 - Triplet	Model 2 - Singlet	Model 2 - Triplet	Homo. - Singlet	Homo. - Triplet
Ni-H	-12366.8292	-12366.84394	-13278.17982	-13278.2009	-3256.26644	-3256.29125
Ni(H)(η^2-Et)	-12445.3349	-	-13356.68308	-	-3334.78592	-3334.74107
H-insertion	-12445.3140	-12445.29394	-13356.67346	N/A	-3334.77284	N/A
Ni-Et	-12445.3405	-12445.35236	-13356.70059	-13356.7079	-3334.79210	-3334.80090
Ni(Et)(η^2-Et)	-12523.8267	-	-13435.17513	-	-3413.28239	-3413.25003
Et-insertion	-12523.7699	-12523.77768	-13435.12051	N/A	-3413.24892	-3413.23060
Ni-1°-Bu	-12523.8435	-12523.84806	-13435.20953	-13435.2195	-3413.30084	-3413.30981
BHE	-12523.8207	-12523.80116	N/A	-13435.1646	-3413.28116	-3413.26354

Ni(H)(η^2-1-Bu)	-12523.8277	-	N/A	-	-3413.29104	-3413.18480
Ni(Bu)(η^2-Et)	-12602.3491	-	-13513.70864	-	-3491.78917	-3491.78168
BHT	-12602.2457	N/A	N/A	N/A	N/A	N/A
Propagation	-12602.2774	-12602.31364	-13513.62897		-3491.75386	-3491.74361
Ni-Hex	-12602.3559	-12602.36504	-13513.71762	-13513.7256	-3491.80655	-3491.81550
BHE (C6)	-12602.3226	N/A	-13513.68837	N/A	-3491.78930	N/A
Ni(H)(η^2-Hex)	-12602.3367	-	N/A	-	-3491.79752	-3491.69022
Isomerization	-12523.8123	-12523.7919	N/A	N/A	-3413.27331	-3413.24069
Ni-2°-Bu	-12523.8311	-12523.85055	N/A	N/A	-3413.30354	-3413.30086
BHE (2°-alkyl)	-12523.8189	-12523.79944	N/A	N/A	-3413.25629	N/A
Ni(H)(η^2-2-Bu)	-12523.8357	-	N/A	-	-3413.29621	-
Ethylene	-78.484661					
1-Butene	-156.993975					
2-Butene	-157.003572					
1-Hexene	-235.500229					

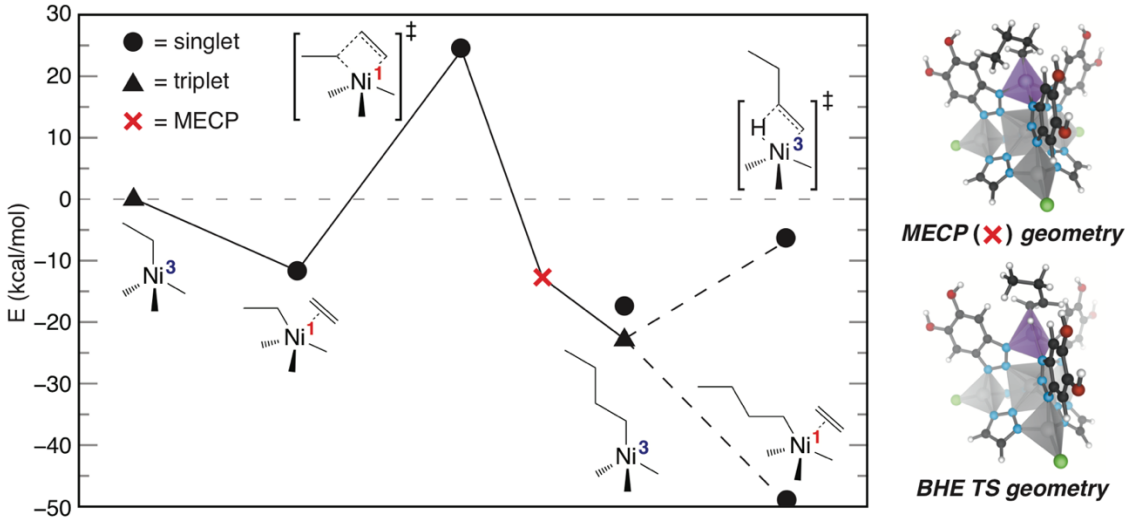

Figure A4: Scanning the PES along the high and low spin energy surfaces between known intermediates of opposite spin-state recovers a minimum energy crossing point, an approximation of the transition state energy along the adiabatic spin surface. The MECP between ethylene insertion on the singlet surface and the Ni(II)-butyl species on the triplet surface is marked by the red X with its structure shown. This structure also offers access to the BHE transition state through a forming β-agostic interaction which can facilitate BHE along the singlet surface from a perhaps transient Ni(II)-butyl species.

Table A4: Tabulated raw electronic energy (Hartree) values recovered for structures reported in Figure A4.

Raw Total Energy	Singlet	Triplet
Ni-Et	N/A	-12445.7982250
Ni(Et)(η^2-Et)	-12524.3311113	N/A
Et-insertion	-12524.2728738	N/A
MECP	-12524.3321121	-12524.3321121
Ni-1°-Bu	-12524.3398394	-12524.3484676
Ni(Bu)(η^2-Et)	-12602.9026766	N/A
BHE	-12524.3212801	N/A
Ethylene	-78.5130510282	N/A

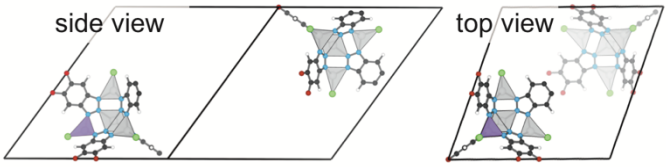

Figure A5: The computational unit cell for geometric optimization of Ni(II)-MFU-4*l* was built by substituting a single metal ion in one of the two pentanuclear Zn(II) clusters of the parent MFU-4*l* scaffold.

APPENDIX E

EXPERIMENTAL DETAILS AND SUPPLEMENTARY INFORMATION FOR:

A Structural Mimic of Carbonic Anhydrase in a Metal-Organic Framework

Ashley M. Wright, Zhenwei Wu, Guanghui Zhang, Jenna L. Mancuso, Robert J. Comito, Robert W. Day, Christopher H. Hendon, Jeffrey T. Miller, and Mircea Dincă

Experimental Discussion Omitted from Main Text

Fitting a 77 K N_2 adsorption isotherm of **2** to the Brunauer-Emmett-Teller equation gave a surface area of 2,739 m^2/g, which, although lower than that of **1** (3,525 m^2/g), confirmed the retention of porosity after treatment with base (Figure S2). Thermogravimetric analysis of **2** revealed that it is less stable than its parent **1**; its extrapolated onset decomposition temperature occurs at 250°C, approximately 100°C lower than for **1** (Figure S6). Energy-dispersive X-ray spectroscopy and X-ray photoelectron spectroscopy of **2** confirmed the quantitative replacement of chloride with hydroxide and revealed no chlorine-specific peaks (Figures S4 and S5). Finally, diffuse reflectance infrared Fourier transform spectroscopy (DRIFTS) of **2** revealed a hydroxide

O–H stretching band at 3,699 cm^{-1}, a signal that was not observed in the DRIFTS data for **1** (Figure S9). Indeed, the frequency of this band is comparable to that of the OH stretch found in the homologous molecular compound $Tp^{tBu,Me}Zn(OH)$ (3,676 cm^{-1}).[703,704]

To further characterize the incorporation of a Zn–OH site in **2**, we analyzed the material by X-ray absorption spectroscopy (XAS). Whereas both **1** and **2** had the same Zn K-edge energy (9,663.6 eV), indicating a common oxidation state on zinc in both materials (Figure 2A), a significant difference in the zinc coordination environment became apparent when we compared the white line and near-edge regions for the two materials: **2** exhibited a lower and broader white line than **1** and a near-edge feature (~9,668 eV) higher than that of **1** (Figure 2A). Moreover, the extended X-ray absorption fine structure (EXAFS) spectra of **1** and **2** indicated a difference in the primary coordination sphere of zinc. In **2**, the first shell peak shifted to a lower radial distance and was less intense than the corresponding peak in **1** (Figure 2B), consistent with a shorter Zn–X bond and scattering by a lighter element, such as oxygen. Quantitative fitting of the EXAFS region for **2** was challenging because there were two Zn^{2+} sites (N_3ZnX and N_6Zn) with distinct coordination environments, and the small difference between the Zn–N bond length of the two sites made it difficult to fit them as one path or separate paths. Consequently, we chose to fit the difference spectrum of **1** and **2**; the similar coordination environments of the two Zn sites removed the disordered Zn–N scattering in the data, and the fit provided information regarding the Zn–X bond (see Figures A7 and A8 for further details).

To probe the nature of the interaction between CO_2 and **2** their reaction was monitored by DRIFTS. Exposing **2** to incremental increases in [CO_2] from 1,000 to 4,000 ppm in an

argon carrier gas resulted in the formation of new bands in the DRIFT spectrum (Figure A21). By contrast, the addition of CO_2 to **1** under the same conditions resulted in no spectral changes (Figs. A22 and A23). The new spectral features in **2** are consistent with the formation of a zinc bicarbonate. Specifically, a new band at 3,626 cm^{-1} was assigned to the O–H stretch.[706] Bands at 1,660 and 1,245 cm^{-1} corresponded to the O=C–O asymmetric and symmetric stretches, respectively.[706] Additionally, bands at 1,018 and 1,423 cm^{-1} were associated with bending and stretching vibrations of the COH group in bicarbonate. The observed stretches were comparable to those of the molecular analog $^{t\text{Bu,Me}}$TpZn(OCO_2H), which featured asymmetric and symmetric O=C–O stretches at 1,675 and 1,302 cm^{-1}, respectively.[706] In addition, the IR spectrum of $[Mn^{II}M^{III}(OCO_2H)Cl_2(bbta)]$ (M = Mn, Co) featured stretches at 3,682 (O–H), 1,224 (symmetric O–C=O), and 1,050 cm^{-1} (O–H bending).[711] Purging the DRIFTS setup with 100% argon flow resulted in the loss of the new signals and reformation of the starting spectrum, consistent with a reversible reaction with CO_2.

To gain more insight into the framework-adsorbate interaction, we determined the coverage-dependent CO_2 adsorption enthalpy (Q_{st}) by measuring the CO_2 adsorption isotherms at three different temperatures (288, 298, and 308 K) and fitting the isotherm data to the virial equation (Figures A13 and A14).[841,842] Other fitting routines, including the Langmuir, Langmuir-Freundlich, and two-site Langmuir models, provided less satisfactory fits (Figures A11 and A12). With the virial equation, Q_{st} at zero CO_2 coverage is 81 kJ/mol, a value much higher than those typically observed in MOFs and other microporous materials[843] and consistent with a chemisorption event. Indeed,

the Q_{st} for CO_2 insertion into metal–hydroxide bonds in $[Mn^{II}Mn^{III}(OH)Cl_2(bbta)]$ and $[Co^{II}Co^{III}(OH)Cl_2(bbta)]$ (H_2bbta = 1*H*,5*H*-benzo(1,2-d:4,5-d)bistriazole) is 99 and 110 kJ/mol, respectively.[711] Notably, the coverage-dependent Q_s suggests a bimodal adsorption profile (Figure A15). With increasing coverage, Q_{st} stays relatively constant up to ~0.5 equiv of CO_2 per SBU and then gradually decreases until it reaches ranges between 62 and 35 kJ/mol for the second CO_2 equivalent and between 35 and 20 kJ/mol for the third CO_2 equivalent. The large, bimodal variation in Q_{st} suggests that the adsorption mechanism changes with increasing CO_2 coverage.

We investigated the ability of **1** and **2** to perform CA-like reactivity. The central function of CA is to rapidly interconvert H_2O and CO_2 as well as bicarbonate and protons. We mimicked the interconversion *in vitro* by studying the exchange of ^{18}O-labeled H_2O with gaseous CO_2 and periodically sampling the headspace to monitor the distribution of CO_2 isotopologues by gas chromatography-mass spectroscopy. Notably, in the presence of **2**, the time to reach an equilibrium mixture of the three possible CO_2 isotopologues ($C^{16}O_2$, $C^{16,18}O_2$, and $C^{18}O_2$) was significantly reduced to 5 hr from 10 hr without **2** (Figures S28–S31). Consequently, there must be a rapid equilibrium for the Zn–OH + CO_2 ⇌ Zn–OCO_2H and Zn–OCO_2H + H_2O ⇌ Zn–OH + H_2CO_3 reactions. It should be noted that **1** also decreased the time taken to reach an equilibrium mixture of the isotopologues but was not as effective as **2** because it reduced the equilibrium time to 7 hr. This could be attributed to partial hydrolysis of the Zn–Cl bond under the reaction conditions.

General Procedures Materials

$ZnCl_2 \cdot 6H_2O$ (99.9%, Alfa Aesar), HCl (32-35%, BDH – VWR Analytic) methanol (99.9%, VWR), *N,N*- dimethylformamide (DMF, 99.8%, Millipore), ethanol (ACS grade, Mallinckrodt), tetra-*n*-butylammonium hydroxide (1.5 M, water, Sigma Aldrich) were used as received. MFU-4*l* was synthesized using previously published procedures.[844]

Powder X-ray Diffraction (PXRD) patterns were recorded with a Bruker Advance II diffractometer equipped with a θ/2θ Bragg-Brentano geometry and Ni-filtered CuKα radiation (Kα1 = 1.5406 Å, Kα2 = 1.5444 Å, Kα1/ Kα2 = 0.5). The tube voltage and current were 40 kV and 40 mA, respectively. Samples for PXRD were prepared by placing a thin layer of the appropriate material on a zero-background silicon crystal plate.

Gas adsorption isotherms were measured by a volumetric method using a Micromeritics ASAP 2020 gas sorption analyzer. Typical samples of ca. 40–80 mg, preactivated at >100°C to remove all residual solvent, were transferred in an Ar-filled glovebox to a pre-weighed analysis tube. The tube with sample inside was weighed again to determine the mass of the sample. The tube was capped with a Micromeritics TranSealTM, brought out of the glovebox, and transferred to the analysis port of the gas sorption analyzer. Free space correction measurements were performed using ultra-high purity He gas (UHP grade 5, 99.999% pure). Nitrogen isotherms were measured using UHP grade Nitrogen. All nitrogen analyses were performed using a liquid nitrogen bath at 77 K. Carbon dioxide isotherms were measured using Research grade carbon dioxide (99.999%). Carbon dioxide

analyses were performed at varying temperatures in a water/ethylene glycol isothermal bath. Oil-free vacuum pumps were used to prevent contamination of sample or feed gases.

Thermogravimetric Analysis (TGA) was performed on a TA Instruments Q500 Thermogravimetric Analyzer at a heating rate of 2 °C/min under a nitrogen gas flow of 10 mL/min.

Diffuse reflectance infrared Fourier transform spectroscopy (DRIFTS) measurements were performed on a Bruker Tensor 37 with a mercury cadmium telluride detector cooled to 77 K. Data were collected in "MIR_DRIFTS" mode with a 6mm aperture setting and a KBr beam splitter using a DiffusIR accessory made by Pike Technologies in an in-situ cell equipped with a ZnSe window. Data was averaged over 32 scans between 4000 and 600 cm^{-1}. Samples were diluted with KBr to ~5% by weight and loaded in to ceramic sample cup. A background of KBr was subtracted from the data.

Synthesis of MFU-4*l*-(OH) (2).

tetrabutylammonium hydroxide (2.7 mL, 4.1 mmol, 20 equiv.) was added dropwise to a gently stirring suspension of MFU-4*l* (1) (255 mg, 0.202 mmol) in methanol under a nitrogen atmosphere. The mixture was slowly stirred for 18 hours, then the solid was isolated on a medium porosity frit in air. The solid was washed with MeOH (12 × 30 mL portions) over 48 hours to remove [TBA][Cl] and excess [TBA][OH]. The solid was dried under vacuum at 110 °C for 18 hours and stored in an argon glove box prior to use. Amount isolated: 200 mg, 85% yield.

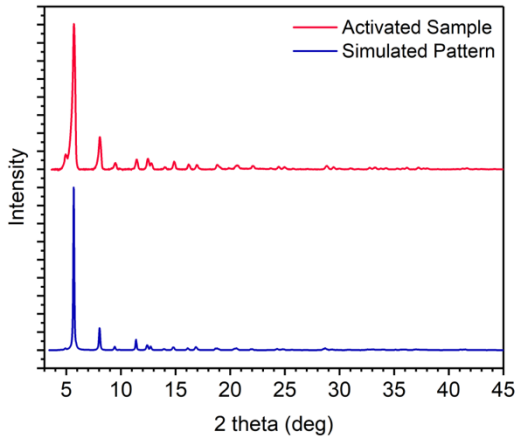

Figure A1. Powder X-ray diffraction pattern of an activated sample of MFU-4*l*-(OH) (2) (top trace, red) and the simulated pattern of MFU-4*l*-(OH) (2) (bottom trace, blue) as determined from the DFT extended lattice model.

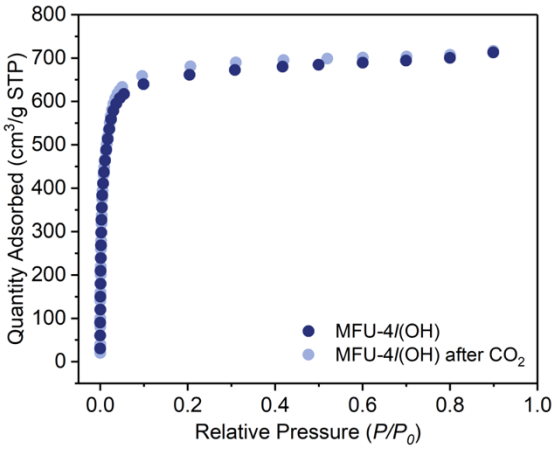

Figure A2. N2 adsorption isotherm at 77 K before (blue circles) and after exposure to CO2 (light blue circles). BET surface areas: before, 2739 m^2/g; after 2875 m^2/g.

Table A1. BET parameters and pressure ranges used for the calculation of the BET surface area for MFU-4*l*- (OH).

Materials	**MFU-4*l*-(OH) before CO_2**	**MFU-4*l*-(OH) after CO_2**
BET surface area	2739 m^2/g	2875 m^2/g
P/P_0 range	0.009 – 0.055	0.009 – 0.051
C	244.4	206.2
V_m	629 m^2/g	661 m^2/g
P/P_0 (@ V_m)	0.07	0.096
$1/(\sqrt{C}+1)$	0.060	0.065

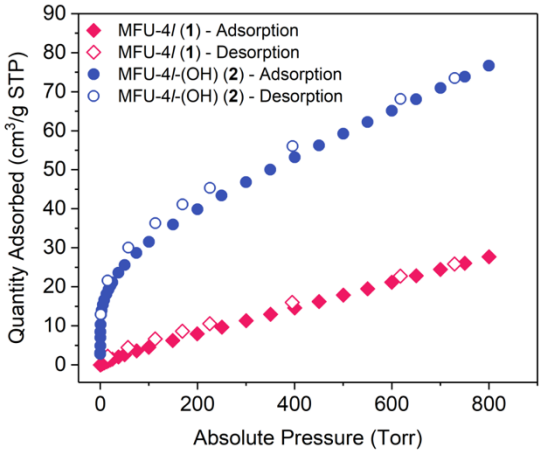

Figure A3. Comparison of the CO_2 adsorption isotherms of MFU-4*l*-(OH) (2) (blue circles) and MFU-4*l* (1) (red diamonds) at 298 K. The closed symbols denote the adsorption phase and the open symbols represent the desorption phase.

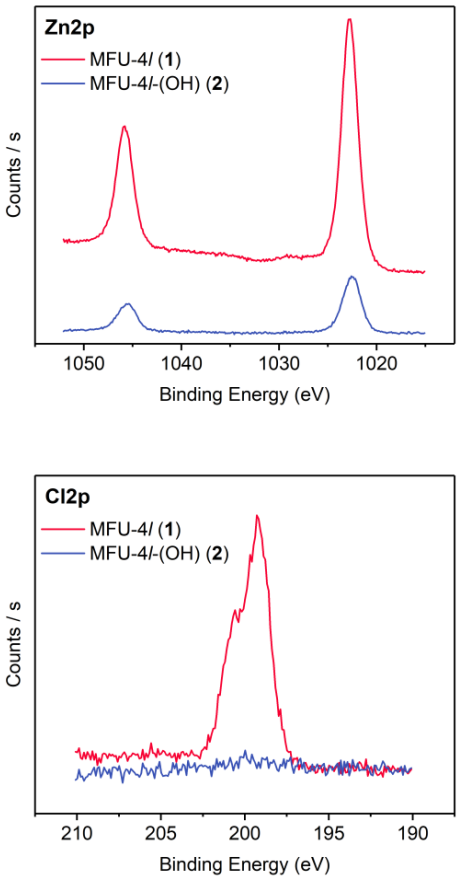

Figure A4. High resolution XPS spectra of MFU-4*l* (1, red line) and MFU-4*l*-(OH) (2, blue line) in the Zn2p and Cl2p regions. The lack of signal in the Cl2p region for 2 is consistent with no chloride present.

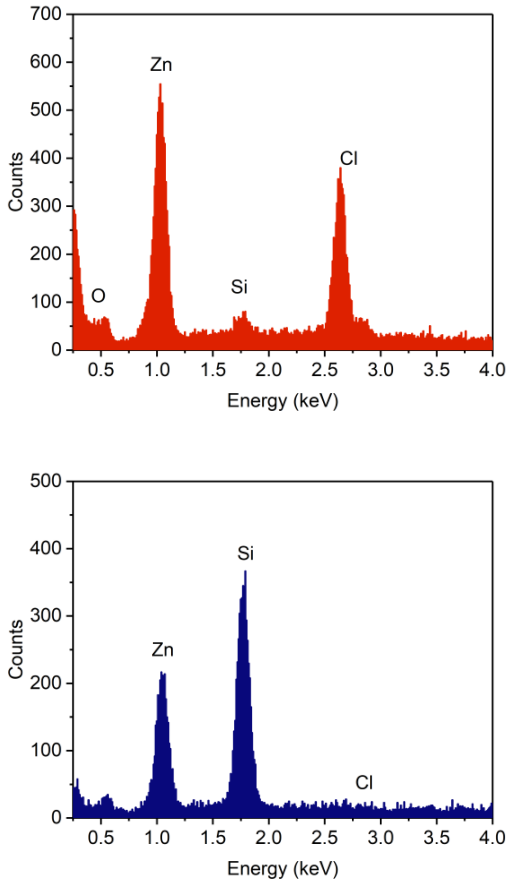

Figure A5. Energy-dispersive X-ray spectroscopy of MFU-4*l* (1) (left, red) and MFU-4*l*-(OH) (2) (right, blue). The EDXS spectrum of 2 indicates no chloride in the bulk sample supporting exchange of OH for Cl. The Si signal is from the substrate material.

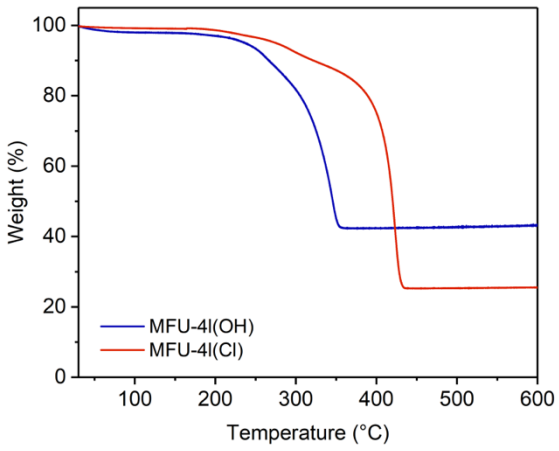

Figure A6. Thermogravimetric analysis (TGA) curves for MFU-4*l* (1, red) and MFU-4*l*-(OH) (2, blue).

X-ray Absorption Spectroscopy (XAS) Analysis of MFU-4*l*-(OH) and MFU-4*l*

X-ray absorption spectroscopy measurements at the Zn K edge (9658.6 eV) were performed on the 10-ID line of the Materials Research Collaborative Access Team (MRCAT) at the Advanced Photo Source (APS), Argonne National Laboratory. Below are the XANES plot of MFU-4*l* (1) and MFU-4*l*-(OH) (2) (Figure S7). Both samples have the same edge energy of 9663.6 eV characteristic of Zn(II). The whiteline and near edge features, however, are different between the two samples. The MFU-4*l*-(OH) has slightly lower and broader whiteline compared to MFU-4*l*. The near edge feature after whiteline is higher, which is evident of changes in the coordination environment around Zn. More information is obtained from the EXAFS spectra (Figure S8). Compared to MFU-4*l*, the

first shell EXAFS peak of MFU-4*l*-(OH) sample shift to lower radial distance, which corresponds to a shorter average bond distance and is consistent with the proposed ligand replacement of Cl by OH. In addition, the first shell peak of MFU-4*l*-(OH) sample decreases slightly in intensity, again consistent with oxygen being a lighter scatter compared to Cl.

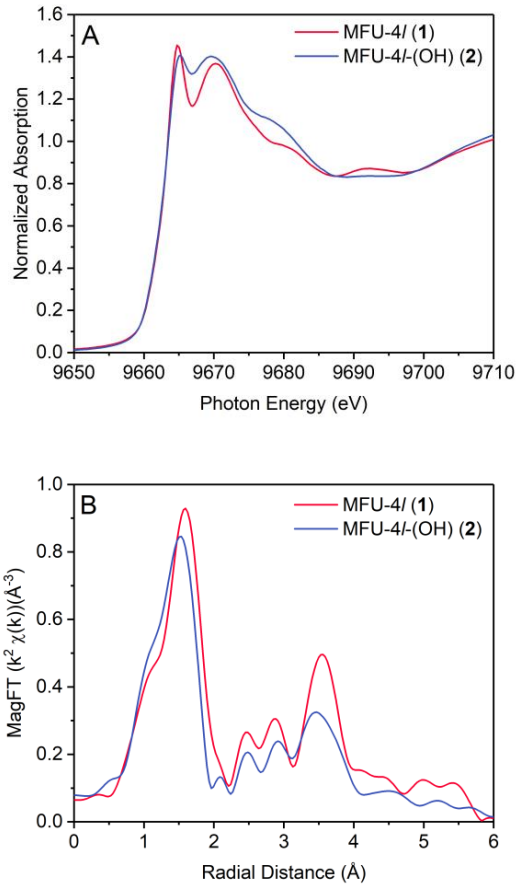

Figure A7. (A) XANES plot of the zinc K-edge for MFU-4*l* (red trace) and MFU-4*l*(OH) (blue trace). (B) Magnitude of Fourier transform of k^2 weighted EXAFS spectra of MFU-4*l* (1) vs MFU-4*l*-OH (2).

Quantitative EXAFS fitting.

To directly examine the coordination environment around Zn and obtain quantitative information, we turn to EXAFS fitting. In a typical fitting approach, we examine the EXAFS data of a certain sample and how close it is to the simulation from a proposed structure model. Briefly, an initial bond length and coordination number from certain structure model is used in the fits and fitting the data gives the amplitude reduction factor S_0^2, energy shift ΔE_0, bond distance difference ΔR and Debye-Waller factor σ^2 values, which are all reflective of whether the model is physically close to the real sample. A good fit is obtained by adjusting the model (coordination number as well as bond distances) until reasonable S_0^2, ΔE_0, ΔR and σ^2 values are obtained.

For this sample, direct fitting of the EXAFS data of a certain sample is very challenging due to the presence of two types of Zn with distinct coordination environments (central Zn in an N_6Zn environment and peripheral Zn in a N_3ZnX environment). These two types of Zn have Zn—N bonds in two sets of different distances, but the bond distances do not differ significantly, making it hard to fit them as either one path or separate paths. Alternatively, we take the difference between the EXAFS ($\chi(k)$) of MFU-4*l* and MFU-4*l*-OH and fit the difference spectrum (Figure S8A). Due to the presumably similar overall Zn coordination environment between the two samples, taking this difference should, at best if not totally, remove the same multiple Zn—N scatterings in the data. According to the proposed sample structure, this difference EXAFS represents the coordination change due to the anion exchange, corresponding to 0.8 Zn—Cl scattering plus – 0.8 Zn—O

scattering. The coordination number is 0.8 instead of 1 since the one Zn—X coordination change on each four peripheral Zn is averaged to all five Zn in each SBU in EXAFS which is a bulk average technique. The "negative" Zn—O scattering is due to the data subtraction and equivalent to a Zn—O scattering with inverse phase shift and can be simulated and fit in the Artemis software.[1] Figure S8b shows the imaginary part of the fit summing an inverse Zn-O path and a Zn-Cl path.

The approach of fitting of the difference spectrum resulted in a satisfactory fit of Zn—Cl bond of 2.17 Å and Zn—O bond of 1.93 Å, with an amplitude reduction factor of 0.93. The obtained Zn—Cl bond distance is very similar to the calculated bond distance for MFU-4*l* as well as the Ni—Cl and Co—Cl bond distances obtained from previous EXAFS fitting of the Ni and Co-MFU-4*l* samples (~2.15 Å). The Zn—O bond distance is longer than the value from DFT calculation but is within the reasonable range for Zn—O bonds in tetrahedral geometry. For instance, ZnO has tetrahedral Zn—O bonds of 1.97 Å. Other common compounds of late 3d transitional metals in tetrahedral geometry also feature O bonds in a distance between 1.9 and 2.0 Å. The amplitude reduction factor S_0^2 in the fit is also close to the value obtained from ZnO reference (0.97), confirming that this is a physically reasonable fit. In addition, the fit well explains the dip at around 1.5 Å (phase uncorrected distance) in the magnitude of k^2 weighted difference EXAFS (Figure S8a). This feature comes from a strong deconstructive interference between Zn—Cl and inverse phase Zn—O scattering as shown in Figure S8b. The fit is also consistent with varied data range in k and R space of the data.

Overall, both qualitative and quantitative analysis of the XAS data verifies that in the MFU-4*l*-(OH) sample, the original Cl ligand attached to the Zn in the ion exchange site of MFU-4l has been replaced by OH ligand.

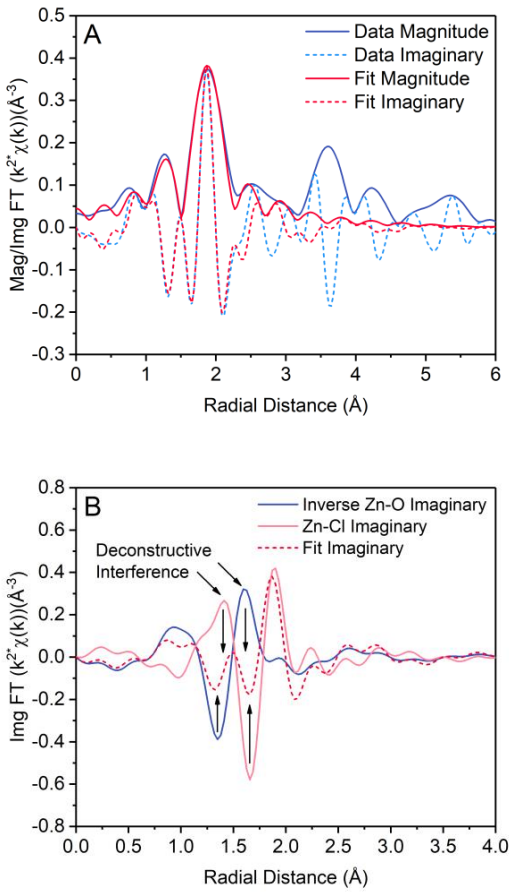

Figure A8. (A) Fitting results (red) of the difference EXAFS spectra between MFU-4*l* and MFU-4*l*-OH (blue), the plots show the magnitude (solid) and imaginary part (dash) of the Fourier transform of k^2 weighted EXAFS, k: 2.7 – 10.0 $Å^{-1}$, R: 1.0 - 2.3 Å; (B) Comparison between the summed imaginary part with that of the Zn—O and Zn—Cl scattering path. The two different paths happen to show strong deconstructive interference between 1.1 Å and 1.7 Å.

Table A2. Fitting results for the difference EXAFS between MFU-4*l* (1) and MFU-4*l*-(OH) (2) and ZnO reference.

Sample	Scattering Pair	S_0^2*	CN	Bond Length (Å)*	ΔE_0 (eV)*	σ^2 (Å^2)*
ZnO	Zn—O	0.97	4	1.97	3.0	0.005
MFU-4*l*	Zn—Cl	0.93	0.8	2.17	1.6	0.004
MFU-4*l*-OH	Zn—O	0.93	0.8	1.93	1.6	0.005

*The average error in S_o^2 is 0.2, in bond length is 0.2 Å, in ΔE_0 is 2.0 eV, in σ^2 is 0.002 Å

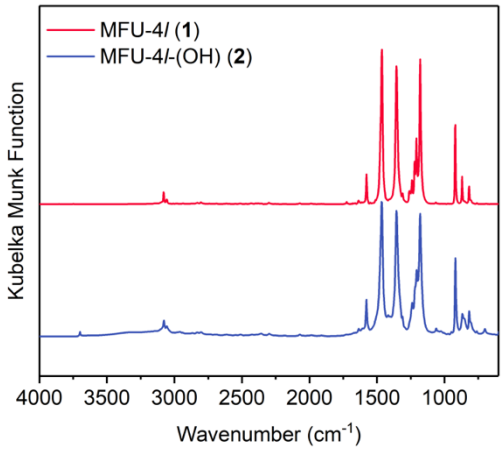

Figure A9. DRIFT spectrum of MFU-4*l* (1) (top, red trace) and MFU-4*l*-(OH) (2) (bottom, blue trace).

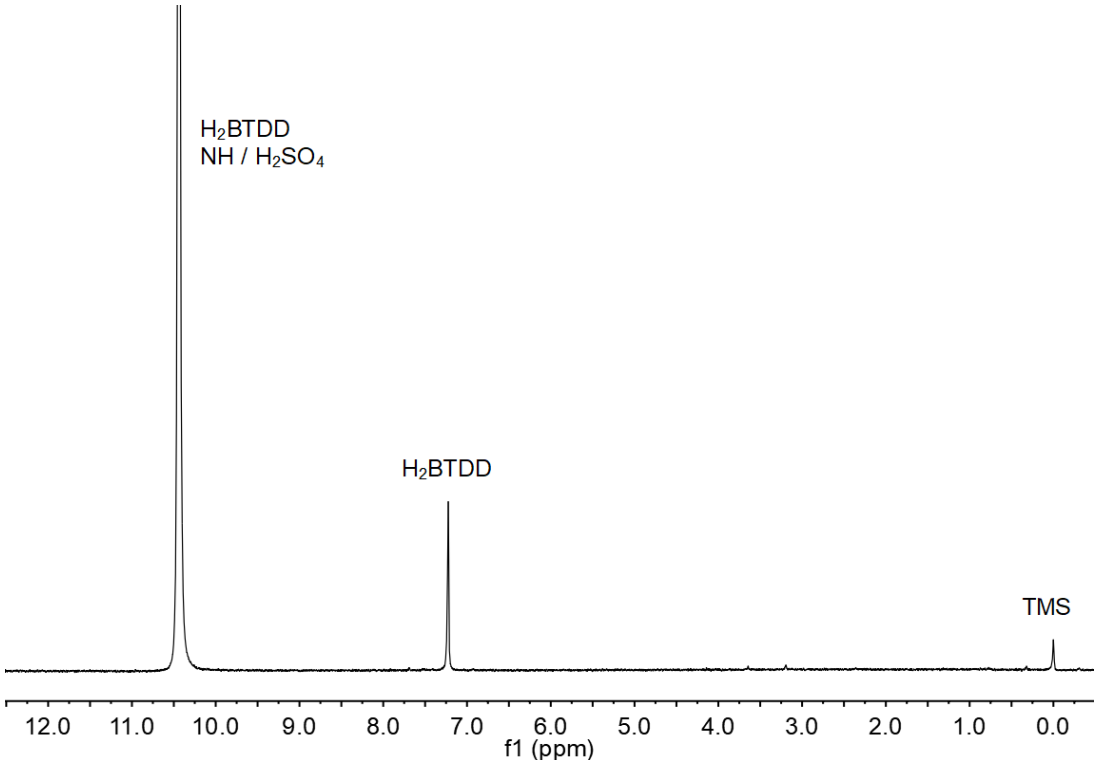

Figure A10. Digestion of MFU-4*l*-(OH) in D_2SO_4. ^1H NMR spectrum (D2SO4, 300 MHz) of MFU-4*l*-(OH) (~3.5 mg) digested in D2SO4. The ^1H NMR spectrum shows the presence of the ligand in the digested sample. No signals corresponding to the ^{n}Bu4N$^+$ cation was observed in the spectrum revealing the cation does not remain in the MOF after anion exchange.

Isosteric Heats of Adsorption Calculations

To determine the isosteric heat of adsorption (Qst) for substrate binding, we measured isotherm data for each material at a minimum of three different temperatures. Initial attempts to fit the adsorption isotherm data to the Dual-Site Langmuir model (eq. 1)

resulted in a poor fit in the low-pressure region (Figure A11) producing heat of adsorption values (Figure A12) of questionable accuracy. As a result, the adsorption isotherms at three temperatures were simultaneously fitted to a Virial-type expression (eq. 2).[841] The virial model has been extensively used to calculate heats of adsorption from isotherm data as the isotherms plot coverage as a function of pressure and provides more reasonable values of Qst irrespective of the adsorption mechanism.[842] Fitting with the virial equation provided better low pressures fits (Figure A13)

$$n = \frac{q_A b_A P}{1+b_A} + \frac{q_B b_B P}{1+b_B} \quad (1)$$

$$\ln p = \ln n + \left(\frac{1}{T}\right) \sum_{i=0}^{m} a_i n^i + \sum_{i=0}^{n} b n^i \quad (2)$$

$$Q_{st} = -R \sum_{i=0}^{m} a_i N^i \quad (3)$$

The fitting parameters for each adsorbent is given below the respective figure. The number of virial coefficients was considered satisfactory when the fit did not improve with added a or b parameters. The quality of the fit was evaluated by comparing adjusted R^2 values and the residual sum of squares, in addition, to visually inspection of the fit. It should be noted; some fits feature significant derivations between the virial model and the experimental data at higher pressures. The values of the virial coefficients a_0 through a_m were then used to calculate the isosteric heat of adsorption using equation 3.

For CO_2 adsorption of MFU-4*l*, the heat of adsorption at the zero-coverage limit was also calculated from the Henry's constant KH (cm g^{-1} kPa^{-1}), which can be determined from the linear region of the isotherm at very low pressures. In the linear region the amount

adsorbed follows Henry's Law (eq. 4). The heat of adsorption is calculated using the Clausius-Clapeyron equation.

$$n = K_H P \tag{4}$$

CO_2 adsorption for MFU-4l-(OH)

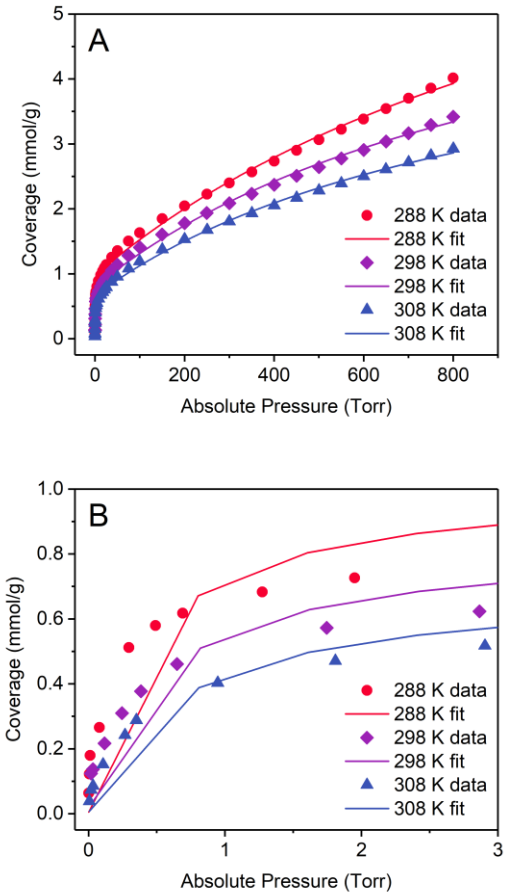

Figure A11. CO_2 adsorption isotherms of 2 measured at 288 K (red circles), 298 K (purple diamonds), and 308 K (blue triangles). (a) shows the full pressure range and (b) shows the low-pressure region. The symbols represent data and the lines represent the DSL model fit.

Given the poor fits at low pressure, the DSL model provided an unreasonable Q_{st} (Figure S12). As a result, we did not use the DSL model to determine the Q_{st}.

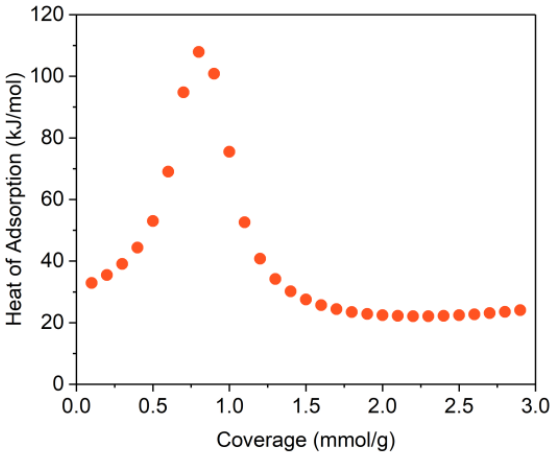

Figure A12. Coverage-dependent CO_2 adsorption enthalpy for 2 as obtained from Dual-Site Langmuir model of the CO_2 sorption isotherms. Poor fit in the low-pressure region indicates heat of adsorption between 0 and 1 mmol/g coverage is of questionable accuracy.

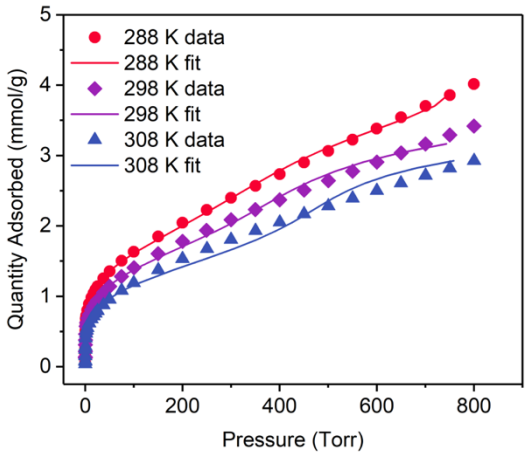

Figure A13. CO_2 adsorption isotherms of 2 measured at 288 K (red circles), 298 K (purple diamonds), and 308 K (blue triangles). The lines represent Virial fitting.

Table A3. Virial fitting parameters for the adsorption of carbon dioxide by MFU-4*l*-(OH).

index	a_i	b_i	Standard error a_i	Standard error b_i
0	-9730.85061	29.74961	726.0938	2.42089
1	541.98762	7.09937	1978.2961	6.57413
2	3045.31104	-12.86594	1459.1224	4.78533
3	-973.31472	2.91462	339.78303	0.98805
4	83.64366		49.61208	
5	-9.7301		5.08917	
R^2	0.9971			
chi squared	0.0377			

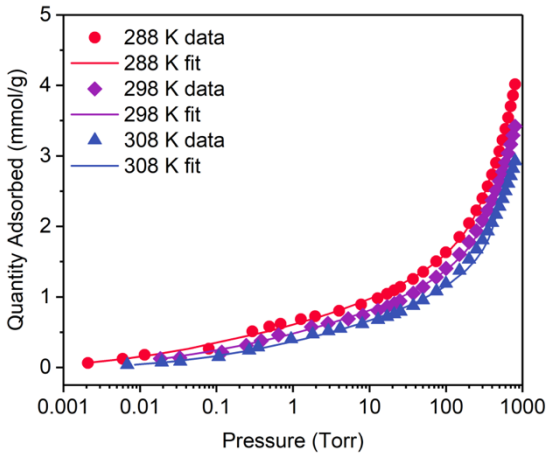

Figure A14. CO_2 adsorption isotherms of 2 measured at 288 K (red circles), 298 K (purple diamonds), and 308 K (blue triangles). The logarithmic scale is shown to display the good fit at low pressures. The lines represent the Virial fitting of the adsorption isotherms.

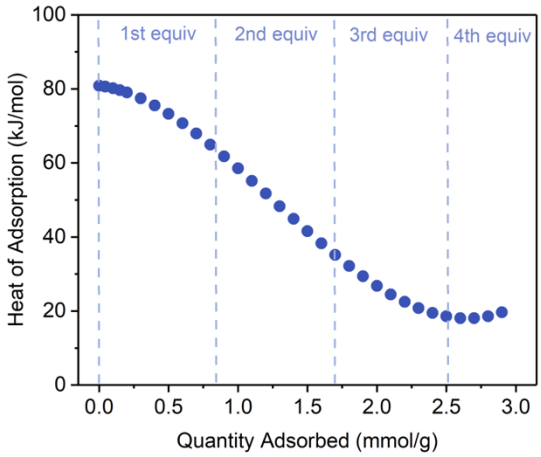

Figure A15. Coverage-dependent CO_2 adsorption enthalpy for 2 as obtained from fitting the Virial equation to three different temperature CO_2 isotherms. The lines indicate the number of equivalents of CO_2 per metal node (1^{st} equiv., 0.85 mmol/g; 2^{nd} equiv., 1.70 mmol/g; 3^{rd} equiv., 2.55 mmol/g). The total number of Zn—OH sites is 3.41 mmol/g.

CO_2 adsorption MFU-4*l*

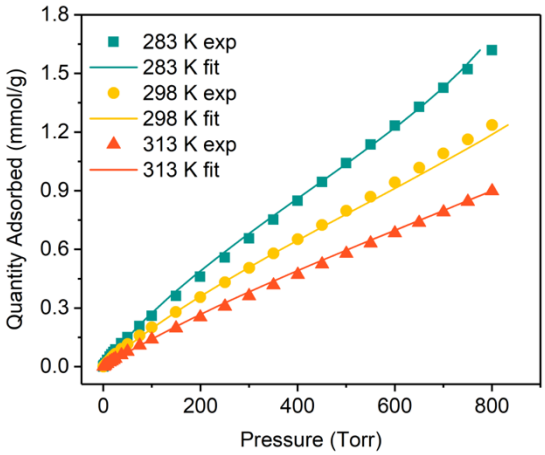

Figure A16. CO_2 adsorption isotherms of 1 measured at 283 K (turquoise squares), 298 K (yellow circles), and 313 K (orange triangles). The lines represent the Virial fitting.

Table A4. Virial fitting parameters for the adsorption of carbon dioxide by MFU-4*l*

index	a_i	b_i	Standard error a_i	Standard error b_i
0	-2266.96577	13.72805	726.0938	1.00388
1	497.43778	-1.02126	1978.2961	2.18717
2	-79.71544		57.70613	
R^2	0.9879			
chi squared	0.0758			

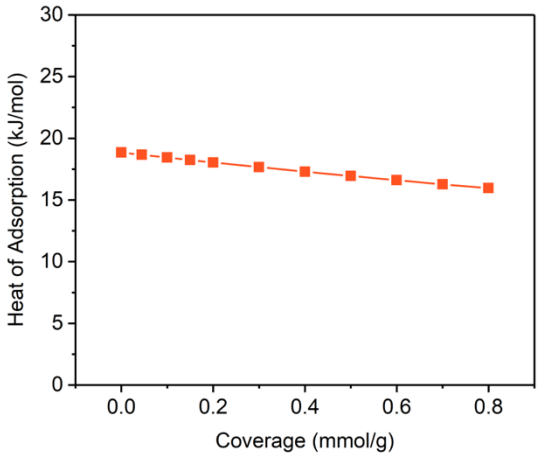

Figure A17. Coverage-dependent CO_2 heat of adsorption for 1 as obtained from fitting the Virial equation to three different temperature CO_2 isotherms. The Q_{st} at zero coverage is 18.8 kJ/mol.

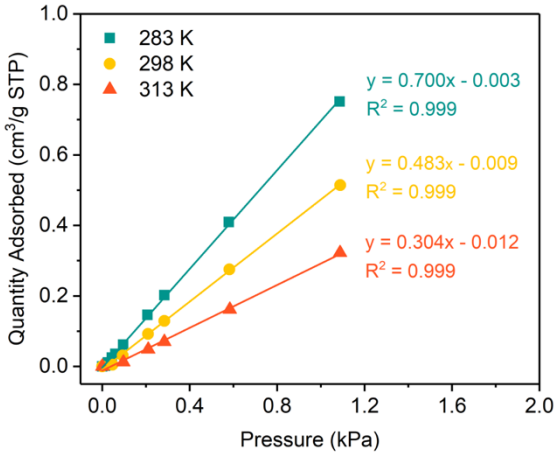

Figure A18. Determination of the Henry's constant for CO_2 adsorption in MFU-4*l* (1).

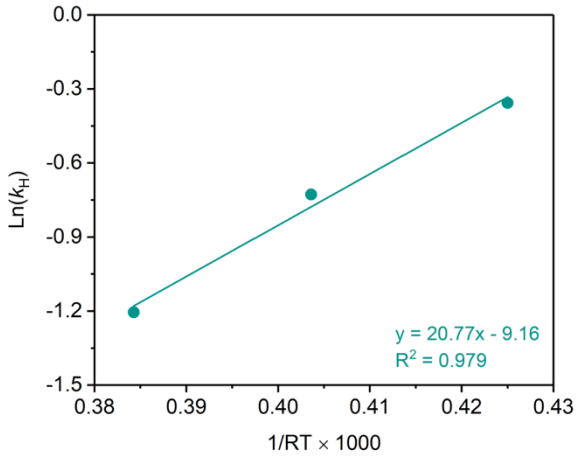

Figure A19. lnK_H versus 1/RT plots for CO_2 adsorption in MFU-4*l*. Using Henry's constant method, the heat of adsorption at zero coverage is 20.8 ± 2 kJ/mol.

Diffuse Reflectance IR Spectroscopy

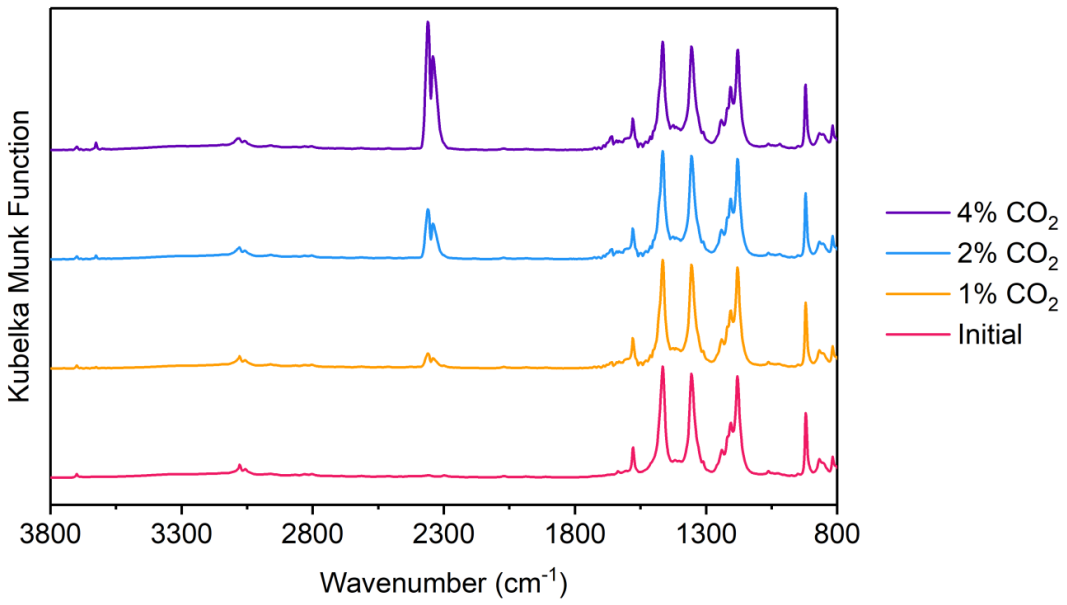

Figure A20. DRIFT spectra for CO_2 adsorption by MFU-4*l*-(OH) (2) at different concentrations of CO_2. The concentration was increased from 1 to 2 to 4%. The difference spectrum in Figure S21 reveals the formation of bicarbonate ligand.

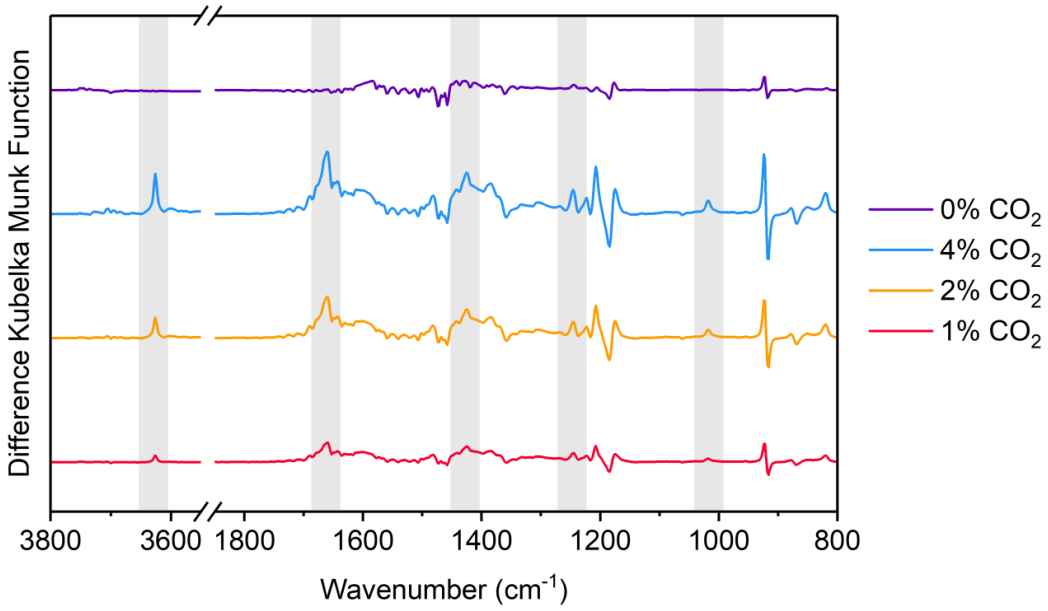

Figure A21. Difference DRIFT spectra for CO_2 adsorption by MFU-4*l*-(OH) (2) at different concentrations of CO_2 in argon. The concentration was increased from 1 to 2 to 4% and then decreased to 0% CO_2. The shaded areas represent new bands that grow in with increasing CO_2 concentration that are associated with a Zn—CO_3H group, notably, these disappear when exposed to 100% argon flow.

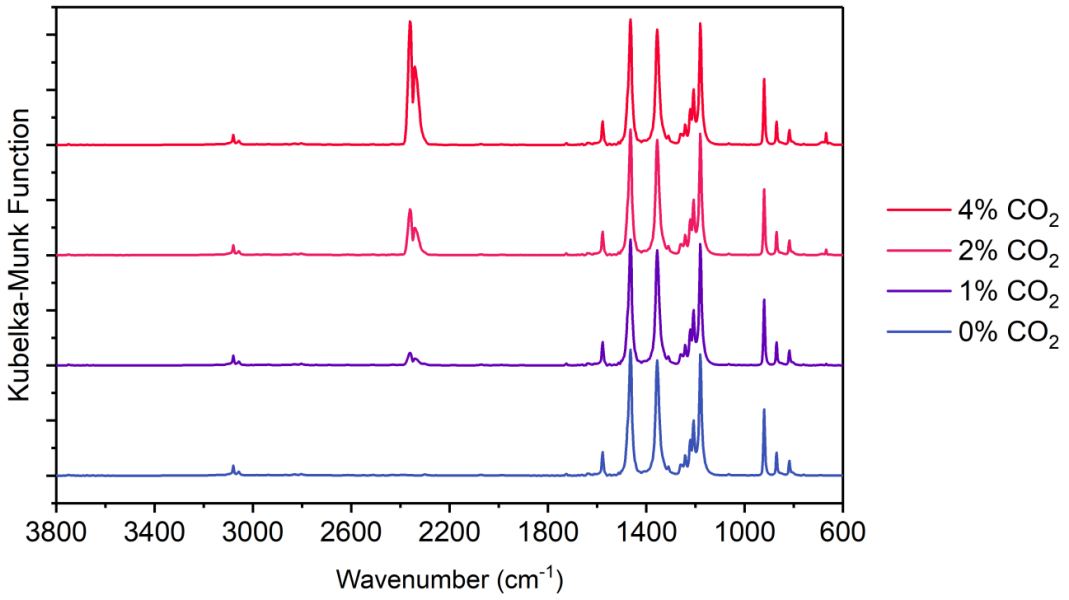

Figure A22. DRIFT spectra of MFU-4*l* (1) with increasing concentrations of CO_2. The peak at 2362 cm^{-1} is the asymmetric stretch of gaseous CO_2 and indicates no reaction with the MFU-4*l* framework. The difference spectrum is given below in Figure S23.

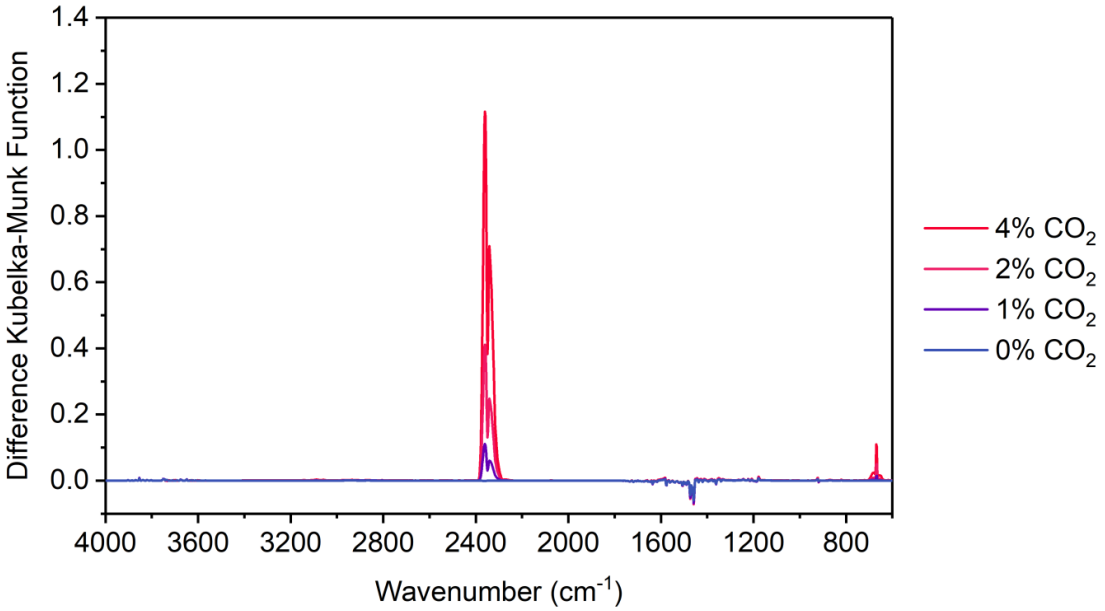

Figure A23. Difference DRIFT spectra of MFU-4*l* (1) under increasing concentrations of CO_2. The peak at 2362 cm^{-1} is the asymmetric stretch of gaseous CO_2. No other peaks are observed indicating no reaction between CO_2 and MFU-4*l*.

Water Stability of MFU-4*l*-(OH)

MFU-4*l*-(OH) was submerged in water for a set period (6 & 24 hours) and then analyzed by powder X-ray diffraction. Prior to recording the PXRD pattern, the material was washed with methanol (3 × 2 mL) to allow for better drop casting on to the ZBH plate.

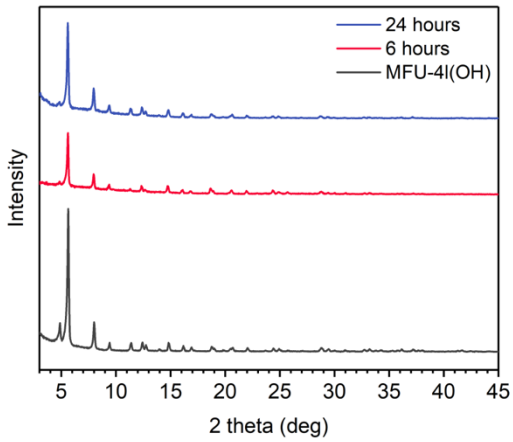

Figure A24. Powder X-ray diffraction patterns for MFU-4*l*-(OH) (grey trace), after submersion in water for 6 hours (red trace), and after submersion in water for 24 hours (blue trace). The materials remained crystalline after submersion in water.

Buffer Stability Studies

The stability of MFU-4*l*-(OH) in a variety of different buffer systems was examined. Buffer systems with pH of 8.0–9.0 were tested. A sample of MFU-4*l*-(OH) (~15 mg) was submerged in a buffer solution (3 mL) for 3 hours. The solution was decanted, and the MOF was washed with MeOH (3 × 10 mL). A material was analyzed by PXRD.

Table A5. Buffer systems tested for water stability of MFU-4*l*-OH

Entry	Buffer System	Buffer Concentration	pH
1	K_3PO_4 / NaOH	1.0 M	8.0
2	TRIS-HCl	1.0 M	8.0
3	$NaHCO_3$ / Na_2CO_3	0.2 M	9.0
4	HEPES	50 mM	8.0
5	Pure water	n/a	7.0

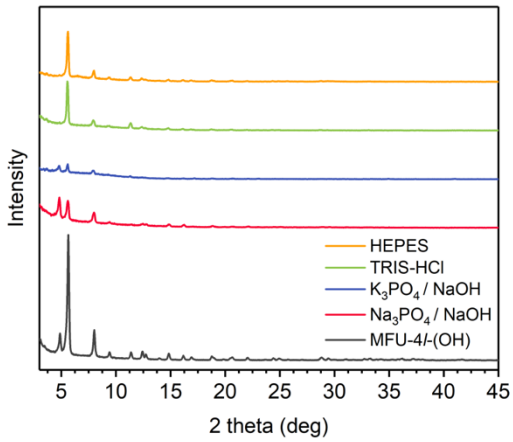

Figure A25. Powder X-ray diffraction of MFU-4*l*-(OH) (2) after submersion in buffer solution. After submersion in HEPES and TRIS-HCl the crystallinity is retained as indicated by the PXRD pattern. The phosphate buffers lead to a significant increase in the feature at ~4.8°, which is ascribed to the exchange of the hydroxide ligand for phosphate of the buffer. These materials exhibit IR stretches consistent with phosphate post-exposure.

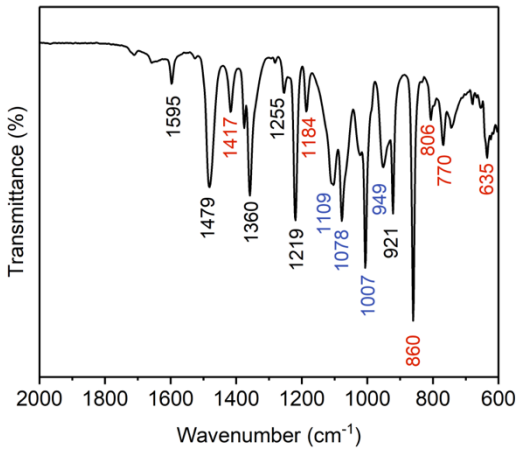

Figure A26. IR spectra of MFU-4*l*-(OH) after submersion in sodium phosphate / sodium hydroxide buffer solution. The wavenumbers marked in black are associated with the MOF framework and those marked in blue are assignable to phosphate stretches. Bands denoted by red are unknown new features.

^{18}O exchange between H_2O and CO_2 catalyzed by MFU-4*l*-(OH)

A custom-made batch reactor (Figure S27) was charged with MOF (~10 mg), MeCN (0.5 mL), and $H_2{}^{18}O$ (0.1 mL). The solution was degassed by three nitrogen / vacuum cycles, and then backfilled with CO_2 (15 psig). The distribution of carbon dioxide isotopologues was monitored periodically using gas chromatography-mass spectrometry (GC/MS). The ratio of its isotopologues, $C^{18}O_2$, $C^{16,18}O_2$, and $C^{18}O_2$, was determined from the relative abundances of *m/z* 44, 46, and 48 in the mass spectrum.

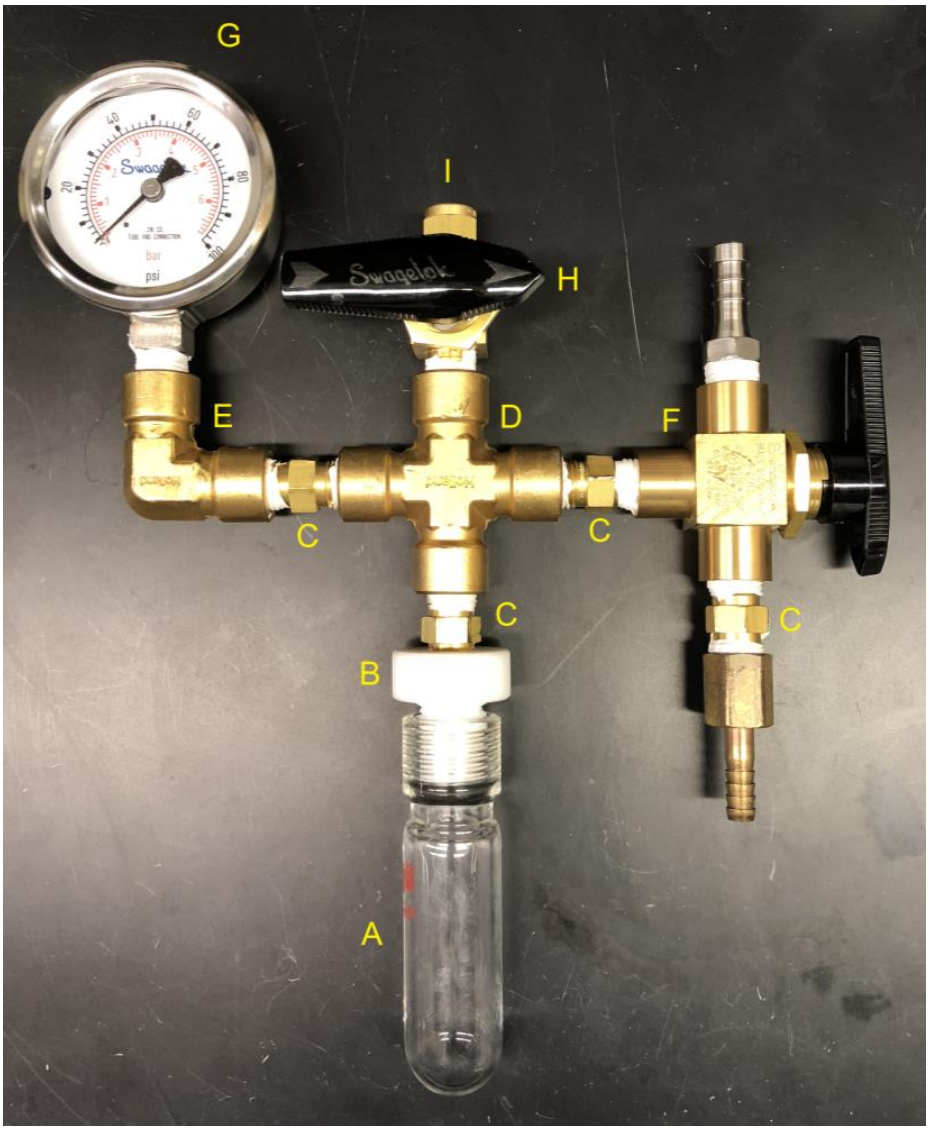

Figure S27. Picture of the custom-made reactor setup. (A) 15 mL Pressure Tube (Ace Glass, 8648 product family); (B) Adapter NPT tubing to Ace-Thred (Ace Glass, 5844-74); (C) 1⁄4" Brass Male Hex Nipple NPT (Swagelok, B-4-HN); (D) Brass Pipe Fitting, Cross 1⁄4", Female NPT (Swagelok, B-4-CS); (E) Brass Pipe Elbow 1⁄4", Female NPT (Swagelok, B-4-E); (F) Brass 1-Piece 40 Series 3-way Ball Valve (Swagelok, B-43XF4); (G) 100 psig SS Gauge (Swagelok, PGI-63C-PG100-LAOX); (H) Brass 1-Piece 40 Series Ball Valve (Swagelok, B- 43M4-S4); (I) Septum 9.5 mm.

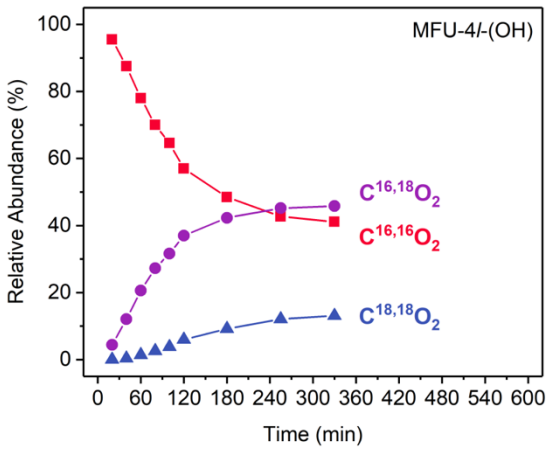

Figure A28. Normalized relative abundance of the carbon dioxide isotopologues upon exposure of carbon dioxide to $H_2{}^{18}O$ and MFU-4*l*-(OH) (2) in MeCN. Time taken to reach an equilibrium mixture of CO_2 isotopologues was 5.5 hours.

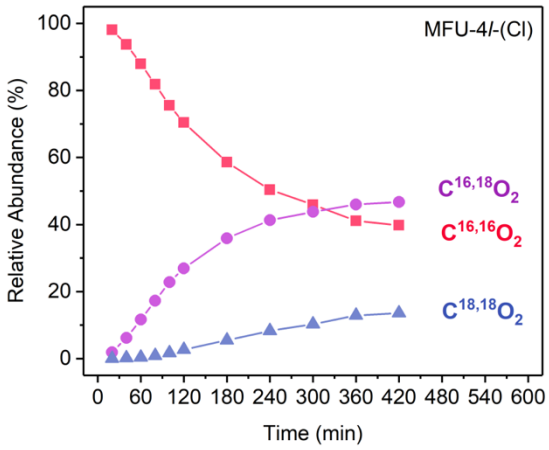

Figure A29. Normalized relative abundance of the carbon dioxide isotopologues upon exposure of carbon dioxide to $H_2{}^{18}O$ and MFU-4*l*-(Cl) (1) in MeCN. Time taken to reach an equilibrium mixture of CO_2 isotopologues was ~7 hours.

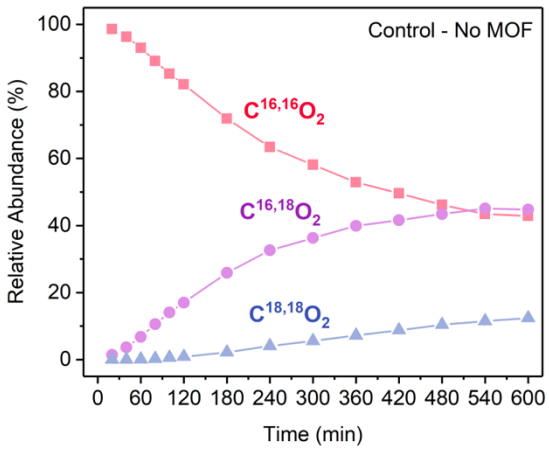

Figure A30. Relative abundance of the carbon dioxide isotopologues versus time for the control reaction between $H_2{}^{18}O$ and CO_2 in MeCN.

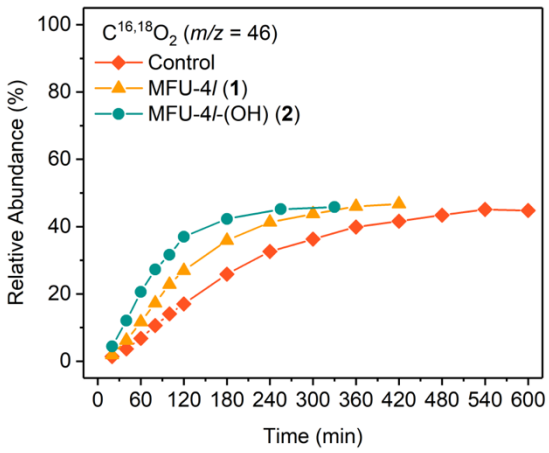

Figure A31. Comparison of the increase in relative abundance of $C^{16,18}O_2$ for reactions with 1, 2, and the control.

Catalytic hydrolysis of 4-nitrophenyl acetate

The hydrolysis reactions were performed in 50 mL centrifuge tubes with added 4-NPA in acetonitrile and 50 mM HEPES buffer solution. The concentration of 4-nitrophenol was monitored by time-dependent UV-vis spectroscopy by measuring its absorption band at 405 nm. A calibration curve was first prepared using known quantities of 4-nitrophenol in 50 mM HEPES solution.

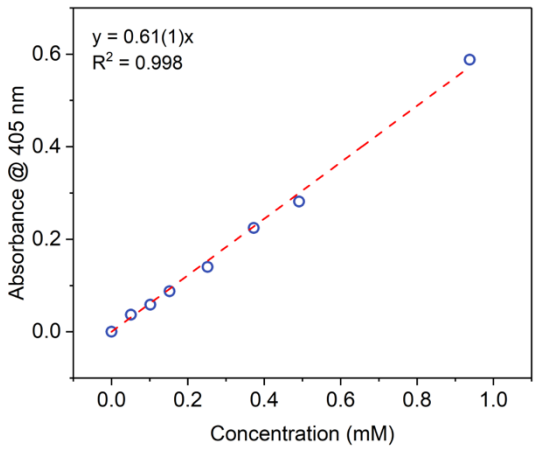

Figure A32. Calibration curve for 4-nitrophenol in 50 mM HEPES buffer solution. The calculated extinction coefficient is 627 M^{-1} cm^{-1}.

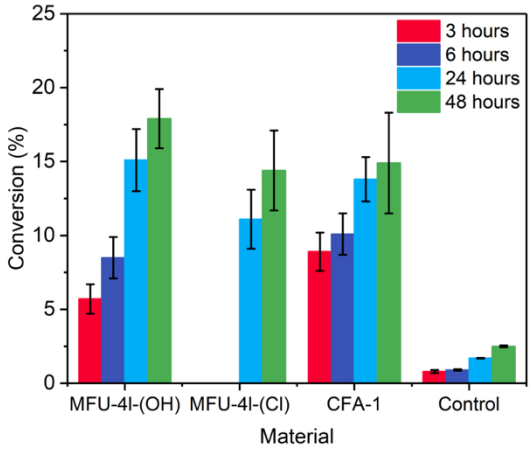

Figure A33. The percent conversion of 4-nitrophenyl acetate to 4-nitrophenol under four different conditions (catalysts: MFU-4*l*-(OH) (2), MFU-4*l* (1), CFA-1, and control) at four different time points (3, 6, 24, and 48 hours). Conditions: catalyst loading, 8-10 mol% (MFU-4*l*-(OH) (2) and MFU-4*l* (1)) or 12-14 mol% (CFA-1), 50 mM HEPES buffer, 1 mM 4-NPA. The mol% catalyst is calculated from the number of peripheral Zn–X sites (four per molecular formula). Each experiment run was repeated a minimum of three times and the error bars represent one standard deviation. Small particles of MFU-4*l* interfered with UV-vis measurements at 3 and 6-hour time points in all three measurements. Notably, the control reaction indicates the hydrolysis of 4-nitrophenyl acetate occurs with very low conversion without a MOF.

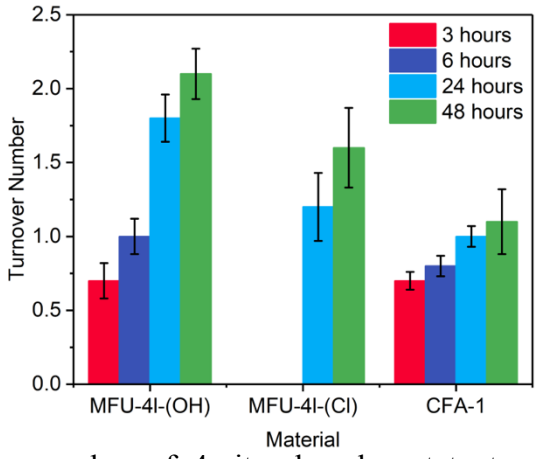

Figure A34. Turnover number of 4-nitrophenyl acetate to 4-nitrophenol under four different conditions (catalysts: MFU-4*l*-(OH), MFU-4*l*-(Cl), CFA-1, and control) at four different time points (3, 6, 24, and 48 hours). Conditions: catalyst loading, 8-10 mol% (MFU-4*l*-(OH) (2) and MFU-4*l* (1)) or 12-14 mol% (CFA-1), 50 mM HEPES buffer, 1 mM 4-NPA. The mol% catalyst is calculated from the number of peripheral Zn—X sites (four per molecular formula). Each experiment run was repeated a minimum of three times and the error bars represent one standard deviation.

Table A6. Data for the hydrolysis of 4-nitrophenyl acetate using different MOF catalysts

Material	**Conversion (mmol/mmol) 3 hours**	**Conversion (mmol/mmol) 6 hours**	**Conversion (mmol/mmol) 24 hours**	**Conversion (mmol/mmol) 48 hours**
Control	0.8 ± 0.1 % (n/a)	0.9 ± 0.1 % (n/a)	1.7 ± 0.2 % (n/a)	2.5 ± 0.1 % (n/a)
MFU-4*l*-OH	5.7 ± 1.0 % (0.7 ± 0.1)	8.5 ± 1.4 % (1.0 ± 0.1)	15.1 ± 2.1 % (1.8 ± 0.2)	17.9 ± 2.1 % (2.1 ± 0.2)
MFU-4*l*	n/a	n/a	11.1 ± 2.2 % (1.2 ± 0.2)	14.4 ± 2.7 % (1.6 ± 0.3)
CFA-1	8.9 ± 1.4 % (0.7 ± 0.1)	10.1 ± 1.4 % (0.8 ± 0.1)	13.8 ± 1.5 % (1.0 ± 0.1)	14.4 ± 2.7 % (1.6 ± 0.3)

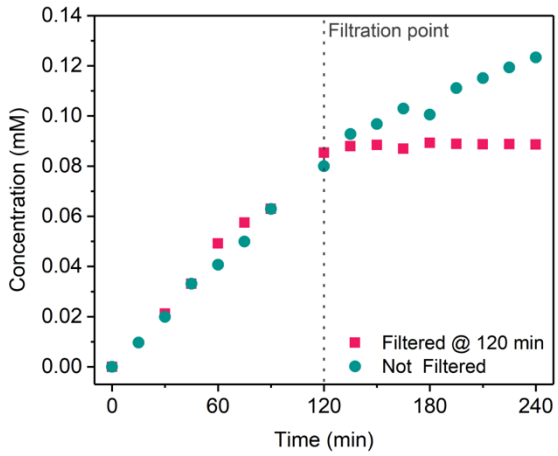

Figure A35. Change in absorbance over time for the hydrolysis of 4-nitrophenyl acetate in the presence of MFU- 4*l*-(OH) (2). Two reaction vessels were charged with 45 mL of 50 mM HEPES buffer and 5 mL of 4-nitrophenyl acetate in acetonitrile ([4-NPA] = 1 mM, 0.05 mmol) and 2 (3 mg, 0.003 mmol, 24 mol% per Zn-OH site). One reaction flask was filtered after 120 minutes and the other was left as is. The reaction was monitored by tracking the 405 nm signal of 4-nitrophenol by UV-vis spectroscopy. The observed initial reaction rate is 0.7 μM/min.

Table A7. Binding energies for sequential addition of CO_2 to $Zn_5(OH)_4(bibta)_3$ cluster

Addition of CO_2	**Binding Energy (kJ/mol) using PBE/6-31G****	**Binding Energy (kJ/mol) using PBE/6-311G****
First	−56.7	−50.4
Second	−48.2	−42.0
Third	−48.6	−42.0
Fourth	−46.1	−37.8

APPENDIX F

EXPERIMENTAL DETAILS AND SUPPLEMENTARY INFORMATION FOR:

Record-Setting Sorbents for Reversible Water Uptake by Systematic Anion-Exchanges in Metal-Organic Frameworks

Adam J. Rieth, Ashley M. Wright, Grigorii Skorupskii, **Jenna L. Mancuso**, Christopher H. Hendon, and Mircea Dincă

Section A1. General Information. Materials and Methods

$NiCl_2 \cdot 6H_2O$ (Strem Chemicals), HCl (32-35%, BDH – VWR Analytic) methanol (99.9%, VWR), *N*,*N*-dimethylformamide (99.8%, Millipore), 1-chloro-2,4-dinitrobenzene (99%, TCI), Catechol (99%, Sigma-Aldrich), K_2CO_3 (99%, Sigma-Aldrich), Sn Powder (150 micron, 99.5%, Sigma-Aldrich), diethyl ether (99%, Sigma-Aldrich), Trimethylsilyl bromide (97%, Sigma- Aldrich), Acetone (ACS grade, Macron Chemical), Fuming HNO_3 (90% min, Macron), H_2SO_4 (95-98%, BDH Chemicals), Acetic Acid (ACS grade, VWR BDH Chemicals), $NaNO_2$ (98%, Alfa Aesar), Ethanol (200 proof, Koptec), KOH (ACS grade, BDH chemicals), CsF (99%, Beantown Chemicals) were used as received. Benzene

(ACS grade, EMD) was purged with argon, and subjected to three freeze-pump-thaw cycles before bringing into a nitrogen-filled glovebox and stored over 3 Å molecular sieves.

Powder X-ray diffraction (PXRD) patterns were recorded with a Bruker D8 Advance II diffractometer equipped with a θ/2θ Bragg-Brentano geometry and Ni-filtered CuKα radiation ($K\alpha_1$ = 1.5406 Å, $K\alpha_2$ = 1.5444 Å, $K\alpha_2/K\alpha_1$ = 0.5). The tube voltage and current were 40 kV and 40 mA, respectively. Samples for PXRD were prepared by placing a thin layer of the appropriate material on a zero-background silicon crystal plate.

Nitrogen adsorption isotherms were measured by a volumetric method using a Micromeritics ASAP 2020 gas sorption analyzer. A typical sample of ca. 40 mg of metal-organic framework, pre-activated at 100°C to remove all residual solvent, was transferred in an Ar filled glovebox to a pre-weighed analysis tube. The tube with sample inside was weighed again to determine the mass of the sample. The tube was capped with a Micromeritics TranSeal, brought out of the glovebox, and transferred to the analysis port of the gas sorption analyzer. Free space correction measurements were performed using ultra-high purity He gas (UHP grade 5, 99.999% pure). Nitrogen isotherms were measured using UHP grade nitrogen. All nitrogen analyses were performed using a liquid nitrogen bath at 77 K. Oil-free vacuum pumps were used to prevent contamination of sample or feed gases.

Water vapor adsorption and desorption isotherms were measured by a volumetric method using a Micromeritics ASAP 2020 gas sorption analyzer with a vapor dose option and a heated manifold. A typical sample of ca. 40 mg of metal-organic framework, pre-

activated at 100°C to remove all residual solvent, was transferred in an Ar filled glovebox to a pre-weighed analysis tube. The tube with sample inside was weighed again to determine the mass of the sample. The tube was capped with a Micromeritics TranSeal, brought out of the glovebox, and transferred to the analysis port of the gas sorption analyzer. Free space correction measurements were performed using ultra-high purity He gas (UHP grade 5, 99.999% pure). Water vapor adsorption isotherms were measured using Milli-Q water. The water was degassed on the ASAP 2020 manifold prior to measurement. All water analyses were performed using water baths held at constant temperature with a recirculating chiller. The manifold was held 10 °C above the temperature of the sample water bath, and the vapor dosing tube was held 15 °C above the temperature of the sample water bath. Oil-free vacuum pumps were used to prevent contamination of sample or feed gases.

Variable-temperature water vapor adsorption isotherms as well as all water cycling experiments were measured by a gravimetric method using a Hiden Analytical XEMIS microbalance with a vapor dose option and a heated manifold. A typical sample of ca. 5 mg of metal-organic framework, pre-activated at 100°C to remove all residual solvent, but later exposed to air, was loaded into the microbalance basket. All water analyses were performed using a programmable water bath with a recirculating chiller. Oil-free vacuum pumps were used to prevent contamination of sample or feed gases.

Diffuse reflectance infrared Fourier transform spectroscopy (DRIFTS) measurements were performed using a Bruker Tensor 37 IR spectrometer equipped with a liquid nitrogen

cooled mercury cadmium telluride detector and a Pike DiffusIR accessory. A sample of Co_2Cl_2BTDD, pre-activated at 150 °C under vacuum to remove all water, was diluted with KBr in a ratio of approximately 1:5 (MOF:KBr) in an argon-filled glovebox. The resulting solid solution was then packed into a ceramic cup and sealed in the DiffusIR cell. The cell was brought out of the box, and a static dry spectrum was recorded with the cell sealed. Two gas streams of flowing argon (UHP grade 5.0, Airgas), one wet (bubbled through a fine frit through MilliQ H_2O) and one dry, were each flow controlled using mass flow controllers (MFCs), and joined together at a T fitting before connecting to the DRIFTS cell. The wet stream and dry stream were controlled via the mass flow controllers (MFCs) to change relative humidity (RH) every 20 minutes (a time period previously demonstrated to result in saturation of the IR spectrum at all loadings). The MFCs were controlled such that the total flow rate was constant at 1 liter per minute (LPM) (e.g. for 40% RH, 0.4 LPM wet, 0.6 LPM dry). The temperature for all measurements was 20 °C. Spectra were recorded at the end of the period at which the sample atmosphere was at each RH, every 20 minutes. Data was transformed using the Kubelka-Munk function.[845]

Energy dispersive X-ray spectroscopy (EDS) analyses were conducted using a FEI Tecnai Multipurpose Digital TEM, using the EDAX system (Windowless detector) with Team software, operated with an acceleration voltage of 100 keV. Samples were drop-cast onto Cu TEM grids from powder dispersed in methanol.

X-ray photoelectron spectroscopy (XPS) was performed at the Harvard Center for NanoscaleSystems (Cambridge, MA, USA) on a Thermo Scientific K-Alpha system

equipped with an Al source and 180° double focusing hemispherical analyzer and 128-channel detector using a 400 μm X-ray spot size.

NMR Spectroscopy was performed in the Massachusetts Institute of Technology (MIT) Department of Chemistry Instrumentation Facility (DCIF) using a Bruker AVANCE NEO 400 MHz spectrometer equipped with a broadband probe.

High-resolution synchrotron powder X-ray spectroscopy was performed using the mail-in program at beamline 11-BM at the Argonne National Laboratory (ANL) Advanced Photon Source (APS). Samples were packed into a Kapton capillary and the ends were sealed using epoxy. Samples were mounted into Kapton capillary sample holders provided by the beamline and shipped to the beamline. Powder patterns were collected with the standard automated experimental setup[102,812,813] at 100 K using 0.412805 Å X-rays.

Thermogravimetric analysis (TGA) was performed on a TA Instruments Q500 Thermogravimetric Analyzer at a heating rate of 1 °C/min under a nitrogen gas flow of 90 mL/min.

Elemental Analyses were performed by Robertson Microlit Laboratories, Ledgewood NJ.

	%C	**%H**	**%N**
Ni_2Cl_2BTDD			
Calc. (Dry)	31.85	0.89	18.57
Calc. (2.38 H_2O)	29.08	1.79	16.96
Found	29.45	2.52	16.74
Ni_2F_2BTDD			
Calc. (Dry)	34.35	0.96	20.03
Calc. (2.26 H_2O)	31.31	1.87	18.26
Found	32.10	2.72	17.34
Ni_2Br_2BTDD			
Calc. (Dry)	26.62	0.74	15.52
Calc. (2.61 H_2O)	24.49	1.58	14.28
Found	24.88	1.77	13.74
$Ni_2(OH)_2BTDD$			
Calc. (Dry)	34.68	1.46	20.22
Calc. (2.13 H_2O)	31.73	2.28	18.51
Found	32.59	2.76	17.28

Calculation of the Characteristic Curve

In order to make the loading dependent on only one free variable ("energy") rather than two (p,T), we constructed a characteristic curve.[715,717,747] The energy parameter used is the adsorption potential (*A*), which is the Gibbs free energy of adsorption with the inverse sign:

$$A = RT \ln\left(\frac{p_o(T)}{p}\right)$$

p_o is the saturation vapor pressure of the working fluid at the temperature of analysis, p is the pressure at each loading value, R is the ideal gas constant, and T is the analysis temperature.

Isotherms measured at different temperatures should collapse onto a single characteristic curve. Water isotherms for **Ni2Cl2BTDD** and **Ni2Br2BTDD** were measured at 283 K, 293 K, and 298 K. After calculating the characteristic curve using each of these isotherms, it is evident that they all collapse into a single characteristic curve confirming the validity of the characteristic curve model.

Calculation of the Enthalpy of Adsorption

The Clausius-Clayperon equation was used to determine the enthalpy of adsorption (ΔH_{012}). Loadings at two different temperatures were calculated from the characteristic curve, and these values were then used to calculate the heat of adsorption according to the integrated Clausius- Clayperon equation:

$$ln\frac{P_1}{P_2} = -\frac{\Delta H_{ads}}{R}\ln\left(\frac{1}{T_1} - \frac{1}{T_2}\right)$$

Section A2. Synthetic Methods.

Improved Synthetic Pathway to the Ligand H2BTDD

Literature methods for the synthesis of H2BTDD normally begin with the relatively expensive dibenzodioxin core.[844] We synthesized the ligand using more scalable methods beginning with 1-chloro-2,4-dinitrobenzene (**1**) according to the following scheme:

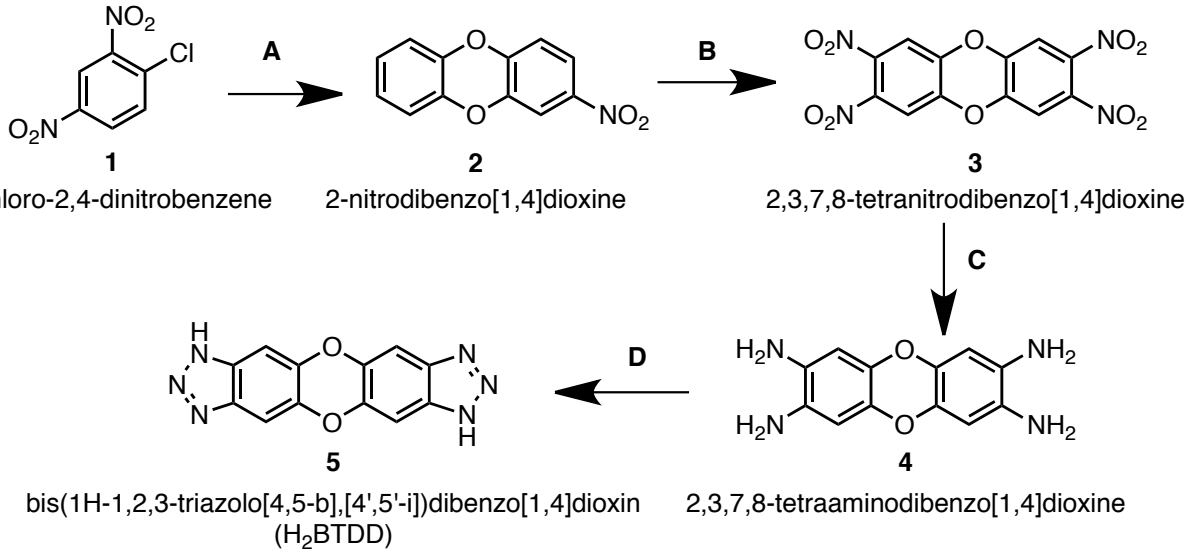

Scheme A1. Novel synthesis pathways to H_2BTDD, compound 5

Reaction A. To a warm (60 °C) stirring solution of 11.9 g catechol and 30.02 g potassium carbonate in 120 mL N-N-dimethylformamide in a 250 mL round bottom flask was added 20 g 1-chloro-2,4-dinitrobenzene. The mixture was heated to reflux for 3 hours, then cooled to room temperature. The mixture was then poured into 250 mL crushed ice. The solids were separated by filtration and washed with deionized water. The yellow solids obtained were dissolved in 1000 mL hot acetone, which was cooled to RT and 400mL DI water was slowly added. The resulting precipitate was filtered, washed with deionized water, and dried to obtain 22.9 g of 2-nitrodibenzo[1,4]dioxin (**2**). Purification can also proceed by recrystallization from a 50:50 mixture of chloroform and methanol to obtain yellow crystals.

Reaction B. In a 500mL RBF, 90 mL fuming nitric acid was added to 22.9 g 2-nitrodibenzo[1,4]dioxin. A condenser was equipped and 60 mL sulfuric acid added slowly

through the top of condenser. The reaction was heated at 70 °C overnight, then cooled to room temperature. The mixture was then filtered to obtain the product, 2,3,7,8-tetranitrodibenzo[1,4]dioxin (**3**).

Reaction C. In a 500 mL 2 neck round bottom flask, 9.2 g 2,3,7,8-tetranitrodibenzo[1,4]dioxin was added to 190 mL hydrochloric acid and a stir bar. A condenser was equipped. 48 g powdered Sn was added in small portions while stirring, slowly to minimize foaming of the reaction mixture. After all Sn was added and the off-gassing had subsided, the mixture was heated to reflux in an oil bath overnight. Then, the mixture was cooled to room temperature, then cooled in an ice bath, filtered, and washed with concentrated hydrochloric acid, ethanol, then diethyl ether. The obtained solids, the tetra-hydrochloric acid salt of 2,3,7,8- tetraaminodibenzo[1,4]dioxin (**4**), were dried under vacuum.

Reaction D. *Normally performed directly after isolation of product from D.* To a suspension of 6.4 g of the tetra-hydrochloric acid salt of 2,3,7,8-tetraaminodibenzo[1,4]dioxin, 60 mL acetic acid, and 20 mL deionized water in a 250 mL round bottom flask on a salted ice bath was added a solution of 2.75 g $NaNO_2$ and water (20 mL) over ten minutes. Note that before addition of the oxidant, the reaction is a white, free-flowing suspension and that over the addition (which was carried out drop wise) the reaction changes color from green to orange to brown. After addition was complete, the reaction was allowed to stir an additional 30 minutes at this temperature, then diluted with 50 mL H_2O. The product was filtered, washed with water, ethanol, and diethyl ether. Tan

solids were obtained that were the product, bis(1H-1,2,3-triazolo[4,5-b],[4′,5′-i])dibenzo[1,4]dioxin), or H2BTDD (**5**).

Synthesis of Ni_2X_2BTDD MOFs.

The synthesis of Ni2Cl2BTDD broadly followed methods in the literature[11] with increased acid concentration and temperature. In a typical synthesis, 200 mg H2BTDD (0.75 mmol) was dissolved in 200 mL N,N'-dimethylformamide (DMF) in a 500 mL jar by stirring and heating to approximately 100°C. The clear solution was then cooled to room temperature. In a separate 500 mL jar, 1.65 mmol (2.2 eq.) nickel chloride hydrate was dissolved in a solution of 200 mL methanol and 128 mL concentrated hydrochloric acid. The clear solutions were combined, capped, and heated to 100°C in an oven for 2 days. After this time, the reaction mixture was removed from the oven and filtered to collect the solids. The solids were washed with DMF and methanol. Solvent exchange of DMF was carried out by Soxhlet extraction with methanol for approximately 48 hours. The materials were then activated under dynamic vacuum at 150°C for 24 hours.

The synthesis of Ni2(OH)2BTDD followed the methods for the synthesis of Co2(OH)2BTDD and the smaller pore $Co_2(OH)_2$BBTA reported in the literature.[846] Briefly, beginning with the as-synthesized Ni2Cl2BTDD material, 10 eq. of KOH per Cl^- were dissolved in deionized water and added to a suspension of MOF in deionized water to form a 0.05 M hydroxide solution. The suspension was stirred overnight, then filtered, the solids were washed with DMF and methanol, and then activated at 100°C under dynamic vacuum.

To synthesize Ni_2F_2BTDD, 0.751 mmol as-synthesized Ni_2Cl_2BTDD material was suspended in 80 mL DMF. 5.7 g CsF (25 eq. per Cl^-) was added to the suspension, and it was stirred for 12 hours at room temperature. The suspension was then filtered on a frit and washed with 10 × 20 mL DMF and 10 × 20 mL methanol. The resulting powder was activated at 100 °C under dynamic vacuum.

To synthesize Ni_2Br_2BTDD, 100 mg of activated Ni_2F_2BTDD in a nitrogen-filled glovebox was suspended in 5 mL dry, degassed benzene. 0.066 mL (1.05 eq. per F^-) trimethylsilyl bromide was added from a syringe in one portion. The vial was left overnight, then filtered on a frit and the solids were washed with benzene. The resulting powder was activated at 100 °C under dynamic vacuum.

Section A3. Powder X-ray Diffraction Data.

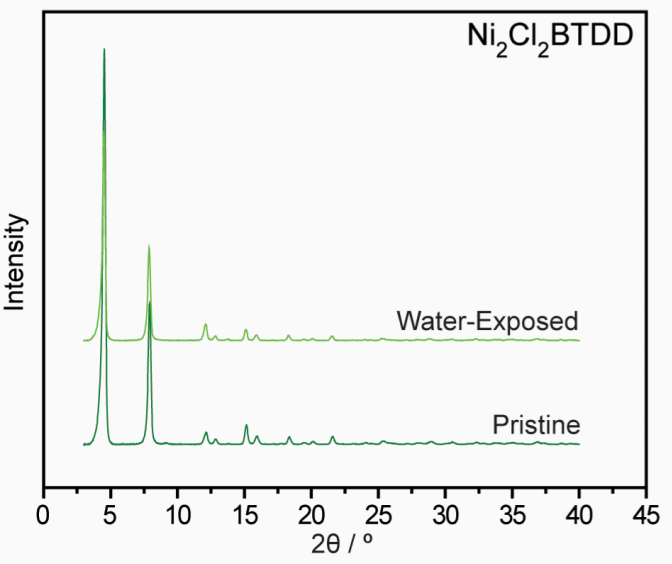

Figure A3.1. Powder X-ray diffractograms for activated samples of pristine Ni2Cl2BTDD (dark green), and after a single water isotherm (light green).

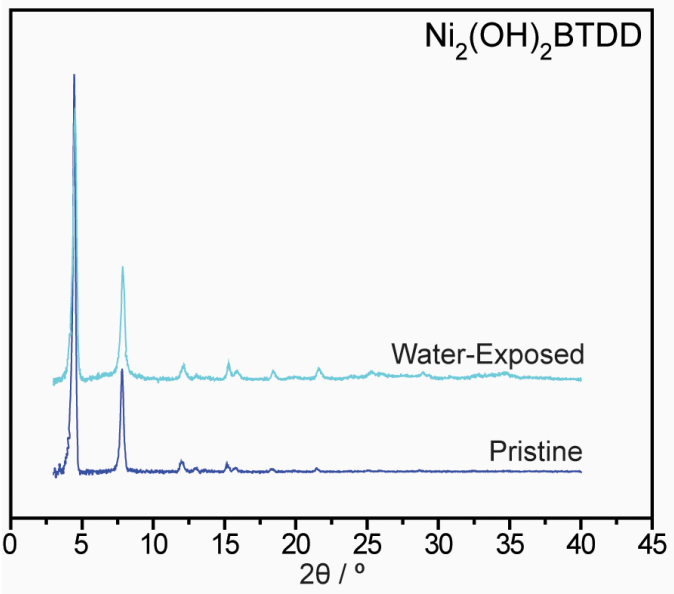

Figure A3.2. Powder X-ray diffractograms for activated samples of pristine Ni2(OH)2BTDD (dark blue), and after a single water isotherm (light blue).

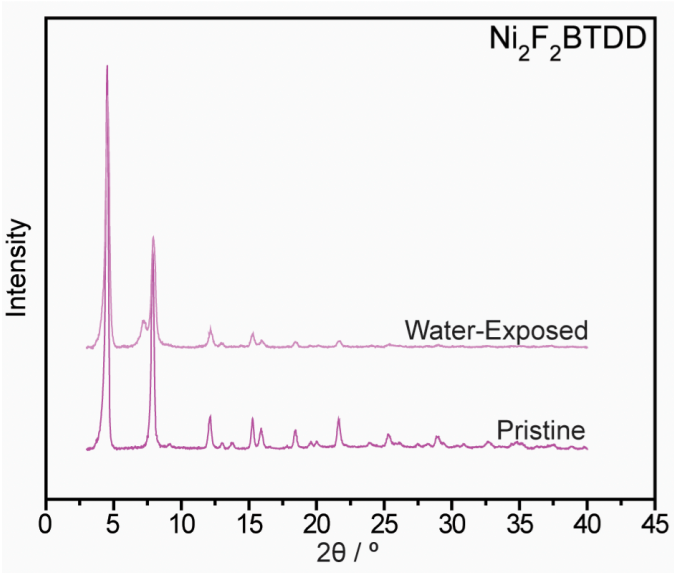

Figure A3.3. Powder X-ray diffractograms for activated samples of pristine Ni2F2BTDD (dark pink), and after a single water isotherm (light pink).

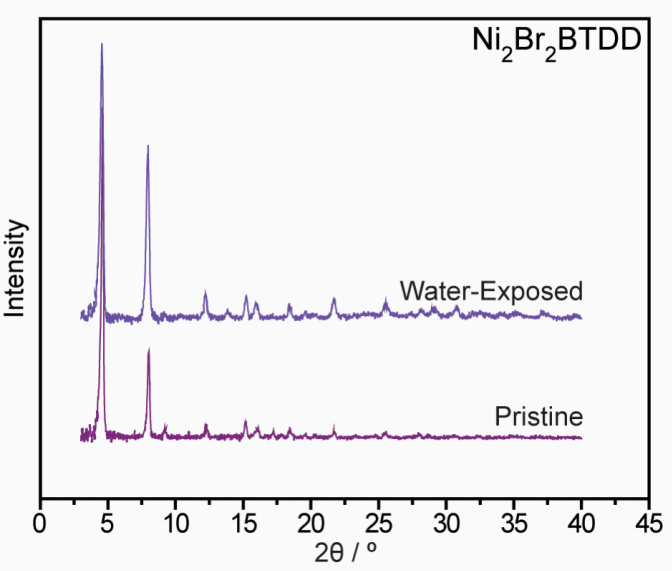

Figure A3.4. Powder X-ray diffractograms for activated samples of pristine Ni2Br2BTDD (dark purple), and after a single water isotherm (light purple).

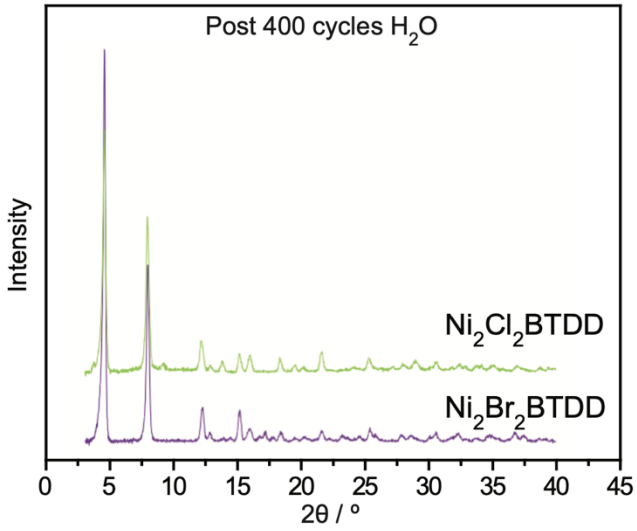

Figure A3.5. Powder X-ray diffractograms for samples after 400 cycles of water uptake and release of Ni2Br2BTDD (purple), and Ni2Br2BTDD (green).

Section A4. Nitrogen Isotherm Data.

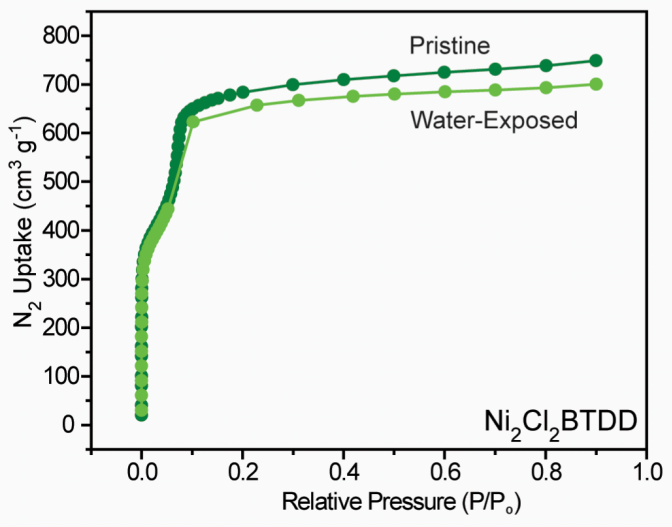

Figure A4.1. N2 adsorption isotherms for activated samples of pristine Ni2Cl2BTDD (dark green), and after a single water isotherm (light green).

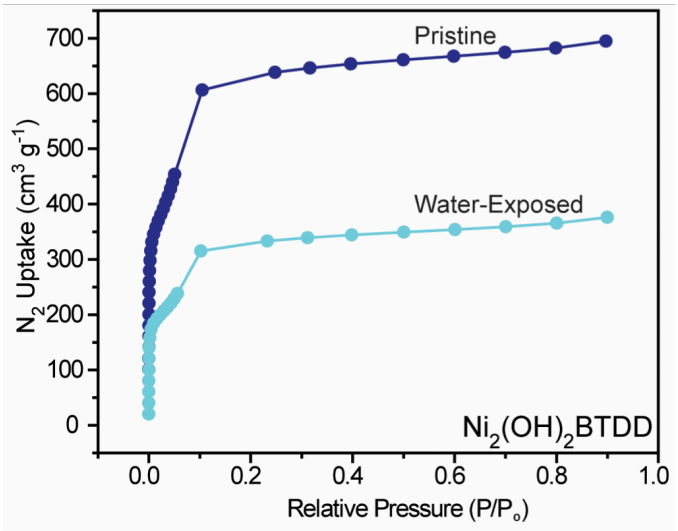

Figure A4.2. N2 adsorption isotherms for activated samples of pristine Ni2(OH)2BTDD (dark blue), and after a single water isotherm (light blue).

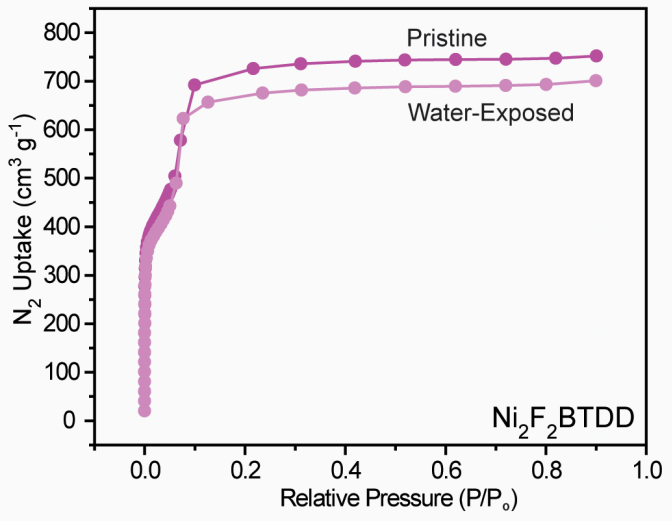

Figure A4.3. N2 adsorption isotherms for activated samples of pristine Ni2F2BTDD (dark pink), and after a single water isotherm (light pink).

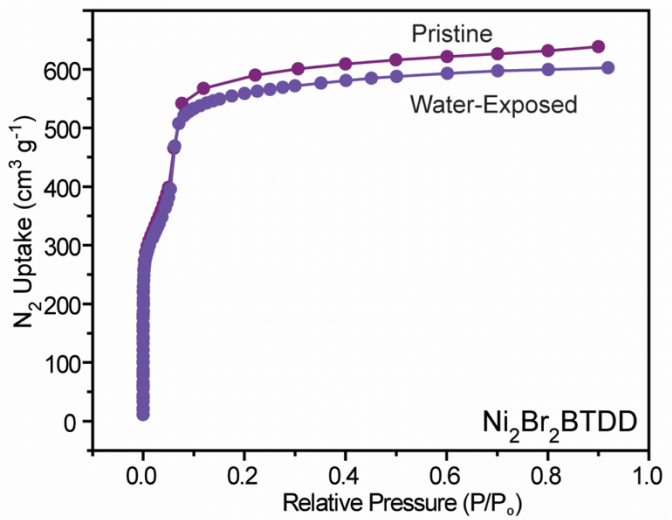

Figure A4.4. N2 adsorption isotherms for activated samples of pristine Ni2Br2BTDD (dark purple), and after a single water isotherm (light purple).

Section A5. X-ray Photoelectron Spectroscopy Data.

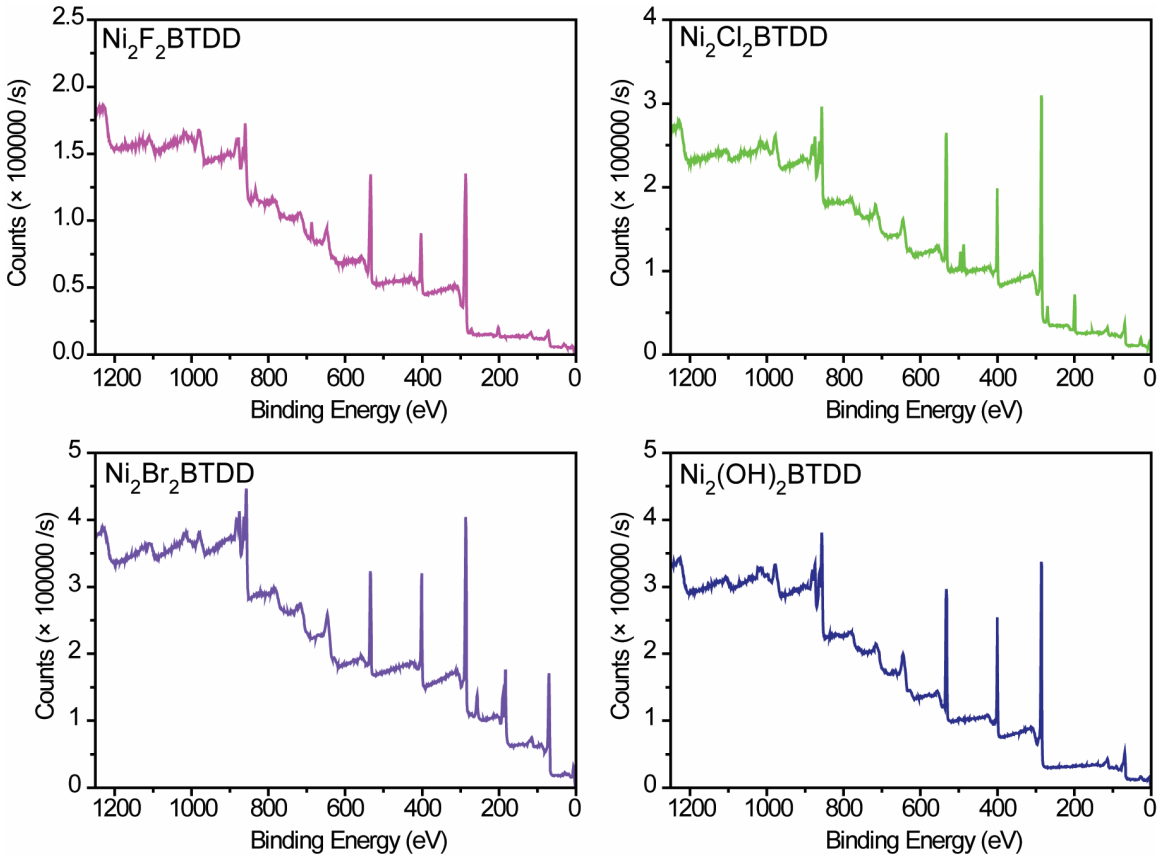

Figure A5.1: Survey X-ray photoelectron spectroscopy (XPS) for Ni2F2BTDD (pink), Ni2Cl2BTDD (green), Ni2Br2BTDD (purple), and Ni2(OH)2BTDD (navy).

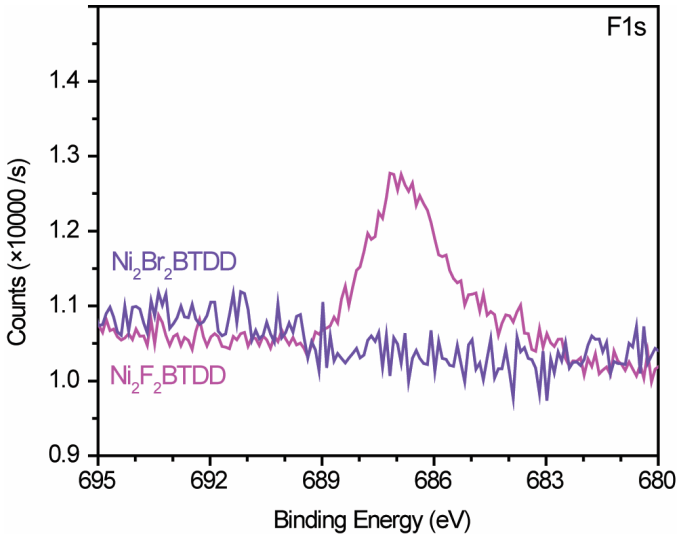

Figure A5.2: Fluoride F1s energy X-ray photoelectron spectroscopy (XPS) for Ni2F2BTDD (pink) and Ni2Br2BTDD (purple).

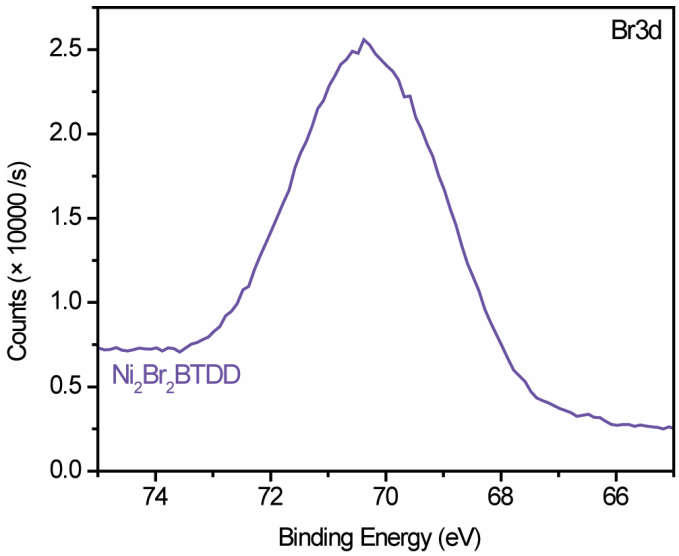

Figure A5.3: Bromide Br3d energy X-ray photoelectron spectroscopy (XPS) for Ni2Br2BTDD (purple).

Section A6. Infrared Spectroscopy Data.

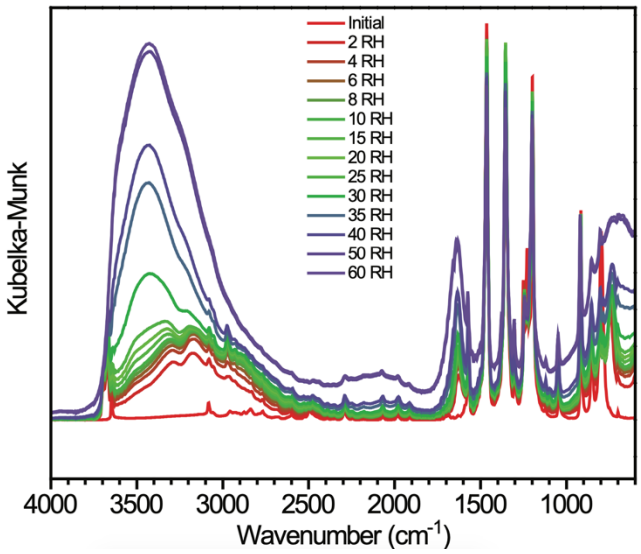

Figure A6.1. Diffuse-Reflectance Infrared Spectroscopy (DRIFTS) of the water adsorption process in $Ni_2(OH)_2BTDD$ under controlled relative humidity (RH).

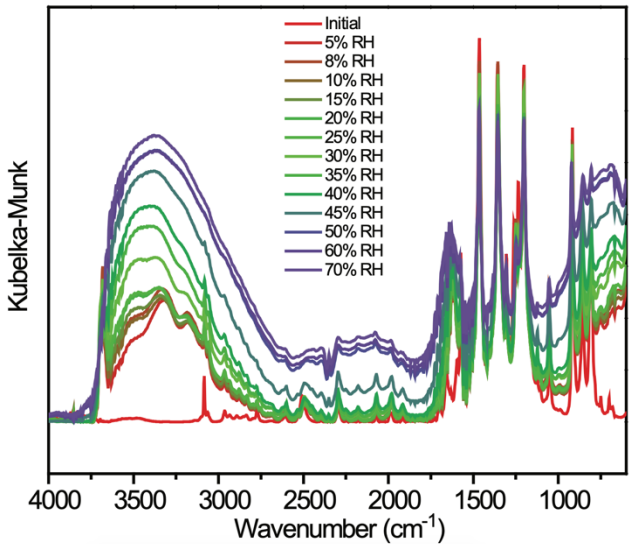

Figure A6.2. Diffuse-Reflectance Infrared Spectroscopy (DRIFTS) of the water adsorption process in Ni_2F_2BTDD under controlled relative humidity (RH).

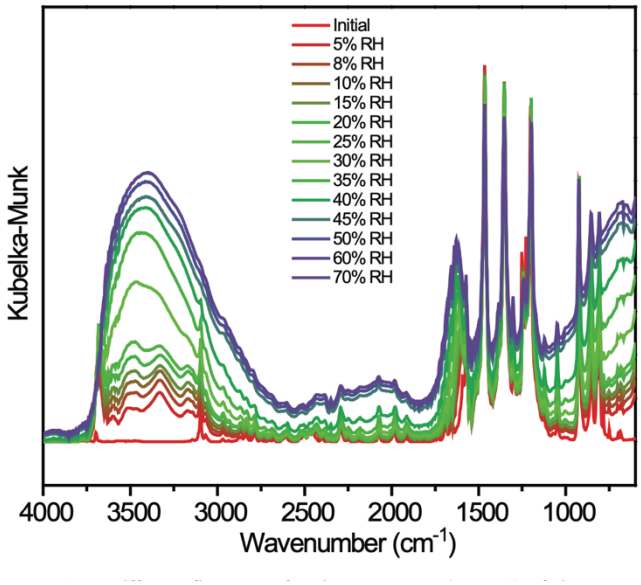

Figure A6.3. Diffuse-Reflectance Infrared Spectroscopy (DRIFTS) of the water adsorption process in Ni_2Cl_2BTDD under controlled relative humidity (RH).

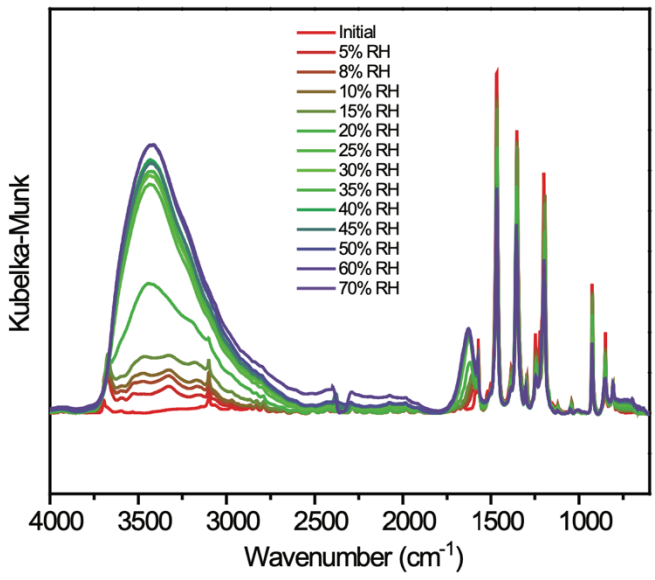

Figure A6.4. Diffuse-Reflectance Infrared Spectroscopy (DRIFTS) of the water adsorption process in Ni_2Br_2BTDD under controlled relative humidity (RH).

Section A7. Additional Water Cycling Data.

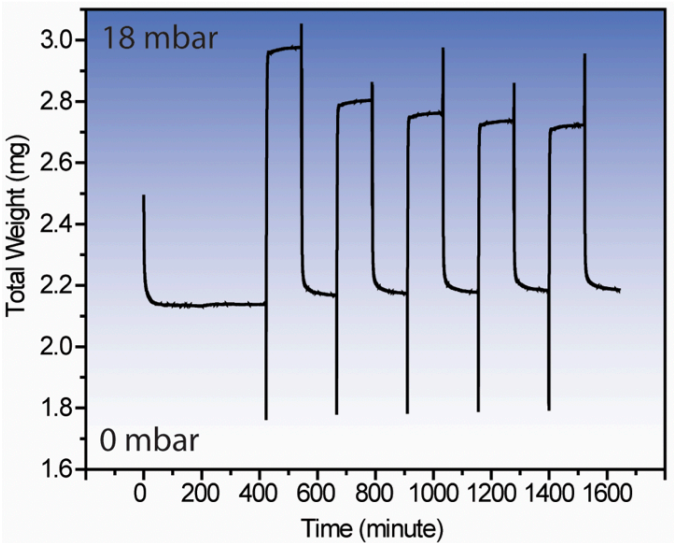

Figure A7.1: Water cycling in $Ni_2(OH)_2BTDD$, switching from 0 mbar H_2O to 18 mbar H_2O every two hours. Initial cycle was measured after a water isotherm at 25 °C. Spikes in data are microbalance anomalies caused by pressure changes.

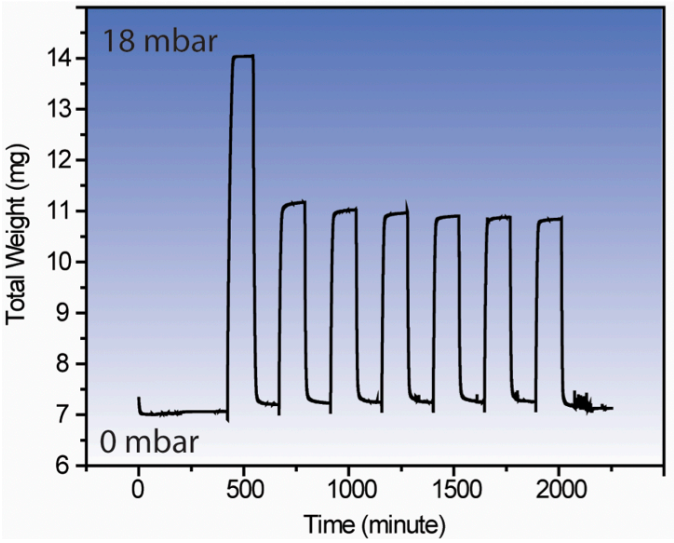

Figure A7.2: Water cycling in Ni_2F_2BTDD, switching from 0 mbar H_2O to 18 mbar H_2O every two hours. Initial cycle was measured after a water isotherm at 25 °C. Spikes in data are microbalance anomalies caused by pressure changes.

Section A8. Nuclear Magnetic Resonance Data.

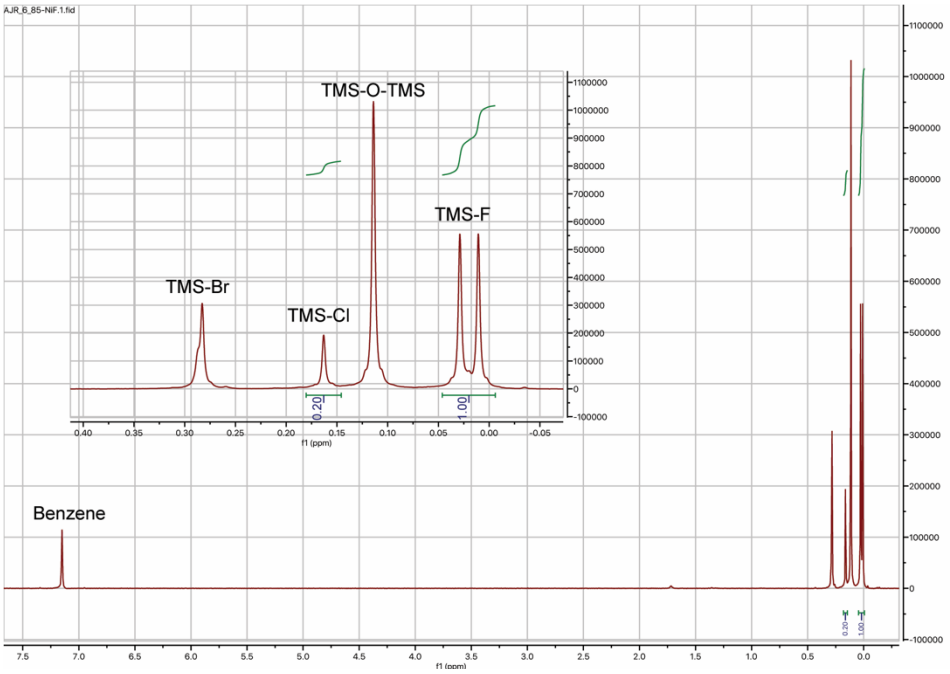

Figure A8.1: Nuclear Magnetic Resonance spectrum acquired at 400 MHz of the filtrate after treatment of Ni_2F_2BTDD with trimethylsilyl bromide (TMS-Br) in deuterated benzene.

Section A9. Rietveld Refinement of Synchrotron Powder X-ray Diffraction Data. Due to relatively small crystal size, structures of **Ni_2X_2(BTDD)** were obtained from synchrotron powder X-ray diffraction data. Obtained patterns were refined in TOPAS Academic V6

(Coelho Software).[847] An anisotropic strain broadening model by Stephens et al. was used to improve profile fit.[848] Reported structures for **Co_2Cl_2(BTDD)**[690] and **Cu_2Cl_2(BTDD)**[849] were used as a starting point for the Rietveld refinement.[850] Structures were initially refined using a rigid body description of the ligand, with bond lengths and angles constrained to literature[849] values. After the orientation and position of the ligand were refined, the rigid body constraints were lifted, and all atom positions were refined, subject to geometric bond length and angle restraints. Distances and angles in the linker were restrained to literature values; [849] Ni-N1 and Ni-X distances were restrained to average Cambridge Structural Database[851] distances for the relevant Ni environments. Additional oxygen atoms representing adsorbed water molecules were placed in the MOF pores based on the difference Fourier map. For **Ni_2F_2(BTDD)**, the bridging halide was refined as a disorder between Cl and F to match the results of the NMR study. Initially, the occupancies of the halides were constrained to the experimental 1:5 ratio. The constraint was relaxed to a restraint in the final stage of the refinement. For **Ni_2Br_2(BTDD)**, the fit significantly improved with introduction of Ni and Br vacancies, and addition of a small amount of terminal Br (Br_2) atoms disordered with the terminal water groups (O_2) to keep the structure charge balanced. Thermal parameters were refined isotropically for all structures, with similarity restraints applied separately on heavy atoms and on light atoms. Experimental details and structural information are presented in **Table A9.1**. Final Rietveld plots for the three compounds are presented in **Figs. A9.1** (**Ni_2Cl_2(BTDD)**), **A9.2** (**Ni_2F_2(BTDD)**), and **A9.3** (**Ni_2Br_2(BTDD)**).

Table A9.1. Experimental details and structural information for Ni_2X_2(BTDD).

Material	**Ni_2F_2(BTDD)**	**Ni_2Cl_2(BTDD)**	**Ni_2Br_2(BTDD)**
Diffraction instrument	APS 11-BM		
Radiation type	Synchrotron X-ray		
Wavelength	0.412805 Å		
Temperature	100.0		
Formula	$C_{12}Cl_{0.38}F_{1.62}N_6Ni_2O_{8.56}$	$C_{12}Cl_2N_6Ni_2O11.48$	$C_{12}Br_{1.68}N_6Ni_{1.81}O_{8.69}$
M_r, g/mol	526.79	600.19	603.91
Z	9		
Crystal system	Trigonal		
Space group	*R3m (no. 166; hexagonal setting)*		
a, Å	38.6092(5)	38.5282(5)	38.42498(19)
c, Å	8.09293(13)	8.18879(13)	8.20774(6)
V, Å^3	10447.6(3)	10527.1(3)	10494.98(13)
D_c, g/cm^3	0.75348	0.85204	0.85948
μ, mm^{-1}	0.196	0.215	0.496
2θ range, °	1 – 18	0.5 – 20	0.5 – 25
Refl. Obs.	628	846	1583
No. of parameters	65	65	71
No. of restraints	28	28	29
R_{wp}, %	7.08	7.71	7.83
R_{exp}, %	5.86	7.60	6.19
R_p, %	4.87	5.12	5.54
R_{Bragg}, %	0.91	1.38	1.92
G_0F (χ)	1.21	1.01	1.27

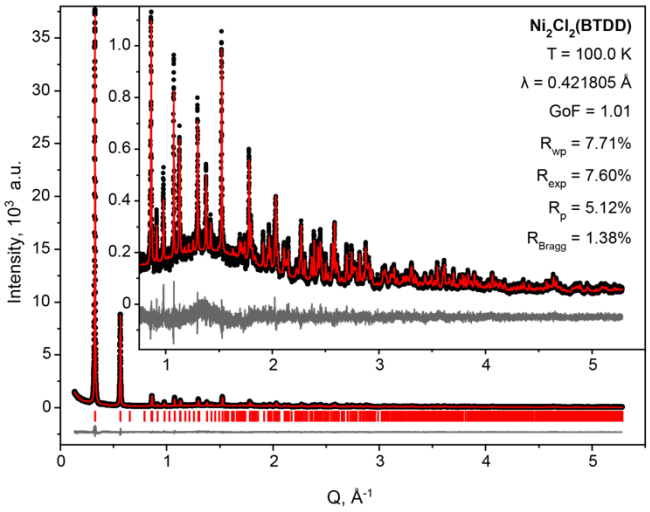

Figure A9.1. Rietveld fit of Ni_2Cl_2(BTDD). Red line: calculated intensities; black circles: experimental intensities; grey line: difference; red ticks: calculated reflection positions. Select fit parameters are presented on the plot.

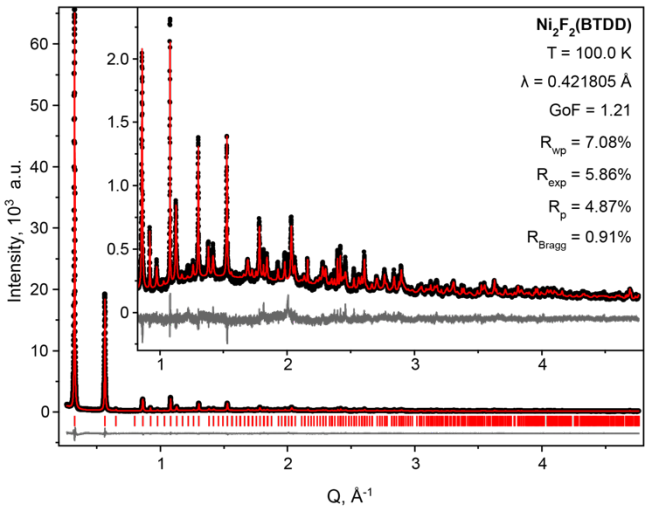

Figure A9.2. Rietveld fit of Ni_2F_2(BTDD). Red line: calculated intensities; black circles: experimental intensities; grey line: difference; red ticks: calculated reflection positions. Select fit parameters are presented on the plot.

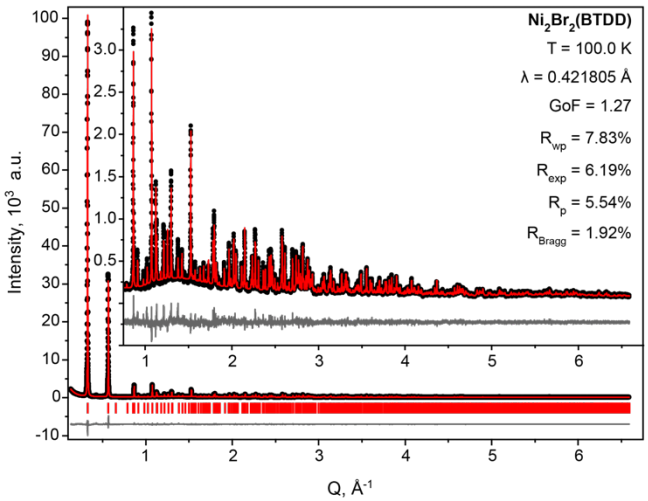

Figure A9.3. Rietveld fit of Ni_2Br_2(BTDD). Red line: calculated intensities; black circles: experimental intensities; grey line: difference; red ticks: calculated reflection positions. Select fit parameters are presented on the plot.

Section A10. Additional Water Uptake Data, Heat of Adsorption.

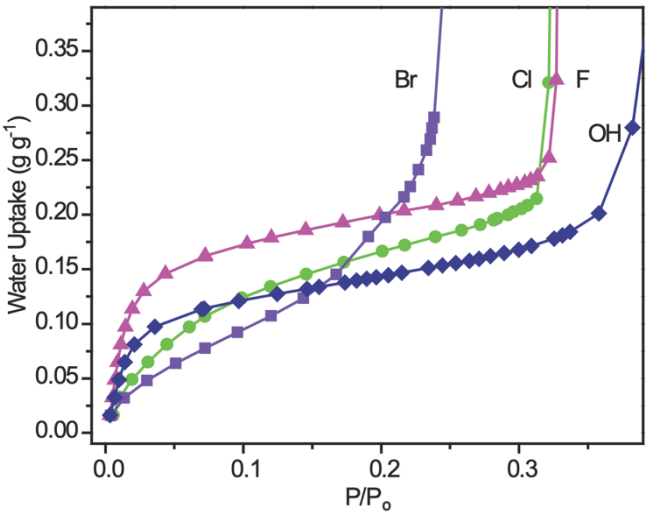

Figure A10.1: Zoom in on the low-pressure region of water adsorption isotherms in gravimetric units for Ni_2F_2BTDD (pink), Ni_2Cl_2BTDD (green), Ni_2Br_2BTDD (purple), and $Ni_2(OH)_2$BTDD (navy).

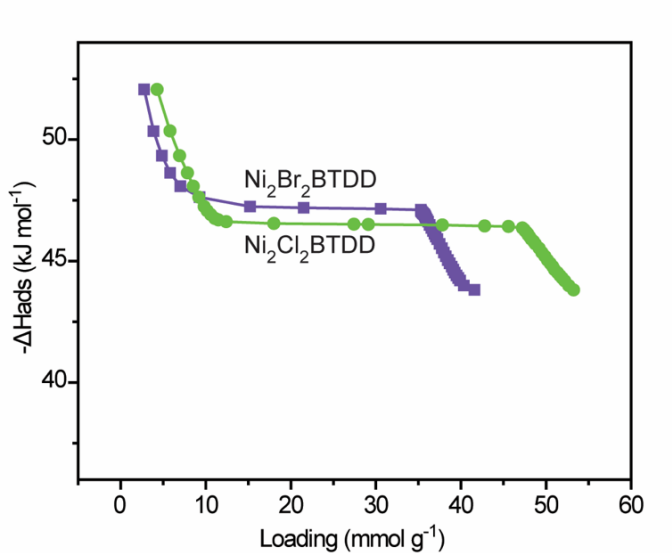

Figure A10.2: Heat of adsorption (ΔH_{012}) of water in Ni_2Cl_2BTDD (green), or Ni_2Br_2BTDD (purple).

APPENDIX G

SUPPLEMENTARY INFORMATION FOR:

Tuning Adsorbate Binding Interactions by Anion Exchange in the Metal-Organic Framework, Ni_2X_2BTDD

Julian Oppenheim*, **Jenna L. Mancuso***, Christopher H. Hendon, and Mircea Dincă

*Co-first authors

Experimental Discussion Omitted from Main Text

To test the impact of the anion on the binding strength of various adsorbates, we measured variable temperature adsorption isotherms with activated samples of **1-X** (X = OH, F, Cl, Br) at 283, 288, 293, 298, and 308 K for CO and C_2H_4, and at 77 and 87 K for H_2. Each material displayed a type I isotherm upon dosing with each of the three gases (**Figure 60**). The adsorbate uptake capacities at 1 bar and 298 K also show that the coverage is substoichiometric with respect to the metal sites ranging from 14-59% for CO and 43-74% for ethylene (**Table 2**). Notably, the uptake capacity is considerably reduced for **1-OH**, possibly indicating a weakened interaction between **1-OH** and each adsorbate. The

H_2 capacity at 1 bar and 77 K is in excess of the metal content, ranging from 174-252% per metal site, suggesting the formation of a multilayer or the presence of BTDD-bound sites

To gain insight into the adsorbate binding energy, we modeled the variable temperature adsorption data to extract isosteric enthalpies of adsorption. For each of the **1-X** materials, the data was fit using the Dual Site Langmuir (DSL), Sips (also known as Langmuir-Freundlich), Unilan, and Virial isotherms (Appendix G Section A6). Isosteric enthalpies of adsorption were then calculated using the Clausius-Clapeyron relation for the DSL, Sips, and Unilan models and directly for the Virial model. In order to exclude sources of error, the isosteric enthalpies of adsorption were all interpolated at a coverage of 0.01 mmol/g and were averaged over the results of all four fitting models in an effort to minimize systematic error (**Figure 61**, unfilled shapes).[852]

Section A1. General Experimental Information.

Materials and Methods. $NiCl_2$•$6H_2O$ (Strem Chemicals), HCl (32-35%, BDH – VWR Analytic) methanol (99.9%, VWR), N,N-dimethylformamide (99.8%, Millipore), 1-chloro-2,4-dinitrobenzene (99%, TCI), catechol (99%, Sigma-Aldrich), K_2CO_3 (99%, Sigma-Aldrich), Sn Powder (150 micron, 99.5%, Sigma-Aldrich), diethyl ether (99%, Sigma-Aldrich), trimethylsilyl bromide (97%, SigmaAldrich), acetone (ACS grade, Macron Chemical), fuming HNO_3 (90% min, Macron), H_2SO_4 (95-98%, BDH Chemicals), acetic acid (ACS grade, VWR BDH Chemicals), $NaNO_2$ (98%, Alfa Aesar), ethanol (200 proof, Koptec), KOH (ACS grade, BDH chemicals), CsF (99%, Beantown Chemicals) were used as received. Benzene (ACS grade, EMD) was purged with argon, and subjected

to three freeze-pump-thaw cycles before bringing into a nitrogen-filled glovebox and stored over 3 Å molecular sieves.

Gas adsorption isotherms were measured by a volumetric method using a Micromeritics ASAP 2020 gas sorption analyzer. Typical samples of ca. 40–80 mg, preactivated at >100°C to remove all residual solvent, were transferred in an Ar-filled glovebox to a pre-weighed analysis tube. The tube with sample inside was weighed again to determine the mass of the sample. The tube was capped with a Micromeritics TranSeal™, brought out of the glovebox, and transferred to the analysis port of the gas sorption analyzer. Free space correction measurements were performed using ultra-high purity He gas (UHP grade 5, 99.999% pure). Nitrogen isotherms were measured using UHP grade Nitrogen. All nitrogen analyses were performed using a liquid nitrogen bath at 77 K. Carbon monoxide and ethylene isotherms were measured at varying temperatures in a water/ethylene glycol isothermal bath using high purity gases (carbon monoxide, 99.99%; ethylene 99.9%). Hydrogen (H_2, 99.999%) isotherms were performed using a liquid nitrogen bath (77 K) or a liquid argon bath (87 K). Oil-free vacuum pumps were used to prevent contamination of sample or feed gases.

Diffuse reflectance infrared Fourier transform spectroscopy (DRIFTS) measurements were performed using a Bruker Tensor 37 IR spectrometer equipped with a liquid nitrogen cooled mercury cadmium S4 telluride detector and a Pike DiffusIR accessory. A sample of MOF, pre-activated under vacuum to remove all solvent, was diluted with KBr in a ratio

of approximately 1:50-100 (MOF:KBr) in an argon-filled glovebox. The resulting solid solution was then packed into a ceramic cup and sealed in the DiffusIR cell. The cell was brought out of the box, and a static dry spectrum was recorded with the cell sealed. Known volumes of CO was dosed into the cell through an airtight port using a gas tight syringe. The temperature for all measurements was 20 °C. Data was transformed using the Kubelka-Munk function.

Section A2. Computations

Table A2.1: Comparative tabulation of adsorption energies recovered from experiment and theory for halide exchanged frameworks.

	Adsorbate	**Experiment**	**Theory (HSE06)**
OH	CO	16.42 ± 1.17	31.79
	H_2	7.00 ± 0.01	-
	Et	23.23 ± 1.14	13.06
F	CO	31.00 ± 1.61	32.74
	H_2	7.09 ± 0.02	9.78
	Et	32.98 ± 0.40	25.07
Cl	CO	39.02 ± 0.16	41.44
	H_2	7.63 ± 0.01	12.90
	Et	22.31 ± 0.24	23.62
Br	CO	44.56 ± 0.75	44.42
	H_2	7.62 ± 0.01	12.38
	Et	19.8 ± 0.65	20.79
I	CO	-	51.00
	H_2	-	13.83
	Et	-	17.14

Table A2.2: Total valence electrons on nickel atom for the empty framework and those with carbon monoxide and ethylene bound showing an increase in electron density with σ-donation from CO and a decrease in electron density associated with π-backbonding from ethylene.

	Model	Electrons on Ni	Spin on Ni
OH	CO	9.268	1.573
	Empty	9.148	1.630
	Et	9.160	1.631
F	CO	9.211	1.628
	H_2	9.117	1.662
	Empty	9.126	1.665
	Et	9.012	1.663
Cl	CO	9.241	1.556
	H_2	9.135	1.598
	Empty	9.128	1.606
	Et	9.123	1.607
Br	CO	9.238	1.526
	H_2	9.121	1.547
	Empty	9.102	1.588
	Et	9.004	1.595
I	CO	9.247	1.470
	H_2	9.114	1.526
	Empty	9.081	1.553
	Et	8.972	1.562

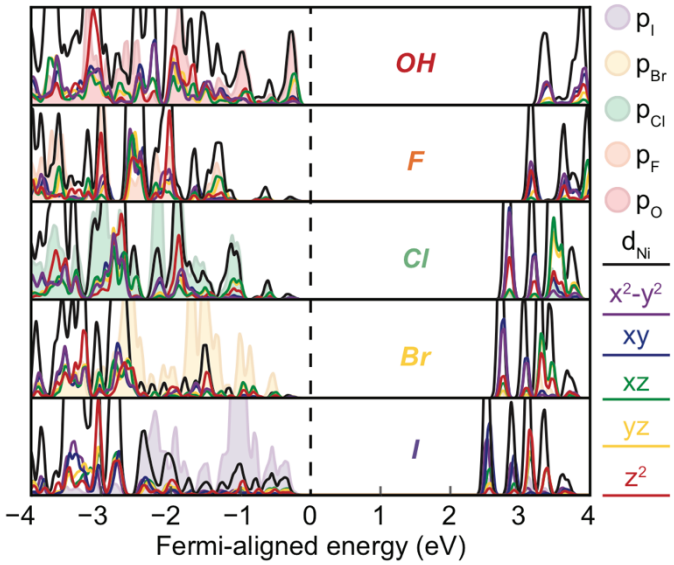

Figure A2.1: Fermi-aligned orbital-decomposed DOS plots depicting the sum of p-states from halide and hydroxyl ligands, sum of nickel d-states (black), and contribution of each d-orbital to the summed d-DOS at the HSEsol06 level of theory.

Table A2.3: Structure parameters for active site "openness" as a function of halide exchange recovered from structures fully equilibrated with the PBE-D3 functional.

	Ni-Ni distance	**Linker-Linker dihedral**
OH	3.11 Å	113.0°
F	3.10 Å	109.8°
Cl	3.24 Å	102.6°
Br	3.29 Å	97.3°
I	3.37 Å	88.3°

Section A3. Diffuse reflectance infrared Fourier transform (DRIFTS)

To a sample of **1-Cl** (2.6 mg, 0.0057 mmol), 750 µL of CO (~3 eq.) were dosed in and a DRIFT spectrum was recorded 5 times in increments of 120 seconds

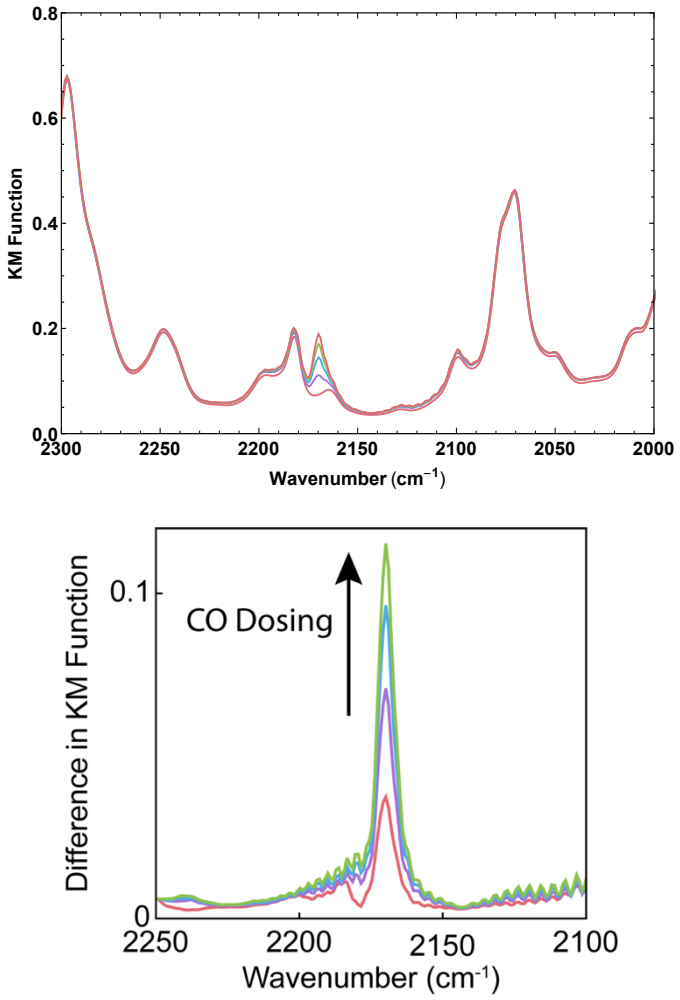

Figure A3.1: DRIFTS measurement of CO in **1-Cl** on left and a close up of the 2100-2250 cm^{-1} region showing the difference in Kubelka-Munk intensity of with increasing carbon monoxide dosing on right

Section A4. Non-classical Metal Carbonyl Correlation

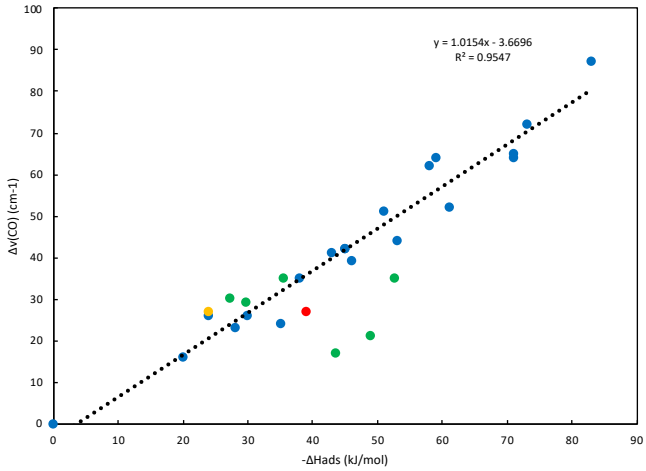

Figure A4.1: Δν -ΔH_{ads} linear relationship: red (**1-Cl**, this work), blue[785], green[777], yellow[853].

Section A5. Typical isosteric enthalpies

Table A5.1: Selection of literature isosteric enthalpy of adsorption values for CO.

Framework	**CO Q_{st} (kJ/mol)**	**Method/Notes[a]**
Zeolite 5A[854]	70	One of Langmuir or Freundlich, 194.5/237/298 K
Zeolite 13X[854]	70	One of Langmuir or Freundlich, 194.5/237/298 K
Ni-MOF-74[777]	52.7	Two or three site(?) temperature dependent Langmuir model, 298/308/318 K
Cu(I)/MIL-100(Fe)[855]	50	DSLF, 288/298/308 K
Cu doped Al_2O_3[856]	48.8	Modeling kinetics with linear driving force model
Co-MOF-74[777]	48.8	Two or three site(?) temperature dependent Langmuir model, 298/308/318 K
Fe-MOF-74[777]	43.6	Two or three site(?) temperature dependent Langmuir model, 298/308/318 K
MIL-100(Fe)[855]	38	DSLF, 288/298/308 K
Mg-MOF-74[777]	35.4	Two or three site(?) temperature dependent Langmuir model, 298/308/318 K
Mn-MOF-74[777]	29.7	Two or three site(?) temperature dependent Langmuir model, 298/308/318 K
Mg-MOF-74[857]	29	Variable temperature IR, $-\Delta S^0$ = 133 J/molK
Zn-MOF-74[777]	27.2	Two or three site(?) temperature dependent Langmuir model, 298/308/318 K
Zn-MOF-177[854]	22	One of Langmuir or Freundlich, 194.5/237/298 K
Zn-MOF-5[854]	16	One of Langmuir or Freundlich, 194.5/237/298 K
Ag doped Al_2O_3[856]	37.3/36.1	Modeling kinetics with linear driving force model

[a] DSL = Dual-site Langmuir, DSLF = Dual-site Langmuir-Freundlich = Dual-site Sips

Table A5.2: Selection of literature isosteric enthalpy of adsorption values for ethylene.

Framework	C_2H_4 Q_{st} (kJ/mol)	Method/Notes
Cr-MIL-101-SO_3Ag[858]	120	DSLF, 293/303/313 K
PAF-1-SO_3Ag[859]	106	DSLF, 296/318 K, Ag on PAF
MIL-101-Cr-SO_3Ag[860]	63	DSLF, 296/318 K
HUS-6(Hf)-Ag[861]	56.5	Virial, 283/298 K
Co-MOF-74[862]	47	Virial, 298/308/318 K
Fe-MOF-74[778]	45	DSLF, 318/333/353 K, Caption for Fig. S3 is confusing
Mg-MOF-74[863]	42.6	DSLF, 278/298/318 K
Cu^+@Cr-MIL-101[864]	40	DSL, 303/313/323 K, CuCl loaded
Cr-MIL-101-SO_3H[858]	35	DSLF, 298/303/313 K
Cu-MOF-74[862]	30	Virial, 298/308/318 K
Fe-MIL-142A[865]	26	DSLF, 278/288/298 K, typo in text body, value taken from figure
PAF-1-SO_3H[859]	23	DSLF, 296/318 K, PAF
Fe-PCN-250[866]	21.1	DSLF, 273/298 K
PAF-1[859]	14	DSLF, 296/318 K, PAF, also known as PPN-6
Cr-MIL-101-SO_3H[860]	10	DSLF, 296/318 K

Section A6. Isosteric enthalpy of adsorption calculations

The Langmuir model is defined as $n = \frac{U_1 a_1 p}{1+a_1 p}$, where *n* is the quantity of adsorbate adsorbed onto the adsorbent surface and *p* is the pressure. This model can be derived from the steady state of $\frac{dn}{dt} = k_1 p(U_1 - n) - k_2 n$, in which the rate of adsorption is limited by the number of available sites.[867] The Langmuir model can be extended to a heterogeneous system in which there are two adsorption sites to form the Dual-Site Langmuir model, $n = \frac{U_1 a_1 p}{1+a_1 p} +$

$\frac{U_2 a_2 p}{1+a_2 p}$. Chemically a two site model in the Ni_2X_2BTDD system can be interpreted as distinct adsorption to the Ni sites and the BTDD sites, however this interpretation is not necessarily precise. Distinct adsorption sites may be added to the model until the limit of continuous energy distribution is reached. In this limit, the Unilan isotherm is derived, $n = \frac{\int_{-s}^{+s} \frac{U e^j p}{a+e^j p} dj}{\int_{-s}^{+s} dj} = \frac{U}{2s} \ln \frac{1+pe^s/a}{1+pe^{-s}/a}$. The Sips (also known as Langmuir-Freundlich) isotherm is a mixture of the Langmuir and Freundlich isotherms, $n = \frac{U a p^s}{1+a p^s}$. In this model, the factor *s* introduces heterogeneity.[868] These particular models were chosen as the inverse, P(n), can be expressed analytically, which allows for facile error propagation. The errors of the isotherm fits were calculated using the variance-covariance matrix of the fit, $\Sigma^f = J \Sigma^X J^T$, where Σ^f is a vector of the variance for each variable, J is the Jacobian ($\frac{dF}{da_i}$), and Σ^X is the variance-covariance matrix.[869] For each of these models, the isosteric enthalpy of adsorption is calculated using the Clausius-Clapeyron relation, $\ln P(n) = \frac{\Delta H_{ads}(n)}{R} \frac{1}{T} + C$. The variances calculated from the variance-covariance calculation were used as the weights in the Clausius-Clapeyron linear fit. The last model used in this study is a virial-type equation, $\ln p = \ln n + \frac{1}{T} \sum_{i=0}^{x} a_i n^i + \sum_{i=0}^{y} b_i n^i$. Unlike the abovementioned models, the virial analysis simultaneously fits the isothermal data for all temperatures. We have determined that $x = 4$ and $y = 1$ fits the data sufficiently with our data set. The isosteric enthalpy of adsorption is calculated as $\Delta H_{ads}(n) = R \sum_{i=0}^{x} a_i n^i$.

The various isotherm models were fit using the Nonlinearmodelfit function in Mathematica (which minimizes the sum of the squares of the residuals). Each fit is

weighted by 1/quantity adsorbed in order to ensure an appropriate model fit at the lowest pressures in order to achieve accurate isosteric enthalpy of adsorptions.

Table A6.1: Summary of isosteric enthalpy of adsorption (kJ/mol).

Gas	X	Unilan	Virial	Sips	DSL	Average
CO	F	33.67 ± 2.12	26.19 ± 1.84	35.04 ± 5.12	29.08 ± 2.67	31.00 ± 1.61
	Cl	37.91 ± 0.21	37.69 ± 0.40	43.05 ± 0.41	37.42 ± 0.16	39.02 ± 0.16
	Br	40.18 ± 0.55	46.09 ± 1.16	50.97 ± 2.57	41.00 ± 0.86	44.56 ± 0.75
	OH	17.92 ± 3.02	14.96 ± 2.95	16.00 ± 0.14	16.78 ± 2.01	16.42 ± 1.17
C_2H_4	F	27.21 ± 0.96	32.14 ± 0.49	43.20 ± 1.04	29.38 ± 0.51	32.98 ± 0.40
	Cl	21.28 ± 0.63	22.81 ± 0.16	22.99 ± 0.49	22.17 ± 0.53	22.31 ± 0.24
	Br	18.91 ± 0.51	21.44 ± 0.34	18.27 ± 2.02	20.57 ± 1.54	19.80 ± 0.65
	OH	16.96 ± 1.31	22.56 ± 0.39	29.60 ± 3.98	23.78 ± 1.80	23.23 ± 1.14
H_2	F	6.86 ± 0.00	7.11 ± 0.08	7.78 ± 0.01	6.60 ± 0.00	7.09 ± 0.02
	Cl	7.42 ± 0.00	7.46 ± 0.03	8.73 ± 0.00	6.91 ± 0.00	7.63 ± 0.01
	Br	7.34 ± 0.00	7.43 ± 0.02	8.54 ± 0.01	7.16 ± 0.00	7.62 ± 0.01
	OH	6.22 ± 0.01	6.73 ± 0.03	8.66 ± 0.01	6.40 ± 0.00	7.00 ± 0.01

[a]-ΔH_{ads} (kJ/mol) determined at 0.01 mmol/g (this point was chosen rather than 0 mmol/g to prevent error resulting in extrapolation to ranges outside of measurement)

Table A6.2: Summary of mean absolute percentage error (MAPE) for each model (in %). Expressed as $\frac{100}{N}\sum\left|\frac{q_{meas}-q_{fit}}{q_{meas}}\right|$ (for Unilan, Sips, DSL) and $\frac{100}{N}\sum\left|\frac{p_{meas}-p_{fit}}{p_{meas}}\right|$ (for virial).

Gas	X	Unilan	Virial	Sips	DSL	Average
Average		**5.37**	**4.00**	**5.00**	**2.93**	4.32
CO	F	7.68	13.65	7.17	6.90	8.85
	Cl	1.61	2.55	5.64	1.78	2.90
	Br	5.11	8.43	4.66	4.94	5.79
	OH	11.78	11.10	14.01	10.33	11.81
C_2H_4	F	4.61	2.22	4.26	1.19	3.07
	Cl	3.12	1.12	0.66	0.34	1.31
	Br	5.78	1.86	1.41	0.77	2.46
	OH	11.02	2.17	2.00	0.53	**3.93**
H_2	F	2.09	2.31	6.85	2.61	3.47
	Cl	2.82	1.05	3.27	2.30	2.36
	Br	2.01	0.58	4.24	1.57	2.10
	OH	6.78	0.98	5.78	1.84	3.85

Figure A6.1: Summary of isosteric enthalpy of adsorption across models.

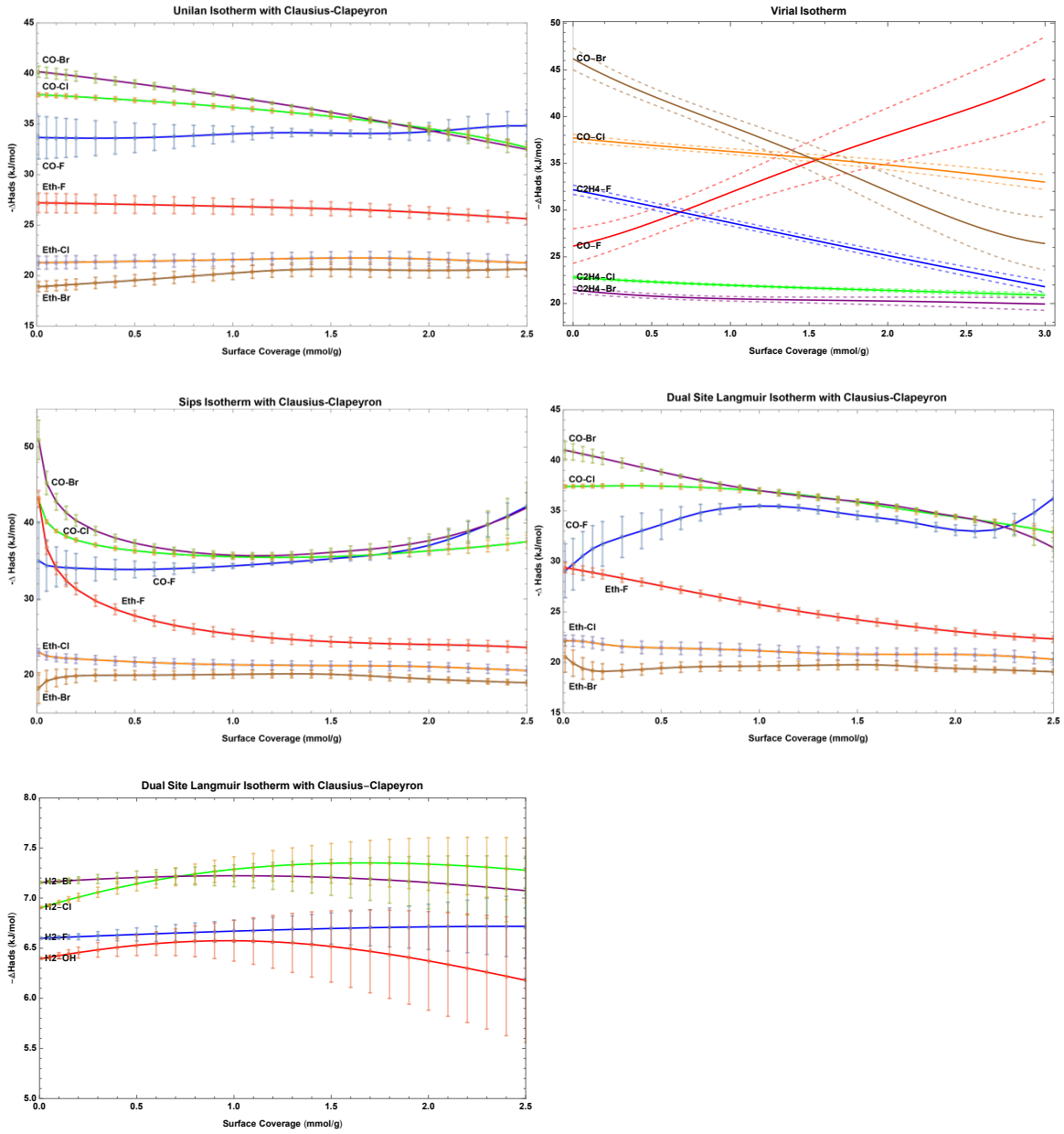

Unilan Models for Isosteric Enthalpy of Adsorption

$$n = \frac{U}{2s} \ln \frac{1+pe^{s}/a}{1+pe^{-s}/a}$$

n = quantity adsorbed (mmol/g)

p = pressure (kPa)

U = maximum adsorption capacity

a = Unilan constant

s = difference between minimum and maximum adsorption energy

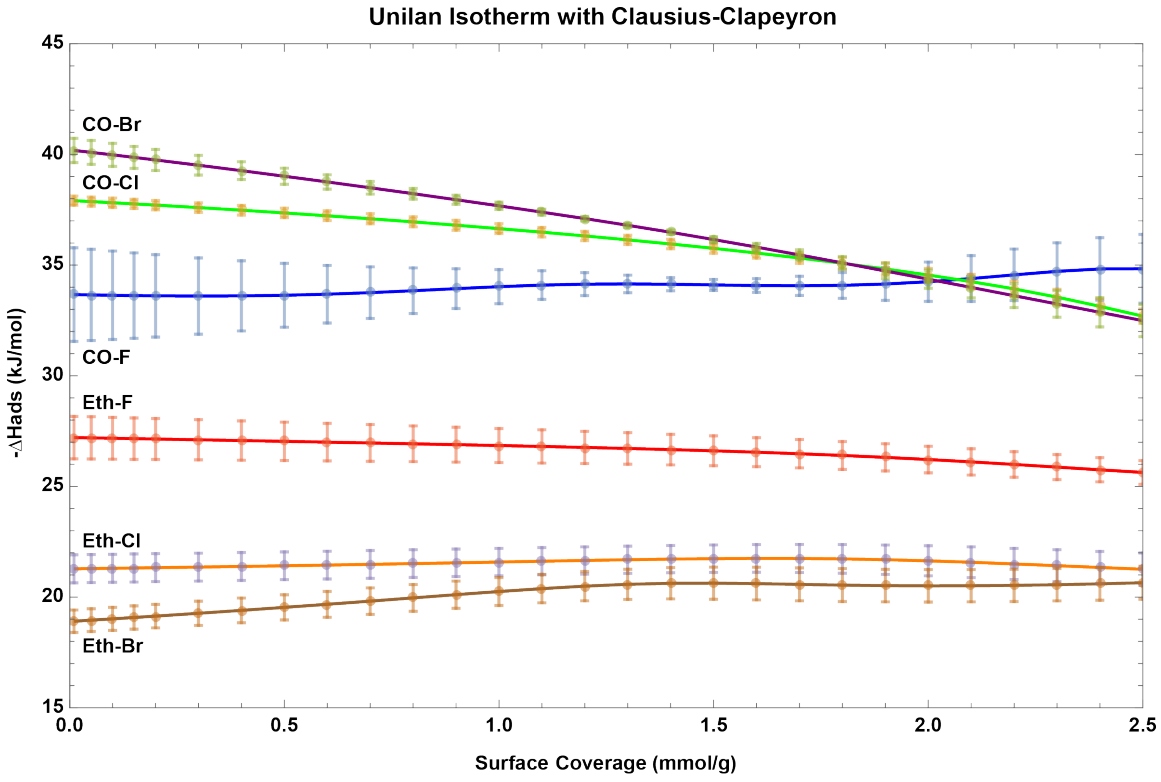

Summary of all Unilan/CC calculations. Error bars show one standard deviation.

G = CO, X = F

	283 K	288 K	293 K	298 K	308 K
U	5.63278	20.8899	21.5268	21.5705	20.6312
s	3.15121	12.527	12.569	12.2529	11.846
a	110.263	$1.46024*10^6$	$2.04597*10^6$	$2.00405*10^6$	$2.07604*10^6$
R^2	0.99977	0.999813	0.999864	0.99969	0.999467

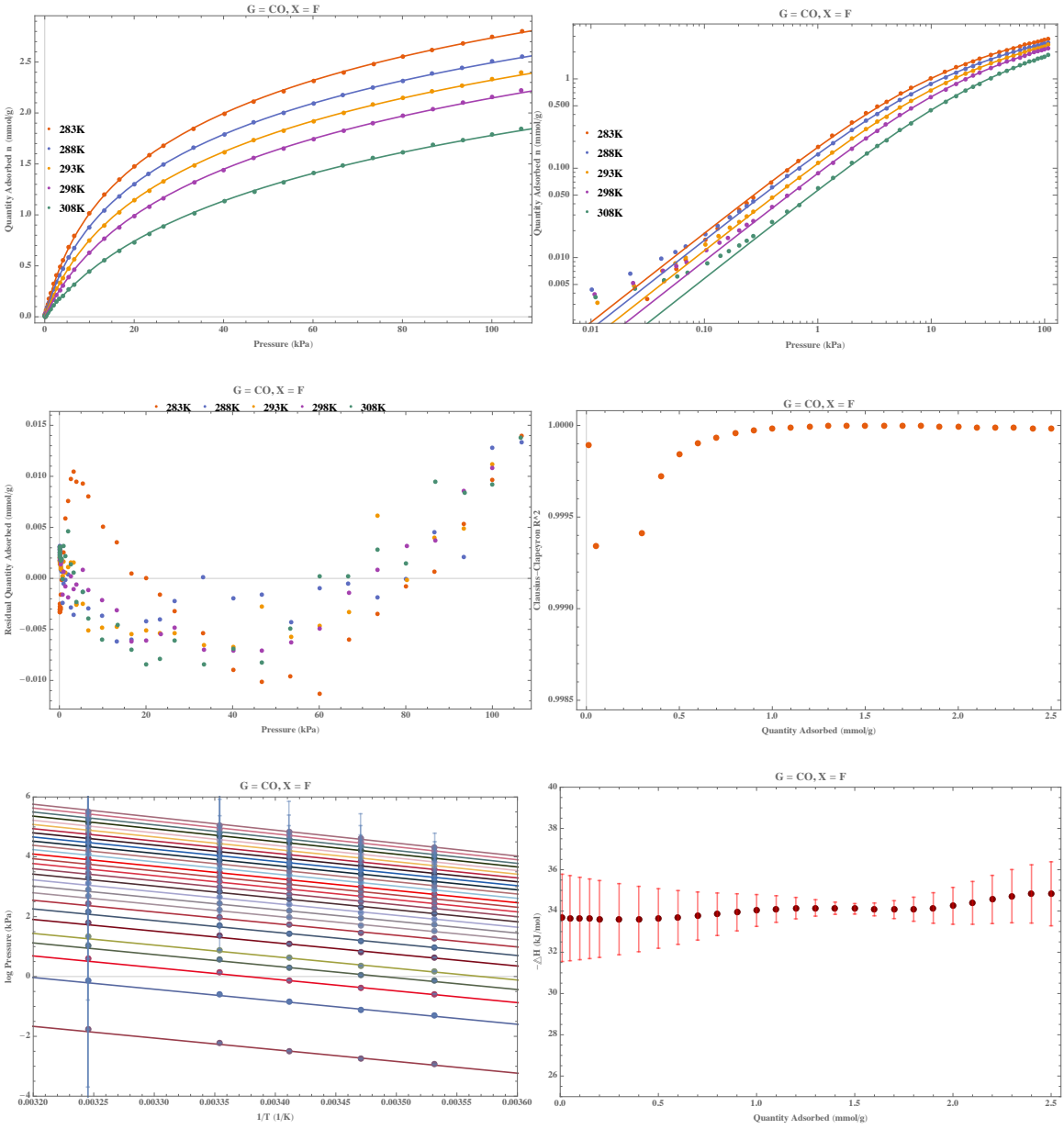

G = CO, X = Cl

	283 K	288 K	293 K	298 K	308 K
U	5.0222	5.19379	5.72677	7.27046	24.7394
s	2.58975	2.62905	2.88274	3.67202	12.0629
a	44.5242	62.6492	105.847	307.017	$2.27772*10^6$
R^2	0.999995	0.999995	0.999996	0.999967	0.999986

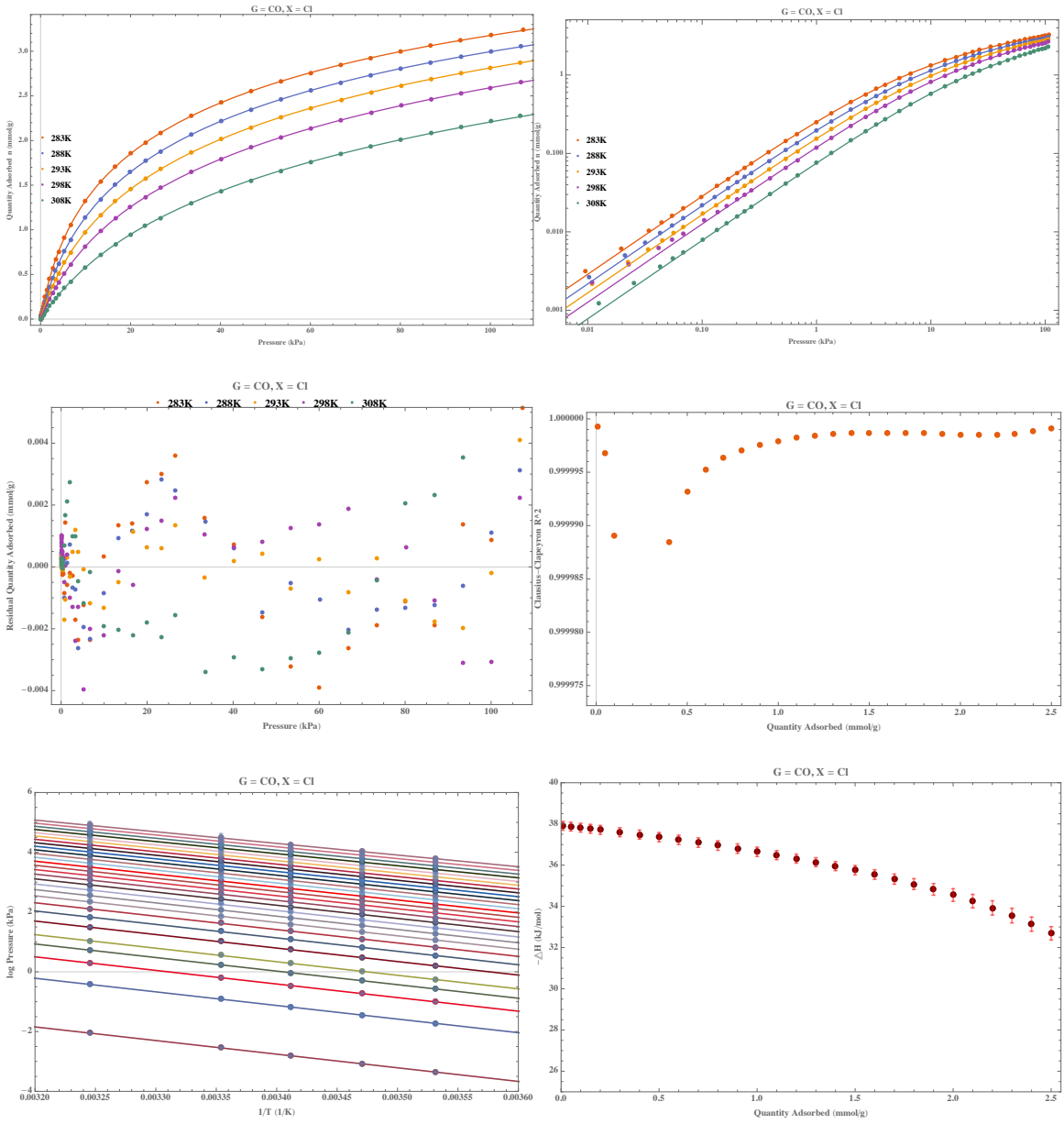

G = CO, X = Br

	283 K	288 K	293 K	298 K	308 K
U	17.8139	19.2549	18.099	18.813	17.7014
s	12.5083	13.0374	11.8569	12.3436	11.0933
a	724520	$1.74737*10^6$	746012	$1.54856*10^6$	794747
R^2	0.99974	0.9996667	0.999947	0.99984	0.999984

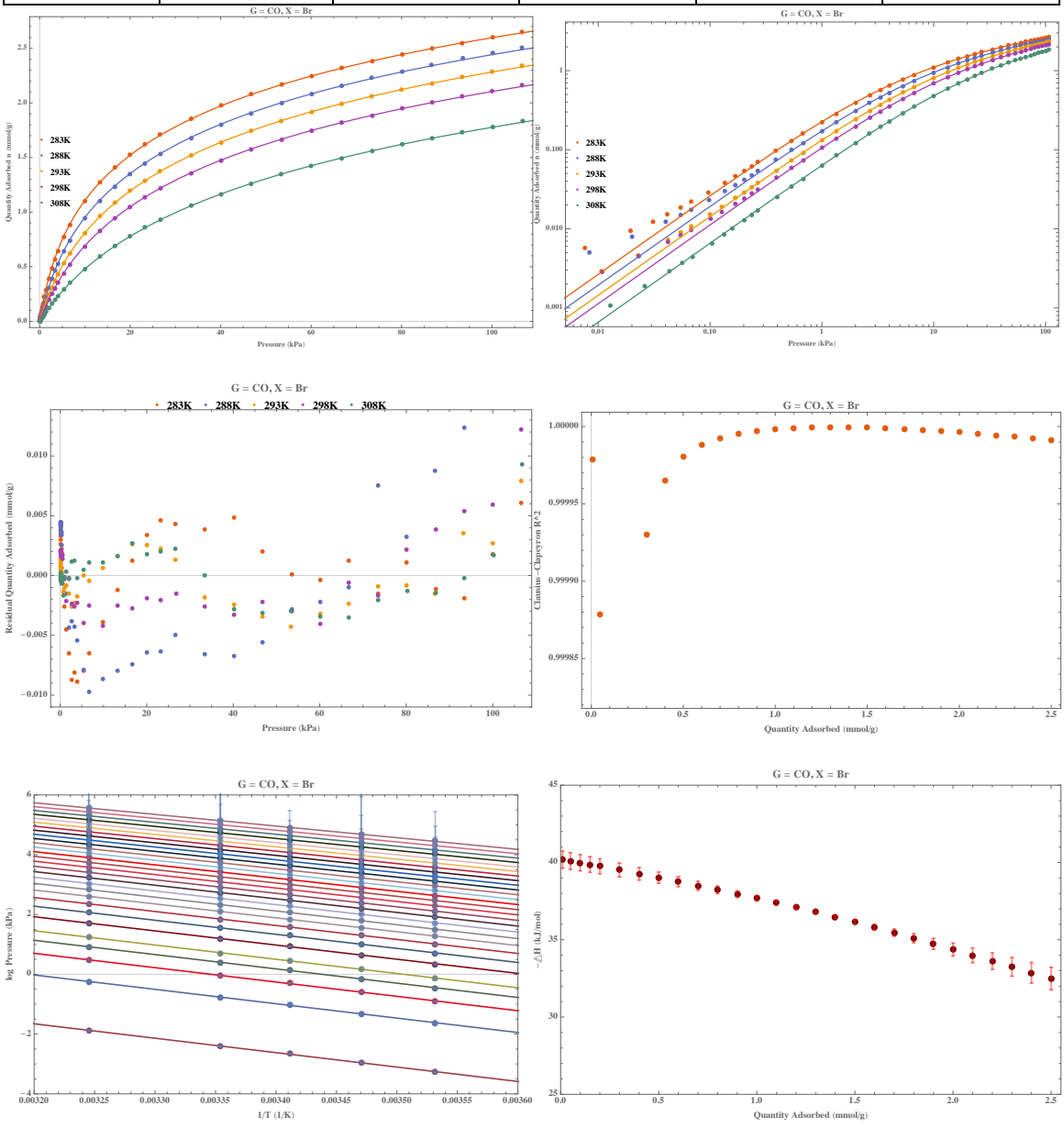

G = ethylene, X = F

	283 K	288 K	293 K	298 K	308 K
U	65.3984	64.2953	63.6257	63.9649	63.2723
s	12.6045	12.482	12.3199	12.1315	11.1287
a	$6.41561*10^6$	$6.72536*10^6$	$6.82727*10^6$	$6.90939*10^6$	$4.0884*10^6$
R^2	0.998638	0.99899	0.999373	0.999493	0.999799

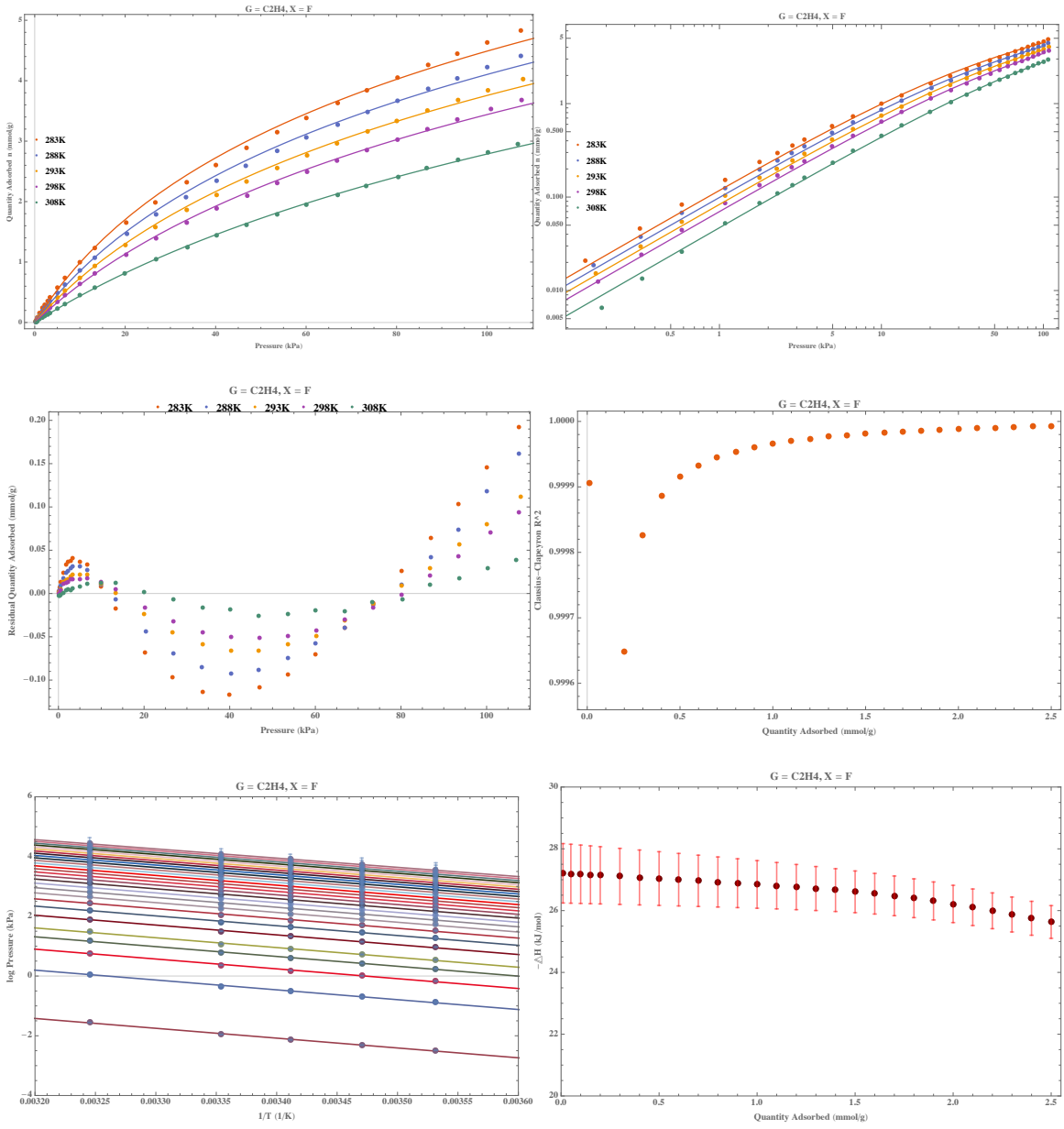

G = ethylene, X = Cl

	283 K	288 K	293 K	298 K	308 K
U	133.335	130.957	126.82	126.815	116.632
s	10.7864	10.6319	10.3772	10.2796	10.0138
a	$4.63904*10^6$	$4.55355*10^6$	$4.03451*10^6$	$4.35625*10^6$	$4.2323*10^6$
R^2	0.999788	0.999805	0.999806	0.999806	0.999819

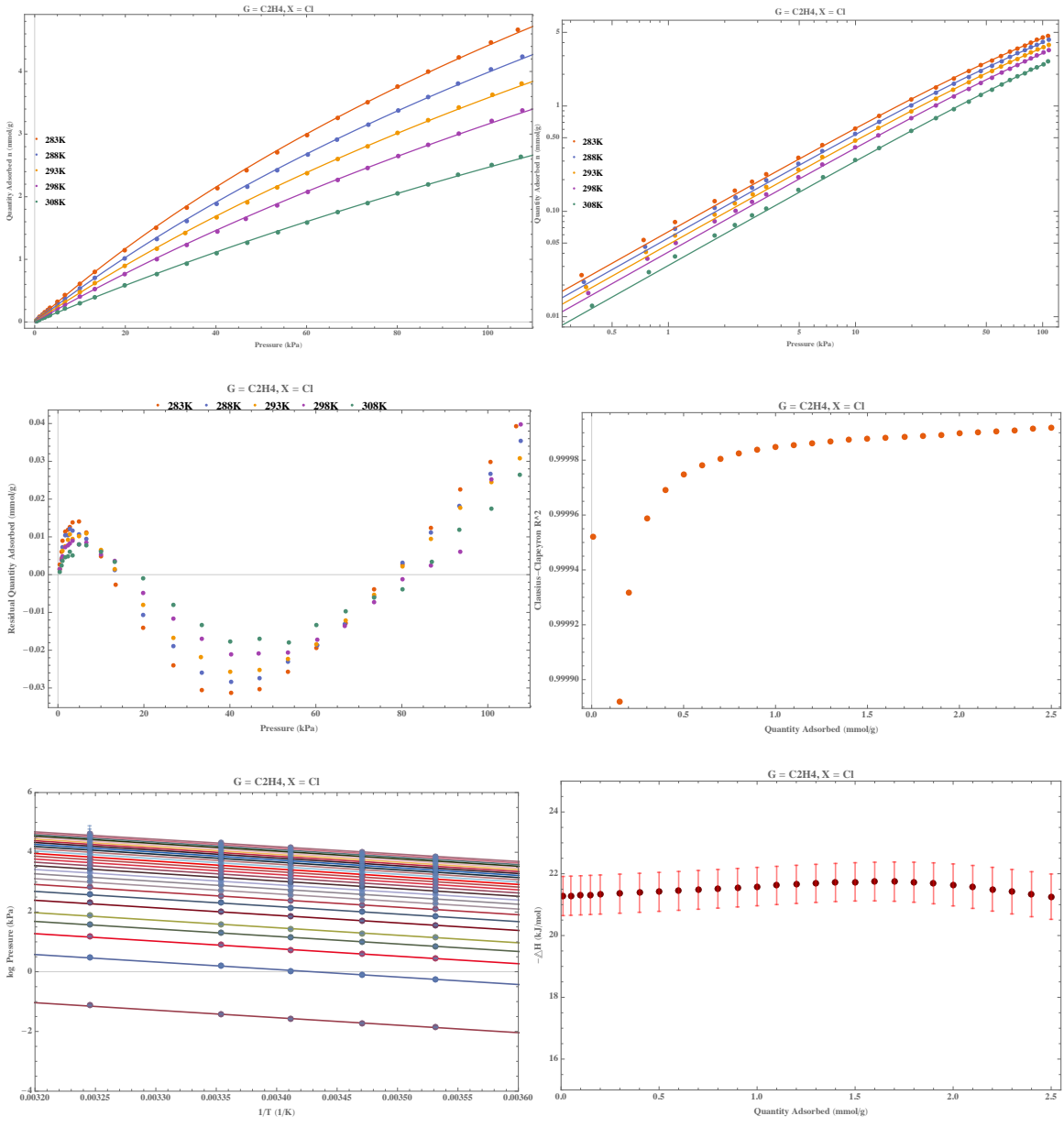

G = ethylene, X = Br

	283 K	288 K	293 K	298 K	308 K
U	142.249	136.116	123.941	110.549	90.9118
s	10.2099	10.1586	10.1083	10.1124	10.0267
a	$4.19987*10^6$	$4.37677*10^6$	$4.33957*10^6$	$4.38547*10^6$	$4.43476*10^6$
R^2	0.999489	0.999276	0.999322	0.999205	0.999373

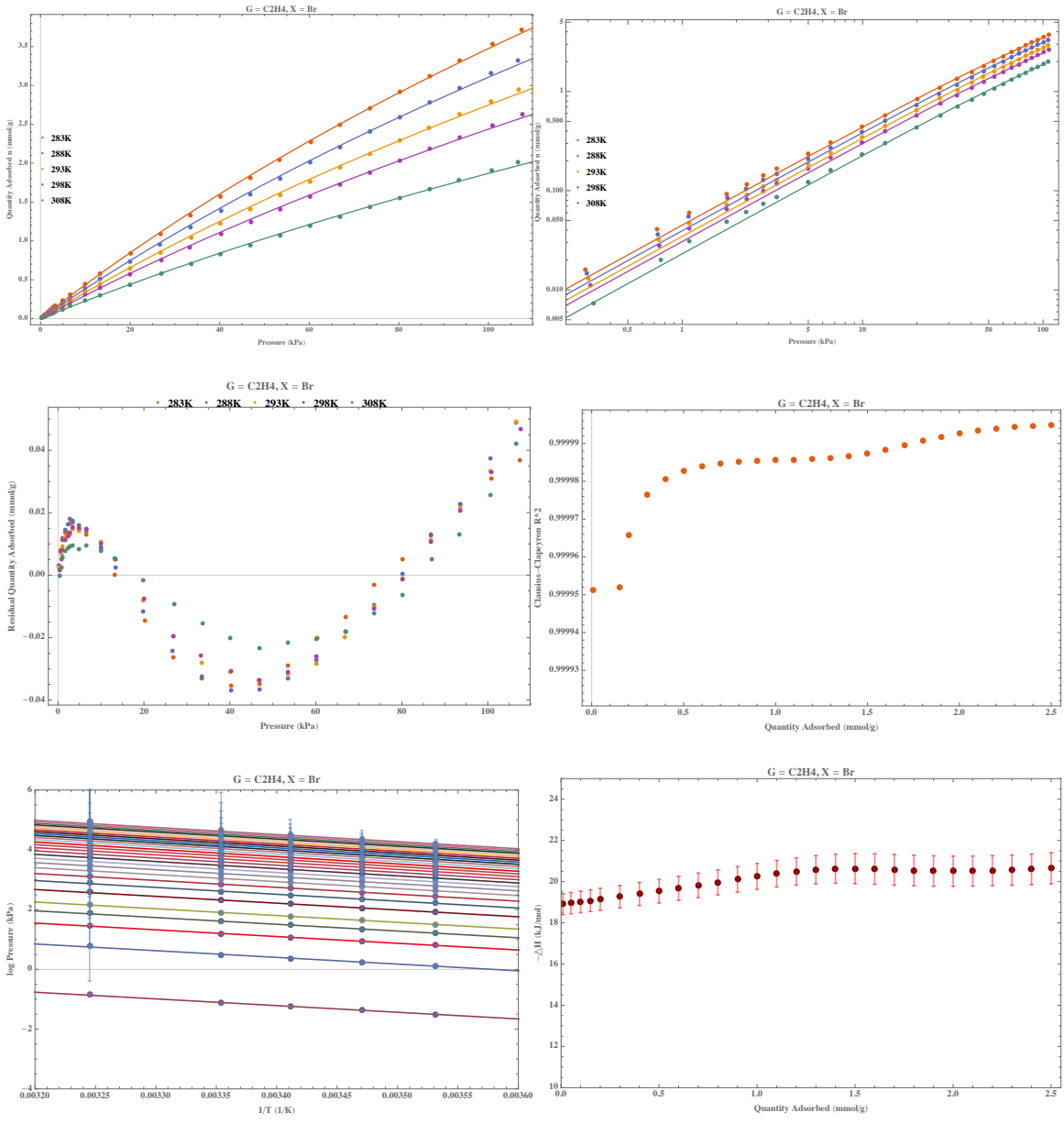

Virial Model for Isosteric Enthalpy of Adsorption

$$\ln p = \ln n + \frac{1}{T}\sum_{i=0}^{4} a_i n^i + \sum_{i=0}^{1} b_i n^i$$

$$\Delta H_{ads}(n) = R\sum_{i=0}^{4} a_i n^i$$

n = quantity adsorbed (mmol/g)

p = pressure (kPa)

T = temperature (K)

a_i, b_i = virial coefficients (K/mol^i)

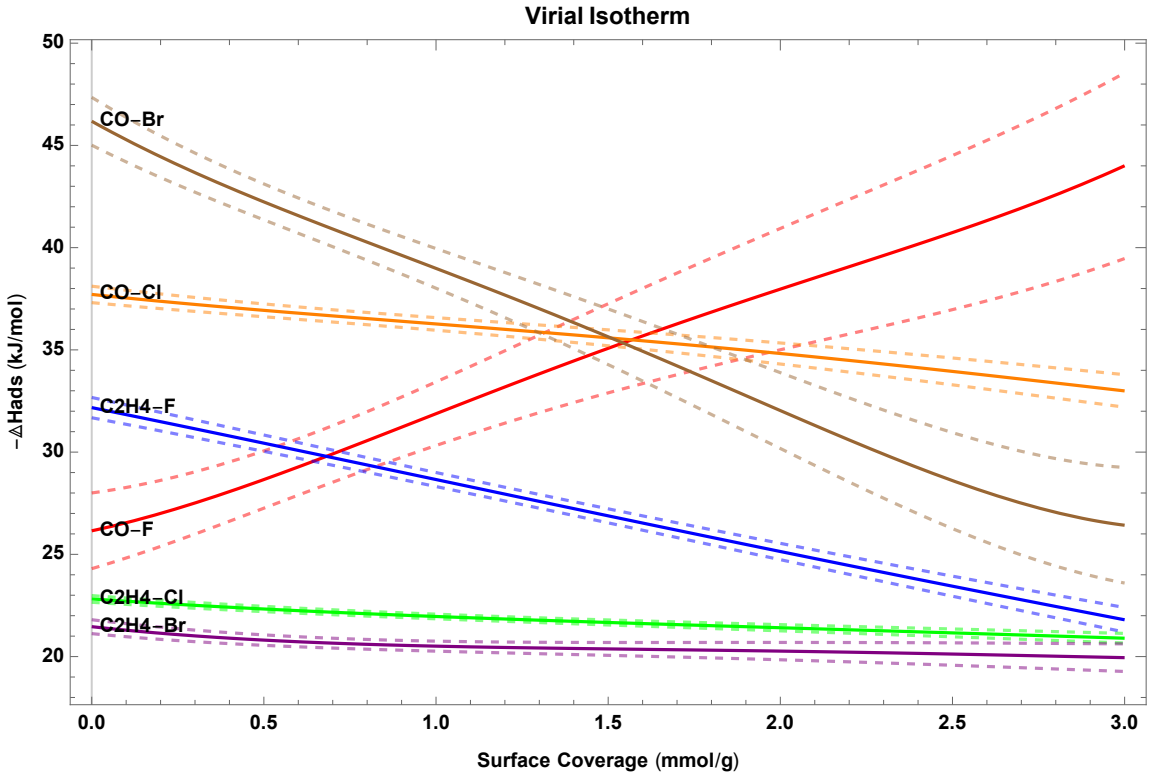

Summary of Virial Isotherm Fits. Dotted lines are one standard deviation.

G = CO, X = F

	Estimate	Standard Error
a_0	-3145.29	222.67
a_1	-430.24	246.012
a_2	-450.004	141.225
a_3	228.036	84.4302
a_4	-36.5873	16.0848
b_0	12.6571	0.754852
b_1	3.21696	0.792216

$R^2 = 0.994755$

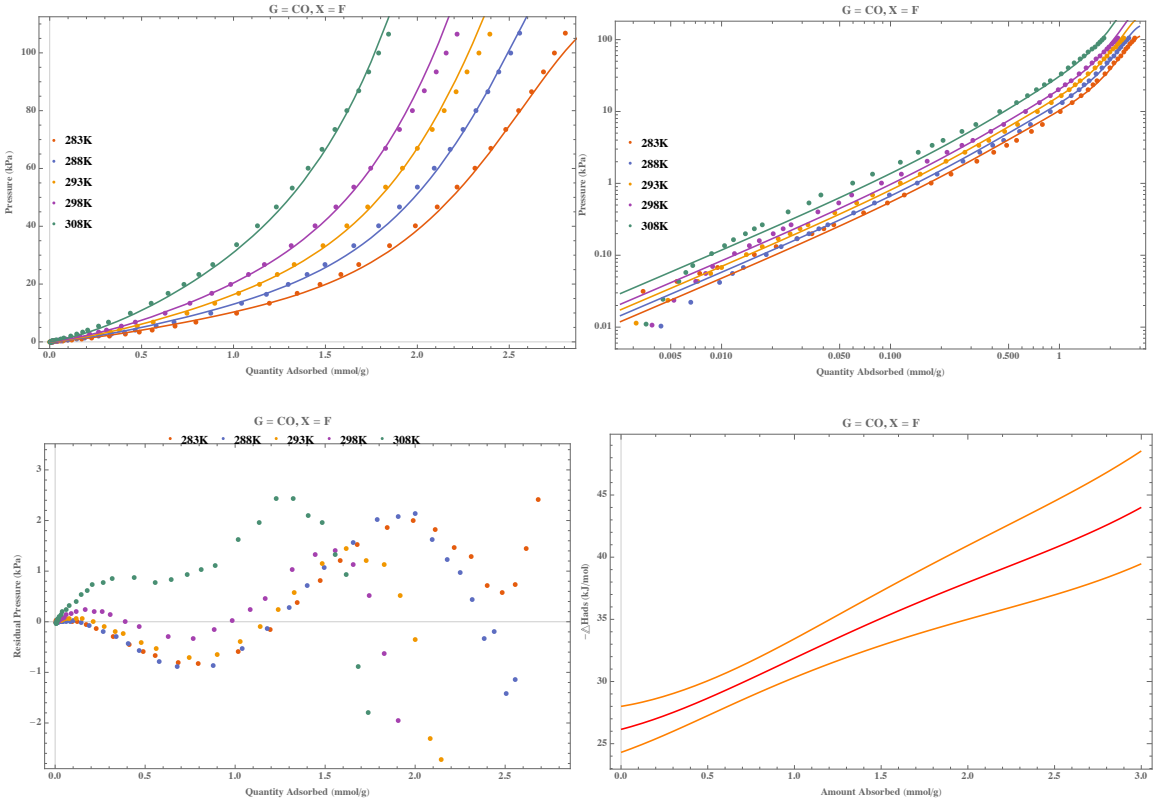

G = CO, X = Cl

	Estimate	Standard Error
a_0	-4535.79	48.3746
a_1	214.899	44.1429
a_2	-70.4058	23.1363
a_3	33.5374	11.9493
a_4	-4.30791	1.96507
b_0	17.2152	0.16415
b_1	0.0257865	0.140197

$R^2 = 0.999749$

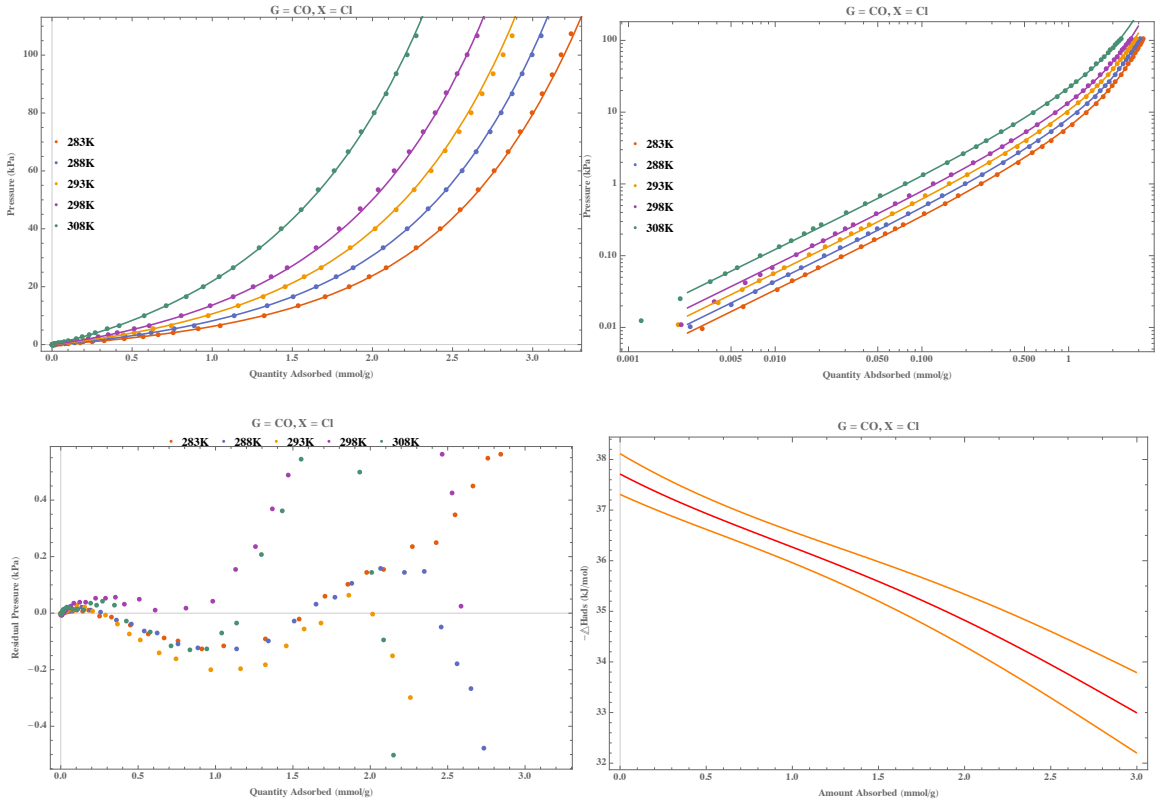

G = CO, X = Br

	Estimate	Standard Error
a_0	-5554.49	140.656
a_1	1132.74	157.623
a_2	-492.002	100.465
a_3	274.374	63.2769
a_4	-49.405	12.7042
b_0	20.6528	0.476755
b_1	-1.98746	0.498593

$R^2 = 0.997923$

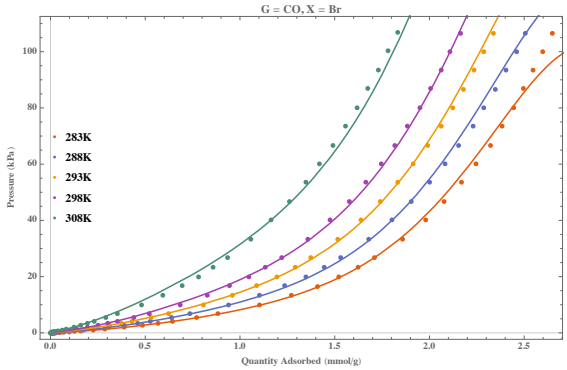

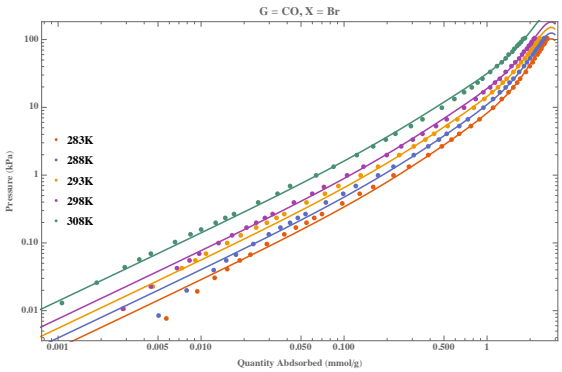

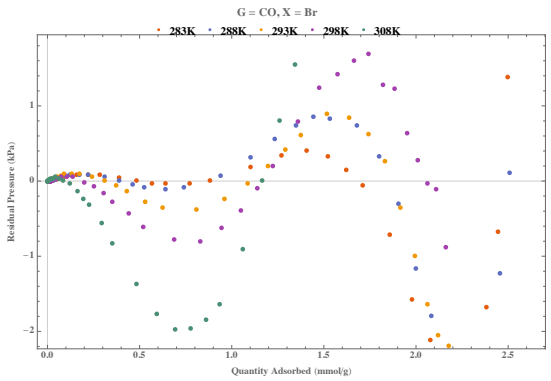

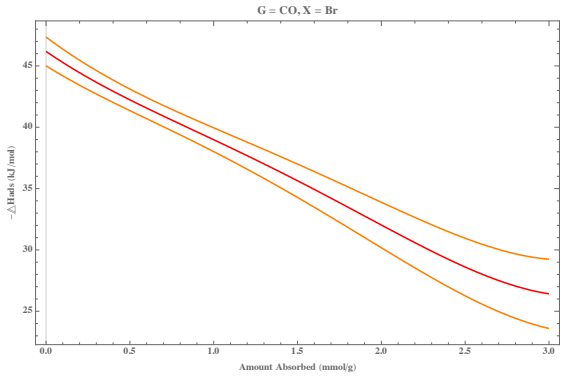

G = C_2H_4 X = F

	Estimate	Standard Error
a_0	-3869.99	59.6324
a_1	410.376	36.8163
a_2	20.9295	11.6294
a_3	-9.05943	3.93495
a_4	0.903879	0.429069
b_0	15.5967	0.201573
b_1	-1.1733	0.11743

R^2 = 0.999828

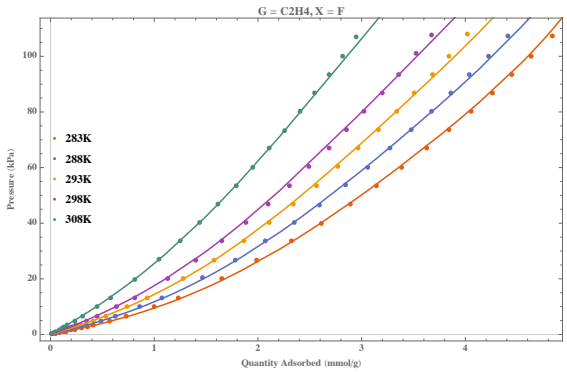

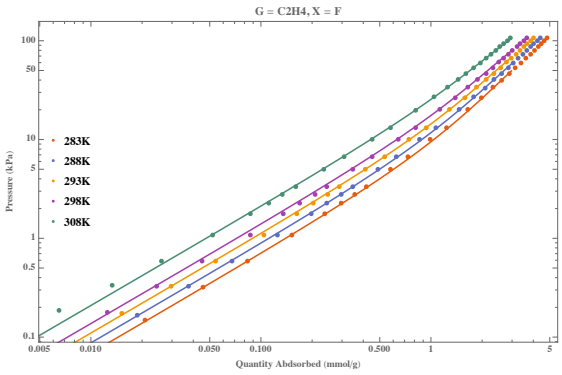

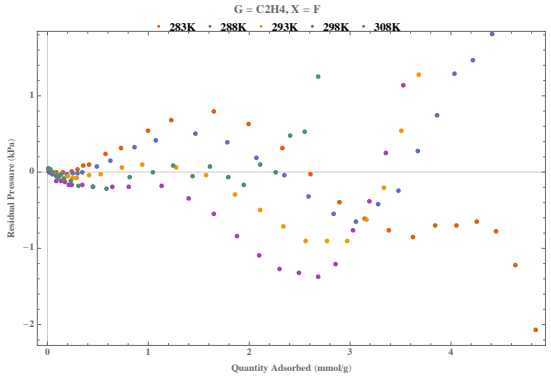

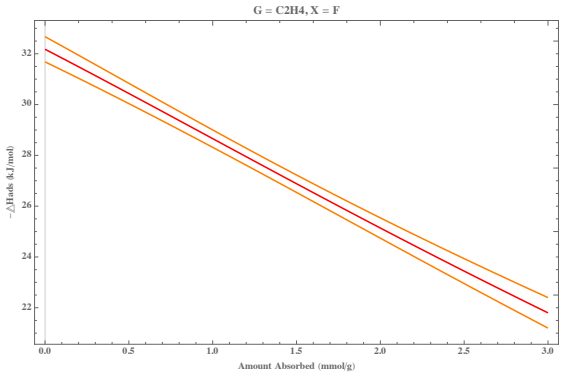

G = C_2H_4, X = Cl

	Estimate	Standard Error
a_0	-2744.61	19.6555
a_1	138.707	13.6658
a_2	-45.7346	4.35165
a_3	11.3473	1.53692
a_4	-0.983806	0.174077
b_0	12.2969	0.0666057
b_1	-0.14488	0.0442618

R^2 = 0.999981

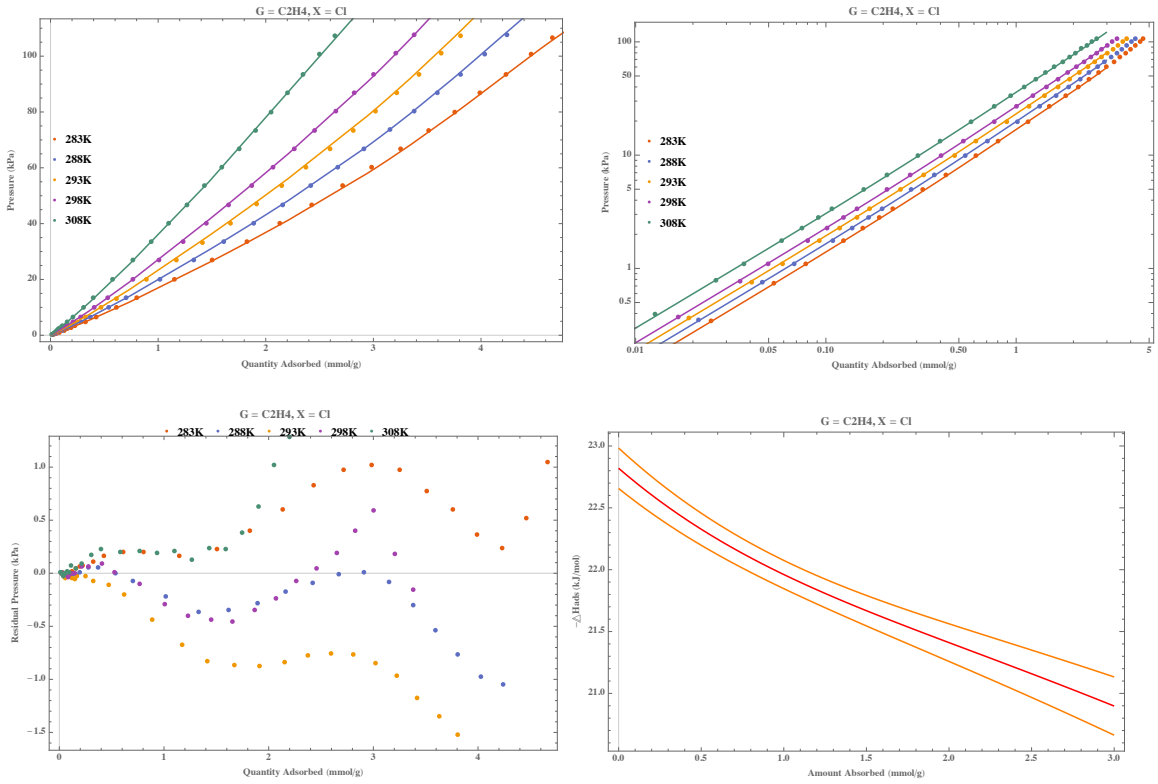

G = C_2H_4, X = Br

	Estimate	Standard Error
a_0	-2581.4	40.8822
a_1	222.15	37.1675
a_2	-150.99	14.3773
a_3	48.9921	6.141441
a_4	-5.53159	0.915535
b_0	11.9703	0.138634
b_1	-0.058865	0.121385

R^2 = 0.999918

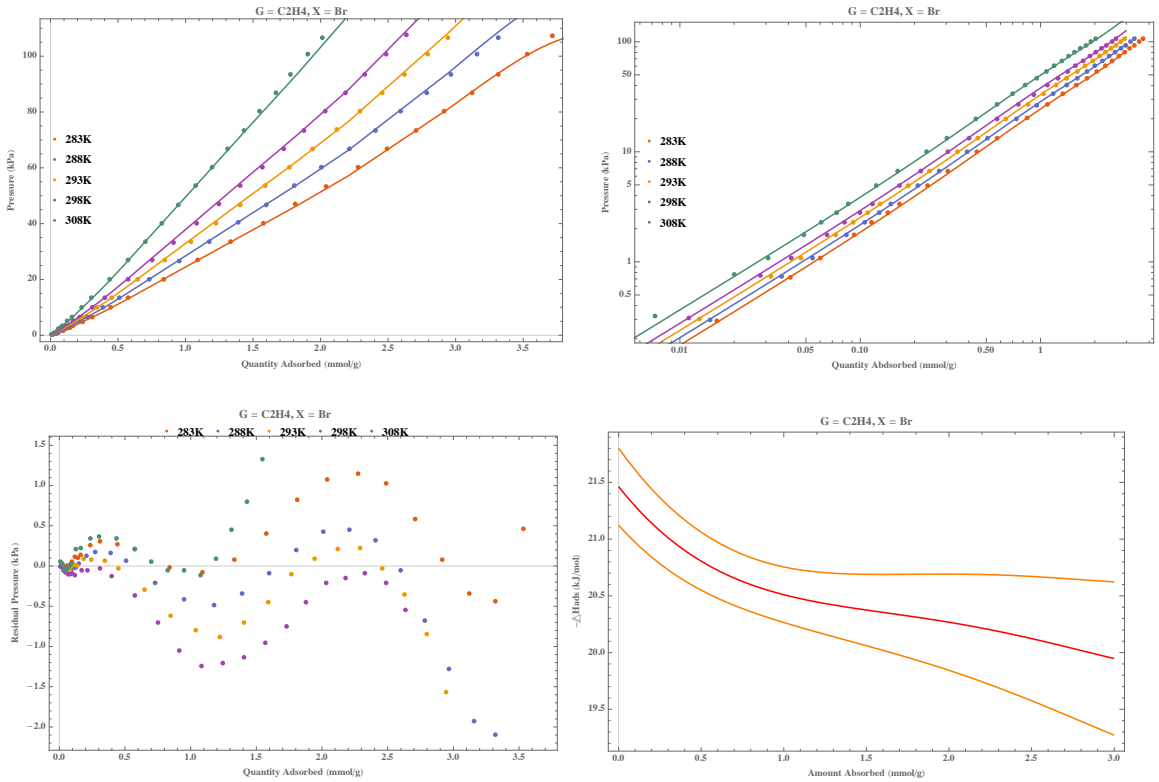

Sips (Langmuir-Freundlich) Models for Isosteric Enthalpy of Adsorption

$$n = \frac{Uap^s}{1+ap^s}$$

n = quantity adsorbed (mmol/g)

p = pressure (kPa)

U = maximum adsorption capacity

a = Sips constant

s = heterogeneity factor

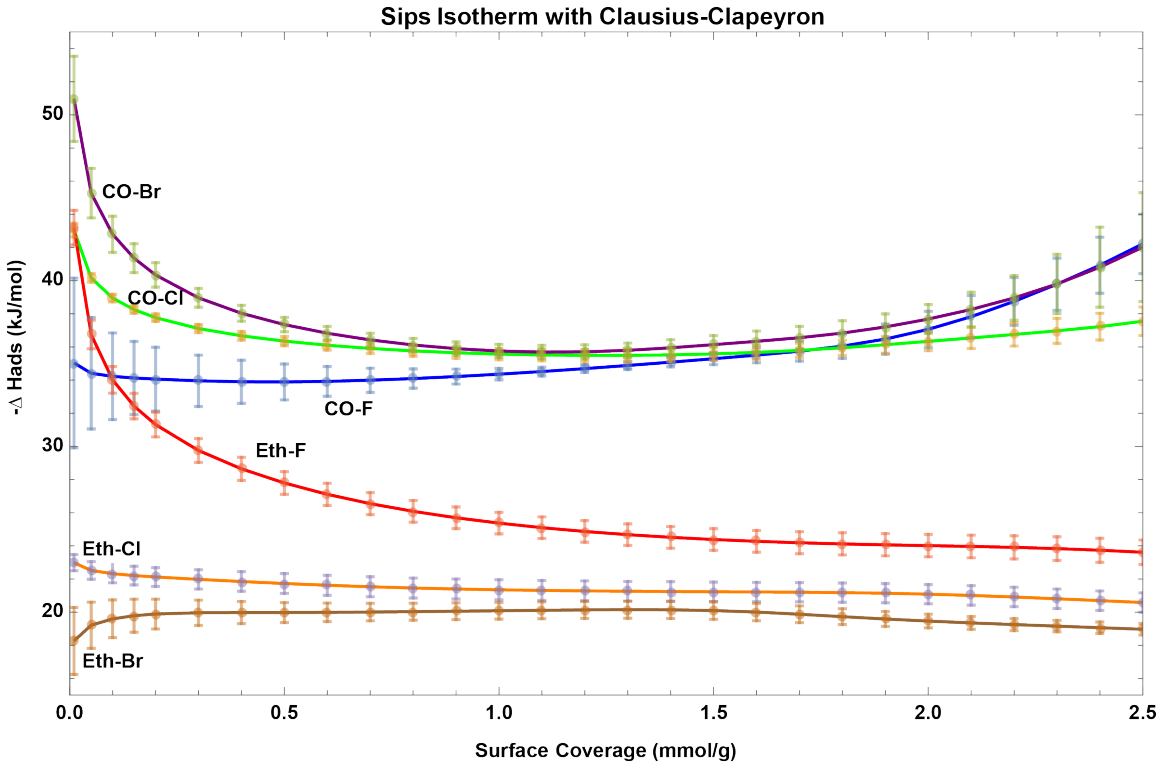

Summary of all Sips/CC calculations. Error bars show one standard deviation.

G = CO, X = F

	283 K	288 K	293 K	298 K	308 K
U	3.44571	3.41418	3.34023	3.30429	3.14974
s	0.917805	0.880539	0.894853	0.902536	0.907754
a	0.0497797	0.04447	0.0356671	0.0284464	0.0198512
R^2	0.998692	0.999592	0.99966	0.999667	0.999712

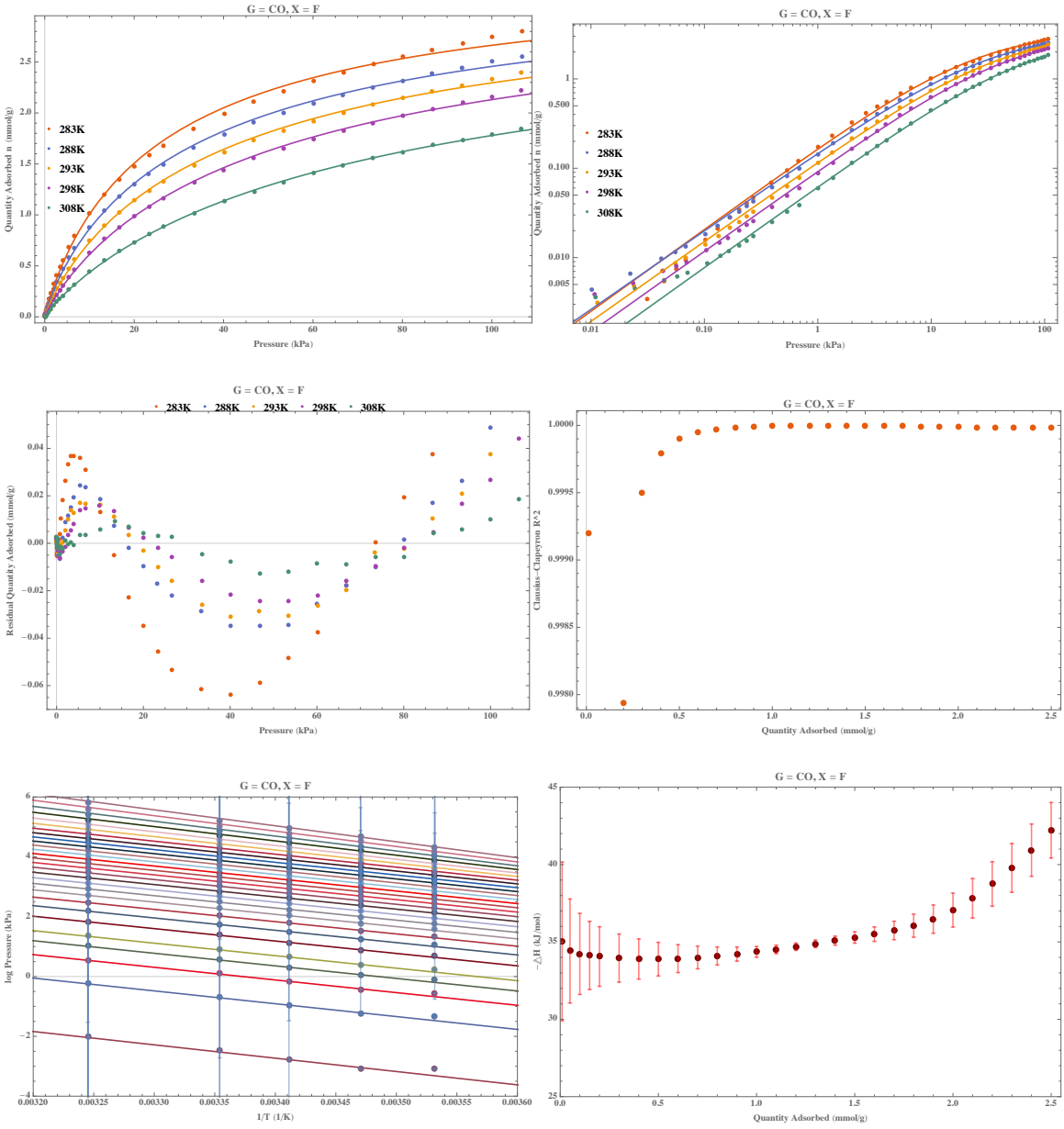

G = CO, X = Cl

	283 K	288 K	293 K	298 K	308 K
U	3.90009	3.82286	3.7482	3.67129	3.48608
s	0.88546	0.898632	0.910116	0.914805	0.936993
a	0.0664391	0.0527782	0.0423251	0.0337662	0.0224625
R^2	0.999395	0.999513	0.99957	0.999744	0.999795

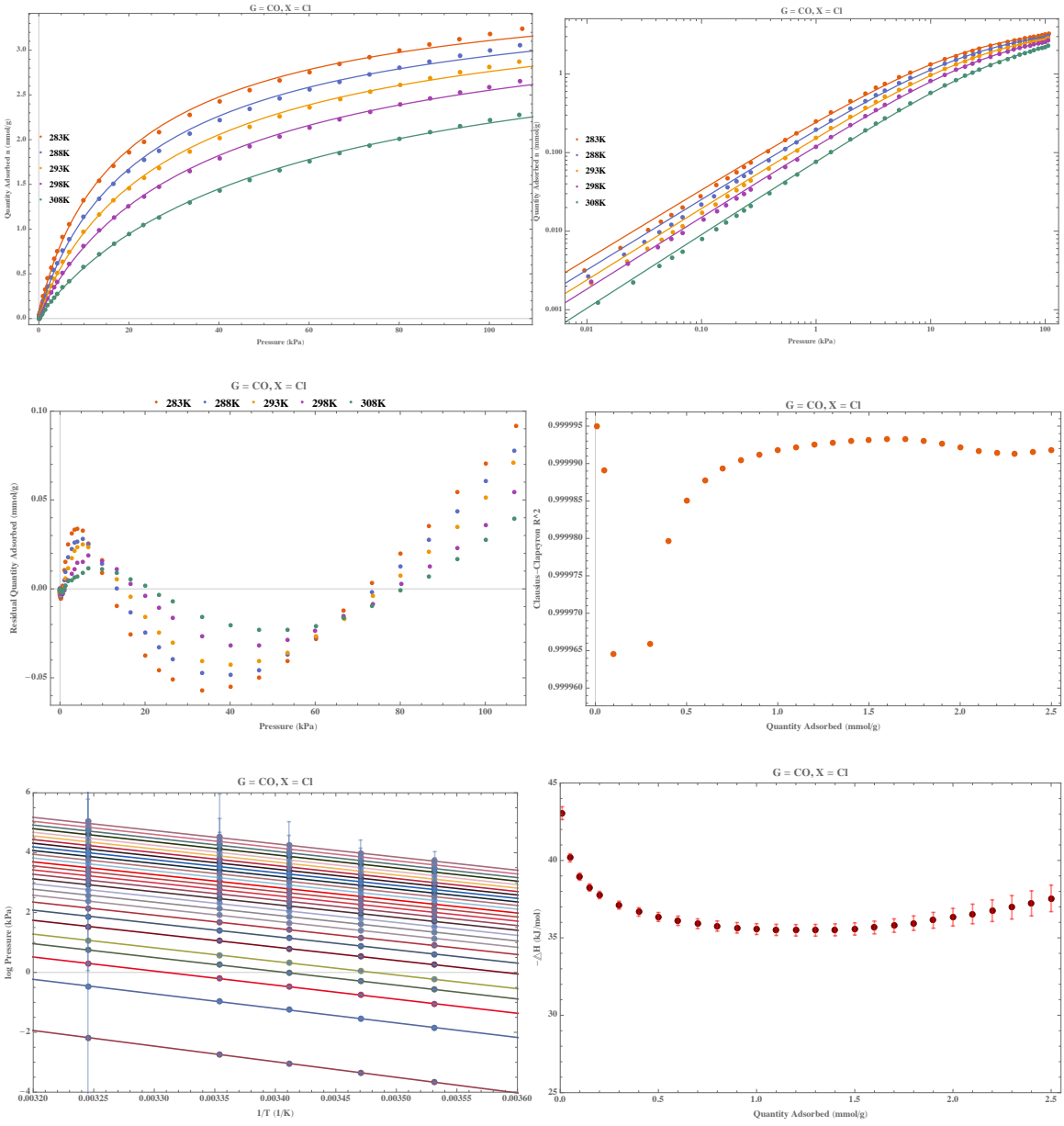

G = CO, X = Br

	283 K	288 K	293 K	298 K	308 K
U	3.27187	3.27314	3.05511	2.99641	2.69418
s	0.84281	0.849174	0.893861	0.892136	0.943709
a	0.0719193	0.0558379	0.0448456	0.0372138	0.0241213
R^2	0.999502	0.999556	0.999552	0.999717	0.999704

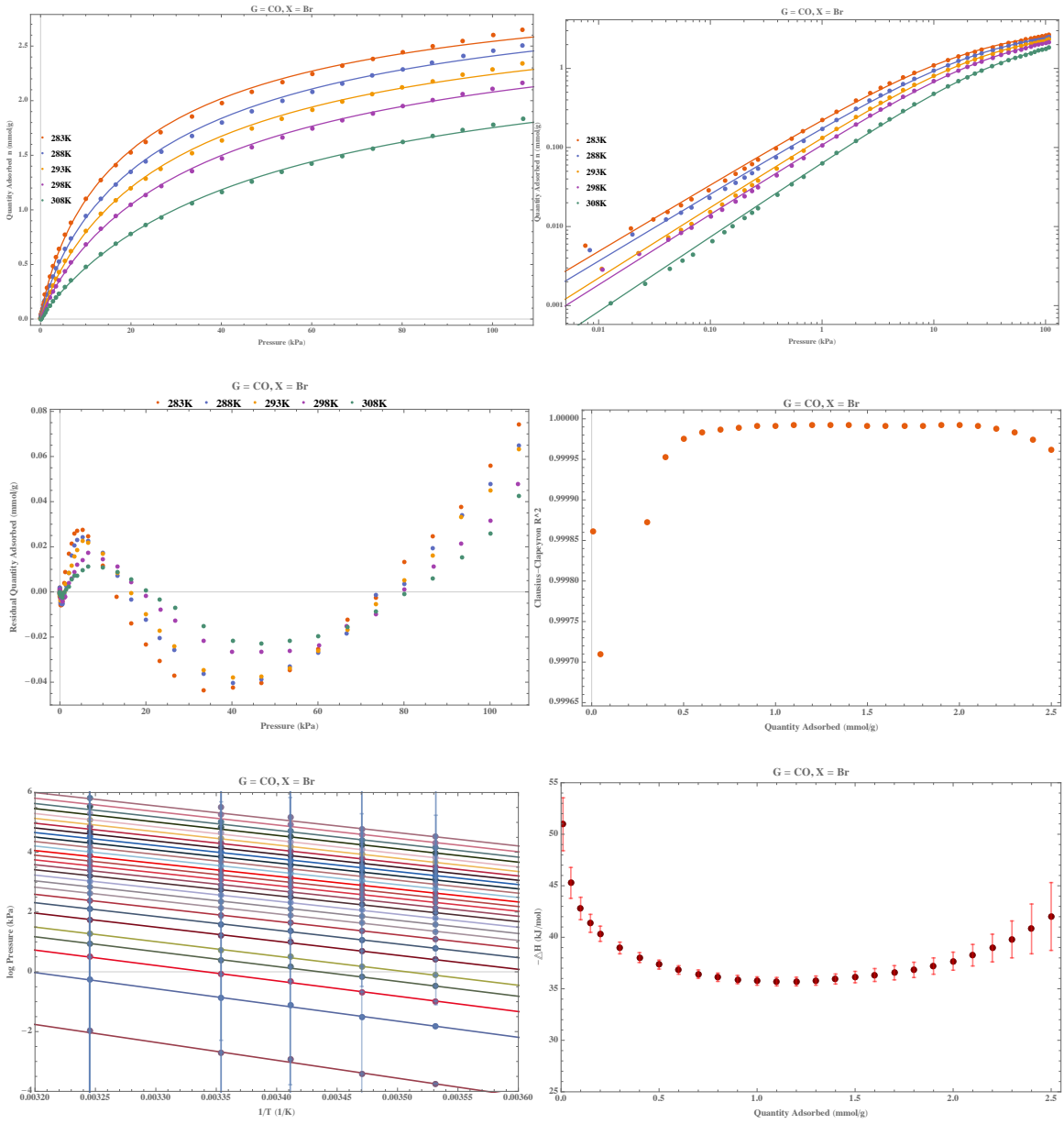

G = C_2H_4, X = F

	283 K	288 K	293 K	298 K	308 K
U	12.3524	11.3064	10.1453	9.86665	8.21607
s	0.844591	0.866797	0.893866	0.908688	0.964091
a	0.0120794	0.0108159	0.00977922	0.00828876	0.00608007
R^2	0.999643	0.999701	0.999769	0.999798	0.999768

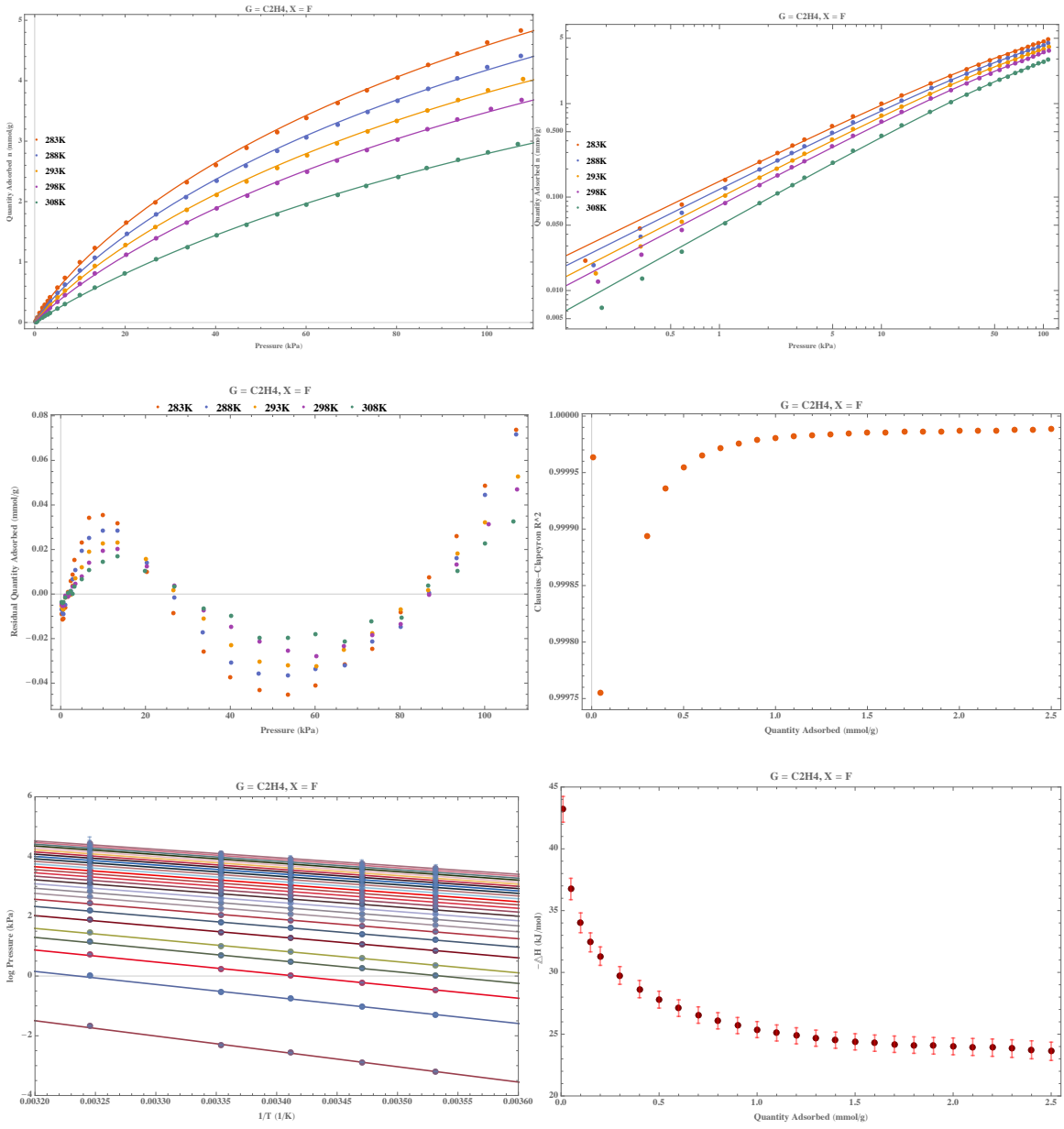

G = C_2H_4, X = Cl

	283 K	288 K	293 K	298 K	308 K
U	21.7058	21.6453	22.2085	24.016	24.5239
s	0.943901	0.947855	0.949111	0.950006	0.953837
a	0.00333629	0.00289391	0.00244852	0.00192215	0.00139425
R^2	0.999995	0.999991	0.999993	0.999995	0.999989

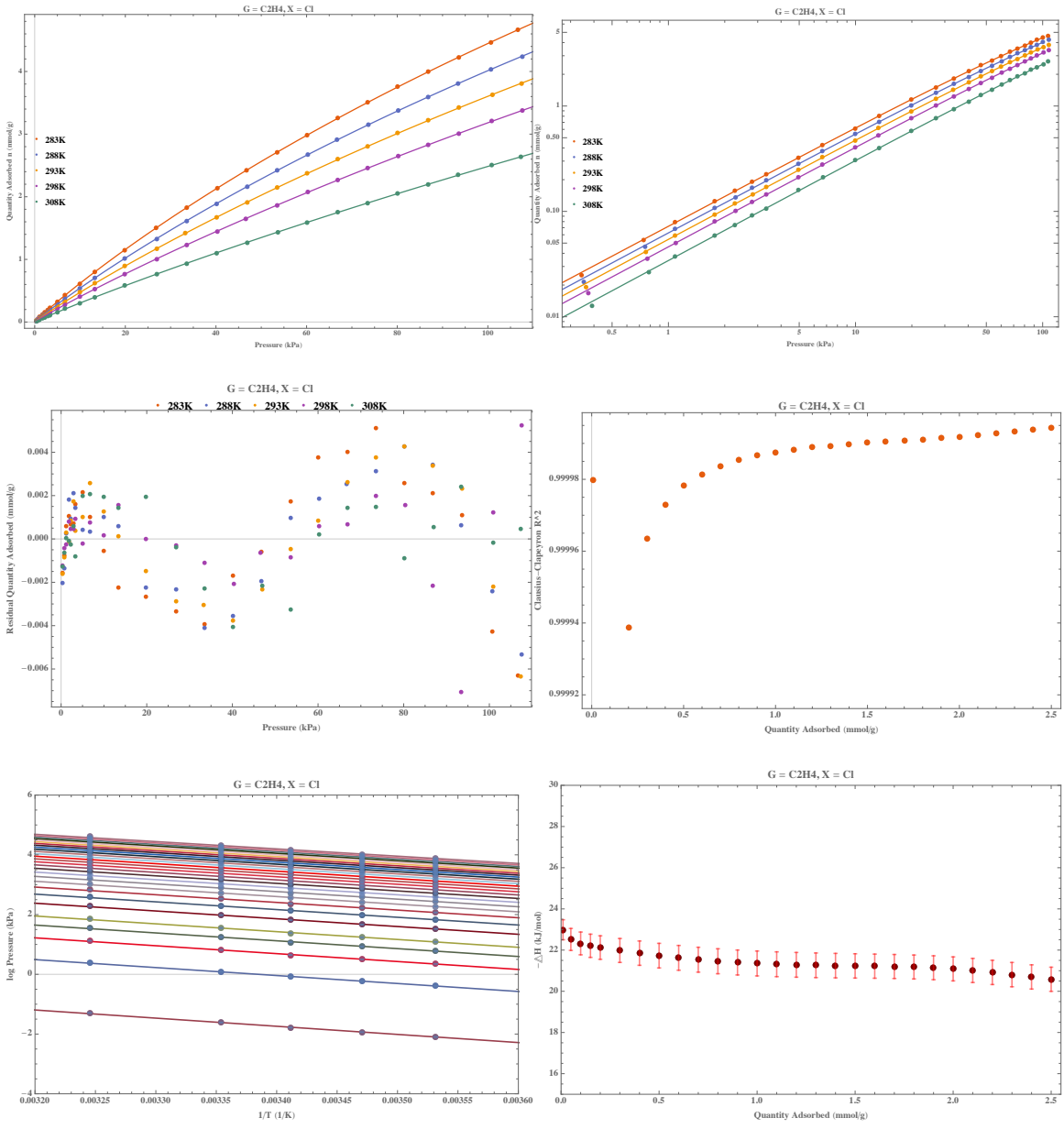

G = C_2H_4, X = Br

	283 K	288 K	293 K	298 K	308 K
U	49.8223	152.321	149.263	429.556	94.3708
s	0.923228	0.908901	0.911411	0.906088	0.919935
a	0.00108089	0.000321164	0.000286022	0.0000892223	0.000295874
R^2	0.999971	0.999972	0.999985	0.999966	0.999929

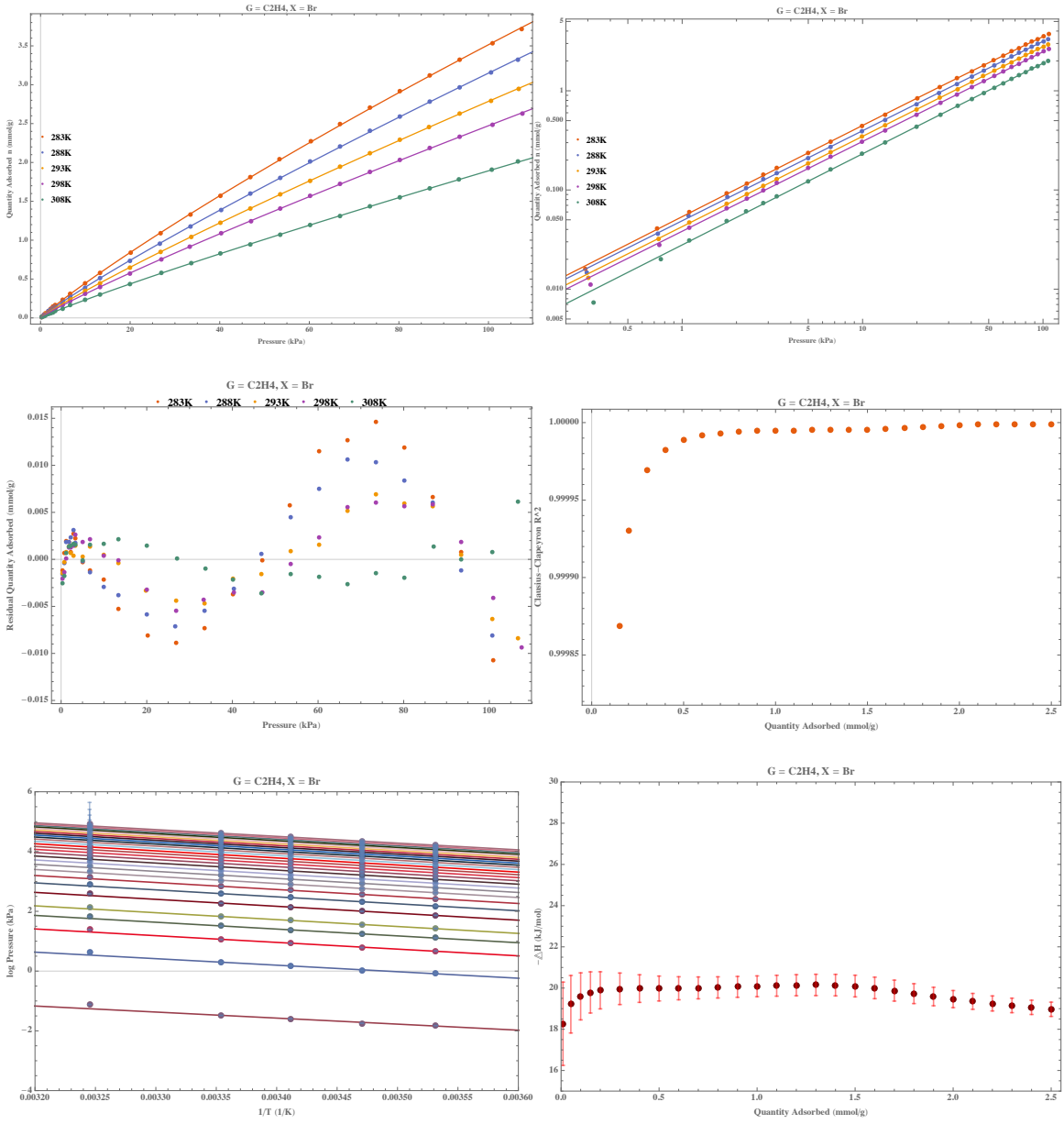

Dual-Site Langmuir Model for Isosteric Enthalpy of Adsorption

$$n = \frac{U_1 a_1 p}{1+a_1 p} + \frac{U_2 a_2 p}{1+a_2 p}$$

n = quantity adsorbed (mmol/g)

p = pressure (kPa)

U_1 = maximum adsorption capacity site 1

a_1 = Langmuir constant for site 1

U_2 = maximum adsorption capacity site 2

a_2 = Langmuir constant for site 2

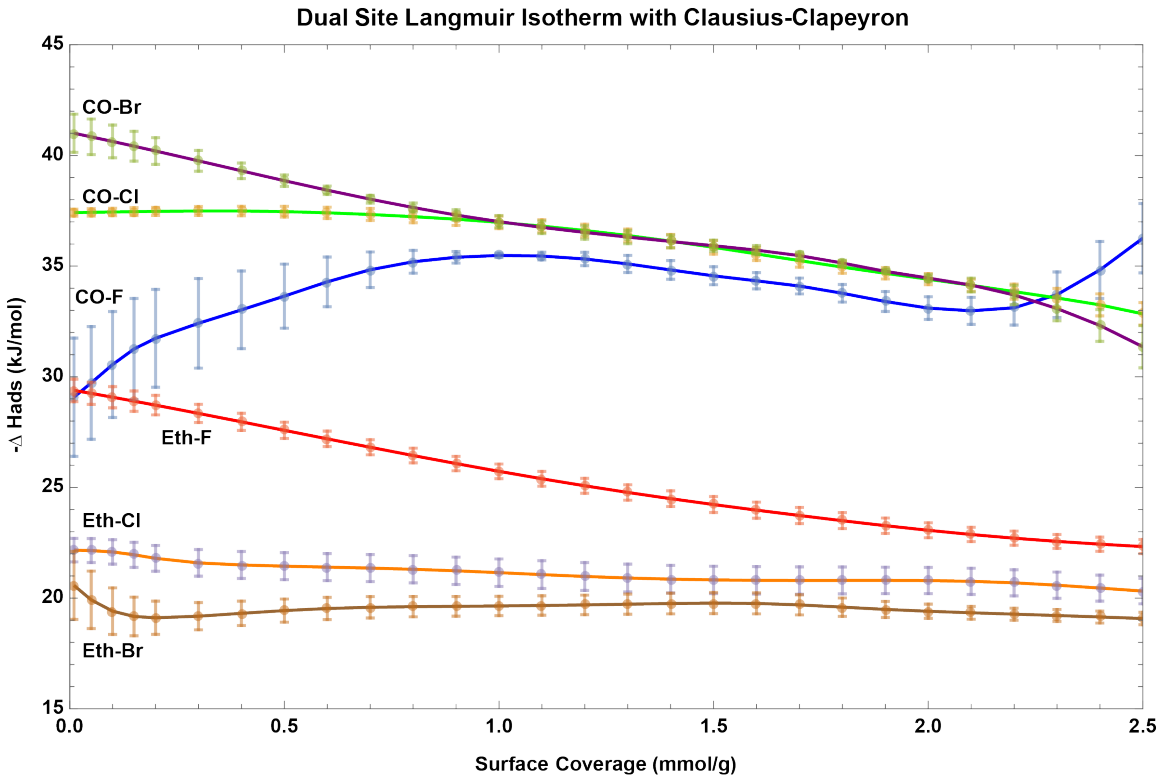

Summary of all DSL/CC calculations. Error bars show one standard deviation.

G = CO, X = F

	283 K	288 K	293 K	298 K	308 K
U_1	1.76323	2.7173	2.78848	2.84011	2.83802
a_1	0.0935967	0.0127078	0.0104615	0.00894128	0.0130336
U_2	3.12837	1.05535	0.999907	0.923821	0.187816
a_2	0.00584444	0.118544	0.0937149	0.0746356	0.147748
R^2	0.999826	0.999814	0.999884	0.999718	0.999587

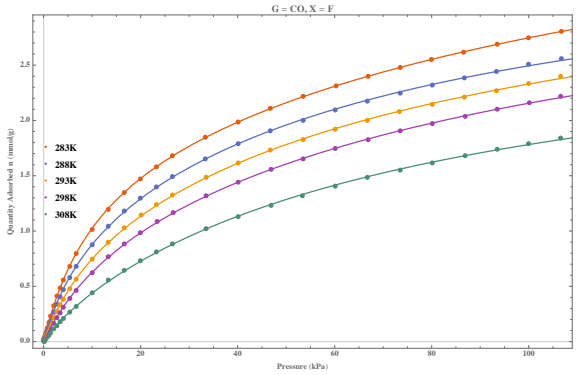

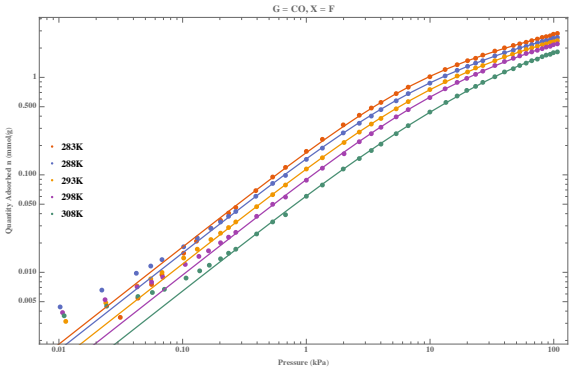

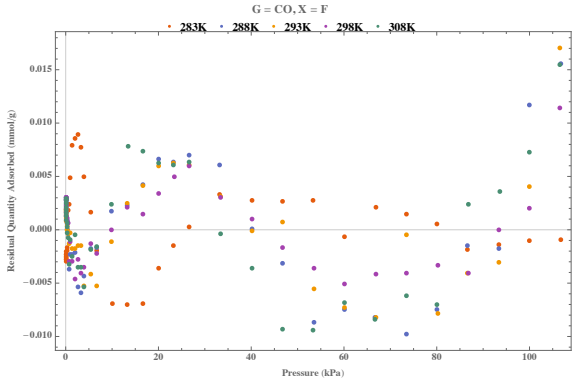

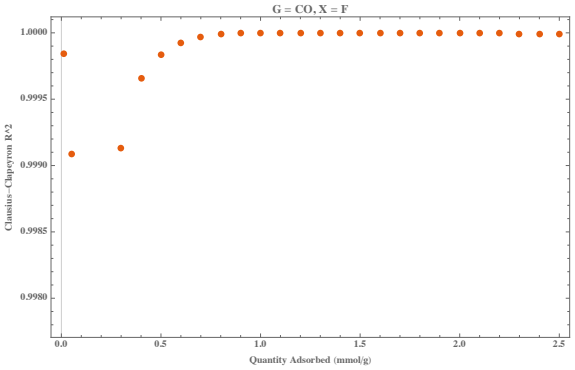

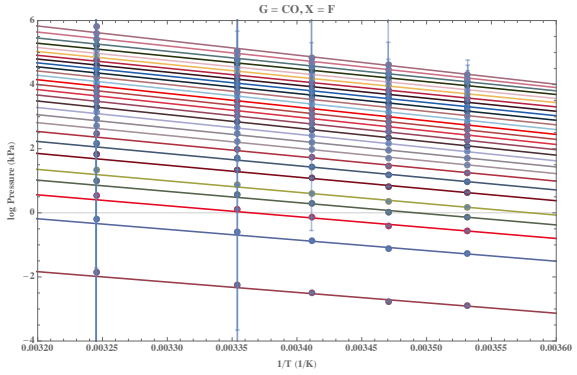

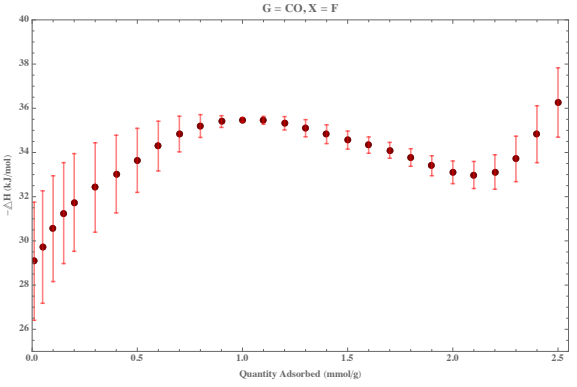

G = CO, X = Cl

	283 K	288 K	293 K	298 K	308 K
U_1	2.79425	1.45672	1.44297	2.9624	3.11188
a_1	0.016538	0.121102	0.0931956	0.0104458	0.00687372
U_2	1.52	2.83829	2.91287	1.20834	1.13045
a_2	0.157121	0.0137755	0.0107251	0.0793118	0.0506936
R^2	0.999985	0.999988	0.999993	0.999963	0.999991

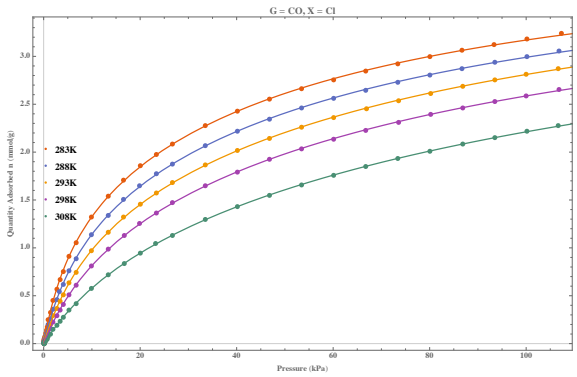

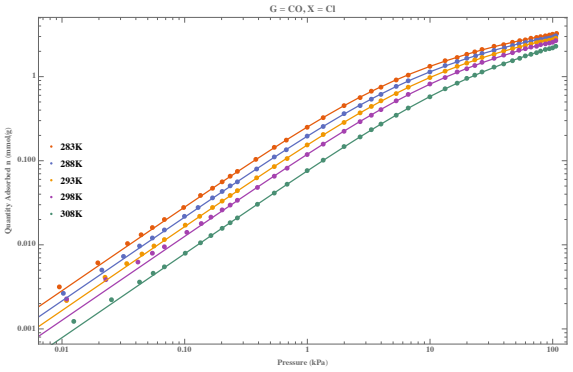

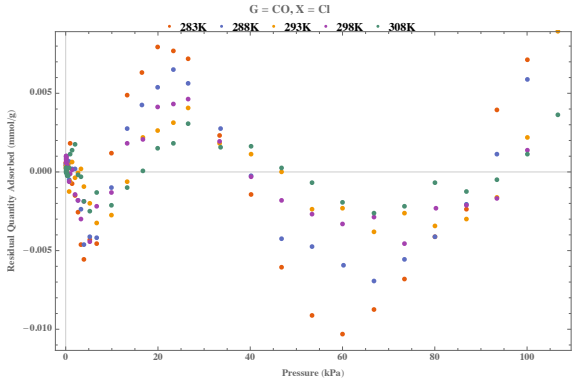

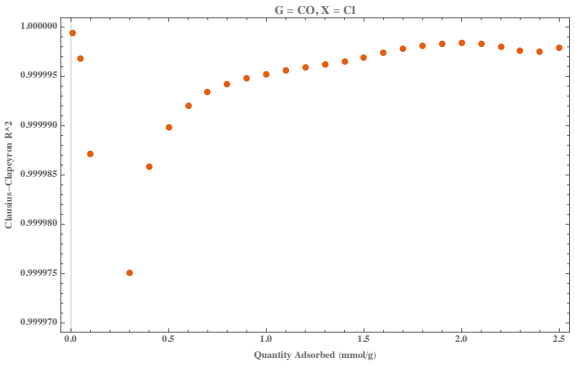

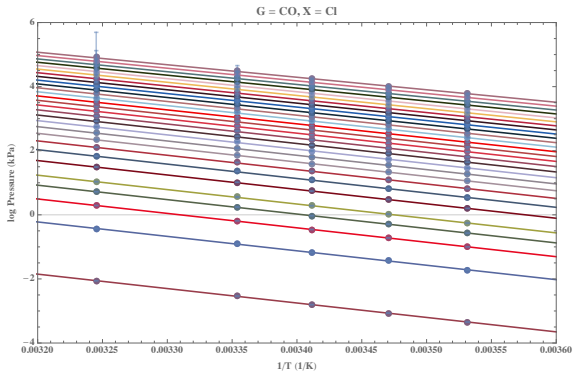

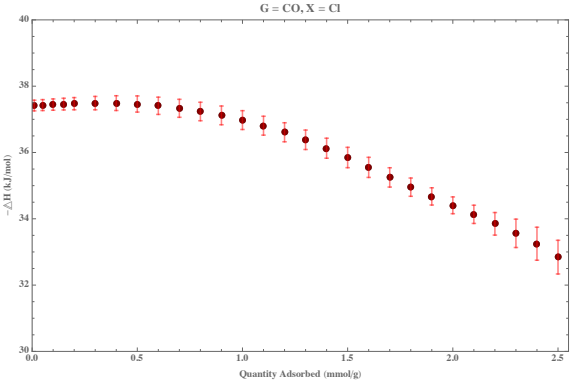

G = CO, X = Br

	283 K	288 K	293 K	298 K	308 K
U_1	2.46217	2.56768	2.418	2.44229	2.89267
a_1	0.02135	0.0170786	0.00987337	0.0117264	0.00330234
U_2	0.943152	0.868636	1.19003	0.866496	1.31304
a_2	0.231705	0.182158	0.0998768	0.0096256	0.0423484
R^2	0.999722	0.999698	0.999937	0.999844	0.999991

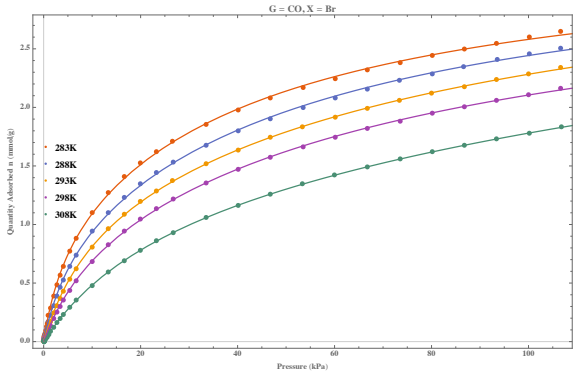

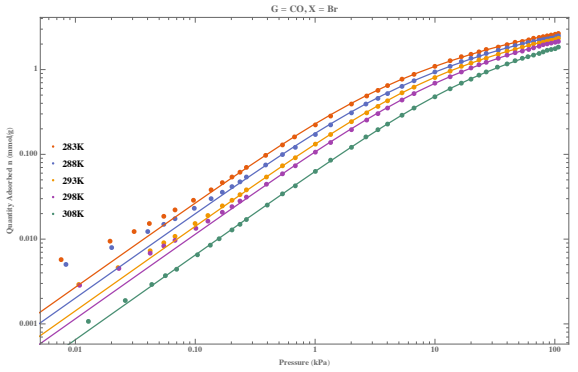

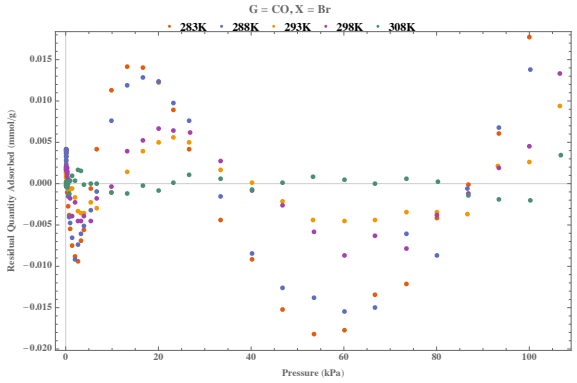

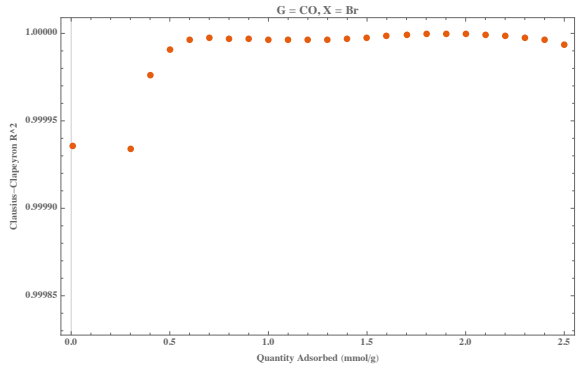

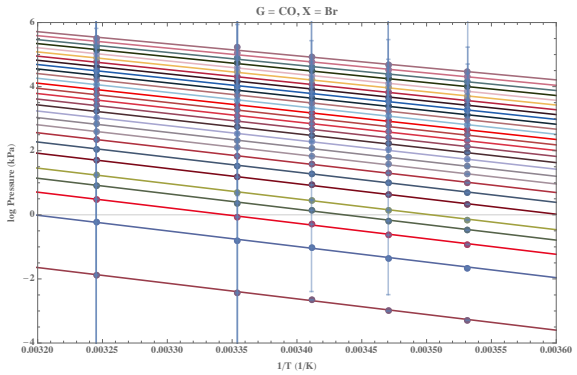

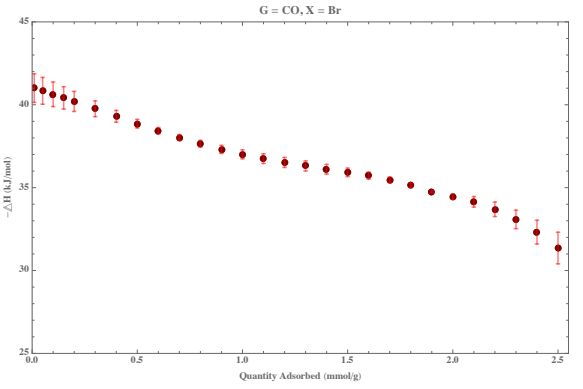

G = C_2H_4, X = F

	283 K	288 K	293 K	298 K	308 K
U_1	13.1321	1.08773	1.05136	1.02448	1028.92
a_1	0.00384017	0.0689303	0.0540611	0.044034	0.0000145715
U_2	1.10213	13.0558	12.1511	12.9691	2.14487
a_2	0.0872416	0.00333717	0.00320464	0.00259274	0.00259274
R^2	0.999997	0.999996	0.999992	0.999988	0.99992

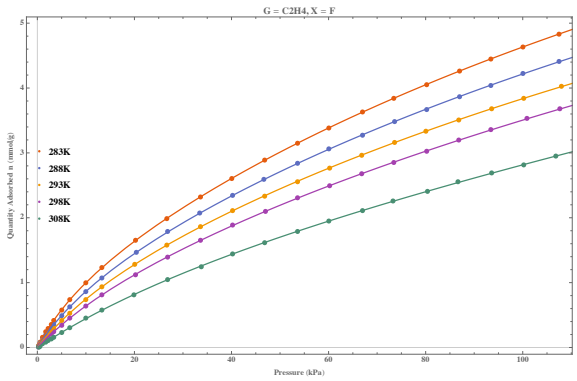

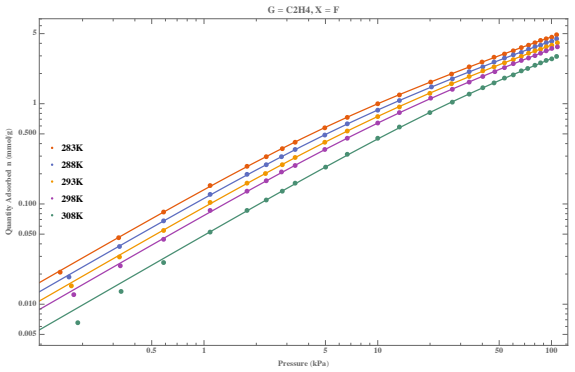

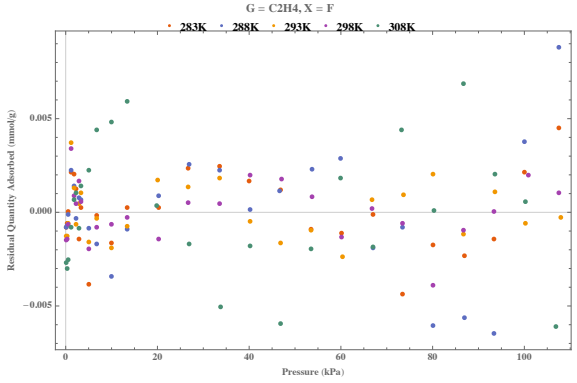

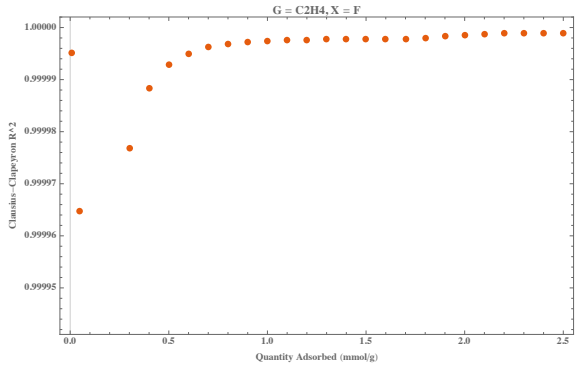

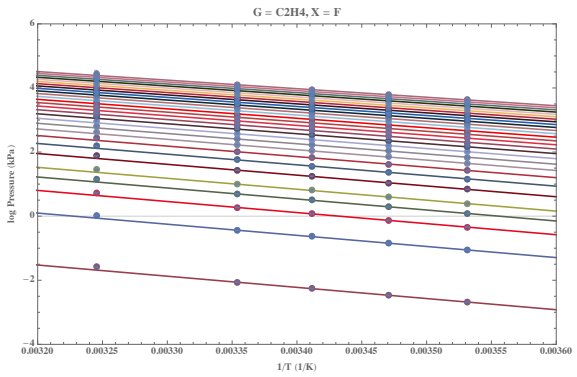

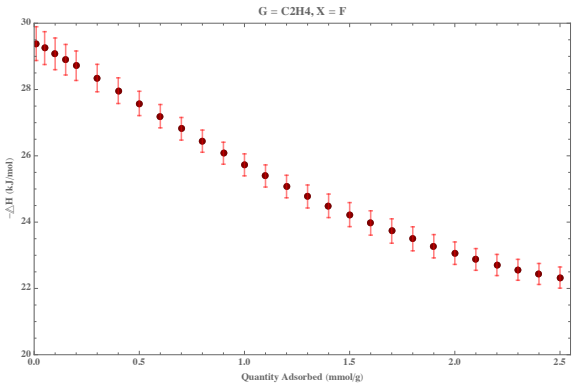

G = C_2H_4, X = Cl

	283 K	288 K	293 K	298 K	308 K
U_1	0.0889428	17.9032	0.0774436	18.8628	0.0706771
a_1	0.19005	0.00281494	0.146105	0.00198009	0.0914834
U_2	17.7817	0.0848068	18.0982	0.0678695	20.0265
a_2	0.00324847	0.158996	0.00242382	0.136973	0.00137576
R^2	0.999999	0.999997	0.999998	0.999997	0.999997

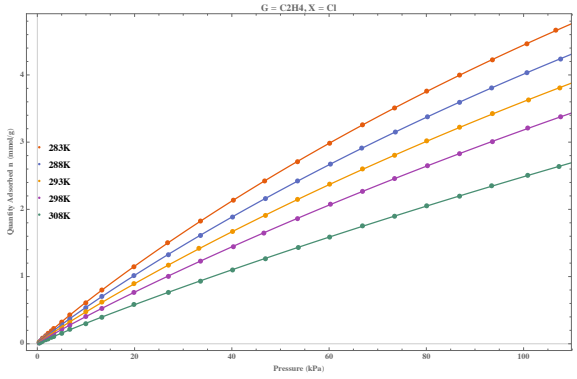

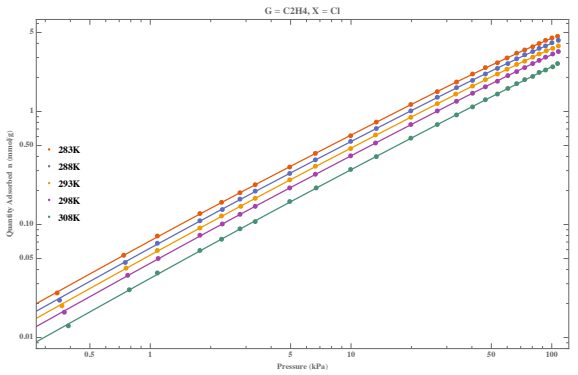

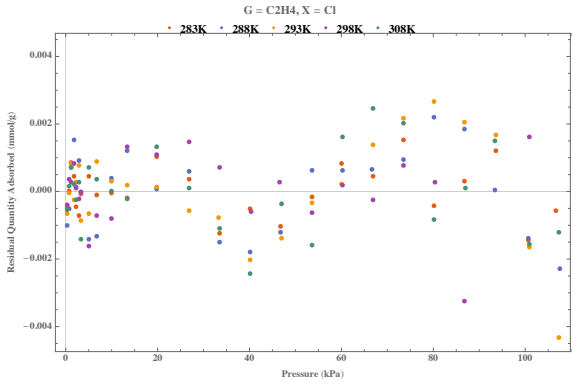

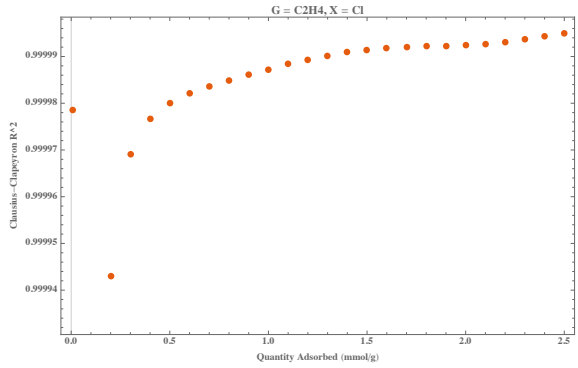

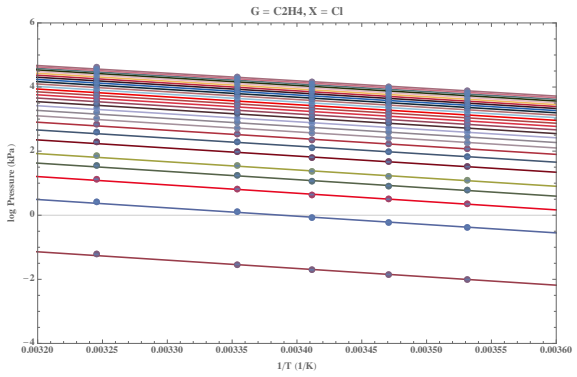

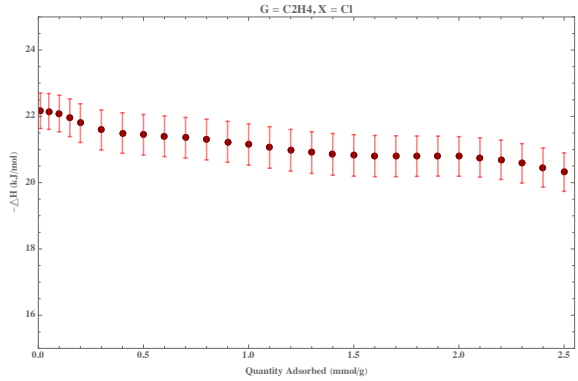

G = C_2H_4, X = Br

	283 K	288 K	293 K	298 K	308 K
U_1	22.9129	26.4185	26.6506	27.8703	30.7648
a_1	0.00177518	0.00132047	0.00113493	0.000941937	0.000627983
U_2	0.0565859	0.0647446	0.0702615	0.076716	0.0843938
a_2	0.33456	0.292574	0.210294	0.177744	0.10093
R^2	0.999993	0.999995	0.999996	0.999993	0.999967

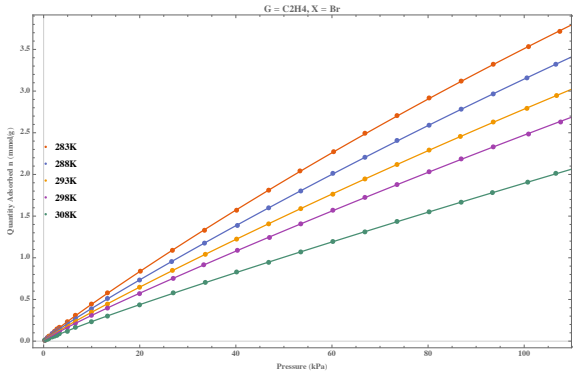

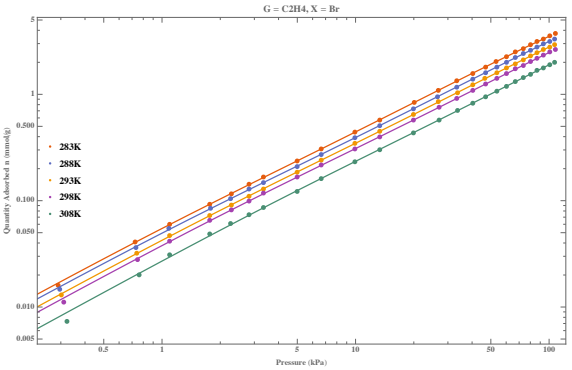

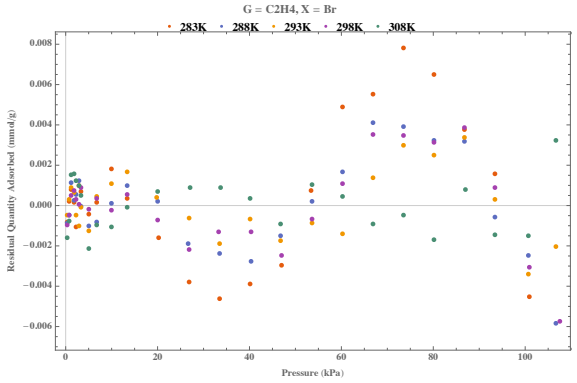

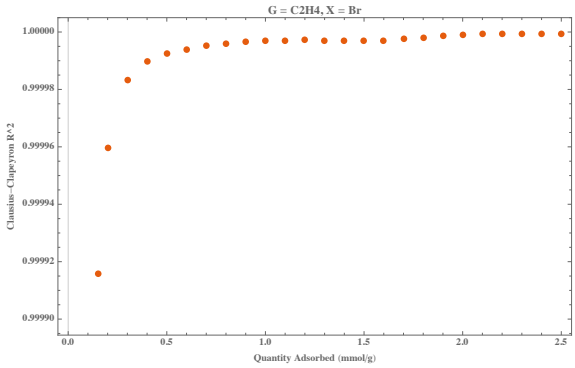

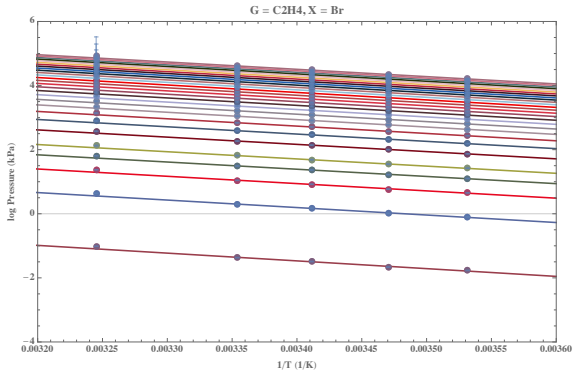

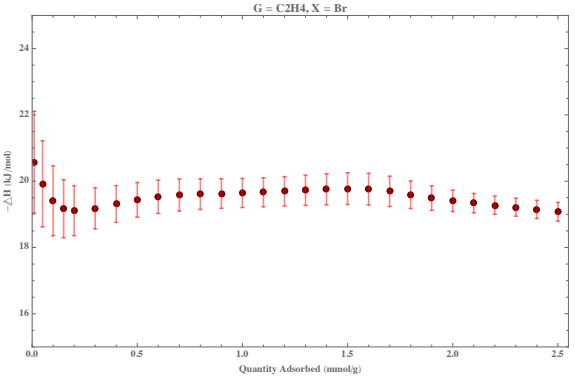

REFERENCES CITED

(1) Yaghi, O. M.; Li, G.; Li, H. Selective Binding and Removal of Guests in a Microporous Metal–Organic Framework. *Nature* **1995**, *378* (6558), 703–706. https://doi.org/10.1038/378703a0.

(2) Furukawa, H.; Cordova, K. E.; O'Keeffe, M.; Yaghi, O. M. The Chemistry and Applications of Metal-Organic Frameworks. *Science* **2013**, *341* (6149), 1230444–1230444. https://doi.org/10.1126/science.1230444.

(3) Kitagawa, S.; Kitaura, R.; Noro, S. Functional Porous Coordination Polymers. *Angewandte Chemie International Edition* **2004**, *43* (18), 2334–2375. https://doi.org/10.1002/anie.200300610.

(4) Li, H.; Eddaoudi, M.; O'Keeffe, M.; Yaghi, O. M. Design and Synthesis of an Exceptionally Stable and Highly Porous Metal-Organic Framework. *Nature* **1999**, *402* (6759), 276–279. https://doi.org/10.1038/46248.

(5) Eddaoudi, M.; Moler, D. B.; Li, H.; Chen, B.; Reineke, T. M.; O'Keeffe, M.; Yaghi, O. M. Modular Chemistry: Secondary Building Units as a Basis for the Design of Highly Porous and Robust Metal−Organic Carboxylate Frameworks. *Accounts of Chemical Research* **2001**, *34* (4), 319–330. https://doi.org/10.1021/ar000034b.

(6) Tranchemontagne, D. J.; Mendoza-Cortés, J. L.; O'Keeffe, M.; Yaghi, O. M. Secondary Building Units, Nets and Bonding in the Chemistry of Metal–Organic Frameworks. *Chemical Society Reviews* **2009**, *38* (5), 1257. https://doi.org/10.1039/b817735j.

(7) Kawano, M.; Kawamichi, T.; Haneda, T.; Kojima, T.; Fujita, M. The Modular Synthesis of Functional Porous Coordination Networks. *Journal of the American Chemical Society* **2007**, *129* (50), 15418–15419. https://doi.org/10.1021/ja0752540.

(8) Furukawa, H.; Ko, N.; Go, Y. B.; Aratani, N.; Choi, S. B.; Choi, E.; Yazaydin, A. O.; Snurr, R. Q.; O'Keeffe, M.; Kim, J.; Yaghi, O. M. Ultrahigh Porosity in Metal-Organic Frameworks. *Science* **2010**, *329* (5990), 424–428. https://doi.org/10.1126/science.1192160.

(9) Eddaoudi, M.; Li, H.; Yaghi, O. M. Highly Porous and Stable Metal−Organic Frameworks: Structure Design and Sorption Properties. *Journal of the American Chemical Society* **2000**, *122* (7), 1391–1397. https://doi.org/10.1021/ja9933386.

(10) Farha, O. K.; Özgür Yazaydın, A.; Eryazici, I.; Malliakas, C. D.; Hauser, B. G.; Kanatzidis, M. G.; Nguyen, S. T.; Snurr, R. Q.; Hupp, J. T. De Novo Synthesis of a Metal–Organic Framework Material Featuring Ultrahigh Surface Area and Gas Storage Capacities. *Nature Chemistry* **2010**, *2* (11), 944–948. https://doi.org/10.1038/nchem.834.

(11) Mason, J. A.; Veenstra, M.; Long, J. R. Evaluating Metal–Organic Frameworks for Natural Gas Storage. *Chemical Science* **2014**, *5* (1), 32–51. https://doi.org/10.1039/C3SC52633J.

(12) Rosi, N. L. Hydrogen Storage in Microporous Metal-Organic Frameworks. *Science* **2003**, *300* (5622), 1127–1129. https://doi.org/10.1126/science.1083440.

(13) Li, J.-R.; Kuppler, R. J.; Zhou, H.-C. Selective Gas Adsorption and Separation in Metal–Organic Frameworks. *Chemical Society Reviews* **2009**, *38* (5), 1477. https://doi.org/10.1039/b802426j.

(14) Li, J.-R.; Sculley, J.; Zhou, H.-C. Metal–Organic Frameworks for Separations. *Chemical Reviews* **2012**, *112* (2), 869–932. https://doi.org/10.1021/cr200190s.

(15) Chughtai, A. H.; Ahmad, N.; Younus, H. A.; Laypkov, A.; Verpoort, F. Metal–Organic Frameworks: Versatile Heterogeneous Catalysts for Efficient Catalytic Organic Transformations. *Chemical Society Reviews* **2015**, *44* (19), 6804–6849. https://doi.org/10.1039/C4CS00395K.

(16) Corma, A.; García, H.; Llabrés i Xamena, F. X. Engineering Metal Organic Frameworks for Heterogeneous Catalysis. *Chemical Reviews* **2010**, *110* (8), 4606–4655. https://doi.org/10.1021/cr9003924.

(17) Farrusseng, D.; Aguado, S.; Pinel, C. Metal-Organic Frameworks: Opportunities for Catalysis. *Angewandte Chemie International Edition* **2009**, *48* (41), 7502–7513. https://doi.org/10.1002/anie.200806063.

(18) Gascon, J.; Corma, A.; Kapteijn, F.; Llabrés i Xamena, F. X. Metal Organic Framework Catalysis: *Quo Vadis*? *ACS Catalysis* **2014**, *4* (2), 361–378. https://doi.org/10.1021/cs400959k.

(19) Chen, S.; Dai, J.; Zeng, X. C. Metal–Organic Kagome Lattices M_3(2,3,6,7,10,11-Hexaiminotriphenylene)$_2$ (M = Ni and Cu): From Semiconducting to Metallic by Metal Substitution. *Physical Chemistry Chemical Physics* **2015**, *17* (8), 5954–5958. https://doi.org/10.1039/C4CP05328A.

(20) Stassen, I.; Burtch, N.; Talin, A.; Falcaro, P.; Allendorf, M.; Ameloot, R. An Updated Roadmap for the Integration of Metal–Organic Frameworks with Electronic Devices and Chemical Sensors. *Chemical Society Reviews* **2017**, *46* (11), 3185–3241. https://doi.org/10.1039/C7CS00122C.

(21) Hendon, C. H.; Rieth, A. J.; Korzyński, M. D.; Dincă, M. Grand Challenges and Future Opportunities for Metal–Organic Frameworks. *ACS Central Science* **2017**, *3* (6), 554–563. https://doi.org/10.1021/acscentsci.7b00197.

(22) Liu, L.; Zhou, Y.; Liu, S.; Xu, M. The Applications of Metal−Organic Frameworks in Electrochemical Sensors. *ChemElectroChem* **2018**, *5* (1), 6–19. https://doi.org/10.1002/celc.201700931.

(23) Choi, K. M.; Jeong, H. M.; Park, J. H.; Zhang, Y.-B.; Kang, J. K.; Yaghi, O. M. Supercapacitors of Nanocrystalline Metal–Organic Frameworks. *ACS Nano* **2014**, *8* (7), 7451–7457. https://doi.org/10.1021/nn5027092.

(24) Sheberla, D.; Bachman, J. C.; Elias, J. S.; Sun, C.-J.; Shao-Horn, Y.; Dincă, M. Conductive MOF Electrodes for Stable Supercapacitors with High Areal Capacitance. *Nature Materials* **2017**, *16* (2), 220–224. https://doi.org/10.1038/nmat4766.

(25) Wang, L.; Han, Y.; Feng, X.; Zhou, J.; Qi, P.; Wang, B. Metal–Organic Frameworks for Energy Storage: Batteries and Supercapacitors. *Coordination Chemistry Reviews* **2016**, *307*, 361–381. https://doi.org/10.1016/j.ccr.2015.09.002.

(26) Xia, W.; Mahmood, A.; Zou, R.; Xu, Q. Metal–Organic Frameworks and Their Derived Nanostructures for Electrochemical Energy Storage and Conversion. *Energy & Environmental Science* **2015**, *8* (7), 1837–1866. https://doi.org/10.1039/C5EE00762C.

(27) Xu, Y.; Li, Q.; Xue, H.; Pang, H. Metal-Organic Frameworks for Direct Electrochemical Applications. *Coordination Chemistry Reviews* **2018**, *376*, 292–318. https://doi.org/10.1016/j.ccr.2018.08.010.

(28) Lu, W.; Wei, Z.; Gu, Z.-Y.; Liu, T.-F.; Park, J.; Park, J.; Tian, J.; Zhang, M.; Zhang, Q.; Gentle III, T.; Bosch, M.; Zhou, H.-C. Tuning the Structure and Function of Metal–Organic Frameworks via Linker Design. *Chemical Society Reviews* **2014**, *43* (16), 5561–5593. https://doi.org/10.1039/C4CS00003J.

(29) Burnett, B. J.; Barron, P. M.; Hu, C.; Choe, W. Stepwise Synthesis of Metal–Organic Frameworks: Replacement of Structural Organic Linkers. *Journal of the American Chemical Society* **2011**, *133* (26), 9984–9987. https://doi.org/10.1021/ja201911v.

(30) Colón, Y. J.; Snurr, R. Q. High-Throughput Computational Screening of Metal–Organic Frameworks. *Chemical Society Reviews* **2014**, *43* (16), 5735–5749. https://doi.org/10.1039/C4CS00070F.

(31) Wilmer, C. E.; Leaf, M.; Lee, C. Y.; Farha, O. K.; Hauser, B. G.; Hupp, J. T.; Snurr, R. Q. Large-Scale Screening of Hypothetical Metal–Organic Frameworks. *Nature Chemistry* **2012**, *4* (2), 83–89. https://doi.org/10.1038/nchem.1192.

(32) Lalonde, M.; Bury, W.; Karagiaridi, O.; Brown, Z.; Hupp, J. T.; Farha, O. K. Transmetalation: Routes to Metal Exchange within Metal–Organic Frameworks. *Journal of Materials Chemistry A* **2013**, *1* (18), 5453. https://doi.org/10.1039/c3ta10784a.

(33) Grancha, T.; Ferrando-Soria, J.; Zhou, H.-C.; Gascon, J.; Seoane, B.; Pasán, J.; Fabelo, O.; Julve, M.; Pardo, E. Postsynthetic Improvement of the Physical Properties in a Metal-Organic Framework through a Single Crystal to Single Crystal Transmetallation. *Angewandte Chemie International Edition* **2015**, *54* (22), 6521–6525. https://doi.org/10.1002/anie.201501691.

(34) Asha, K. S.; Bhattacharjee, R.; Mandal, S. Complete Transmetalation in a Metal-Organic Framework by Metal Ion Metathesis in a Single Crystal for Selective Sensing of Phosphate Ions in Aqueous Media. *Angewandte Chemie International Edition* **2016**, *55* (38), 11528–11532. https://doi.org/10.1002/anie.201606185.

(35) Das, S.; Kim, H.; Kim, K. Metathesis in Single Crystal: Complete and Reversible Exchange of Metal Ions Constituting the Frameworks of Metal−Organic Frameworks. *Journal of the American Chemical Society* **2009**, *131* (11), 3814–3815. https://doi.org/10.1021/ja808995d.

(36) Doonan, C. J.; Morris, W.; Furukawa, H.; Yaghi, O. M. Isoreticular Metalation of Metal−Organic Frameworks. *Journal of the American Chemical Society* **2009**, *131* (27), 9492–9493. https://doi.org/10.1021/ja903251e.

(37) Islamoglu, T.; Goswami, S.; Li, Z.; Howarth, A. J.; Farha, O. K.; Hupp, J. T. Postsynthetic Tuning of Metal–Organic Frameworks for Targeted Applications. *Accounts of Chemical Research* **2017**, *50* (4), 805–813. https://doi.org/10.1021/acs.accounts.6b00577.

(38) Kim, M.; Cahill, J. F.; Fei, H.; Prather, K. A.; Cohen, S. M. Postsynthetic Ligand and Cation Exchange in Robust Metal–Organic Frameworks. *Journal of the American Chemical Society* **2012**, *134* (43), 18082–18088. https://doi.org/10.1021/ja3079219.

(39) Colombo, V.; Montoro, C.; Maspero, A.; Palmisano, G.; Masciocchi, N.; Galli, S.; Barea, E.; Navarro, J. A. R. Tuning the Adsorption Properties of Isoreticular Pyrazolate-Based Metal–Organic Frameworks through Ligand Modification. *Journal of the American Chemical Society* **2012**, *134* (30), 12830–12843. https://doi.org/10.1021/ja305267m.

(40) Eddaoudi, M. Systematic Design of Pore Size and Functionality in Isoreticular MOFs and Their Application in Methane Storage. *Science* **2002**, *295* (5554), 469–472. https://doi.org/10.1126/science.1067208.

(41) Garibay, S. J.; Cohen, S. M. Isoreticular Synthesis and Modification of Frameworks with the UiO-66 Topology. *Chemical Communications* **2010**, *46* (41), 7700. https://doi.org/10.1039/c0cc02990d.

(42) Sagara, T.; Klassen, J.; Ortony, J.; Ganz, E. Binding Energies of Hydrogen Molecules to Isoreticular Metal-Organic Framework Materials. *The Journal of Chemical Physics* **2005**, *123* (1), 014701. https://doi.org/10.1063/1.1944730.

(43) Burtch, N. C.; Jasuja, H.; Walton, K. S. Water Stability and Adsorption in Metal–Organic Frameworks. *Chemical Reviews* **2014**, *114* (20), 10575–10612. https://doi.org/10.1021/cr5002589.

(44) Furukawa, H.; Gándara, F.; Zhang, Y.-B.; Jiang, J.; Queen, W. L.; Hudson, M. R.; Yaghi, O. M. Water Adsorption in Porous Metal–Organic Frameworks and Related Materials. *Journal of the American Chemical Society* **2014**, *136* (11), 4369–4381. https://doi.org/10.1021/ja500330a.

(45) Hanikel, N.; Prévot, M. S.; Fathieh, F.; Kapustin, E. A.; Lyu, H.; Wang, H.; Diercks, N. J.; Glover, T. G.; Yaghi, O. M. Rapid Cycling and Exceptional Yield in a Metal-Organic Framework Water Harvester. *ACS Central Science* **2019**, *5* (10), 1699–1706. https://doi.org/10.1021/acscentsci.9b00745.

(46) Ma, L.; Abney, C.; Lin, W. Enantioselective Catalysis with Homochiral Metal–Organic Frameworks. *Chemical Society Reviews* **2009**, *38* (5), 1248. https://doi.org/10.1039/b807083k.

(47) Zhang, T.; Lin, W. Metal–Organic Frameworks for Artificial Photosynthesis and Photocatalysis. *Chemical Society Reviews* **2014**, *43* (16), 5982–5993. https://doi.org/10.1039/C4CS00103F.

(48) Zhu, L.; Liu, X.-Q.; Jiang, H.-L.; Sun, L.-B. Metal–Organic Frameworks for Heterogeneous Basic Catalysis. *Chemical Reviews* **2017**, *117* (12), 8129–8176. https://doi.org/10.1021/acs.chemrev.7b00091.

(49) Howarth, A. J.; Liu, Y.; Li, P.; Li, Z.; Wang, T. C.; Hupp, J. T.; Farha, O. K. Chemical, Thermal and Mechanical Stabilities of Metal–Organic Frameworks. *Nature Reviews Materials* **2016**, *1* (3). https://doi.org/10.1038/natrevmats.2015.18.

(50) Valvekens, P.; Vermoortele, F.; De Vos, D. Metal–Organic Frameworks as Catalysts: The Role of Metal Active Sites. *Catalysis Science & Technology* **2013**, *3* (6), 1435. https://doi.org/10.1039/c3cy20813c.

(51) Jiao, L.; Wang, Y.; Jiang, H.-L.; Xu, Q. Metal-Organic Frameworks as Platforms for Catalytic Applications. *Advanced Materials* **2018**, *30* (37), 1703663. https://doi.org/10.1002/adma.201703663.

(52) Manna, K.; Zhang, T.; Greene, F. X.; Lin, W. Bipyridine- and Phenanthroline-Based Metal–Organic Frameworks for Highly Efficient and Tandem Catalytic Organic Transformations via Directed C–H Activation. *Journal of the American Chemical Society* **2015**, *137* (7), 2665–2673. https://doi.org/10.1021/ja512478y.

(53) Feng, D.; Chung, W.-C.; Wei, Z.; Gu, Z.-Y.; Jiang, H.-L.; Chen, Y.-P.; Darensbourg, D. J.; Zhou, H.-C. Construction of Ultrastable Porphyrin Zr Metal–Organic Frameworks through Linker Elimination. *Journal of the American Chemical Society* **2013**, *135* (45), 17105–17110. https://doi.org/10.1021/ja408084j.

(54) Klet, R. C.; Wang, T. C.; Fernandez, L. E.; Truhlar, D. G.; Hupp, J. T.; Farha, O. K. Synthetic Access to Atomically Dispersed Metals in Metal–Organic Frameworks via a Combined Atomic-Layer-Deposition-in-MOF and Metal-Exchange Approach. *Chemistry of Materials* **2016**, *28* (4), 1213–1219. https://doi.org/10.1021/acs.chemmater.5b04887.

(55) Mondloch, J. E.; Bury, W.; Fairen-Jimenez, D.; Kwon, S.; DeMarco, E. J.; Weston, M. H.; Sarjeant, A. A.; Nguyen, S. T.; Stair, P. C.; Snurr, R. Q.; Farha, O. K.; Hupp, J. T. Vapor-Phase Metalation by Atomic Layer Deposition in a Metal–Organic Framework. *Journal of the American Chemical Society* **2013**, *135* (28), 10294–10297. https://doi.org/10.1021/ja4050828.

(56) Pal, T. K.; De, D.; Neogi, S.; Pachfule, P.; Senthilkumar, S.; Xu, Q.; Bharadwaj, P. K. Significant Gas Adsorption and Catalytic Performance by a Robust Cu^{II}-MOF Derived through Single-Crystal to Single-Crystal Transmetalation of a Thermally Less-Stable Zn^{II}-MOF. *Chemistry - A European Journal* **2015**, *21* (52), 19064–19070. https://doi.org/10.1002/chem.201503163.

(57) Pal, T. K.; De, D.; Senthilkumar, S.; Neogi, S.; Bharadwaj, P. K. A Partially Fluorinated, Water-Stable Cu(II)–MOF Derived via Transmetalation: Significant Gas Adsorption with High CO_2 Selectivity and Catalysis of Biginelli Reactions. *Inorganic Chemistry* **2016**, *55* (16), 7835–7842. https://doi.org/10.1021/acs.inorgchem.6b00154.

(58) Xu, Y.; Howarth, A. J.; Islamoglu, T.; da Silva, C. T.; Hupp, J. T.; Farha, O. K. Combining Solvent-Assisted Linker Exchange and Transmetallation Strategies to Obtain a New Non-Catenated Nickel(II) Pillared-Paddlewheel MOF. *Inorganic Chemistry Communications* **2016**, *67*, 60–63. https://doi.org/10.1016/j.inoche.2016.03.002.

(59) Lee, C. Y.; Farha, O. K.; Hong, B. J.; Sarjeant, A. A.; Nguyen, S. T.; Hupp, J. T. Light-Harvesting Metal–Organic Frameworks (MOFs): Efficient Strut-to-Strut Energy Transfer in Bodipy and Porphyrin-Based MOFs. *Journal of the American Chemical Society* **2011**, *133* (40), 15858–15861. https://doi.org/10.1021/ja206029a.

(60) Metzger, E. D.; Brozek, C. K.; Comito, R. J.; Dincă, M. Selective Dimerization of Ethylene to 1-Butene with a Porous Catalyst. *ACS Central Science* **2016**, *2* (3), 148–153. https://doi.org/10.1021/acscentsci.6b00012.

(61) Benoit, F. Substituent Effects in Mass Spectrometry—III: Substituent Effects in the Dissociation of the Molecular Ions Ofpara Andmeta Substituted Benzoic Acids. *Organic Mass Spectrometry* **1973**, *7* (3), 295–303. https://doi.org/10.1002/oms.1210070308.

(62) Dan-Hardi, M.; Serre, C.; Frot, T.; Rozes, L.; Maurin, G.; Sanchez, C.; Férey, G. A New Photoactive Crystalline Highly Porous Titanium(IV) Dicarboxylate. *Journal of the American Chemical Society* **2009**, *131* (31), 10857–10859. https://doi.org/10.1021/ja903726m.

(63) Cavka, J. H.; Jakobsen, S.; Olsbye, U.; Guillou, N.; Lamberti, C.; Bordiga, S.; Lillerud, K. P. A New Zirconium Inorganic Building Brick Forming Metal Organic Frameworks with Exceptional Stability. *Journal of the American Chemical Society* **2008**, *130* (42), 13850–13851. https://doi.org/10.1021/ja8057953.

(64) Walsh, A.; Butler, K. T.; Hendon, C. H. Chemical Principles for Electroactive Metal–Organic Frameworks. *MRS Bulletin* **2016**, *41* (11), 870–876. https://doi.org/10.1557/mrs.2016.243.

(65) Chen, B.; Wang, L.; Zapata, F.; Qian, G.; Lobkovsky, E. B. A Luminescent Microporous Metal−Organic Framework for the Recognition and Sensing of Anions. *Journal of the American Chemical Society* **2008**, *130* (21), 6718–6719. https://doi.org/10.1021/ja802035e.

(66) Allendorf, M. D.; Bauer, C. A.; Bhakta, R. K.; Houk, R. J. T. Luminescent Metal–Organic Frameworks. *Chemical Society Reviews* **2009**, *38* (5), 1330. https://doi.org/10.1039/b802352m.

(67) Hendon, C. H.; Tiana, D.; Fontecave, M.; Sanchez, C.; D'arras, L.; Sassoye, C.; Rozes, L.; Mellot-Draznieks, C.; Walsh, A. Engineering the Optical Response of the Titanium-MIL-125 Metal–Organic Framework through Ligand Functionalization. *Journal of the American Chemical Society* **2013**, *135* (30), 10942–10945. https://doi.org/10.1021/ja405350u.

(68) Li, Y.; Xu, H.; Ouyang, S.; Ye, J. Metal–Organic Frameworks for Photocatalysis. *Physical Chemistry Chemical Physics* **2016**, *18* (11), 7563–7572. https://doi.org/10.1039/C5CP05885F.

(69) Xiao, J.-D.; Jiang, H.-L. Metal–Organic Frameworks for Photocatalysis and Photothermal Catalysis. *Accounts of Chemical Research* **2019**, *52* (2), 356–366. https://doi.org/10.1021/acs.accounts.8b00521.

(70) Ziebel, M. E.; Gaggioli, C. A.; Turkiewicz, A. B.; Ryu, W.; Gagliardi, L.; Long, J. R. Effects of Covalency on Anionic Redox Chemistry in Semiquinoid-Based Metal–Organic Frameworks. *Journal of the American Chemical Society* **2020**, *142* (5), 2653–2664. https://doi.org/10.1021/jacs.9b13050.

(71) Tranchemontagne, D. J.; Hunt, J. R.; Yaghi, O. M. Room Temperature Synthesis of Metal-Organic Frameworks: MOF-5, MOF-74, MOF-177, MOF-199, and IRMOF-0. *Tetrahedron* **2008**, *64* (36), 8553–8557. https://doi.org/10.1016/j.tet.2008.06.036.

(72) Hmadeh, M.; Lu, Z.; Liu, Z.; Gándara, F.; Furukawa, H.; Wan, S.; Augustyn, V.; Chang, R.; Liao, L.; Zhou, F.; Perre, E.; Ozolins, V.; Suenaga, K.; Duan, X.; Dunn, B.; Yamamto, Y.; Terasaki, O.; Yaghi, O. M. New Porous Crystals of Extended Metal-Catecholates. *Chemistry of Materials* **2012**, *24* (18), 3511–3513. https://doi.org/10.1021/cm301194a.

(73) Sheberla, D.; Sun, L.; Blood-Forsythe, M. A.; Er, S.; Wade, C. R.; Brozek, C. K.; Aspuru-Guzik, A.; Dincă, M. High Electrical Conductivity in Ni_3(2,3,6,7,10,11-Hexaiminotriphenylene)$_2$, a Semiconducting Metal–Organic Graphene Analogue. *Journal of the American Chemical Society* **2014**, *136* (25), 8859–8862. https://doi.org/10.1021/ja502765n.

(74) Herebian, D.; Bothe, E.; Neese, F.; Weyhermüller, T.; Wieghardt, K. Molecular and Electronic Structures of Bis-(*o*-Diiminobenzosemiquinonato)Metal(II) Complexes (Ni, Pd, Pt), Their Monocations and -Anions, and of Dimeric Dications Containing Weak Metal−Metal Bonds. *Journal of the American Chemical Society* **2003**, *125* (30), 9116–9128. https://doi.org/10.1021/ja030123u.

(75) Stiefel, E. I.; Waters, J. H.; Billig, E.; Gray, H. B. The Myth of Nickel(III) and Nickel(IV) in Planar Complexes. *Journal of the American Chemical Society* **1965**, *87* (13), 3016–3017. https://doi.org/10.1021/ja01091a047.

(76) Hendon, C. H.; Tiana, D.; Walsh, A. Conductive Metal–Organic Frameworks and Networks: Fact or Fantasy? *Physical Chemistry Chemical Physics* **2012**, *14* (38), 13120. https://doi.org/10.1039/c2cp41099k.

(77) Lin, C.-K.; Zhao, D.; Gao, W.-Y.; Yang, Z.; Ye, J.; Xu, T.; Ge, Q.; Ma, S.; Liu, D.-J. Tunability of Band Gaps in Metal–Organic Frameworks. *Inorganic Chemistry* **2012**, *51* (16), 9039–9044. https://doi.org/10.1021/ic301189m.

(78) Bohr, N. I. *On the Constitution of Atoms and Molecules*. *The London, Edinburgh, and Dublin Philosophical Magazine and Journal of Science* **1913**, *26* (151), 1–25. https://doi.org/10.1080/14786441308634955.

(79) Einstein, A. Über einen die Erzeugung und Verwandlung des Lichtes betreffenden heuristischen Gesichtspunkt. *Annalen der Physik* **1905**, *322* (6), 132–148. https://doi.org/10.1002/andp.19053220607.

(80) de Broglie, L. The Reinterpretation of Wave Mechanics. *Foundations of Physics* **1970**, *1* (1), 5–15. https://doi.org/10.1007/BF00708650.

(81) Schrödinger, E. An Undulatory Theory of the Mechanics of Atoms and Molecules. *Physical Review* **1926**, *28* (6), 1049–1070. https://doi.org/10.1103/PhysRev.28.1049.

(82) Eisberg, R. M.; Resnick, R. *Quantum Physics of Atoms, Molecules, Solids, Nuclei, and Particles*, 2nd ed.; Wiley: New York, 1985.

(83) Schrödinger, E. Quantisierung als Eigenwertproblem. *Annalen der Physik* **1926**, *384* (4), 361–376. https://doi.org/10.1002/andp.19263840404.

(84) Balmer, J. J. Notiz Über Die Spectrallinien Des Wasserstoffs. *Annalen der Physik* **1885**, *261* (5), 80–87. https://doi.org/10.1002/andp.18852610506.

(85) Andreev, A. V. *Atomic Spectroscopy: Introduction to the Theory of Hyperfine Structure*; Springer Science+Business Media: New York, 2006.

(86) Pauli, W. Über den Zusammenhang des Abschlusses der Elektronengruppen im Atom mit der Komplexstruktur der Spektren. *Zeitschrift für Physik* **1925**, *31* (1), 765–783. https://doi.org/10.1007/BF02980631.

(87) Born, M.; Oppenheimer, R. Zur Quantentheorie der Molekeln. *Annalen der Physik* **1927**, *389* (20), 457–484. https://doi.org/10.1002/andp.19273892002.

(88) Scherrer, A.; Agostini, F.; Sebastiani, D.; Gross, E. K. U.; Vuilleumier, R. On the Mass of Atoms in Molecules: Beyond the Born-Oppenheimer Approximation. *Physical Review X* **2017**, *7* (3), 031035. https://doi.org/10.1103/PhysRevX.7.031035.

(89) Hartree, D. R. The Wave Mechanics of an Atom with a Non-Coulomb Central Field. Part III. Term Values and Intensities in Series in Optical Spectra. *Mathematical Proceedings of the Cambridge Philosophical Society* **1928**, *24* (3), 426–437. https://doi.org/10.1017/S0305004100015954.

(90) Fock, V. Näherungsmethode zur Lösung des quantenmechanischen Mehrkörperproblems. *Zeitschrift für Physik* **1930**, *61* (1–2), 126–148. https://doi.org/10.1007/BF01340294.

(91) Slater, J. C. Note on Hartree's Method. *Physical Review* **1930**, *35* (2), 210–211. https://doi.org/10.1103/PhysRev.35.210.2.

(92) Møller, Chr.; Plesset, M. S. Note on an Approximation Treatment for Many-Electron Systems. *Physical Review* **1934**, *46* (7), 618–622. https://doi.org/10.1103/PhysRev.46.618.

(93) Maurice, D.; Head-Gordon, M. Analytical Second Derivatives for Excited Electronic States Using the Single Excitation Configuration Interaction Method: Theory and Application to Benzo[a]Pyrene and Chalcone. *Molecular Physics* **1999**, *96* (10), 1533–1541. https://doi.org/10.1080/00268979909483096.

(94) Purvis, G. D.; Bartlett, R. J. A Full Coupled-cluster Singles and Doubles Model: The Inclusion of Disconnected Triples. *The Journal of Chemical Physics* **1982**, *76* (4), 1910–1918. https://doi.org/10.1063/1.443164.

(95) Curtiss, L. A.; Raghavachari, K.; Trucks, G. W.; Pople, J. A. Gaussian-2 Theory for Molecular Energies of First- and Second-row Compounds. *The Journal of Chemical Physics* **1991**, *94* (11), 7221–7230. https://doi.org/10.1063/1.460205.

(96) Hohenberg, P.; Kohn, W. Inhomogeneous Electron Gas. *Physical Review* **1964**, *136* (3B), B864–B871. https://doi.org/10.1103/PhysRev.136.B864.

(97) Perdew, J. P.; Ruzsinszky, A.; Tao, J.; Staroverov, V. N.; Scuseria, G. E.; Csonka, G. I. Prescription for the Design and Selection of Density Functional Approximations: More Constraint Satisfaction with Fewer Fits. *The Journal of Chemical Physics* **2005**, *123* (6), 062201. https://doi.org/10.1063/1.1904565.

(98) Vosko, S. H.; Wilk, L.; Nusair, M. Accurate Spin-Dependent Electron Liquid Correlation Energies for Local Spin Density Calculations: A Critical Analysis. *Can. J. Phys.* **1980**, *58* (8), 1200–1211. https://doi.org/10.1139/p80-159.

(99) Watson, R. E.; Fernando, G. W.; Weinert, M.; Wang, Y. J.; Davenport, J. W. Local-Density Approximation: Cohesion in the Transition Metals and $s \rightarrow d$ Promotion in the Transition-Metal Atoms. *Physical Review B* **1991**, *43* (2), 1455–1462. https://doi.org/10.1103/PhysRevB.43.1455.

(100) Perdew, J. P.; Ruzsinszky, A.; Constantin, L. A.; Sun, J.; Csonka, G. I. Some Fundamental Issues in Ground-State Density Functional Theory: A Guide for the Perplexed. *Journal of Chemical Theory and Computation* **2009**, *5* (4), 902–908. https://doi.org/10.1021/ct800531s.

(101) Perdew, J. P.; Burke, K.; Ernzerhof, M. Generalized Gradient Approximation Made Simple. *Physical Review Letters* **1996**, *77* (18), 3865–3868. https://doi.org/10.1103/PhysRevLett.77.3865.

(102) Perdew, J. P.; Ruzsinszky, A.; Csonka, G. I.; Vydrov, O. A.; Scuseria, G. E.; Constantin, L. A.; Zhou, X.; Burke, K. Restoring the Density-Gradient Expansion for Exchange in Solids and Surfaces. *Physical Review Letters* **2008**, *100* (13), 136406. https://doi.org/10.1103/PhysRevLett.100.136406.

(103) Zhao, Y.; Truhlar, D. G. A New Local Density Functional for Main-Group Thermochemistry, Transition Metal Bonding, Thermochemical Kinetics, and Noncovalent Interactions. *The Journal of Chemical Physics* **2006**, *125* (19), 194101. https://doi.org/10.1063/1.2370993.

(104) Hao, P.; Sun, J.; Xiao, B.; Ruzsinszky, A.; Csonka, G. I.; Tao, J.; Glindmeyer, S.; Perdew, J. P. Performance of Meta-GGA Functionals on General Main Group Thermochemistry, Kinetics, and Noncovalent Interactions. *Journal of Chemical Theory and Computation* **2013**, *9* (1), 355–363. https://doi.org/10.1021/ct300868x.

(105) Heyd, J.; Scuseria, G. E.; Ernzerhof, M. Hybrid Functionals Based on a Screened Coulomb Potential. *The Journal of Chemical Physics* **2003**, *118* (18), 8207–8215. https://doi.org/10.1063/1.1564060.

(106) Gori-Giorgi, P.; Savin, A. Properties of Short-Range and Long-Range Correlation Energy Density Functionals from Electron-Electron Coalescence. *Physical Review A* **2006**, *73* (3), 032506. https://doi.org/10.1103/PhysRevA.73.032506.

(107) Ditchfield, R.; Hehre, W. J.; Pople, J. A. Self-Consistent Molecular-Orbital Methods. IX. An Extended Gaussian-Type Basis for Molecular-Orbital Studies of Organic Molecules. *The Journal of Chemical Physics* **1971**, *54* (2), 724–728. https://doi.org/10.1063/1.1674902.

(108) Pietro, W. J.; Francl, M. M.; Hehre, W. J.; DeFrees, D. J.; Pople, J. A.; Binkley, J. S. Self-Consistent Molecular Orbital Methods. 24. Supplemented Small Split-Valence Basis Sets for Second-Row Elements. *Journal of the American Chemical Society* **1982**, *104* (19), 5039–5048. https://doi.org/10.1021/ja00383a007.

(109) Collins, J. B.; von R. Schleyer, P.; Binkley, J. S.; Pople, J. A. Self-consistent Molecular Orbital Methods. XVII. Geometries and Binding Energies of Second-row Molecules. A Comparison of Three Basis Sets. *The Journal of Chemical Physics* **1976**, *64* (12), 5142–5151. https://doi.org/10.1063/1.432189.

(110) Mancuso, J. L.; Mroz, A. M.; Le, K. N.; Hendon, C. H. Electronic Structure Modeling of Metal–Organic Frameworks. *Chemical Reviews* **2020**, *120* (16), 8641–8715. https://doi.org/10.1021/acs.chemrev.0c00148.

(111) Hamann, D. R.; Schlüter, M.; Chiang, C. Norm-Conserving Pseudopotentials. *Physical Review Letters* **1979**, *43* (20), 1494–1497. https://doi.org/10.1103/PhysRevLett.43.1494.

(112) Bachelet, G. B.; Hamann, D. R.; Schlüter, M. Pseudopotentials That Work: From H to Pu. *Physical Review B* **1982**, *26* (8), 4199–4228. https://doi.org/10.1103/PhysRevB.26.4199.

(113) Kresse, G.; Joubert, D. From Ultrasoft Pseudopotentials to the Projector Augmented-Wave Method. *Physical Review B* **1999**, *59* (3), 1758–1775. https://doi.org/10.1103/PhysRevB.59.1758.

(114) Farha, O. K.; Hupp, J. T. Rational Design, Synthesis, Purification, and Activation of Metal−Organic Framework Materials. *Accounts of Chemical Research* **2010**, *43* (8), 1166–1175. https://doi.org/10.1021/ar1000617.

(115) Canepa, P.; Chabal, Y. J.; Thonhauser, T. When Metal Organic Frameworks Turn into Linear Magnets. *Physical Review B* **2013**, *87* (9), 094407. https://doi.org/10.1103/PhysRevB.87.094407.

(116) Tian, Y.; Wang, W.; Chai, Y.; Cong, J.; Shen, S.; Yan, L.; Wang, S.; Han, X.; Sun, Y. Quantum Tunneling of Magnetization in a Metal-Organic Framework. *Physical Review Letters* **2014**, *112* (1). https://doi.org/10.1103/PhysRevLett.112.017202.

(117) Makov, G.; Payne, M. C. Periodic Boundary Conditions in *Ab Initio* Calculations. *Physical Review B* **1995**, *51* (7), 4014–4022. https://doi.org/10.1103/PhysRevB.51.4014.

(118) *Computer Modelling of Microporous Materials*, 1st ed.; Catlow, C. R. A., Santen, R. A. van, Smit, B. J., Eds.; Elsevier : Academic Press: Amsterdam ; Boston, 2004.

(119) Hinchliffe, A. *Molecular Modelling for Beginners*; Wiley: Chichester, West Sussex, England ; Hoboken, NJ, 2003.

(120) Truhlar, D. G.; Garrett, B. C.; Klippenstein, S. J. Current Status of Transition-State Theory. **1996**, *100* (31), 12771–12800. https://doi.org/10.1021/jp953748q.

(121) Bennett, T. D.; Cheetham, A. K. Amorphous Metal–Organic Frameworks. *Accounts of Chemical Research* **2014**, *47* (5), 1555–1562. https://doi.org/10.1021/ar5000314.

(122) Bennett, T. D.; Horike, S. Liquid, Glass and Amorphous Solid States of Coordination Polymers and Metal–Organic Frameworks. *Nature Reviews Materials* **2018**, *3* (11), 431–440. https://doi.org/10.1038/s41578-018-0054-3.

(123) Bennett, T. D.; Yue, Y.; Li, P.; Qiao, A.; Tao, H.; Greaves, N. G.; Richards, T.; Lampronti, G. I.; Redfern, S. A. T.; Blanc, F.; Farha, O. K.; Hupp, J. T.; Cheetham, A. K.; Keen, D. A. Melt-Quenched Glasses of Metal–Organic Frameworks. *Journal of the American Chemical Society* **2016**, *138* (10), 3484–3492. https://doi.org/10.1021/jacs.5b13220.

(124) Gaillac, R.; Pullumbi, P.; Beyer, K. A.; Chapman, K. W.; Keen, D. A.; Bennett, T. D.; Coudert, F.-X. Liquid Metal–Organic Frameworks. *Nature Materials* **2017**, *16* (11), 1149–1154. https://doi.org/10.1038/nmat4998.

(125) Umeyama, D.; Horike, S.; Inukai, M.; Itakura, T.; Kitagawa, S. Reversible Solid-to-Liquid Phase Transition of Coordination Polymer Crystals. *Journal of the American Chemical Society* **2015**, *137* (2), 864–870. https://doi.org/10.1021/ja511019u.

(126) Bloch, F. Über die Quantenmechanik der Elektronen in Kristallgittern. *Zeitschrift für Physik* **1929**, *52* (7–8), 555–600. https://doi.org/10.1007/BF01339455.

(127) Ashcroft, N. W.; Mermin, N. D. *Solid State Physics*; Holt, Rinehart and Winston: New York, 1976.

(128) Zhang, X.-G.; Varga, K.; Pantelides, S. T. Generalized Bloch Theorem for Complex Periodic Potentials: A Powerful Application to Quantum Transport Calculations. *Physical Review B* **2007**, *76* (3), 035108. https://doi.org/10.1103/PhysRevB.76.035108.

(129) Kratzer, P.; Neugebauer, J. The Basics of Electronic Structure Theory for Periodic Systems. *Frontiers in Chemistry* **2019**, *7*, 106. https://doi.org/10.3389/fchem.2019.00106.

(130) Baldereschi, A. Mean-Value Point in the Brillouin Zone. *Physical Review B* **1973**, *7* (12), 5212–5215. https://doi.org/10.1103/PhysRevB.7.5212.

(131) Aroyo, M. I.; Orobengoa, D.; de la Flor, G.; Tasci, E. S.; Perez-Mato, J. M.; Wondratschek, H. Brillouin-Zone Database on the *Bilbao Crystallographic Server*. *Acta Crystallographica Section A* **2014**, *70* (2), 126–137. https://doi.org/10.1107/S205327331303091X.

(132) Biswas, S.; Ahnfeldt, T.; Stock, N. New Functionalized Flexible Al-MIL-53-X (X = -Cl, -Br, $-CH_3$, $-NO_2$, $-(OH)_2$) Solids: Syntheses, Characterization, Sorption, and Breathing Behavior. *Inorganic Chemistry* **2011**, *50* (19), 9518–9526. https://doi.org/10.1021/ic201219g.

(133) Tulchinsky, Y.; Hendon, C. H.; Lomachenko, K. A.; Borfecchia, E.; Melot, B. C.; Hudson, M. R.; Tarver, J. D.; Korzyński, M. D.; Stubbs, A. W.; Kagan, J. J.; Lamberti, C.; Brown, C. M.; Dincă, M. Reversible Capture and Release of Cl_2 and Br_2 with a Redox-Active Metal–Organic Framework. *Journal of the American Chemical Society* **2017**, *139* (16), 5992–5997. https://doi.org/10.1021/jacs.7b02161.

(134) Chadi, D. J. Special Points for Brillouin-Zone Integrations. *Physical Review B* **1977**, *16* (4), 1746–1747. https://doi.org/10.1103/PhysRevB.16.1746.

(135) Monkhorst, H. J.; Pack, J. D. Special Points for Brillouin-Zone Integrations. *Physical Review B* **1976**, *13* (12), 5188–5192. https://doi.org/10.1103/PhysRevB.13.5188.

(136) Genova, A.; Pavanello, M. Exploiting the Locality of Periodic Subsystem Density-Functional Theory: Efficient Sampling of the Brillouin Zone. *Journal of Physics: Condensed Matter* **2015**, *27* (49), 495501. https://doi.org/10.1088/0953-8984/27/49/495501.

(137) Takahashi, K.; Yoshikawa, A.; Sandhu, A. *Wide Bandgap Semiconductors: Fundamental Properties and Modern Photonic and Electronic Devices*; Springer: Berlin, 2007.

(138) Spoerke, E. D.; Small, L. J.; Foster, M. E.; Wheeler, J.; Ullman, A. M.; Stavila, V.; Rodriguez, M.; Allendorf, M. D. MOF-Sensitized Solar Cells Enabled by a Pillared Porphyrin Framework. *Journal of Physical Chemistry C* **2017**, *121* (9), 4816–4824. https://doi.org/10.1021/acs.jpcc.6b11251.

(139) Foster, M. E.; Azoulay, J. D.; Wong, B. M.; Allendorf, M. D. Novel Metal–Organic Framework Linkers for Light Harvesting Applications. *Chemical Science* **2014**, *5* (5), 2081–2090. https://doi.org/10.1039/C4SC00333K.

(140) Stavila, V.; Talin, A. A.; Allendorf, M. D. MOF-Based Electronic and Opto-Electronic Devices. *Chemical Society Reviews* **2014**, *43* (16), 5994–6010. https://doi.org/10.1039/C4CS00096J.

(141) Butler, K. T.; Hendon, C. H.; Walsh, A. Designing Porous Electronic Thin-Film Devices: Band Offsets and Heteroepitaxy. *Faraday Discussions* **2017**, *201*, 207–219. https://doi.org/10.1039/C7FD00019G.

(142) Bredas, J.-L. Mind the Gap! *Materials Horizons* **2014**, *1* (1), 17–19. https://doi.org/10.1039/C3MH00098B.

(143) Mori-Sánchez, P.; Cohen, A. J. The Derivative Discontinuity of the Exchange–Correlation Functional. *Physical Chemistry Chemical Physics* **2014**, *16* (28), 14378–14387. https://doi.org/10.1039/C4CP01170H.

(144) Mori-Sánchez, P.; Cohen, A. J.; Yang, W. Localization and Delocalization Errors in Density Functional Theory and Implications for Band-Gap Prediction. *Physical Review Letters* **2008**, *100* (14), 146401. https://doi.org/10.1103/PhysRevLett.100.146401.

(145) Yamada, K. *Electron Correlation in Metals*; Cambridge University Press: Leiden, 2004.

(146) Matsuda, Y.; Tahir-Kheli, J.; Goddard, W. A. Definitive Band Gaps for Single-Wall Carbon Nanotubes. *Journal of Physical Chemistry Letters* **2010**, *1* (19), 2946–2950. https://doi.org/10.1021/jz100889u.

(147) Godby, R. W.; Schlüter, M.; Sham, L. J. Accurate Exchange-Correlation Potential for Silicon and Its Discontinuity on Addition of an Electron. *Physical Review Letters* **1986**, *56* (22), 2415–2418. https://doi.org/10.1103/PhysRevLett.56.2415.

(148) Fritsch, D.; Morgan, B. J.; Walsh, A. Self-Consistent Hybrid Functional Calculations: Implications for Structural, Electronic, and Optical Properties of Oxide Semiconductors. *Nanoscale Research Letters* **2017**, *12* (1), 19. https://doi.org/10.1186/s11671-016-1779-9.

(149) Monserrat, B.; Dreyer, C. E.; Rabe, K. M. Phonon-Assisted Optical Absorption in BaSnO 3 from First Principles. *Physical Review B* **2018**, *97* (10), 104310. https://doi.org/10.1103/PhysRevB.97.104310.

(150) Morris, A. J.; Monserrat, B. Optical Absorption Driven by Dynamical Symmetry Breaking in Indium Oxide. *Physical Review B* **2018**, *98* (16), 161203. https://doi.org/10.1103/PhysRevB.98.161203.

(151) Pathak, A.; Shen, J.-W.; Usman, M.; Wei, L.-F.; Mendiratta, S.; Chang, Y.-S.; Sainbileg, B.; Ngue, C.-M.; Chen, R.-S.; Hayashi, M.; Luo, T.-T.; Chen, F.-R.; Chen, K.-H.; Tseng, T.-W.; Chen, L.-C.; Lu, K.-L. Integration of a (–Cu–S–)n Plane in a Metal–Organic Framework Affords High Electrical Conductivity. *Nature Communications* **2019**, *10* (1), 1721. https://doi.org/10.1038/s41467-019-09682-0.

(152) Haldar, R.; Batra, K.; Marschner, S. M.; Kuc, A. B.; Zahn, S.; Fischer, R. A.; Bräse, S.; Heine, T.; Wöll, C. Bridging the Green Gap: Metal–Organic Framework Heteromultilayers Assembled from Porphyrinic Linkers Identified by Using Computational Screening. *Chemistry — A European Journal* **2019**, *25* (33), 7847–7851. https://doi.org/10.1002/chem.201901585.

(153) Dhakshinamoorthy, A.; Li, Z.; Garcia, H. Catalysis and Photocatalysis by Metal Organic Frameworks. *Chemical Society Reviews* **2018**, *47* (22), 8134–8172. https://doi.org/10.1039/C8CS00256H.

(154) Wang, H.; Zhu, Q.-L.; Zou, R.; Xu, Q. Metal-Organic Frameworks for Energy Applications. *Chem* **2017**, *2* (1), 52–80. https://doi.org/10.1016/j.chempr.2016.12.002.

(155) Liu, W.; Yin, X.-B. Metal–Organic Frameworks for Electrochemical Applications. *TrAC Trends in Analytical Chemistry* **2016**, *75*, 86–96. https://doi.org/10.1016/j.trac.2015.07.011.

(156) Zeng, L.; Guo, X.; He, C.; Duan, C. Metal–Organic Frameworks: Versatile Materials for Heterogeneous Photocatalysis. *ACS Catalysis* **2016**, *6* (11), 7935–7947. https://doi.org/10.1021/acscatal.6b02228.

(157) Usman, M.; Mendiratta, S.; Lu, K.-L. Semiconductor Metal-Organic Frameworks: Future Low-Bandgap Materials. *Advanced Materials* **2017**, *29* (6), 1605071. https://doi.org/10.1002/adma.201605071.

(158) Madelung, O. *Introduction to Solid-State Theory*; Solid-State Sciences; Springer, 1978; Vol. 2.

(159) Rosenberg, H. M. *The Solid State*, 3rd ed.; Oxford Physics; Oxford Science, 1988; Vol. 9.

(160) Aziz, A.; Ruiz-Salvador, A. R.; Hernández, N. C.; Calero, S.; Hamad, S.; Grau-Crespo, R. Porphyrin-Based Metal-Organic Frameworks for Solar Fuel Synthesis Photocatalysis: Band Gap Tuning via Iron Substitutions. *Journal of Materials Chemistry A* **2017**, *5* (23), 11894–11904. https://doi.org/10.1039/C7TA01278K.

(161) Hamad, S.; Hernandez, N. C.; Aziz, A.; Ruiz-Salvador, A. R.; Calero, S.; Grau-Crespo, R. Electronic Structure of Porphyrin-Based Metal–Organic Frameworks and Their Suitability for Solar Fuel Production Photocatalysis. *Journal of Materials Chemistry A* **2015**, *3* (46), 23458–23465. https://doi.org/10.1039/C5TA06982C.

(162) Syzgantseva, M. A.; Ireland, C. P.; Ebrahim, F. M.; Smit, B.; Syzgantseva, O. A. Metal Substitution as the Method of Modifying Electronic Structure of Metal–Organic Frameworks. *Journal of the American Chemical Society* **2019**, *141* (15), 6271–6278. https://doi.org/10.1021/jacs.8b13667.

(163) Yang, L.-M.; Ravindran, P.; Vajeeston, P.; Tilset, M. Properties of IRMOF-14 and Its Analogues M-IRMOF-14 (M = Cd, Alkaline Earth Metals): Electronic Structure, Structural Stability, Chemical Bonding, and Optical Properties. *Physical Chemistry Chemical Physics* **2012**, *14* (14), 4713. https://doi.org/10.1039/c2cp24091b.

(164) Chong, S.; Kim, J. Rational Modifications of PCN-700 to Induce Electrical Conductivity: A Computational Study. *Dalton Transactions* **2020**, *49* (1), 102–113. https://doi.org/10.1039/C9DT03865E.

(165) Choi, J. H.; Choi, Y. J.; Lee, J. W.; Shin, W. H.; Kang, J. K. Tunability of Electronic Band Gaps from Semiconducting to Metallic States via Tailoring Zn Ions in MOFs with Co Ions. *Physical Chemistry Chemical Physics* **2009**, *11* (4), 628–631. https://doi.org/10.1039/B816668D.

(166) Li, J.; Musho, T.; Bright, J.; Wu, N. Functionalization of a Metal-Organic Framework Semiconductor for Tuned Band Structure and Catalytic Activity. *Journal of The Electrochemical Society* **2019**, *166* (5), H3029–H3034. https://doi.org/10.1149/2.0051905jes.

(167) Li, Y.; Fu, Y.; Ni, B.; Ding, K.; Chen, W.; Wu, K.; Huang, X.; Zhang, Y. Effects of Ligand Functionalization on the Photocatalytic Properties of Titanium-Based MOF: A Density Functional Theory Study. *AIP Advances* **2018**, *8* (3), 035012. https://doi.org/10.1063/1.5021098.

(168) Mu, X.; Jiang, J.; Chao, F.; Lou, Y.; Chen, J. Ligand Modification of UiO-66 with an Unusual Visible Light Photocatalytic Behavior for RhB Degradation. *Dalton Transactions* **2018**, *47* (6), 1895–1902. https://doi.org/10.1039/C7DT04477A.

(169) Musho, T.; Li, J.; Wu, N. Band Gap Modulation of Functionalized Metal–Organic Frameworks. *Physical Chemistry Chemical Physics* **2014**, *16* (43), 23646–23653. https://doi.org/10.1039/C4CP03110E.

(170) Taddei, M.; Schukraft, G. M.; Warwick, M. E. A.; Tiana, D.; McPherson, M. J.; Jones, D. R.; Petit, C. Band Gap Modulation in Zirconium-Based Metal–Organic Frameworks by Defect Engineering. *Journal of Materials Chemistry A* **2019**, *7* (41), 23781–23786. https://doi.org/10.1039/C9TA05216J.

(171) Zhang, G.; Chan, J. M. W. Reversibly Thermochromic Bismuth-Organic Materials with Tunable Optical Gaps. *Journal of Materials Chemistry C* **2017**, *5* (38), 10007–10015. https://doi.org/10.1039/C7TC03277C.

(172) Grau-Crespo, R.; Aziz, A.; Collins, A. W.; Crespo-Otero, R.; Hernández, N. C.; Rodriguez-Albelo, L. M.; Ruiz-Salvador, A. R.; Calero, S.; Hamad, S. Modelling a Linker Mix-and-Match Approach for Controlling the Optical Excitation Gaps and Band Alignment of Zeolitic Imidazolate Frameworks. *Angewandte Chemie International Edition* **2016**, *55* (52), 16012–16016. https://doi.org/10.1002/anie.201609439.

(173) Hendrickx, K.; Vanpoucke, D. E. P.; Leus, K.; Lejaeghere, K.; Van Yperen-De Deyne, A.; Van Speybroeck, V.; Van Der Voort, P.; Hemelsoet, K. Understanding Intrinsic Light Absorption Properties of UiO-66 Frameworks: A Combined Theoretical and Experimental Study. *Inorganic Chemistry* **2015**, *54* (22), 10701–10710. https://doi.org/10.1021/acs.inorgchem.5b01593.

(174) Taddei, M.; Tiana, D.; Casati, N.; van Bokhoven, J. A.; Smit, B.; Ranocchiari, M. Mixed-Linker UiO-66: Structure–Property Relationships Revealed by a Combination of High-Resolution Powder X-Ray Diffraction and Density Functional Theory Calculations. *Physical Chemistry Chemical Physics* **2017**, *19* (2), 1551–1559. https://doi.org/10.1039/C6CP07801J.

(175) Choi, J. H.; Jeon, H. J.; Choi, K. M.; Kang, J. K. Metal–Organic Frameworks for Visible Light Absorption via Anion Substitution. *Journal of Materials Chemistry* **2012**, *22* (20), 10144. https://doi.org/10.1039/c2jm16245h.

(176) Botas, J. A.; Calleja, G.; Sánchez-Sánchez, M.; Orcajo, M. G. Cobalt Doping of the MOF-5 Framework and Its Effect on Gas-Adsorption Properties. *Langmuir* **2010**, *26* (8), 5300–5303. https://doi.org/10.1021/la100423a.

(177) Venkataramanan, N. S.; Sahara, R.; Mizuseki, H.; Kawazoe, Y. Probing the Structure, Stability and Hydrogen Adsorption of Lithium Functionalized Isoreticular MOF-5 (Fe, Cu, Co, Ni and Zn) by Density Functional Theory. *International Journal of Molecular Sciences* **2009**, *10* (4), 1601–1608. https://doi.org/10.3390/ijms10041601.

(178) Pham, H. Q.; Mai, T.; Pham-Tran, N.-N.; Kawazoe, Y.; Mizuseki, H.; Nguyen-Manh, D. Engineering of Band Gap in Metal–Organic Frameworks by Functionalizing Organic Linker: A Systematic Density Functional Theory Investigation. *Journal of Physical Chemistry C* **2014**, *118* (9), 4567–4577. https://doi.org/10.1021/jp405997r.

(179) Gascon, J.; Hernández-Alonso, M. D.; Almeida, A. R.; van Klink, G. P. M.; Kapteijn, F.; Mul, G. Isoreticular MOFs as Efficient Photocatalysts with Tunable Band Gap: An Operando FTIR Study of the Photoinduced Oxidation of Propylene. *ChemSusChem* **2008**, *1* (12), 981–983. https://doi.org/10.1002/cssc.200800203.

(180) Yang, L.-M.; Ravindran, P.; Vajeeston, P.; Tilset, M. Ab Initio Investigations on the Crystal Structure, Formation Enthalpy, Electronic Structure, Chemical Bonding, and Optical Properties of Experimentally Synthesized Isoreticular Metal–Organic Framework-10 and Its Analogues: M-IRMOF-10 (M = Zn, Cd, Be, Mg, Ca, Sr and Ba). *RSC Advances* **2012**, *2* (4), 1618–1631. https://doi.org/10.1039/C1RA00187F.

(181) Salih, Z. I.; Guo, Y.-J.; Zheng, J.-J.; Zhao, X. Effect of Modified Linkers of MOF-5 on Enhancing Interaction Energies: A Theoretical Study. *Computational and Theoretical Chemistry* **2015**, *1058*, 28–33. https://doi.org/10.1016/j.comptc.2015.01.022.

(182) Yang, L.-M.; Fang, G.-Y.; Ma, J.; Ganz, E.; Han, S. S. Band Gap Engineering of Paradigm MOF-5. *Crystal Growth & Design* **2014**, *14* (5), 2532–2541. https://doi.org/10.1021/cg500243s.

(183) Brozek, C. K.; Michaelis, V. K.; Ong, T.-C.; Bellarosa, L.; López, N.; Griffin, R. G.; Dincă, M. Dynamic DMF Binding in MOF-5 Enables the Formation of Metastable Cobalt-Substituted MOF-5 Analogues. *ACS Central Science* **2015**, *1* (5), 252–260. https://doi.org/10.1021/acscentsci.5b00247.

(184) Dodson, R. A.; Wong-Foy, A. G.; Matzger, A. J. The Metal–Organic Framework Collapse Continuum: Insights from Two-Dimensional Powder X-Ray Diffraction. *Chemistry of Materials* **2018**, *30* (18), 6559–6565. https://doi.org/10.1021/acs.chemmater.8b03378.

(185) Yasin, A. S.; Li, J.; Wu, N.; Musho, T. Study of the Inorganic Substitution in a Functionalized UiO-66 Metal–Organic Framework. *Physical Chemistry Chemical Physics* **2016**, *18* (18), 12748–12754. https://doi.org/10.1039/C5CP08070C.

(186) Trousselet, F.; Archereau, A.; Boutin, A.; Coudert, F.-X. Heterometallic Metal–Organic Frameworks of MOF-5 and UiO-66 Families: Insight from Computational Chemistry. *Journal of Physical Chemistry C* **2016**, *120* (43), 24885–24894. https://doi.org/10.1021/acs.jpcc.6b08594.

(187) Yang, L.-M.; Ganz, E.; Svelle, S.; Tilset, M. Computational Exploration of Newly Synthesized Zirconium Metal–Organic Frameworks UiO-66, -67, -68 and Analogues. *Journal of Materials Chemistry C* **2014**, *2* (34), 7111–7125. https://doi.org/10.1039/C4TC00902A.

(188) Santaclara, J. G.; Olivos-Suarez, A. I.; Gonzalez-Nelson, A.; Osadchii, D.; Nasalevich, M. A.; van der Veen, M. A.; Kapteijn, F.; Sheveleva, A. M.; Veber, S. L.; Fedin, M. V.; Murray, A. T.; Hendon, C. H.; Walsh, A.; Gascon, J. Revisiting the Incorporation of Ti(IV) in UiO-Type Metal–Organic Frameworks: Metal Exchange versus Grafting and Their Implications on Photocatalysis. *Chemistry of Materials* **2017**, *29* (21), 8963–8967. https://doi.org/10.1021/acs.chemmater.7b03320.

(189) Lammert, M.; Wharmby, M. T.; Smolders, S.; Bueken, B.; Lieb, A.; Lomachenko, K. A.; Vos, D. D.; Stock, N. Cerium-Based Metal Organic Frameworks with UiO-66 Architecture: Synthesis, Properties and Redox Catalytic Activity. *Chemical Communications* **2015**, *51* (63), 12578–12581. https://doi.org/10.1039/C5CC02606G.

(190) Campanelli, M.; Del Giacco, T.; De Angelis, F.; Mosconi, E.; Taddei, M.; Marmottini, F.; D'Amato, R.; Costantino, F. Solvent-Free Synthetic Route for Cerium(IV) Metal–Organic Frameworks with UiO-66 Architecture and Their Photocatalytic Applications. *ACS Applied Materials & Interfaces* **2019**, *11* (48), 45031–45037. https://doi.org/10.1021/acsami.9b13730.

(191) Tu, J.; Zeng, X.; Xu, F.; Wu, X.; Tian, Y.; Hou, X.; Long, Z. Microwave-Induced Fast Incorporation of Titanium into UiO-66 Metal–Organic Frameworks for Enhanced Photocatalytic Properties. *Chemical Communications* **2017**, *53* (23), 3361–3364. https://doi.org/10.1039/C7CC00076F.

(192) Kim, M.; Cahill, J. F.; Su, Y.; Prather, K. A.; Cohen, S. M. Postsynthetic Ligand Exchange as a Route to Functionalization of 'Inert' Metal–Organic Frameworks. *Chemical Science* **2012**, *3* (1), 126–130. https://doi.org/10.1039/C1SC00394A.

(193) Tanabe, K. K.; Cohen, S. M. Engineering a Metal-Organic Framework Catalyst by Using Postsynthetic Modification. *Angewandte Chemie International Edition* **2009**, *48* (40), 7424–7427. https://doi.org/10.1002/anie.200903433.

(194) Karagiaridi, O.; Bury, W.; Mondloch, J. E.; Hupp, J. T.; Farha, O. K. Solvent-Assisted Linker Exchange: An Alternative to the De Novo Synthesis of Unattainable Metal-Organic Frameworks. *Angewandte Chemie International Edition* **2014**, *53* (18), 4530–4540. https://doi.org/10.1002/anie.201306923.

(195) Ortiz, A. U.; Boutin, A.; Fuchs, A. H.; Coudert, F.-X. Metal–Organic Frameworks with Wine-Rack Motif: What Determines Their Flexibility and Elastic Properties? *The Journal of Chemical Physics* **2013**, *138* (17), 174703. https://doi.org/10.1063/1.4802770.

(196) Coudert, F.-X. Responsive Metal–Organic Frameworks and Framework Materials: Under Pressure, Taking the Heat, in the Spotlight, with Friends. *Chemistry of Materials* **2015**, *27* (6), 1905–1916. https://doi.org/10.1021/acs.chemmater.5b00046.

(197) Coudert, F.-X.; Boutin, A.; Jeffroy, M.; Mellot-Draznieks, C.; Fuchs, A. H. Thermodynamic Methods and Models to Study Flexible Metal-Organic Frameworks. *ChemPhysChem* **2011**, *12* (2), 247–258. https://doi.org/10.1002/cphc.201000590.

(198) Ling, S.; Slater, B. Unusually Large Band Gap Changes in Breathing Metal–Organic Framework Materials. *Journal of Physical Chemistry C* **2015**, *119* (29), 16667–16677. https://doi.org/10.1021/acs.jpcc.5b04050.

(199) Butler, K. T.; Hendon, C. H.; Walsh, A. Electronic Structure Modulation of Metal–Organic Frameworks for Hybrid Devices. *ACS Applied Materials & Interfaces* **2014**, *6* (24), 22044–22050. https://doi.org/10.1021/am507016r.

(200) Clough, A. J.; Skelton, J. M.; Downes, C. A.; de la Rosa, A. A.; Yoo, J. W.; Walsh, A.; Melot, B. C.; Marinescu, S. C. Metallic Conductivity in a Two-Dimensional Cobalt Dithiolene Metal–Organic Framework. *Journal of the American Chemical Society* **2017**, *139* (31), 10863–10867. https://doi.org/10.1021/jacs.7b05742.

(201) Clough, A. J.; Orchanian, N. M.; Skelton, J. M.; Neer, A. J.; Howard, S. A.; Downes, C. A.; Piper, L. F. J.; Walsh, A.; Melot, B. C.; Marinescu, S. C. Room Temperature Metallic Conductivity in a Metal–Organic Framework Induced by Oxidation. *Journal of the American Chemical Society* **2019**, *141* (41), 16323–16330. https://doi.org/10.1021/jacs.9b06898.

(202) Li, W.; Sun, L.; Qi, J.; Jarillo-Herrero, P.; Dincă, M.; Li, J. High Temperature Ferromagnetism in π-Conjugated Two-Dimensional Metal–Organic Frameworks. *Chemical Science* **2017**, *8* (4), 2859–2867. https://doi.org/10.1039/C6SC05080H.

(203) DeGayner, J. A.; Jeon, I.-R.; Sun, L.; Dincă, M.; Harris, T. D. 2D Conductive Iron-Quinoid Magnets Ordering up to T_c = 105 K via Heterogenous Redox Chemistry. *Journal of the American Chemical Society* **2017**, *139* (11), 4175–4184. https://doi.org/10.1021/jacs.7b00705.

(204) Liu, L.; DeGayner, J. A.; Sun, L.; Zee, D. Z.; Harris, T. D. Reversible Redox Switching of Magnetic Order and Electrical Conductivity in a 2D Manganese Benzoquinoid Framework. *Chemical Science* **2019**, *10* (17), 4652–4661. https://doi.org/10.1039/C9SC00606K.

(205) Tie, D. Y.; Chen, Z. First Principles Study of the Electronic Properties of a Ni_3(2,3,6,7,10,11-Hexaaminotriphenylene)$_2$ Monolayer under Biaxial Strain. *RSC Advances* **2015**, *5* (68), 55186–55190. https://doi.org/10.1039/C5RA09824F.

(206) Zhou, Q.; Wang, J.; Chwee, T. S.; Wu, G.; Wang, X.; Ye, Q.; Xu, J.; Yang, S.-W. Topological Insulators Based on 2D Shape-Persistent Organic Ligand Complexes. *Nanoscale* **2015**, *7* (2), 727–735. https://doi.org/10.1039/C4NR05247A.

(207) Zhang, X.; Wang, Z.; Zhao, M.; Liu, F. Tunable Topological States in Electron-Doped HTT-Pt. *Physical Review B* **2016**, *93* (16). https://doi.org/10.1103/PhysRevB.93.165401.

(208) Clough, A. J.; Yoo, J. W.; Mecklenburg, M. H.; Marinescu, S. C. Two-Dimensional Metal–Organic Surfaces for Efficient Hydrogen Evolution from Water. *Journal of the American Chemical Society* **2015**, *137* (1), 118–121. https://doi.org/10.1021/ja5116937.

(209) Wu, M.; Wang, Z.; Liu, J.; Li, W.; Fu, H.; Sun, L.; Liu, X.; Pan, M.; Weng, H.; Dincă, M.; Fu, L.; Li, J. Conetronics in 2D Metal-Organic Frameworks: Double/Half Dirac Cones and Quantum Anomalous Hall Effect. *2D Mater.* **2016**, *4* (1), 015015. https://doi.org/10.1088/2053-1583/4/1/015015.

(210) Adjizian, J.-J.; Briddon, P.; Humbert, B.; Duvail, J.-L.; Wagner, P.; Adda, C.; Ewels, C. Dirac Cones in Two-Dimensional Conjugated Polymer Networks. *Nature Communications* **2014**, *5* (1). https://doi.org/10.1038/ncomms6842.

(211) Huang, X.; Sheng, P.; Tu, Z.; Zhang, F.; Wang, J.; Geng, H.; Zou, Y.; Di, C.; Yi, Y.; Sun, Y.; Xu, W.; Zhu, D. A Two-Dimensional π–d Conjugated Coordination Polymer with Extremely High Electrical Conductivity and Ambipolar Transport Behaviour. *Nature Communications* **2015**, *6* (1), 7408. https://doi.org/10.1038/ncomms8408.

(212) Zhao, B.; Zhang, J.; Feng, W.; Yao, Y.; Yang, Z. Quantum Spin Hall and Z_2 Metallic States in an Organic Material. *Physical Review B* **2014**, *90* (20), 201403. https://doi.org/10.1103/PhysRevB.90.201403.

(213) Lopez, M. F.; Merino, J. From Quantum Anomalous Hall Phases to Topological Metals in Interacting Decorated Honeycomb Lattices. *Physical Review B* **2019**, *100* (7), 075154. https://doi.org/10.1103/PhysRevB.100.075154.

(214) Wang, Z. F.; Liu, Z.; Liu, F. Quantum Anomalous Hall Effect in 2D Organic Topological Insulators. *Physical Review Letters* **2013**, *110* (19). https://doi.org/10.1103/PhysRevLett.110.196801.

(215) Young, S. M.; Kane, C. L. Dirac Semimetals in Two Dimensions. *Physical Review Letters* **2015**, *115* (12). https://doi.org/10.1103/PhysRevLett.115.126803.

(216) Young, S. M.; Zaheer, S.; Teo, J. C. Y.; Kane, C. L.; Mele, E. J.; Rappe, A. M. Dirac Semimetal in Three Dimensions. *Physical Review Letters* **2012**, *108* (14). https://doi.org/10.1103/PhysRevLett.108.140405.

(217) *Topological Insulators: Fundamentals and Perspectives*; Ortmann, F., Roche, S., Valenzuela, S. O., Eds.; Wiley-VCH Verlag GmbH & Co. KGaA: Weinheim, 2015.

(218) Dou, J.-H.; Sun, L.; Ge, Y.; Li, W.; Hendon, C. H.; Li, J.; Gul, S.; Yano, J.; Stach, E. A.; Dincă, M. Signature of Metallic Behavior in the Metal–Organic Frameworks M_3(Hexaiminobenzene)$_2$ (M = Ni, Cu). *Journal of the American Chemical Society* **2017**, *139* (39), 13608–13611. https://doi.org/10.1021/jacs.7b07234.

(219) Foster, M. E.; Sohlberg, K.; Allendorf, M. D.; Talin, A. A. Unraveling the Semiconducting/Metallic Discrepancy in $Ni_3(HITP)_2$. *Journal of Physical Chemistry Letters* **2018**, *9* (3), 481–486. https://doi.org/10.1021/acs.jpclett.7b03140.

(220) Foster, M. E.; Sohlberg, K.; Spataru, C. D.; Allendorf, M. D. Proposed Modification of the Graphene Analogue $Ni_3(HITP)_2$ To Yield a Semiconducting Material. *Journal of Physical Chemistry C* **2016**, *120* (27), 15001–15008. https://doi.org/10.1021/acs.jpcc.6b05746.

(221) Feng, D.; Lei, T.; Lukatskaya, M. R.; Park, J.; Huang, Z.; Lee, M.; Shaw, L.; Chen, S.; Yakovenko, A. A.; Kulkarni, A.; Xiao, J.; Fredrickson, K.; Tok, J. B.; Zou, X.; Cui, Y.; Bao, Z. Robust and Conductive Two-Dimensional Metal−organic Frameworks with Exceptionally High Volumetric and Areal Capacitance. *Nature Energy* **2018**, *3* (1), 30–36. https://doi.org/10.1038/s41560-017-0044-5.

(222) Liu, J.; Lukose, B.; Shekhah, O.; Arslan, H. K.; Weidler, P.; Gliemann, H.; Bräse, S.; Grosjean, S.; Godt, A.; Feng, X.; Müllen, K.; Magdau, I.-B.; Heine, T.; Wöll, C. A Novel Series of Isoreticular Metal Organic Frameworks: Realizing Metastable Structures by Liquid Phase Epitaxy. *Science Reports* **2012**, *2* (1), 921. https://doi.org/10.1038/srep00921.

(223) Kapustin, E. A.; Lee, S.; Alshammari, A. S.; Yaghi, O. M. Molecular Retrofitting Adapts a Metal–Organic Framework to Extreme Pressure. *ACS Central Science* **2017**, *3* (6), 662–667. https://doi.org/10.1021/acscentsci.7b00169.

(224) Schneider, C.; Bodesheim, D.; Keupp, J.; Schmid, R.; Kieslich, G. Retrofitting Metal-Organic Frameworks. *Nature Communications* **2019**, *10* (1). https://doi.org/10.1038/s41467-019-12876-1.

(225) Schneider, C.; Bodesheim, D.; Ehrenreich, M. G.; Crocellà, V.; Mink, J.; Fischer, R. A.; Butler, K. T.; Kieslich, G. Tuning the Negative Thermal Expansion Behavior of the Metal–Organic Framework Cu_3BTC_2 by Retrofitting. *Journal of the American Chemical Society* **2019**, *141* (26), 10504–10509. https://doi.org/10.1021/jacs.9b04755.

(226) Dong, L.; Kim, Y.; Er, D.; Rappe, A. M.; Shenoy, V. B. Two-Dimensional π - Conjugated Covalent-Organic Frameworks as Quantum Anomalous Hall Topological Insulators. *Physical Review Letters* **2016**, *116* (9), 096601. https://doi.org/10.1103/PhysRevLett.116.096601.

(227) Kambe, T.; Sakamoto, R.; Kusamoto, T.; Pal, T.; Fukui, N.; Hoshiko, K.; Shimojima, T.; Wang, Z.; Hirahara, T.; Ishizaka, K.; Hasegawa, S.; Liu, F.; Nishihara, H. Redox Control and High Conductivity of Nickel Bis(Dithiolene) Complex π-Nanosheet: A Potential Organic Two-Dimensional Topological Insulator. *Journal of the American Chemical Society* **2014**, *136* (41), 14357–14360. https://doi.org/10.1021/ja507619d.

(228) Wang, Z. F.; Su, N.; Liu, F. Prediction of a Two-Dimensional Organic Topological Insulator. *Nano Letters* **2013**, *13* (6), 2842–2845. https://doi.org/10.1021/nl401147u.

(229) Liu, Z.; Wang, Z.-F.; Mei, J.-W.; Wu, Y.-S.; Liu, F. Flat Chern Band in a Two-Dimensional Organometallic Framework. *Physical Review Letters* **2013**, *110* (10), 106804. https://doi.org/10.1103/PhysRevLett.110.106804.

(230) Yang, L.; He, X.; Dincă, M. Triphenylene-Bridged Trinuclear Complexes of Cu: Models for Spin Interactions in Two-Dimensional Electrically Conductive Metal–Organic Frameworks. *Journal of the American Chemical Society* **2019**, *141* (26), 10475–10480. https://doi.org/10.1021/jacs.9b04822.

(231) Yu, S.; Li, S.; Meng, X.; Wan, C.; Ju, X. Tuning the Hydrogen Adsorption Properties of Zn–Based Metal–Organic Frameworks: Combined DFT and GCMC Simulations. *Journal of Solid-State Chemistry* **2018**, *266*, 31–36. https://doi.org/10.1016/j.jssc.2018.04.033.

(232) Erkartal, M.; Durandurdu, M. Pressure-Induced Amorphization of MOF-5: A First Principles Study. *Chemistry Select* **2018**, *3* (28), 8056–8063. https://doi.org/10.1002/slct.201801381.

(233) Xie, L. S.; Sun, L.; Wan, R.; Park, S. S.; DeGayner, J. A.; Hendon, C. H.; Dincă, M. Tunable Mixed-Valence Doping toward Record Electrical Conductivity in a Three-Dimensional Metal–Organic Framework. *Journal of the American Chemical Society* **2018**, *140* (24), 7411–7414. https://doi.org/10.1021/jacs.8b03604.

(234) Zhao, M.; Wang, A.; Zhang, X. Half-Metallicity of a Kagome Spin Lattice: The Case of a Manganese Bis-Dithiolene Monolayer. *Nanoscale* **2013**, *5* (21), 10404. https://doi.org/10.1039/c3nr03323f.

(235) Zhang, L.-C.; Zhang, L.; Qin, G.; Zheng, Q.-R.; Hu, M.; Yan, Q.-B.; Su, G. Two-Dimensional Magnetic Metal–Organic Frameworks with the Shastry-Sutherland Lattice. *Chemical Science* **2019**, *10* (44), 10381–10387. https://doi.org/10.1039/C9SC03816G.

(236) Žutić, I.; Fabian, J.; Das Sarma, S. Spintronics: Fundamentals and Applications. *Reviews of Modern Physics* **2004**, *76* (2), 323–410. https://doi.org/10.1103/RevModPhys.76.323.

(237) Zhang, Y.; Riduan, S. N.; Wang, J. Redox Active Metal- and Covalent Organic Frameworks for Energy Storage: Balancing Porosity and Electrical Conductivity. *Chemistry — A European Journal* **2017**, *23* (65), 16419–16431. https://doi.org/10.1002/chem.201702919.

(238) Darago, L. E.; Aubrey, M. L.; Yu, C. J.; Gonzalez, M. I.; Long, J. R. Electronic Conductivity, Ferrimagnetic Ordering, and Reductive Insertion Mediated by Organic Mixed-Valence in a Ferric Semiquinoid Metal–Organic Framework. *Journal of the American Chemical Society* **2015**, *137* (50), 15703–15711. https://doi.org/10.1021/jacs.5b10385.

(239) Usov, P. M.; Huffman, B.; Epley, C. C.; Kessinger, M. C.; Zhu, J.; Maza, W. A.; Morris, A. J. Study of Electrocatalytic Properties of Metal–Organic Framework PCN-223 for the Oxygen Reduction Reaction. *ACS Applied Materials & Interfaces* **2017**, *9* (39), 33539–33543. https://doi.org/10.1021/acsami.7b01547.

(240) Lin, S.; Usov, P. M.; Morris, A. J. The Role of Redox Hopping in Metal–Organic Framework Electrocatalysis. *Chemical Communications* **2018**, *54* (51), 6965–6974. https://doi.org/10.1039/C8CC01664J.

(241) Sun, L.; Hendon, C. H.; Park, S. S.; Tulchinsky, Y.; Wan, R. Is Iron Unique in Promoting Electrical Conductivity in MOFs? *Chemical Science* **2017**, *8* (6), 4450–4457. https://doi.org/10.1039/c7sc00647k.

(242) Hod, I.; Farha, O. K.; Hupp, J. T. Modulating the Rate of Charge Transport in a Metal–Organic Framework Thin Film Using Host:Guest Chemistry. *Chemical Communications* **2016**, *52* (8), 1705–1708. https://doi.org/10.1039/C5CC09695B.

(243) Gándara, F.; Uribe-Romo, F. J.; Britt, D. K.; Furukawa, H.; Lei, L.; Cheng, R.; Duan, X.; O'Keeffe, M.; Yaghi, O. M. Porous, Conductive Metal-Triazolates and Their Structural Elucidation by the Charge-Flipping Method. *Chemistry - A European Journal* **2012**, *18* (34), 10595–10601. https://doi.org/10.1002/chem.201103433.

(244) Park, J. G.; Aubrey, M. L.; Oktawiec, J.; Chakarawet, K.; Darago, L. E.; Grandjean, F.; Long, G. J.; Long, J. R. Charge Delocalization and Bulk Electronic Conductivity in the Mixed-Valence Metal–Organic Framework Fe(1,2,3-Triazolate)$_2$(BF_4)$_x$. *Journal of the American Chemical Society* **2018**, *140* (27), 8526–8534. https://doi.org/10.1021/jacs.8b03696.

(245) Sun, L.; Hendon, C. H.; Dincă, M. Coordination-Induced Reversible Electrical Conductivity Variation in the MOF-74 Analogue Fe_2(DSBDC). *Dalton Transactions* **2018**, *47* (34), 11739–11743. https://doi.org/10.1039/C8DT02197J.

(246) Sun, L.; Hendon, C. H.; Minier, M. A.; Walsh, A.; Dincă, M. Million-Fold Electrical Conductivity Enhancement in Fe $_2$ (DEBDC) versus Mn_2(DEBDC) (E = S, O). *Journal of the American Chemical Society* **2015**, *137* (19), 6164–6167. https://doi.org/10.1021/jacs.5b02897.

(247) Aubrey, M. L.; Wiers, B. M.; Andrews, S. C.; Sakurai, T.; Reyes-Lillo, S. E.; Hamed, S. M.; Yu, C.-J.; Darago, L. E.; Mason, J. A.; Baeg, J.-O.; Grandjean, F.; Long, G. J.; Seki, S.; Neaton, J. B.; Yang, P.; Long, J. R. Electron Delocalization and Charge Mobility as a Function of Reduction in a Metal–Organic Framework. *Nature Materials* **2018**, *17* (7), 625–632. https://doi.org/10.1038/s41563-018-0098-1.

(248) Creutz, C. Mixed Valence Complexes of d^5 - d^6 Metal Centers. In *Progress in Inorganic Chemistry*; Lippard, S. J., Ed.; John Wiley & Sons, Inc.: Hoboken, NJ, USA, 2007; pp 1–73. https://doi.org/10.1002/9780470166314.ch1.

(249) Narayan, T. C.; Miyakai, T.; Seki, S.; Dincă, M. High Charge Mobility in a Tetrathiafulvalene-Based Microporous Metal–Organic Framework. *Journal of the American Chemical Society* **2012**, *134* (31), 12932–12935. https://doi.org/10.1021/ja3059827.

(250) Park, S. S.; Hontz, E. R.; Sun, L.; Henson, C. H.; Walsh, A. Cation-Dependent Intrinsic Electrical Conductivity in Isostructural Tetrathiafulvalene-Based Microporous Metal–Organic Frameworks. *Journal of the American Chemical Society* **2015**, *137* (5), 1774–1777. https://doi.org/10.1021/ja512437u.

(251) Cadiau, A.; Xie, L. S.; Kolobov, N.; Shkurenko, A.; Qureshi, M.; Tchalala, M. R.; Park, S. S.; Bavykina, A.; Eddaoudi, M.; Dincă, M.; Hendon, C. H.; Gascon, J. Toward New 2D Zirconium-Based Metal–Organic Frameworks: Synthesis, Structures, and Electronic Properties. *Chemistry of Materials* **2020**, *32* (1), 97–104. https://doi.org/10.1021/acs.chemmater.9b02462.

(252) Zhao, S.; Wang, Y.; Dong, J.; He, C.-T.; Yin, H.; An, P.; Zhao, K.; Zhang, X.; Gao, C.; Zhang, L.; Lv, J.; Wang, J.; Zhang, J.; Khattak, A. M.; Khan, N. A.; Wei, Z.; Zhang, J.; Liu, S.; Zhao, H.; Tang, Z. Ultrathin Metal–Organic Framework Nanosheets for Electrocatalytic Oxygen Evolution. *Nature Energy* **2016**, *1* (12), 16184. https://doi.org/10.1038/nenergy.2016.184.

(253) Nasalevich, M. A.; van der Veen, M.; Kapteijn, F.; Gascon, J. Metal–Organic Frameworks as Heterogeneous Photocatalysts: Advantages and Challenges. *CrystEngComm* **2014**, *16* (23), 4919–4926. https://doi.org/10.1039/C4CE00032C.

(254) Feldblyum, J. I.; Liu, M.; Gidley, D. W.; Matzger, A. J. Reconciling the Discrepancies between Crystallographic Porosity and Guest Access As Exemplified by Zn-HKUST-1. *Journal of the American Chemical Society* **2011**, *133* (45), 18257–18263. https://doi.org/10.1021/ja2055935.

(255) Edgar, M.; Mitchell, R.; Slawin, A. M. Z.; Lightfoot, P.; Wright, P. A. Solid-State Transformations of Zinc 1,4-Benzenedicarboxylates Mediated by Hydrogen-Bond-Forming Molecules. *Chemistry - A European Journal* **2001**, *7* (23), 5168–5175. https://doi.org/10.1002/1521-3765(20011203)7:23<5168::AID-CHEM5168>3.0.CO;2-S.

(256) Lee, Y.-G.; Moon, H. R.; Cheon, Y. E.; Suh, M. P. A Comparison of the H_2 Sorption Capacities of Isostructural Metal-Organic Frameworks With and Without Accessible Metal Sites: $[\{Zn_2(Abtc)(Dmf)_2\}_3]$ and $[\{Cu_2(Abtc)(Dmf)_2\}_3]$ versus $[\{Cu_2(Abtc)\}_3]$. *Angewandte Chemie International Edition* **2008**, *47* (40), 7741–7745. https://doi.org/10.1002/anie.200801488.

(257) Nazarian, D.; Ganesh, P.; Sholl, D. S. Benchmarking Density Functional Theory Predictions of Framework Structures and Properties in a Chemically Diverse Test Set of Metal–Organic Frameworks. *Journal of Materials Chemistry A* **2015**, *3* (44), 22432–22440. https://doi.org/10.1039/C5TA03864B.

(258) Jensen, J. H. Predicting Accurate Absolute Binding Energies in Aqueous Solution: Thermodynamic Considerations for Electronic Structure Methods. *Physical Chemistry Chemical Physics* **2015**, *17* (19), 12441–12451. https://doi.org/10.1039/C5CP00628G.

(259) Xiao, D. J.; Bloch, E. D.; Mason, J. A.; Queen, W. L.; Hudson, M. R.; Planas, N.; Borycz, J.; Dzubak, A. L.; Verma, P.; Lee, K.; Bonino, F.; Crocellà, V.; Yano, J.; Bordiga, S.; Truhlar, D. G.; Gagliardi, L.; Brown, C. M.; Long, J. R. Oxidation of Ethane to Ethanol by N_2O in a Metal–Organic Framework with Coordinatively Unsaturated Iron(II) Sites. *Nature Chemistry* **2014**, *6* (7), 590–595. https://doi.org/10.1038/nchem.1956.

(260) Ortuño, M. A.; Bernales, V.; Gagliardi, L.; Cramer, C. J. Computational Study of First-Row Transition Metals Supported on MOF NU-1000 for Catalytic Acceptorless Alcohol Dehydrogenation. *The Journal of Physical Chemistry C* **2016**, *120* (43), 24697–24705. https://doi.org/10.1021/acs.jpcc.6b06381.

(261) Mondloch, J. E.; Katz, M. J.; Isley III, W. C.; Ghosh, P.; Liao, P.; Bury, W.; Wagner, G. W.; Hall, M. G.; DeCoste, J. B.; Peterson, G. W.; Snurr, R. Q.; Cramer, C. J.; Hupp, J. T.; Farha, O. K. Destruction of Chemical Warfare Agents Using Metal–Organic Frameworks. *Nature Materials* **2015**, *14* (5), 512–516. https://doi.org/10.1038/nmat4238.

(262) Kim, I. S.; Borycz, J.; Platero-Prats, A. E.; Tussupbayev, S.; Wang, T. C.; Farha, O. K.; Hupp, J. T.; Gagliardi, L.; Chapman, K. W.; Cramer, C. J.; Martinson, A. B. F. Targeted Single-Site MOF Node Modification: Trivalent Metal Loading via Atomic Layer Deposition. *Chemistry of Materials* **2015**, *27* (13), 4772–4778. https://doi.org/10.1021/acs.chemmater.5b01560.

(263) Jackson, A. J.; Skelton, J. M.; Hendon, C. H.; Butler, K. T.; Walsh, A. Crystal Structure Optimisation Using an Auxiliary Equation of State. *The Journal of Chemical Physics* **2015**, *143* (18), 184101. https://doi.org/10.1063/1.4934716.

(264) Schreiner, P. R. Relative Energy Computations with Approximate Density Functional Theory—A Caveat! *Angewandte Chemie International Edition* **2007**, *46* (23), 4217–4219. https://doi.org/10.1002/anie.200700386.

(265) Odoh, S. O.; Cramer, C. J.; Truhlar, D. G.; Gagliardi, L. Quantum-Chemical Characterization of the Properties and Reactivities of Metal–Organic Frameworks. *Chemical Reviews* **2015**, *115* (12), 6051–6111. https://doi.org/10.1021/cr500551h.

(266) De Santis, E.; Edwards, A. A.; Alexander, B. D.; Holder, S. J.; Biesse-Martin, A.-S.; Nielsen, B. V.; Mistry, D.; Waters, L.; Siligardi, G.; Hussain, R.; Faure, S.; Taillefumier, C. Selective Complexation of Divalent Cations by a Cyclic α,β-Peptoid Hexamer: A Spectroscopic and Computational Study. *Organic and Biomolecular Chemistry* **2016**, *14* (48), 11371–11380. https://doi.org/10.1039/C6OB01954D.

(267) Oxford, G. A. E.; Snurr, R. Q.; Broadbelt, L. J. Hybrid Quantum Mechanics/Molecular Mechanics Investigation of (Salen)Mn for Use in Metal−Organic Frameworks. *Industrial & Engineering Chemistry Research* **2010**, *49* (21), 10965–10973. https://doi.org/10.1021/ie100165j.

(268) Bennett, T. D.; Cheetham, A. K.; Fuchs, A. H.; Coudert, F.-X. Interplay between Defects, Disorder and Flexibility in Metal-Organic Frameworks. *Nature Chemistry* **2017**, *9*, 11–16.

(269) Cinar, Z. The Role of Molecular Modeling in TiO_2 Photocatalysis. *Molecules* **2017**, *22* (4), 556. https://doi.org/10.3390/molecules22040556.

(270) Liu, L.; Mi, W.; Hao, C.; Qiu, J. Theoretical Studies on How Excited State Hydrogen and Coordination Bonds Affect Luminescent Properties of Metal Organic Framework $Cu_4(L)_4$•2EtOH. *Inorganic Chemistry Communications* **2013**, *31*, 69–73. https://doi.org/10.1016/j.inoche.2013.02.023.

(271) Wang, B.; Truhlar, D. G. Combined Quantum Mechanical and Molecular Mechanical Methods for Calculating Potential Energy Surfaces: Tuned and Balanced Redistributed-Charge Algorithm. *Journal of Chemical Theory and Computation* **2010**, *6* (2), 359–369. https://doi.org/10.1021/ct900366m.

(272) Théry, V.; Rinaldi, D.; Rivail, J.-L.; Maigret, B.; Ferenczy, G. G. Quantum Mechanical Computations on Very Large Molecular Systems: The Local Self-Consistent Field Method: Quantum Mechanical Computations. *Journal of Computational Chemistry* **1994**, *15* (3), 269–282. https://doi.org/10.1002/jcc.540150303.

(273) Amara, P.; Field, M. J.; Alhambra, C.; Gao, J. The Generalized Hybrid Orbital Method for Combined Quantum Mechanical/Molecular Mechanical Calculations: Formulation and Tests of the Analytical Derivatives. *Theoretical Chemistry Accounts: Theory, Computation, and Modeling (Theoretica Chimica Acta)* **2000**, *104* (5), 336–343. https://doi.org/10.1007/s002140000153.

(274) Yang, D.; Odoh, S. O.; Wang, T. C.; Farha, O. K.; Hupp, J. T.; Cramer, C. J.; Gagliardi, L.; Gates, B. C. Metal–Organic Framework Nodes as Nearly Ideal Supports for Molecular Catalysts: NU-1000- and UiO-66-Supported Iridium Complexes. *Journal of the American Chemical Society* **2015**, *137* (23), 7391–7396. https://doi.org/10.1021/jacs.5b02956.

(275) Momeni, M. R.; Pahls, D. R.; Yang, D.; Wang, T. C.; Farha, O. K.; Hupp, J. T.; Cramer, C. J.; Gagliardi, L.; Gates, B. C. Correction to "Metal–Organic Framework Nodes as Nearly Ideal Supports for Molecular Catalysts: NU-1000- and UiO-66-Supported Iridium Complexes." *Journal of the American Chemical Society* **2017**, *139* (50), 18406–18406. https://doi.org/10.1021/jacs.7b02871.

(276) Qian, J.; Li, Q.; Liang, L.; Li, T.-T.; Hu, Y.; Huang, S. A Microporous MOF with Open Metal Sites and Lewis Basic Sites for Selective CO_2 Capture. *Dalton Transactions* **2017**, *46* (41), 14102–14106. https://doi.org/10.1039/C7DT03255B.

(277) Strauss, I.; Mundstock, A.; Treger, M.; Lange, K.; Hwang, S.; Chmelik, C.; Rusch, P.; Bigall, N. C.; Pichler, T.; Shiozawa, H.; Caro, J. Metal–Organic Framework Co-MOF-74-Based Host–Guest Composites for Resistive Gas Sensing. *ACS Applied Materials & Interfaces* **2019**, *11* (15), 14175–14181. https://doi.org/10.1021/acsami.8b22002.

(278) Shustova, N. B.; Ong, T.-C.; Cozzolino, A. F.; Michaelis, V. K.; Griffin, R. G.; Dincă, M. Phenyl Ring Dynamics in a Tetraphenylethylene-Bridged Metal–Organic Framework: Implications for the Mechanism of Aggregation-Induced Emission. *Journal of the American Chemical Society* **2012**, *134* (36), 15061–15070. https://doi.org/10.1021/ja306042w.

(279) Vogiatzis, K. D.; Haldoupis, E.; Xiao, D. J.; Long, J. R.; Siepmann, J. I.; Gagliardi, L. Accelerated Computational Analysis of Metal–Organic Frameworks for Oxidation Catalysis. *The Journal of Physical Chemistry C* **2016**, *120* (33), 18707–18712. https://doi.org/10.1021/acs.jpcc.6b07115.

(280) Vermoortele, F.; Vandichel, M.; Van de Voorde, B.; Ameloot, R.; Waroquier, M.; Van Speybroeck, V.; De Vos, D. E. Electronic Effects of Linker Substitution on Lewis Acid Catalysis with Metal-Organic Frameworks. *Angewandte Chemie International Edition* **2012**, *51* (20), 4887–4890. https://doi.org/10.1002/anie.201108565.

(281) Hajek, J.; Vandichel, M.; Van de Voorde, B.; Bueken, B.; De Vos, D.; Waroquier, M.; Van Speybroeck, V. Mechanistic Studies of Aldol Condensations in UiO-66 and UiO-66-NH_2 Metal Organic Frameworks. *Journal of Catalysis* **2015**, *331*, 1–12. https://doi.org/10.1016/j.jcat.2015.08.015.

(282) Caratelli, C.; Hajek, J.; Cirujano, F. G.; Waroquier, M.; Llabres i Xamena, F. X.; Van Speybroeck, V. Nature of Active Sites on UiO-66 and Beneficial Influence of Water in the Catalysis of Fischer Esterification. *Journal of Catalysis* **2017**, *352*, 401–414.

(283) Dolgopolova, E. A.; Moore, T. M.; Ejegbavwo, O. A.; Pellechia, P. J.; Smith, M. D.; Shustova, N. B. A Metal–Organic Framework as a Flask: Photophysics of Confined Chromophores with a Benzylidene Imidazolinone Core. *Chemical Communications* **2017**, *53* (53), 7361–7364. https://doi.org/10.1039/C7CC02253K.

(284) Gu, Z.-G.; Heinke, L.; Wöll, C.; Neumann, T.; Wenzel, W.; Li, Q.; Fink, K.; Gordan, O. D.; Zahn, D. R. T. Experimental and Theoretical Investigations of the Electronic Band Structure of Metal-Organic Frameworks of HKUST-1 Type. *Applied Physics Letters* **2015**, *107* (18), 183301. https://doi.org/10.1063/1.4934737.

(285) Braglia, L.; Borfecchia, E.; Martini, A.; Bugaev, A. L.; Soldatov, A. V.; Øien-Ødegaard, S.; Lønstad-Bleken, B. T.; Olsbye, U.; Lillerud, K. P.; Lomachenko, K. A.; Agostini, G.; Manzoli, M.; Lamberti, C. The Duality of UiO-67-Pt MOFs: Connecting Treatment Conditions and Encapsulated Pt Species by *Operando* XAS. *Physical Chemistry Chemical Physics* **2017**, *19* (40), 27489–27507. https://doi.org/10.1039/C7CP05185A.

(286) Borfecchia, E.; Øien, S.; Svelle, S.; Mino, L.; Braglia, L.; Agostini, G.; Gallo, E.; Lomachenko, K. A.; Bordiga, S.; Guda, A. A.; Soldatov, M. A.; Soldatov, A. V.; Olsbye, U.; Lillerud, K. P.; Lamberti, C. A XAFS Study of the Local Environment and Reactivity of Pt- Sites in Functionalized UiO-67 MOFs. *Journal of Physics: Conference Series* **2016**, *712*, 012125. https://doi.org/10.1088/1742-6596/712/1/012125.

(287) Øien, S.; Agostini, G.; Svelle, S.; Borfecchia, E.; Lomachenko, K. A.; Mino, L.; Gallo, E.; Bordiga, S.; Olsbye, U.; Lillerud, K. P.; Lamberti, C. Probing Reactive Platinum Sites in UiO-67 Zirconium Metal–Organic Frameworks. *Chemistry of Materials* **2015**, *27* (3), 1042–1056. https://doi.org/10.1021/cm504362j.

(288) Xu, C.; Liu, H.; Li, D.; Su, J.-H.; Jiang, H.-L. Direct Evidence of Charge Separation in a Metal–Organic Framework: Efficient and Selective Photocatalytic Oxidative Coupling of Amines *via* Charge and Energy Transfer. *Chemical Science* **2018**, *9* (12), 3152–3158. https://doi.org/10.1039/C7SC05296K.

(289) Ye, J.; Johnson, J. K. Design of Lewis Pair-Functionalized Metal Organic Frameworks for CO_2 Hydrogenation. *ACS Catalysis* **2015**, *5* (5), 2921–2928. https://doi.org/10.1021/acscatal.5b00396.

(290) Ye, J.; Johnson, J. K. Catalytic Hydrogenation of CO_2 to Methanol in a Lewis Pair Functionalized MOF. *Catalysis Science & Technology* **2016**, *6* (24), 8392–8405. https://doi.org/10.1039/C6CY01245K.

(291) Dybtsev, D. N.; Nuzhdin, A. L.; Chun, H.; Bryliakov, K. P.; Talsi, E. P.; Fedin, V. P.; Kim, K. A Homochiral Metal–Organic Material with Permanent Porosity, Enantioselective Sorption Properties, and Catalytic Activity. *Angewandte Chemie* **2006**, *118* (6), 930–934. https://doi.org/10.1002/ange.200503023.

(292) Seo, J. S.; Whang, D.; Lee, H.; Jun, S. I.; Oh, J.; Jeon, Y. J.; Kim, K. A Homochiral Metal–Organic Porous Material for Enantioselective Separation and Catalysis. *Nature* **2000**, *404* (6781), 982–986. https://doi.org/10.1038/35010088.

(293) Horike, S.; Dincă, M.; Tamaki, K.; Long, J. R. Size-Selective Lewis Acid Catalysis in a Microporous Metal-Organic Framework with Exposed Mn^{2+} Coordination Sites. *Journal of the American Chemical Society* **2008**, *130* (18), 5854–5855. https://doi.org/10.1021/ja800669j.

(294) Zhang, X.; Huang, Z.; Ferrandon, M.; Yang, D.; Robison, L.; Li, P.; Wang, T. C.; Delferro, M.; Farha, O. K. Catalytic Chemoselective Functionalization of Methane in a Metal−organic Framework. *Nature Catalysis* **2018**, *1* (5), 356–362. https://doi.org/10.1038/s41929-018-0069-6.

(295) Yang, B.; Wu, X.-P.; Gagliardi, L.; Truhlar, D. G. Methane Functionalization by an Ir(III) Catalyst Supported on a Metal–Organic Framework: An Alternative Explanation of Steric Confinement Effects. *Theoretical Chemistry Accounts* **2019**, *138* (9), 107. https://doi.org/10.1007/s00214-019-2498-y.

(296) Supronowicz, B.; Mavrandonakis, A.; Heine, T. Interaction of Small Gases with the Unsaturated Metal Centers of the HKUST-1 Metal Organic Framework. *Journal of Physical Chemistry C* **2013**, *117* (28), 14570–14578. https://doi.org/10.1021/jp4018037.

(297) Maihom, T.; Probst, M.; Limtrakul, J. Computational Study of the Carbonyl–Ene Reaction between Formaldehyde and Propylene Encapsulated in Coordinatively Unsaturated Metal–Organic Frameworks $M_3(BTC)_2$ (M = Fe, Co, Ni, Cu and Zn). *Physical Chemistry Chemical Physics* **2019**, *21* (5), 2783–2789. https://doi.org/10.1039/C8CP06841K.

(298) Položij, M.; Rubeš, M.; Čejka, J.; Nachtigall, P. Catalysis by Dynamically Formed Defects in a Metal-Organic Framework Structure: Knoevenagel Reaction Catalyzed by Copper Benzene-1,3,5-Tricarboxylate. *ChemCatChem* **2014**, *6* (10), 2821–2824. https://doi.org/10.1002/cctc.201402411.

(299) Liu, Y.; Klet, R. C.; Hupp, J. T.; Farha, O. Probing the Correlations between the Defects in Metal–Organic Frameworks and Their Catalytic Activity by an Epoxide Ring-Opening Reaction. *Chemical Communications* **2016**, *52* (50), 7806–7809. https://doi.org/10.1039/C6CC03727E.

(300) Wu, H.; Chua, Y. S.; Krungleviciute, V.; Tyagi, M.; Chen, P.; Yildirim, T.; Zhou, W. Unusual and Highly Tunable Missing-Linker Defects in Zirconium Metal–Organic Framework UiO-66 and Their Important Effects on Gas Adsorption. *Journal of the American Chemical Society* **2013**, *135* (28), 10525–10532. https://doi.org/10.1021/ja404514r.

(301) Canivet, J.; Vandichel, M.; Farrusseng, D. Origin of Highly Active Metal–Organic Framework Catalysts: Defects? Defects! *Dalton Transactions* **2016**, *45* (10), 4090–4099. https://doi.org/10.1039/C5DT03522H.

(302) Svane, K. L.; Bristow, J. K.; Gale, J. D.; Walsh, A. Vacancy Defect Configurations in the Metal–Organic Framework UiO-66: Energetics and Electronic Structure. *Journal of Materials Chemistry A* **2018**, *6* (18), 8507–8513. https://doi.org/10.1039/c7ta11155j.

(303) Noh, H.; Cui, Y.; Peters, A. W.; Pahls, D. R.; Ortuño, M. A.; Vermeulen, N. A.; Cramer, C. J.; Gagliardi, L.; Hupp, J. T.; Farha, O. K. An Exceptionally Stable Metal–Organic Framework Supported Molybdenum(VI) Oxide Catalyst for Cyclohexene Epoxidation. *Journal of the American Chemical Society* **2016**, *138* (44), 14720–14726. https://doi.org/10.1021/jacs.6b08898.

(304) Platero-Prats, A. E.; League, A. B.; Bernales, V.; Ye, J.; Gallington, L. C.; Vjunov, A.; Schweitzer, N. M.; Li, Z.; Zheng, J.; Mehdi, B. L.; Stevens, A. J.; Dohnalkova, A.; Balasubramanian, M.; Farha, O. K.; Hupp, J. T.; Browning, N. D.; Fulton, J. L.; Camaioni, D. M.; Lercher, J. A.; Truhlar, D. G.; Gagliardi, L.; Cramer, C. J.; Chapman, K. W. Bridging Zirconia Nodes within a Metal–Organic Framework via Catalytic Ni-Hydroxo Clusters to Form Heterobimetallic Nanowires. *Journal of the American Chemical Society* **2017**, *139* (30), 10410–10418. https://doi.org/10.1021/jacs.7b04997.

(305) Li, Z.; Schweitzer, N. M.; League, A. B.; Bernales, V.; Peters, A. W.; Getsoian, A. "Bean"; Wang, T. C.; Miller, J. T.; Vjunov, A.; Fulton, J. L.; Lercher, J. A.; Cramer, C. J.; Gagliardi, L.; Hupp, J. T.; Farha, O. K. Sintering-Resistant Single-Site Nickel Catalyst Supported by Metal–Organic Framework. *Journal of the American Chemical Society* **2016**, *138* (6), 1977–1982. https://doi.org/10.1021/jacs.5b12515.

(306) Yang, D.; Odoh, S. O.; Borycz, J.; Wang, T. C.; Farha, O. K.; Hupp, J. T.; Cramer, C. J.; Gagliardi, L.; Gates, B. C. Tuning Zr $_6$ Metal–Organic Framework (MOF) Nodes as Catalyst Supports: Site Densities and Electron-Donor Properties Influence Molecular Iridium Complexes as Ethylene Conversion Catalysts. *ACS Catalysis* **2016**, *6* (1), 235–247. https://doi.org/10.1021/acscatal.5b02243.

(307) Vermoortele, F.; Bueken, B.; Le Bars, G.; Van de Voorde, B.; Vandichel, M.; Houthoofd, K.; Vimont, A.; Daturi, M.; Waroquier, M.; Van Speybroeck, V.; Kirschhock, C.; De Vos, D. E. Synthesis Modulation as a Tool To Increase the Catalytic Activity of Metal–Organic Frameworks: The Unique Case of UiO-66(Zr). *Journal of the American Chemical Society* **2013**, *135* (31), 11465–11468. https://doi.org/10.1021/ja405078u.

(308) Ling, S.; Slater, B. Dynamic Acidity in Defective UiO-66. *Chemical Science* **2016**, *7* (7), 4706–4712. https://doi.org/10.1039/C5SC04953A.

(309) Troya, D. Reaction Mechanism of Nerve-Agent Decomposition with Zr-Based Metal Organic Frameworks. *Journal of Physical Chemistry C* **2016**, *120* (51), 29312–29323. https://doi.org/10.1021/acs.jpcc.6b10530.

(310) Terranova, Z. L.; Paesani, F. The Effects of Framework Dynamics on the Behavior of Water Adsorbed in the [Zn(l-L)(Cl)] and Co-MOF-74 Metal–Organic Frameworks. *Physical Chemistry Chemical Physics* **2016**, *18* (11), 8196–8204. https://doi.org/10.1039/C5CP07681A.

(311) Islamoglu, T.; Ortuño, M. A.; Proussaloglou, E.; Howarth, A. J.; Vermeulen, N. A.; Atilgan, A.; Asiri, A. M.; Cramer, C. J.; Farha, O. K. Presence versus Proximity: The Role of Pendant Amines in the Catalytic Hydrolysis of a Nerve Agent Simulant. *Angewandte Chemie International Edition* **2018**, *57* (7), 1949–1953. https://doi.org/10.1002/anie.201712645.

(312) de Koning, M. C.; van Grol, M.; Breijaert, T. Degradation of Paraoxon and the Chemical Warfare Agents VX, Tabun, and Soman by the Metal–Organic Frameworks UiO-66-NH_2, MOF-808, NU-1000, and PCN-777. *Inorganic Chemistry* **2017**, *56* (19), 11804–11809. https://doi.org/10.1021/acs.inorgchem.7b01809.

(313) Sadakiyo, M.; Yamada, T.; Honda, K.; Matsui, H.; Kitagawa, H. Control of Crystalline Proton-Conducting Pathways by Water-Induced Transformations of Hydrogen-Bonding Networks in a Metal–Organic Framework. *Journal of the American Chemical Society* **2014**, *136* (21), 7701–7707. https://doi.org/10.1021/ja5022014.

(314) Wang, G.; Sharp, C.; Plonka, A. M.; Wang, Q.; Frenkel, A. I.; Guo, W.; Hill, C.; Smith, C.; Kollar, J.; Troya, D.; Morris, J. R. Mechanism and Kinetics for Reaction of the Chemical Warfare Agent Simulant, DMMP(*g*), with Zirconium(IV) MOFs: An Ultrahigh-Vacuum and DFT Study. *Journal of Physical Chemistry C* **2017**, *121* (21), 11261–11272. https://doi.org/10.1021/acs.jpcc.7b00070.

(315) Plonka, A. M.; Grissom, T. G.; Musaev, D. G.; Balboa, A.; Gordon, W. O.; Collins-Wildman, D. L.; Ghose, S. K.; Tian, Y.; Ebrahim, A. M.; Mitchell, M. B.; Hill, C. L.; Morris, J. R.; Frenkel, A. I. Effect of Carbon Dioxide on the Degradation of Chemical Warfare Agent Simulant in the Presence of Zr Metal Organic Framework MOF-808. *Chemistry of Materials* **2019**, *31* (23), 9904–9914. https://doi.org/10.1021/acs.chemmater.9b04565.

(316) Chen, H.; Liao, P.; Mendonca, M. L.; Snurr, R. Q. Insights into Catalytic Hydrolysis of Organophosphate Warfare Agents by Metal–Organic Framework NU-1000. *Journal of Physical Chemistry C* **2018**, *122* (23), 12362–12368. https://doi.org/10.1021/acs.jpcc.8b03641.

(317) Barea, E.; Maldonado, C. R.; Navarro, J. A. R. MOFs for the Capture and Degradation of Chemical Warfare Agents. In *Metal-Organic Frameworks*; García, H., Navalón, S., Eds.; Wiley-VCH Verlag GmbH & Co. KGaA: Weinheim, Germany, 2018; pp 199–221. https://doi.org/10.1002/9783527809097.ch7.

(318) Ketrat, S.; Maihom, T.; Wannakao, S.; Probst, M.; Nokbin, S.; Limtrakul, J. Coordinatively Unsaturated Metal–Organic Frameworks $M_3(BTC)_2$ (M = Cr, Fe, Co, Ni, Cu, and Zn) Catalyzing the Oxidation of CO by N_2O: Insight from DFT Calculations. *Inorganic Chemistry* **2017**, *56* (22), 14005–14012. https://doi.org/10.1021/acs.inorgchem.7b02143.

(319) Ryu, U. J.; Kim, S. J.; Lim, H.-K.; Kim, H.; Choi, K. M.; Kang, J. K. Synergistic Interaction of Re Complex and Amine Functionalized Multiple Ligands in Metal-Organic Frameworks for Conversion of Carbon Dioxide. *Science Reports* **2017**, *7* (1), 612. https://doi.org/10.1038/s41598-017-00574-1.

(320) Yilmaz, G.; Peh, S. B.; Zhao, D.; Ho, G. W. Atomic- and Molecular-Level Design of Functional Metal–Organic Frameworks (MOFs) and Derivatives for Energy and Environmental Applications. *Advanced Science* **2019**, *6* (21), 1901129. https://doi.org/10.1002/advs.201901129.

(321) Santaclara, J. G.; Kapteijn, F.; Gascon, J.; van der Veen, M. A. Understanding Metal–Organic Frameworks for Photocatalytic Solar Fuel Production. *CrystEngComm* **2017**, *19* (29), 4118–4125. https://doi.org/10.1039/C7CE00006E.

(322) Evarestov, R. A.; Smirnov, V. P. Special points of the brillouin zone and their use in the solid-state theory. *physica status solidi (b)* **1983**, *119* (1), 9–40. https://doi.org/10.1002/pssb.2221190102.

(323) Chadi, D. J.; Cohen, M. L. Special Points in the Brillouin Zone. *Physical Review B* **1973**, *8* (12), 5747–5753. https://doi.org/10.1103/PhysRevB.8.5747.

(324) Hoffmann, R. How Chemistry and Physics Meet in the Solid State. *Angewandte Chemie International Edition in English* **1987**, *26* (9), 846–878. https://doi.org/10.1002/anie.198708461.

(325) Hoffmann, R. Interaction of Orbitals through Space and through Bonds. *Accounts of Chemical Research* **1971**, *4* (1), 1–9. https://doi.org/10.1021/ar50037a001.

(326) Sun, L.; Campbell, M. G.; Dincă, M. Electrically Conductive Porous Metal-Organic Frameworks. *Angewandte Chemie International Edition* **2016**, *55* (11), 3566–3579. https://doi.org/10.1002/anie.201506219.

(327) Skorupskii, G.; Trump, B. A.; Kasel, T. W.; Brown, C. M.; Hendon, C. H.; Dincă, M. Efficient and Tunable One-Dimensional Charge Transport in Layered Lanthanide Metal–Organic Frameworks. *Nature Chemistry* **2020**, *12* (2), 131–136. https://doi.org/10.1038/s41557-019-0372-0.

(328) Ivanov, M. V.; Wadumethrige, S. H.; Wang, D.; Rathore, R. Through-Space or Through-Bond? The Important Role of Cofaciality in Orbital Reordering and Its Implications for Hole (De)Stabilization in Polychromophoric Assemblies. *The Journal of Physical Chemistry C* **2017**, *121* (29), 15639–15643. https://doi.org/10.1021/acs.jpcc.7b05804.

(329) Scholes, G. D.; Ghiggino, K. P.; Oliver, A. M.; Paddon-Row, M. N. Through-Space and through-Bond Effects on Exciton Interactions in Rigidly Linked Dinaphthyl Molecules. *Journal of the American Chemical Society* **1993**, *115* (10), 4345–4349. https://doi.org/10.1021/ja00063a061.

(330) Hmadeh, M.; Lu, Z.; Liu, Z.; Gándara, F.; Furukawa, H.; Wan, S.; Augustyn, V.; Chang, R.; Liao, L.; Zhou, F.; Perre, E.; Ozolins, V.; Suenaga, K.; Duan, X.; Dunn, B.; Yamamto, Y.; Terasaki, O.; Yaghi, O. M. New Porous Crystals of Extended Metal-Catecholates. *Chemistry of Materials* **2012**, *24* (18), 3511–3513. https://doi.org/10.1021/cm301194a.

(331) Sheberla, D.; Sun, L.; Blood-Forsythe, M. A.; Er, S.; Wade, C. R.; Brozek, C. K.; Aspuru-Guzik, A.; Dincă, M. High Electrical Conductivity in Ni_3 (2,3,6,7,10,11-Hexaiminotriphenylene)$_2$, a Semiconducting Metal–Organic Graphene Analogue. *Journal of the American Chemical Society* **2014**, *136* (25), 8859–8862. https://doi.org/10.1021/ja502765n.

(332) Dong, R.; Han, P.; Arora, H.; Ballabio, M.; Karakus, M.; Zhang, Z.; Shekhar, C.; Adler, P.; Petkov, P. St.; Erbe, A.; Mannsfeld, S. C. B.; Felser, C.; Heine, T.; Bonn, M.; Feng, X.; Cánovas, E. High-Mobility Band-like Charge Transport in a Semiconducting Two-Dimensional Metal–Organic Framework. *Nature Materials* **2018**, *17* (11), 1027–1032. https://doi.org/10.1038/s41563-018-0189-z.

(333) Kambe, T.; Sakamoto, R.; Hoshiko, K.; Takada, K.; Miyachi, M.; Ryu, J.-H.; Sasaki, S.; Kim, J.; Nakazato, K.; Takata, M.; Nishihara, H. π-Conjugated Nickel Bis(Dithiolene) Complex Nanosheet. *Journal of the American Chemical Society* **2013**, *135* (7), 2462–2465. https://doi.org/10.1021/ja312380b.

(334) Talin, A. A.; Centrone, A.; Ford, A. C.; Foster, M. E.; Stavila, V.; Haney, P.; Kinney, R. A.; Szalai, V.; El Gabaly, F.; Yoon, H. P.; Léonard, F.; Allendorf, M. D. Tunable Electrical Conductivity in Metal-Organic Framework Thin-Film Devices. *Science* **2014**, *343* (6166), 66–69. https://doi.org/10.1126/science.1246738.

(335) Aubrey, M. L.; Wiers, B. M.; Andrews, S. C.; Sakurai, T.; Reyes-Lillo, S. E.; Hamed, S. M.; Yu, C.-J.; Darago, L. E.; Mason, J. A.; Baeg, J.-O.; Grandjean, F.; Long, G. J.; Seki, S.; Neaton, J. B.; Yang, P.; Long, J. R. Electron Delocalization and Charge Mobility as a Function of Reduction in a Metal–Organic Framework. *Nature Materials* **2018**, *17* (7), 625–632. https://doi.org/10.1038/s41563-018-0098-1.

(336) Nam, K. W.; Park, S. S.; dos Reis, R.; Dravid, V. P.; Kim, H.; Mirkin, C. A.; Stoddart, J. F. Conductive 2D Metal-Organic Framework for High-Performance Cathodes in Aqueous Rechargeable Zinc Batteries. *Nature Communications* **2019**, *10* (1), 4948. https://doi.org/10.1038/s41467-019-12857-4.

(337) Wada, K.; Sakaushi, K.; Sasaki, S.; Nishihara, H. Multielectron-Transfer-based Rechargeable Energy Storage of Two-Dimensional Coordination Frameworks with Non-Innocent Ligands. *Angewandte Chemie International Edition* **2018**, *57* (29), 8886–8890. https://doi.org/10.1002/anie.201802521.

(338) Pomerantseva, E.; Bonaccorso, F.; Feng, X.; Cui, Y.; Gogotsi, Y. Energy Storage: The Future Enabled by Nanomaterials. *Science* **2019**, *366* (6468), eaan8285. https://doi.org/10.1126/science.aan8285.

(339) Sheberla, D.; Bachman, J. C.; Elias, J. S.; Sun, C.-J.; Shao-Horn, Y.; Dincă, M. Conductive MOF Electrodes for Stable Supercapacitors with High Areal Capacitance. *Nature Materials* **2017**, *16* (2), 220–224. https://doi.org/10.1038/nmat4766.

(340) Wang, H.; Zhu, Q.-L.; Zou, R.; Xu, Q. Metal-Organic Frameworks for Energy Applications. *Chem* **2017**, *2* (1), 52–80. https://doi.org/10.1016/j.chempr.2016.12.002.

(341) Feng, D.; Lei, T.; Lukatskaya, M. R.; Park, J.; Huang, Z.; Lee, M.; Shaw, L.; Chen, S.; Yakovenko, A. A.; Kulkarni, A.; Xiao, J.; Fredrickson, K.; Tok, J. B.; Zou, X.; Cui, Y.; Bao, Z. Robust and Conductive Two-Dimensional Metal−organic Frameworks with Exceptionally High Volumetric and Areal Capacitance. *Nature Energy* **2018**, *3* (1), 30–36. https://doi.org/10.1038/s41560-017-0044-5.

(342) Miner, E. M.; Fukushima, T.; Sheberla, D.; Sun, L.; Surendranath, Y.; Dincă, M. Electrochemical Oxygen Reduction Catalysed by Ni3(Hexaiminotriphenylene)2. *Nature Communications* **2016**, *7* (1), 10942. https://doi.org/10.1038/ncomms10942.

(343) Stassen, I.; Burtch, N.; Talin, A.; Falcaro, P.; Allendorf, M.; Ameloot, R. An Updated Roadmap for the Integration of Metal–Organic Frameworks with Electronic Devices and Chemical Sensors. *Chemical Society Reviews* **2017**, *46* (11), 3185–3241. https://doi.org/10.1039/C7CS00122C.

(344) Evans, A. M.; Parent, L. R.; Flanders, N. C.; Bisbey, R. P.; Vitaku, E.; Kirschner, M. S.; Schaller, R. D.; Chen, L. X.; Gianneschi, N. C.; Dichtel, W. R. Seeded Growth of Single-Crystal Two-Dimensional Covalent Organic Frameworks. *Science* **2018**, *361* (6397), 52–57. https://doi.org/10.1126/science.aar7883.

(345) Ma, T.; Kapustin, E. A.; Yin, S. X.; Liang, L.; Zhou, Z.; Niu, J.; Li, L.-H.; Wang, Y.; Su, J.; Li, J.; Wang, X.; Wang, W. D.; Wang, W.; Sun, J.; Yaghi, O. M. Single-Crystal x-Ray Diffraction Structures of Covalent Organic Frameworks. *Science* **2018**, *361* (6397), 48–52. https://doi.org/10.1126/science.aat7679.

(346) Zhao, M.; Huang, Y.; Peng, Y.; Huang, Z.; Ma, Q.; Zhang, H. Two-Dimensional Metal–Organic Framework Nanosheets: Synthesis and Applications. *Chemical Society Reviews* **2018**, *47* (16), 6267–6295. https://doi.org/10.1039/C8CS00268A.

(347) Zhong, Y.; Cheng, B.; Park, C.; Ray, A.; Brown, S.; Mujid, F.; Lee, J.-U.; Zhou, H.; Suh, J.; Lee, K.-H.; Mannix, A. J.; Kang, K.; Sibener, S. J.; Muller, D. A.; Park, J. Wafer-Scale Synthesis of Monolayer Two-Dimensional Porphyrin Polymers for Hybrid Superlattices. *Science* **2019**, *366* (6471), 1379–1384. https://doi.org/10.1126/science.aax9385.

(348) Dou, J.-H.; Sun, L.; Ge, Y.; Li, W.; Hendon, C. H.; Li, J.; Gul, S.; Yano, J.; Stach, E. A.; Dincă, M. Signature of Metallic Behavior in the Metal–Organic Frameworks M_3(Hexaiminobenzene)$_2$ (M = Ni, Cu). *Journal of the American Chemical Society* **2017**, *139* (39), 13608–13611. https://doi.org/10.1021/jacs.7b07234.

(349) Day, R. W.; Bediako, D. K.; Rezaee, M.; Parent, L. R.; Skorupskii, G.; Arguilla, M. Q.; Hendon, C. H.; Stassen, I.; Gianneschi, N. C.; Kim, P.; Dincă, M. Single Crystals of Electrically Conductive Two-Dimensional Metal–Organic Frameworks: Structural and Electrical Transport Properties. *ACS Central Science* **2019**, *5* (12), 1959–1964. https://doi.org/10.1021/acscentsci.9b01006.

(350) Miao, Q. Ten Years of N-Heteropentacenes as Semiconductors for Organic Thin-Film Transistors. *Advanced Materials* **2014**, *26* (31), 5541–5549. https://doi.org/10.1002/adma.201305497.

(351) Wang, C.; Dong, H.; Jiang, L.; Hu, W. Organic Semiconductor Crystals. *Chemical Society Reviews* **2018**, *47* (2), 422–500. https://doi.org/10.1039/C7CS00490G.

(352) Watson, M. D.; Fechtenkötter, A.; Müllen, K. Big Is Beautiful−"Aromaticity" Revisited from the Viewpoint of Macromolecular and Supramolecular Benzene Chemistry. *Chemical Reviews* **2001**, *101* (5), 1267–1300. https://doi.org/10.1021/cr990322p.

(353) Okamoto, T.; Kumagai, S.; Fukuzaki, E.; Ishii, H.; Watanabe, G.; Niitsu, N.; Annaka, T.; Yamagishi, M.; Tani, Y.; Sugiura, H.; Watanabe, T.; Watanabe, S.; Takeya, J. Robust, High-Performance n-Type Organic Semiconductors. *Science Advances* **2020**, *6* (18), eaaz0632. https://doi.org/10.1126/sciadv.aaz0632.

(354) Rieth, A. J.; Wright, A. M.; Dincă, M. Kinetic Stability of Metal–Organic Frameworks for Corrosive and Coordinating Gas Capture. *Nature Reviews Materials* **2019**, *4* (11), 708–725. https://doi.org/10.1038/s41578-019-0140-1.

(355) Pliego, J. R. Thermodynamic Cycles and the Calculation of PKa. *Chemical Physics Letters* **2003**, *367* (1–2), 145–149. https://doi.org/10.1016/S0009-2614(02)01686-X.

(356) Romero, R.; Salgado, P. R.; Soto, C.; Contreras, D.; Melin, V. An Experimental Validated Computational Method for PKa Determination of Substituted 1,2-Dihydroxybenzenes. *Frontiers in Chemistry* **2018**, *6*, 208. https://doi.org/10.3389/fchem.2018.00208.

(357) Van Vleet, M. J.; Weng, T.; Li, X.; Schmidt, J. R. In Situ, Time-Resolved, and Mechanistic Studies of Metal–Organic Framework Nucleation and Growth. *Chemical Reviews* **2018**, *118* (7), 3681–3721. https://doi.org/10.1021/acs.chemrev.7b00582.

(358) Hestand, N. J.; Spano, F. C. Expanded Theory of H- and J-Molecular Aggregates: The Effects of Vibronic Coupling and Intermolecular Charge Transfer. *Chemical Reviews* **2018**, *118* (15), 7069–7163. https://doi.org/10.1021/acs.chemrev.7b00581.

(359) Xie, L. S.; Skorupskii, G.; Dincă, M. Electrically Conductive Metal–Organic Frameworks. *Chemical Reviews* **2020**, *120* (16), 8536–8580. https://doi.org/10.1021/acs.chemrev.9b00766.

(360) Stavila, V.; Talin, A. A.; Allendorf, M. D. MOF-Based Electronic and Opto-Electronic Devices. *Chemical Society Reviews* **2014**, *43* (16), 5994–6010. https://doi.org/10.1039/C4CS00096J.

(361) Allendorf, M. D.; Schwartzberg, A.; Stavila, V.; Talin, A. A. A Roadmap to Implementing Metal-Organic Frameworks in Electronic Devices: Challenges and Critical Directions. *Chemistry — A European Journal* **2011**, *17* (41), 11372–11388. https://doi.org/10.1002/chem.201101595.

(362) Clough, A. J.; Orchanian, N. M.; Skelton, J. M.; Neer, A. J.; Howard, S. A.; Downes, C. A.; Piper, L. F. J.; Walsh, A.; Melot, B. C.; Marinescu, S. C. Room Temperature Metallic Conductivity in a Metal–Organic Framework Induced by Oxidation. *Journal of the American Chemical Society* **2019**, *141* (41), 16323–16330. https://doi.org/10.1021/jacs.9b06898.

(363) Huang, X.; Sheng, P.; Tu, Z.; Zhang, F.; Wang, J.; Geng, H.; Zou, Y.; Di, C.; Yi, Y.; Sun, Y.; Xu, W.; Zhu, D. A Two-Dimensional π–d Conjugated Coordination Polymer with Extremely High Electrical Conductivity and Ambipolar Transport Behaviour. *Nature Communications* **2015**, *6* (1), 7408. https://doi.org/10.1038/ncomms8408.

(364) Murase, R.; Leong, C. F.; D'Alessandro, D. M. Mixed Valency as a Strategy for Achieving Charge Delocalization in Semiconducting and Conducting Framework Materials. *Inorganic Chemistry* **2017**, *56* (23), 14373–14382. https://doi.org/10.1021/acs.inorgchem.7b02090.

(365) Kung, C.-W.; Otake, K.; Buru, C. T.; Goswami, S.; Cui, Y.; Hupp, J. T.; Spokoyny, A. M.; Farha, O. K. Increased Electrical Conductivity in a Mesoporous Metal–Organic Framework Featuring Metallacarboranes Guests. *Journal of the American Chemical Society* **2018**, *140* (11), 3871–3875. https://doi.org/10.1021/jacs.8b00605.

(366) Le Ouay, B.; Boudot, M.; Kitao, T.; Yanagida, T.; Kitagawa, S.; Uemura, T. Nanostructuration of PEDOT in Porous Coordination Polymers for Tunable Porosity and Conductivity. *Journal of the American Chemical Society* **2016**, *138* (32), 10088–10091. https://doi.org/10.1021/jacs.6b05552.

(367) Wang, T. C.; Hod, I.; Audu, C. O.; Vermeulen, N. A.; Nguyen, S. T.; Farha, O. K.; Hupp, J. T. Rendering High Surface Area, Mesoporous Metal–Organic Frameworks Electronically Conductive. *ACS Applied Materials & Interfaces* **2017**, *9* (14), 12584–12591. https://doi.org/10.1021/acsami.6b16834.

(368) D'Alessandro, D. M. Exploiting Redox Activity in Metal–Organic Frameworks: Concepts, Trends and Perspectives. *Chemical Communications* **2016**, *52* (58), 8957–8971. https://doi.org/10.1039/C6CC00805D.

(369) Sun, L.; Hendon, C. H.; Park, S. S.; Tulchinsky, Y.; Wan, R.; Wang, F.; Walsh, A.; Dincă, M. Is Iron Unique in Promoting Electrical Conductivity in MOFs? *Chemical Science* **2017**, *8* (6), 4450–4457. https://doi.org/10.1039/C7SC00647K.

(370) Xie, L. S.; Sun, L.; Wan, R.; Park, S. S.; DeGayner, J. A.; Hendon, C. H.; Dincă, M. Tunable Mixed-Valence Doping toward Record Electrical Conductivity in a Three-Dimensional Metal–Organic Framework. *Journal of the American Chemical Society* **2018**, *140* (24), 7411–7414. https://doi.org/10.1021/jacs.8b03604.

(371) Kobayashi, Y.; Jacobs, B.; Allendorf, M. D.; Long, J. R. Conductivity, Doping, and Redox Chemistry of a Microporous Dithiolene-Based Metal−Organic Framework. *Chemistry of Materials* **2010**, *22* (14), 4120–4122. https://doi.org/10.1021/cm101238m.

(372) Darago, L. E.; Aubrey, M. L.; Yu, C. J.; Gonzalez, M. I.; Long, J. R. Electronic Conductivity, Ferrimagnetic Ordering, and Reductive Insertion Mediated by Organic Mixed-Valence in a Ferric Semiquinoid Metal–Organic Framework. *Journal of the American Chemical Society* **2015**, *137* (50), 15703–15711. https://doi.org/10.1021/jacs.5b10385.

(373) Jeon, I.-R.; Sun, L.; Negru, B.; Van Duyne, R. P.; Dincă, M.; Harris, T. D. Solid-State Redox Switching of Magnetic Exchange and Electronic Conductivity in a Benzoquinoid-Bridged Mn ^{II} Chain Compound. *Journal of the American Chemical Society* **2016**, *138* (20), 6583–6590. https://doi.org/10.1021/jacs.6b02485.

(374) Liu, L.; DeGayner, J. A.; Sun, L.; Zee, D. Z.; Harris, T. D. Reversible Redox Switching of Magnetic Order and Electrical Conductivity in a 2D Manganese Benzoquinoid Framework. *Chemical Science* **2019**, *10* (17), 4652–4661. https://doi.org/10.1039/C9SC00606K.

(375) Wade, C. R.; Li, M.; Dincă, M. Facile Deposition of Multicolored Electrochromic Metal-Organic Framework Thin Films. *Angewandte Chemie International Edition* **2013**, *52* (50), 13377–13381. https://doi.org/10.1002/anie.201306162.

(376) AlKaabi, K.; Wade, C. R.; Dincă, M. Transparent-to-Dark Electrochromic Behavior in Naphthalene-Diimide-Based Mesoporous MOF-74 Analogs. *Chem* **2016**, *1* (2), 264–272. https://doi.org/10.1016/j.chempr.2016.06.013.

(377) Johnson, B. A.; Bhunia, A.; Fei, H.; Cohen, S. M.; Ott, S. Development of a UiO-Type Thin Film Electrocatalysis Platform with Redox-Active Linkers. *Journal of the American Chemical Society* **2018**, *140* (8), 2985–2994. https://doi.org/10.1021/jacs.7b13077.

(378) Guha, S.; Saha, S. Fluoride Ion Sensing by an Anion−π Interaction. *Journal of the American Chemical Society* **2010**, *132* (50), 17674–17677. https://doi.org/10.1021/ja107382x.

(379) Wentz, H. C.; Campbell, M. G. Fluoride Detection with a Redox-Active Naphthalene Diimide Metal–Organic Framework. *Polyhedron* **2018**, *154*, 309–313. https://doi.org/10.1016/j.poly.2018.08.005.

(380) Saha, S. Anion-Induced Electron Transfer. *Accounts of Chemical Research* **2018**, *51* (9), 2225–2236. https://doi.org/10.1021/acs.accounts.8b00197.

(381) Bélanger-Chabot, G.; Ali, A.; Gabbaï, F. P. On the Reaction of Naphthalene Diimides with Fluoride Ions: Acid/Base versus Redox Reactions. *Angewandte Chemie International Edition* **2017**, *56* (33), 9958–9961. https://doi.org/10.1002/anie.201705223.

(382) Song, Q.; Li, F.; Wang, Z.; Zhang, X. A Supramolecular Strategy for Tuning the Energy Level of Naphthalenediimide: Promoted Formation of Radical Anions with Extraordinary Stability. *Chemical Science* **2015**, *6* (6), 3342–3346. https://doi.org/10.1039/C5SC00862J.

(383) Zhong, C. J.; Kwan, W. S. V.; Miller, L. L. Self-Assembly of Delocalized Pi.-Stacks in Solution. Assessment of Structural Effects. *Chemistry of Materials* **1992**, *4* (6), 1423–1428. https://doi.org/10.1021/cm00024a052.

(384) Andric, G.; Boas, J. F.; Bond, A. M.; Fallon, G. D.; Ghiggino, K. P.; Hogan, C. F.; Hutchison, J. A.; Lee, M. A.-P.; Langford, S. J.; Pilbrow, J. R.; Troup, G. J.; Woodward, C. P. Spectroscopy of Naphthalene Diimides and Their Anion Radicals. *Australian Journal of Chemistry* **2004**, *57* (10), 1011. https://doi.org/10.1071/CH04130.

(385) Narayan, T. C.; Miyakai, T.; Seki, S.; Dincă, M. High Charge Mobility in a Tetrathiafulvalene-Based Microporous Metal–Organic Framework. *Journal of the American Chemical Society* **2012**, *134* (31), 12932–12935. https://doi.org/10.1021/ja3059827.

(386) Park, S. S.; Hontz, E. R.; Sun, L.; Hendon, C. H.; Walsh, A.; Van Voorhis, T.; Dincă, M. Cation-Dependent Intrinsic Electrical Conductivity in Isostructural Tetrathiafulvalene-Based Microporous Metal–Organic Frameworks. *Journal of the American Chemical Society* **2015**, *137* (5), 1774–1777. https://doi.org/10.1021/ja512437u.

(387) Sun, L.; Park, S. S.; Sheberla, D.; Dincă, M. Measuring and Reporting Electrical Conductivity in Metal–Organic Frameworks: Cd_2(TTFTB) as a Case Study. *Journal of the American Chemical Society* **2016**, *138* (44), 14772–14782. https://doi.org/10.1021/jacs.6b09345.

(388) Xie, L. S.; Dincă, M. Novel Topology in Semiconducting Tetrathiafulvalene Lanthanide Metal-Organic Frameworks. *Israel Journal of Chemistry* **2018**, *58* (9–10), 1119–1122. https://doi.org/10.1002/ijch.201800068.

(389) Xie, L. S.; Alexandrov, E. V.; Skorupskii, G.; Proserpio, D. M.; Dincă, M. Diverse π–π Stacking Motifs Modulate Electrical Conductivity in Tetrathiafulvalene-Based Metal–Organic Frameworks. *Chemical Science* **2019**, *10* (37), 8558–8565. https://doi.org/10.1039/C9SC03348C.

(390) Kresse, G.; Furthmüller, J. Efficiency of Ab-Initio Total Energy Calculations for Metals and Semiconductors Using a Plane-Wave Basis Set. *Computational Materials Science* **1996**, *6* (1), 15–50. https://doi.org/10.1016/0927-0256(96)00008-0.

(391) Kresse, G.; Furthmüller, J. Efficient Iterative Schemes for *Ab Initio* Total-Energy Calculations Using a Plane-Wave Basis Set. *Physical Review B* **1996**, *54* (16), 11169–11186. https://doi.org/10.1103/PhysRevB.54.11169.

(392) Kresse, G.; Hafner, J. Ab Initio Molecular-Dynamics Simulation of the Liquid-Metal--Amorphous-Semiconductor Transition in Germanium. *Physical Review B* **1994**, *49* (20), 14251–14269. https://doi.org/10.1103/PhysRevB.49.14251.

(393) Blöchl, P. E. Projector Augmented-Wave Method. *Physical Review B* **1994**, *50* (24), 17953–17979. https://doi.org/10.1103/PhysRevB.50.17953.

(394) Krukau, A. V.; Vydrov, O. A.; Izmaylov, A. F.; Scuseria, G. E. Influence of the Exchange Screening Parameter on the Performance of Screened Hybrid Functionals. *The Journal of Chemical Physics* **2006**, *125* (22), 224106. https://doi.org/10.1063/1.2404663.

(395) Butler, K. T.; Hendon, C. H.; Walsh, A. Electronic Chemical Potentials of Porous Metal–Organic Frameworks. *Journal of the American Chemical Society* **2014**, *136* (7), 2703–2706. https://doi.org/10.1021/ja4110073.

(396) Bard, A. J. Thermodynamic Potential for the Anodic Dissolution of N-Type Semiconductors. *Journal of the Electrochemical Society* **1977**, *124* (11), 1706. https://doi.org/10.1149/1.2133140.

(397) Hao, J.; Xu, X.; Fei, H.; Li, L.; Yan, B. Functionalization of Metal-Organic Frameworks for Photoactive Materials. *Advanced Materials* **2018**, *30* (17), 1705634. https://doi.org/10.1002/adma.201705634.

(398) Wang, S.; Wang, X. Multifunctional Metal-Organic Frameworks for Photocatalysis. *Small* **2015**, *11* (26), 3097–3112. https://doi.org/10.1002/smll.201500084.

(399) Kong, X.-J.; Lin, Z.; Zhang, Z.-M.; Zhang, T.; Lin, W. Hierarchical Integration of Photosensitizing Metal-Organic Frameworks and Nickel-Containing Polyoxometalates for Efficient Visible-Light-Driven Hydrogen Evolution. *Angewandte Chemie International Edition* **2016**, *55* (22), 6411–6416. https://doi.org/10.1002/anie.201600431.

(400) Gu, X.; Lu, Z.-H.; Jiang, H.-L.; Akita, T.; Xu, Q. Synergistic Catalysis of Metal–Organic Framework-Immobilized Au–Pd Nanoparticles in Dehydrogenation of Formic Acid for Chemical Hydrogen Storage. *Journal of the American Chemical Society* **2011**, *133* (31), 11822–11825. https://doi.org/10.1021/ja200122f.

(401) Dhakshinamoorthy, A.; Asiri, A. M.; García, H. Metal-Organic Framework (MOF) Compounds: Photocatalysts for Redox Reactions and Solar Fuel Production. *Angewandte Chemie International Edition* **2016**, *55* (18), 5414–5445. https://doi.org/10.1002/anie.201505581.

(402) Sham, L. J.; Schluter, M. Density-Functional Theory of the Energy Gap. *Physical Review Letters* **1983**, *51*, 1888–1891.

(403) Runge, E.; Gross, E. K. U. Density-Functional Theory for Time-Dependent Systems. *Physical Review Letters* **1984**, *52* (12), 997–1000. https://doi.org/10.1103/PhysRevLett.52.997.

(404) Rüger, R.; Niehaus, T.; van Lenthe, E.; Heine, T.; Visscher, L. Vibrationally Resolved UV/Vis Spectroscopy with Time-Dependent Density Functional Based Tight Binding. *The Journal of Chemical Physics* **2016**, *145* (18), 184102. https://doi.org/10.1063/1.4966918.

(405) Hendon, C. H.; Walsh, A. Chemical Principles Underpinning the Performance of the Metal–Organic Framework HKUST-1. *Chemical Science* **2015**, *6* (7), 3674–3683. https://doi.org/10.1039/C5SC01489A.

(406) Peterson, G. W.; DeCoste, J. B.; Glover, T. G.; Huang, Y.; Jasuja, H.; Walton, K. S. Effects of Pelletization Pressure on the Physical and Chemical Properties of the Metal–Organic Frameworks $Cu_3(BTC)_2$ and UiO-66. *Microporous and Mesoporous Materials* **2013**, *179*, 48–53. https://doi.org/10.1016/j.micromeso.2013.02.025.

(407) Liu, J.; Zhou, W.; Liu, J.; Howard, I.; Kilibarda, G.; Schlabach, S.; Coupry, D.; Addicoat, M.; Yoneda, S.; Tsutsui, Y.; Sakurai, T.; Seki, S.; Wang, Z.; Lindemann, P.; Redel, E.; Heine, T.; Wöll, C. Photoinduced Charge-Carrier Generation in Epitaxial MOF Thin Films: High Efficiency as a Result of an Indirect Electronic Band Gap? *Angewandte Chemie International Edition* **2015**, *54* (25), 7441–7445. https://doi.org/10.1002/anie.201501862.

(408) Flage−Larsen, E.; Røyset, A.; Cavka, J. H.; Thorshaug, K. Band Gap Modulations in UiO Metal–Organic Frameworks. *Journal of Physical Chemistry C* **2013**, *117* (40), 20610–20616. https://doi.org/10.1021/jp405335q.

(409) Yan, D.; Lloyd, G. O.; Delori, A.; Jones, W.; Duan, X. Tuning Fluorescent Molecules by Inclusion in a Metal-Organic Framework: An Experimental and Computational Study. *ChemPlusChem* **2012**, *77* (12), 1112–1118. https://doi.org/10.1002/cplu.201200245.

(410) Wei, Z.; Gu, Z.-Y.; Arvapally, R. K.; Chen, Y.-P.; McDougald, R. N.; Ivy, J. F.; Yakovenko, A. A.; Feng, D.; Omary, M. A.; Zhou, H.-C. Rigidifying Fluorescent Linkers by Metal–Organic Framework Formation for Fluorescence Blue Shift and Quantum Yield Enhancement. *Journal of the American Chemical Society* **2014**, *136* (23), 8269–8276. https://doi.org/10.1021/ja5006866.

(411) Brozek, C. K.; Michaelis, V. K.; Ong, T.-C.; Bellarosa, L.; López, N.; Griffin, R. G.; Dincă, M. Dynamic DMF Binding in MOF-5 Enables the Formation of Metastable Cobalt-Substituted MOF-5 Analogues. *ACS Central Science* **2015**, *1* (5), 252–260. https://doi.org/10.1021/acscentsci.5b00247.

(412) Brozek, C. K.; Dincă, M. Ti^{3+}-, $V^{2+/3+}$-, $Cr^{2+/3+}$-, Mn^{2+}-, and Fe^{2+}-Substituted MOF-5 and Redox Reactivity in Cr- and Fe-MOF-5. *Journal of the American Chemical Society* **2013**, *135* (34), 12886–12891. https://doi.org/10.1021/ja4064475.

(413) Van Wyk, A.; Smith, T.; Park, J.; Deria, P. Charge-Transfer within Zr-Based Metal–Organic Framework: The Role of Polar Node. *Journal of the American Chemical Society* **2018**, *140* (8), 2756–2760. https://doi.org/10.1021/jacs.7b13211.

(414) Cozzolino, A. F.; Brozek, C. K.; Palmer, R. D.; Yano, J.; Li, M.; Dincă, M. Ligand Redox Non-Innocence in the Stoichiometric Oxidation of Mn_2(2,5-Dioxidoterephthalate) (Mn-MOF-74). *Journal of the American Chemical Society* **2014**, *136* (9), 3334–3337. https://doi.org/10.1021/ja411808r.

(415) Saouma, C. T.; Richard, S.; Smolders, S.; Delley, M. F.; Ameloot, R.; Vermoortele, F.; De Vos, D. E.; Mayer, J. M. Bulk-to-Surface Proton-Coupled Electron Transfer Reactivity of the Metal–Organic Framework MIL-125. *Journal of the American Chemical Society* **2018**, *140* (47), 16184–16189. https://doi.org/10.1021/jacs.8b09120.

(416) Saouma, C. T.; Tsou, C.-C.; Richard, S.; Ameloot, R.; Vermoortele, F.; Smolders, S.; Bueken, B.; DiPasquale, A. G.; Kaminsky, W.; Valdez, C. N.; De Vos, D. E.; Mayer, J. M. Sodium-Coupled Electron Transfer Reactivity of Metal–Organic Frameworks Containing Titanium Clusters: The Importance of Cations in Redox Chemistry. *Chemical Science* **2019**, *10* (5), 1322–1331. https://doi.org/10.1039/C8SC04138E.

(417) Gong, Y.-N.; Ouyang, T.; He, C.-T.; Lu, T.-B. Photoinduced Water Oxidation by an Organic Ligand Incorporated into the Framework of a Stable Metal–Organic Framework. *Chemical Science* **2016**, *7* (2), 1070–1075. https://doi.org/10.1039/C5SC02679B.

(418) Scholes, G. D.; Rumbles, G. Excitons in Nanoscale Systems. *Nature Materials* **2006**, *5* (9), 683–696. https://doi.org/10.1038/nmat1710.

(419) Izquierdo, M. A.; Broer, R.; Havenith, R. W. A. Theoretical Study of the Charge Transfer Exciton Binding Energy in Semiconductor Materials for Polymer: Fullerene-Based Bulk Heterojunction Solar Cells. *Journal of Physical Chemistry A* **2019**, *123* (6), 1233–1242.

(420) Koch, S. W.; Kira, M.; Khitrova, G.; Gibbs, H. M. Semiconductor Excitons in New Light. *Nature Materials* **2006**, *5* (7), 523–531. https://doi.org/10.1038/nmat1658.

(421) Nasalevich, M. A.; Hendon, C. H.; Santaclara, J. G.; Svane, K.; van der Linden, B.; Veber, S. L.; Fedin, M. V.; Houtepen, A. J.; van der Veen, M. A.; Kapteijn, F.; Walsh, A.; Gascon, J. Electronic Origins of Photocatalytic Activity in d 0 Metal Organic Frameworks. *Scientific Reports* **2016**, *6* (1), 23676. https://doi.org/10.1038/srep23676.

(422) Civalleri, B.; Napoli, F.; Noël, Y.; Roetti, C.; Dovesi, R. Ab-Initio Prediction of Materials Properties with CRYSTAL: MOF-5 as a Case Study. *CrystEngComm* **2006**, *8* (5), 364–371. https://doi.org/10.1039/B603150C.

(423) Wang, G.; Sun, Q.; Liu, Y.; Huang, B.; Dai, Y.; Zhang, X.; Qin, X. A Bismuth-Based Metal-Organic Framework as an Efficient Visible-Light-Driven Photocatalyst. *Chemistry — A European Journal* **2015**, *21* (6), 2364–2367. https://doi.org/10.1002/chem.201405047.

(424) Fischer, R. A.; Wöll, C. Layer-by-Layer Liquid-Phase Epitaxy of Crystalline Coordination Polymers at Surfaces. *Angewandte Chemie International Edition* **2009**, *48* (34), 6205–6208. https://doi.org/10.1002/anie.200901090.

(425) Zhou, E.-H.; Li, B.-H.; Chen, W.-X.; Luo, Z.; Liu, J.; Singh, A.; Kumar, A.; Jin, J.-C. Photocatalytic Degradation of Organic Dyes by a Stable and Biocompatible Zn(II) MOF Having Ferulic Acid: Experimental Findings and Theoretical Correlation. *Journal of Molecular Structure* **2017**, *1149*, 352–356. https://doi.org/10.1016/j.molstruc.2017.07.105.

(426) Williams, D. E.; Dolgopolova, E. A.; Pellechia, P. J.; Palukoshka, A.; Wilson, T. J.; Tan, R.; Maier, J. M.; Greytak, A. B.; Smith, M. D.; Krause, J. A.; Shustova, N. B. Mimic of the Green Fluorescent Protein Beta-Barrel: Photophysics and Dynamics of Confined Chromophores Defined by a Rigid Porous Scaffold. *Journal of the American Chemical Society* **2015**, *137* (6), 2223–2226.

(427) Chambers, M. B.; Wang, X.; Elgrishi, N.; Hendon, C. H.; Walsh, A.; Bonnefoy, J.; Canivet, J.; Quadrelli, E. A.; Farrusseng, D.; Mellot-Draznieks, C.; Fontecave, M. Photocatalytic Carbon Dioxide Reduction with Rhodium-Based Catalysts in Solution and Heterogenized within Metal-Organic Frameworks. *ChemSusChem* **2015**, *8* (4), 603–608. https://doi.org/10.1002/cssc.201403345.

(428) Jin, J.-C.; Wu, J.; Liu, W.-C.; Ma, A.-Q.; Liu, J.-Q.; Singh, A.; Kumar, A. A New Zn(II) Metal–Organic Framework Having 3D $CdSO_4$ Topology as Luminescent Sensor and Photocatalyst for Degradation of Organic Dyes. *New J. Chem.* **2018**, *42* (4), 2767–2775. https://doi.org/10.1039/C7NJ04355D.

(429) Bordiga, S.; Lamberti, C.; Ricchiardi, G.; Regli, L.; Bonino, F.; Damin, A.; Lillerud, K.-P.; Bjorgen, M.; Zecchina, A. Electronic and Vibrational Properties of a MOF-5 Metal–Organic Framework: ZnO Quantum Dot Behaviour. *Chemical Communications* **2004**, No. 20, 2300–2301. https://doi.org/10.1039/B407246D.

(430) Tachikawa, T.; Choi, J. R.; Fujitsuka, M.; Majima, T. Photoinduced Charge-Transfer Processes on MOF-5 Nanoparticles: Elucidating Differences between Metal-Organic Frameworks and Semiconductor Metal Oxides. *Journal of Physical Chemistry C* **2008**, *112* (36), 14090–14101. https://doi.org/10.1021/jp803620v.

(431) Yang, L.-M.; Vajeeston, P.; Ravindran, P.; Fjellvåg, H.; Tilset, M. Theoretical Investigations on the Chemical Bonding, Electronic Structure, And Optical Properties of the Metal−Organic Framework MOF-5. *Inorganic Chemistry* **2010**, *49* (22), 10283–10290. https://doi.org/10.1021/ic100694w.

(432) Ji, M.; Lan, X.; Han, Z.; Hao, C.; Qiu, J. Luminescent Properties of Metal–Organic Framework MOF-5: Relativistic Time-Dependent Density Functional Theory Investigations. *Inorganic Chemistry* **2012**, *51* (22), 12389–12394. https://doi.org/10.1021/ic301771b.

(433) De Vos, A.; Hendrickx, K.; Van Der Voort, P.; Van Speybroeck, V.; Lejaeghere, K. Missing Linkers: An Alternative Pathway to UiO-66 Electronic Structure Engineering. *Chemistry of Materials* **2017**, *29* (7), 3006–3019. https://doi.org/10.1021/acs.chemmater.6b05444.

(434) Walsh, A.; Catlow, C. R. A. Photostimulated Reduction Processes in a Titania Hybrid Metal-Organic Framework. *Chemistry — A European Journal of Chem. Phys.* **2010**, *11* (11), 2341–2344. https://doi.org/10.1002/cphc.201000306.

(435) Komatsu, T.; Taylor, J. M.; Kitagawa, H. Design of a Conducting Metal–Organic Framework: Orbital-Level Matching in MIL-140A Derivatives. *Inorganic Chemistry* **2016**, *55* (2), 546–548. https://doi.org/10.1021/acs.inorgchem.5b02265.

(436) Wang, S.; Kitao, T.; Guillou, N.; Wahiduzzaman, M.; Martineau-Corcos, C.; Nouar, F.; Tissot, A.; Binet, L.; Ramsahye, N.; Devautour-Vinot, S.; Kitagawa, S.; Seki, S.; Tsutsui, Y.; Briois, V.; Steunou, N.; Maurin, G.; Uemura, T.; Serre, C. A Phase Transformable Ultrastable Titanium-Carboxylate Framework for Photoconduction. *Nature Communications* **2018**, *9* (1), 1660. https://doi.org/10.1038/s41467-018-04034-w.

(437) Gao, J.; Miao, J.; Li, P.-Z.; Teng, W. Y.; Yang, L.; Zhao, Y.; Liu, B.; Zhang, Q. A P-Type Ti(IV)-Based Metal–Organic Framework with Visible-Light Photo-Response. *Chemical Communications* **2014**, *50* (29), 3786–3788. https://doi.org/10.1039/C3CC49440C.

(438) Wu, X.-P.; Gagliardi, L.; Truhlar, D. G. Cerium Metal–Organic Framework for Photocatalysis. *Journal of the American Chemical Society* **2018**, *140* (25), 7904–7912. https://doi.org/10.1021/jacs.8b03613.

(439) Padial, N. M.; Castells-Gil, J.; Almora-Barrios, N.; Romero-Angel, M.; da Silva, I.; Barawi, M.; García-Sánchez, A.; de la Peña O'Shea, V. A.; Martí-Gastaldo, C. Hydroxamate Titanium–Organic Frameworks and the Effect of Siderophore-Type Linkers over Their Photocatalytic Activity. *Journal of the American Chemical Society* **2019**, *141* (33), 13124–13133. https://doi.org/10.1021/jacs.9b04915.

(440) Fu, Y.; Sun, D.; Chen, Y.; Huang, R.; Ding, Z.; Fu, X.; Li, Z. An Amine-Functionalized Titanium Metal-Organic Framework Photocatalyst with Visible-Light-Induced Activity for CO_2 Reduction. *Angewandte Chemie International Edition* **2012**, *51* (14), 3364–3367. https://doi.org/10.1002/anie.201108357.

(441) Shi, L.; Wang, T.; Zhang, H.; Chang, K.; Meng, X.; Liu, H.; Ye, J. An Amine-Functionalized Iron(III) Metal-Organic Framework as Efficient Visible-Light Photocatalyst for Cr(VI) Reduction. *Advanced Science* **2015**, *2* (3), 1500006. https://doi.org/10.1002/advs.201500006.

(442) Sun, M.; Yan, S.; Sun, Y.; Yang, X.; Guo, Z.; Du, J.; Chen, D.; Chen, P.; Xing, H. Enhancement of Visible-Light-Driven CO_2 Reduction Performance Using an Amine-Functionalized Zirconium Metal–Organic Framework. *Dalton Transactions* **2018**, *47* (3), 909–915. https://doi.org/10.1039/C7DT04062H.

(443) Shen, L.; Liang, S.; Wu, W.; Liang, R.; Wu, L. Multifunctional NH2-Mediated Zirconium Metal–Organic Framework as an Efficient Visible-Light-Driven Photocatalyst for Selective Oxidation of Alcohols and Reduction of Aqueous Cr(Vi). *Dalton Transactions* **2013**, *42* (37), 13649. https://doi.org/10.1039/c3dt51479j.

(444) Liang, R.; Shen, L.; Jing, F.; Wu, W.; Qin, N.; Lin, R.; Wu, L. NH 2 -Mediated Indium Metal–Organic Framework as a Novel Visible-Light-Driven Photocatalyst for Reduction of the Aqueous Cr(VI). *Applied Catalysis B: Environmental* **2015**, *162*, 245–251. https://doi.org/10.1016/j.apcatb.2014.06.049.

(445) Hendon, C. H.; Tiana, D.; Fontecave, M.; Sanchez, C.; D'arras, L.; Sassoye, C.; Rozes, L.; Mellot-Draznieks, C.; Walsh, A. Engineering the Optical Response of the Titanium-MIL-125 Metal–Organic Framework through Ligand Functionalization. *Journal of the American Chemical Society* **2013**, *135* (30), 10942–10945. https://doi.org/10.1021/ja405350u.

(446) Chambers, M. B.; Wang, X.; Ellezam, L.; Ersen, O.; Fontecave, M.; Sanchez, C.; Rozes, L.; Mellot-Draznieks, C. Maximizing the Photocatalytic Activity of Metal–Organic Frameworks with Aminated-Functionalized Linkers: Substoichiometric Effects in MIL-125-NH $_2$. *Journal of the American Chemical Society* **2017**, *139* (24), 8222–8228. https://doi.org/10.1021/jacs.7b02186.

(447) Yoon, T. P.; Ischay, M. A.; Du, J. Visible Light Photocatalysis as a Greener Approach to Photochemical Synthesis. *Nature Chemistry* **2010**, *2* (7), 527–532. https://doi.org/10.1038/nchem.687.

(448) Mills, A.; Davies, R. H.; Worsley, D. Water Purification by Semiconductor Photocatalysis. *Chemical Society Reviews* **1993**, *22* (6), 417. https://doi.org/10.1039/cs9932200417.

(449) Fujishima, A.; Honda, K. Electrochemical Photolysis of Water at a Semiconductor Electrode. *Nature* **1972**, *238* (5358), 37–38. https://doi.org/10.1038/238037a0.

(450) Ampelli, C.; Centi, G.; Passalacqua, R.; Perathoner, S. Synthesis of Solar Fuels by a Novel Photoelectrocatalytic Approach. *Energy & Environmental Science* **2010**, *3* (3), 292–301. https://doi.org/10.1039/b925470f.

(451) Joya, K. S.; Joya, Y. F.; Ocakoglu, K.; van de Krol, R. Water-Splitting Catalysis and Solar Fuel Devices: Artificial Leaves on the Move. *Angewandte Chemie International Edition* **2013**, *52* (40), 10426–10437. https://doi.org/10.1002/anie.201300136.

(452) Navalón, S.; Dhakshinamoorthy, A.; Álvaro, M.; Garcia, H. Photocatalytic CO_2 Reduction Using Non-Titanium Metal Oxides and Sulfides. *ChemSusChem* **2013**, *6* (4), 562–577. https://doi.org/10.1002/cssc.201200670.

(453) Kim, D.; Sakimoto, K. K.; Hong, D.; Yang, P. Artificial Photosynthesis for Sustainable Fuel and Chemical Production. *Angewandte Chemie International Edition* **2015**, *54* (11), 3259–3266. https://doi.org/10.1002/anie.201409116.

(454) Tahir, M.; Amin, N. S. Recycling of Carbon Dioxide to Renewable Fuels by Photocatalysis: Prospects and Challenges. *Renewable and Sustainable Energy Reviews* **2013**, *25*, 560–579. https://doi.org/10.1016/j.rser.2013.05.027.

(455) Marzo, L.; Pagire, S. K.; Reiser, O.; König, B. Visible-Light Photocatalysis: Does It Make a Difference in Organic Synthesis? *Angewandte Chemie International Edition* **2018**, *57* (32), 10034–10072. https://doi.org/10.1002/anie.201709766.

(456) Khan, M. M.; Adil, S. F.; Al-Mayouf, A. Metal Oxides as Photocatalysts. *Journal of Saudi Chemical Society* **2015**, *19* (5), 462–464. https://doi.org/10.1016/j.jscs.2015.04.003.

(457) Navalón, S.; Dhakshinamoorthy, A.; Álvaro, M.; Garcia, H. Photocatalytic CO_2 Reduction Using Non-Titanium Metal Oxides and Sulfides. *ChemSusChem* **2013**, *6* (4), 562–577. https://doi.org/10.1002/cssc.201200670.

(458) Toroker, M. C.; Kanan, D. K.; Alidoust, N.; Isseroff, L. Y.; Liao, P.; Carter, E. A. First Principles Scheme to Evaluate Band Edge Positions in Potential Transition Metal Oxide Photocatalysts and Photoelectrodes. *Physical Chemistry Chemical Physics* **2011**, *13* (37), 16644. https://doi.org/10.1039/c1cp22128k.

(459) Allen, N. S.; Edge, M.; Verran, J.; Caballero, L.; Abrusci, C.; Stratton, J.; Maltby, J.; Bygott, C. Photocatalytic Surfaces: Environmental Benefits of Nanotitania. *The Open Materials Science Journal* **2010**, *3* (1), 6–27. https://doi.org/10.2174/1874088X00903010006.

(460) Ariga, H.; Taniike, T.; Morikawa, H.; Tada, M.; Min, B. K.; Watanabe, K.; Matsumoto, Y.; Ikeda, S.; Saiki, K.; Iwasawa, Y. Surface-Mediated Visible-Light Photo-Oxidation on Pure TiO_2 (001). *Journal of the American Chemical Society* **2009**, *131* (41), 14670–14672. https://doi.org/10.1021/ja9066805.

(461) Howe, R. F.; Gratzel, Michael. EPR Study of Hydrated Anatase under UV Irradiation. *Journal of Physical Chemistry* **1987**, *91* (14), 3906–3909. https://doi.org/10.1021/j100298a035.

(462) Xing, M.; Fang, W.; Nasir, M.; Ma, Y.; Zhang, J.; Anpo, M. Self-Doped Ti^{3+}-Enhanced TiO_2 Nanoparticles with a High-Performance Photocatalysis. *Journal of Catalysis* **2013**, *297*, 236–243. https://doi.org/10.1016/j.jcat.2012.10.014.

(463) Scanlon, D. O.; Dunnill, C. W.; Buckeridge, J.; Shevlin, S. A.; Logsdail, A. J.; Woodley, S. M.; Catlow, C. R. A.; Powell, Michael. J.; Palgrave, R. G.; Parkin, I. P.; Watson, G. W.; Keal, T. W.; Sherwood, P.; Walsh, A.; Sokol, A. A. Band Alignment of Rutile and Anatase TiO_2. *Nature Materials* **2013**, *12* (9), 798–801. https://doi.org/10.1038/nmat3697.

(464) Anpo, M.; Takeuchi, M. The Design and Development of Highly Reactive Titanium Oxide Photocatalysts Operating under Visible Light Irradiation. *Journal of Catalysis* **2003**, *216* (1–2), 505–516. https://doi.org/10.1016/S0021-9517(02)00104-5.

(465) Guayaquil-Sosa, J. F.; Serrano-Rosales, B.; Valadés-Pelayo, P. J.; de Lasa, H. Photocatalytic Hydrogen Production Using Mesoporous TiO2 Doped with Pt. *Applied Catalysis B: Environmental* **2017**, *211*, 337–348. https://doi.org/10.1016/j.apcatb.2017.04.029.

(466) Hernández-Alonso, M. D.; Fresno, F.; Suárez, S.; Coronado, J. M. Development of Alternative Photocatalysts to TiO_2: Challenges and Opportunities. *Energy & Environmental Science* **2009**, *2* (12), 1231–1257. https://doi.org/10.1039/b907933e.

(467) Di Valentin, C.; Pacchioni, G.; Selloni, A. Origin of the Different Photoactivity of N -Doped Anatase and Rutile TiO_2. *Physical Review B* **2004**, *70* (8), 085116. https://doi.org/10.1103/PhysRevB.70.085116.

(468) Wang, H.; Yuan, X.; Wu, Y.; Zeng, G.; Chen, X.; Leng, L.; Wu, Z.; Jiang, L.; Li, H. Facile Synthesis of Amino-Functionalized Titanium Metal-Organic Frameworks and Their Superior Visible-Light Photocatalytic Activity for Cr(VI) Reduction. *Journal of Hazardous Materials* **2015**, *286*, 187–194. https://doi.org/10.1016/j.jhazmat.2014.11.039.

(469) Sun, D.; Ye, L.; Li, Z. Visible-Light-Assisted Aerobic Photocatalytic Oxidation of Amines to Imines over NH_2 -MIL-125(Ti). *Applied Catalysis B: Environmental* **2015**, *164*, 428–432. https://doi.org/10.1016/j.apcatb.2014.09.054.

(470) Bueken, B.; Vermoortele, F.; Vanpoucke, D. E. P.; Reinsch, H.; Tsou, C.-C.; Valvekens, P.; De Baerdemaeker, T.; Ameloot, R.; Kirschhock, C. E. A.; Van Speybroeck, V.; Mayer, J. M.; De Vos, D. A Flexible Photoactive Titanium Metal-Organic Framework Based on a $[Ti^{IV}_3(\mu^3\text{-}O)(O)_2(COO)_6]$ Cluster. *Angewandte Chemie International Edition* **2015**, *54* (47), 13912–13917. https://doi.org/10.1002/anie.201505512.

(471) Yuan, S.; Qin, J.-S.; Xu, H.-Q.; Su, J.; Rossi, D.; Chen, Y.; Zhang, L.; Lollar, C.; Wang, Q.; Jiang, H.-L.; Son, D. H.; Xu, H.; Huang, Z.; Zou, X.; Zhou, H.-C. $[Ti_8Zr_2O_{12}(COO)_{16}]$ Cluster: An Ideal Inorganic Building Unit for Photoactive Metal–Organic Frameworks. *ACS Central Science* **2018**, *4* (1), 105–111. https://doi.org/10.1021/acscentsci.7b00497.

(472) Cavka, J. H.; Jakobsen, S.; Olsbye, U.; Guillou, N.; Lamberti, C.; Bordiga, S.; Lillerud, K. P. A New Zirconium Inorganic Building Brick Forming Metal Organic Frameworks with Exceptional Stability. *Journal of the American Chemical Society* **2008**, *130* (42), 13850–13851. https://doi.org/10.1021/ja8057953.

(473) Jakobsen, S.; Gianolio, D.; Wragg, D. S.; Nilsen, M. H.; Emerich, H.; Bordiga, S.; Lamberti, C.; Olsbye, U.; Tilset, M.; Lillerud, K. P. Structural Determination of a Highly Stable Metal-Organic Framework with Possible Application to Interim Radioactive Waste Scavenging: Hf-UiO-66. *Physical Review B* **2012**, *86* (12), 125429. https://doi.org/10.1103/PhysRevB.86.125429.

(474) Kim, M.; Cahill, J. F.; Fei, H.; Prather, K. A.; Cohen, S. M. Postsynthetic Ligand and Cation Exchange in Robust Metal–Organic Frameworks. *Journal of the American Chemical Society* **2012**, *134* (43), 18082–18088. https://doi.org/10.1021/ja3079219.

(475) Rosi, N. L. Hydrogen Storage in Microporous Metal-Organic Frameworks. *Science* **2003**, *300* (5622), 1127–1129. https://doi.org/10.1126/science.1083440.

(476) Zou, L.; Feng, D.; Liu, T.-F.; Chen, Y.-P.; Yuan, S.; Wang, K.; Wang, X.; Fordham, S.; Zhou, H.-C. A Versatile Synthetic Route for the Preparation of Titanium Metal–Organic Frameworks. *Chemical Science* **2016**, *7* (2), 1063–1069. https://doi.org/10.1039/C5SC03620H.

(477) Mondloch, J. E.; Bury, W.; Fairen-Jimenez, D.; Kwon, S.; DeMarco, E. J.; Weston, M. H.; Sarjeant, A. A.; Nguyen, S. T.; Stair, P. C.; Snurr, R. Q.; Farha, O. K.; Hupp, J. T. Vapor-Phase Metalation by Atomic Layer Deposition in a Metal–Organic Framework. *Journal of the American Chemical Society* **2013**, *135* (28), 10294–10297. https://doi.org/10.1021/ja4050828.

(478) Syzgantseva, M. A.; Ireland, C. P.; Ebrahim, F. M.; Smit, B.; Syzgantseva, O. A. Metal Substitution as the Method of Modifying Electronic Structure of Metal–Organic Frameworks. *Journal of the American Chemical Society* **2019**, *141* (15), 6271–6278. https://doi.org/10.1021/jacs.8b13667.

(479) Comito, R. J.; Fritzsching, K. J.; Sundell, B. J.; Schmidt-Rohr, K.; Dincă, M. Single-Site Heterogeneous Catalysts for Olefin Polymerization Enabled by Cation Exchange in a Metal-Organic Framework. *Journal of the American Chemical Society* **2016**, *138* (32), 10232–10237. https://doi.org/10.1021/jacs.6b05200.

(480) Kresse, G.; Hafner, J. *Ab Initio* Molecular Dynamics for Liquid Metals. *Physical Review B* **1993**, *47* (1), 558–561. https://doi.org/10.1103/PhysRevB.47.558.

(481) Sun, D.; Liu, W.; Qiu, M.; Zhang, Y.; Li, Z. Introduction of a Mediator for Enhancing Photocatalytic Performance via Post-Synthetic Metal Exchange in Metal–Organic Frameworks (MOFs). *Chemical Communications* **2015**, *51* (11), 2056–2059. https://doi.org/10.1039/C4CC09407G.

(482) Keum, Y.; Park, S.; Chen, Y.-P.; Park, J. Titanium-Carboxylate Metal-Organic Framework Based on an Unprecedented Ti-Oxo Chain Cluster. *Angewandte Chemie International Edition* **2018**, *57* (45), 14852–14856. https://doi.org/10.1002/anie.201809762.

(483) Assi, H.; Pardo Pérez, L. C.; Mouchaham, G.; Ragon, F.; Nasalevich, M.; Guillou, N.; Martineau, C.; Chevreau, H.; Kapteijn, F.; Gascon, J.; Fertey, P.; Elkaim, E.; Serre, C.; Devic, T. Investigating the Case of Titanium(IV) Carboxyphenolate Photoactive Coordination Polymers. *Inorganic Chemistry* **2016**, *55* (15), 7192–7199. https://doi.org/10.1021/acs.inorgchem.6b01060.

(484) Yuan, S.; Liu, T.-F.; Feng, D.; Tian, J.; Wang, K.; Qin, J.; Zhang, Q.; Chen, Y.-P.; Bosch, M.; Zou, L.; Teat, S. J.; Dalgarno, S. J.; Zhou, H.-C. A Single Crystalline Porphyrinic Titanium Metal–Organic Framework. *Chemical Science* **2015**, *6* (7), 3926–3930. https://doi.org/10.1039/C5SC00916B.

(485) Nguyen, H. L.; Gándara, F.; Furukawa, H.; Doan, T. L. H.; Cordova, K. E.; Yaghi, O. M. A Titanium–Organic Framework as an Exemplar of Combining the Chemistry of Metal– and Covalent–Organic Frameworks. *Journal of the American Chemical Society* **2016**, *138* (13), 4330–4333. https://doi.org/10.1021/jacs.6b01233.

(486) Song, Y.; Li, Z.; Zhu, Y.; Feng, X.; Chen, J. S.; Kaufmann, M.; Wang, C.; Lin, W. Titanium Hydroxide Secondary Building Units in Metal–Organic Frameworks Catalyze Hydrogen Evolution under Visible Light. *Journal of the American Chemical Society* **2019**, *141* (31), 12219–12223. https://doi.org/10.1021/jacs.9b05964.

(487) Brozek, C. K.; Dincă, M. Thermodynamic Parameters of Cation Exchange in MOF-5 and MFU-4l. *Chemical Communications* **2015**, *51* (59), 11780–11782. https://doi.org/10.1039/C5CC04249F.

(488) Denysenko, D.; Jelic, J.; Reuter, K.; Volkmer, D. Postsynthetic Metal and Ligand Exchange in MFU-4*l*: A Screening Approach toward Functional Metal-Organic Frameworks Comprising Single-Site Active Centers. *Chemistry — A European Journal* **2015**, *21* (22), 8188–8199. https://doi.org/10.1002/chem.201406564.

(489) Brus, L. E. Electron–Electron and Electron-hole Interactions in Small Semiconductor Crystallites: The Size Dependence of the Lowest Excited Electronic State. *The Journal of Chemical Physics* **1984**, *80* (9), 4403–4409. https://doi.org/10.1063/1.447218.

(490) Weinberg, D. R.; Gagliardi, C. J.; Hull, J. F.; Murphy, C. F.; Kent, C. A.; Westlake, B. C.; Paul, A.; Ess, D. H.; McCafferty, D. G.; Meyer, T. J. Proton-Coupled Electron Transfer. *Chemical Reviews* **2012**, *112* (7), 4016–4093. https://doi.org/10.1021/cr200177j.

(491) Siegbahn, P. E. M.; Blomberg, M. R. A. Quantum Chemical Studies of Proton-Coupled Electron Transfer in Metalloenzymes. *Chemical Reviews* **2010**, *110* (12), 7040–7061. https://doi.org/10.1021/cr100070p.

(492) Warren, J. J.; Tronic, T. A.; Mayer, J. M. Thermochemistry of Proton-Coupled Electron Transfer Reagents and Its Implications. *Chemical Reviews* **2010**, *110* (12), 6961–7001. https://doi.org/10.1021/cr100085k.

(493) Feher, G.; Allen, J. P.; Okamura, M. Y.; Rees, D. C. Structure and Function of Bacterial Photosynthetic Reaction Centres. *Nature* **1989**, *339* (6220), 111–116. https://doi.org/10.1038/339111a0.

(494) Meyer, T. J.; Huynh, M. H. V.; Thorp, H. H. The Possible Role of Proton-Coupled Electron Transfer (PCET) in Water Oxidation by Photosystem II. *Angewandte Chemie International Edition* **2007**, *46* (28), 5284–5304. https://doi.org/10.1002/anie.200600917.

(495) Gagliardi, C. J.; Westlake, B. C.; Kent, C. A.; Paul, J. J.; Papanikolas, J. M.; Meyer, T. J. Integrating Proton Coupled Electron Transfer (PCET) and Excited States. *Coordination Chemistry Reviews* **2010**, *254* (21–22), 2459–2471. https://doi.org/10.1016/j.ccr.2010.03.001.

(496) Gentry, E. C.; Knowles, R. R. Synthetic Applications of Proton-Coupled Electron Transfer. *Accounts of Chemical Research* **2016**, *49* (8), 1546–1556. https://doi.org/10.1021/acs.accounts.6b00272.

(497) Hoffmann, N. Proton-Coupled Electron Transfer in Photoredox Catalytic Reactions: Proton-Coupled Electron Transfer in Photoredox Catalytic Reactions. *European Journal of Organic Chemistry* **2017**, *2017* (15), 1982–1992. https://doi.org/10.1002/ejoc.201601445.

(498) Yayla, H.; Knowles, R. Proton-Coupled Electron Transfer in Organic Synthesis: Novel Homolytic Bond Activations and Catalytic Asymmetric Reactions with Free Radicals. *Synthetic Letters* **2014**, *25* (20), 2819–2826. https://doi.org/10.1055/s-0034-1379304.

(499) Valdez, C. N.; Schimpf, A. M.; Gamelin, D. R.; Mayer, J. M. Proton-Controlled Reduction of ZnO Nanocrystals: Effects of Molecular Reductants, Cations, and Thermodynamic Limitations. *Journal of the American Chemical Society* **2016**, *138* (4), 1377–1385. https://doi.org/10.1021/jacs.5b12182.

(500) Song, Y.; Sanyal, U.; Pangotra, D.; Holladay, J. D.; Camaioni, D. M.; Gutiérrez, O. Y.; Lercher, J. A. Hydrogenation of Benzaldehyde via Electrocatalysis and Thermal Catalysis on Carbon-Supported Metals. *Journal of Catalysis* **2018**, *359*, 68–75. https://doi.org/10.1016/j.jcat.2017.12.026.

(501) Feng, J.; He, Y.; Liu, Y.; Du, Y.; Li, D. Supported Catalysts Based on Layered Double Hydroxides for Catalytic Oxidation and Hydrogenation: General Functionality and Promising Application Prospects. *Chemical Society Reviews* **2015**, *44* (15), 5291–5319. https://doi.org/10.1039/C5CS00268K.

(502) Dubouis, N.; Grimaud, A. The Hydrogen Evolution Reaction: From Material to Interfacial Descriptors. *Chemical Science* **2019**, *10* (40), 9165–9181. https://doi.org/10.1039/C9SC03831K.

(503) Huynh, M. H. V.; Meyer, T. J. Proton-Coupled Electron Transfer. *Chemical Reviews* **2007**, *107* (11), 5004–5064. https://doi.org/10.1021/cr0500030.

(504) Choi, C.; Back, S.; Kim, N.-Y.; Lim, J.; Kim, Y.-H.; Jung, Y. Suppression of Hydrogen Evolution Reaction in Electrochemical N_2 Reduction Using Single-Atom Catalysts: A Computational Guideline. *ACS Catalysis* **2018**, *8* (8), 7517–7525. https://doi.org/10.1021/acscatal.8b00905.

(505) *IUPAC Compendium of Chemical Terminology: Gold Book*, 2.1.0.; Nič, M., Jirát, J., Košata, B., Jenkins, A., McNaught, A., Eds.; IUPAC: Research Triagle Park, NC, 2009. https://doi.org/10.1351/goldbook.

(506) Batzill, M. Fundamental Aspects of Surface Engineering of Transition Metal Oxide Photocatalysts. *Energy & Environmental Science* **2011**, *4* (9), 3275. https://doi.org/10.1039/c1ee01577j.

(507) Copéret, C.; Chabanas, M.; Petroff Saint-Arroman, R.; Basset, J.-M. Homogeneous and Heterogeneous Catalysis: Bridging the Gap through Surface Organometallic Chemistry. *Angewandte Chemie International Edition* **2003**, *42* (2), 156–181. https://doi.org/10.1002/anie.200390072.

(508) Cui, X.; Li, W.; Ryabchuk, P.; Junge, K.; Beller, M. Bridging Homogeneous and Heterogeneous Catalysis by Heterogeneous Single-Metal-Site Catalysts. *Nature Catalysis* **2018**, *1* (6), 385–397. https://doi.org/10.1038/s41929-018-0090-9.

(509) Yin, Z.; Wan, S.; Yang, J.; Kurmoo, M.; Zeng, M.-H. Recent Advances in Post-Synthetic Modification of Metal–Organic Frameworks: New Types and Tandem Reactions. *Coordination Chemistry Reviews* **2019**, *378*, 500–512. https://doi.org/10.1016/j.ccr.2017.11.015.

(510) Tanabe, K. K.; Cohen, S. M. Engineering a Metal-Organic Framework Catalyst by Using Postsynthetic Modification. *Angewandte Chemie International Edition* **2009**, *48* (40), 7424–7427. https://doi.org/10.1002/anie.200903433.

(511) Lee, J.; Farha, O. K.; Roberts, J.; Scheidt, K. A.; Nguyen, S. T.; Hupp, J. T. Metal–Organic Framework Materials as Catalysts. *Chemical Society Reviews* **2009**, *38* (5), 1450. https://doi.org/10.1039/b807080f.

(512) Wang, Z.; Cohen, S. M. Postsynthetic Covalent Modification of a Neutral Metal−Organic Framework. *Journal of the American Chemical Society* **2007**, *129* (41), 12368–12369. https://doi.org/10.1021/ja074366o.

(513) Mancuso, J. L.; Hendon, C. H. Titanium(IV) Inclusion as a Versatile Route to Photoactivity in Metal–Organic Frameworks. *Advanced Theory & Simulation* **2019**, *2* (11), 1900126. https://doi.org/10.1002/adts.201900126.

(514) García-García, P.; Müller, M.; Corma, A. MOF Catalysis in Relation to Their Homogeneous Counterparts and Conventional Solid Catalysts. *Chemical Science* **2014**, *5* (8), 2979. https://doi.org/10.1039/c4sc00265b.

(515) Drake, T.; Ji, P.; Lin, W. Site Isolation in Metal–Organic Frameworks Enables Novel Transition Metal Catalysis. *Accounts of Chemical Research* **2018**. https://doi.org/10.1021/acs.accounts.8b00297.

(516) Otake, K.; Ye, J.; Mandal, M.; Islamoglu, T.; Buru, C. T.; Hupp, J. T.; Delferro, M.; Truhlar, D. G.; Cramer, C. J.; Farha, O. K. Enhanced Activity of Heterogeneous Pd(II) Catalysts on Acid-Functionalized Metal–Organic Frameworks. *ACS Catalysis* **2019**, *9* (6), 5383–5390. https://doi.org/10.1021/acscatal.9b01043.

(517) Ji, P.; Song, Y.; Drake, T.; Veroneau, S. S.; Lin, Z.; Pan, X.; Lin, W. Titanium(III)-Oxo Clusters in a Metal–Organic Framework Support Single-Site Co(II)-Hydride Catalysts for Arene Hydrogenation. *Journal of the American Chemical Society* **2018**, *140* (1), 433–440. https://doi.org/10.1021/jacs.7b11241.

(518) Feng, X.; Song, Y.; Chen, J. S.; Xu, Z.; Dunn, S. J.; Lin, W. Rational Construction of an Artificial Binuclear Copper Monooxygenase in a Metal–Organic Framework. *Journal of the American Chemical Society* **2021**, *143* (2), 1107–1118. https://doi.org/10.1021/jacs.0c11920.

(519) Fang, Y.; Ma, Y.; Zheng, M.; Yang, P.; Asiri, A. M.; Wang, X. Metal–Organic Frameworks for Solar Energy Conversion by Photoredox Catalysis. *Coordination Chemistry Reviews* **2018**, *373*, 83–115. https://doi.org/10.1016/j.ccr.2017.09.013.

(520) Meng, Z.; Luo, J.; Li, W.; Mirica, K. A. Hierarchical Tuning of the Performance of Electrochemical Carbon Dioxide Reduction Using Conductive Two-Dimensional Metallophthalocyanine Based Metal–Organic Frameworks. *Journal of the American Chemical Society* **2020**, *142* (52), 21656–21669. https://doi.org/10.1021/jacs.0c07041.

(521) Fan, Y.; Ren, Y.; Li, J.; Yue, C.; Jiang, H. Enhanced Activity and Enantioselectivity of Henry Reaction by the Postsynthetic Reduction Modification for a Chiral Cu(Salen)-Based Metal–Organic Framework. *Inorganic Chemistry* **2018**, *57* (19), 11986–11994. https://doi.org/10.1021/acs.inorgchem.8b01551.

(522) Huang, R.; Peng, Y.; Wang, C.; Shi, Z.; Lin, W. A Rhenium-Functionalized Metal-Organic Framework as a Single-Site Catalyst for Photochemical Reduction of Carbon Dioxide: A Rhenium-Functionalized Metal-Organic Framework as a Single-Site Catalyst for Photochemical Reduction of Carbon Dioxide. *Eur. J. Inorganic Chemistry* **2016**, *2016* (27), 4358–4362. https://doi.org/10.1002/ejic.201600064.

(523) Celis-Salazar, P. J.; Epley, C. C.; Ahrenholtz, S. R.; Maza, W. A.; Usov, P. M.; Morris, A. J. Proton-Coupled Electron Transport in Anthraquinone-Based Zirconium Metal–Organic Frameworks. *Inorganic Chemistry* **2017**, *56* (22), 13741–13747. https://doi.org/10.1021/acs.inorgchem.7b01656.

(524) Gaggioli, C. A.; Sauer, J.; Gagliardi, L. Hydrogen Atom or Proton Coupled Electron Transfer? C–H Bond Activation by Transition-Metal Oxides. *Journal of the American Chemical Society* **2019**, *141* (37), 14603–14611. https://doi.org/10.1021/jacs.9b04006.

(525) Horiuchi, Y.; Toyao, T.; Saito, M.; Mochizuki, K.; Iwata, M.; Higashimura, H.; Anpo, M.; Matsuoka, M. Visible-Light-Promoted Photocatalytic Hydrogen Production by Using an Amino-Functionalized Ti(IV) Metal–Organic Framework. *Journal of Physical Chemistry C* **2012**, *116* (39), 20848–20853. https://doi.org/10.1021/jp3046005.

(526) Shao, Z.; Wu, Q.; Han, X.; Zhao, Y.; Xie, Q.; Wang, H.; Hou, H. Proton Coupled Electron Transfer: Novel Photochromic Performance in a Host–Guest Collaborative MOF. *Chemical Communications* **2019**, *55* (73), 10948–10951. https://doi.org/10.1039/C9CC05498G.

(527) Liang, Z.; Qu, C.; Xia, D.; Zou, R.; Xu, Q. Atomically Dispersed Metal Sites in MOF-Based Materials for Electrocatalytic and Photocatalytic Energy Conversion. *Angewandte Chemie International Edition* **2018**, *57* (31), 9604–9633. https://doi.org/10.1002/anie.201800269.

(528) Llabrés i Xamena, F. X.; Corma, A.; Garcia, H. Applications for Metal−Organic Frameworks (MOFs) as Quantum Dot Semiconductors. *The Journal of Physical Chemistry C* **2007**, *111* (1), 80–85. https://doi.org/10.1021/jp063600e.

(529) Ding, C.-W.; Luo, W.; Zhou, J.-Y.; Ma, X.-J.; Chen, G.-H.; Zhou, X.-P.; Li, D. Hydroxo Iron(III) Sites in a Metal–Organic Framework: Proton-Coupled Electron Transfer and Catalytic Oxidation of Alcohol with Molecular Oxygen. *ACS Applied Materials & Interfaces* **2019**, *11* (49), 45621–45628. https://doi.org/10.1021/acsami.9b15311.

(530) Ghosh, S.; Castillo-Lora, J.; Soudackov, A. V.; Mayer, J. M.; Hammes-Schiffer, S. Theoretical Insights into Proton-Coupled Electron Transfer from a Photoreduced ZnO Nanocrystal to an Organic Radical. *Nano Letters* **2017**, *17* (9), 5762–5767. https://doi.org/10.1021/acs.nanolett.7b02642.

(531) Zhang, Z.; Yoshikawa, H.; Awaga, K. Monitoring the Solid-State Electrochemistry of Cu(2,7-AQDC) (AQDC = Anthraquinone Dicarboxylate) in a Lithium Battery: Coexistence of Metal and Ligand Redox Activities in a Metal–Organic Framework. *Journal of the American Chemical Society* **2014**, *136* (46), 16112–16115. https://doi.org/10.1021/ja508197w.

(532) Hirao, H.; Ng, W. K. H.; Moeljadi, A. M. P.; Bureekaew, S. Multiscale Model for a Metal–Organic Framework: High-Spin Rebound Mechanism in the Reaction of the Oxoiron(IV) Species of Fe-MOF-74. *ACS Catalysis* **2015**, *5* (6), 3287–3291. https://doi.org/10.1021/acscatal.5b00475.

(533) Kurtz, D. M. Oxo- and Hydroxo-Bridged Diiron Complexes: A Chemical Perspective on a Biological Unit. *Chemical Reviews* **1990**, *90* (4), 585–606. https://doi.org/10.1021/cr00102a002.

(534) An, Y.; Xu, B.; Liu, Y.; Wang, Z.; Wang, P.; Dai, Y.; Qin, X.; Zhang, X.; Huang, B. Photocatalytic Overall Water Splitting over MIL-125(Ti) upon CoPi and Pt Co-Catalyst Deposition. *ChemistryOpen* **2017**, *6* (6), 701–705. https://doi.org/10.1002/open.201700100.

(535) Shen, L.; Luo, M.; Huang, L.; Feng, P.; Wu, L. A Clean and General Strategy To Decorate a Titanium Metal–Organic Framework with Noble-Metal Nanoparticles for Versatile Photocatalytic Applications. *Inorganic Chemistry* **2015**, *54* (4), 1191–1193. https://doi.org/10.1021/ic502609a.

(536) Koopmans, T. Über die Zuordnung von Wellenfunktionen und Eigenwerten zu den Einzelnen Elektronen Eines Atoms. *Physica* **1934**, *1* (1–6), 104–113. https://doi.org/10.1016/S0031-8914(34)90011-2.

(537) Janak, J. F. Proof That $\partial E/\partial n_i = \varepsilon$ in Density-Functional Theory. *Physical Review B* **1978**, *18* (12), 7165–7168. https://doi.org/10.1103/PhysRevB.18.7165.

(538) Paul, A.; Borrelli, R.; Bouyanfif, H.; Gottis, S.; Sauvage, F. Tunable Redox Potential, Optical Properties, and Enhanced Stability of Modified Ferrocene-Based Complexes. *ACS Omega* **2019**, *4* (12), 14780–14789. https://doi.org/10.1021/acsomega.9b01341.

(539) Carroll, G. M.; Brozek, C. K.; Hartstein, K. H.; Tsui, E. Y.; Gamelin, D. R. Potentiometric Measurements of Semiconductor Nanocrystal Redox Potentials. *Journal of the American Chemical Society* **2016**, *138* (13), 4310–4313. https://doi.org/10.1021/jacs.6b00936.

(540) Carroll, G. M.; Schimpf, A. M.; Tsui, E. Y.; Gamelin, D. R. Redox Potentials of Colloidal N-Type ZnO Nanocrystals: Effects of Confinement, Electron Density, and Fermi-Level Pinning by Aldehyde Hydrogenation. *Journal of the American Chemical Society* **2015**, *137* (34), 11163–11169. https://doi.org/10.1021/jacs.5b06715.

(541) Pavlishchuk, V. V.; Addison, A. W. Conversion Constants for Redox Potentials Measured versus Different Reference Electrodes in Acetonitrile Solutions at 25°C. *Inorganica Chimica Acta* **2000**, *298* (1), 97–102. https://doi.org/10.1016/S0020-1693(99)00407-7.

(542) Qi, K.; Hou, R.; Zaman, S.; Qiu, Y.; Xia, B. Y.; Duan, H. Construction of Metal–Organic Framework/Conductive Polymer Hybrid for All-Solid-State Fabric Supercapacitor. *ACS Applied Materials & Interfaces* **2018**, *10* (21), 18021–18028. https://doi.org/10.1021/acsami.8b05802.

(543) Yan, Y.; Gu, P.; Zheng, S.; Zheng, M.; Pang, H.; Xue, H. Facile Synthesis of an Accordion-like Ni-MOF Superstructure for High-Performance Flexible Supercapacitors. *Journal of Materials Chemistry A* **2016**, *4* (48), 19078–19085. https://doi.org/10.1039/C6TA08331E.

(544) Miner, E. M.; Gul, S.; Ricke, N. D.; Pastor, E.; Yano, J.; Yachandra, V. K.; Van Voorhis, T.; Dincă, M. Mechanistic Evidence for Ligand-Centered Electrocatalytic Oxygen Reduction with the Conductive MOF Ni_3(Hexaiminotriphenylene)$_2$. *ACS Catalysis* **2017**, *7* (11), 7726–7731. https://doi.org/10.1021/acscatal.7b02647.

(545) Lu, X. F.; Xia, B. Y.; Zang, S.-Q.; Lou, X. W. D. Metal-Organic Frameworks Based Electrocatalysts for the Oxygen Reduction Reaction. *Angewandte Chemie International Edition* **2019**. https://doi.org/10.1002/anie.201910309.

(546) Aiyappa, H. B.; Masa, J.; Andronescu, C.; Muhler, M.; Fischer, R. A.; Schuhmann, W. MOFs for Electrocatalysis: From Serendipity to Design Strategies. *Small Methods* **2019**, *3* (8), 1800415. https://doi.org/10.1002/smtd.201800415.

(547) Hu, Z.; Zhao, D. Metal–Organic Frameworks with Lewis Acidity: Synthesis, Characterization, and Catalytic Applications. *CrystEngComm* **2017**, *19* (29), 4066–4081. https://doi.org/10.1039/C6CE02660E.

(548) Li, P.-Z.; Wang, X.-J.; Liu, J.; Lim, J. S.; Zou, R.; Zhao, Y. A Triazole-Containing Metal–Organic Framework as a Highly Effective and Substrate Size-Dependent Catalyst for CO_2 Conversion. *Journal of the American Chemical Society* **2016**, *138* (7), 2142–2145. https://doi.org/10.1021/jacs.5b13335.

(549) Zhu, L.; Liu, X.-Q.; Jiang, H.-L.; Sun, L.-B. Metal–Organic Frameworks for Heterogeneous Basic Catalysis. *Chemical Reviews* **2017**, *117* (12), 8129–8176. https://doi.org/10.1021/acs.chemrev.7b00091.

(550) Oxford, G. A. E.; Snurr, R. Q.; Broadbelt, L. J. Hybrid Quantum Mechanics/Molecular Mechanics Investigation of (Salen)Mn for Use in Metal−Organic Frameworks. *Industrial & Engineering Chemistry Research* **2010**, *49* (21), 10965–10973. https://doi.org/10.1021/ie100165j.

(551) Metzger, E. D.; Brozek, C. K.; Comito, R. J.; Dincă, M. Selective Dimerization of Ethylene to 1-Butene with a Porous Catalyst. *ACS Central Science* **2016**, *2* (3), 148–153. https://doi.org/10.1021/acscentsci.6b00012.

(552) Zheng, S.; Yang, P.; Zhang, F.; Chen, D.-L.; Zhu, W. Pd Nanoparticles Encaged within Amine-Functionalized Metal-Organic Frameworks: Catalytic Activity and Reaction Mechanism in the Hydrogenation of 2,3,5-Trimethylbenzoquinone. *Chemical Engineering Journal* **2017**, *328*, 977–987. https://doi.org/10.1016/j.cej.2017.07.099.

(553) Jiang, D.; Fang, G.; Tong, Y.; Wu, X.; Wang, Y.; Hong, D.; Leng, W.; Liang, Z.; Tu, P.; Liu, L.; Xu, K.; Ni, J.; Li, X. Multifunctional Pd@UiO-66 Catalysts for Continuous Catalytic Upgrading of Ethanol to *n* -Butanol. *ACS Catalysis* **2018**, 11973–11978. https://doi.org/10.1021/acscatal.8b04014.

(554) Genna, D. T.; Wong-Foy, A. G.; Matzger, A. J.; Sanford, M. S. Heterogenization of Homogeneous Catalysts in Metal–Organic Frameworks via Cation Exchange. *Journal of the American Chemical Society* **2013**, *135* (29), 10586–10589. https://doi.org/10.1021/ja402577s.

(555) Bury, W.; Fairen-Jimenez, D.; Lalonde, M. B.; Snurr, R. Q.; Farha, O. K.; Hupp, J. T. Control over Catenation in Pillared Paddlewheel Metal–Organic Framework Materials via Solvent-Assisted Linker Exchange. *Chemistry of Materials* **2013**, *25* (5), 739–744. https://doi.org/10.1021/cm303749m.

(556) Takaishi, S.; DeMarco, E. J.; Pellin, M. J.; Farha, O. K.; Hupp, J. T. Solvent-Assisted Linker Exchange (SALE) and Post-Assembly Metallation in Porphyrinic Metal–Organic Framework Materials. *Chemical Science* **2013**, *4* (4), 1509. https://doi.org/10.1039/c2sc21516k.

(557) Beloqui Redondo, A.; Morel, F. L.; Ranocchiari, M.; van Bokhoven, J. A. Functionalized Ruthenium–Phosphine Metal–Organic Framework for Continuous Vapor-Phase Dehydrogenation of Formic Acid. *ACS Catalysis* **2015**, *5* (12), 7099–7103. https://doi.org/10.1021/acscatal.5b01987.

(558) Wang, Z.; Cohen, S. M. Tandem Modification of Metal–Organic Frameworks by a Postsynthetic Approach. *Angewandte Chemie* **2008**, *120* (25), 4777–4780. https://doi.org/10.1002/ange.200800686.

(559) Goesten, M. G.; Juan-Alcañiz, J.; Ramos-Fernandez, E. V.; Sai Sankar Gupta, K. B.; Stavitski, E.; van Bekkum, H.; Gascon, J.; Kapteijn, F. Sulfation of Metal–Organic Frameworks: Opportunities for Acid Catalysis and Proton Conductivity. *Journal of Catalysis* **2011**, *281* (1), 177–187. https://doi.org/10.1016/j.jcat.2011.04.015.

(560) Eyring, H. The Activated Complex in Chemical Reactions. *The Journal of Chemical Physics* **1935**, *3* (2), 107–115. https://doi.org/10.1063/1.1749604.

(561) Manna, K.; Zhang, T.; Lin, W. Postsynthetic Metalation of Bipyridyl-Containing Metal–Organic Frameworks for Highly Efficient Catalytic Organic Transformations. *Journal of the American Chemical Society* **2014**, *136* (18), 6566–6569. https://doi.org/10.1021/ja5018267.

(562) Guan, Q.; Wang, B.; Chai, X.; Liu, J.; Gu, J.; Ning, P. Comparison of Pd-UiO-66 and Pd-UiO-66-NH 2 Catalysts Performance for Phenol Hydrogenation in Aqueous Medium. *Fuel* **2017**, *205*, 130–141. https://doi.org/10.1016/j.fuel.2017.05.029.

(563) Shen, L.; Wu, W.; Liang, R.; Lin, R.; Wu, L. Highly Dispersed Palladium Nanoparticles Anchored on UiO-66(NH_2) Metal-Organic Framework as a Reusable and Dual Functional Visible-Light-Driven Photocatalyst. *Nanoscale* **2013**, *5* (19), 9374. https://doi.org/10.1039/c3nr03153e.

(564) Bernales, V.; Ortuño, M. A.; Truhlar, D. G.; Cramer, C. J.; Gagliardi, L. Computational Design of Functionalized Metal–Organic Framework Nodes for Catalysis. *ACS Central Science* **2018**, *4* (1), 5–19. https://doi.org/10.1021/acscentsci.7b00500.

(565) Jensen, F. *Introduction to Computational Chemistry*, 2nd ed.; John Wiley & Sons: Chichester, England ; Hoboken, NJ, 2007.

(566) Cruz-Olvera, D.; de la Trinidad Vasquez, A.; Geudtner, G.; Vásquez-Pérez, J. M.; Calaminici, P.; Köster, A. M. Transition-State Searches in Metal Clusters by First-Principle Methods. *The Journal of Physical Chemistry A* **2015**, *119* (9), 1494–1501. https://doi.org/10.1021/jp506121f.

(567) Wales, D. J. *Energy Landscapes*; Cambridge molecular science; Cambridge University Press: Cambridge, UK; New York, 2003.

(568) E, W.; Ren, W.; Vanden-Eijnden, E. String Method for the Study of Rare Events. *Physical Review B* **2002**, *66* (5). https://doi.org/10.1103/PhysRevB.66.052301.

(569) E, W.; Ren, W.; Vanden-Eijnden, E. Simplified and Improved String Method for Computing the Minimum Energy Paths in Barrier-Crossing Events. *The Journal of Chemical Physics* **2007**, *126* (16), 164103. https://doi.org/10.1063/1.2720838.

(570) Peters, B.; Heyden, A.; Bell, A. T.; Chakraborty, A. A Growing String Method for Determining Transition States: Comparison to the Nudged Elastic Band and String Methods. *The Journal of Chemical Physics* **2004**, *120* (17), 7877–7886. https://doi.org/10.1063/1.1691018.

(571) Henkelman, G.; Jónsson, H. Improved Tangent Estimate in the Nudged Elastic Band Method for Finding Minimum Energy Paths and Saddle Points. *The Journal of Chemical Physics* **2000**, *113* (22), 9978–9985. https://doi.org/10.1063/1.1323224.

(572) Henkelman, G.; Uberuaga, B. P.; Jónsson, H. A Climbing Image Nudged Elastic Band Method for Finding Saddle Points and Minimum Energy Paths. *The Journal of Chemical Physics* **2000**, *113* (22), 9901–9904. https://doi.org/10.1063/1.1329672.

(573) Trygubenko, S. A.; Wales, D. J. A Doubly Nudged Elastic Band Method for Finding Transition States. *The Journal of Chemical Physics* **2004**, *120* (5), 2082–2094. https://doi.org/10.1063/1.1636455.

(574) Jonsson, H.; Mills, G.; Jacobsen, K. W. Classical and Quantum Dynamics in Condensed Phase Simulations. In *Classical and Quantum Dynamics in Condensed Phase Simulations*; World Scientific: Singapore, 1998; pp 385–404.

(575) Ulissi, Z. W.; Medford, A. J.; Bligaard, T.; Nørskov, J. K. To Address Surface Reaction Network Complexity Using Scaling Relations Machine Learning and DFT Calculations. *Nature Communications* **2017**, *8* (1). https://doi.org/10.1038/ncomms14621.

(576) Ji, Z.; Li, J.-Q. Density Functional Study of CO Oxidation on Pt and PtMo. *Chemical Physics Letters* **2006**, *424* (1–3), 111–114. https://doi.org/10.1016/j.cplett.2006.04.049.

(577) Lee, D. H.; Xu, J.; Meng, Y. S. An Advanced Cathode for Na-Ion Batteries with High Rate and Excellent Structural Stability. *Physical Chemistry Chemical Physics* **2013**, *15* (9), 3304. https://doi.org/10.1039/c2cp44467d.

(578) Rong, Z.; Malik, R.; Canepa, P.; Sai Gautam, G.; Liu, M.; Jain, A.; Persson, K.; Ceder, G. Materials Design Rules for Multivalent Ion Mobility in Intercalation Structures. *Chemistry of Materials* **2015**, *27* (17), 6016–6021. https://doi.org/10.1021/acs.chemmater.5b02342.

(579) Eames, C.; Frost, J. M.; Barnes, P. R. F.; O'Regan, B. C.; Walsh, A.; Islam, M. S. Ionic Transport in Hybrid Lead Iodide Perovskite Solar Cells. *Nature Communications* **2015**, *6* (1). https://doi.org/10.1038/ncomms8497.

(580) Vilhelmsen, L. B.; Walton, K. S.; Sholl, D. S. Structure and Mobility of Metal Clusters in MOFs: Au, Pd, and AuPd Clusters in MOF-74. *Journal of the American Chemical Society* **2012**, *134* (30), 12807–12816. https://doi.org/10.1021/ja305004a.

(581) Ming, Y.; Kumar, N.; Siegel, D. J. Water Adsorption and Insertion in MOF-5. *ACS Omega* **2017**, *2* (8), 4921–4928. https://doi.org/10.1021/acsomega.7b01129.

(582) Li, Y.; Wang, X.; Xu, D.; Chung, J. D.; Kaviany, M.; Huang, B. H_2O Adsorption/Desorption in MOF-74: *Ab Initio* Molecular Dynamics and Experiments. *The Journal of Physical Chemistry C* **2015**, *119* (23), 13021–13031. https://doi.org/10.1021/acs.jpcc.5b02069.

(583) Ren, W.; Vanden-Eijnden, E. A Climbing String Method for Saddle Point Search. *The Journal of Chemical Physics* **2013**, *138* (13), 134105. https://doi.org/10.1063/1.4798344.

(584) Tian, Y.; Xu, X.; Wu, J. Thermodynamic Route to Efficient Prediction of Gas Diffusivity in Nanoporous Materials. *Langmuir* **2017**, *33* (42), 11797–11803. https://doi.org/10.1021/acs.langmuir.7b02428.

(585) Zhou, M.; Tian, Y.; Fei, W.; Wu, J. Fractionation of Isotopic Methanes with Metal–Organic Frameworks. *Journal of Physical Chemistry C* **2019**, *123* (12), 7397–7407. https://doi.org/10.1021/acs.jpcc.8b11393.

(586) Zhou, M.; Vassallo, A.; Wu, J. Toward the Inverse Design of MOF Membranes for Efficient D2/H2 Separation by Combination of Physics-Based and Data-Driven Modeling. *Journal of Membrane Science* **2019**, 117675. https://doi.org/10.1016/j.memsci.2019.117675.

(587) Smidstrup, S.; Pedersen, A.; Stokbro, K.; Jónsson, H. Improved Initial Guess for Minimum Energy Path Calculations. *The Journal of Chemical Physics* **2014**, *140* (21), 214106. https://doi.org/10.1063/1.4878664.

(588) Maragakis, P.; Andreev, S. A.; Brumer, Y.; Reichman, D. R.; Kaxiras, E. Adaptive Nudged Elastic Band Approach for Transition State Calculation. *The Journal of Chemical Physics* **2002**, *117* (10), 4651–4658. https://doi.org/10.1063/1.1495401.

(589) Sheppard, D.; Terrell, R.; Henkelman, G. Optimization Methods for Finding Minimum Energy Paths. *The Journal of Chemical Physics* **2008**, *128* (13), 134106. https://doi.org/10.1063/1.2841941.

(590) Torrisi, A.; Mellot-Draznieks, C.; Bell, R. G. Impact of Ligands on CO_2 Adsorption in Metal-Organic Frameworks: First Principles Study of the Interaction of CO_2 with Functionalized Benzenes. I. Inductive Effects on the Aromatic Ring. *The Journal of Chemical Physics* **2009**, *130* (19), 194703. https://doi.org/10.1063/1.3120909.

(591) Lee, K.; Kim, Y.-H.; Sun, Y. Y.; West, D.; Zhao, Y.; Chen, Z.; Zhang, S. B. Hole-Mediated Hydrogen Spillover Mechanism in Metal-Organic Frameworks. *Physical Review Letters* **2010**, *104* (23). https://doi.org/10.1103/PhysRevLett.104.236101.

(592) Ye, J.; Johnson, J. K. Design of Lewis Pair-Functionalized Metal Organic Frameworks for CO_2 Hydrogenation. *ACS Catalysis* **2015**, *5* (5), 2921–2928. https://doi.org/10.1021/acscatal.5b00396.

(593) Grimme, S. Semiempirical GGA-Type Density Functional Constructed with a Long-Range Dispersion Correction. *Journal of Computational Chemistry* **2006**, *27* (15), 1787–1799. https://doi.org/10.1002/jcc.20495.

(594) Simons, J.; Nichols, J. Strategies for Walking on Potential Energy Surfaces Using Local Quadratic Approximations. *International Journal of Quantum Chemistry* **1990**, *38* (S24), 263–276. https://doi.org/10.1002/qua.560382427.

(595) Baker, J. An Algorithm for the Location of Transition States. *Journal of Computational Chemistry* **1986**, *7* (4), 385–395. https://doi.org/10.1002/jcc.540070402.

(596) Nichols, J.; Taylor, H.; Schmidt, P.; Simons, J. Walking on Potential Energy Surfaces. *Journal of Physical Chemistry* **1990**, *92*, 2745–2753. https://doi.org/10.1021/j100238a013.

(597) Banerjee, A.; Adams, N.; Simons, J.; Shepard, R. Search for Stationary Points on Surfaces. *Journal of Physical Chemistry* **1985**, *89* (1), 52–57. https://doi.org/10.1021/j100247a015.

(598) Cramer, C. J. *Essentials of Computational Chemistry: Theories and Models*, Second Edition.; Wiley: West Sussex, 2004.

(599) Cerjan, C. J.; Miller, W. H. On Finding Transition States. *The Journal of Chemical Physics* **1981**, *75* (6), 2800–2806. https://doi.org/10.1063/1.442352.

(600) Henkelman, G.; Jónsson, H. A Dimer Method for Finding Saddle Points on High Dimensional Potential Surfaces Using Only First Derivatives. *The Journal of Chemical Physics* **1999**, *111* (15), 7010–7022. https://doi.org/10.1063/1.480097.

(601) Sun, D.; Liu, W.; Fu, Y.; Fang, Z.; Sun, F.; Fu, X.; Zhang, Y.; Li, Z. Noble Metals Can Have Different Effects on Photocatalysis Over Metal-Organic Frameworks (MOFs): A Case Study on M/NH_2 -MIL-125(Ti) (M=Pt and Au). *Chemistry — A European Journal* **2014**, *20* (16), 4780–4788. https://doi.org/10.1002/chem.201304067.

(602) Heyden, A.; Bell, A. T.; Keil, F. J. Efficient Methods for Finding Transition States in Chemical Reactions: Comparison of Improved Dimer Method and Partitioned Rational Function Optimization Method. *The Journal of Chemical Physics* **2005**, *123* (22), 224101. https://doi.org/10.1063/1.2104507.

(603) *Gaussian 09, Revision A.02, M. J. Frisch, G. W. Trucks, H. B. Schlegel, G. E. Scuseria, M. A. Robb, J. R. Cheeseman, G. Scalmani, V. Barone, G. A. Petersson, H. Nakatsuji, X. Li, M. Caricato, A. Marenich, J. Bloino, B. G. Janesko, R. Gomperts, B. Mennucci, H. P. Hratchian, J. V. Ortiz, A. F. Izmaylov, J. L. Sonnenberg, D. Williams-Young, F. Ding, F. Lipparini, F. Egidi, J. Goings, B. Peng, A. Petrone, T. Henderson, D. Ranasinghe, V. G. Zakrzewski, J. Gao, N. Rega, G. Zheng, W. Liang, M. Hada, M. Ehara, K. Toyota, R. Fukuda, J. Hasegawa, M. Ishida, T. Nakajima, Y. Honda, O. Kitao, H. Nakai, T. Vreven, K. Throssell, J. A. Montgomery, Jr., J. E. Peralta, F. Ogliaro, M. Bearpark, J. J. Heyd, E. Brothers, K. N. Kudin, V. N. Staroverov, T. Keith, R. Kobayashi, J. Normand, K. Raghavachari, A. Rendell, J. C. Burant, S. S. Iyengar, J. Tomasi, M. Cossi, J. M. Millam, M. Klene, C. Adamo, R. Cammi, J. W. Ochterski, R. L. Martin, K. Morokuma, O. Farkas, J. B. Foresman, and D. J. Fox, Gaussian, Inc., Wallingford CT, 2016.*

(604) Peng, C.; Bernhard Schlegel, H. Combining Synchronous Transit and Quasi-Newton Methods to Find Transition States. *Israel Journal of Chemistry* **1993**, *33* (4), 449–454. https://doi.org/10.1002/ijch.199300051.

(605) Schlegel, H. B. Optimization of Equilibrium Geometries and Transition Structures. *Journal of Computational Chemistry* **1982**, *3* (2), 214–218. https://doi.org/10.1002/jcc.540030212.

(606) Halgren, T. A.; Lipscomb, W. N. The Synchronous-Transit Method for Determining Reaction Pathways and Locating Molecular Transition States. *Chemical Physics Letters* **1977**, *49* (2), 225–232. https://doi.org/10.1016/0009-2614(77)80574-5.

(607) Baker, J.; Hehre, W. J. Geometry Optimization in Cartesian Coordinates: The End of TheZ-Matrix? *Journal of Computational Chemistry* **1991**, *12* (5), 606–610. https://doi.org/10.1002/jcc.540120510.

(608) Foresman, J. B.; Frisch, Ae. *Exploring Chemistry with Electronic Structure Methods*, Third edition.; Gaussian, Inc: Wallingford, CT, 2015.

(609) Li, X.; Cheetham, A. K.; Jiang, J. CO_2 Cycloaddition with Propylene Oxide to Form Propylene Carbonate on a Copper Metal-Organic Framework: A Density Functional Theory Study. *Molecular Catalysis* **2019**, *463*, 37–44. https://doi.org/10.1016/j.mcat.2018.11.015.

(610) Barona, M.; Ahn, S.; Morris, W.; Hoover, W.; Notestein, J. M.; Farha, O. K.; Snurr, R. Q. Computational Predictions and Experimental Validation of Alkane Oxidative Dehydrogenation by Fe $_2$ M MOF Nodes. *ACS Catalysis* **2020**, *10* (2), 1460–1469. https://doi.org/10.1021/acscatal.9b03932.

(611) Rosen, A. S.; Notestein, J. M.; Snurr, R. Q. Identifying Promising Metal–Organic Frameworks for Heterogeneous Catalysis via High-throughput Periodic Density Functional Theory. *Journal of Computational Chemistry* **2019**, *40* (12), 1305–1318. https://doi.org/10.1002/jcc.25787.

(612) Zong, S.; Zhang, Y.; Lu, N.; Ma, P.; Wang, J.; Shi, X.-R. A DFT Screening of M-HKUST-1 MOFs for Nitrogen-Containing Compounds Adsorption. *Nanomaterials* **2018**, *8* (11), 958. https://doi.org/10.3390/nano8110958.

(613) Latimer, A. A.; Kulkarni, A. R.; Aljama, H.; Montoya, J. H.; Yoo, J. S.; Tsai, C.; Abild-Pedersen, F.; Studt, F.; Nørskov, J. K. Understanding Trends in C–H Bond Activation in Heterogeneous Catalysis. *Nature Materials* **2017**, *16* (2), 225–229. https://doi.org/10.1038/nmat4760.

(614) Shafiee, S.; Topal, E. When Will Fossil Fuel Reserves Be Diminished? *Energy Policy* **2009**, *37* (1), 181–189. https://doi.org/10.1016/j.enpol.2008.08.016.

(615) Bender, M. An Overview of Industrial Processes for the Production of Olefins - C_4 Hydrocarbons. *ChemBioEng Reviews* **2014**, *1* (4), 136–147. https://doi.org/10.1002/cben.201400016.

(616) Liu, L.; Harris, T. D. Metal–Organic Frameworks as Potential Catalysts for Industrial 1-Butene Production. *ACS Central Science* **2016**, *2* (3), 125–127. https://doi.org/10.1021/acscentsci.6b00052.

(617) Muraza, O. Maximizing Diesel Production through Oligomerization: A Landmark Opportunity for Zeolite Research. *Industrial & Engineering Chemistry Research* **2015**, *54* (3), 781–789. https://doi.org/10.1021/ie5041226.

(618) Britovsek, G. J. P.; Malinowski, R.; McGuinness, D. S.; Nobbs, J. D.; Tomov, A. K.; Wadsley, A. W.; Young, C. T. Ethylene Oligomerization beyond Schulz–Flory Distributions. *ACS Catalysis* **2015**, *5* (11), 6922–6925. https://doi.org/10.1021/acscatal.5b02203.

(619) Gollwitzer, A.; Dietel, T.; Kretschmer, W. P.; Kempe, R. A Broadly Tunable Synthesis of Linear α-Olefins. *Nature Communications* **2017**, *8* (1), 1226. https://doi.org/10.1038/s41467-017-01507-2.

(620) Mohsenzadeh, A.; Zamani, A.; Taherzadeh, M. J. Bioethylene Production from Ethanol: A Review and Techno-Economical Evaluation. *ChemBioEng Reviews* **2017**, *4* (2), 75–91. https://doi.org/10.1002/cben.201600025.

(621) Hulea, V. Toward Platform Chemicals from Bio-Based Ethylene: Heterogeneous Catalysts and Processes. *ACS Catalysis* **2018**, *8* (4), 3263–3279. https://doi.org/10.1021/acscatal.7b04294.

(622) Fischer, K.; Jonas, K.; Misbach, P.; Stabba, R.; Wilke, G. The 'Nickel Effect' *Angewandte Chemie International Edition.* **1973**, *12* (12), 943–953. https://doi.org/10.1002/anie.197309431.

(623) Ziegler, K. Aluminium-organische Synthese im Bereich olefinischer Kohlenwasserstoffe. *Angewandte Chemie* **1952**, *64* (12), 323–329. https://doi.org/10.1002/ange.19520641202.

(624) Ziegler, K.; Holzkamp, E.; Breil, H.; Martin, H. Das Mülheimer Normaldruck-Polyäthylen-Verfahren. *Angewandte Chemie* **1955**, *67* (19–20), 541–547. https://doi.org/10.1002/ange.19550671902.

(625) Kaiser, S. K.; Chen, Z.; Faust Akl, D.; Mitchell, S.; Pérez-Ramírez, J. Single-Atom Catalysts across the Periodic Table. *Chemical Reviews* **2020**, *120* (21), 11703–11809. https://doi.org/10.1021/acs.chemrev.0c00576.

(626) Bordiga, S.; Groppo, E.; Agostini, G.; van Bokhoven, J. A.; Lamberti, C. Reactivity of Surface Species in Heterogeneous Catalysts Probed by In Situ X-Ray Absorption Techniques. *Chemical Reviews* **2013**, *113* (3), 1736–1850. https://doi.org/10.1021/cr2000898.

(627) Qin, R.; Liu, K.; Wu, Q.; Zheng, N. Surface Coordination Chemistry of Atomically Dispersed Metal Catalysts. *Chemical Reviews* **2020**, *120* (21), 11810–11899. https://doi.org/10.1021/acs.chemrev.0c00094.

(628) Farha, O. K.; Eryazici, I.; Jeong, N. C.; Hauser, B. G.; Wilmer, C. E.; Sarjeant, A. A.; Snurr, R. Q.; Nguyen, S. T.; Yazaydın, A. Ö.; Hupp, J. T. Metal–Organic Framework Materials with Ultrahigh Surface Areas: Is the Sky the Limit? *Journal of the American Chemical Society* **2012**, *134* (36), 15016–15021. https://doi.org/10.1021/ja3055639.

(629) Stubbs, A. W.; Braglia, L.; Borfecchia, E.; Meyer, R. J.; Román- Leshkov, Y.; Lamberti, C.; Dincă, M. Selective Catalytic Olefin Epoxidation with Mn^{II} -Exchanged MOF-5. *ACS Catalysis* **2018**, *8* (1), 596–601. https://doi.org/10.1021/acscatal.7b02946.

(630) Manna, K.; Ji, P.; Lin, Z.; Greene, F. X.; Urban, A.; Thacker, N. C.; Lin, W. Chemoselective Single-Site Earth-Abundant Metal Catalysts at Metal–Organic Framework Nodes. *Nature Communications* **2016**, *7* (1), 12610. https://doi.org/10.1038/ncomms12610.

(631) Yang, D.; Gates, B. C. Catalysis by Metal Organic Frameworks: Perspective and Suggestions for Future Research. *ACS Catalysis* **2019**, *9* (3), 1779–1798. https://doi.org/10.1021/acscatal.8b04515.

(632) Konnerth, H.; Matsagar, B. M.; Chen, S. S.; Prechtl, M. H. G.; Shieh, F.-K.; Wu, K. C.-W. Metal-Organic Framework (MOF)-Derived Catalysts for Fine Chemical Production. *Coordination Chemistry Reviews* **2020**, *416*, 213319. https://doi.org/10.1016/j.ccr.2020.213319.

(633) Pascanu, V.; González Miera, G.; Inge, A. K.; Martín-Matute, B. Metal–Organic Frameworks as Catalysts for Organic Synthesis: A Critical Perspective. *Journal of the American Chemical Society* **2019**, *141* (18), 7223–7234. https://doi.org/10.1021/jacs.9b00733.

(634) Kalaj, M.; Cohen, S. M. Postsynthetic Modification: An Enabling Technology for the Advancement of Metal–Organic Frameworks. *ACS Central Science* **2020**, *6* (7), 1046–1057. https://doi.org/10.1021/acscentsci.0c00690.

(635) Yaghi, O. M.; O'Keeffe, M.; Ockwig, N. W.; Chae, H. K.; Eddaoudi, M.; Kim, J. Reticular Synthesis and the Design of New Materials. *Nature* **2003**, *423* (6941), 705–714. https://doi.org/10.1038/nature01650.

(636) Forestière, A.; Olivier-Bourbigou, H.; Saussine, L. Oligomerization of Monoolefins by Homogeneous Catalysts. *Oil & Gas Science and Technology - Revue de l'IFP* **2009**, *64* (6), 649–667. https://doi.org/10.2516/ogst/2009027.

(637) Al-Sherehy, F. A. IFP-SABIC Process for the Selective Ethylene Dimerization to Butene-1. In *Studies in Surface Science and Catalysis*; Elsevier, 1996; Vol. 100, pp 515–523. https://doi.org/10.1016/S0167-2991(96)80052-8.

(638) Suttil, J. A.; McGuinness, D. S. Mechanism of Ethylene Dimerization Catalyzed by $Ti(OR')_4/AlR_3$. *Organometallics* **2012**, *31* (19), 7004–7010. https://doi.org/10.1021/om3008508.

(639) Griffin, S. L.; Champness, N. R. A Periodic Table of Metal-Organic Frameworks. *Coordination Chemistry Reviews* **2020**, *414*, 213295. https://doi.org/10.1016/j.ccr.2020.213295.

(640) Madrahimov, S. T.; Gallagher, J. R.; Zhang, G.; Meinhart, Z.; Garibay, S. J.; Delferro, M.; Miller, J. T.; Farha, O. K.; Hupp, J. T.; Nguyen, S. T. Gas-Phase Dimerization of Ethylene under Mild Conditions Catalyzed by MOF Materials Containing $(Bpy)Ni^{II}$ Complexes. *ACS Catalysis* **2015**, *5* (11), 6713–6718. https://doi.org/10.1021/acscatal.5b01604.

(641) Evans, J. D.; Sumby, C. J.; Doonan, C. J. Post-Synthetic Metalation of Metal–Organic Frameworks. *Chemical Society Reviews* **2014**, *43* (16), 5933–5951. https://doi.org/10.1039/C4CS00076E.

(642) Bernales, V.; League, A. B.; Li, Z.; Schweitzer, N. M.; Peters, A. W.; Carlson, R. K.; Hupp, J. T.; Cramer, C. J.; Farha, O. K.; Gagliardi, L. Computationally Guided Discovery of a Catalytic Cobalt-Decorated Metal–Organic Framework for Ethylene Dimerization. *The Journal of Physical Chemistry C* **2016**, *120* (41), 23576–23583. https://doi.org/10.1021/acs.jpcc.6b07362.

(643) Metzger, E. D.; Comito, R. J.; Hendon, C. H.; Dincă, M. Mechanism of Single-Site Molecule-Like Catalytic Ethylene Dimerization in Ni-MFU-4 *l*. *Journal of the American Chemical Society* **2017**, *139* (2), 757–762. https://doi.org/10.1021/jacs.6b10300.

(644) Bunzen, H.; Grzywa, M.; Kalytta-Mewes, A.; Volkmer, D. One-Pot Synthesis of Ultrastable Pentanuclear Alkylzinc Complexes. *Dalton Transactions* **2017**, *46* (8), 2618–2625. https://doi.org/10.1039/C6DT04778E.

(645) Liu, Y.-Y.; Grzywa, M.; Tonigold, M.; Sastre, G.; Schüttrigkeit, T.; Leeson, N. S.; Volkmer, D. Photophysical Properties of Kuratowski-Type Coordination Compounds $[M^{II}Zn_4Cl_4(Me_2bta)_6]$ (M^{II} = Zn or Ru) Featuring Long-Lived Excited Electronic States. *Dalton Transactions* **2011**, *40* (22), 5926. https://doi.org/10.1039/c0dt01750g.

(646) Kunrath, F. A.; de Souza, R. F.; Casagrande, O. L.; Brooks, N. R.; Young, V. G. Highly Selective Nickel Ethylene Oligomerization Catalysts Based on Sterically Hindered Tris(Pyrazolyl)Borate Ligands. *Organometallics* **2003**, *22* (23), 4739–4743. https://doi.org/10.1021/om034035u.

(647) Biswas, S.; Tonigold, M.; Speldrich, M.; Kögerler, P.; Weil, M.; Volkmer, D. Syntheses and Magnetostructural Investigations on Kuratowski-Type Homo- and Heteropentanuclear Coordination Compounds $[MZn_4Cl_4(L)_6]$ (M^{II} = Zn, Fe, Co, Ni, or Cu; L = 5,6-Dimethyl-1,2,3-Benzotriazolate) Represented by the Nonplanar $K_{3,3}$ Graph. *Inorganic Chemistry* **2010**, *49* (16), 7424–7434. https://doi.org/10.1021/ic100749k.

(648) Arrozi, U. S. F.; Bon, V.; Kutzscher, C.; Senkovska, I.; Kaskel, S. Towards Highly Active and Stable Nickel-Based Metal–Organic Frameworks as Ethylene Oligomerization Catalysts. *Dalton Transactions* **2019**, *48* (10), 3415–3421. https://doi.org/10.1039/C8DT03866J.

(649) Brandenburg, H.; Krahmer, J.; Fischer, K.; Schwager, B.; Flöser, B.; Näther, C.; Tuczek, F. Coordination-Induced Spin-State Switching with Nickel(II) Salpn Complexes: Electronic versus Steric Effects and Influence of Intermolecular Interactions: Coordination-Induced Spin-State Switching with Nickel(II) Salpn Complexes: Electronic versus Steric Effects and Influence of Intermolecular Interactio. *Eur. J. Inorganic Chemistry* **2018**, *2018* (5), 576–585. https://doi.org/10.1002/ejic.201701281.

(650) Dommaschk, M.; Schütt, C.; Venkataramani, S.; Jana, U.; Näther, C.; Sönnichsen, F. D.; Herges, R. Rational Design of a Room Temperature Molecular Spin Switch. The Light-Driven Coordination Induced Spin State Switch (LD-CISSS) Approach. *Dalton Transactions* **2014**, *43* (46), 17395–17405. https://doi.org/10.1039/C4DT03048F.

(651) Farcaș, A.-A.; Bende, A. Improving the Light-Induced Spin Transition Efficiency in Ni(II)-Based Macrocyclic-Ligand Complexes. *Molecules* **2019**, *24* (23), 4249. https://doi.org/10.3390/molecules24234249.

(652) Homma, Y.; Ishida, T. A New $S = 0 \rightleftarrows S = 2$ "Spin-Crossover" Scenario Found in a Nickel(II) Bis(Nitroxide) System. *Chemistry of Materials* **2018**, *30* (6), 1835–1838. https://doi.org/10.1021/acs.chemmater.7b05357.

(653) Gray, H. B.; Ballhausen, C. J. A Molecular Orbital Theory for Square Planar Metal Complexes. *Journal of the American Chemical Society* **1963**, *85* (3), 260–265. https://doi.org/10.1021/ja00886a002.

(654) Wilke, G.; Bogdanović, B.; Hardt, P.; Heimbach, P.; Keim, W.; Kröner, M.; Oberkirch, W.; Tanaka, K.; Steinrücke, E.; Walter, D.; Zimmermann, H. Allyl-Transition Metal Systems. *Angewandte Chemie International Edition English* **1966**, *5* (2), 151–164. https://doi.org/10.1002/anie.196601511.

(655) Weigend, F.; Ahlrichs, R. Balanced Basis Sets of Split Valence, Triple Zeta Valence and Quadruple Zeta Valence Quality for H to Rn: Design and Assessment of Accuracy. *Physical Chemistry Chemical Physics* **2005**, *7* (18), 3297–3305. https://doi.org/10.1039/b508541a.

(656) Breitenfeld, J.; Vechorkin, O.; Corminboeuf, C.; Scopelliti, R.; Hu, X. Why Are (NN $_2$)Ni Pincer Complexes Active for Alkyl−Alkyl Coupling: β-H Elimination Is Kinetically Accessible but Thermodynamically Uphill. *Organometallics* **2010**, *29* (17), 3686–3689. https://doi.org/10.1021/om1007506.

(657) Comito, R. J.; Metzger, E. D.; Wu, Z.; Zhang, G.; Hendon, C. H.; Miller, J. T.; Dincă, M. Selective Dimerization of Propylene with Ni-MFU-4 *l*. *Organometallics* **2017**, *36* (9), 1681–1683. https://doi.org/10.1021/acs.organomet.7b00178.

(658) Venkataramani, S.; Jana, U.; Dommaschk, M.; Sonnichsen, F. D.; Tuczek, F.; Herges, R. Magnetic Bistability of Molecules in Homogeneous Solution at Room Temperature. *Science* **2011**, *331* (6016), 445–448. https://doi.org/10.1126/science.1201180.

(659) Thies, S.; Bornholdt, C.; Köhler, F.; Sönnichsen, F. D.; Näther, C.; Tuczek, F.; Herges, R. Coordination-Induced Spin Crossover (CISCO) through Axial Bonding of Substituted Pyridines to Nickel-Porphyrins: σ-Donor versus π-Acceptor Effects. *Chemistry — A European Journal* **2010**, *16* (33), 10074–10083. https://doi.org/10.1002/chem.201000603.

(660) Gaggioli, C. A.; Belpassi, L.; Tarantelli, F.; Harvey, J. N.; Belanzoni, P. Spin-Forbidden Reactions: Adiabatic Transition States Using Spin-Orbit Coupled Density Functional Theory. *Chemistry — A European Journal* **2018**, *24* (20), 5006–5015. https://doi.org/10.1002/chem.201704608.

(661) Harvey, J. N.; Aschi, M.; Schwarz, H.; Koch, W. The Singlet and Triplet States of Phenyl Cation. A Hybrid Approach for Locating Minimum Energy Crossing Points between Non-Interacting Potential Energy Surfaces. *Theoretical Chemistry Accounts: Theory, Computation, and Modeling (Theoretica Chimica Acta)* **1998**, *99* (2), 95–99. https://doi.org/10.1007/s002140050309.

(662) Brogaard, R. Y.; Kømurcu, M.; Dyballa, M. M.; Botan, A.; Van Speybroeck, V.; Olsbye, U.; De Wispelaere, K. Ethene Dimerization on Zeolite-Hosted Ni Ions: Reversible Mobilization of the Active Site. *ACS Catalysis* **2019**, *9* (6), 5645–5650. https://doi.org/10.1021/acscatal.9b00721.

(663) Cossee, P. Ziegler-Natta Catalysis I. Mechanism of Polymerization of a-Olefins with Ziegler-Natta Catalysts. *Journal of Catalysis* **1964**, *3*, 80–88.

(664) Grubbs, R.; Tumas, W. Polymer Synthesis and Organotransition Metal Chemistry. *Science* **1989**, *243* (4893), 907–915. https://doi.org/10.1126/science.2645643.

(665) Ng, F. T. T.; Creaser, D. C. Ethylene Dimerization: Kinetics and Selectivity for 1-Butene. In *Studies in Surface Science and Catalysis*; Elsevier, 1992; Vol. 73, pp 123–131. https://doi.org/10.1016/S0167-2991(08)60805-8.

(666) Mlinar, A. N.; Keitz, B. K.; Gygi, D.; Bloch, E. D.; Long, J. R.; Bell, A. T. Selective Propene Oligomerization with Nickel(II)-Based Metal–Organic Frameworks. *ACS Catalysis* **2014**, *4* (3), 717–721. https://doi.org/10.1021/cs401189a.

(667) Gonzalez, M. I.; Oktawiec, J.; Long, J. R. Ethylene Oligomerization in Metal–Organic Frameworks Bearing Nickel(II) 2,2′-Bipyridine Complexes. *Faraday Discussions* **2017**, *201*, 351–367. https://doi.org/10.1039/C7FD00061H.

(668) Wright, A. M.; Rieth, A. J.; Yang, S.; Wang, E. N.; Dincă, M. Precise Control of Pore Hydrophilicity Enabled by Post-Synthetic Cation Exchange in Metal–Organic Frameworks. *Chemical Science* **2018**, *9* (15), 3856–3859. https://doi.org/10.1039/C8SC00112J.

(669) Wang, Y.; Cui, H.; Wei, Z.-W.; Wang, H.-P.; Zhang, L.; Su, C.-Y. Engineering Catalytic Coordination Space in a Chemically Stable Ir-Porphyrin MOF with a Confinement Effect Inverting Conventional Si–H Insertion Chemoselectivity. *Chemical Science* **2017**, *8* (1), 775–780. https://doi.org/10.1039/C6SC03288E.

(670) Agirrezabal-Telleria, I.; Iglesia, E. Stabilization of Active, Selective, and Regenerable Ni-Based Dimerization Catalysts by Condensation of Ethene Withinordered Mesopores. *Journal of Catalysis* **2017**, *352*, 505–514. https://doi.org/10.1016/j.jcat.2017.06.025.

(671) Agirrezabal-Telleria, I.; Luz, I.; Ortuño, M. A.; Oregui-Bengoechea, M.; Gandarias, I.; López, N.; Lail, M. A.; Soukri, M. Gas Reactions under Intrapore Condensation Regime within Tailored Metal–Organic Framework Catalysts. *Nature Communications* **2019**, *10* (1), 2076. https://doi.org/10.1038/s41467-019-10013-6.

(672) Killian, C. M.; Johnson, L. K.; Brookhart, M. Preparation of Linear α-Olefins Using Cationic Nickel(II) α-Diimine Catalysts. *Organometallics* **1997**, *16* (10), 2005–2007. https://doi.org/10.1021/om961057q.

(673) Chen, C. Designing Catalysts for Olefin Polymerization and Copolymerization: Beyond Electronic and Steric Tuning. *Nature Reviews Chemistry* **2018**, *2* (5), 6–14. https://doi.org/10.1038/s41570-018-0003-0.

(674) Ma, H.; Petersen, J. L.; Young, V. G.; Yee, G. T.; Jensen, M. P. Solid-State Spin Crossover of Ni(II) in a Bioinspired N_3S_2 Ligand Field. *Journal of the American Chemical Society* **2011**, *133* (15), 5644–5647. https://doi.org/10.1021/ja110890v.

(675) Vitek, A. K.; Leone, A. K.; McNeil, A. J.; Zimmerman, P. M. Spin-Switching Transmetalation at Ni Diimine Catalysts. *ACS Catalysis* **2018**, *8* (4), 3655–3666. https://doi.org/10.1021/acscatal.7b03974.

(676) Hill, E. A.; Zhao, N.; Filatov, A. S.; Anderson, J. S. Nickel(II)-Methyl Complexes Adopting Unusual Seesaw Geometries. *Chemical Communications* **2020**, *56* (57), 7861–7864. https://doi.org/10.1039/C9CC09249H.

(677) Jiang, X.; Hao, G.; Wang, X.; Mosey, A.; Zhang, X.; Yu, L.; Yost, A. J.; Zhang, X.; DiChiara, A. D.; N'Diaye, A. T.; Cheng, X.; Zhang, J.; Cheng, R.; Xu, X.; Dowben, P. A. Tunable Spin-State Bistability in a Spin Crossover Molecular Complex. *Journal of Physics: Condensed Matter* **2019**, *31* (31), 315401. https://doi.org/10.1088/1361-648X/ab1a7d.

(678) Wang, J.; Alam, F.; Chang, Q.; Chen, Y.; Jiang, T. Catalytic Behavior Tuning via Structural Modifications of Silylated-diphosphine Ni(II) Complexes for Ethylene Selective Dimerization. *Applied Organometallic Chemistry* **2020**, *34* (8). https://doi.org/10.1002/aoc.5722.

(679) Froese, R. D. J.; Musaev, D. G.; Morokuma, K. Theoretical Study of Substituent Effects in the Diimine−M(II) Catalyzed Ethylene Polymerization Reaction Using the IMOMM Method. *Journal of the American Chemical Society* **1998**, *120* (7), 1581–1587. https://doi.org/10.1021/ja9728334.

(680) Helm, M. L.; Stewart, M. P.; Bullock, R. M.; DuBois, M. R.; DuBois, D. L. A Synthetic Nickel Electrocatalyst with a Turnover Frequency Above 100,000 s-1 for H2 Production. *Science* **2011**, *333* (6044), 863–866. https://doi.org/10.1126/science.1205864.

(681) Hou, J.; Fang, M.; Cardenas, A. J. P.; Shaw, W. J.; Helm, M. L.; Bullock, R. M.; Roberts, J. A. S.; O'Hagan, M. Electrocatalytic H_2 Production with a Turnover Frequency $>10^7$ s^{-1}: The Medium Provides an Increase in Rate but Not Overpotential. *Energy & Environmental Science* **2014**, *7* (12), 4013–4017. https://doi.org/10.1039/C4EE01899K.

(682) Abrahams, B. F.; Hoskins, B. F.; Michail, D. M.; Robson, R. Assembly of Porphyrin Building Blocks into Network Structures with Large Channels. *Nature* **1994**, *369* (6483), 727–729. https://doi.org/10.1038/369727a0.

(683) Gardner, G. B.; Venkataraman, D.; Moore, J. S.; Lee, S. Spontaneous Assembly of a Hinged Coordination Network. *Nature* **1995**, *374* (6525), 792–795. https://doi.org/10.1038/374792a0.

(684) Eddaoudi, M. Systematic Design of Pore Size and Functionality in Isoreticular MOFs and Their Application in Methane Storage. *Science* **2002**, *295* (5554), 469–472. https://doi.org/10.1126/science.1067208.

(685) Cadiau, A.; Adil, K.; Bhatt, P. M.; Belmabkhout, Y.; Eddaoudi, M. A Metal-Organic Framework-Based Splitter for Separating Propylene from Propane. *Science* **2016**, *353* (6295), 137–140. https://doi.org/10.1126/science.aaf6323.

(686) Ye, Y.; Ma, Z.; Lin, R.-B.; Krishna, R.; Zhou, W.; Lin, Q.; Zhang, Z.; Xiang, S.; Chen, B. Pore Space Partition within a Metal–Organic Framework for Highly Efficient C_2H_2/CO_2 Separation. *Journal of the American Chemical Society* **2019**, *141* (9), 4130–4136. https://doi.org/10.1021/jacs.9b00232.

(687) Li, J.-R.; Sculley, J.; Zhou, H.-C. Metal–Organic Frameworks for Separations. *Chemical Reviews* **2012**, *112* (2), 869–932.

(688) Bloch, E. D.; Queen, W. L.; Krishna, R.; Zadrozny, J. M.; Brown, C. M.; Long, J. R. Hydrocarbon Separations in a Metal-Organic Framework with Open Iron(II) Coordination Sites. *Science* **2012**, *335* (6076), 1606–1610. https://doi.org/10.1126/science.1217544.

(689) Matsuda, R.; Kitaura, R.; Kitagawa, S.; Kubota, Y.; Belosludov, R. V.; Kobayashi, T. C.; Sakamoto, H.; Chiba, T.; Takata, M.; Kawazoe, Y.; Mita, Y. Highly Controlled Acetylene Accommodation in a Metal–Organic Microporous Material. *Nature* **2005**, *436* (7048), 238–241. https://doi.org/10.1038/nature03852.

(690) Rieth, A. J.; Tulchinsky, Y.; Dincă, M. High and Reversible Ammonia Uptake in Mesoporous Azolate Metal–Organic Frameworks with Open Mn, Co, and Ni Sites. *Journal of the American Chemical Society* **2016**, *138* (30), 9401–9404. https://doi.org/10.1021/jacs.6b05723.

(691) Tulchinsky, Y.; Hendon, C. H.; Lomachenko, K. A.; Borfecchia, E.; Melot, B. C.; Hudson, M. R.; Tarver, J. D.; Korzyński, M. D.; Stubbs, A. W.; Kagan, J. J.; Lamberti, C.; Brown, C. M.; Dincă, M. Reversible Capture and Release of Cl_2 and Br_2 with a Redox-Active Metal–Organic Framework. *Journal of the American Chemical Society* **2017**, *139* (16), 5992–5997. https://doi.org/10.1021/jacs.7b02161.

(692) Rieth, A. J.; Wright, A. M.; Skorupskii, G.; Mancuso, J. L.; Hendon, C. H.; Dincă, M. Record-Setting Sorbents for Reversible Water Uptake by Systematic Anion Exchanges in Metal–Organic Frameworks. *Journal of the American Chemical Society* **2019**, *141* (35), 13858–13866.

(693) Nath, I.; Chakraborty, J.; Verpoort, F. Metal Organic Frameworks Mimicking Natural Enzymes: A Structural and Functional Analogy. *Chemical Society Reviews* **2016**, *45* (15), 4127–4170. https://doi.org/10.1039/C6CS00047A.

(694) Chen, Y.; Ma, S. Biomimetic Catalysis of Metal–Organic Frameworks. *Dalton Transactions* **2016**, *45* (24), 9744–9753. https://doi.org/10.1039/C6DT00325G.

(695) Chen, K.; Wu, C.-D. Designed Fabrication of Biomimetic Metal–Organic Frameworks for Catalytic Applications. *Coordination Chemistry Reviews* **2019**, *378*, 445–465. https://doi.org/10.1016/j.ccr.2018.01.016.

(696) Zhao, M.; Ou, S.; Wu, C.-D. Porous Metal–Organic Frameworks for Heterogeneous Biomimetic Catalysis. *Accounts of Chemical Research* **2014**, *47* (4), 1199–1207. https://doi.org/10.1021/ar400265x.

(697) Gu, Z.-Y.; Park, J.; Raiff, A.; Wei, Z.; Zhou, H.-C. Metal-Organic Frameworks as Biomimetic Catalysts. *ChemCatChem* **2014**, *6* (1), 67–75. https://doi.org/10.1002/cctc.201300493.

(698) Lykourinou, V.; Chen, Y.; Wang, X.-S.; Meng, L.; Hoang, T.; Ming, L.-J.; Musselman, R. L.; Ma, S. Immobilization of MP-11 into a Mesoporous Metal–Organic Framework, MP-11@mesoMOF: A New Platform for Enzymatic Catalysis. *Journal of the American Chemical Society* **2011**, *133* (27), 10382–10385. https://doi.org/10.1021/ja2038003.

(699) Li, P.; Modica, J. A.; Howarth, A. J.; Vargas L., E.; Moghadam, P. Z.; Snurr, R. Q.; Mrksich, M.; Hupp, J. T.; Farha, O. K. Toward Design Rules for Enzyme Immobilization in Hierarchical Mesoporous Metal-Organic Frameworks. *Chem* **2016**, *1* (1), 154–169. https://doi.org/10.1016/j.chempr.2016.05.001.

(700) Mehta, J.; Bhardwaj, N.; Bhardwaj, S. K.; Kim, K.-H.; Deep, A. Recent Advances in Enzyme Immobilization Techniques: Metal-Organic Frameworks as Novel Substrates. *Coordination Chemistry Reviews* **2016**, *322*, 30–40. https://doi.org/10.1016/j.ccr.2016.05.007.

(701) Li, P.; Moon, S.-Y.; Guelta, M. A.; Lin, L.; Gómez-Gualdrón, D. A.; Snurr, R. Q.; Harvey, S. P.; Hupp, J. T.; Farha, O. K. Nanosizing a Metal–Organic Framework Enzyme Carrier for Accelerating Nerve Agent Hydrolysis. *ACS Nano* **2016**, *10* (10), 9174–9182. https://doi.org/10.1021/acsnano.6b04996.

(702) Liang, J. Y.; Lipscomb, W. N. Binding of Substrate CO2 to the Active Site of Human Carbonic Anhydrase II: A Molecular Dynamics Study. *Proceedings of the National Academy of Sciences* **1990**, *87* (10), 3675–3679. https://doi.org/10.1073/pnas.87.10.3675.

(703) Parkin, G. Synthetic Analogues Relevant to the Structure and Function of Zinc Enzymes. *Chemical Reviews* **2004**, *104* (2), 699–768. https://doi.org/10.1021/cr0206263.

(704) Alsfasser, R.; Trofimenko, S.; Looney, A.; Parkin, G.; Vahrenkamp, H. A Mononuclear Zinc Hydroxide Complex Stabilized by a Highly Substituted Tris(Pyrazolyl)Hydroborato Ligand: Analogies with the Enzyme Carbonic Anhydrase. *Inorganic Chemistry* **1991**, *30* (21), 4098–4100. https://doi.org/10.1021/ic00021a026.

(705) Looney, A.; Han, R.; McNeill, K.; Parkin, G. Tris(Pyrazolyl)Hydroboratozinc Hydroxide Complexes as Functional Models for Carbonic Anhydrase: On the Nature of the Bicarbonate Intermediate. *Journal of the American Chemical Society* **1993**, *115* (11), 4690–4697. https://doi.org/10.1021/ja00064a033.

(706) Looney, A.; Parkin, G.; Alsfasser, R.; Ruf, M.; Vahrenkamp, H. Zinc Pyrazolylborate Complexes Relevant to the Biological Function of Carbonic Anhydrase. *Angewandte Chemie International Edition Engl.* **1992**, *31* (1), 92–93. https://doi.org/10.1002/anie.199200921.

(707) Biswas, S.; Grzywa, M.; Nayek, H. P.; Dehnen, S.; Senkovska, I.; Kaskel, S.; Volkmer, D. A Cubic Coordination Framework Constructed from Benzobistriazolate Ligands and Zinc Ions Having Selective Gas Sorption Properties. *Dalton Transactions* **2009**, No. 33, 6487. https://doi.org/10.1039/b904280f.

(708) Denysenko, D.; Werner, T.; Grzywa, M.; Puls, A.; Hagen, V.; Eickerling, G.; Jelic, J.; Reuter, K.; Volkmer, D. Reversible Gas-Phase Redox Processes Catalyzed by Co-Exchanged MFU-4l(arge). *Chemical Communications* **2012**, *48* (9), 1236–1238. https://doi.org/10.1039/C2CC16235K.

(709) Denysenko, D.; Grzywa, M.; Jelic, J.; Reuter, K.; Volkmer, D. Scorpionate-Type Coordination in MFU-4*l* Metal-Organic Frameworks: Small-Molecule Binding and Activation upon the Thermally Activated Formation of Open Metal Sites. *Angewandte Chemie International Edition* **2014**, *53* (23), 5832–5836. https://doi.org/10.1002/anie.201310004.

(710) Dubey, R. J.-C.; Comito, R. J.; Wu, Z.; Zhang, G.; Rieth, A. J.; Hendon, C. H.; Miller, J. T.; Dincă, M. Highly Stereoselective Heterogeneous Diene Polymerization by Co-MFU-4*l*: A Single-Site Catalyst Prepared by Cation Exchange. *Journal of the American Chemical Society* **2017**, *139* (36), 12664–12669. https://doi.org/10.1021/jacs.7b06841.

(711) Liao, P.-Q.; Chen, H.; Zhou, D.-D.; Liu, S.-Y.; He, C.-T.; Rui, Z.; Ji, H.; Zhang, J.-P.; Chen, X.-M. Monodentate Hydroxide as a Super Strong yet Reversible Active Site for CO_2 Capture from High-Humidity Flue Gas. *Energy & Environmental Science* **2015**, *8* (3), 1011–1016. https://doi.org/10.1039/C4EE02717E.

(712) Bräuer, M.; Pérez-Lustres, J. L.; Weston, J.; Anders, E. Quantitative Reactivity Model for the Hydration of Carbon Dioxide by Biomimetic Zinc Complexes. *Inorganic Chemistry* **2002**, *41* (6), 1454–1463. https://doi.org/10.1021/ic0010510.

(713) Rieth, A. J.; Wright, A. M.; Rao, S.; Kim, H.; LaPotin, A. D.; Wang, E. N.; Dincă, M. Tunable Metal–Organic Frameworks Enable High-Efficiency Cascaded Adsorption Heat Pumps. *Journal of the American Chemical Society* **2018**, *140* (50), 17591–17596. https://doi.org/10.1021/jacs.8b09655.

(714) Rieth, A. J.; Yang, S.; Wang, E. N.; Dincă, M. Record Atmospheric Fresh Water Capture and Heat Transfer with a Material Operating at the Water Uptake Reversibility Limit. *ACS Central Science* **2017**, *3* (6), 668–672. https://doi.org/10.1021/acscentsci.7b00186.

(715) de Lange, M. F.; van Velzen, B. L.; Ottevanger, C. P.; Verouden, K. J. F. M.; Lin, L.-C.; Vlugt, T. J. H.; Gascon, J.; Kapteijn, F. Metal–Organic Frameworks in Adsorption-Driven Heat Pumps: The Potential of Alcohols as Working Fluids. *Langmuir* **2015**, *31* (46), 12783–12796. https://doi.org/10.1021/acs.langmuir.5b03272.

(716) Wang, S.; Lee, J. S.; Wahiduzzaman, M.; Park, J.; Muschi, M.; Martineau-Corcos, C.; Tissot, A.; Cho, K. H.; Marrot, J.; Shepard, W.; Maurin, G.; Chang, J.-S.; Serre, C. A Robust Large-Pore Zirconium Carboxylate Metal–Organic Framework for Energy-Efficient Water-Sorption-Driven Refrigeration. *Nature Energy* **2018**, *3* (11), 985–993. https://doi.org/10.1038/s41560-018-0261-6.

(717) Cadiau, A.; Lee, J. S.; Damasceno Borges, D.; Fabry, P.; Devic, T.; Wharmby, M. T.; Martineau, C.; Foucher, D.; Taulelle, F.; Jun, C.-H.; Hwang, Y. K.; Stock, N.; De Lange, M. F.; Kapteijn, F.; Gascon, J.; Maurin, G.; Chang, J.-S.; Serre, C. Design of Hydrophilic Metal Organic Framework Water Adsorbents for Heat Reallocation. *Advanced Materials* **2015**, *27* (32), 4775–4780. https://doi.org/10.1002/adma.201502418.

(718) Khutia, A.; Rammelberg, H. U.; Schmidt, T.; Henninger, S.; Janiak, C. Water Sorption Cycle Measurements on Functionalized MIL-101Cr for Heat Transformation Application. *Chemistry of Materials* **2013**, *25* (5), 790–798. https://doi.org/10.1021/cm304055k.

(719) Jeremias, F.; Khutia, A.; Henninger, S. K.; Janiak, C. MIL-100(Al, Fe) as Water Adsorbents for Heat Transformation Purposes—a Promising Application. *Journal of Materials Chemistry* **2012**, *22* (20), 10148–10151. https://doi.org/10.1039/C2JM15615F.

(720) Kummer, H.; Jeremias, F.; Warlo, A.; Füldner, G.; Fröhlich, D.; Janiak, C.; Gläser, R.; Henninger, S. K. A Functional Full-Scale Heat Exchanger Coated with Aluminum Fumarate Metal–Organic Framework for Adsorption Heat Transformation. *Industrial & Engineering Chemistry Research* **2017**, *56* (29), 8393–8398. https://doi.org/10.1021/acs.iecr.7b00106.

(721) Kim, H.; Yang, S.; Rao, S. R.; Narayanan, S.; Kapustin, E. A.; Furukawa, H.; Umans, A. S.; Yaghi, O. M.; Wang, E. N. Water Harvesting from Air with Metal-Organic Frameworks Powered by Natural Sunlight. *Science* **2017**, *356* (6336), 430–434. https://doi.org/10.1126/science.aam8743.

(722) Furukawa, H.; Gándara, F.; Zhang, Y.-B.; Jiang, J.; Queen, W. L.; Hudson, M. R.; Yaghi, O. M. Water Adsorption in Porous Metal–Organic Frameworks and Related Materials. *Journal of the American Chemical Society* **2014**, *136* (11), 4369–4381. https://doi.org/10.1021/ja500330a.

(723) Kalmutzki, M. J.; Diercks, C. S.; Yaghi, O. M. Metal-Organic Frameworks for Water Harvesting from Air. *Advanced Materials* **2018**, *30* (37), 1704304. https://doi.org/10.1002/adma.201704304.

(724) Kim, H.; Rao, S. R.; Kapustin, E. A.; Zhao, L.; Yang, S.; Yaghi, O. M.; Wang, E. N. Adsorption-Based Atmospheric Water Harvesting Device for Arid Climates. *Nature Communications* **2018**, *9* (1), 1191. https://doi.org/10.1038/s41467-018-03162-7.

(725) Fathieh, F.; Kalmutzki, M. J.; Kapustin, E. A.; Waller, P. J.; Yang, J.; Yaghi, O. M. Practical Water Production from Desert Air. *Science Advances* **2018**, *4* (6), eaat3198. https://doi.org/10.1126/sciadv.aat3198.

(726) Cui, S.; Qin, M.; Marandi, A.; Steggles, V.; Wang, S.; Feng, X.; Nouar, F.; Serre, C. Metal-Organic Frameworks as Advanced Moisture Sorbents for Energy-Efficient High Temperature Cooling. *Science Reports* **2018**, *8* (1), 15284. https://doi.org/10.1038/s41598-018-33704-4.

(727) Towsif Abtab, S. M.; Alezi, D.; Bhatt, P. M.; Shkurenko, A.; Belmabkhout, Y.; Aggarwal, H.; Weseliński, Ł. J.; Alsadun, N.; Samin, U.; Hedhili, M. N.; Eddaoudi, M. Reticular Chemistry in Action: A Hydrolytically Stable MOF Capturing Twice Its Weight in Adsorbed Water. *Chem* **2018**, *4* (1), 94–105. https://doi.org/10.1016/j.chempr.2017.11.005.

(728) Chen, Z.; Li, P.; Zhang, X.; Li, P.; Wasson, M. C.; Islamoglu, T.; Stoddart, J. F.; Farha, O. K. Reticular Access to Highly Porous **Acs** -MOFs with Rigid Trigonal Prismatic Linkers for Water Sorption. *Journal of the American Chemical Society* **2019**, *141* (7), 2900–2905. https://doi.org/10.1021/jacs.8b13710.

(729) AbdulHalim, R. G.; Bhatt, P. M.; Belmabkhout, Y.; Shkurenko, A.; Adil, K.; Barbour, L. J.; Eddaoudi, M. A Fine-Tuned Metal–Organic Framework for Autonomous Indoor Moisture Control. *Journal of the American Chemical Society* **2017**, *139* (31), 10715–10722. https://doi.org/10.1021/jacs.7b04132.

(730) Seo, Y.-K.; Yoon, J. W.; Lee, J. S.; Hwang, Y. K.; Jun, C.-H.; Chang, J.-S.; Wuttke, S.; Bazin, P.; Vimont, A.; Daturi, M.; Bourrelly, S.; Llewellyn, P. L.; Horcajada, P.; Serre, C.; Férey, G. Energy-Efficient Dehumidification over Hierachically Porous Metal-Organic Frameworks as Advanced Water Adsorbents. *Advanced Materials* **2012**, *24* (6), 806–810. https://doi.org/10.1002/adma.201104084.

(731) Ceriotti, M.; Fang, W.; Kusalik, P. G.; McKenzie, R. H.; Michaelides, A.; Morales, M. A.; Markland, T. E. Nuclear Quantum Effects in Water and Aqueous Systems: Experiment, Theory, and Current Challenges. *Chemical Reviews* **2016**, *116* (13), 7529–7550. https://doi.org/10.1021/acs.chemrev.5b00674.

(732) Cisneros, G. A.; Wikfeldt, K. T.; Ojamäe, L.; Lu, J.; Xu, Y.; Torabifard, H.; Bartók, A. P.; Csányi, G.; Molinero, V.; Paesani, F. Modeling Molecular Interactions in Water: From Pairwise to Many-Body Potential Energy Functions. *Chemical Reviews* **2016**, *116* (13), 7501–7528. https://doi.org/10.1021/acs.chemrev.5b00644.

(733) Wade, C. R.; Corrales-Sanchez, T.; Narayan, T. C.; Dincă, M. Postsynthetic Tuning of Hydrophilicity in Pyrazolate MOFs to Modulate Water Adsorption Properties. *Energy & Environmental Science* **2013**, *6* (7), 2172. https://doi.org/10.1039/c3ee40876k.

(734) Akiyama, G.; Matsuda, R.; Sato, H.; Hori, A.; Takata, M.; Kitagawa, S. Effect of Functional Groups in MIL-101 on Water Sorption Behavior. *Microporous and Mesoporous Materials* **2012**, *157*, 89–93. https://doi.org/10.1016/j.micromeso.2012.01.015.

(735) Canivet, J.; Bonnefoy, J.; Daniel, C.; Legrand, A.; Coasne, B.; Farrusseng, D. Structure–Property Relationships of Water Adsorption in Metal–Organic Frameworks. *New Journal of Chemistry* **2014**, *38* (7), 3102–3111. https://doi.org/10.1039/C4NJ00076E.

(736) Douss, N.; Meunier, F. Experimental Study of Cascading Adsorption Cycles. *Chemical Engineering Science* **1989**, *44* (2), 225–235. https://doi.org/10.1016/0009-2509(89)85060-2.

(737) Critoph, R. E. Evaluation of Alternative Refrigerant—Adsorbent Pairs for Refrigeration Cycles. *Applied Thermal Engineering* **1996**, *16* (11), 891–900. https://doi.org/10.1016/1359-4311(96)00008-7.

(738) Padial, N. M.; Quartapelle Procopio, E.; Montoro, C.; López, E.; Oltra, J. E.; Colombo, V.; Maspero, A.; Masciocchi, N.; Galli, S.; Senkovska, I.; Kaskel, S.; Barea, E.; Navarro, J. A. R. Highly Hydrophobic Isoreticular Porous Metal-Organic Frameworks for the Capture of Harmful Volatile Organic Compounds. *Angewandte Chemie International Edition* **2013**, *52* (32), 8290–8294. https://doi.org/10.1002/anie.201303484.

(739) Zhang, Y.-Z.; He, T.; Kong, X.-J.; Lv, X.-L.; Wu, X.-Q.; Li, J.-R. Tuning Water Sorption in Highly Stable Zr(IV)-Metal–Organic Frameworks through Local Functionalization of Metal Clusters. *ACS Applied Materials & Interfaces* **2018**, *10* (33), 27868–27874. https://doi.org/10.1021/acsami.8b09333.

(740) Davis, J. G.; Gierszal, K. P.; Wang, P.; Ben-Amotz, D. Water Structural Transformation at Molecular Hydrophobic Interfaces. *Nature* **2012**, *491* (7425), 582–585. https://doi.org/10.1038/nature11570.

(741) Koga, K.; Gao, G. T.; Tanaka, H.; Zeng, X. C. Formation of Ordered Ice Nanotubes inside Carbon Nanotubes. *Nature* **2001**, *412* (6849), 802–805. https://doi.org/10.1038/35090532.

(742) Furukawa, H.; Cordova, K. E.; O'Keeffe, M.; Yaghi, O. M. The Chemistry and Applications of Metal-Organic Frameworks. *Science* **2013**, *341* (6149), 1230444. https://doi.org/10.1126/science.1230444.

(743) LaPotin, A.; Kim, H.; Rao, S. R.; Wang, E. N. Adsorption-Based Atmospheric Water Harvesting: Impact of Material and Component Properties on System-Level Performance. *Accounts of Chemical Research* **2019**, *52* (6), 1588–1597. https://doi.org/10.1021/acs.accounts.9b00062.

(744) Coasne, B.; Gubbins, K. E.; Pellenq, R. J.-M. Temperature Effect on Adsorption/Desorption Isotherms for a Simple Fluid Confined within Various Nanopores. *Adsorption* **2005**, *11* (S1), 289–294. https://doi.org/10.1007/s10450-005-5939-y.

(745) Eigen, M. Fast Elementary Steps in Chemical Reaction Mechanisms. *Pure and Applied Chemistry* **1963**, *6* (1), 97–116. https://doi.org/10.1351/pac196306010097.

(746) Perdew, J. P.; Ruzsinszky, A.; Csonka, G. I.; Vydrov, O. A.; Scuseria, G. E.; Constantin, L. A.; Zhou, X.; Burke, K. Restoring the Density-Gradient Expansion for Exchange in Solids and Surfaces. *Physical review letters* **2008**, *100* (13), 136406.

(747) de Lange, M. F.; Verouden, K. J. F. M.; Vlugt, T. J. H.; Gascon, J.; Kapteijn, F. Adsorption-Driven Heat Pumps: The Potential of Metal–Organic Frameworks. *Chemical Reviews* **2015**, *115* (22), 12205–12250. https://doi.org/10.1021/acs.chemrev.5b00059.

(748) Li, J.-R.; J. Kuppler, R.; Zhou, H.-C. Selective Gas Adsorption and Separation in Metal–Organic Frameworks. *Chemical Society Reviews* **2009**, *38* (5), 1477–1504. https://doi.org/10.1039/B802426J.

(749) Kuppler, R. J.; Timmons, D. J.; Fang, Q.-R.; Li, J.-R.; Makal, T. A.; Young, M. D.; Yuan, D.; Zhao, D.; Zhuang, W.; Zhou, H.-C. Potential Applications of Metal-Organic Frameworks. *Coordination Chemistry Reviews* **2009**, *253* (23), 3042–3066. https://doi.org/10.1016/j.ccr.2009.05.019.

(750) Trickett, C. A.; Helal, A.; Al-Maythalony, B. A.; Yamani, Z. H.; Cordova, K. E.; Yaghi, O. M. The Chemistry of Metal–Organic Frameworks for CO 2 Capture, Regeneration and Conversion. *Nature Reviews Materials* **2017**, *2* (8), 1–16. https://doi.org/10.1038/natrevmats.2017.45.

(751) You, W.; Liu, Y.; Howe, J. D.; Tang, D.; Sholl, D. S. Tuning Binding Tendencies of Small Molecules in Metal–Organic Frameworks with Open Metal Sites by Metal Substitution and Linker Functionalization. *Journal of Physical Chemistry C* **2018**, *122* (48), 27486–27494. https://doi.org/10.1021/acs.jpcc.8b08855.

(752) Sours, T.; Patel, A.; Nørskov, J.; Siahrostami, S.; Kulkarni, A. Circumventing Scaling Relations in Oxygen Electrochemistry Using Metal–Organic Frameworks. *The Journal of Physical Chemistry Letters* **2020**, *11* (23), 10029–10036.

(753) Poloni, R.; Lee, K.; Berger, R. F.; Smit, B.; Neaton, J. B. Understanding Trends in CO2 Adsorption in Metal–Organic Frameworks with Open-Metal Sites. *The Journal of Physical Chemistry Letters* **2014**, *5* (5), 861–865.

(754) Sholl, D. S.; Lively, R. P. Seven Chemical Separations to Change the World. *Nature News* **2016**, *532* (7600), 435.

(755) Hinchliffe, A.; Porter, K. A Comparison of Membrane Separation and Distillation. *Chemical Engineering Research and Design* **2000**, *78* (2), 255–268.

(756) Kandasamy, S.; Samudrala, S. P.; Bhattacharya, S. The Route towards Sustainable Production of Ethylene Glycol from a Renewable Resource, Biodiesel Waste: A Review. *Catalysis Science & Technology* **2019**, *9* (3), 567–577. https://doi.org/10.1039/C8CY02035C.

(757) Production: Growth is the Norm. *Chemical Engineering News Archive* **2006**, *84* (28), 59–68. https://doi.org/10.1021/cen-v084n028.p059.

(758) Xie, T.; McAuley, K. B.; Hsu, J. C. C.; Bacon, D. W. Gas Phase Ethylene Polymerization: Production Processes, Polymer Properties, and Reactor Modeling. *Industrial & Engineering Chemistry Research* **1994**, *33* (3), 449–479. https://doi.org/10.1021/ie00027a001.

(759) Service, R. F. Can the world make the chemicals it needs without oil? https://www.sciencemag.org/news/2019/09/can-world-make-chemicals-it-needs-without-oil (accessed 2021 -06 -17).

(760) Wills, R. B.; Golding, J. B. Reduction of Energy Usage in Postharvest Horticulture through Management of Ethylene. *Journal of the Science of Food and Agriculture* **2015**, *95* (7), 1379–1384. https://doi.org/10.1002/jsfa.6930.

(761) Caprioli, F.; Quercia, L. Ethylene Detection Methods in Post-Harvest Technology: A Review. *Sensors and Actuators B: Chemical* **2014**, *203*, 187–196. https://doi.org/10.1016/j.snb.2014.06.109.

(762) Riyazuddin, R.; Verma, R.; Singh, K.; Nisha, N.; Keisham, M.; Bhati, K. K.; Kim, S. T.; Gupta, R. Ethylene: A Master Regulator of Salinity Stress Tolerance in Plants. *Biomolecules* **2020**, *10* (6), 959. https://doi.org/10.3390/biom10060959.

(763) Chen, R.; Su, H.-Y.; Liu, D.; Huang, R.; Meng, X.; Cui, X.; Tian, Z.-Q.; Zhang, D. H.; Deng, D. Highly Selective Production of Ethylene by the Electroreduction of Carbon Monoxide. *Angewandte Chemie International Edition* **2020**, *59* (1), 154–160. https://doi.org/10.1002/anie.201910662.

(764) Shetsiri, S.; Thivasasith, A.; Saenluang, K.; Wannapakdee, W.; Salakhum, S.; Wetchasat, P.; Nokbin, S.; Limtrakul, J.; Wattanakit, C. Sustainable Production of Ethylene from Bioethanol over Hierarchical ZSM-5 Nanosheets. *Sustainable Energy Fuels* **2018**, *3* (1), 115–126. https://doi.org/10.1039/C8SE00392K.

(765) Farrell, B. L.; Igenegbai, V. O.; Linic, S. A Viewpoint on Direct Methane Conversion to Ethane and Ethylene Using Oxidative Coupling on Solid Catalysts. *ACS Catalysis* **2016**, *6* (7), 4340–4346. https://doi.org/10.1021/acscatal.6b01087.

(766) Bachman, J. E.; Reed, D. A.; Kapelewski, M. T.; Chachra, G.; Jonnavittula, D.; Radaelli, G.; Long, J. R. Enabling Alternative Ethylene Production through Its Selective Adsorption in the Metal–Organic Framework Mn_2(*m*-Dobdc). *Energy & Environmental Science* **2018**, *11* (9), 2423–2431. https://doi.org/10.1039/C8EE01332B.

(767) Outlook, I. For Biogas and Biomethane: Prospects for Organic Growth. **2020**.

(768) Ma, W.; Xie, S.; Liu, T.; Fan, Q.; Ye, J.; Sun, F.; Jiang, Z.; Zhang, Q.; Cheng, J.; Wang, Y. Electrocatalytic Reduction of CO 2 to Ethylene and Ethanol through Hydrogen-Assisted C–C Coupling over Fluorine-Modified Copper. *Nature Catalysis* **2020**, *3* (6), 478–487. https://doi.org/10.1038/s41929-020-0450-0.

(769) You, W.; Liu, Y.; Howe, J. D.; Sholl, D. S. Competitive Binding of Ethylene, Water, and Carbon Monoxide in Metal–Organic Framework Materials with Open Cu Sites. *The Journal of Physical Chemistry C* **2018**, *122* (16), 8960–8966.

(770) Rieth, A. J.; Tulchinsky, Y.; Dincă, M. High and Reversible Ammonia Uptake in Mesoporous Azolate Metal–Organic Frameworks with Open Mn, Co, and Ni Sites. *Journal of the American Chemical Society* **2016**, *138* (30), 9401–9404.

(771) Barnett, B. R.; Parker, S. T.; Paley, M. V.; Gonzalez, M. I.; Biggins, N.; Oktawiec, J.; Long, J. R. Thermodynamic Separation of 1-Butene from 2-Butene in Metal–Organic Frameworks with Open Metal Sites. *Journal of the American Chemical Society* **2019**, *141* (45), 18325–18333.

(772) Rosen, A. S.; Mian, M. R.; Islamoglu, T.; Chen, H.; Farha, O. K.; Notestein, J. M.; Snurr, R. Q. Tuning the Redox Activity of Metal–Organic Frameworks for Enhanced, Selective O2 Binding: Design Rules and Ambient Temperature O_2 Chemisorption in a Cobalt–Triazolate Framework. *Journal of the American Chemical Society* **2020**, *142* (9), 4317–4328.

(773) Sun, L.; Hendon, C. H.; Minier, M. A.; Walsh, A.; Dincă, M. Million-Fold Electrical Conductivity Enhancement in Fe_2(DEBDC) versus Mn_2(DEBDC) (E = S, O). *Journal of the American Chemical Society* **2015**, *137* (19), 6164–6167. https://doi.org/10.1021/jacs.5b02897.

(774) Li, D.; Nielsen, M. H.; Lee, J. R.; Frandsen, C.; Banfield, J. F.; De Yoreo, J. J. Direction-Specific Interactions Control Crystal Growth by Oriented Attachment. *Science* **2012**, *336* (6084), 1014–1018.

(775) Gygi, D.; Bloch, E. D.; Mason, J. A.; Hudson, M. R.; Gonzalez, M. I.; Siegelman, R. L.; Darwish, T. A.; Queen, W. L.; Brown, C. M.; Long, J. R. Hydrogen Storage in the Expanded Pore Metal–Organic Frameworks M_2(Dobpdc) (M = Mg, Mn, Fe, Co, Ni, Zn). *Chemistry of Materials* **2016**, *28* (4), 1128–1138. https://doi.org/10.1021/acs.chemmater.5b04538.

(776) Thommes, M.; Kaneko, K.; Neimark, A. V.; Olivier, J. P.; Rodriguez-Reinoso, F.; Rouquerol, J.; Sing, K. S. Physisorption of Gases, with Special Reference to the Evaluation of Surface Area and Pore Size Distribution (IUPAC Technical Report). *Pure and Applied Chemistry* **2015**, *87* (9–10), 1051–1069.

(777) Bloch, E. D.; Hudson, M. R.; Mason, J. A.; Chavan, S.; Crocellà, V.; Howe, J. D.; Lee, K.; Dzubak, A. L.; Queen, W. L.; Zadrozny, J. M.; others. Reversible CO Binding Enables Tunable CO/H_2 and CO/N_2 Separations in Metal–Organic Frameworks with Exposed Divalent Metal Cations. *Journal of the American Chemical Society* **2014**, *136* (30), 10752–10761.

(778) Bloch, E. D.; Queen, W. L.; Krishna, R.; Zadrozny, J. M.; Brown, C. M.; Long, J. R. Hydrocarbon Separations in a Metal-Organic Framework with Open Iron(II) Coordination Sites. *Science* **2012**, *335* (6076), 1606–1610.

(779) Kapelewski, M. T.; Runčevski, T.; Tarver, J. D.; Jiang, H. Z.; Hurst, K. E.; Parilla, P. A.; Ayala, A.; Gennett, T.; FitzGerald, S. A.; Brown, C. M.; others. Record High Hydrogen Storage Capacity in the Metal–Organic Framework Ni_2(*m*-DOBDC) at near-Ambient Temperatures. *Chemistry of Materials* **2018**, *30* (22), 8179–8189.

(780) Rosnes, M. H.; Opitz, M.; Frontzek, M.; Lohstroh, W.; Embs, J. P.; Georgiev, P. A.; Dietzel, P. D. Intriguing Differences in Hydrogen Adsorption in CPO-27 Materials Induced by Metal Substitution. *Journal of Materials Chemistry A* **2015**, *3* (9), 4827–4839.

(781) Areμn, C. O.; Chavan, S.; Cabello, C. P.; Garrone, E.; Palomino, G. T. Thermodynamics of Hydrogen Adsorption on Metal-Organic Frameworks. *ChemPhysChem* **2010**, *11* (15), 3237-3242. https://doi.org/10.1002/cphc.20100523.

(782) Kresse, G.; Furthmüller, J. Efficient Iterative Schemes for Ab Initio Total-Energy Calculations Using a Plane-Wave Basis Set. *Physical Review B* **1996**, *54* (16), 11169.

(783) Becker, T. M.; Heinen, J.; Dubbeldam, D.; Lin, L.-C.; Vlugt, T. J. Polarizable Force Fields for CO_2 and CH_4 Adsorption in M-MOF-74. *The Journal of Physical Chemistry C* **2017**, *121* (8), 4659–4673.

(784) Hadjiivanov, K. I.; Panayotov, D. A.; Mihaylov, M. Y.; Ivanova, E. Z.; Chakarova, K. K.; Andonova, S. M.; Drenchev, N. L. Power of Infrared and Raman Spectroscopies to Characterize Metal-Organic Frameworks and Investigate Their Interaction with Guest Molecules. *Chemical Reviews* **2021**, *121* (3), 1286-1424. https://doi.org/10.1021/acs.chemrev.0c00487.

(785) Zecchina, A.; Scarano, D.; Bordiga, S.; Spoto, G.; Lamberti, C. Surface Structures of Oxides and Halides and Their Relationships to Catalytic Properties. *Advances in Catalysis* **2001**, *46*, 265-397. https://doi.org/10.1016/S0360-0564(02)46024-5.

(786) Yao, M.; Xiu, J.; Huang, Q.; Li, W.; Wu, W.; Wu, A.; Cao, L.; Deng, W.; Wang, G.; Xu, G. Van Der Waals Heterostructured MOF-on-MOF Thin Films: Cascading Functionality to Realize Advanced Chemiresistive Sensing. *Angewandte Chemie* **2019**, *131* (42), 15057–15061. https://doi.org/10.1002/ange.201907772.

(787) Campbell, M. G.; Sheberla, D.; Liu, S. F.; Swager, T. M.; Dincă, M. Cu_3(Hexaiminotriphenylene)$_2$: An Electrically Conductive 2D Metal-Organic Framework for Chemiresistive Sensing. *Angewandte Chemie International Edition* **2015**, *54* (14), 4349–4352. https://doi.org/10.1002/anie.201411854.

(788) Zhao, Q.; Li, S.-H.; Chai, R.-L.; Ren, X.; Zhang, C. Two-Dimensional Conductive Metal–Organic Frameworks Based on Truxene. *ACS Applied Materials & Interfaces* **2020**, *12* (6), 7504–7509. https://doi.org/10.1021/acsami.9b23416.

(789) Jia, X.; Lynch, A.; Huang, Y.; Danielson, M.; Lang'at, I.; Milder, A.; Ruby, A. E.; Wang, H.; Friedler, S. A.; Norquist, A. J.; Schrier, J. Anthropogenic Biases in Chemical Reaction Data Hinder Exploratory Inorganic Synthesis. *Nature* **2019**, *573* (7773), 251–255. https://doi.org/10.1038/s41586-019-1540-5.

(790) Le, K. N.; Mancuso, J. L.; Hendon, C. H. Electronic Challenges of Retrofitting 2D Electrically Conductive MOFs to Form 3D Conductive Lattices. *ACS Appl. Electron. Mater.* **2021**, *3* (5), 2017–2023. https://doi.org/10.1021/acsaelm.0c01135.

(791) Chen, T.; Dou, J.-H.; Yang, L.; Sun, C.; Libretto, N. J.; Skorupskii, G.; Miller, J. T.; Dincă, M. Continuous Electrical Conductivity Variation in M_3(Hexaiminotriphenylene)$_2$ (M = Co, Ni, Cu) MOF Alloys. *Journal of the American Chemical Society* **2020**, *142* (28), 12367–12373. https://doi.org/10.1021/jacs.0c04458.

(792) McCallum, T.; Wu, X.; Lin, S. Recent Advances in Titanium Radical Redox Catalysis. *Journal of Organic Chemistry* **2019**, *84* (22), 14369–14380. https://doi.org/10.1021/acs.joc.9b02465.

(793) Xie, J.; Jin, R.; Li, A.; Bi, Y.; Ruan, Q.; Deng, Y.; Zhang, Y.; Yao, S.; Sankar, G.; Ma, D.; Tang, J. Highly Selective Oxidation of Methane to Methanol at Ambient Conditions by Titanium Dioxide-Supported Iron Species. *Nature Catalysis* **2018**, *1* (11), 889–896. https://doi.org/10.1038/s41929-018-0170-x.

(794) Li, P.; Xin, Y.; Li, Q.; Wang, Z.; Zhang, Z.; Zheng, L. Ce–Ti Amorphous Oxides for Selective Catalytic Reduction of NO with NH_3: Confirmation of Ce–O–Ti Active Sites. *Environ. Sci. Technol.* **2012**, *46* (17), 9600–9605. https://doi.org/10.1021/es301661r.

(795) Yu, M.-H.; Space, B.; Franz, D.; Zhou, W.; He, C.; Li, L.; Krishna, R.; Chang, Z.; Li, W.; Hu, T.-L.; Bu, X.-H. Enhanced Gas Uptake in a Microporous Metal–Organic Framework *via* a Sorbate Induced-Fit Mechanism. *Journal of the American Chemical Society* **2019**, *141* (44), 17703–17712. https://doi.org/10.1021/jacs.9b07807.

(796) Ortiz, A. U.; Boutin, A.; Coudert, F.-X. Prediction of Flexibility of Metal–Organic Frameworks CAU-13 and NOTT-300 by First Principles Molecular Simulations. *Chemical Communications* **2014**, *50* (44), 5867. https://doi.org/10.1039/c4cc00734d.

(797) Wang, K.; Huang, H.; Xue, W.; Liu, D.; Zhao, X.; Xiao, Y.; Li, Z.; Yang, Q.; Wang, L.; Zhong, C. An Ultrastable Zr Metal–Organic Framework with a Thiophene-Type Ligand Containing Methyl Groups. *CrystEngComm* **2015**, *17* (19), 3586–3590. https://doi.org/10.1039/C5CE00269A.

(798) Wang, K.; Huang, H.; Zhou, X.; Wang, Q.; Li, G.; Shen, H.; She, Y.; Zhong, C. Highly Chemically Stable MOFs with Trifluoromethyl Groups: Effect of Position of Trifluoromethyl Groups on Chemical Stability. *Inorganic Chemistry* **2019**, *58* (9), 5725–5732. https://doi.org/10.1021/acs.inorgchem.9b00088.

(799) Li, M.; Li, D.; O'Keeffe, M.; Yaghi, O. M. Topological Analysis of Metal–Organic Frameworks with Polytopic Linkers and/or Multiple Building Units and the Minimal Transitivity Principle. *Chemical Reviews* **2014**, *114* (2), 1343–1370. https://doi.org/10.1021/cr400392k.

(800) Zhang, D.; Zhu, Y.; Liu, L.; Ying, X.; Hsiung, C.-E.; Sougrat, R.; Li, K.; Han, Y. Atomic-Resolution Transmission Electron Microscopy of Electron Beam–Sensitive Crystalline Materials. *Science* **2018**, *359* (6376), 675–679. https://doi.org/10.1126/science.aao0865.

(801) Liu, K.; Qi, H.; Dong, R.; Shivhare, R.; Addicoat, M.; Zhang, T.; Sahabudeen, H.; Heine, T.; Mannsfeld, S.; Kaiser, U.; Zheng, Z.; Feng, X. On-Water Surface Synthesis of Crystalline, Few-Layer Two-Dimensional Polymers Assisted by Surfactant Monolayers. *Nature Chemistry* **2019**, *11* (11), 994–1000. https://doi.org/10.1038/s41557-019-0327-5.

(802) Lebedev, O. I.; Millange, F.; Serre, C.; Van Tendeloo, G.; Férey, G. First Direct Imaging of Giant Pores of the Metal−Organic Framework MIL-101. *Chemistry of Materials* **2005**, *17* (26), 6525–6527. https://doi.org/10.1021/cm051870o.

(803) Wiktor, C.; Meledina, M.; Turner, S.; Lebedev, O. I.; Fischer, R. A. Transmission Electron Microscopy on Metal–Organic Frameworks – a Review. *Journal of Materials Chemistry A* **2017**, *5* (29), 14969–14989. https://doi.org/10.1039/C7TA00194K.

(804) Liu, L.; Chen, Z.; Wang, J.; Zhang, D.; Zhu, Y.; Ling, S.; Huang, K.-W.; Belmabkhout, Y.; Adil, K.; Zhang, Y.; Slater, B.; Eddaoudi, M.; Han, Y. Imaging Defects and Their Evolution in a Metal–Organic Framework at Sub-Unit-Cell Resolution. *Nature Chemistry* **2019**, *11* (7), 622–628. https://doi.org/10.1038/s41557-019-0263-4.

(805) Li, Y.; Wang, K.; Zhou, W.; Li, Y.; Vila, R.; Huang, W.; Wang, H.; Chen, G.; Wu, G.-H.; Tsao, Y.; Wang, H.; Sinclair, R.; Chiu, W.; Cui, Y. Cryo-EM Structures of Atomic Surfaces and Host-Guest Chemistry in Metal-Organic Frameworks. *Matter* **2019**, *1* (2), 428–438. https://doi.org/10.1016/j.matt.2019.06.001.

(806) Mayoral, A.; Mahugo, R.; Sánchez-Sánchez, M.; Díaz, I. C_s-Corrected STEM Imaging of Both Pure and Silver-Supported Metal-Organic Framework MIL-100(Fe). *ChemCatChem* **2017**, *9* (18), 3497–3502. https://doi.org/10.1002/cctc.201700519.

(807) Shen, B.; Chen, X.; Shen, K.; Xiong, H.; Wei, F. Imaging the Node-Linker Coordination in the Bulk and Local Structures of Metal-Organic Frameworks. *Nature Communications* **2020**, *11* (1), 2692. https://doi.org/10.1038/s41467-020-16531-y.

(808) Zhou, Y.; Xu, X.; Carlsson, A.; Lazar, S.; Pan, Z.; Ma, Y.; Terasaki, O.; Deng, H. Local Structure Evolvement in MOF Single Crystals Unveiled by Scanning Transmission Electron Microscopy. *Chemistry of Materials* **2020**, *32* (12), 4966–4972. https://doi.org/10.1021/acs.chemmater.9b04665.

(809) Cao, Y.; Fatemi, V.; Fang, S.; Watanabe, K.; Taniguchi, T.; Kaxiras, E.; Jarillo-Herrero, P. Unconventional Superconductivity in Magic-Angle Graphene Superlattices. *Nature* **2018**, *556* (7699), 43–50. https://doi.org/10.1038/nature26160.

(810) Brunauer, S.; Emmett, P. H.; Teller, E. Adsorption of Gases in Multimolecular Layers. *Journal of the American Chemical Society* **1938**, *60* (2), 309–319. https://doi.org/10.1021/ja01269a023.

(811) Rouquerol, J.; Llewellyn, P.; Rouquerol, F. Is the Bet Equation Applicable to Microporous Adsorbents? In *Studies in Surface Science and Catalysis*; Elsevier, 2007; Vol. 160, pp 49–56. https://doi.org/10.1016/S0167-2991(07)80008-5.

(812) Wang, J.; Toby, B. H.; Lee, P. L.; Ribaud, L.; Antao, S. M.; Kurtz, C.; Ramanathan, M.; Von Dreele, R. B.; Beno, M. A. A Dedicated Powder Diffraction Beamline at the Advanced Photon Source: Commissioning and Early Operational Results. *Review of Scientific Instruments* **2008**, *79* (8), 085105. https://doi.org/10.1063/1.2969260.

(813) Lee, P. L.; Shu, D.; Ramanathan, M.; Preissner, C.; Wang, J.; Beno, M. A.; Von Dreele, R. B.; Ribaud, L.; Kurtz, C.; Antao, S. M.; Jiao, X.; Toby, B. H. A Twelve-Analyzer Detector System for High-Resolution Powder Diffraction. *J Synchrotron Rad* **2008**, *15* (5), 427–432. https://doi.org/10.1107/S0909049508018438.

(814) Shu, D.; Maser, J.; Holt, M.; Winarski, R.; Preissner, C.; Lai, B.; Vogt, S.; Stephenson, G. B. A Robot-Based Detector Manipulator System for a Hard X-Ray Nanoprobe Instrument. *Nuclear Instruments and Methods in Physics Research Section A: Accelerators, Spectrometers, Detectors and Associated Equipment* **2007**, *582* (1), 159–161. https://doi.org/10.1016/j.nima.2007.08.097.

(815) Dalesio, L. R.; Hill, J. O.; Kraimer, M.; Lewis, S.; Murray, D.; Hunt, S.; Watson, W.; Clausen, M.; Dalesio, J. The Experimental Physics and Industrial Control System Architecture: Past, Present, and Future. *Nuclear Instruments and Methods in Physics Research Section A: Accelerators, Spectrometers, Detectors and Associated Equipment* **1994**, *352* (1–2), 179–184. https://doi.org/10.1016/0168-9002(94)91493-1.

(816) Werner, P. E.; Eriksson, L.; Westdahl, M. TREOR, a Semi-Exhaustive Trial-and-Error Powder Indexing Program for All Symmetries. *Journal of Applied Crystallography* **1985**, *18* (5), 367–370. https://doi.org/10.1107/S0021889885010512.

(817) Petříček, V.; Dušek, M.; Palatinus, L. Crystallographic Computing System JANA2006: General Features. *Zeitschrift für Kristallographie - Crystalline Materials* **2014**, *229* (5), 345–352. https://doi.org/10.1515/zkri-2014-1737.

(818) Sheldrick, G. M. *SHELXT* – Integrated Space-Group and Crystal-Structure Determination. *Acta Crystallographica A* **2015**, *71* (1), 3–8. https://doi.org/10.1107/S2053273314026370.

(819) Sheldrick, G. M. Crystal Structure Refinement with *SHELXL*. *Acta Crstyallographica C* **2015**, *71* (1), 3–8. https://doi.org/10.1107/S2053229614024218.

(820) Wang, Y.; Takki, S.; Cheung, O.; Xu, H.; Wan, W.; Öhrström, L.; Inge, A. K. Elucidation of the Elusive Structure and Formula of the Active Pharmaceutical Ingredient Bismuth Subgallate by Continuous Rotation Electron Diffraction. *Chemical Communications* **2017**, *53* (52), 7018–7021. https://doi.org/10.1039/C7CC03180G.

(821) Smeets, S.; Zou, X.; Wan, W. Serial Electron Crystallography for Structure Determination and Phase Analysis of Nanocrystalline Materials. *Journal of Applied Crystallography* **2018**, *51* (5), 1262–1273. https://doi.org/10.1107/S1600576718009500.

(822) Wan, W.; Sun, J.; Su, J.; Hovmöller, S.; Zou, X. Three-Dimensional Rotation Electron Diffraction: Software *RED* for Automated Data Collection and Data Processing. *Journal of Applied Crystallography* **2013**, *46* (6), 1863–1873. https://doi.org/10.1107/S0021889813027714.

(823) Kabsch, W. *XDS*. *Acta Crstyallographica D* **2010**, *66* (2), 125–132. https://doi.org/10.1107/S0907444909047337.

(824) Kumar, S.; Shankar Rao, D. S.; Krishna Prasad, S. New Branched Chain Tricycloquinazoline Derivatives: A Room Temperature Electron Deficient Discotic System. *Journal of Materials Chemistry* **1999**, *9* (11), 2751–2754. https://doi.org/10.1039/a904405a.

(825) Zhao, Y.; Wang, J.; Pei, R. Micron-Sized Ultrathin Metal–Organic Framework Sheet. *Journal of the American Chemical Society* **2020**, *142* (23), 10331–10336. https://doi.org/10.1021/jacs.0c04442.

(826) Dong, W.-K.; Lan, P.-F.; Zhou, W.-M.; Zhang, Y. Salamo-Type Trinuclear and Tetranuclear Cobalt(II) Complexes Based on a New Asymmetry Salamo-Type Ligand: Syntheses, Crystal Structures, and Fluorescence Properties. *Journal of Coordination Chemistry* **2016**, *69* (7), 1272–1283. https://doi.org/10.1080/00958972.2016.1168520.

(827) Sasmal, A.; Garribba, E.; Ugone, V.; Rizzoli, C.; Mitra, S. Synthesis, Crystal Structures, EPR and DFT Studies of First Row Transition Metal Complexes of Lignin Model Compound Ethylvanillin. *Polyhedron* **2017**, *121*, 107–114. https://doi.org/10.1016/j.poly.2016.09.041.

(828) Brückner, C.; Caulder, D. L.; Raymond, K. N. Preparation and Structural Characterization of Nickel(II) Catecholates. *Inorganic Chemistry* **1998**, *37* (26), 6759–6764. https://doi.org/10.1021/ic980620p.

(829) Zhang, C.; Wang, F.; Patil, R. S.; Barnes, C. L.; Li, T.; Atwood, J. L. Hierarchical Self-Assembly of Supramolecular Coordination Polymers Using Giant Metal-Organic Nanocapsules as Building Blocks. *Chemistry — A European Journal* **2018**, *24* (54), 14335–14340. https://doi.org/10.1002/chem.201803942.

(830) Zhang, C.; Patil, R. S.; Li, T.; Barnes, C. L.; Atwood, J. L. Self-Assembly of Magnesium-Seamed Hexameric Pyrogallol[4]Arene Nanocapsules. *Chemical Communications* **2017**, *53* (31), 4312–4314. https://doi.org/10.1039/C7CC01208J.

(831) Zhang, C.; Patil, R. S.; Li, T.; Barnes, C. L.; Teat, S. J.; Atwood, J. L. Preparation of Magnesium-Seamed *C* -Alkylpyrogallol[4]Arene Nanocapsules with Varying Chain Lengths. *Chemistry — A European Journal* **2017**, *23* (35), 8520–8524. https://doi.org/10.1002/chem.201701765.

(832) Lp, Y.; Yamauchi, J.; Azuma, N. ESR Spectra and Structures of $[Cu(B15C5)(H_2O)_2](ClO_4)_2$ in $[Mg(B_{15}C_5)(H_2O)_2](ClO_4)_2$ Crystal in Frozen 60% $HClO_4$. *Journal of Coordination Chemistry* **1997**, *42* (4), 291–301. https://doi.org/10.1080/00958979708022859.

(833) Costes, J.-P.; Vendier, L.; Wernsdorfer, W. Structural and Magnetic Studies of Original Tetranuclear Co^{II}–Ln^{III} Complexes (Ln^{III} = Gd, Tb, Y). *Dalton Transactions* **2011**, *40* (8), 1700. https://doi.org/10.1039/c0dt01253j.

(834) Kobayashi, F.; Ohtani, R.; Kusumoto, S.; Lindoy, L. F.; Hayami, S.; Nakamura, M. Wheel-Type Heterometallic Ferromagnetic Clusters: $[Ni_{7-x}M_x(HL)_6(\mu^3\text{-}OMe)_4(\mu^3\text{-}OH)_2]Cl_2$ (M = Zn, Co, Mn; x = 1, 3). *Dalton Transactions* **2018**, *47* (46), 16422–16428. https://doi.org/10.1039/C8DT03275K.

(835) Meally, S. T.; Karotsis, G.; Brechin, E. K.; Papaefstathiou, G. S.; Dunne, P. W.; McArdle, P.; Jones, L. F. Planar [Ni7] Discs as Double-Bowl, Pseudometallacalix[6]Arenehost Cavities. *CrystEngComm* **2010**, *12* (1), 59–63. https://doi.org/10.1039/B914538A.

(836) Barrett, E. P.; Joyner, L. G.; Halenda, P. P. The Determination of Pore Volume and Area Distributions in Porous Substances. I. Computations from Nitrogen Isotherms. *Journal of the American Chemical Society* **1951**, *73* (1), 373–380. https://doi.org/10.1021/ja01145a126.

(837) Kruk, M.; Jaroniec, M.; Sayari, A. Application of Large Pore MCM-41 Molecular Sieves to Improve Pore Size Analysis Using Nitrogen Adsorption Measurements. *Langmuir* **1997**, *13* (23), 6267–6273. https://doi.org/10.1021/la970776m.

(838) Hovmöller, S. CRISP: Crystallographic Image Processing on a Personal Computer. *Ultramicroscopy* **1992**, *41* (1–3), 121–135. https://doi.org/10.1016/0304-3991(92)90102-P.

(839) Pangborn, A. B.; Giardello, M. A.; Grubbs, R. H.; Rosen, R. K.; Timmers, F. J. Safe and Convenient Procedure for Solvent Purification. *Organometallics* **1996**, *15* (5), 1518–1520. https://doi.org/10.1021/om9503712.

(840) Wudl, F.; Bryce, M. R. Apparatus for Two-Probe Conductivity Measurements on Compressed Powders. *Journal of Chemical Education* **1990**, *67* (8), 717. https://doi.org/10.1021/ed067p717.

(841) Czepirski, L.; JagieŁŁo, J. Virial-Type Thermal Equation of Gas—Solid Adsorption. *Chemical Engineering Science* **1989**, *44* (4), 797–801. https://doi.org/10.1016/0009-2509(89)85253-4.

(842) Dincă, M.; Dailly, A.; Liu, Y.; Brown, C. M.; Neumann, Dan. A.; Long, J. R. Hydrogen Storage in a Microporous Metal−Organic Framework with Exposed Mn^{2+} Coordination Sites. *Journal of the American Chemical Society* **2006**, *128* (51), 16876–16883. https://doi.org/10.1021/ja0656853.

(843) Sumida, K.; Rogow, D. L.; Mason, J. A.; McDonald, T. M.; Bloch, E. D.; Herm, Z. R.; Bae, T.-H.; Long, J. R. Carbon Dioxide Capture in Metal–Organic Frameworks. *Chemical Reviews* **2012**, *112* (2), 724–781. https://doi.org/10.1021/cr2003272.

(844) Denysenko, D.; Grzywa, M.; Tonigold, M.; Streppel, B.; Krkljus, I.; Hirscher, M.; Mugnaioli, E.; Kolb, U.; Hanss, J.; Volkmer, D. Elucidating Gating Effects for Hydrogen Sorption in MFU-4-Type Triazolate-Based Metal-Organic Frameworks Featuring Different Pore Sizes. *Chemistry — A European Journal* **2011**, *17* (6), 1837–1848. https://doi.org/10.1002/chem.201001872.

(845) Kubelka, P.; Munk, F. Ein Beitrag Zur Optik Der Farbanstriche. *Z. Techn. Phys. 12*, 593–601.

(846) Wang, Y.; Huang, N.-Y.; Shen, J.-Q.; Liao, P.-Q.; Chen, X.-M.; Zhang, J.-P. Hydroxide Ligands Cooperate with Catalytic Centers in Metal–Organic Frameworks for Efficient Photocatalytic CO_2 Reduction. *Journal of the American Chemical Society* **2018**, *140* (1), 38–41. https://doi.org/10.1021/jacs.7b10107.

(847) Coelho, A. *Topas Academic V6*; Coellho Software, 2017.

(848) Stephens, P. W. Phenomenological Model of Anisotropic Peak Broadening in Powder Diffraction. *Journal of Applied Crystallography* **1999**, *32* (2), 281–289. https://doi.org/10.1107/S0021889898006001.

(849) Park, S. S.; Tulchinsky, Y.; Dincă, M. Single-Ion Li^+, Na^+, and Mg^{2+} Solid Electrolytes Supported by a Mesoporous Anionic Cu–Azolate Metal–Organic Framework. *Journal of the American Chemical Society* **2017**, *139* (38), 13260–13263. https://doi.org/10.1021/jacs.7b06197.

(850) Rietveld, H. M. A Profile Refinement Method for Nuclear and Magnetic Structures. *Journal of Applied Crystallography* **1969**, *2* (2), 65–71. https://doi.org/10.1107/S0021889869006558.

(851) Groom, C. R.; Bruno, I. J.; Lightfoot, M. P.; Ward, S. C. The Cambridge Structural Database. *Acta Crstyallographica B* **2016**, *72* (2), 171–179. https://doi.org/10.1107/S2052520616003954.

(852) Nuhnen, A.; Janiak, C. A Practical Guide to Calculate the Isosteric Heat/Enthalpy of Adsorption via Adsorption Isotherms in Metal–Organic Frameworks, MOFs. *Dalton Transactions* **2020**, *49* (30), 10295–10307.

(853) Miller, S. R.; Pearce, G. M.; Wright, P. A.; Bonino, F.; Chavan, S.; Bordiga, S.; Margiolaki, I.; Guillou, N.; Férey, G.; Bourrelly, S.; others. Structural Transformations and Adsorption of Fuel-Related Gases of a Structurally Responsive Nickel Phosphonate Metal- Organic Framework, Ni-STA-12. *Journal of the American Chemical Society* **2008**, *130* (47), 15967–15981.

(854) Saha, D.; Deng, S. Adsorption Equilibria and Kinetics of Carbon Monoxide on Zeolite 5A, 13X, MOF-5, and MOF-177. *Journal of Chemical & Engineering Data* **2009**, *54* (8), 2245–2250.

(855) Peng, J.; Xian, S.; Xiao, J.; Huang, Y.; Xia, Q.; Wang, H.; Li, Z. A Supported Cu (I)@ MIL-100 (Fe) Adsorbent with High CO Adsorption Capacity and CO/N_2 Selectivity. *Chemical Engineering Journal* **2015**, *270*, 282–289.

(856) Deng, S.; Lin, Y. Sol-Gel Preparation and Properties of Alumina Adsorbents for Gas Separation. *AIChE Journal* **1995**, *41* (3), 559–570.

(857) Valenzano, L.; Civalleri, B.; Chavan, S.; Palomino, G. T.; Areán, C. O.; Bordiga, S. Computational and Experimental Studies on the Adsorption of CO, N2, and CO2 on Mg-MOF-74. *The Journal of Physical Chemistry C* **2010**, *114* (25), 11185–11191.

(858) Chang, G.; Huang, M.; Su, Y.; Xing, H.; Su, B.; Zhang, Z.; Yang, Q.; Yang, Y.; Ren, Q.; Bao, Z.; others. Immobilization of Ag(I) into a Metal–Organic Framework with–SO 3 H Sites for Highly Selective Olefin–Paraffin Separation at Room Temperature. *Chemical Communications* **2015**, *51* (14), 2859–2862.

(859) Li, B.; Zhang, Y.; Ma, D.; Wu, Z.; Ma, S. Ag (I) Ion Functionalized Porous Organic Polymers as a New Platform for Highly Selective Adsorption of Ethylene over Ethane. *Journal of the American Chemical Society* **2014**, *136* (24).

(860) Zhang, Y.; Li, B.; Krishna, R.; Wu, Z.; Ma, D.; Shi, Z.; Pham, T.; Forrest, K.; Space, B.; Ma, S. Highly Selective Adsorption of Ethylene over Ethane in a MOF Featuring the Combination of Open Metal Site and π-Complexation. *Chemical communications* **2015**, *51* (13), 2714–2717.

(861) Wang, Y.; Hu, Z.; Cheng, Y.; Zhao, D. Silver-Decorated Hafnium Metal–Organic Framework for Ethylene/Ethane Separation. *Industrial & Engineering Chemistry Research* **2017**, *56* (15), 4508–4516.

(862) Liao, Y.; Zhang, L.; Weston, M. H.; Morris, W.; Hupp, J. T.; Farha, O. K. Tuning Ethylene Gas Adsorption via Metal Node Modulation: Cu-MOF-74 for a High Ethylene Deliverable Capacity. *Chemical Communications* **2017**, *53* (67), 9376–9379.

(863) Bao, Z.; Alnemrat, S.; Yu, L.; Vasiliev, I.; Ren, Q.; Lu, X.; Deng, S. Adsorption of Ethane, Ethylene, Propane, and Propylene on a Magnesium-Based Metal–Organic Framework. *Langmuir* **2011**, *27* (22), 13554–13562.

(864) Chang, G.; Bao, Z.; Ren, Q.; Deng, S.; Zhang, Z.; Su, B.; Xing, H.; Yang, Y. Fabrication of Cuprous Nanoparticles in MIL-101: An Efficient Adsorbent for the Separation of Olefin–Paraffin Mixtures. *RSC advances* **2014**, *4* (39), 20230–20233.

(865) Chen, Y.; Wu, H.; Lv, D.; Shi, R.; Chen, Y.; Xia, Q.; Li, Z. Highly Adsorptive Separation of Ethane/Ethylene by an Ethane-Selective MOF MIL-142A. *Industrial & Engineering Chemistry Research* **2018**, *57* (11), 4063–4069.

(866) Chen, Y.; Qiao, Z.; Wu, H.; Lv, D.; Shi, R.; Xia, Q.; Zhou, J.; Li, Z. An Ethane-Trapping MOF PCN-250 for Highly Selective Adsorption of Ethane over Ethylene. *Chemical Engineering Science* **2018**, *175*, 110–117.

(867) Skopp, J. Derivation of the Freundlich Adsorption Isotherm from Kinetics. *Journal of Chemical Education* **2009**, *86* (11), 1341.

(868) Sreńscek-Nazzal, J.; Narkiewicz, U.; Morawski, A. W.; Wróbel, R. J.; Michalkiewicz, B. Comparison of Optimized Isotherm Models and Error Functions for Carbon Dioxide Adsorption on Activated Carbon. *Journal of Chemical & Engineering Data* **2015**, *60* (11), 3148–3158.

(869) Ochoa, B.; Belongie, S. Covariance Propagation for Guided Matching. In *Proceedings of the Workshop on Statistical Methods in Multi-Image and Video Processing (SMVP)*; 2006; Vol. 83.